

Studies in Computational Intelligence 531

Teresa Orłowska-Kowalska
Frede Blaabjerg
José Rodríguez *Editors*

Advanced and Intelligent Control in Power Electronics and Drives

 Springer

Studies in Computational Intelligence

Volume 531

Series editor

Janusz Kacprzyk, Polish Academy of Sciences, Warsaw, Poland
e-mail: kacprzyk@ibspan.waw.pl

For further volumes:
<http://www.springer.com/series/7092>

About this Series

The series “Studies in Computational Intelligence” (SCI) publishes new developments and advances in the various areas of computational intelligence—quickly and with a high quality. The intent is to cover the theory, applications, and design methods of computational intelligence, as embedded in the fields of engineering, computer science, physics and life sciences, as well as the methodologies behind them. The series contains monographs, lecture notes and edited volumes in computational intelligence spanning the areas of neural networks, connectionist systems, genetic algorithms, evolutionary computation, artificial intelligence, cellular automata, self-organizing systems, soft computing, fuzzy systems, and hybrid intelligent systems. Of particular value to both the contributors and the readership are the short publication timeframe and the world-wide distribution, which enable both wide and rapid dissemination of research output.

Teresa Orłowska-Kowalska
Frede Blaabjerg · José Rodríguez
Editors

Advanced and Intelligent Control in Power Electronics and Drives

 Springer

Editors

Teresa Orłowska-Kowalska
Institute of Electrical Machines, Drives
and Measurements
Wrocław University of Technology
Wrocław
Poland

José Rodríguez
Department of Electronics Engineering
Universidad Técnica Federico Santa María
Valparaíso
Chile

Frede Blaabjerg
Department of Energy Technology Power
Electronic Systems
Aalborg University
Aalborg East
Denmark

ISSN 1860-949X

ISBN 978-3-319-03400-3

DOI 10.1007/978-3-319-03401-0

Springer Cham Heidelberg New York Dordrecht London

ISSN 1860-9503 (electronic)

ISBN 978-3-319-03401-0 (eBook)

Library of Congress Control Number: 2013957126

© Springer International Publishing Switzerland 2014

This work is subject to copyright. All rights are reserved by the Publisher, whether the whole or part of the material is concerned, specifically the rights of translation, reprinting, reuse of illustrations, recitation, broadcasting, reproduction on microfilms or in any other physical way, and transmission or information storage and retrieval, electronic adaptation, computer software, or by similar or dissimilar methodology now known or hereafter developed. Exempted from this legal reservation are brief excerpts in connection with reviews or scholarly analysis or material supplied specifically for the purpose of being entered and executed on a computer system, for exclusive use by the purchaser of the work. Duplication of this publication or parts thereof is permitted only under the provisions of the Copyright Law of the Publisher's location, in its current version, and permission for use must always be obtained from Springer. Permissions for use may be obtained through RightsLink at the Copyright Clearance Center. Violations are liable to prosecution under the respective Copyright Law. The use of general descriptive names, registered names, trademarks, service marks, etc. in this publication does not imply, even in the absence of a specific statement, that such names are exempt from the relevant protective laws and regulations and therefore free for general use.

While the advice and information in this book are believed to be true and accurate at the date of publication, neither the authors nor the editors nor the publisher can accept any legal responsibility for any errors or omissions that may be made. The publisher makes no warranty, express or implied, with respect to the material contained herein.

Printed on acid-free paper

Springer is part of Springer Science+Business Media (www.springer.com)

Foreword

It is my great honor and pleasure to write the foreword for this state-of-the-art book “Advanced and Intelligent Control in Power Electronics and Drives.” The control of power electronics and drives is a complex and multidisciplinary field. As it is not sufficient to describe power electronics as well as electrical drives by simple and linear transfer functions, a detailed knowledge of these systems is necessary to control them properly.

The 11 chapters of the book are divided into three parts: *Advanced Power Electronic Control in Renewable Energy Sources* (Chaps. 1–4), *Predictive Control of Power Converters and Drives* (Chaps. 5–7), and *Neuro and Nonlinear Control of Power Converters and Drives* (Chaps. 8–11). The first two chapters are co-authored by world-renowned expert in so-called renewable energy applications Prof. Frede Blaabjerg. The introduction to this field of energy conversion is followed by a report on modern control strategies for wind power and photovoltaic applications. Chapters dealing with the control of grid side converters and on fault diagnosis in the respective converters are a reasonable completion of this part. The Part II of the book begins with chapters providing a highly interesting overview of predictive control strategies, which is co-authored by young emerging specialist Dr. Tobias Geyer. The next chapter deals with a couple of very interesting applications for predictive control algorithms; this chapter is co-authored by world-known specialist Prof. José Rodríguez and Prof. Haitham Abu-Rub. The last chapter of this part is co-authored by Teresa Orłowska-Kowalska, who is also known worldwide for being an expert in the area of predictive control. Here the application of predictive control to a mechanical system is presented. The Part III of the book is dedicated to research activities of several Institutes in Poland dealing with neuro and nonlinear control strategies. After introducing chapter co-authored by Teresa Orłowska-Kowalska, which explains the fundamental concepts and ideas behind this class of nonlinear control, this part contains chapters on control strategies of Voltage Source Inverters (VSI) and Multilevel Inverters. These types of power electronic converters are widely used and highly interesting for industry today. The final chapter discusses and presents discontinuous control methods for induction motor drives, which is a rather special topic, but nevertheless a valuable completion of this part.

The work gives a highly valuable overview on modern nonlinear control strategies for power electronics and AC drives. It discusses several aspects of the

authors' current research containing innovative and original concepts. A good description style as well as good illustrations make the book easy to read and attractive for researchers, engineering professionals, and graduate students of Electrical Engineering and Power Electronics.

I would like to express my appreciation for the initiative taken by the editors in this timely book to cover a rather new, but in the long term very essential area of power electronics control. The Editors obviously succeeded in publishing an impressive collection of reports belonging to the edge of research. This work is directing to a field getting more and more importance and providing better understanding of “Advanced and Intelligent Control in Power Electronics and Drives”—hopefully it will contribute to the creation of even more new solutions with high further research and application potential.

Germany

Ralph Kennel
Technische Universität München

Preface I

Power electronics and variable frequency drives are continuously developing multidisciplinary fields in electrical engineering, and it is practically not possible to write a book covering the entire area by one individual specialist. Especially, as recently we observe fast-development in neighboring fields like control theory, computational intelligence, and signal processing, which all strongly influence new solutions in control of power electronics and drives. Therefore, the book is written by key specialists working in the area of modern advanced control methods that penetrate current implementation of power converters and drives. Although some of the presented methods are still not adopted by the industry, they create new solutions with high further research and application potential.

The material of the book is presented in the following three parts:

Part I: Advanced Power Electronic Control in Renewable Energy Sources (Chaps. 1–4),

Part II: Predictive Control of Power Converters and Drives (Chaps. 5–7),

Part III: Neurocontrol and Nonlinear Control of Power Converters and Drives (Chaps. 8–11).

In [Chap. 1](#) the state-of-the-arts of renewable energy are reviewed in respect to the installed power and market share, where wind power and photovoltaic power generation are the focus due to the fast growing speed and large share of installed capacity. Some basic principles of operation, mission profiles, as well as power electronics solutions and corresponding controls are discussed, respectively, in the case of wind power and photovoltaic power systems. Finally, a few development trends for renewable energy conversion systems are also given from a power electronics point of view. It is concluded that as the quick development of renewable energy, wind power and PV power both show great potential to be largely integrated into the power grid. Power electronics is playing an essential role in both systems to achieve more controllable, efficient, and reliable energy production—which is crucial for the cost reduction and spread use of renewable energies, because their fluctuated and unpredicted features are un-preferred for the operation of the power grid. Meanwhile, there are also some other emerging challenges and considerations in the renewable energy conversion systems, calling for more advanced controls as well as configurations of power electronics converters.

Chapter 2 presents advanced control of photovoltaic and wind turbine power systems, which can enable power conversion efficiently and reliably. For both PV and wind turbine power systems, advanced controls are addressed in order to enhance the integration of those technologies. Related grid demands have been presented first, where much more attention has been paid on specific requirements, like Low Voltage Ride-Through (LVRT) and reactive power injection capability. To perform the functions of such systems, advanced control strategies are presented with much more emphasis on the LVRT operation with reactive power injection for both single-phase and three-phase systems. Other advanced control strategies like constant power generation control for PV systems to further increase the penetration level, and the improvements in LVRT performance for a doubly fed induction generator-based wind turbine system by means of hardware protection solutions are also discussed in this chapter.

In **Chap. 3** operation of a reliable control method of a Grid Connected Converter (GCC) under grid voltage disturbances is presented. As GCC authors understand, power electronic AC-DC converter with AC side filter and DC-link capacitor operate as an interface between the electrical grid and Active Loads (AL). The chosen modeling approach of a GCC is discussed and the example of passive components calculation is provided. Next, a brief review of a basic GCC control method is described. A new reliable (robust to selected grid voltage disturbances such as dips, higher harmonics) control method is proposed—Robust Direct Power Control with Space Vector Modulation (RDPC-SVM). This new control method can assure sinusoidal like and balanced AC current in extremely distorted grid voltage. Moreover, the quality of current and power is considerably improved in comparison to classical methods. Hence, the negative impact of the GCC on the grid voltage is significantly reduced, i.e., lower Total Harmonics Distortion (THD) factor of the grid current, more accurate control of active and reactive power flow assure good quality of integration with the grid even, in case of increased impedance within operation limits.

At the end of Part I, **Chap. 4** discusses the faults and diagnosis systems in power converters used in renewable energy systems and drive systems. Increasing efforts have been put to improve these systems in terms of reliability in order to achieve high power, source availability, reduce the cost of energy, and also increase the reliability of overall systems. The chapter describes failures in power converters, like a power device and a capacitor faults, as well as their detection in order to do fault handling and still be able to run a power electronic system, increasing the reliability of power electronics. In this chapter, the diagnosis methods for power device faults are discussed by dividing them into open- and short-circuit faults. Then, the condition monitoring methods of DC-link electrolytic capacitor are also introduced. The chapter is supported with a number of examples including the three-level NPC converter.

Part II of this book is focused on predictive control methods applied in power electronics and drive systems.

Chapter 5 introduces the reader to basic principles and methods of model predictive control with a view toward applications in power electronics and drives.

The simplest predictive control formulations use horizon-one cost functions, which can be related to well-established dead-beat controllers. Model predictive control using larger horizons has the potential to give significant performance benefits, but requires more computations at each sampling instant to solve the associated optimization problems. For particular classes of system models, practical algorithms are discussed, which make long-horizon predictive control suitable for power electronics.

Chapter 6 presents a general application of predictive control in power electronics. The analyzed application is an energy conversion system from alternate current to direct current and to alternate current again. This example has been carefully selected because a number of predictive control principles can be clearly explained using this topology and later expanded to a wide variety of converter topologies. The chapter includes mathematical models and a clear presentation of the advanced control strategies. The results show that the use of predictive control introduces a conceptually different solution which allows for the control of electrical energy without using pulse-width modulation and linear controllers.

In **Chap. 7** a long-horizon Model Predictive Control strategy for speed regulation of a drive system with an elastic transmission is applied. Torsional vibrations caused by elastic connection of the driven motor and loading machine are evident in many industrial drive systems: starting from traditional rolling-mill drives, conveyer belt drives, machines for paper and textile industry, deep space antenna drives, the windmill generators, modern servo drives, and robotic applications. The flexible modes affect the performances of the drive, and in some situations can even lead to the failure of the entire drive system. The mathematical model and short characteristic of the control problems of such drive system are given in the chapter. Next, the advanced methodology for robust control strategy design is presented, based on suitable selection of the explicit form of MPC, which enables the drive's safety and physical limitations to be directly incorporated into control algorithm synthesis. The simulation and experimental results show that the long-horizon MPC is very effective in torsional vibration damping and controlling the load speed of the drive system with elastic coupling for a wide-range of the changes of the load side inertia, ensuring a suitable dynamics and constraints fulfillment.

Part III of this book consists of four chapters which concern the application of artificial intelligence and nonlinear control methods for power converters and drive systems.

In **Chap. 8** basic principles of neurocontrol are revised and discussed from the point of view of application in converter-fed drive systems. The neural network structures used as neural controllers are classified into two groups: off-line and on-line trained controllers. From the point of view of drive system uncertainties, caused by simplifying assumptions under mathematical model formulation, errors in drive parameters identification, and changes in the models and their parameters under different operation conditions, on-line adaptive neural controllers are recommended for practical applications. Different neural structures and their on-line training methods are discussed. The chosen neurocontrollers are verified in

simulation and experimental tests for converter-fed drives with rigid and resilient mechanical connections between the driving motor and loading machine.

Chapter 9 presents the application of a particle swarm optimization (PSO) to a controller tuning in selected power electronic and drive systems. An example of PSO used for optimization of selected learning parameters in the adaptive neural network-based online trained speed controller for urban vehicle (3D problem) is presented. Next, this algorithm is applied to selecting penalty factors in the LQR with augmented state for a three-phase four-leg sine wave inverter (15D problem). It is demonstrated for these case studies why and where the PSO, or any other similar population-based stochastic search algorithm can be beneficial. This chapter illustrates that in some cases it is relatively easy to reduce the non-straightforward controller tuning tasks into the objective function selection problem and automatically determine the relevant controller parameters by the PSO.

Chapter 10 is devoted to the Space Vector Modulation (SVM) in three-phase three-level flying capacitor converter-fed adjustable speed drive. First the classical and adaptive SVM, which minimizes number of switching and thus reduces the switching losses in FCC are described. Next, elimination of DC sources unbalance in full range of operation of the Voltage Source Converters and minimization of the flying capacitor voltage pulsation is presented. Taking into account the requirements of the demanding drive application, like low speed operation without phase current distortion and high speed operation over the linear range of the converter with reference output voltage amplitude, the additional features for both modulation techniques: the dead-time effect and semiconductor devices voltage drop compensation as well as the overmodulation algorithm are shown.

In the last **Chap. 11** several applications of nonlinear control methods for induction motor drive are described, such as feedback linearization (FLC) and sliding mode control (SMC). The FLC guarantees the exact decoupling of the motor speed and rotor flux control. Thus this control method gives a possibility to get very good behavior in both dynamic and steady states. The SMC approach assures direct control of inverter legs and allows using a simple table instead of performing complicated PWM calculation. Moreover, the SMC is robust to drive uncertainties. Thus the SMC and FLC, both together and separately, offer an interesting perspective in the converter-fed drive applications, and these approaches are also a good alternative to other solutions, such as predictive and adaptive systems, and soft computing-based methods.

The book has strong monograph attributes and is intended for engineers, researchers, and students in the field of power electronics and drives who are interested in the use of advanced control methods and also for specialists from the control theory area who like to explore new areas of applications. Some parts of the content can be considered as part of graduate and undergraduate studies in electrical engineering, robotics, and mechatronics faculties.

We would like to express our sincere thanks to the chapter contributors for their enthusiastic response, cooperation, and timeliness. Special thanks is directed to Prof. Janusz Kacprzyk, the Editor of Springer Book Series “Studies in Computational Intelligence” for his interest and motivation to write this book. Thanks

also to Dr. Thomas Ditzinger and Dr. Leontina Di Cecco, both from Springer Applied Sciences and Engineering, for support during implementation of this project. Finally, we are very thankful to our families for their cooperation.

Wrocław, Poland
Aalborg East, Denmark
Valparaíso, Chile

Teresa Orłowska-Kowalska
Frede Blaabjerg
José Rodríguez

Preface II



It is our great honor and pleasure to dedicate this book to Prof. Marian P. Kaźmierkowski on the occasion of his 70th anniversary. He is one of the most prominent and world-recognized researchers in the area of industrial electronics, power electronics, and electrical drives. His professional and scientific career has been associated with the Institute of Control and Industrial Electronics of the Warsaw University of Technology. There, having completed his Ph.D. studies (1969–1972), he continued research as assistant professor (since 1973), associated professor (since 1988), and next full professor (since 1995). In 1987–1990 and in 1996–2008 he was

Director of the Institute of Control and Industrial Electronics and now he still holds the position of full professor there. He has also cooperated with the Electrotechnical Institute in Warsaw-Miedzylesie, as a researcher in 1967–1969, and since 1996—as professor-consultant and member of the Scientific Board.

In the years 1980–1982 he was granted the Humboldt Foundation scholarship at the RTWH Aachen (Germany) and later completed there a 2-year DFG scientific research project. Later, he was often invited as visiting professor to various universities: NTH Trondheim (Norway), University of Minnesota, Minneapolis (USA), University of Padova (Italy), University of Aalborg (Denmark), University of Bologna (Italy), ENSEEIHT/LEEI Toulouse (France), University of Sevilla, LSE/ENIT Tunis, Texas A&M University at Qatar, Doha.

The main areas of his interest include problems of vector control of the converter-fed induction motor and permanent magnet synchronous motor drives, including real-time sensorless control, new topologies of multilevel converters, modulation techniques focused on current control, active rectifiers with unity power factor, artificial intelligence and predictive control applications in power electronics, advanced control methods of power electronics devices for renewable energy systems, and recently also contactless energy transfer systems. To all these topics Prof. Kaźmierkowski has contributed with important publications (more than 400 papers in peer review journals and conference proceedings) and 11 books. Among the most popular books are: *Automatic Control of Converter fed Drives*,

ELSEVIER-PWN, 1994, and *Control in Power Electronics*, Academic Press, USA, 2002.

Professor Kaźmierkowski has been active in cooperation with the industry (*ABB Research Centre*, Krakow; *APATOR*, Torun; *Huettinger Electronics*, Warsaw; *TWERD*, Torun) and has been granted 16 patents. He has also conducted many research projects, international (5): Maria Skłodowska-Curie Found II, NSF-PAN Phare-SCI-TECH II; the V and VI European Union Framework, and national (15) founded by: the Committee of Scientific Research (KBN), Ministry of Science and Higher Education, Foundation of Polish Science, National Centre for Research and Development.

The activities of Prof. Kaźmierkowski in research and education have been appreciated by the highest scientific committees in Poland. He was elected a Member of the T-10 Council for Research Projects Evaluation in Electrical Energy and Measurements, the Ministry of Science and Technology (KBN), Warsaw, (1996–2004). In 1993 he became a member of the Electrical Engineering Committee of the Polish Academy of Sciences, and in 1999–2011 he was the chairman of the Power Electronics and Electrical Drives Section of this Committee. In 2007 he was elected a *corresponding member* of the Polish Academy of Sciences and since 2011 he has been the Dean of the *Division IV Engineering Sciences* of this Academy.

In his international activities he served as Vice-President for Publications of the *IEEE Industrial Electronics Society* 1999–2001 Editor-in-Chief (2004–2006) and the Past Editor-in-Chief (2006–2009) of the *IEEE Transactions on Industrial Electronics*. Currently, he is member of the editorial boards of international journals: *IEEE Transactions on Industrial Electronics*, *IEEE Transactions on Industrial Informatics*, *IEEE Industrial Electronics Magazine*, *Bulletin of the Polish Academy of Science, Technical Science* (Warsaw, Poland), *Journal of Power Electronics* (JPE—Seoul, Korea), *Acta Electrotechnica et Informatica* (Technical University of Košice, Slovak Republic). Since 1996 he is an active member of *Power Electronics and Motion Control Council (EPE-PEMC)* organizing series of PEMC conferences in East and Middle Europe.

For outstanding papers in international journals and activity in the IEEE Prof. Kaźmierkowski has received a number of international awards and distinctions, just to mention: *IEE F.C. Williams Premium*—for the best paper 1989 (UK); *Best Paper Award* at the Conf. IEEE-IECON'2000 in Nagoya (Japan); 2013 *Best Paper Award* in the IEEE Industrial Electronics Magazine (USA); *Dr. Eugene Mittelmann Achievements Award*—IEEE Industrial Electronics Society 2005; IEEE Industrial Electronics Society *Anthony J. Hornfeck Service Award*, 2007. Also, in Poland he was honored with prestigious awards, including *Research Award of Siemens* (2007) and the *Technical Science Subsidies* by the Polish Science Foundation (FNP) in 2001–2004. In 1998, he received the *Fellow Member Grade* of the IEEE, USA; in 2001 he was elected the member of the *International Academy of Electrotechnical Sciences—Moscow, Russia*, and in 2010—Honorary Member of *Hungarian Academy of Science*. He has been granted honorary doctorates of European universities, like: University of Aalborg, Denmark (2004),

Institute National Polytechnique Toulouse (INPT), France (2010), and the University of Zielona Gora, Poland (2012).

Professor Kaźmierkowski is undoubtedly one of the greatest scientists specializing in power electronics and electrical drives. He is an outstanding lecturer, warmly remembered by many generations of students and conference participants. On his 70th birthday, we wish him all the best—many happy years to come, with continuous scientific success and satisfaction of his and his students' achievements in the field of power electronics and electrical drives.

Wrocław, Poland
Aalborg East, Denmark
Valparaíso, Chile

Teresa Orłowska-Kowalska
Frede Blaabjerg
José Rodríguez

Contents

Part I Advanced Power Electronic Control in Renewable Energy Sources

1 Introduction to Renewable Energy Systems	3
Ke Ma, Yongheng Yang and Frede Blaabjerg	
2 Advanced Control of Photovoltaic and Wind Turbines Power Systems	41
Yongheng Yang, Wenjie Chen and Frede Blaabjerg	
3 Control of Grid Connected Converter (GCC) Under Grid Voltage Disturbances	91
Marek Jasiński, Grzegorz Wrona and Szymon Piasecki	
4 Faults and Diagnosis Systems in Power Converters	143
Kyo-Beum Lee and Ui-Min Choi	

Part II Predictive Control of Power Converters and Drives

5 Predictive Control in Power Electronics and Drives: Basic Concepts, Theory, and Methods	181
Daniel E. Quevedo, Ricardo P. Aguilera and Tobias Geyer	
6 Application of Predictive Control in Power Electronics: An AC-DC-AC Converter System	227
José Rodríguez, Haitham Abu-Rub, Marcelo A. Perez and Samir Kouro	
7 Application of the Long-Horizon Predictive Control to the Drive System with Elastic Joint	249
Krzysztof Szabat, Piotr Serkies and Teresa Orłowska-Kowalska	

Part III Neuro and Nonlinear Control of Power Converters and Drives

8 Adaptive Neurocontrollers for Drive Systems: Basic Concepts, Theory and Applications. 269
Teresa Orłowska-Kowalska and Marcin Kamiński

9 Advanced Control and Optimization Techniques in AC Drives and DC/AC Sine Wave Voltage Inverters: Selected Problems. . . . 303
Bartłomiej Ufnalski, Lech M. Grzesiak and Arkadiusz Kaszewski

10 Space Vector Modulation in Three-Phase Three-Level Flying Capacitor Converter-Fed Adjustable Speed Drive 335
Sebastian Styński and Mariusz Malinowski

11 Some Aspects of Nonlinear and Discontinuous Control with Induction Motor Applications 375
Dariusz L. Sobczuk

About the Editors 409

Contributors

Haitham Abu-Rub Texas A&M in Qatar, Doha, Qatar

Ricardo P. Aguilera Technical University Federico Santa Maria, Valpariso, Chile

Frede Blaabjerg University of Aalborg, Aalborg East, Denmark

Wenjie Chen Zhejiang University, Hangzhou, China

Ui-Min Choi University of Aalborg, Aalborg East, Denmark

Tobias Geyer ABB, Corporate Research, Dattwil, Switzerland

Lech M. Grzesiak Warsaw University of Technology, Warsaw, Poland

Marek Jasiński Warsaw University of Technology, Warsaw, Poland

Marcin Kamiński Wrocław University of Technology, Wrocław, Poland

Arkadiusz Kaszewski Warsaw University of Technology, Wrocław, Poland

Samir Kouro Technical University Federico Santa Maria, Valpariso, Chile

Kyo-Beum Lee Ajou University, Suwon, Korea

Ke Ma University of Aalborg, Aalborg East, Denmark

Mariusz Malinowski Warsaw University of Technology, Warsaw, Poland

Teresa Orłowska-Kowalska Wrocław University of Technology, Wrocław, Poland

Szymon Piasecki Warsaw University of Technology, Warsaw, Poland

Marcelo A. Pérez Technical University Federico Santa Maria, Valpariso, Chile

Daniel E. Quevedo Technical University Federico Santa Maria, Valpariso, Chile

José Rodríguez Technical University Federico Santa Maria, Valpariso, Chile

Piotr Serkies Wrocław University of Technology, Wrocław, Poland

Dariusz L. Sobczuk Warsaw University of Technology, Warsaw, Poland

Sebastian Styński Warsaw University of Technology, Warsaw, Poland
Krzysztof Szabat Warsaw University of Technology, Wrocław, Poland
Barłomiej Ufnalski Warsaw University of Technology, Warsaw, Poland
Grzegorz Wrona Warsaw University of Technology, Warsaw, Poland
Yongheng Yang University of Aalborg, Aalborg East, Denmark

Part I
Advanced Power Electronic Control in
Renewable Energy Sources

Chapter 1

Introduction to Renewable Energy Systems

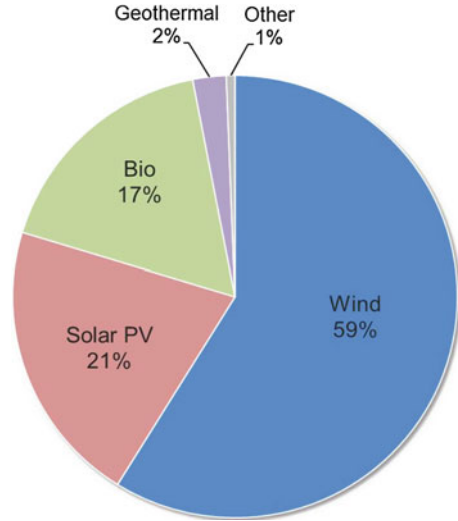
Ke Ma, Yongheng Yang and Frede Blaabjerg

Abstract In this chapter, the state-of-the-arts developments of renewable energy are reviewed in respect to the installed power and market share, where wind power and photovoltaic power generation are the main focuses due to the fast growing speed and large share of installed capacity. Some basic principles of operation, mission profiles, as well as power electronics solutions and corresponding controls are discussed respectively in the case of wind power and photovoltaic power systems. Finally a few development trends for renewable energy conversions are also given from a power electronics point of view. It is concluded that as the quick development of renewable energy, wind power and PV power both show great potential to be largely integrated into the power grid. Power electronics is playing essential role in both of the systems to achieve more controllable, efficient, and reliable energy production—which is crucial for the cost reduction and spread use of renewable energies, because their fluctuated and unpredicted features are un-preferred for the operation of the power grid. Meanwhile there are also some emerging challenges and considerations in the renewable energy conversion system, calling for more advanced controls as well as configurations of power electronics converter.

Due to the shortage of inexhaustible resources and environmental problems caused by the emissions, the traditional power generations which are based on fossil fuel are generally considered to be unsustainable in the long term. As a result, many efforts are made worldwide and lots of countries have being introducing more renewable energies such as wind power, solar photovoltaic (PV) power, hydro-power, biomass power, and ocean power, etc. into their electric grids [1–3]. The installed capacity of the renewable energy is growing so fast in the last decade—by

K. Ma (✉) · Y. Yang · F. Blaabjerg
Aalborg University, Aalborg, Denmark
e-mail: kema@et.aau.dk

Fig. 1 Accumulated capacity share of different renewables by 2012 (480 GW total installed capacity without hydro-power) [3]



2012 the worldwide non-hydro power generation based on renewables has exceeded 480 Giga Watts (GW), which supplies 5.2 % of the global electricity consumption and accounts for almost half of the newly established generation capacity [3].

Among various renewable energy sources, the hydro power had a large installation in the past and nowadays accounts for the largest share of 67 % in renewables capacity. However, due to the special requirements for locations with river/lake resources, the worldwide growth of hydro power nowadays is very slow and it is considered to be close to the capacity limit. Differently, with fewer requirements for the locations, broader distribution of resources, fewer impacts of the environment, and more untapped capacities, wind power and solar power seems to be more promising to be largely utilized in the future.

The accumulated capacity of different renewables without hydro power by 2012 is shown in Fig. 1 [3]. It can be clearly seen that the wind power and solar PV have already accounted for 80 % of the total power production by non-hydro renewables. Moreover, among the major renewable energy technologies, the worldwide wind and PV power generation achieved the fastest growth rate at 25 and 60 % respectively in the last five years, as indicated in Fig. 2. As two extreme examples, by 2012 Denmark and Italy have more than 30 and 5.6 % of their electricity production covered by wind and solar PV, respectively, meanwhile some other countries like Germany, U.S., Spain and China are catching up and have also shown promising growth. Therefore these two renewables will be the main focus in this chapter in order to describe the technology enabling its grid interconnection including power electronics and system control.

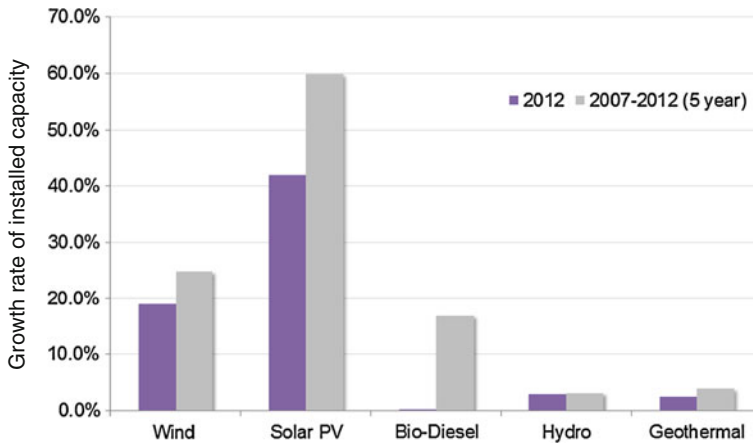


Fig. 2 Worldwide growth rate of installed capacity for different renewable technologies in 2012 and between 2007 and 2012 [3]

1 Status of Wind Power and Photovoltaic Generation

1.1 Wind Power

The cumulative wind power capacity globally from 1999 to 2020 is shown in Fig. 3 [3], and it can be seen that the wind power has grown to a capacity of 283 GW with around 45 GW installed only in 2012, which accounted for 39 % of newly added renewable power capacity. Generally the wind power grows more significantly than any other renewables in many countries, and right now it is no longer an ancillary but an important player in the modern energy supply system.

In respect to the markets and manufacturers, U.S. is the largest market with over 13.1 GW capacity installed in 2012, together with China (13 GW) and EU (11.9 GW) sharing around 87 % of the global market. The Danish company Vestas first gives out the first position among the biggest manufacturers since 2000, while GE takes over the top position due to the strong market of U.S. in 2012. Figure 4 summarizes the worldwide top suppliers of wind turbines in 2012. It can be seen that there are four Chinese companies in the Top 10 manufacturers with a total market share of 16.6 %, which is a significant drop compared to the 26 % in 2011 [3].

1.2 Photovoltaic Power

The development of solar photovoltaic (PV) power has also been progressive especially in the recent five years. By 2012 it has already accounted for 26 % of

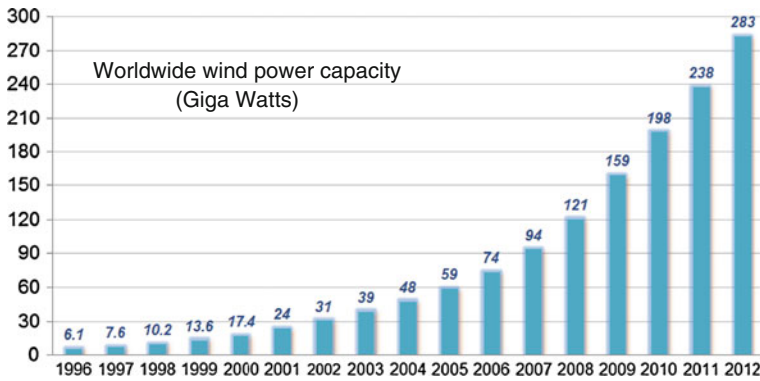
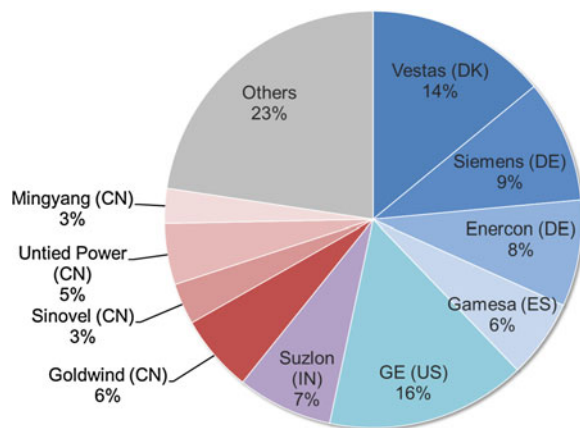


Fig. 3 Cumulative installed wind power capacity from 1996 to 2012 worldwide [1]

Fig. 4 Distribution of wind turbine market share by manufacturers in 2012 (total capacity of 45 GW) [3]



newly added renewables and has reached the 100 GW milestone of capacity. This number makes PV power the third largest renewable energy source in terms of capacity after hydro and wind power. Figure 5 shows the cumulative PV installed capacity from 1996 to 2012, a boost of growing can be clearly observed after 2009.

Different from wind power, Germany and Italy are the top two markets in respect to PV power, with over 7.6 and 3.8 GW installed respectively in 2012. The PV markets in 2012 by different countries are summarized in Fig. 6, where it can be seen that the Europe still dominates the PV markets and accounts for 70 % of the global PV capacity. The U.S., China, and Japan are also important markets with around 7 % market share each by 2012.

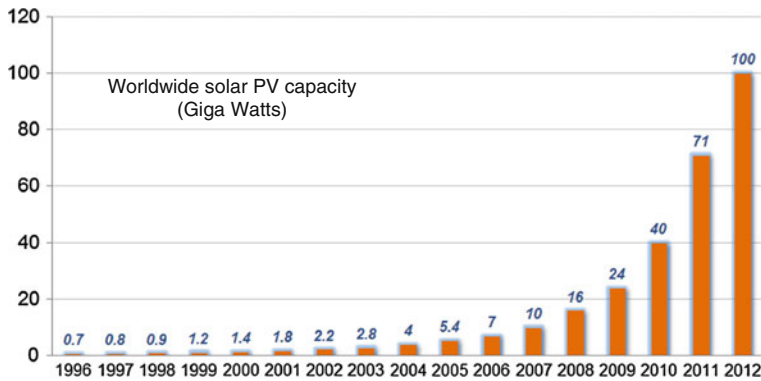
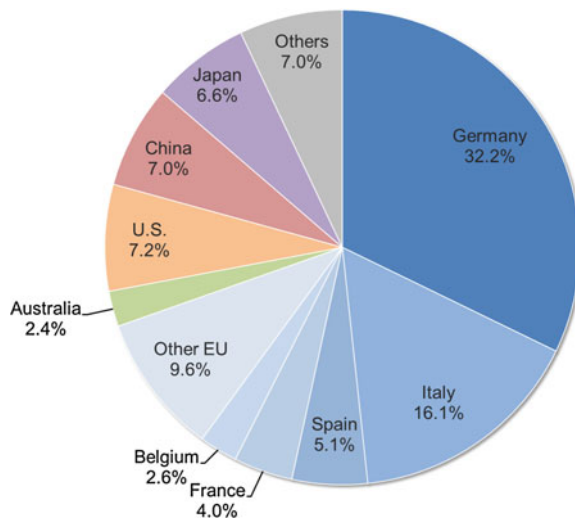


Fig. 5 Cumulative installed PV capacity from 1996 to 2012 [3]

Fig. 6 PV markets shared by different countries in 2012 (total 29 GW capacity) [3]



2 Wind Power Generation

The power conversion stages for a typical wind turbine system are shown in Fig. 7, in which the wind energy captured from the nature is the input, and electrical power injected into the power grid is the output. There are mainly two types of energy conversion in the system, including both the mechanical and electrical parts.

As illustrated in Fig. 7, the wind turbine first captures the wind power by means of aero-dynamical blades and converts it to mechanical power in the rotating shaft of the generator. For typical multi-MW wind turbines, the rotational speed of turbine rotor is relative low and normally ranges in 5–16 rpm, which may result in bulky generator solutions and increase the installation cost. Therefore a gearbox in

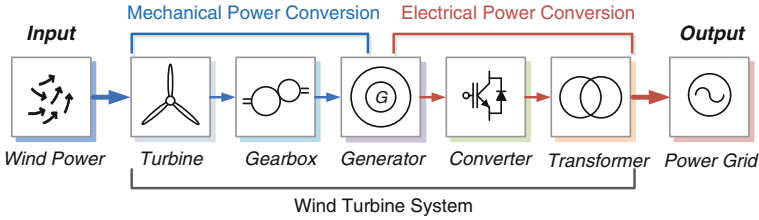


Fig. 7 Converting wind power into electrical power in a wind turbine system

Fig. 7 may be needed to convert the mechanical power to the one with higher-speed and lower-torque, which will contribute to the size and weight reduction of the generator [4].

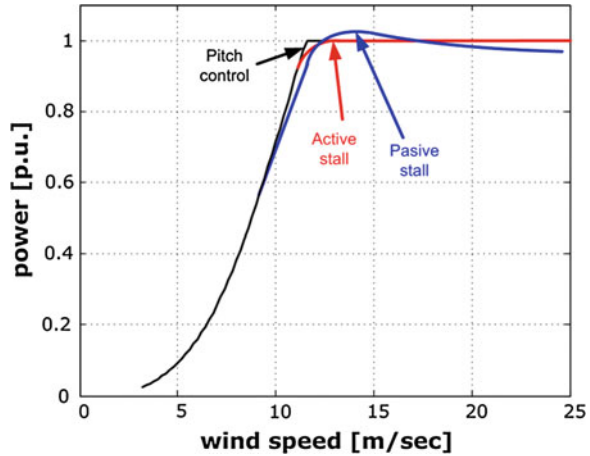
The electrical power produced by the generator also needs to be regulated in order to be injected into the power grid. As shown in Fig. 7, a power electronics converter is normally used which enables certain controllability of the electrical power in the system. Finally a transformer is generally used by manufacturers to boost the voltage level, achieving more efficient power transmission in the power grid. Consequently, the wind energy is refined by the wind turbine system to more controlled and regulated electrical power.

2.1 Basic Operation of Wind Turbine System

In a wind turbine system there are a few control variables to ensure a reliable, controllable, and efficient power production. It is essential first to be able to limit the mechanical power generated by wind turbines under higher wind speeds in order to prevent overloading. The power limitation is done either by Stall Control (the blade position is fixed but stall of the wind appears along the blade), Active Stall Control (The blade angle is adjusted in order to create stall along the blades) or Pitch Control (the blades are turned out of the wind). The characteristics of the output mechanical power using the three types of power limitation methods are compared in Fig. 8 [5]. It can be clearly seen that the pitch control approach can achieve the best power limitation performance and it has already become the dominant technology solution in the newly established wind turbines.

Another control variable of the wind turbines is the rotational speed of turbine rotor. In the past this control freedom is not utilized and the rotational speed is fixed during the whole operation range of wind speeds. Although the fixed speed wind turbines have the advantages of simple, robust and low cost of the electrical parts, the drawbacks are even more significant like the uncontrollable electrical power, large mechanical stress during wind gusts and unsatisfactory power quality of output.

Fig. 8 Power limitations by different methods (Passive stall is based on fixed speed operation) [5]



Nowadays the variable speed wind turbines are widely used in order to achieve better aerodynamic efficiency and also overall control performance. By introducing the variable speed operation, it is possible to continuously adapt the rotational speed of the wind turbine to the wind speed, in such a way that the tip speed ratio is kept constant to achieve the maximum power coefficient of the blades and thereby maximum power extracting efficiency of wind turbine. The power variations in wind will be absorbed by changing rotational speed of the rotor, the mechanical stress and acoustical noise can be thereby reduced. Additionally, the power converters used for speed adjustment can also provide higher quality electrical power in order to fulfill the higher technical demands imposed by the grid operators. This feature is becoming a determining factor in the development of the modern wind power technologies [4].

2.2 Mission Profile for Wind Turbine System

2.2.1 Wind Speed Profiles

As the input of the whole wind turbine system, the wind energy quantified by the wind speed is an important factor that can determine the design, control, maintenance, energy yield and also the cost of the whole system. A field recorded 1-year wind speeds is illustrated in Fig. 9 [6], which is based on 3 h averaged at 80 m hub height, and it was designated for the wind farm located near Thyborøn, Denmark with latitude 56.71° and longitude 8.20° . The chosen hub wind speed belongs to the wind class IEC I with average wind speed of 8.5–10 m/s. It can be seen that the wind speed fluctuates largely from 0 up to 28 m/s. Without proper controls of the mechanical and electrical parts, this significant fluctuation may be transferred to the grid and cause grid stability problems. Moreover the components in the

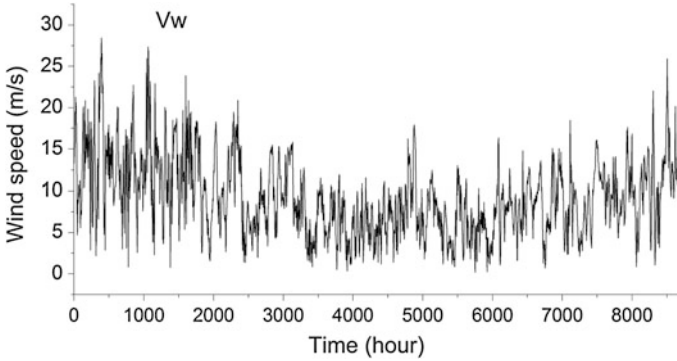


Fig. 9 One year mission profile of wind speed and ambient temperature from a wind farm of Denmark (3-h averaged)

system may suffer from largely cyclical loadings which may quickly trigger reliability problems [7–11]. As a result, the roughness and fluctuation of wind speeds should be carefully taken into account in the control and design of the power electronics converter [12].

2.2.2 Requirements for Modern Wind Power Converter

As the quick development of capacity and technology in the wind power generation, the power electronics converter is becoming more essential. On the other hand, the power electronics converters also need to satisfy much tougher requirements than ever before. These requirements can be generally characterized as shown in Fig. 10 [13, 14]:

(A) *General requirements*

For the generator side, the current flowing in the generator rotor or stator should be regulated to control the electromagnetic torque, not only for maximizing the extracted power from the wind turbines, but also for the energy balancing in case of dynamics due to the inertia mismatch between mechanical and electrical power conversions. For the grid side, the converter must emulate the behaviors of conventional power plants regardless of the wind speed. This means it should help to maintain the frequency as well as voltage amplitude of the grid, and also withstand the grid faults or even contribute the faults recovery [4, 15–19].

(B) *Special considerations*

Due to relative large power capacity, the failures of wind power conversion system may impose strong impacts to grid stability and result in high cost to repair, thereby the reliability performance is especially emphasized. Because of high power capacity, the voltage level of generator may need to be boosted up to facilitate the power transmission, thus step-up transformer are normally

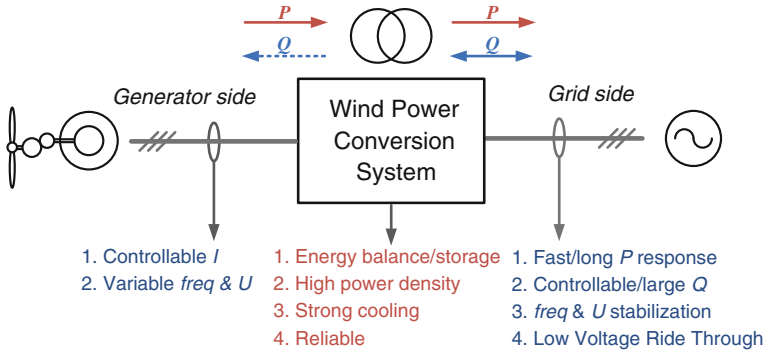


Fig. 10 Demands for modern wind power converters

required in wind turbine system. Furthermore, because the space is limited in the nacelle or tower of wind turbines, the power density and cooling ability are crucial performance for power converter. Finally because of the mismatching power inertia between the turbine and grid, energy storage and balancing is an important issue and may result in extra cost of the system.

2.3 Wind Turbine Concepts and Topologies

2.3.1 Popular Wind Turbine Concepts

The development of the wind turbine technology has been steady for the last 35 years [4, 5, 13, 14]. Depending on the types of generator, power electronics, speed controllability and the way in which the aerodynamic power is limited, the wind turbine designs can generally be categorized into several concepts [5, 20]. In these wind turbine concepts the power electronics play quite different role and has various power rating coverage of the system. Up until now the configuration of Doubly Fed Induction Generator (DFIG) equipped with partial-scale power converter is dominating on the market, but in very near future the configuration with Synchronous Generator (SG) and full-scale power converter is expected to take over to be the dominant solution [4, 14]. In the following these two state-of-the-art wind turbine concepts are going to be introduced.

(A) *Doubly-Fed Induction-Generator with partial-scale power converter*

This wind turbine concept is the most adopted solution nowadays and it has been used extensively since 2000s. As shown in Fig. 11, a power electronics converter is adopted in conjunction with the Doubly-Fed Induction Generator (DFIG). The stator windings of DFIG are directly connected to the power grid, while the rotor windings are connected to the power grid by the

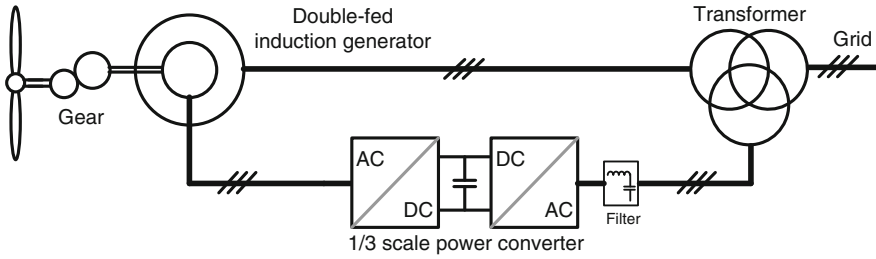


Fig. 11 Variable speed wind turbine with partial-scale power converter and a doubly fed induction generator

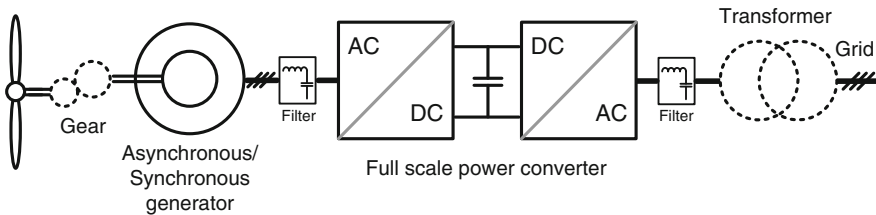


Fig. 12 Variable speed wind turbine with full-scale power converter

converter with normally 30 % capacity of the wind turbine [21–25]. In this concept, the frequency and the current in the rotor can be flexible regulated and thus the variable speed range can be extended to a satisfactory level. The smaller converter capacity makes this concept attractive seen from a cost point of view. However, its main drawbacks are the use of slip-rings and the insufficient power controllability in the case of grid faults—these disadvantages may comprise the reliability and may be difficult to completely satisfy the future grid requirements as claimed in [26, 27].

(B) *Asynchronous/synchronous generator with full-scale power converter*

The second important concept that is popular for the newly developed and installed wind turbines is shown in Fig. 12. It introduces a full-scale power converter to interconnect the power grid and stator windings of generator, thus all the generated power from the wind turbine can be regulated. The Asynchronous Generator, Wound Rotor Synchronous Generator (WRSG) or Permanent Magnet Synchronous Generator (PMSG) have been reported to be used. The elimination of slip rings, simpler or even eliminated gearbox, full power and speed controllability as well as better grid support ability are the main advantages compared to the DFIG based concept. However, the more stressed and expensive power electronic components as well as the higher power losses in the converter are the main drawbacks of this concept.

2.3.2 Power Converters for Wind Turbines

(A) *Two-level power converter*

The Two-Level Pulse-Width-Modulation Voltage-Source-Converter (2L-PWM-VSC) is the most used converter topology so far for the DFIG based wind turbine concept as the power rating requirement for the converter is limited. Normally, two 2L-PWM-VSCs are configured in a back-to-back structure in the wind turbine system, as shown in Fig. 13 which is called 2L-BTB for convenience. A technical advantage of the 2L-BTB solution is the full power controllability (4-quadrant operation) with a relatively simple structure and few components, which contribute to well-proven robust/reliable performances as well as advantage of cost.

As for the full scale converter based concept, the converter needs to carry all the generated power by wind turbines e.g. up to 10 MW, the 2L-BTB converter topology at this power level may suffer from large switching loss and many devices may need to be connected in parallel, also the cabling in case of low voltage level can be a great design/physical challenge. Consequently, it is becoming more and more difficult for a single 2L-BTB topology to achieve acceptable performance for the full-scale wind power converter, even though having the cost advantage.

(B) *Multilevel power converter*

With the abilities to achieve higher voltage and power level, multi-level converters may become more preferred candidates in the full-scale converter based concept [26–28]. The Three-level Neutral Point diode Clamped topology (3L-NPC) is one of the most commercialized multi-level topologies on the market. Similar to the 2L-BTB, it is usually configured as a back-to-back structure in the wind power application, as shown in Fig. 14, which is called 3L-NPC BTB for convenience. The 3L-BTB solution achieves one more output voltage level and less dv/dt stress compared to the counterpart of 2L-BTB, thus it is possible to convert the power at medium voltage with lower current, less paralleled devices, and smaller filter size. The mid-point voltage fluctuation of the DC-bus can be a drawback of the 3L-NPC BTB. This problem has been extensively researched and it is considered to be improved by the controlling of redundant switching states [29–31]. However, it is found that the loss distribution is unequal between the outer and inner switching devices in a switching arm [32–34], and this problem might lead to a de-rated power capacity, when it is practically used.

(C) *Multi-cell converter*

In order to handle the fast growing power capacity, some multi-cell converter configurations (i.e. parallel/series connection of converter cells) are developed and widely adopted by the industry.

Figure 15a shows a multi-cell solution adopted by Gamesa in the 4.5 MW wind turbines [35], which have 2L-BTB single-cell converters paralleled both on the generator side and on the grid side. Siemens also introduce the similar

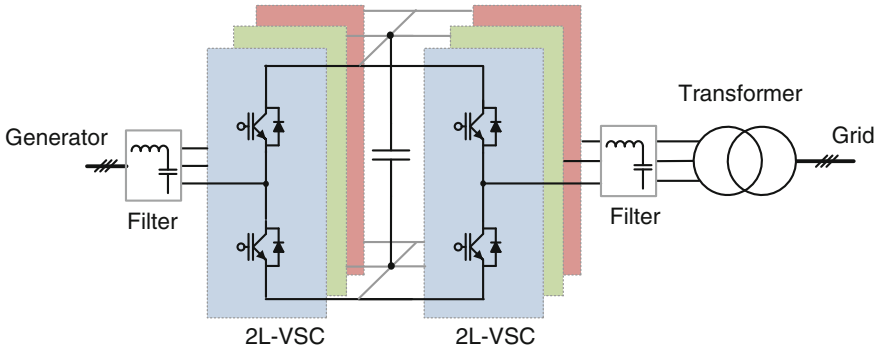


Fig. 13 Two-level back-to-back voltage source converter for wind turbine (2L-BTB)

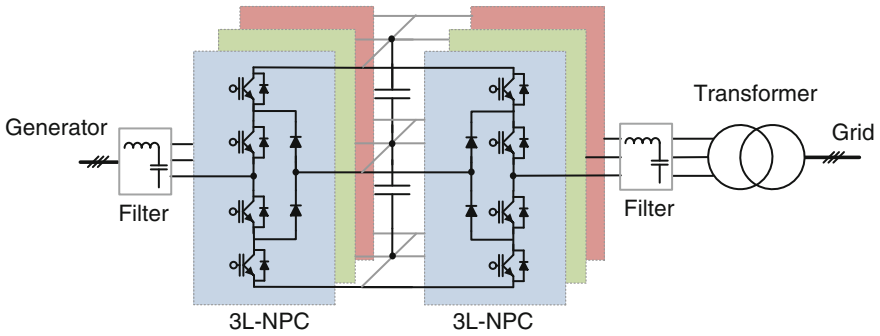


Fig. 14 Three-level neutral point clamped back-to-back converter for wind turbine (3L-NPC BTB)

solution in their best-selling multi-MW wind turbines, as indicated in Fig. 15b [36]. The standard and proven low voltage converter cells as well as redundant and modular characteristics are the main advantages. This converter configuration is the state-of-the-art solution in the industry for the wind turbines with power level higher than 3 MW.

Another multi-cell configuration shares the similar idea with the next generation traction converters [37, 38], and is also proposed in the European UNIFLEX-PM Project [39], as shown in Fig. 16. It is based on a structure of back-to-back Cascaded H-bridge converter, with galvanic insulated DC/DC converters as interface. The DC/DC converters have Medium Frequency Transformer (MFT) operating at several kHz up to dozens of kHz, thereby the transformer size can be significantly reduced in both weight and volume. Moreover, because of the cascaded structure, it can be directly connected to the distribution power grid (10–33 kV) with high output voltage quality, filterless design, and redundant ability [35, 36]. Figure 17 shows another

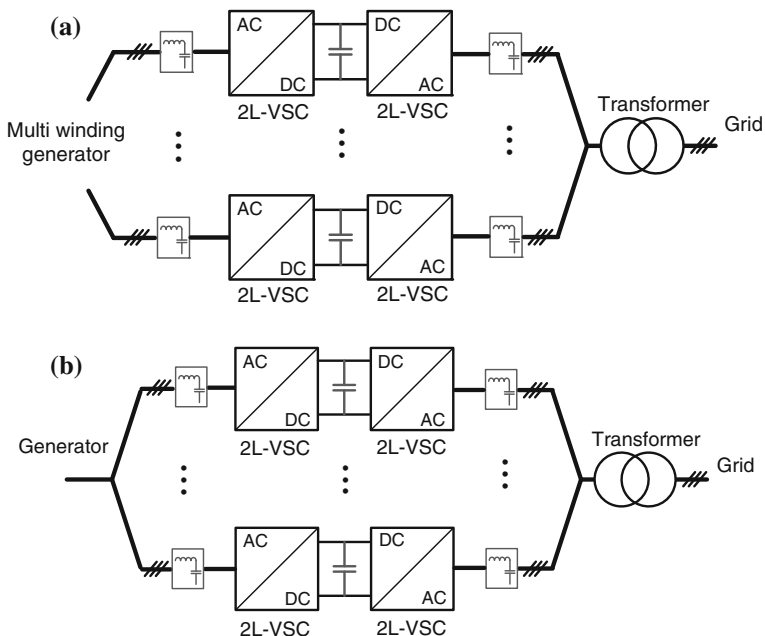


Fig. 15 Multi-cell converter with paralleled converter cells (MC-PCC). **a** Variant 1, **b** Variant 2

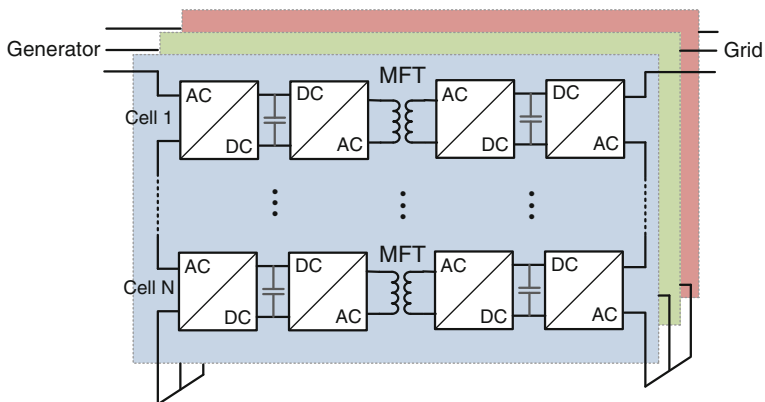
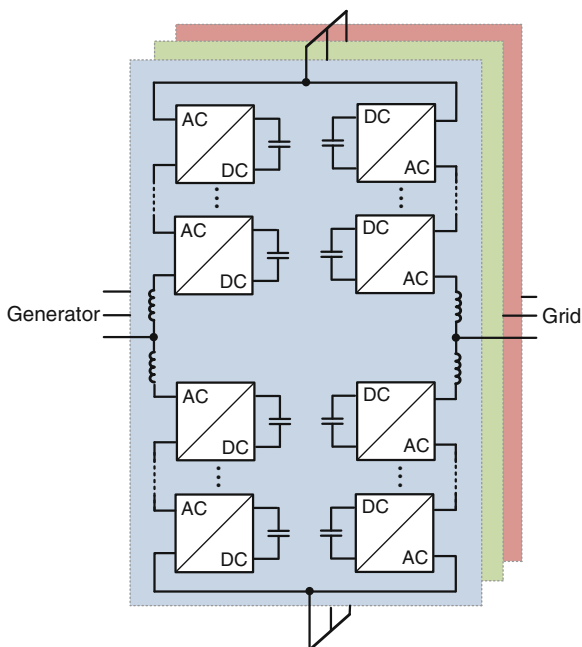


Fig. 16 Cascaded H-bridge converter with medium frequency transformer for wind turbine system (CHB-MFT)

configuration sharing the similar idea with some of the emerging converters used for High Voltage Direct Current (HVDC) Transmission [40, 41]. It is also based on a back-to-back structure with cascaded DC/AC converter cells.

Fig. 17 Modular multilevel converters for wind turbine (MMC)



One advantage of this configuration is the easily scalable voltage/power capability; therefore it can achieve very high power conversion at dozens of kV with good modularity and redundancy.

2.4 General Control Targets of Wind Turbine System

Controlling a wind turbine involves both fast and slow control dynamics [42–50], as indicated in Fig. 18, where a control structure for a wind turbine system including turbine, generator, filter and converter are indicated. Generally the power flowing in and out of the generation system has to be managed. The generated power by the turbines should be controlled by means of mechanical parts (e.g. pitch angle of blades, yawing system, etc.). Meanwhile, the whole system has to follow the power production commands given by Distribution/Transmission System Operators (DSO/TSO).

More advanced features of the control system may be taken into account like the maximization of the generated power, ride through operation of the grid faults and providing grid supporting functions in both normal and abnormal operations of power grid. In the variable speed wind turbine concept, the current in the generator will typically be changed by controlling the generator side converter, and thereby the rotational speed of turbine can be adjusted to achieve maximum power

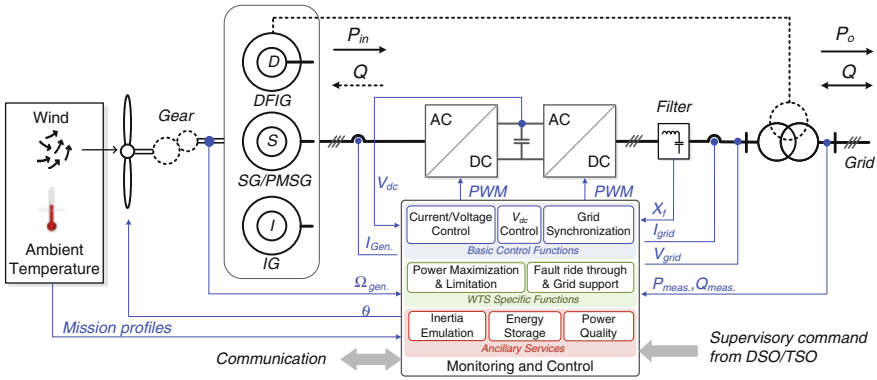


Fig. 18 General control structure for modern wind turbines

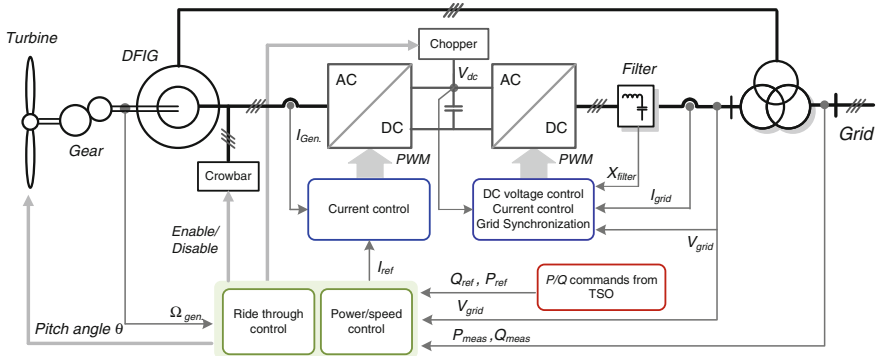


Fig. 19 Control of a wind turbine with doubly-fed induction generator

production. In respect to the operation under grid faults, coordinated control of several subsystems in the wind turbine like the generator/grid side converters, breaking chopper/crowbar, pitch angle controller is necessary.

Finally, the basic controls like current regulation, DC bus stabilization and the grid synchronization have to be quickly performed by the power converter, where the Proportional-Integral (PI) controller and Proportional-Resonant (PR) controllers are typically used.

As an example, the control methods for a DFIG based wind turbine system are shown in Fig. 19. Below maximum power production the wind turbine will typically vary the rotational speed proportional with the wind speed and keep the pitch angle θ fixed. At very low wind speed the rotational speed will be fixed at the maximum allowable slip in order prevent over voltage of generator output. A pitch angle controller is used to limit the power when the turbine output above the nominal power. The total electrical power of the wind turbine system is regulated

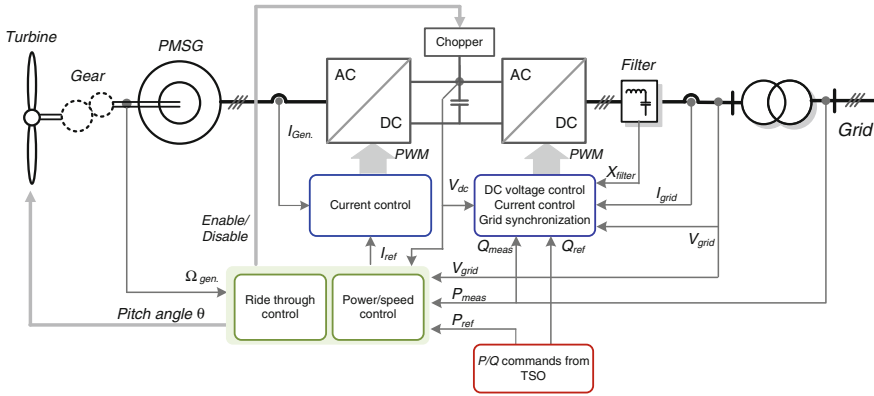


Fig. 20 Control of active and reactive power in a wind turbine with multi-pole synchronous generator

by controlling the DFIG through the rotor-side converter. The control strategy of the grid-side converter is simply just to keep the dc-link voltage fixed. It is noted that a trend is to use a crowbar connected to the rotor of DFIG in order to improve the control performance under grid faults.

Another example for the control structure used for full-scale converter based wind turbine concept is shown in Fig. 20. An advantage of this turbine system is that the dc-link performs some kind of control decoupling between the turbine and the grid. The dc-link will also give an option for the wind turbines to be connected with energy storage units, which can better manage the active power flow injected into the power grid—this feature will further improve the grid supporting abilities of the wind turbines. The generated active power of the wind turbine system is controlled by the generator side converter, while the reactive power is controlled by the grid side converter. It is noted that a DC chopper is normally introduced to prevent over voltage of DC link in case of grid faults, when the extra turbine power needs to be dissipated as the sudden drop of grid voltage.

3 Photovoltaic Power Generation

Due to the cost reduction of Photovoltaic (PV) modules and the development of PV cell technology, the PV power generation has been becoming dominant in the renewable energy supplies of some countries [57–61]. It is expected that the cost of PV technology will continue declining, which will also make the grid-connected PV systems competitive compared to other renewable energy systems.

A grid-connected PV power system has to efficiently and reliably transfer and convert the solar energy, which is highly dependent on the environmental conditions (i.e. irradiance level and ambient temperature). Power electronics systems,

known as PV inverters, together with advanced and intelligent control strategies, are able to enable an effective transferring of the generated PV energy to the grid [4, 5, 58, 60]. Hence, the basic functions of a PV conversion system include: maximum power extraction from PV panels in response to the environmental dependency, grid synchronization, compliance of grid connection requirements, anti-islanding, and etc. [49, 50, 62–64].

In this part, a brief introduction of the PV cell development and the characteristics of solar PV cell are presented firstly, followed by the mission profiles and the demands for PV power conversion systems. An overview of the advanced PV inverters for grid-connected PV systems is demonstrated in Sect. 3.3. Finally, the general control targets of grid-connected PV power conversion systems are given in Sect. 3.4 with some basic control examples. Advanced control strategies for PV systems are detailed in another chapter—*Advanced Control of Photovoltaic and Wind Turbines Power Systems*.

3.1 Photovoltaic Cell Technology and Characteristics

As the core and source of a PV power conversion system, PV panels are typically connected to the DC-AC converter. Depending on the voltage level, a DC-DC stage may be required to boost up the DC-link voltage to an acceptable level of the PV inverter. Similar to this concept, a PV panel/module is an assembly of many PV cells connected in series (increased output voltage) and in parallel (increased output current), as it is shown in Fig. 21a.

Various materials with varying efficiencies and costs can be used to make PV cells. At present, the commonly used materials for PV cells include mono- and poly-crystalline silicon. Those crystalline-silicon-based PV cells can achieve an efficiency of 11–15 % [64, 65]. Another PV cell technology is called thin-film technology, which reduces the amount of required material to create a PV cell. Thin-film PV cells are typically based on cadmium telluride, copper indium gallium selenide, and amorphous silicon [65, 66]. However, the thin-film based PV cells have a relative lower efficiency compared to the crystalline-silicon-based PV cells [64].

The operating principle of all these PV technologies is based on the photovoltaic effect. When a PV cell is exposed to the sunlight, the photons of the semiconductor material are excited, and then jump to the conduction band and become free. Thus, an electromotive force is generated. When the PV cell is connected into a closed loop, the freed electrons will introduce a DC current and the solar energy is converted to electric energy. Hence, the current produced by a PV cell is highly dependent on the solar irradiance level and the ambient temperature. An electrical circuit shown in Fig. 21b can be used to model the characteristics of a PV module or cell. This model has a photo-current source, i_{ph} , in parallel with a diode, a shunt resistance R_p , and a series resistance R_s .

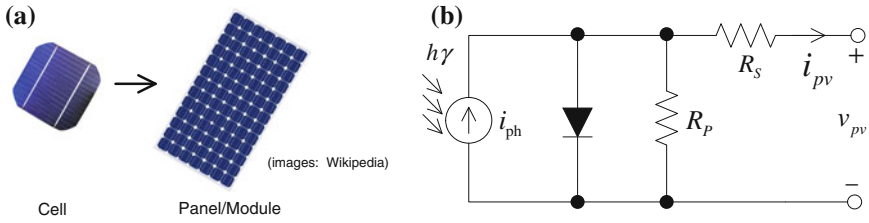


Fig. 21 A PV panel: **a** from solar cells to panel, **b** electrical model

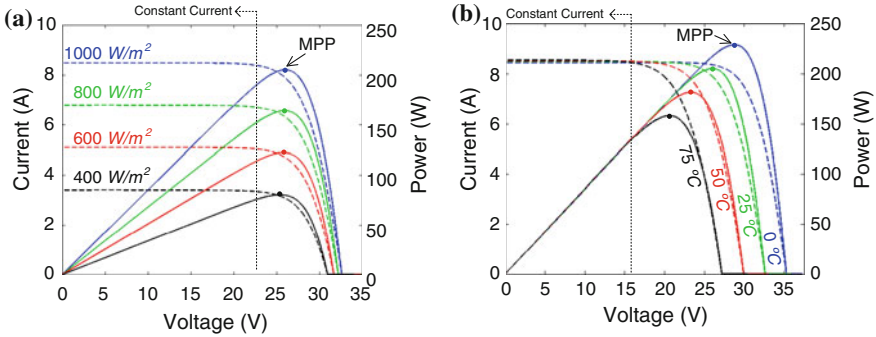


Fig. 22 I-V and P-V characteristics of a PV panel: **a** different solar irradiance levels at 25 °C, **b** different ambient temperatures at 1000 W/m²

As it has been discussed in the previous paragraph, the generated current of a PV panel, and thus the output power, are significantly affected by the solar irradiance level and the ambient temperature. According to Fig. 21b, the electrical characteristics (*I-V* and *P-V* characteristics) of a PV panel are non-linear and also varied with the ambient conditions, as can be observed in Fig. 22. Due to the properties of non-linearity and environmental dependency of the PV panel, a Maximum Power Point Tracking (MPPT) algorithm is necessary to ensure that the solar energy is captured and converted as much as possible—also for the sake of reduction of cost of energy.

It can be seen in Fig. 22 that the power curve of a PV panel is of “hill” form under a given condition. Thus, the *P-V* curve can be divided into three segments: (a) *climbing*—a positive dp/dv , when the PV panel is working as a constant current source, (b) *going-down*—a negative dp/dv , and (c) *the-top*— $dp/dv = 0$, which corresponds to the Maximum Power Point (MPP) for a given ambient condition (e.g. 25 °C, 1000 W/m²). Many proposed MPPT algorithms are based this “hill” characteristic of a PV panel (when the MPP is reached, $dp/dv = 0$), such as the Perturb-and-Observe (P&O) method and the Incremental Conductance (INC) method [67, 68]. The output of the MPPT control system (e.g. power, current or

voltage) is the reference to be controlled by a DC–DC converter or directly a DC–AC inverter, depending on the configuration of the PV system.

However, it should be pointed out that the characteristics shown in Fig. 22 are only for an individual PV panel or module. If many PV panels are connected in series (PV string) or in parallel (PV array) to increase the output power, the MPPs may be different because of panel mismatch. Moreover, the partial shading of the panels increases the MPPT difficulty [66]. Thus, a robust MPPT control algorithm is crucial for PV systems in order to maximize the energy yield of PV strings/arrays with mismatch and partial shading issues.

3.2 Mission Profiles for Photovoltaic Conversion Systems

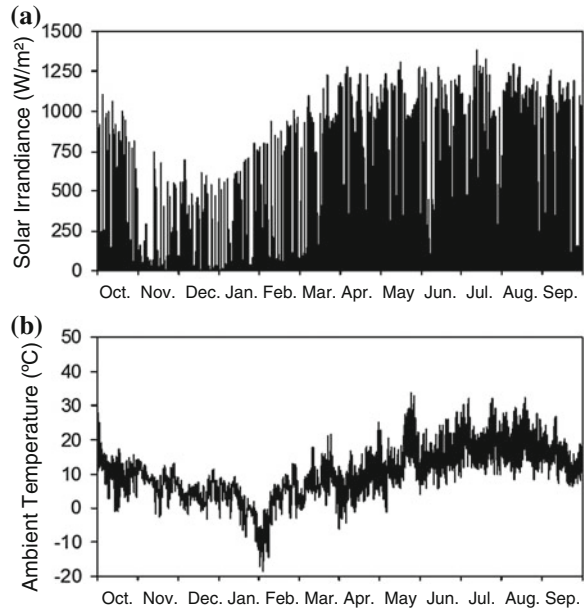
3.2.1 Solar Irradiance and Ambient Temperature Profiles

Since the output power of a PV panel is significantly dependent on the environmental conditions, the knowledge of mission profiles, including solar irradiance level and ambient temperature has become of high importance for the design, control and operation of a PV conversion system. With the accumulation of field experiences and the introduction of more and more real-time monitoring systems, better mission profile data is expected to be available in various kinds of power electronic systems (e.g. PV inverters) [69]. This offers the possibilities to predict the lifetime of a PV inverter and the energy production of a PV system [69, 70].

Figure 23 shows yearly mission profiles for PV systems in Aalborg East, Denmark, from October 2011 to September 2012. The original recorded data has a sampling frequency of 5 Hz [73]. In Fig. 23, the data is resampled every 5 min. It can be observed from Fig. 23 that both the solar irradiance level and the ambient temperature vary significantly through a year. Those fluctuations require dedicated MPPT control systems in order to increase energy yield. Moreover, due to the intermittency, the resultant power, generated by a PV system and then transferred to the grid, may cause grid stability problems—especially when the global PV penetration is getting larger and larger. It is also found that the reliability of a power electronics system has a strong connection with the temperature loading on the power electronics devices [6, 70–72], which is affected by the mission profiles. Hence, different time-scale mission profiles may have an influence on the consumed lifetime of a power electronics system [6].

Consequently, those aspects related to mission profiles have to be carefully taken into considerations in the control and design of the power electronics converters for PV systems. With the development of power electronics technology, the advancement of monitoring techniques, and also intelligent control strategies, further improvement of the lifetime and reduction of energy cost for a PV system can be achieved.

Fig. 23 Yearly mission profiles from recorded data (5 min per sampling data) for PV systems: **a** solar irradiance level, **b** ambient temperature



3.2.2 Requirements for PV Conversion Systems

Grid-connected PV systems are being developed very fast and will soon take a major part of electricity generation in some areas [59, 61]. In order to ensure a reliable and efficient transfer of solar energy to the grid, the power electronics converters (mainly PV inverters) have to comply with much tougher requirements than ever before. These requirements can be generally categorized into the following three parts as shown in Fig. 24.

(A) General requirements

In the PV power conversion the power capacity is not as large as the wind power. Moreover the power inertia of PV output is compatible with the behavior of power grid, and as a result the requirements are less tough when compared to wind turbine systems.

For the PV side, the current or voltage of PV panels should be controlled in order to achieve maximum extracted solar energy. In view of this, a DC–DC converter is commonly used in PV power conversion systems to flexibly track the maximum power, which is strongly dependent on the mission profiles. In this case, the DC voltage should be maintained as a desirable value for the inverter during operation. For the grid side, the requirements are not as stringent as those in wind power systems, but normally the Total Harmonic Distortion (THD) of the output current must be restrained at a lower level (e.g. 5 %) [74]. While for large PV systems with higher power ratings (e.g. hundreds kW connected to medium voltage grid), the grid side also demands

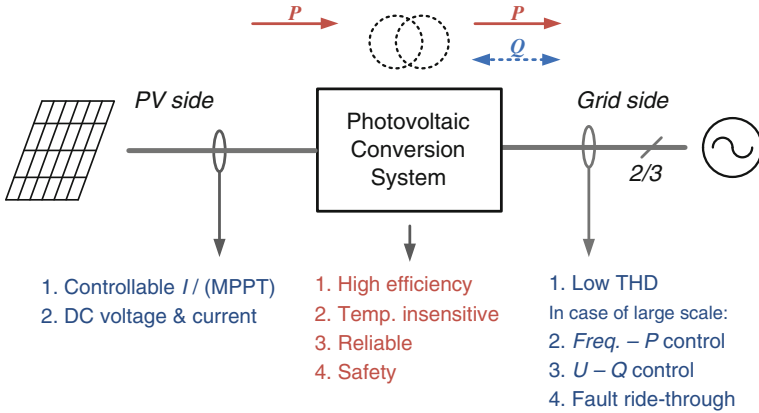


Fig. 24 General demands for the grid-connected PV power conversion system

the PV inverter to stabilize the grid voltage by providing ancillary services. In response to grid faults, the PV inverters have to ride-through voltage faults, when a higher PV penetration level comes to reality [75–78]. Such requirements are expected to cover a wide range of PV applications [77, 78].

(B) *Special considerations*

For PV technology the power capacity per generating unit is relative low but the cost of energy is relative high, as a result there are very strong demands for high efficiency power conversion in order to achieve acceptable price per produced kWh. On the other hand, transformerless PV inverters have gained increasing popularity in the European market (e.g. Germany and Spain) [49, 80] in order to further extend the conversion efficiency. However in this case the safety becomes a more crucial issue because of the lack of galvanic isolation in transformerless PV systems. Reduction of the potential leakage current is generally required [49].

Furthermore, similar to the wind power conversion systems, reliability is also important for power electronics based PV systems, and motivated by extending the total energy production (service time) and reducing the cost. Finally, because of exposure or smaller housing chamber, the PV converter system must be more temperature insensitive, which is beneficial for the reliability performance.

3.3 Photovoltaic Concepts and Topologies

Most of the demands mentioned above for PV systems are performed by the power electronics systems, i.e. PV inverters. Hence, an overview of the basic configurations for grid-connected PV systems is given in the following. This section

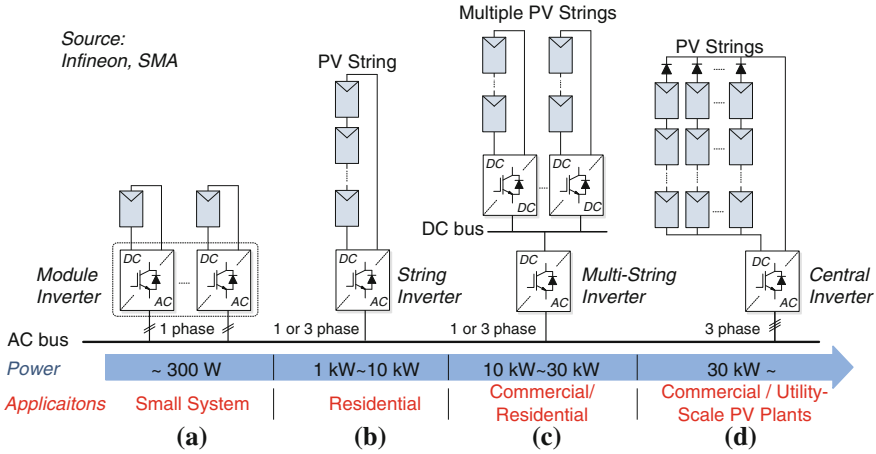


Fig. 25 Different grid-connected PV inverter structures: **a** small system **b** residential **c** commercial/residential **d** commercial/utility scale PV plants

includes dominant PV inverter concepts, covering a wide range of PV applications, and transformerless inverter topologies, which can achieve high efficiency.

3.3.1 PV System Configuration Concepts

Unlike the wind power technology, the solar PV produces much lower power per generating unit (e.g. individual PV panel or PV string), and thereby the PV system is normally composed of many panels connected in parallel and/or series to increase the output power within an acceptable range. According to the state-of-the-art technologies, there are mainly four concepts [63, 64] to organize and deliver the PV power to the public grid, as shown in Fig. 25, each of the concept consists of a series of PV panels or strings and a couple of power electronics converters (DC–DC converters and DC–AC inverters) configured in different structures. Depending on the output voltage level, a boost converter may be required by the string and multi-string inverters.

(A) Central inverter

For this inverter concept, PV panels are arranged in paralleled strings, and are connected to one common central inverter, as shown in Fig. 25d. The central inverter, typically three-phase, is the most widely alternative for large-scale or utility-scale PV power plants, which have high power ratings (e.g. 750 kW SMA Central Inverter [81]). Such inverters have to be equipped with ancillary service functions, like fault ride-through and reactive power injection due to the high power ratings. Adoption of a central inverter is the simplest way

to concentrate a large PV plant with low construction cost. However, the disadvantages of this configuration are also significant and they are listed as follows [63]:

- need for high DC-link voltage (550–850 V) and very long DC cables between PV strings and the central inverter,
- power losses due to a common MPPT applied to the central inverter,
- power loss due to module mismatch,
- losses in the string diodes (blocking diodes), and
- reliability of the whole system depends only on one inverter.

As the capacity of the PV power plants continues growing, various inverter topologies are in those applications to handle high power and high voltage PV systems. Two-level voltage source inverters are currently the most optimal solution for central inverters of large-scale PV power plants. Other multi-level inverters, like three-phase three-level neutral point clamped inverter, which is typically used in wind power systems, can also be adopted in large PV power plants due to the capability to surpass classic semiconductor voltage blocking limits.

(B) *String inverter*

As shown in Fig. 25b, the string inverter concept was first introduced into the European market in 1995. It is based on a modular concept, where PV strings are made up of series-connected PV panels, and are connected to separate string inverters (single- or three-phase). Then, the string inverters are paralleled and connected to the grid. If the PV string terminal voltage is high enough—no voltage boosting is necessary (single-stage), an improvement of the overall system efficiency can be achieved. Moreover, fewer PV panels for each string can also be used, but then a DC–DC boost converter, a DC-AC-DC high-frequency transformer-based converter, or a line frequency transformer is required as the boosting stage, comprising the efficiency performance. The advantages compared to the central inverter are as follows [63]:

- no losses in string diodes (no diodes needed),
- individual MPPT for each string,
- better yield, due to separate MPPTs,
- lower price due to the mass production.

Depending on the grid connection standards, the transformer may be removed in order to further increase the efficiency in some countries (Germany and Spain) where galvanic isolation is not required. This makes the string inverter to be transformerless system, and thus specific design of transformerless inverters and modulation schemes are required in order to eliminate the leakage ground currents due to the parasitic capacitance between the PV panels and the ground [49, 76, 80].

(C) *Multi-string inverter*

Multi-string inverters have recently introduced on the PV market. They are an intermediate solution between string inverters and central inverters.

A multi-string inverter, shown in Fig. 25c, combines the advantages of both string-inverters (high energy production due to individual MPPT control) and central-inverters (low cost), by having many DC–DC converters with individual MPPTs, which feed energy into a common DC-AC inverter. In this way, no matter what the nominal data, string size, PV module technology (e.g. crystalline or thin film), orientation, inclination or weather conditions (e.g. partial shading) of different PV strings are, they can be connected to one common grid-connected inverter [63, 82]. The multi-string concept is a flexible solution, having a high overall efficiency of power extraction, due to the fact that each PV string is individually controlled. The major feature of a multi-string inverter is the multiple DC–DC stages connected in parallel to the DC-link. Thus, transformerless PV inverter technology can also be adopted in the multi-string inverter systems. As mentioned above, the leakage currents should be taken care of during the inverter design and operation.

(D) *Module inverter*

An AC module is made up with an individual solar panel connected to the grid through its own inverter, as shown in Fig. 25a. The advantage of this configuration is that there are no mismatch losses, due to the fact that every single solar panel has its own inverter and MPPT control, thus maximizing the power production. The power extraction is much better optimized than in the case of string inverters. One other advantage is the modular structure, which simplifies the modification and maintenance of the whole system because of its “plug & play” characteristic. One disadvantage is that the price per watt is still higher than in the previous cases [63]. Moreover, due to the low power ratings of PV modules, large voltage amplification units for grid connection are required, and thus making the whole system difficult to achieve high efficiency. In view of those demerits, this inverter configuration has not been widely adopted even for small or medium-scale PV systems.

3.3.2 Transformerless PV Inverter Topologies

To achieve high efficiency, transformerless inverters are introduced to string-inverters and multi-string inverters, where single-phase configurations are more common. As aforementioned, due to the lack of galvanic isolation, leakage currents will appear between the PV panels and the ground and will cause safety issues. Thus, the transformerless inverters are required to reduce the leakage currents either by redesigning the topology or by modifying the modulation schemes. In the following, different single-phase transformerless PV-inverter technologies are discussed.

(A) *H-Bridge topology with bipolar PWM*

The H-Bridge inverter (Fig. 26) is a well-known topology and it is almost the standard solution for the single-phase DC-AC power conversion. It has been widely used in the motor drives and UPS applications. However, in the case of

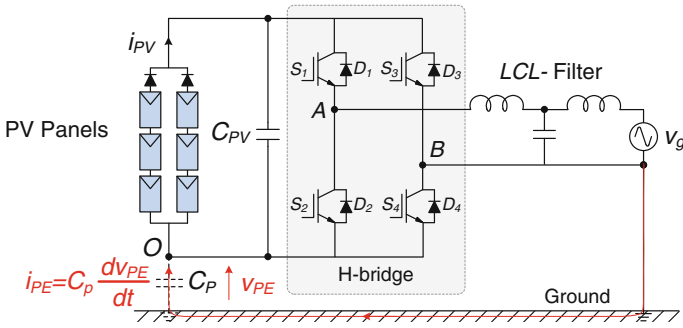


Fig. 26 H-bridge transformerless topology for PV application (V_{PE} common mode voltage, i_{PE} leakage current)

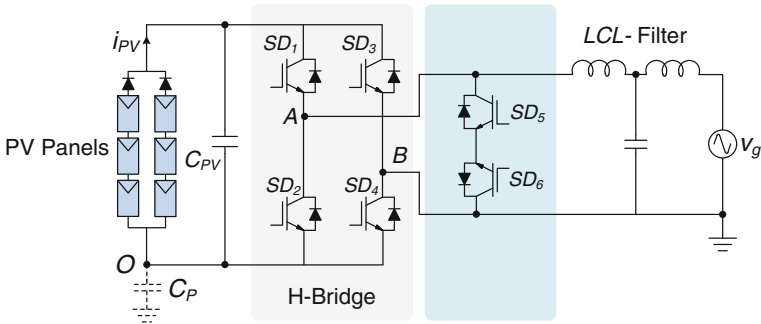


Fig. 27 HERIC transformerless topology for PV applications

the transformerless configuration for PV system, the PWM modulation strategies should be carefully selected, because some popular modulation methods like unipolar PWM may introduce abrupt change of the common mode voltage (high dv/dt) and thus leads to a large leakage current, which are in-preferable in transformerless PV systems and grid connection standards [49, 76]. The bipolar modulation scheme can be adopted in an H-Bridge transformerless inverter with effective elimination of leakage currents, but also with lower efficiency.

In order to improve the common-mode behavior, meanwhile further to increase the efficiency, and to keep all the other merits given by the H- bridge inverter, some modified topologies are proposed in the PV application by adding bypass switches either on the DC side or on the AC side [76, 79, 80, 82–86], as it will be detailed in the following.

(B) *HERIC topology*

The Highly Efficient and Reliable Inverter Concept (HERIC) [87] includes two extra switches (SD_5 – SD_6) on the AC output of the inverter, as it is shown in Fig. 27.

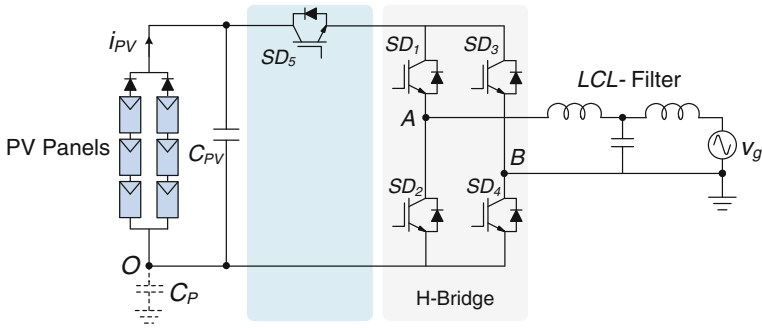


Fig. 28 H5 transformerless topology for PV applications

The common-mode behavior of the HERIC topology is similar to the H-Bridge converter with bipolar PWM, where the voltage to ground of the PV array terminals will only have a sinusoidal shape, while the same high efficiency can be also achieved as the H-bridge converter with unipolar PWM. Therefore, the HERIC topology is more suitable for transformer-less PV system in terms of efficiency (up to 98 % reported) and is widely used for the power range of 2.5–5 kW for single-phase applications [88].

(C) *H5 inverter*

Another suitable topology for the transformer less PV power conversion is called H5 converter, as shown in Fig. 28 [89], which is patented and used by SMA in many of their transformerless inverters. This topology introduces an extra switch (SD_5) on the DC side of H-bridge converter, and it can disconnect the PV panels from the grid during the zero voltage states. Thus, the reduction of leakage currents is achieved.

Similar to the HERIC inverter, the common-mode behavior of the H5 topology is similar to the H-Bridge with bipolar PWM. The voltage to ground of the PV array terminals will only have a sinusoidal shape, while having the same high conversion efficiency as the H-Bridge with unipolar switching. Unipolar output voltage is achieved by disconnecting the PV array from the grid by using a method called DC decoupling.

(D) *H6 inverter*

Another transformerless topology using the DC decoupling method is called the H6 converter [84, 85], which adds two extra switches and two extra diodes to the H-bridge topology as shown in Fig. 29.

The common-mode behavior of the topology is similar to the HERIC and H5 topologies, since the voltage to ground of the PV array has only a sinusoidal shape and the frequency is the grid frequency. It is another suitable solution for transformerless PV systems, and several commercial products are available on the markets with the efficiency of up to 97 %.

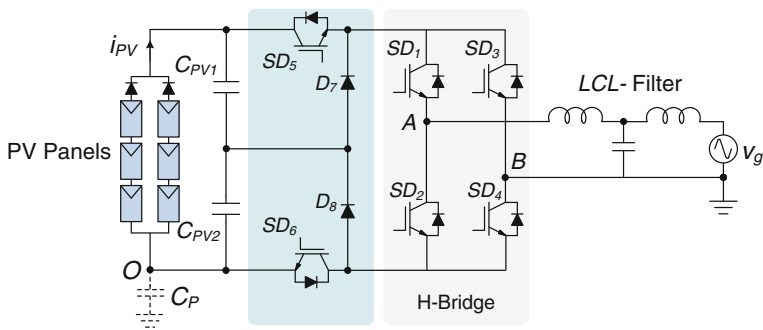


Fig. 29 H6 transformerless topology for PV applications

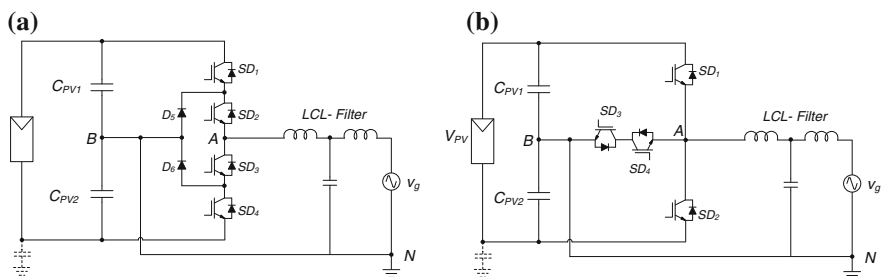


Fig. 30 Neutral Point Clamped transformerless topology for PV application **a** NPC half-bridge inverter **b** Conergy NPC inverter

(E) *Neutral Point Clamped topology*

Besides the H-bridge based topologies, some half bridge solutions are also used in the PV system. The Neutral Point Clamped (NPC) topology shown in Fig. 30a was introduced some years ago in [90]. The voltage to ground measured at both PV array terminals is constant, this is due to the connection of the neutral line of the middle point of the DC-link that fixes the potential of the PV array to the grounded neutral.

The NPC topology is suitable for transformerless PV systems, since the voltage to ground is constant. The only drawback for the single-phase NPC topology is the high DC-link voltage, which has to be more than twice of the grid peak voltage; therefore a boost stage is normally required before the inverter, which will decrease the overall efficiency of the PV system.

A “variant” of the classical NPC topology is also popular in the PV application, as shown in Fig. 30b, which is called Conergy NPC converter [91]. The output voltage of the Conergy converter is clamped to the DC neutral point by a bidirectional switch, which is normally realized with two back-to-back IGBTs, as detailed in [92].

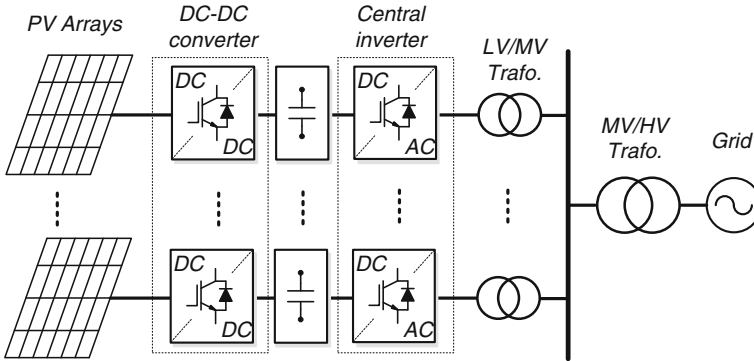


Fig. 31 Typical large-scale PV power plant based on central inverters for utility applications

3.3.3 Central Inverter Topology for High Power PV Applications

Although single-phase configurations are more common for PV applications, some companies like SMA, Sunways, and Kaco are promoting the three-phase PV systems with central inverters for utility-scale applications [81, 88, 93]. For example, the Neuhardenberg solar power plant with a nominal output of 19.69 MWp in Germany uses Powador XP500-HV TL central inverters [93, 94]; the largest European thin-film PV power plant Equipped with 114 Sunny Central 900CP XT inverters from SMA, forming a PV plant of 128 MWp [95]. Those large PV power plants, rated over tens and even hundreds of MW, adopt many central inverters with the power rating of up to 900 kW. A typical large-scale PV power plant is shown in Fig. 31, where DC–DC converters are also used before the central inverters.

3.4 General Control Targets of Photovoltaic Systems

According to the demands for a grid-connected PV system shown in Fig. 24, and also the above discussions, the PV systems should be controlled to perform those functions reliably and efficiently. The variability of PV inverter topologies and system configurations (single- or two-stage) increases the control difficulty. Nonetheless, as it is shown in Fig. 32, the general control objectives for a grid-connected PV system are universal, including MPPT, DC-link control, grid synchronization, voltage/current control, anti-islanding protection, system condition monitoring (grid and PV panels), and ancillary services (especially for a high power PV system). With the increasing PV capacity, the power flowing-in and -out of PV systems has to be managed with other systems (e.g. energy storage systems). Thus, communications are necessary to perform this function. Meanwhile, the

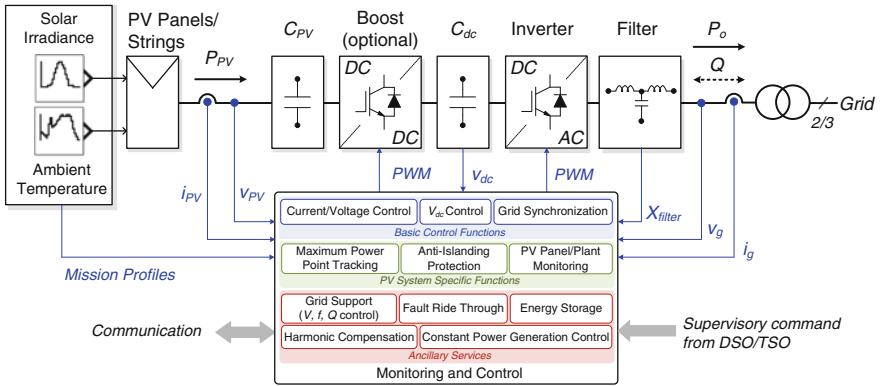


Fig. 32 General control structure of a grid-connected PV system

whole system has to follow the set-point commands given by Distribution/ Transmission System Operators (DSO/TSO) for system stability concern.

More advanced features of the control system, which are required in wind turbine systems, may be taken into consideration at high penetration level of PV systems. For instance, delta power production control, frequency control through active power, voltage control through reactive power, ride-through operation of the grid faults, and the provision of grid support in both normal and abnormal conditions to the grid, have been set for high power PV systems [4, 19, 20, 57, 78]. Some of those features are extended and coming into effectiveness for residential PV applications with low power ratings [75–77]. Typically, those features can be implemented in the outer loop of a cascaded dual-loop control system, which provides a current reference to shape the injected current [50, 76]. Regarding the operation under grid faults, since the PV systems have much lower physical inertia when compared to wind turbine systems, the power of a PV system during fault ride-through operation should be dispatched at least by: (a) modifying the MPPT control, (b) activating DC chopper to absorb power, and (c) managing power exchange between PV systems and the energy storage systems.

Consequently, the basic controls like current regulation (in the inner control loop), DC-link voltage stabilization, grid synchronization, and anti-islanding have to be quickly performed by the power converter.

Since single-phase PV systems are more commonly seen, an example of the control for a single-phase two-stage grid-connected PV system can be observed in Fig. 33, where the control system can be divided into two parts—the boost converter control and the inverter control. The boost converter is controlled to track the maximum power of the PV panels affected by the input solar irradiance level and ambient temperature. The inverter is controlled to maintain the DC-link voltage level. As it is shown in Fig. 32, the injected grid current is synchronized with the grid voltage using a phase-locked-loop system. The current controller is responsible for the injected current quality. The Proportional Resonant (PR),

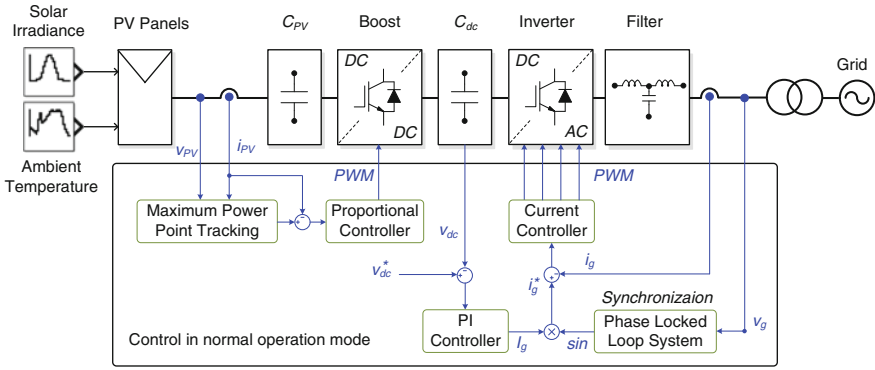


Fig. 33 Basic control structure of a single-phase grid-connected PV system

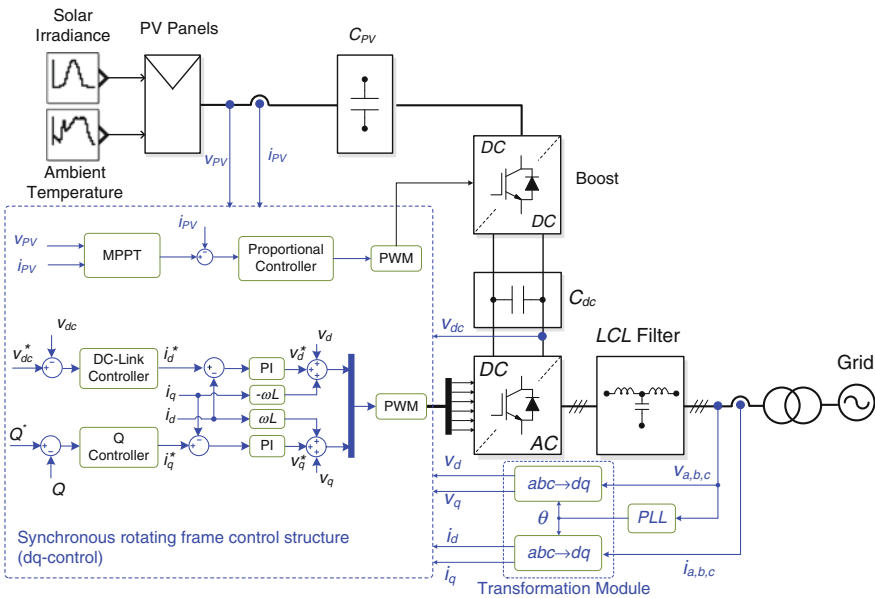


Fig. 34 Basic control structure of a three-phase grid-connected PV system

Resonant Control (RSC), Repetitive Controller (RC), and Deadbeat Controller (DB) can be adopted directly as the current controller, since they are capable to track sinusoidal signals without steady-state errors [49, 50, 76]. By applying the Park transformation ($\alpha\beta \rightarrow dq$) leads to the possibility of Proportional Integral (PI) controllers to regulate the injected current with the help of an orthogonal signal generator. Furthermore, by introducing Harmonic Compensators (HC) for the controller and adding passive damping for the filter, an enhancement of the current controller tracking performance can be achieved [47, 50, 68, 76].

Another example for the control structure used for three-phase PV systems is shown in Fig. 33. Unlike single-phase systems, the Clarke transform and the Park transform can be used in the control of three-phase systems. Hence, the control of a three-phase PV system can be implemented in the synchronous rotating reference frame (dq -control), in the stationary reference frame ($\alpha\beta$ -control), and also in the natural reference frame (abc -control), where the three phase currents are controlled separately [50]. Similarly, for a two-stage system, the control can be divided into two parts. The first one is about the MPPT control by the boost converter. The second one is about the injected current control. In different reference frames, the above mentioned current controllers for single-phase systems can also be adopted here. Those two examples only demonstrate the basic control structure of a grid-connected PV system. In respect to the advanced features and their related control strategies are available in another chapter.

4 Development Trends for Renewable Energies

4.1 More Power Electronics and Advanced Controls

Accompany with the capacity growth, the impacts by renewables to the power grid are also becoming more significant. Unfortunately, the fluctuated and unpredicted features of the renewable energies are un-preferred for the operation of the power grid, thereby technologies which can ensure more reliable and controllable power generating/converting are crucial needs. In the last few decades power electronics gradually become more and more advanced and bring significant performance improvements for the renewable energy production - not only to improve the energy capturing efficiency, but also to enable the whole renewable system to act as a controllable electrical power generation unit in order to be better integrated with the power grid. A good example can be seen from the evolution of wind turbine technology, as shown in Fig. 34 [51, 52], in which the covered power and played role by power electronics are both indicated. It is clear that the power electronics converter already achieved 100 % power coverage in the wind turbine system since 2005, actually in most of the newly established wind turbines and PV panels, power electronics converters have become essential components carrying all of the generated power up to multi-MW.

In order to facilitate the grid integration of renewables, the conventional power grid system which is normally based on centralized and large power plants have to be modified to the structure with more distributed and smaller generation units, thus new demands for grid integration standards, communication, power flow control, and protection are needed. Power electronic converters again play an important role in this technology transformation [4].

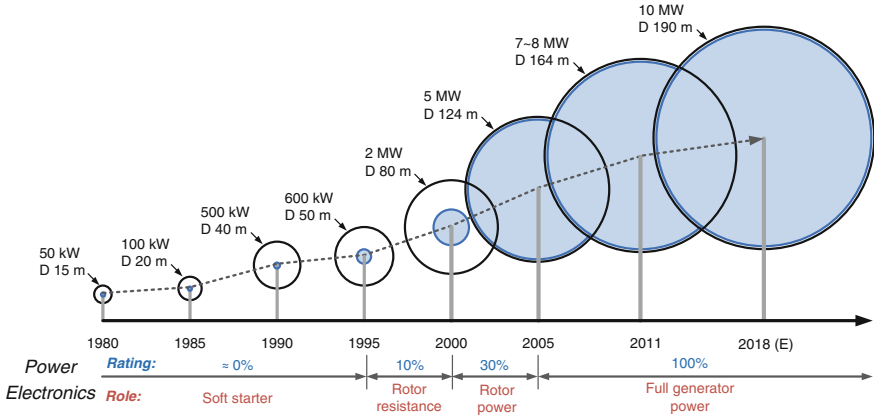


Fig. 35 Evolution of wind turbine size and the power electronics seen from 1980 to 2018 (Estimated), blue circle indicates the power capacity coverage by power electronics

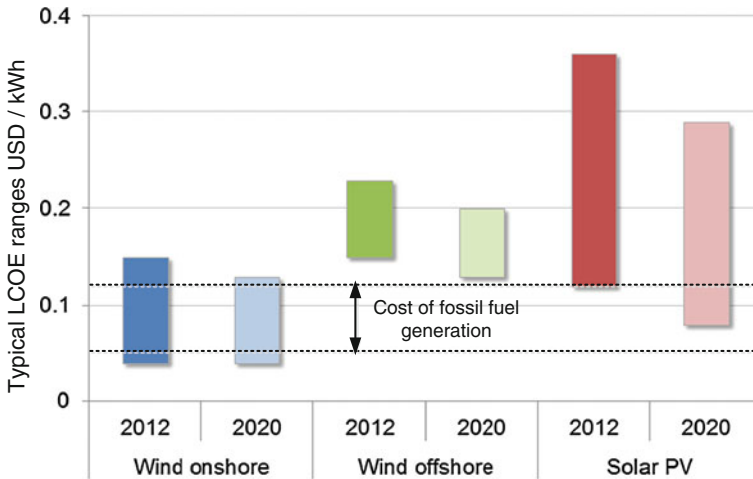


Fig. 36 Levelized cost of energy for several renewable energy technologies in 2012 and 2020 (E) (Source International Renewable Energy Agency IRENA) [54]

4.2 Lower Cost of Energy

Cost is the most important consideration which will strongly determine the wide spread use and installed capacity of certain energy technologies. In order to quantify and compare the cost for different energy technologies, Levelized Cost of Energy (LCOE) index is generally used [53]. LCOE represents the price at which the electricity is generated from a specific energy source over the whole lifetime of the generation unit.

Figure 35 shows the worldwide LCOE ranges for the wind and PV power generations in 2012, as well as the estimations in 2020 [54]. It can be seen that the on-shore wind power technology nowadays is even comparable with the fossil-fuel-based power generation in respect to the cost. The cost advantage is also the main reason why on-shore wind power showed significant growth in the last few decades. However as claimed in [54], the potential for the remaining cost reduction of on-shore wind power until 2020 will not be as large as it was before.

Off-shore wind power and solar PV technologies are still more expensive than the on-shore wind power—not only nowadays but also in the near future. However the potential for cost reduction is larger, as also indicated in Fig. 36.

As power electronics are almost essential with higher power rating and more advanced control features, the cost for the power electronics is no longer ignorable and becomes critical in the renewable energy systems. As the cost is so important for the larger scale utilization of certain renewable energy technology, some special cost considerations should also be taken into account for the design and control of power electronics converters.

4.3 Higher Reliability

The dramatic growth of total installation and also the individual capacity make the failures of renewable system costly or even unacceptable from the point view of the TSO/grid owner. The failures of these renewable generation units will not only cause stability problems of the power grid due to sudden absence of a large amount of power capacity, but also results in high cost for repairing and maintenance especially for those large and remote-located wind turbines or PV panels. Additionally it will cause energy loss to the customer—leading to reduced total/annual energy production and thus it will increase the LCOE. As a result, the reliability performance is another critical performance for the renewable energy system.

Nevertheless, the reliability of power electronics in renewable applications still seems to be unsatisfactory. As an example, when looking at the failure rates and down time distribution in individual wind turbine [55, 56], it is found that the control and power electronic parts tend to have higher failure rate than the other subsystems with a factor of 2-4, therefore the reliability improvements of power electronics will effectively extend the energy production. This is a very helpful approach to further reduce the cost of energy, either for the technologies like onshore wind power where the remaining potential for cost reduction is not so large, or for those technologies like offshore wind and PV power where the cost are still high.

5 Summary

The chapter first illustrates the status of wind power and photovoltaic power generation. Some basic operations, control targets, and technical solutions of the power electronics used in the wind power and photovoltaic power generations are also discussed respectively.

It is concluded that as the quick development of renewable energy technologies and capacity, power electronics is playing essential role to achieve more controllable, efficient, and reliable power production of renewable energies. Meanwhile there are also some emerging challenges and opportunities in respect to the control and design of power electronics system used in renewable application.

References

1. Wikipedia, Renewable Energy, Sep 2013. http://en.wikipedia.org/wiki/Renewable_energy
2. Report of Danish Commission on Climate Change Policy, Green Energy - the road to a Danish energy system without fossil fuels, Sept 2010. <http://www.klimakommissionen.dk/en-US/>
3. REN21 - Renewables 2012 Global Status Report, June 2012. <http://www.ren21.net>
4. F. Blaabjerg, K. Ma, Future on power electronics for wind turbine systems. *IEEE J. Emerg. Sel. Top. Power Electron.* **1**(3), 139–152 (2013)
5. F. Blaabjerg, Z. Chen, S.B. Kjaer, Power Electronics as Efficient Interface in Dispersed Power Generation Systems. *IEEE Trans. Power Electron.* **19**(4), 1184–1194 (2004)
6. K. Ma, M. Liserre, F. Blaabjerg, Lifetime estimation for the power semiconductors considering mission profiles in wind power converter, in *Proceedings of ECCE' 2013*, Sep 2013
7. E. Wolfgang, L. Amigues, N. Seliger, G. Lugert, Building-in reliability into power electronics systems. *The World of Electronic Packaging and System Integration*, pp. 246–252 (2005)
8. D. Hirschmann, D. Tissen, S. Schroder, R.W. De Doncker, Inverter design for hybrid electrical vehicles considering mission profiles, in *IEEE Conference on Vehicle Power and Propulsion*, pp. 1–6, 7–9 Sept 2005
9. C. Busca, R. Teodorescu, F. Blaabjerg, S. Munk-Nielsen, L. Helle, T. Abeyasekera, P. Rodriguez, An overview of the reliability prediction related aspects of high power IGBTs in wind power applications. *Microelectron. Reliab.* **51**(9–11), 1903–1907 (2011)
10. E. Wolfgang, Examples for failures in power electronics systems. Paper presented at ECPE Tutorial on Reliability of Power Electronic Systems, Nuremberg, Germany, April 2007
11. S. Yang, A.T. Bryant, P.A. Mawby, D. Xiang, L. Ran, P. Tavner, An industry-based survey of reliability in power electronic converters. *IEEE Trans. Ind. Appl.* **47**(3), 1441–1451 (2011)
12. A. Isidori, F.M. Rossi, F. Blaabjerg, K. Ma, Thermal loading and reliability of 10 MW multilevel wind power converter at different wind roughness classes. *IEEE Trans. Ind. Appl.* (2013)
13. Z. Chen, J.M. Guerrero, F. Blaabjerg, A review of the state of the art of power electronics for wind turbines. *IEEE Trans. Power Electron.* **24**(8), 1859–1875 (2009)
14. F. Blaabjerg, M. Liserre, K. Ma, Power electronics converters for wind turbine systems. *IEEE Trans. Ind. Appl.* **48**(2), 708–719 (2012)
15. M. Altin, O. Goksu, R. Teodorescu, P. Rodriguez, B. Bak-Jensen, L. Helle, Overview of recent grid codes for wind power integration, in *Proceedings of OPTIM'2010*, pp. 1152–1160 (2010)

16. M. Tsili, A review of grid code technical requirements for wind farms. *IET J. Renew. Power Gener.* **3**(3), 308–332 (2009)
17. Energinet – Wind turbines connected to grids with voltages below 100 kV, Jan 2003
18. Energinet – Technical regulation 3.2.5 for wind power plants with a power output greater than 11 kW, Sept 2010
19. E.ON-Netz – Grid Code. Requirements for offshore grid connections in the E.ON Netz network, April 2008
20. F. Blaabjerg, K. Ma, High power electronics – Key technology for wind turbines, chapter 6, in *Power electronics for renewable energy systems, transportation and industrial applications*. (Wiley, New York, 2013)
21. S. Muller, M. Deicke, R.W. De Doncker, Doubly fed induction generator systems for wind turbines. *IEEE Ind. Appl. Mag.* **8**(3), 26–33 (2002)
22. D. Xiang, L. Ran, P.J. Tavner, S. Yang, Control of a doubly fed induction generator in a wind turbine during grid fault ride-through. *IEEE Trans. Energy Convers.* **21**(3), 652–662 (2006)
23. F.K.A. Lima, A. Luna, P. Rodriguez, E.H. Watanabe, F. Blaabjerg, Rotor voltage dynamics in the doubly fed induction generator during grid faults. *IEEE Trans. Power Electron.* **25**(1), 118–130 (2010)
24. D. Santos-Martin, J.L. Rodriguez-Amenedo, S. Arnaltes, Providing ride-through capability to a doubly fed induction generator under unbalanced voltage dips. *IEEE Trans. Power Electron.* **24**(7), 1747–1757 (2009)
25. R. Pena, J.C. Clare, G.M. Asher, Doubly fed induction generator using back-to-back PWM converters and its application to variable speed wind-energy generation. *Electric Power Application* **143**(3), 231–241 (1996)
26. J. Rodriguez, S. Bernet, W. Bin, J.O. Pontt, S. Kouro, Multilevel voltage-source-converter topologies for industrial medium-voltage drives. *IEEE Trans. Ind. Electron.* **54**(6), 2930–2945 (2007)
27. S. Kouro, M. Malinowski, K. Gopakumar, J. Pou, L.G. Franquelo, B. Wu, J. Rodriguez, M.A. Perez, J.I. Leon, Recent advances and industrial applications of multilevel converters. *IEEE Trans. Power Electron.* **57**(8), 2553–2580 (2010)
28. A. Faulstich, J.K. Stinke, F. Wittwer, Medium voltage converter for permanent magnet wind power generators up to 5 MW, in *Proceedings of EPE 2005*, pp. 1–9 (2005)
29. N. Celanovic, D. Boroyevich, A comprehensive study of neutral-point voltage balancing problem in three-level neutral-point-clamped voltage source PWM inverters. *IEEE Trans. Power Electron.* **15**(2), 242–249 (2000)
30. S. Srikanthan, M.K. Mishra, DC capacitor voltage equalization in neutral clamped inverters for DSTATCOM application. *IEEE Trans. Ind. Electron.* **57**(8), 2768–2775 (2010)
31. J. Zaragoza, J. Pou, S. Ceballos, E. Robles, C. Jaen, M. Corbalan, Voltage-balance compensator for a carrier-based modulation in the neutral-point-clamped converter. *IEEE Trans. Ind. Electron.* **56**(2), 305–314 (2009)
32. K. Ma, F. Blaabjerg, D. Xu, Power devices loading in multilevel converters for 10 MW wind turbines, in *Proceedings of ISIE 2011*, pp. 340–346, June 2011
33. K. Ma, F. Blaabjerg, Multilevel converters for 10 MW wind turbines, in *Proceedings of EPE'2011*, Birmingham, pp. 1–10 (2011)
34. J. Rodriguez, S. Bernet, P.K. Steimer, I.E. Lizama, A survey on neutral-point-clamped inverters. *IEEE Trans. Ind. Electron.* **57**(7), 2219–2230 (2010)
35. B. Andresen, J. Birk, A high power density converter system for the Gamesa G10x 4.5 MW wind turbine, in *Proceedings of EPE'2007*, pp. 1–7 (2007)
36. R. Jones, P. Waite, Optimised power converter for multi-MW direct drive permanent magnet wind turbines, in *Proceedings of EPE'2011*, pp. 1–10 (2011)
37. B. Engel, M. Victor, G. Bachmann, A. Falk, 15 kV/16.7 Hz energy supply system with medium frequency transformer and 6.5 kV IGBTs in resonant operation, in *Proceedings of EPE'2003*, Toulouse, France, 2–4 Sept 2003

38. S. Inoue, H. Akagi, A bidirectional isolated DC–DC converter as a core circuit of the next-generation medium-voltage power conversion system. *IEEE Trans. Power Electron.* **22**(2), 535–542 (2007)
39. F. Iov, F. Blaabjerg, J. Clare, O. Wheeler, A. Rufer, A. Hyde, UNIFLEX-PM-A key-enabling technology for future European electricity networks. *EPE J.* **19**(4), 6–16 (2009)
40. M. Davies, M. Dommaschk, J. Dorn, J. Lang, D. Retzmann, D. Soerangr, HVDC PLUS – Basics and Principles of Operation, Siemens Technical articles (2008)
41. A. Lesnicar, R. Marquardt, An innovative modular multilevel converter topology suitable for a wide power range, in *Proceedings of IEEE Bologna PowerTech Conference*, pp. 1–6 (2003)
42. M.S. El-Moursi, B. Bak-Jensen, M.H. Abdel-Rahman, Novel STATCOM controller for mitigating SSR and damping power system oscillations in a series compensated wind park. *IEEE Trans. Power Electron.* **25**(2), 429–441 (2010)
43. J. Dai, D.D. Xu, B. Wu, A novel control scheme for current-source-converter-based PMSG wind energy conversion systems. *IEEE Trans. Power Electron.* **24**(4), 963–972 (2009)
44. X. Yuan, F. Wang, D. Boroyevich, Y. Li, R. Burgos, DC-link Voltage Control of a Full Power Converter for Wind Generator Operating in Weak-Grid Systems. *IEEE Trans. on Power Electron.* **24**(9), 2178–2192 (2009)
45. P. Rodriguez, A. Timbus, R. Teodorescu, M. Liserre, F. Blaabjerg, Reactive power control for improving wind turbine system behavior under grid faults. *IEEE Trans. Power Electron.* **24**(7), 1798–1801 (2009)
46. A. Timbus, M. Liserre, R. Teodorescu, P. Rodriguez, F. Blaabjerg, Evaluation of current controllers for distributed power generation systems. *IEEE Trans. Power Electron.* **24**(3), 654–664 (2009)
47. M. Liserre, F. Blaabjerg, S. Hansen, Design and control of an LCL-filter-based three-phase active rectifier. *IEEE Trans. Ind. Appl.* **41**(5), 1281–1291 (2005)
48. P. Rodriguez, A.V. Timbus, R. Teodorescu, M. Liserre, F. Blaabjerg, Flexible active power control of distributed power generation systems during grid faults. *IEEE Trans. Ind. Electron.* **54**(5), 2583–2592 (2007)
49. R. Teodorescu, M. Liserre, P. Rodriguez, in *Grid Converters for Photovoltaic and Wind Power Systems*. Wiley, New York (2011)
50. F. Blaabjerg, R. Teodorescu, M. Liserre, A.V. Timbus, Overview of control and grid synchronization for distributed power generation systems. *IEEE Trans. Ind. Electron.* **53**(5), 1398–1409 (2006)
51. Website of Vestas Wind Power, *Wind turbines overview*, April 2011. <http://www.vestas.com/>
52. UpWind project, Design limits and solutions for very large wind turbines, March 2011. http://www.ewea.org/fileadmin/ewea_documents/documents/upwind/21895_UpWind_Report_low_web.pdf
53. Wikipedia Cost of electricity by source, April 2013. http://en.wikipedia.org/wiki/Cost_of_electricity_by_source
54. Report of the International Renewable Energy Agency (IRENA), Renewable Power Generation Costs in 2012: An Overview, Released in 2013. <http://www.irena.org/>
55. S. Faulstich, P. Lyding, B. Hahn, P. Tavner, Reliability of offshore turbines—identifying the risk by onshore experience, in *Proceedings of European Offshore Wind*, Stockholm (2009)
56. B. Hahn, M. Durstewitz, K. Rohrig, Reliability of wind turbines – experience of 15 years with 1500 WTs, in *Wind Energy*, ed. by J. Peinke, P. Schaumann S. Barth (Springer, Berlin, 2007), pp. 329–332
57. K.O. Kovanen, Photovoltaics and power distribution. *Renew. Energy Focus* **14**(3), 20–21 (2013)
58. Y. Xue, K.C. Divya, G. Griepentrog, M. Liviu, S. Suresh, M. Manjrekar, Towards next generation photovoltaic inverters, in *Proceedings of ECCE'11*, pp. 2467–2474, 17–22 Sept 2011
59. C. Winneker, World's solar photovoltaic capacity passes 100-gigawatt landmark after strong year [Online], Feb 2013. <http://www.epia.org/news/>

60. J.D. van Wyk, F.C. Lee, On a future for power electronics. *IEEE J. Emerg. Sel. Top. Power Electron.* **1**(2), 59–72 (2013)
61. M. Braun, T. Stetz, R. Brundlinger, C. Mayr, K. Ogimoto, H. Hatta, H. Kobayashi, B. Kroposki, B. Mather, M. Coddington, K. Lynn, G. Graditi, A. Woyte, I. MacGill, Is the distribution grid ready to accept large-scale photovoltaic deployment? State of the art, progress, and future prospects. *Prog. Photovolt: Res. Appl.* **20**(6), 681–697 (2012)
62. F. Blaabjerg, R. Teodorescu, M. Liserre, A.V. Timbus, Overview of control and grid synchronization for distributed power generation systems. *IEEE Trans. Ind. Electron.* **53**(5), 1398–1409 (2006)
63. S.B. Kjaer, J.K. Pedersen, F. Blaabjerg, A review of single-phase grid-connected inverters for photovoltaic modules. *IEEE Trans. Ind. Appl.* **41**(5), 1292–1306 (2005)
64. S.B. Kjaer, *Design and Control of an Inverter for Photovoltaic Applications*, PhD Thesis, Department of Energy Technology, Aalborg University, Aalborg, Denmark, Jan 2005
65. Wikipedia, Solar cell, Sept 2013. http://en.wikipedia.org/wiki/Solar_cell
66. A. Luque, S. Hegedus, in *Handbook of Photovoltaic Science and Engineering*, second version (Wiley, New York, 2011)
67. F. Iov, M. Ciobotaru, D. Sera, R. Teodorescu, F. Blaabjerg, Power electronics and control of renewable energy systems, in *Proceedings of PEDS'07*, pp. P-6–P-28, 27–30, Nov 2007
68. M. Ciobotaru, R. Teodorescu, F. Blaabjerg, Control of single-stage single-phase PV inverter, in *Proceedings of EPE'05*, pp. P.1–P.10 (2005)
69. E. Koutroulis, F. Blaabjerg, A New technique for tracking the global maximum power point of PV arrays operating under partial-shading conditions. *IEEE J. Photovoltaics* **2**(2), 184–190 (2012)
70. H. Wang, M. Liserre, F. Blaabjerg, Toward reliable power electronics - challenges, design tools and opportunities. *IEEE Ind. Electron. Mag.* **7**(2), 17–26 (2013)
71. H. Huang, P.A. Mawby, A lifetime estimation technique for voltage source inverters. *IEEE Trans. Power Electron.* **28**(8), 4113–4119 (2013)
72. Y. Yang, H. Wang, F. Blaabjerg, and K. Ma, Mission profile based multi-disciplinary analysis of power modules in single-phase transformerless photovoltaic inverters, in *Proceedings of EPE ECCE Europe'13*, pp. P.1–P.10, Sept 2013
73. Photovoltaic Research Group, Department of Energy Technology, Aalborg University. <http://www.et.aau.dk/research-programmes/>
74. IEEE-SA Standards Board, IEEE Std 929-2000: IEEE recommended practice for utility interface of photovoltaic (PV) systems, Jan 2000
75. Y. Yang, F. Blaabjerg, Z. Zou, Benchmarking of grid fault modes in single-phase grid-connected photovoltaic systems. *IEEE Trans. Ind. Appl.* **49**(5), 2167–2176 (2013)
76. Y. Yang, F. Blaabjerg, H. Wang, Low voltage ride-through of single-phase transformerless photovoltaic inverters. *IEEE Trans. Ind. Appl.* May/June 2014. <http://dx.doi.org/10.1109/1139TIA.2013.2282966>
77. N.P. Papanikolaou, Low-voltage ride-through concept in flyback inverter-based alternating current- photovoltaic modules. *IET Power Electron.* **6**(7), 1436–1448 (2013)
78. Y. Bae, T.-K. Vu, R.-Y. Kim, Implemental control strategy for grid stabilization of grid-connected PV system based on german grid code in symmetrical low-to-medium voltage network. *IEEE Trans. Energy Convers.* **28**(3), 619–631 (2013)
79. E. Koutroulis, F. Blaabjerg, Design optimization of transformer-less grid-connected pv inverters including reliability. *IEEE Trans. Power Electron.* **28**(1), 325–335 (2013)
80. D. Meneses, F. Blaabjerg, O. García, J.A. Cobos, Review and comparison of step-up transformerless topologies for photovoltaic AC-module application. *IEEE Trans. Power Electron.* **28**(6), 2649–2663(2013)
81. SMA, SUNNY CENTRAL- High tech solution for solar power stations. Products Category Brochure. <http://www.sma-america.com/>
82. M. Meinhardt, G. Cramer, Multi-string-converter: the next step in evolution of string-converter technology, in *Proceedings of EPE'01*, pp. P.1–P.9 (2001)

83. S.V. Araujo, P. Zacharias, R. Mallwitz, Highly efficient single-phase transformerless inverters for grid-connected PV systems. *IEEE Trans. Ind. Electron.* **57**(9), 3118–3128 (2010)
84. R. Gonzalez, J. Lopez, P. Sanchis, L. Marroyo, Transformerless inverter for single-phase photovoltaic systems. *IEEE Trans. Power Electron.* **22**(2), 693–697 (2007)
85. S.R. Gonzalez, C.J. Coloma, P.L. Marroyo, T.J. Lopez, G.P. Sanchis, Single-phase inverter circuit for conditioning and converting dc electrical energy into ac electrical, International Patent Application, Pub. No. WO/2008/015298, 7 Feb 2008
86. T. Kerekes, R. Teodorescu, P. Rodriguez, G. Vazquez, E. Aldabas, A new high-efficiency single-phase transformerless PV inverter topology. *IEEE Trans. Ind. Electron.* **58**(1), 184–191 (2011)
87. H. Schmidt, S. Christoph, J. Ketterer, Current inverter for direct/alternating currents, has direct and alternating connections with an intermediate power store, a bridge circuit, rectifier diodes and a inductive choke, German Patent DE10 221 592 A1, 4 Dec 2003
88. Sunways, Yield-oriented solar inverters with up to 98% peak efficiency. Product category. <http://www.sunways.eu/en/>
89. M. Victor, F. Greizer, S. Bremicker, U. Hubler, Method of converting a direct current voltage from a source of direct current voltage, more specifically from a photovoltaic source of direct current voltage, into an alternating current voltage, US Patent Application, Pub. No. US 2005/0286281 A1, 29 Dec 2005
90. A. Nabae, H. Magi, I. Takahashi, A new neutral-point-clamped PWM inverter. *IEEE Trans. Ind. Appl.* **17**(5), 518–523 (1981)
91. P. Knaup, International Patent Application, Pub. No. WO 2007/048420 A1, May 2007
92. M. Calais, V.G. Agelidis, M. Meinhardt, Multilevel converters for single-phase grid connected photovoltaic systems: an overview. *Sol. Energy* **66**(5), 325–335 (1999)
93. Kaco, Powador XP500-HV TL central inverter. <http://www.kaco-newenergy.com/products/solar-inverters>
94. Wikipedia, List of photovoltaic power stations, Sept 2013. http://en.wikipedia.org/wiki/List_of_photovoltaic_power_stations
95. SMA news, 114 Sunny Central 900CP XT inverters from SMA, May 2013. <http://www.sma.de/en/newsroom/current-news.html>

Chapter 2

Advanced Control of Photovoltaic and Wind Turbines Power Systems

Yongheng Yang, Wenjie Chen and Frede Blaabjerg

Abstract Much more efforts have been made on the integration of renewable energies into the grid in order to meet the imperative demand of a clean and reliable electricity generation. In this case, the grid stability and robustness may be violated due to the intermittency and interaction of the solar and wind renewables. Thus, in this chapter, advanced control strategies, which can enable the power conversion efficiently and reliably, for both photovoltaic (PV) and wind turbines power systems are addressed in order to enhance the integration of those technologies. Related grid demands have been presented firstly, where much more attention has been paid on specific requirements, like Low Voltage Ride-Through (LVRT) and reactive power injection capability. To perform the functions of those systems, advanced control strategies are presented with much more emphasis on the LVRT operation with reactive power injection for both single-phase and three-phase systems. Other control strategies like constant power generation control for PV systems to further increase the penetration level, and the improvements of LVRT performance for a doubly fed induction generator based wind turbine system by means of hardware protection solutions are also discussed in this chapter.

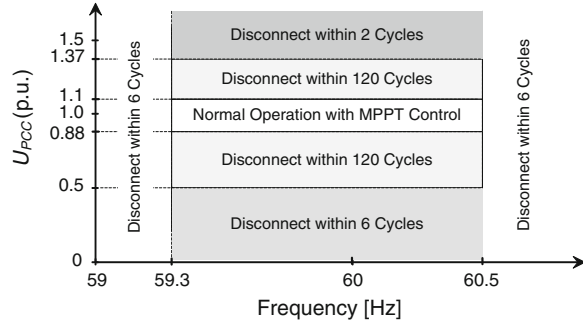
1 Introduction

Driven by a steady demand of clean and reliable electricity generation from renewable energy systems (e.g. photovoltaic and wind turbine systems), the grid requirements regarding the integration of renewable energy systems are going to

Y. Yang (✉) · F. Blaabjerg
Aalborg University, Aalborg, Denmark
e-mail: yoy@et.aau.dk

W. Chen
Zhejiang University, Hangzhou, China

Fig. 1 Example of the voltage and frequency window for PV systems in IEEE Std 929–2000 [1]



be more stringent, and thereby also the control systems. Thus, in this chapter, specific requirements for photovoltaic and wind turbine power systems are addressed firstly. Focuses are put on the advanced and intelligent control solutions for those systems to ensure an efficient and reliable electricity generation both from PV and wind turbine systems.

1.1 Grid Requirements for Photovoltaic Systems

Until currently, in most countries, the photovoltaic (PV) systems still account for a minor part of the overall electricity generation. Therefore, the Distribution/Transmission System Operators (DSOs/TSOs) impose basic grid requirements (i.e. grid codes) on those systems in order to guarantee the quality of the generated power. For example, in IEEE Std 929-2000, the Total Harmonic Distortion (THD) for the injected grid current should be lower than 5 % in normal operation to avoid adverse effects on other equipment connected to the grid [1–3]. Moreover, the boundaries of the grid voltage and frequency are also specified as shown in Fig. 1. In response to abnormal grid conditions, the PV systems are currently required to disconnect from the distributed grid for safety reasons, also known as the islanding protection. Whilst, in normal operation, the PV systems should maximize the output power, known as Maximum Power Point Tracking (MPPT).

With the rapid growth of low-voltage PV systems, the current active grid codes are expected to be modified in order to accept more PV energy in the grid [4, 5]. For the next generation PV systems, it is better to provide ancillary services, such as Low Voltage Ride-Through (LVRT), reactive power control and frequency control through active power control, in order to ensure reliable and efficient power conversion. Similar requirements are currently active for medium- and/or high-voltage applications (e.g. MW wind turbine systems and large PV power plant). For example, in Italy, it is required that the PV generation units serving low-voltage grid with the nominal power exceeding 6 kW have to ride through grid voltage faults [6]. In Germany, the medium- and/or high-voltage systems should have LVRT capability with reactive power injection [7]. Recently, a study

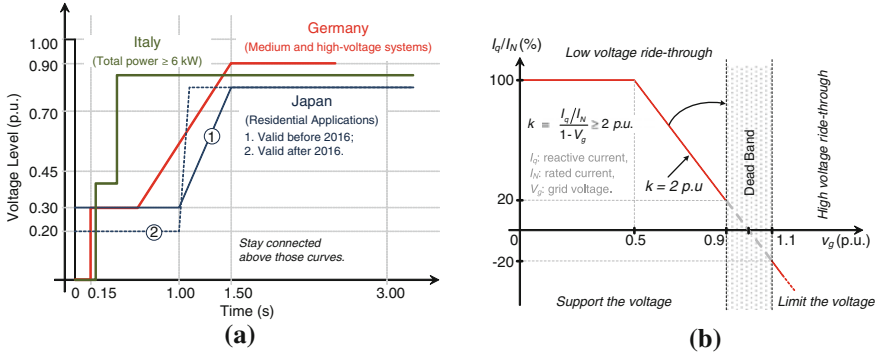


Fig. 2 a Low voltage ride-through requirements in different countries and **b** reactive current injection requirements during low voltage ride-through defined in E.ON grid code for medium and high voltage systems [7]

done in Japan presented the LVRT requirements on PV systems, which are connected to single-phase low-voltage grids [8]. Thus, the DSOs have given priority to find a solution in order to guarantee stable operation of distributed power systems and accept more PV energy. Examples of the requirements are shown in Fig. 2 [7]. Those requirements are imposed to ensure the safety of utility maintenance personnel, to protect the equipment, and also to guarantee utility stability.

Further increasing the PV penetration level can be achieved if the above ancillary services are adopted appropriately. Another solution to accept more PV energy is to reduce the maximum feed-in power from PV systems (e.g. 80 % of the nominal power) since the cut-off energy in a year is limited (e.g. 6.23 % reduction of total energy yield in Aalborg). By doing so, the distributed line capacity is also freed up. Recently, these issues have been discussed in some countries with a high penetration level of PV systems [9], e.g. Germany. In Sect. 2, control strategies are proposed and discussed in order to fulfil the above specific grid requirements.

1.2 Grid Requirements for Wind Turbine Systems

A general demand of the grid requirements for the wind power systems is that the Wind Turbine Systems (WTS) should behave as the synchronous generators based conventional power plants. During normal operation, the WTS is required to generate active and reactive power within a range around the rated voltage and frequency. The active power response speed and the reactive power capacity are restricted as well. Under grid faults, the WTS should remain connected to the grid and provide reactive power to support the grid, also referred as Fault Ride Through (FRT) requirements. The following provides a brief introduction of the grid requirements in a few countries.

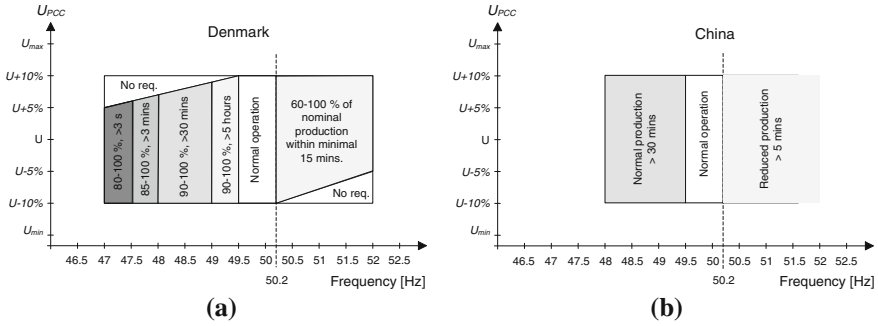


Fig. 3 Examples of voltage-frequency operation windows for WTS in **a** Denmark and **b** China

1.2.1 Grid Requirements for WTS Under Normal Operation

The grid requirements under normal operations include the frequency and voltage deviation, the active power control and the reactive power control. The requirements related to the frequency and voltage deviation demand that the WTS should operate within a range around rated voltage and frequency. Usually, this requirement can be described using three zones: (a) continuous operation zones, (b) time-limited operation zones, and (c) immediate disconnection zones, as it is shown in the example in Fig. 3 [10, 11].

The requirements on active power control demand the WTS must be equipped with active power constraint function, for example, keeping the active power constant during wind speed changes or limiting the ramp rate of the active power. In Denmark [10], three constraint functions are required for the WTS, including the absolute production constraint, the delta production constraint and the power gradient constraint.

The reactive power control requirement demand the wind power plants should regulate the output reactive power Q in response to the grid voltage variation, also known as Automatic Voltage Regulation (AVR). In general, the reactive power requirement is usually given in three different ways:

- Q control. The reactive power should be controlled independently of the active power at the point of connection.
- Power factor control. The reactive power is controlled proportionally to the active power at the point of connection.
- Voltage control. It is a function, which controls the voltage in the voltage reference point by changing the reactive power generation.

It should be noticed that the reactive power control and voltage control functions are mutually exclusive, which means that only one of the above three functions could be activated at a time.

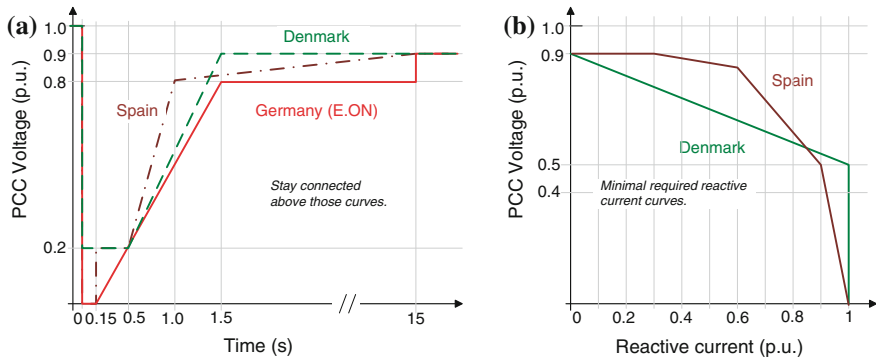


Fig. 4 **a** Low voltage ride-through requirements in different counties and **b** reactive current injection requirements during low voltage ride-through defined in Denmark and Spain

1.2.2 Grid Requirements for WTS Under Grid Faults

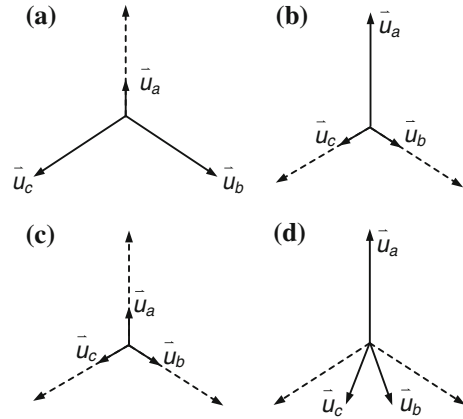
Grid faults will introduce grid voltage sags and/or swells. As more wind power plants have been connected to the grid, the grid code requires that the WTSs have to ride through grid faults for the stability concerns of the power system [5–7, 10–14]. The general requirements can be described as three aspects. (a) The WTS should remain connected during a short time of grid voltage sags and swells, known as LVRT and High Voltage Ride-Through (HVRT), respectively. (b) The WTS should provide an amount of reactive power to support the grid recovery. (c) After the fault clearance, the production of active power should be resumed at a limited rate.

LVRT Requirement

Voltage sags, due to short-circuited faults, are the most common grid faults in a power system. The voltage profiles in Germany, Denmark and Spain are shown in Fig. 4a under grid faults. The German and Spanish grid codes require that the WTSs should ride through zero voltage faults within 0.15 s, while the Danish grid code requires the WTS to ride through voltage sags with 20 % remaining voltage. The WTSs should stay connected to the grid when the voltage levels are above the curves.

Associated with the LVRT requirement, it is also stated in those grid codes (e.g. E.ON., Danish and Spanish grid codes in Figs. 2b and 4b) that the WTS should provide active and/or reactive power during the voltage dips. Normally, the reactive power support must be satisfied with the highest priority during a fault operation. The active power generation can be reduced in order to fulfill this requirement. The reactive power support requirements may differ with grid fault types in three-phase systems (e.g., three-phase fault, two-phase fault, etc.). For example, in Germany, the minimum reactive current under three-phase fault is 1.0 p.u.; while under single- and two-phase fault, the minimum reactive current is only 0.4 p.u.. Typically, the grid sags can be categorized into four fault types as they are shown in Fig. 5.

Fig. 5 Typical voltage sag types in three-phase systems
a single-phase-to-ground fault, **b** two-phase-to-ground fault, **c** three-phase-to-ground fault, **d** phase-to-phase fault



HVRT Requirement

Besides voltage dips, voltage swells are also observed in three-phase systems due to grid faults. Thus, the grid codes specify that the WTS should ride through a short time of high voltage, and at the same time absorb a certain reactive power for the stability concern, referred as HVRT. Figure 6a shows the HVRT requirements for WTSs in Germany and Spain [12, 13]. It is required for WTS to keep connected for at least 0.1 s, if the voltage at the Point of Common Coupling (PCC) reaches to 120 % of its normal value in Germany; while in Spain, the WTS should stay connected to the grid for 0.15 s under a 130 % voltage swell situation.

Similar to the LVRT operation, the WTS have to provide reactive power support to the grid during HVRT. However, instead of delivering reactive power to the grid, the WTS should absorb reactive power during HVRT operation in order to alleviate the voltage rise at PCC, as it is represented in Fig. 6b. The German grid code demands the WTS to absorb at least 1.0 p.u. reactive current during under a 120 % voltage swell situation; while in Spain, the requirement is to absorb about 0.73 p.u. reactive current under a 130 % voltage swell condition.

Recurring Fault Ride-Through

Recurring fault is also a challenge for the WTSs. Thus, the Danish grid has defined that the WTSs should withstand the recurring faults as it is summarized in Table 1 [10], and also illustrated as Fig. 7. The WTS capacity has to be sufficient to comply with the requirements specified in Table 1 if at least two independent faults specified in Table 1 occur within 2 min. The energy provided by auxiliary equipment should be sufficient in order to operate under at least six independent faults specified in Table 1 with time intervals of 5 min [10].

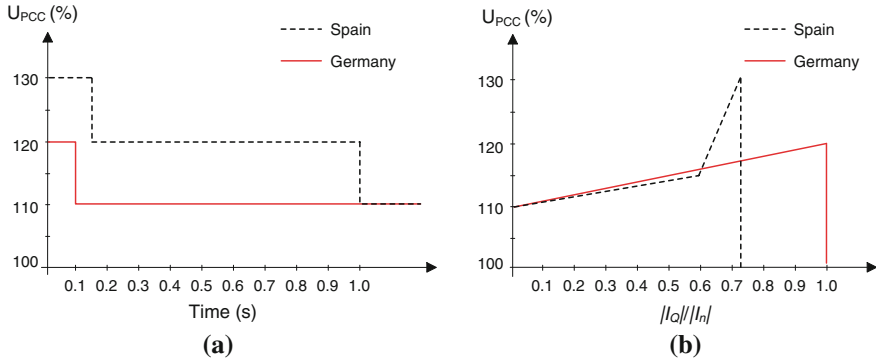
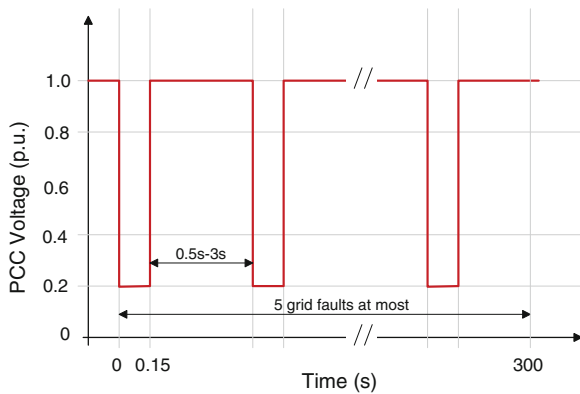


Fig. 6 **a** HVRT requirements for WTS and **b** reactive power requirements during HVRT in Germany (E.ON) and Spain

Table 1 Fault types and durations in the public electricity supply network in Denmark

Type	Fault duration
Three-phase short-circuit	Short-circuit for a period of 150 ms
Two-phase short-circuit with/without earth contact	Short-circuit for a period of 150 ms followed by a new short-circuit fault of 150 ms after 0.5–3 s
Single-phase short-circuit to earth	Single-phase-ground fault of 150 ms followed by a new single-phase-ground fault with the same duration after 0.5–3 s

Fig. 7 Voltage profile of recurring faults in the Danish grid code



2 Control of Photovoltaic Power Systems

Currently, the PV systems are dominantly for residential applications with low power ratings (single-phase, a few kW) and still account for a limited power generation in most countries. Underpinned by modern advanced power electronics

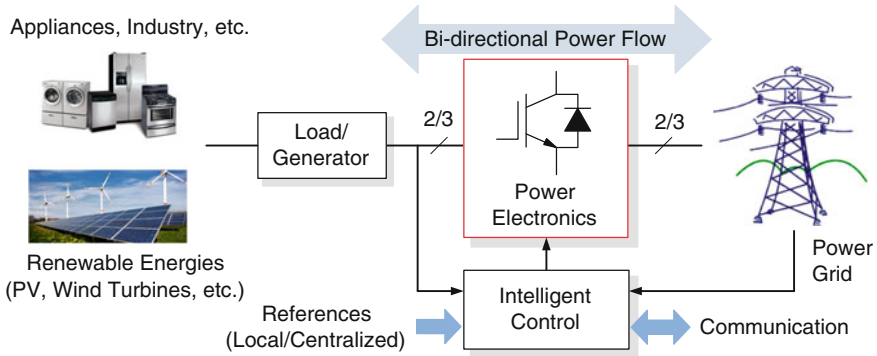


Fig. 8 Advanced modern power electronics technologies and intelligent control techniques to enable an efficient and reliable power generation from renewable energy sources

technologies, the penetration degree of those low-voltage PV systems is increasing in recent decades. Thus, ancillary services provided by PV systems are proposed in some countries [3–5]. As it is shown in Fig. 8, the power electronics converters together with intelligent control techniques in the renewable generation systems (PV systems and wind turbine systems) have this responsibility to enable the power conversion effectively and efficiently.

For a power-electronics based system as shown in Fig. 8, the power converters associated by intelligent control techniques are responsible for:

- Reliable/secure power supply,
- High efficiency, low cost, small volume, and effective protection,
- Control of active and reactive power injected into the grid, and
- Dynamic grid support (ride-through operation) and monitoring.

Therefore, in this section, advanced and intelligent control technologies of single-phase PV systems in the provision of ancillary services are discussed firstly. An overview of three-phase PV systems control technologies is presented as well. Since the injected current from a grid-connected converter is normally required to be synchronized with the grid voltage, the synchronization techniques are also discussed, together with the grid monitoring, which can improve the performance of grid-connected power converters.

2.1 Control of Single-Phase Photovoltaic Systems

Figure 9 presents the overall control diagram and functions that a PV system should provide. As for residential applications, typically, the power ratings range from 3 to 10 kW, and thus a DC/DC converter is necessary to boost the DC voltage level within an allowable range for the PV inverter (e.g. DC voltage range:

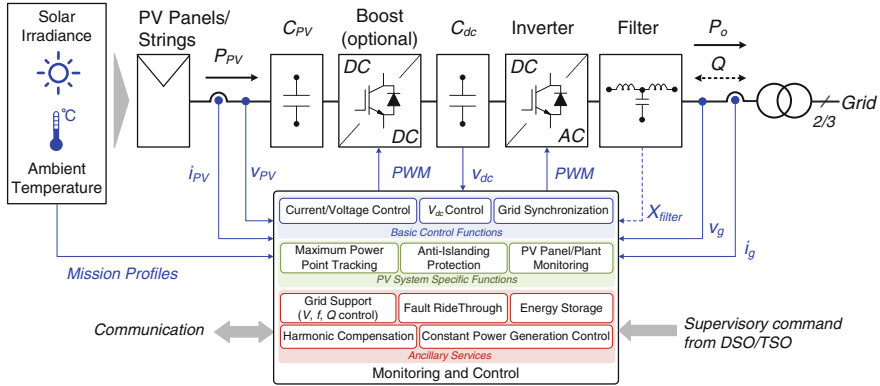


Fig. 9 Hardware schematic and control function blocks of a typical PV system with a DC/DC boost stage

200–600 V) [15, 16]. Moreover, the use of a boost converter offers flexibility to extract maximum power from the PV panels, which is a basic requirement for PV systems and known as Maximum Power Point Tracking (MPPT). There are also other basic requirements for PV systems, which should be complied with during the design and operation, such as power quality issues, grid synchronization and the anti-islanding protection. In order to perform those basic functions for PV systems, an effective monitoring system, which offers the system operation conditions (e.g. grid conditions and mission profiles), is necessary.

2.1.1 Basic Control of Single-Phase Photovoltaic Systems

The control objectives of a single-phase system [3], can be divided into two major parts according to Fig. 9:

- (1) PV-side controller, with the purpose to extract the maximum power from the input source considering mission profiles (ambient temperature and solar irradiance). In general, the protection of the DC/DC converter (boost converter) should also be taken into consideration in this controller.
- (2) Grid-side controller, with the purpose to fulfill the basic requirements. Thus, the grid-side controller can have the following tasks:

- control of the active power delivered to the grid;
- control of the reactive power exchange with the grid;
- high efficiency and high quality of the injected power;
- grid synchronization, and anti-islanding protection.

A conventional control structure for single-phase systems consists of two-cascaded loops as shown in Fig. 10 in order to fulfill the above requirements.

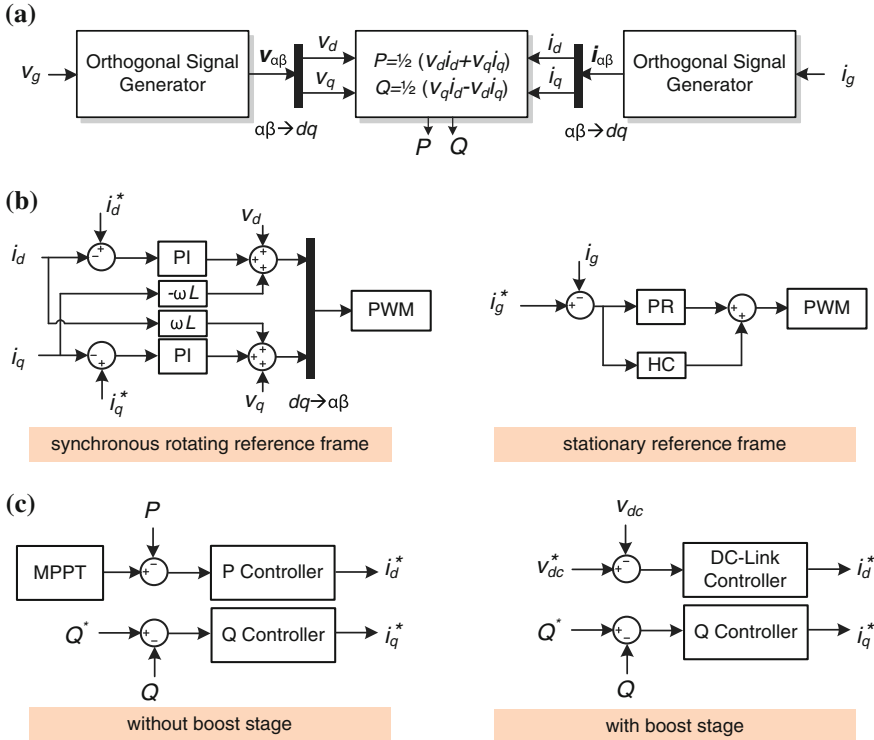


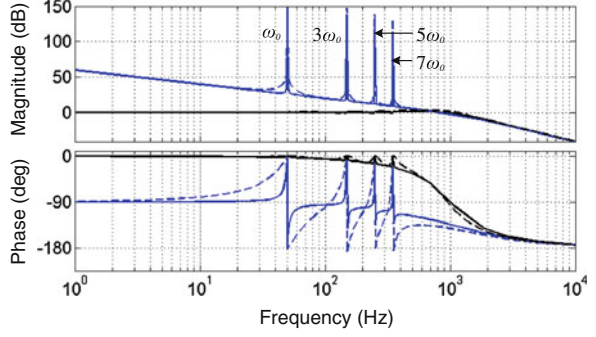
Fig. 10 Conventional single-phase dual-loop control structures with orthogonal signal generators. **a** Power calculation and signal generation. **b** Inner current control loop. **c** Outer control loop for current reference generation

Inner Current Control Loop

For the current control loop, which has the responsibilities of the power quality issues and current protection of the inverter. The existing controllers, such as Proportional Resonant (PR), Resonant Control (RSC), Repetitive Controller (RC), and Deadbeat Controller (DB) can be adopted directly [16–22]. Further, applying a Park transformation ($\alpha\beta \rightarrow dq$) lead to the possibility of Proportional Integral (PI) controllers to regulate the injected current, and afterwards, the modulation reference can be obtained by means of the inverse Park transformation ($dq \rightarrow \alpha\beta$), as it is shown in Fig. 10. Since the current control loop is responsible for the power quality, this responsibility should also be effective and valid in the design of current controllers and the *LCL*-filter. By introducing Harmonic Compensators (HCs) for the controller and adding passive damping for the filter, an enhancement of the current controller tracking performance can be achieved and the background distortion influence is alleviated [3, 16, 17, 20, 22].

The PR controller with Harmonic Compensators (PR + HC) presents a good performance in terms of accurate tracking and fast dynamic response compared to the PI controller [22]. The transfer function of this controller can be given as,

Fig. 11 Open loop (blue) and closed loop (black) Bode diagrams of the PR current controller with different sets of k_{rh} : $k_p = 22$, $k_r = k_{rh} = 500$ (solid line) and $k_r = k_{rh} = 5,000$ (dashed line), where $h = 3, 5, 7$



$$G_i(s) = k_p + k_r \frac{s}{s^2 + \omega_0^2} + \sum_{h=3,5,7,\dots} \frac{k_{rh}s}{s^2 + (h\omega_0)^2} \quad (1)$$

where k_p is the proportional gain, k_r is the fundamental resonant control gain, k_{rh} is the control gain for h -order resonant controller and ω_0 is the grid fundamental frequency. As it is shown in Fig. 11, the cascaded HCs can effectively suppress the harmonics at the corresponding resonant points if the gains are high enough.

Outer Control Loop for Current Reference Generation

The outer voltage/power control loop shown in Fig. 10 provides the system operation conditions (e.g. grid voltage amplitude and grid frequency) and then it generates a current reference, which is subsequently utilized in the inner current control loop. Thus, it offers the possibilities to add control methods into this loop to shape the injected grid current. For example, based on the single-phase PQ theory [21, 22], the injected grid current reference can be produced by regulating the averaged active power and reactive power, as it is shown in Fig. 10. This power control method is intuitive and simple, since the averaged active power and the averaged reactive power references (P^* and Q^*) can directly be set by the operators. With the help of orthogonal signal generator systems (e.g. Hilbert transform) [21], the grid current reference i_g^* can be expressed as,

$$i_g^* = \frac{1}{v_\alpha^2 + v_\beta^2} \begin{bmatrix} v_\alpha & v_\beta \end{bmatrix} \begin{bmatrix} G_P(s)(P - P^*) \\ G_Q(s)(Q - Q^*) \end{bmatrix} \quad (2)$$

where v_α, v_β are the orthogonal components of the grid voltage, respectively, P, Q are the averaged active power and reactive power, P^*, Q^* are the power references and $G_P(s), G_Q(s)$ are PI-based controllers for the active power and the reactive power, respectively. The grid current is then controlled as shown in Fig. 10.

There are also other control possibilities available for the outer control loop of a single-phase system, such as the droop-based control and the instantaneous power control [18, 21]. The droop-based power control method is implemented based on the assumption that the distributed line is mainly inductive [21]. However, in fact, the PV systems have been dominated by residential applications with low rated

power and low voltage grid. In the case of those applications, such assumption is not valid. The instantaneous power control method acts directly on the instantaneous power, and subsequently the reference current is produced. Thus, there is no need to calculate the averaged active power and reactive power for this method [18]. Nevertheless, in respects to the control of grid-connected PV systems, the basic requirements imposed by the Distributed System Operators (DSOs) and/or national committees should be followed as exactly as possible.

Grid Synchronization

The injected current into the grid has to be synchronized with the grid voltage as the standards in the field [3]. Therefore, grid synchronization algorithms play an important role for the PV systems. Moreover, in respect to the above control methods, e.g. the *PQ* control strategies, a fast and accurate synchronization system will strongly contribute to the dynamic performance and the stability margin of the whole control systems. Even for the instantaneous power control method, the syntheses of instantaneous power reference from the averaged active power and reactive power references is affected by the knowledge of the grid conditions.

Different methods to extract the phase angle have been developed and presented in many studies. Here is presented a brief description of the main methods:

- *Zero-Crossing Method*, which has the simplest implementation. However, due to the poor performances mainly when grid voltages register variations such as harmonics, it is not the optimal synchronization method.
- *Filtering of Grid Voltage*, being another possibility to extract the phase angle. With dedicated orthogonal signal generator systems, improved performance of the zero-crossing method in single-phase applications is achieved, but still, the filtering method encounters difficulty when the grid presents variations.
- *Phase Locked Loop (PLL) Technique*, has been the state-of-the-art method to detect the phase angle of the grid voltage [3, 16, 21]. This algorithm has a better rejection of grid harmonics, notches, and any other kind of disturbances. However, for single-phase applications, focuses should be paid on the creation of the orthogonal signal generator systems.

Grid Condition Monitoring (Fault Detection)

Grid condition information is very important for the control system to perform special functionalities. The voltage sag detection is the way to identify a voltage fault and it determines the dynamic performance of the voltage sag compensator for the distributed systems and the behavior of the whole control system [22–24]. For single-phase system, the Root Mean Square (RMS) method, peak value method (OSG based sag detection techniques), the missing voltage technique and wavelet transform method [22, 23] can be used to monitor the grid voltage and detect the fault.

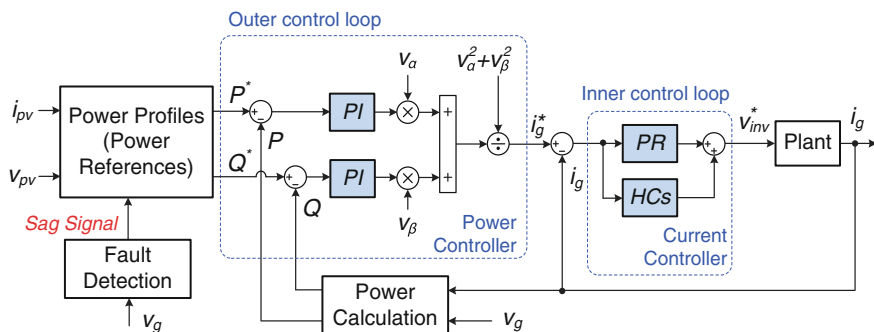


Fig. 12 Dual-loop control system of a single-phase single-stage PV system with low voltage ride through capability based on the single-phase PQ theory and $PR + HC$ current controller

2.1.2 Advanced Control of Single-Phase PV Systems Under Grid Faults

In the case of a wide-scale penetration of single-phase PV systems in the distributed grid, the disconnection due to unintentional anti-islanding protection under grid faults can contribute to: (a) voltage flickers, (b) power outages, and (c) system instability [4, 5, 21]. In order to address those issues, the current active grid codes are suggested to be modified for the PV systems with ancillary services. Some grid standards have been updated already. The next generation PV systems should be capable to ride-through low voltage and provide reactive power to support the grid at the same time. The performance of such systems under grid faults can be enhanced by a better voltage sag detection unit in terms of fast response and accuracy. Referring to Fig. 10, an intuitive and easy way for a single-phase PV system to inject reactive power during grid faults is based on the single-phase PQ theory, as it is shown in Fig. 12, including a fault detection unit.

The “Power Profiles” unit in Fig. 12 is used to generate the average active power and reactive power references for the power controllers, and subsequently, the references are regulated to produce the grid current reference. In the normal operation mode, the average active power reference P^* is the output of a MPPT system and the whole system is required to operate at unity power factor to deliver as much energy as possible to the grid. When a grid voltage fault is detected by the “Fault Detection” unit, the PV system enters into the LVRT operation mode. According to the grid requirements defined in Fig. 2b, three major possibilities are available for single-phase PV systems to inject reactive power [5, 23].

Constant Peak Current Strategy

With this control strategy, there is no risk of inverter shutdown due to overcurrent protection, as the amplitude of the injected grid current (I_{gmax}) is kept constant during the voltage sag. The injected reactive current level (I_q) is dependent of the voltage level. According to Fig. 2b, the grid peak current I_{gmax} can be set as the rated current level I_N of the PV system, for example,

Fig. 13 Representation of the grid current and the grid voltage of a single-phase PV system with constant peak current control strategy ($v_g \geq 0.5$ p.u.)

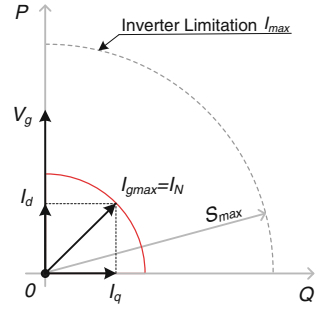
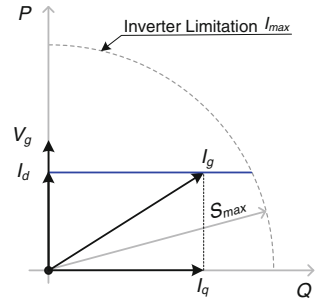


Fig. 14 Representation of the grid current and the grid voltage of a single-phase PV system with constant active current control strategy ($v_g \geq 0.5$ p.u.)



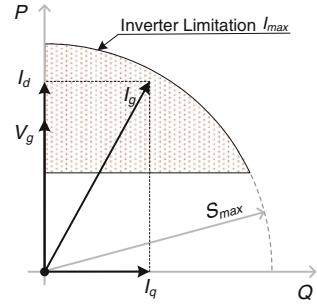
$$\begin{cases} I_{g \max} = I_N \\ I_q = k(1 - v_g)I_N \end{cases} \quad (3)$$

in which v_g is the grid voltage in p.u., $0.5 \text{ p.u.} \leq v_g \leq 0.9 \text{ p.u.}$, and $k \geq 2 \text{ p.u.}$. Based on Fig. 2b, the PV inverter should generate full reactive power ($I_q = I_N$) when $v_g < 0.5 \text{ p.u.}$. The phasor diagram for this control strategy is shown in Fig. 13, from which it can be observed that the output active power decreases ($I_d < I_N$ and $V_g < V_{gn}$) during LVRT.

Constant Active Current Strategy

Another control possibility under LVRT operation is to maintain the active current constant. For the purpose to extract as much energy from the PV panels as possible, the level of active current can be controlled to be that of the rated current ($I_d = I_N$), as it is shown in Fig. 14. The injected reactive current (I_q) is proportional to the voltage sag depth within a voltage range ($0.5 \text{ p.u.} \leq v_g \leq 0.9 \text{ p.u.}$), as it is shown in Fig. 2b. With this reactive power injection strategy, the amplitude of the injected current may exceed the inverter limitation (I_{max}). To avoid inverter shutdown owing to over-current protection, the following condition should be fulfilled during the design and the operation of a PV inverter,

Fig. 15 Representation of the grid current and the grid voltage of a single-phase PV system with constant average active power control strategy ($v_g \geq 0.5$ p.u.)



$$\sqrt{1 + k^2(1 - v_g)^2} \leq \frac{I_{\max}}{I_N} \quad (4)$$

where v_g is the grid voltage in p.u. and $k \geq 2$ p.u..

Considering a pre-designed inverter with a robustness margin, $I_{\max} = 1.25I_N$, and $k = 2$ p.u., it is not possible to utilize this control strategy to inject the required reactive power, since the minimum margin is 1.41 for $k = 2$ p.u.. In such a case, the PV system should also de-rate the active power output in order to generate sufficient reactive power to support the grid voltage recovery. Otherwise, over-rated operations may introduce failures to the whole system and shorten the inverter serving time, and thus the maintenance cost increases.

Constant Average Active Power Strategy

Similar to the constant active current control strategy, a straightforward way to maximize the output energy (i.e., to deliver maximum active power) is to keep the average active power constant during LVRT, as it is shown in Fig. 15. However, the required injection of reactive power might pose a risk of over-current operation with this control strategy. In case of this, the currents can be expressed as,

$$\begin{cases} I_d = \frac{1}{v_g} I_N \\ I_q = k(1 - v_g) I_N \end{cases} \quad (5)$$

in which v_g and k are defined previously. Thus, the following constraint should be satisfied to avoid inverter shutdown due to over-current protection.

$$\frac{1}{v_g} \sqrt{1 + k^2(v_g - v_g^2)^2} \leq \frac{I_{\max}}{I_N} . \quad (6)$$

In the design and the operation of the PV inverters, those above constraints should be considered. Especially, for the next generation PV systems, the provision of reactive power both in normal operation and under grid faults, and the requirements of LVRT will come into force in the near future. If the above aspects are not well considered, the maintenance costs and energy losses may increase.

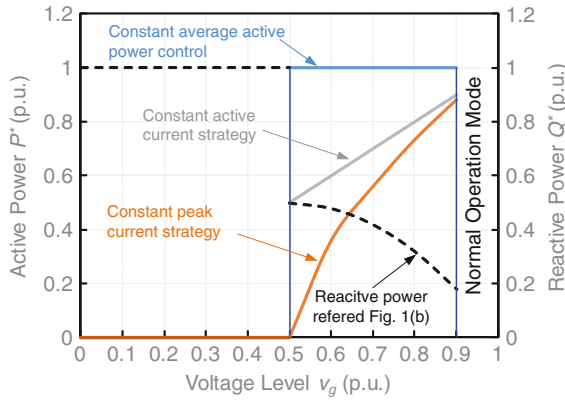


Fig. 16 Reactive power and active power references for a PV inverter under different reactive power injection strategies according to Fig. 2b

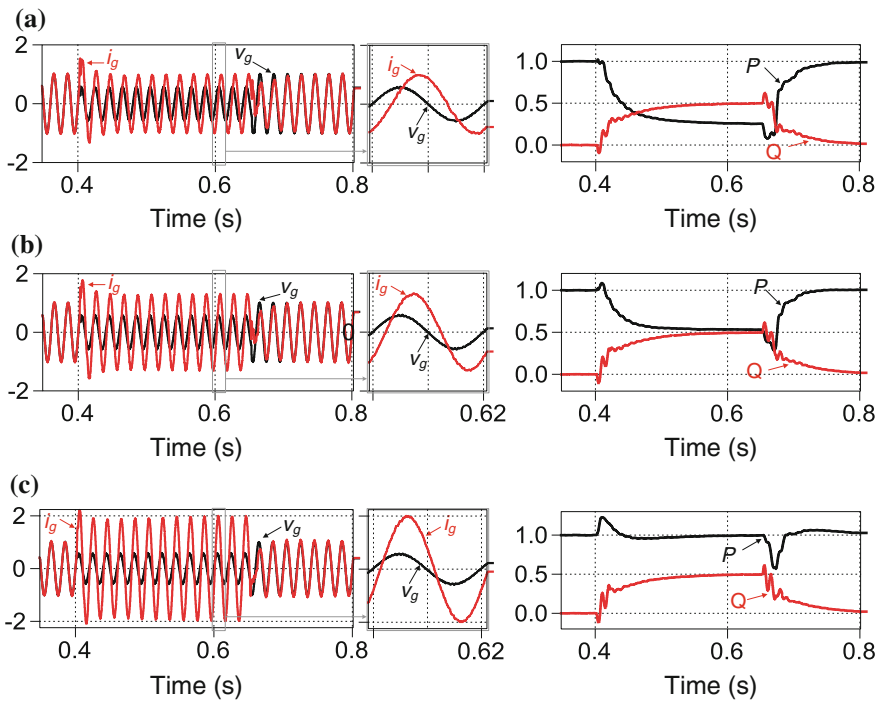


Fig. 17 Simulation results of a single-phase 1 kW PV system in LVRT operation mode with three different reactive power injection strategies: i_g , grid current [p.u.]; v_g , grid voltage [p.u.]; P , average active power [p.u.]; Q , average reactive power [p.u.]; voltage sag level: 0.45 p.u. **a** Constant peak current strategy. **b** Constant active current strategy. **c** Constant average active power strategy

The corresponding active and reactive power under different voltage sag levels for the three reactive power injection strategies discussed above can be given as shown in Fig. 16. Thus, the required reactive power can be injected under different voltage levels according to Figs. 12 and 16. Simulation results of a single-phase PV system in LVRT operation with different reactive power control strategies are given in Fig. 17. The results demonstrate the effectiveness of those reactive power injection strategies for single-phase PV systems.

2.1.3 Constant Power Generation Control of Single-Phase PV Systems

Another issue to cope with for the DSOs is to expand the power infrastructure in order to accept more PV energy in the distributed grid. This challenge is even severe in some countries with an increasing adoption of PV systems, e.g. Germany and Spain [5, 9, 25]. However, the potential cost brought by such line extensions and increased maintenances impose new obstacles. In the light of this, the DSOs are limiting PV installations in order to avoid an extension of the power infrastructure, which is against the goal of the acceptance of more renewable energy resources in those countries. Thus, seen from a total cost perspective, the line extension approach is not the optimal solution to increase PV renewable energy utilizations.

Actually, according to a study of a 3 kW single-phase PV system at a certain place with a yearly mission profile as it is shown in Fig. 18, a 20 % reduction of the maximum feed-in power from PV systems only leads to a limited reduction (6.23 %) of yearly total energy yield. Thus, it is feasible and reasonable to increase PV penetration degree without violating the line capacity by limiting the maximum feed-in power from current existing PV systems. Such issues are already being discussed in some countries where the PV systems share a large electricity generation, e.g. Germany [9]. Thus, the current active PV systems should enter into a Constant Power Generation (CPG) mode when the output reaches a certain level (e.g. 80 % of the peak power) [25, 26, 27]. The cut-off energy can be used in other systems (e.g. energy storage systems), but the total cost will increase. However, the CPG operation control for an individual PV system can be implemented by means of: (a) modifying MPPT control and/or (b) enabling an energy storage system.

With modified MPPT control in the CPG operation mode for an individual PV system, there is no need to install extra devices and thus there are no additional expenses. For a PV system with multi-string inverters connected in parallel, by shutting down a number of string-inverter based PV units, a constant power generation can also be achieved. The flowchart for a PV system with the CPG control by modifying the conventional MPPT algorithm is shown in Fig. 19.

According to Fig. 19, the operation principle is described as following:

When the PV output power P_{pv} exceeds the maximum feed-in power limitation P_{limit} , $P_{pv} > P_{limit}$, the system enters into CPG operation mode and the MPPT control is deactivated. When $P_{pv} \leq P_{limit}$, the system should deliver as much energy as possible to the grid with a MPPT control algorithm, and thus the CPG

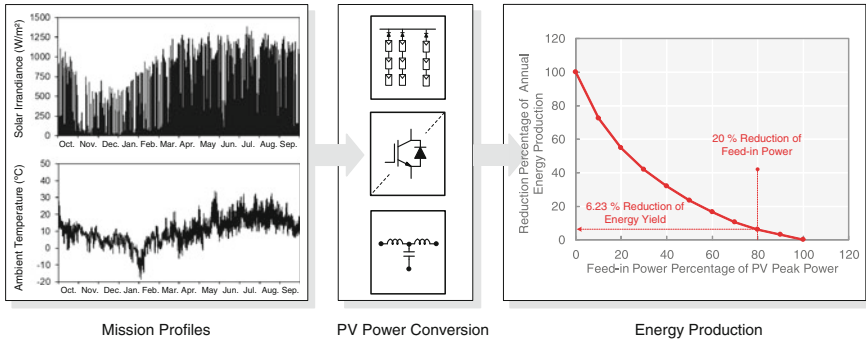
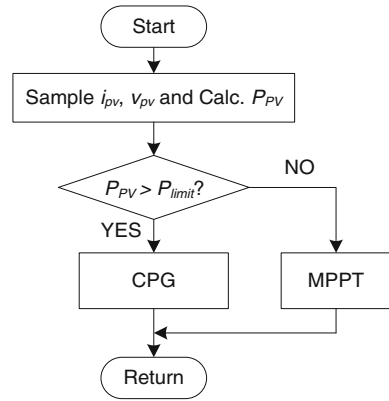


Fig. 18 Energy reduction due to the limitation of maximum feed-in power from a 3 kW single-phase PV system with a yearly mission profiles (Oct. 2011–Sept. 2012) at a certain place in Denmark

Fig. 19 Flowchart of CPG control by modifying MPPT algorithm for a single-phase PV system



control is disabled. During this period, a conventional MPPT algorithm can be adopted, such as the perturb-and-observe and incremental-conductance algorithms.

Study results of a 3 kW single-phase PV system with the CPG control by modifying MPPT algorithm are shown Fig. 20. The study demonstrates the effectiveness of the CPG method by modifying MPPT control. Thus, it is worth to investigate two main issues for the CPG control in order to increase PV penetration level in the future: (a) analyzing the reduction of the energy yield and (b) developing robust CPG control methods. It is also worth to point out that, due to the intermittency, the active power from a large PV system should be constrained to a required value, which is proportional to the possible available power. This control is known as *Delta production control* and is set to avoid imbalances or overloading in the grid in some countries for wind power plants [10]. With the

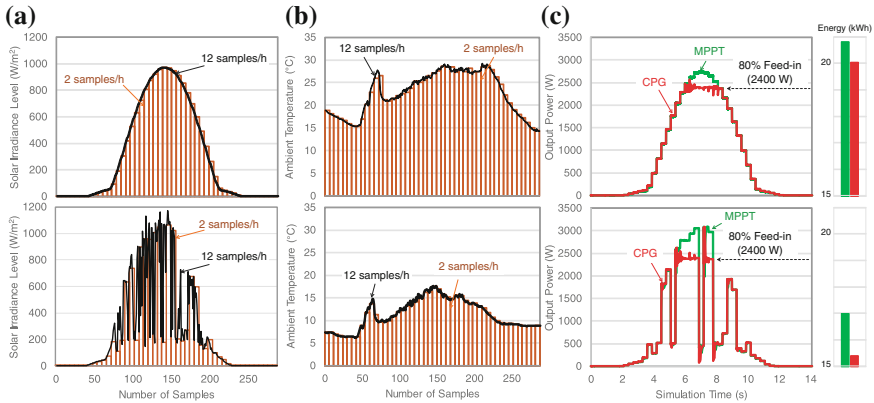


Fig. 20 Output power profiles and energy productions of a 3 kW single-phase PV system with Constant Power Generation (CPG) and MPPT control using measured daily profiles **a** Solar irradiance level (up: clear day,down: cloudy day) **b** Ambient temperature (up: clear day,down: cloudy day) **c** Output power and energy production (up:clear day, down: cloudy day)

same control objectives, such an active power constraint can also be implemented in PV systems, which consist of significantly accumulated small PV units.

2.2 Control of Three-Phase Photovoltaic Systems

Although most of the PV systems are connected to the grid with single-phase converters due to the fact that they are highly used in residential applications, there are also other systems with the same power ratings as those of wind turbine systems. For commercial or industrial purpose, the use of central inverters, ranging from tens to hundreds kilowatts, and up to several megawatts, forms three-phase systems in those applications. Compared to the control of single-phase systems, since there are more control freedoms (grid voltages, grid currents, instantaneous power, etc.), the main control issues of grid-connected three-phase PV converters are transformed through the instantaneous power theory with reference to AC current and voltage controllers [3, 16, 17]. However, since there is an interaction between voltage sequences and current sequences under unbalanced grid faults, which is opt to occur in three-phase systems, either the controlled active power or the controlled reactive power will have oscillations. In other words, the control of three-phase PV systems under grid faults is much more complicated, which will be discussed in the following.

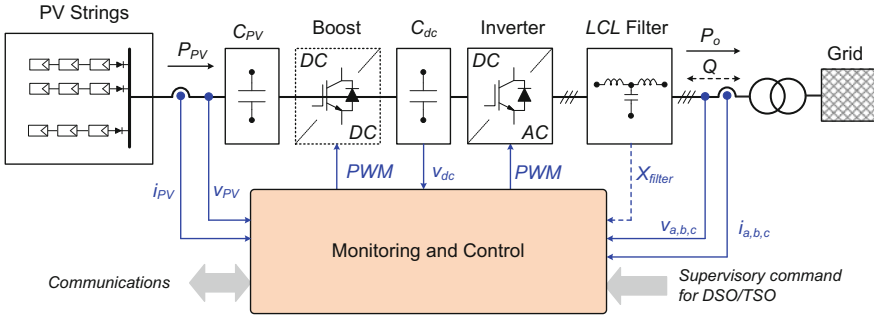


Fig. 21 Hardware schematic and general control structure of a three-phase grid-connected PV system with an *LCL*-filter

2.2.1 Basic Control of Three-Phase PV Systems

Figure 21 shows the general structure of a three-phase PV system with power feed-in functions. The main control features of such a system are similar to those of a single-phase system shown in Fig. 9, such as MPPT control, grid synchronization, reactive power control, and grid supporting features.

The boost stage functions as the input power control stage to extract the maximum power from the PV strings in normal operation. If the input voltage is sufficient for the PV inverter, it might be eliminated but results in the lack of a feasible MPPT control system. The control of the grid-side converter (three-phase PV inverter) is normally implemented by regulating the DC-link voltage in order to maintain the power balance between the PV strings and the grid. It also takes care of the power quality of the generated power by controlling the injected grid current. With the help of the instantaneous power theory and the Clark and Park transformations [3, 16], the synchronization and the control of three-phase PV inverters are easier than that of single-phase PV inverters. The control strategy applied to the three-phase PV inverters more clearly involves two cascaded loops, which have the similar responsibilities as those in single-phase systems. The implementation of the control strategy for such a three-phase PV inverter can be done in different reference frames, such as synchronous rotating (dq -), stationary ($\alpha\beta$ -), and natural (abc -) reference frame [3, 16, 17].

Control Structure in Synchronous Reference Frame

Applying the Park transformation to a three-phase variable (v_{abc} , i_{abc}) leads to the possibility of dq -control for a three-phase system. This control uses the reference frame transformation module ($abc \rightarrow dq$) to transform the grid voltage and current waveforms into a reference frame which rotates synchronously with the grid voltage. Consequently, the control variables are becoming DC quantities. Since every deviation of the grid voltage and/or the grid current will be reflected to the corresponding d - and q -axis components, it leads to an easy solution to filter and control by means of Proportional-Integral (PI) based controllers.

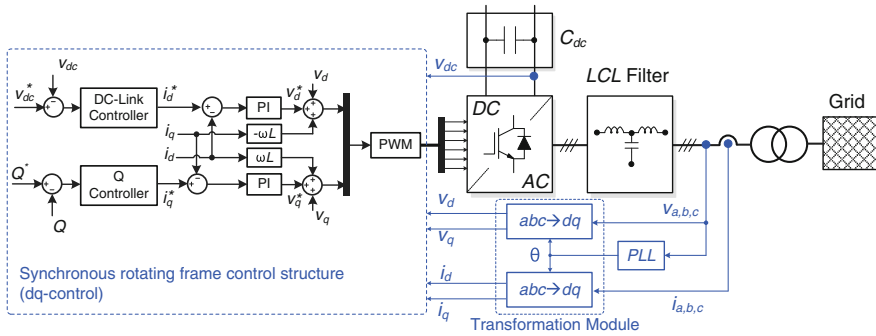


Fig. 22 General control structure of a three-phase PV inverter with synchronous rotating frame control (*dq*-control)

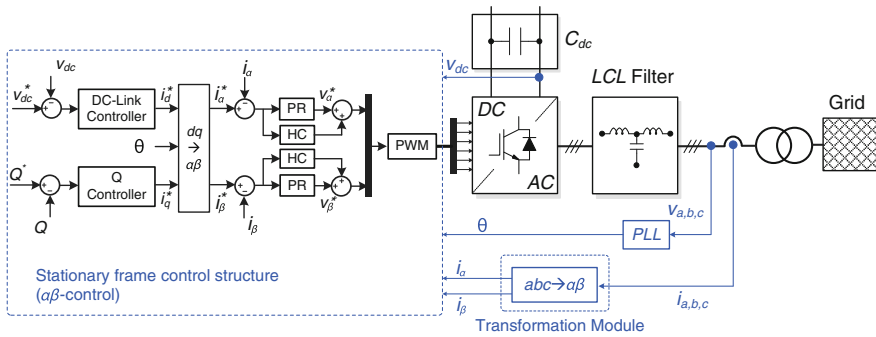


Fig. 23 General structure of a three-phase PV inverter with stationary frame control ($\alpha\beta$ -control)

Figure 22 represents the schematic of the *dq*-control for a three-phase PV inverter. In this structure, the DC-link voltage is controlled in accordance to the necessary output power. Its output is then utilized as the reference for the active current controller, whereas the reactive current reference is usually set to be zero in normal operation. When the reactive power has to be controlled in some cases, a reactive power reference must be imposed to the control system.

Since the grid currents are required to be synchronized with the grid voltage, a Phase-Locked Loop (PLL) system is also included in this control structure. It also provides the grid phase angle, which is necessary for the Park transformation model ($abc \rightarrow dq$). For this control structure, the main drawback is the poor compensation capability of the low-order harmonics in the case of PI based controllers in a grid-connected system, even when cross-coupling terms and voltage feed-forward control are adopted to improve the performance [3, 17, 29].

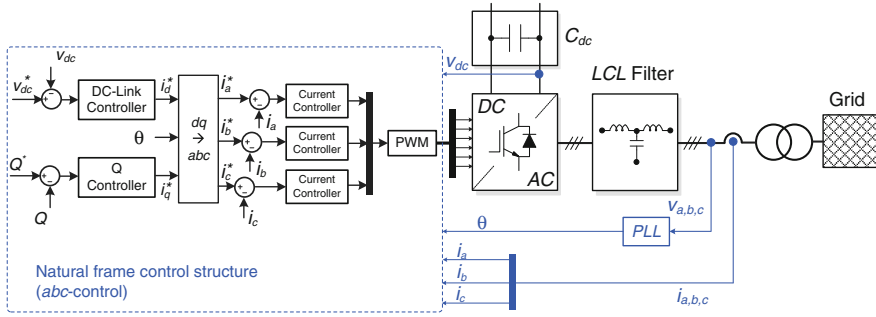


Fig. 24 General structure of a three-phase PV inverter with natural frame control (abc -control)

Control Structure in Stationary Reference Frame

Another implementation of the control loops can be done in a stationary reference frame, also known as $\alpha\beta$ -control, which is shown in Fig. 23. In case of this control structure, the control variables (e.g. grid currents) are transformed using the abc - $\alpha\beta$ module. The resultant components in the $\alpha\beta$ reference frame are sinusoidal. Since the PI controller is not good at removing the steady-state error when the signal is time varying, employment of other controllers is necessary.

As it is discussed in Sect. 2.1.1 and demonstrated in Fig. 11, the PR controller gained a large popularity due to its capability of eliminating the steady-state error when controlling sinusoidal waveforms, which is the case of $\alpha\beta$ -control. To further improve the injected current quality, Harmonic Compensators (HC) for low-order harmonics (e.g. 3rd, 5th, and 7th order harmonics) can be implemented in parallel with the PR controller, as it is shown Fig. 23. The transfer function of a PR controller with HCs (PR + HC) is represented as (1). Proved in Fig. 11, a low integral time constant k_i or k_{ih} leads to a very narrow resonant band, and thus affecting the performance of the resonant controller. Advanced PR controllers in terms of high dynamic characteristics have also been reported [30].

Control Structure in Natural Reference Frame

In the natural reference control strategy (abc -control), an individual controller is applied to each grid current. However, the configurations of the three-phase system structure, e.g. delta, star with or without isolated neutral, etc., pose a challenge for the design of the three individual current controllers. A possible implementation of abc -control is shown in Fig. 24 where the DC-link voltage is controlled to generate the active current reference. Then, the current references in dq -frame are transformed into three current references using the inverse Park transformation and the phase angle of the grid voltages. Each of the current references is compared with the corresponding measured grid current, and the error goes into the current controller, forming the reference Pulse Width Modulation (PWM) signal for the three-phase PV inverter.

In the case of an abc -controlled three-phase PV inverter, three individual current controllers are necessary to create the duty cycles for the PWM pattern, as

it is shown in Fig. 24. The existing controllers, such as PI controller, PR controller, hysteresis controller, dead-beat controller and repetitive controller [3, 17], can be adopted as the three current controllers in the natural reference frame control structure. Selection of those controllers is dependent on the control complexity and its dynamic performance.

2.2.2 Advanced Control of Three-Phase PV Systems Under Grid Faults

As it has been discussed in the previous section, the three-phase instantaneous power theory, the Park transformation and the Clark transformation offer the possibility of feasible control strategies for three-phase PV inverters in normal operations. However, operations under grid faults as required by the TSOs or DSOs increases the control complexity. According to Fig. 5, the grid faults can be classified into two major categories [3]:

- (a) symmetrical/balanced fault is very seldom in the three-phase systems, representing the same amplitude drop on all three grid voltages but no phase shifting;
- (b) asymmetrical/unbalanced fault is when the phases register an unequal amplitude drop together with phase shifting between the faulty voltages. This fault is induced by one or two phases shorted to ground or to each other.

When an asymmetrical fault occurs, the negative-sequence appears in the grid voltages and thus increases the control complexity. In respect to the control strategy under grid faults for three-phase systems, four major possibilities are available. Since the implementation of these strategies gives rise to the injection of unbalanced currents to the grid, specific current control structures, which can properly regulate the positive- and negative-sequence components, are necessary.

Unity Power Factor Control Strategy

One of the control strategies that a three-phase PV system can adopt in the case of grid faults is to maintain a unity power factor during LVRT. According to the instantaneous power theory, the most efficient set of currents, which delivers the instantaneous active power P to the grid, can be given as,

$$\mathbf{i} = g\mathbf{v}, \quad g = \frac{P}{|\mathbf{v}|^2} \quad (7)$$

in which g is the instantaneous conductance and $|\mathbf{v}|$ represents the module of the three-phase voltage vector \mathbf{v} . Under unbalanced grid faults, oscillations at twice the fundamental frequency due to the negative-sequence component will appear in $|\mathbf{v}|$, and thus high-order components will be presented in the injected currents.

It is shown in (7) that the current vector \mathbf{i} is instantaneously proportional to the voltage vector \mathbf{v} . This gives rise to the injection of no reactive power to the grid (unity power factor) since the current vector \mathbf{i} does not have any orthogonal component, which is in relation to the grid voltage. Therefore, in this control

strategy, both active and reactive instantaneous powers are controlled constant during LVRT.

Positive Sequence Control Strategy

The presence of positive-sequence components offers another control strategy for three-phase systems to follow the positive-sequence of the grid voltages. In this case, a better fault detection unit, which can detect the unbalanced grid fault, is necessary. Moreover, the detection system should have high robustness to unbalanced situation and be able to detect the positive sequences of the grid voltages. By this means, the detection of positive- and negative-sequences is the main focus of this control strategy under grid faults.

Since the locked phase angle follows the positive sequence of the grid voltages, the reference currents can be obtained for all control structures for three-phase systems in normal operation, which has been discussed previously, for example, dq -, $\alpha\beta$ -, and abc -control. However, the ripple of the DC-link voltage rises the only problem for this control strategy. This situation can be alleviated by introducing a digital filter. Nonetheless, the DC-link capacitor should be designed with appropriate ratings in order to overcome the second-harmonic ripple presenting during LVRT; otherwise, it may introduce device failures.

With the positive-sequence control, the grid currents will stay sinusoidal and symmetrical during the fault. An increase in amplitude of the grid currents will register due to the amplitude drop of the grid voltages. Since there is an interaction between voltage sequences and current sequences under grid faults, either the controlled active power or the controlled reactive power will present oscillations at twice the grid fundamental frequency during the whole fault period [3, 16, 31]. Thus, in [31], the zero-sequence control path has been introduced in the traditional three-phase system to further increase the control freedoms and to eliminate the oscillations in the controlled power.

Constant Active Power Control Strategy

Another control possibility for three-phase PV systems under grid faults is to maintain the active power constant. In the case of unbalanced grid faults which have been discussed previously, both positive- and negative-sequences will present in the grid voltages, and consequently, leading to unbalanced grid currents. According to the instantaneous power theory, both the active and reactive powers will experience oscillations at twice the grid fundamental frequency due to the unbalanced grid voltages and currents. This gives the rise to the compensation for the double-harmonic components by injecting an amount of negative-sequence in the current reference, which can be expressed as,

$$I^- = -\frac{U^-}{U^+} I^+ \quad (8)$$

where “-” and “+” denote the negative and positive sequence components of both current and voltage.

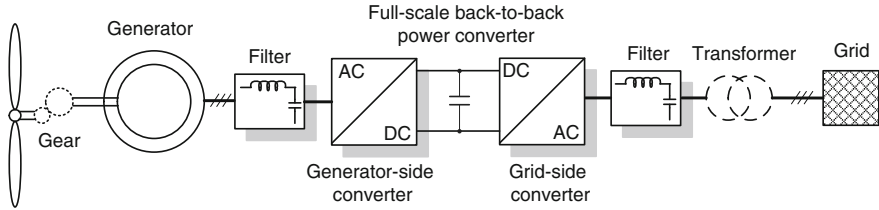


Fig. 25 Basic WTS configuration based on full-scale back-to-back power converters

When this control strategy is applied to a control structure using PI controllers for current regulation, additional controllers for the negative sequence current are needed [3, 16], but the active power can be kept constant during the grid fault. When a control structure based on a PR controller adopts this control strategy, the negative components of the current can be introduced in the current reference since this controller can regulate both positive and negative grid angular frequencies ($+\omega$ and $-\omega$). It is worth to notice that the grid currents are unbalanced during grid faults and that the reactive power presents large oscillations if this control strategy is adopted [3, 31].

Constant Reactive Power Control Strategy

Similar to the case in the constant active power control, an expression can be derived for the reactive power to cancel the double-frequency oscillations. In addition, a current vector, which is orthogonal to the grid voltage vector, can be obtained. Thus, this offers the access to independently control the reactive power if the PV inverters are required to exchange a certain amount of reactive power with the grid. In this case, the reactive power reference is not zero anymore, and it should be set as the desired value according the grid requirements once the grid fault is confirmed.

Consequently, with the above control strategies for three-phase PV systems, the grid codes regarding LVRT under grid faults can be fulfilled. The amount of the injected reactive power should be set depending on the grid requirements imposed by the TSOs or DSOs.

3 Control of Full-Scale Wind Turbine Generation Systems

The full-scale WTS mainly consists of a variable speed controlled generator, which is connected to the grid through a full-scale back-to-back power converter, as it is shown in Fig. 25 [32]. The generator can be an asynchronous generator, an electrically excited synchronous generator (WRSG) or a Permanent Magnet Synchronous Generator (PMSG). The gearbox is not necessary in this case as a heavier direct driven multi-pole generator is adopted. The typical voltage level of the full-scale back-to-back power converter is normally Low-Voltage (LV, below

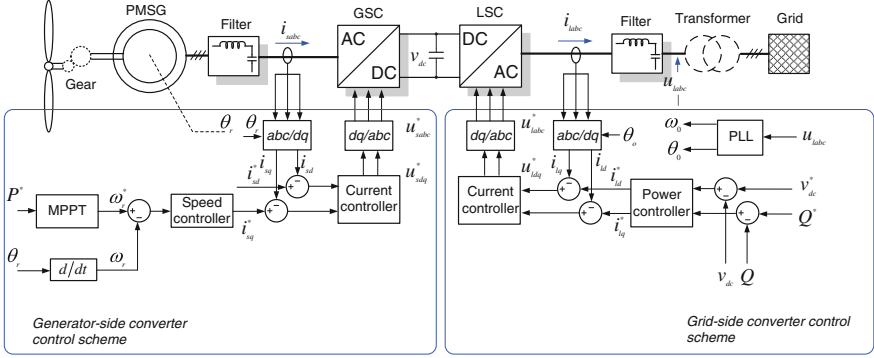


Fig. 26 Control scheme of a PMSG based full-scale back-to-back WTS

1 kV), but systems with Medium-Voltage (MV) level appear also. In the future, the voltage level might be higher so that the system can be connected to the grid without a transformer.

3.1 Basic Control of Full-Scale Back-to-Back WTS

As the full-scale back-to-back power converter works as an interface between the wind power generator and the grid, it must satisfy the requirements of both sides [33–35].

For the Generator Side Converter (GSC) as shown in Fig. 25, the current flowing in the generator stator should be controlled to adjust the generator torque and consequently the rotating speed. This will contribute to the active power balance in normal operation when the maximum power is extracted. The control schemes differ with the generator types. For example, the control structure of a PMSG based full-scale back-to-back WTS is represented in Fig. 26 [35].

When the q -axis is aligned to the rotor magnet flux, the dynamic model for a PMSG based full-scale WTS in dq -reference frames can be described as,

$$\begin{cases} u_{sd} = -R_s i_{sd} - L_s \frac{d}{dt} i_{sd} + L_s \omega_r i_{sq} \\ u_{sq} = -R_s i_{sq} - L_s \frac{d}{dt} i_{sq} + L_s \omega_r i_{sd} + \omega_r \Psi \end{cases} \quad (9)$$

in which, u_{sd} , u_{sq} and i_{sd} , i_{sq} are the stator voltage and current in dq -reference frames, respectively, R_s is the stator resistance and L_s is the stator inductance, and Ψ is the magnet flux. The electromagnetic torque is given as,

$$T_e = \frac{3}{2} p \Psi i_{sq} \quad (10)$$

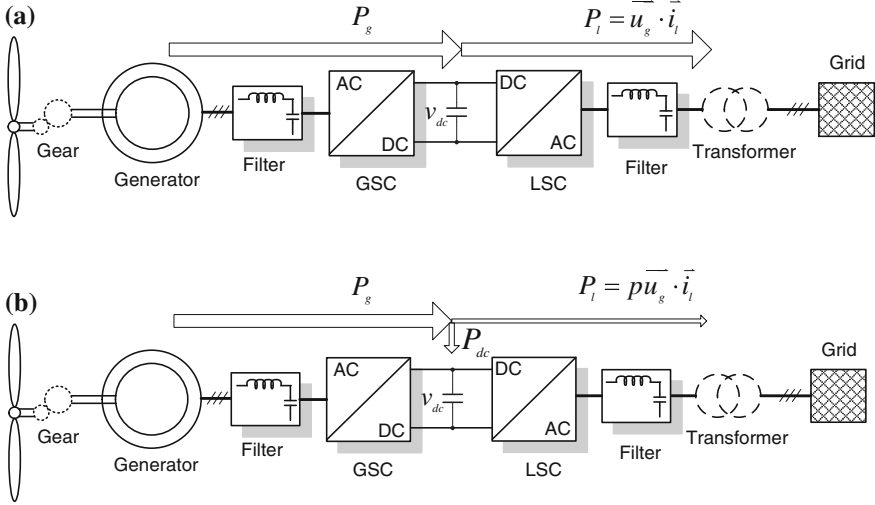


Fig. 27 Power imbalance between the GSC and the LSC of a full-scale back-to-back WTS due to voltage sags. **a** In normal situation. **b** Under grid faults

where p is the pole pairs. It can be concluded from (10) that the torque of the generator, as well as the output active power, can be controlled by controlling the q -axis stator current, as it is shown in Fig. 26.

The control scheme shown in Fig. 26 consists of a speed/power outer loop and a current inner loop. For the GSC, the rotor speed reference ω_r^* is derived from the active power reference P^* controlled by the Maximum Power Point Tracking (MPPT) system. The output of the speed controller is regarded to be the stator q -axis current reference in the inner loop. The output of the inner loop u_{sdq}^* is the voltage reference of the GSC.

For the Line-Side (grid-side) Converter (LSC), it should have the ability to control the DC-link voltage, v_{dc} , in order to ensure that the active power from the GSC can be delivered into the grid. At the same time, the ability of controlling the reactive power is required by the grid codes as well. As shown in Fig. 26, similar to the control of other grid-connected converter, the d -axis is aligned with the grid voltage vector and the DC-link voltage v_{dc} is controlled with the d -axis output current i_{sd} ; while the reactive power Q is controlled by the q -axis current i_{sq} .

3.2 Challenges of Full-Scale WTS Under Grid Faults

In a full-scale WTS shown in Fig. 26, a voltage dip induced by a grid fault has less impact on the generator, since the generator is completely isolated from the grid by the back-to-back converter. However, the power imbalance problem becomes a

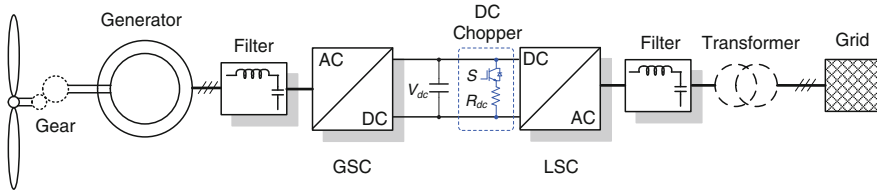


Fig. 28 Full-scale WTS with a DC-chopper for the enhancement of FRT

challenge to the WTS safety. When the grid voltage dip happens, the output active power of the LSC will decrease instantly. Nevertheless, for the generator side, because the generator is connected with the wind turbine, which has a large inertia, the output active power from the generator can only be regulated slowly. Consequently, a power imbalance between the GSC and the LSC will appear, and thus the DC-link voltage may rise, which leads to over-voltage stresses on the switching devices, as it is illustrated by Fig. 27 [36].

For the LSC, the grid voltage dips will introduce power fluctuations and DC-link voltage variations, especially for the unbalanced dips. Its performance under grid faults is similar to that of the three-phase grid-connected PV systems, which has been introduced in Sect. 2.2.

3.3 Advanced Control of Full-Scale WTS in FRT Operation

The main control objectives of a full-scale WTS under grid faults are to balance the power flow between the GSC and the LSC, in order to avoid the DC-link over-voltage, and suppress the power and DC-voltage fluctuations.

3.3.1 FRT of a Full-scale WTS with DC-Choppers

Using a DC-chopper is the simplest way to avoid over-voltage on the DC-link during FRT operation, as it is shown in Fig. 28. When the voltage dip happens and the DC-link voltage v_{dc} rises, the DC-chopper is enabled by switching S , and thus the power from the GSC is dissipated on a series-connected braking resistor R_{dc} . Hence, the energy balance is restored. The braking resistor can also work in the switching mode, and thus the performance of the DC-chopper under different voltage dip levels can be optimized. A pitch control of the wind turbine is another way to limit power from the GSC by directly reducing the input mechanical power, but the response is not fast enough to take away all the power. As a result, it usually works together with a DC-chopper under grid faults in order to enhance the FRT performance [36].

Simulation results of the DC-link voltage in a 2 MW PMSG WTS with a DC-chopper under a 50 % balanced voltage dip is presented in Fig. 29. Compared

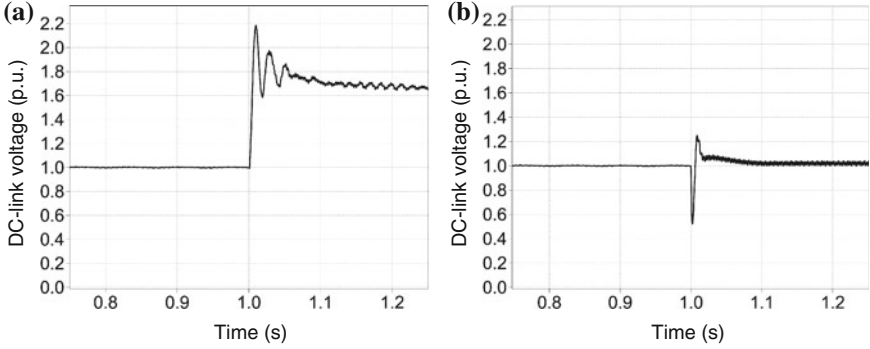


Fig. 29 Performance of a 2 MW PMSG WTS with a DC-chopper in FRT operation mode **a** without a DC-chopper, **b** with a DC-chopper

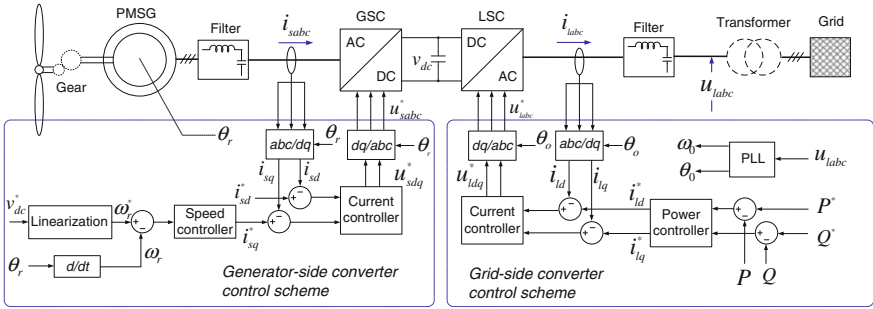


Fig. 30 DC-voltage control scheme of a full-scale PMSG based WTS

with the performance of this system without a DC-chopper in FRT operation, it can be seen that the over-voltage is significant alleviated by the DC-chopper.

3.3.2 DC-Voltage Control of a Full-Scale WTS Under Grid Faults

Another approach to limit the DC-link voltage under grid fault is to use the GSC to control the DC-bus voltage, while the LSC is used to control the output power [37, 38]. The relationship between the DC-voltage v_{dc} and the generator rotor speed ω_r is represented as,

$$C \cdot v_{dc} \cdot \frac{dv_{dc}}{dt} = -J \cdot \omega_r \cdot \frac{d\omega_r}{dt} - P_{load} + \frac{1}{2} \rho \cdot A \cdot C_p(\omega_r) \cdot v_w^3 \quad (11)$$

where C is the DC-link capacitance, J is the system inertia, ρ is the air density, A is the wind turbine swept areas, v_w is the wind speed. $C_p(\omega_r)$ is the power coefficient

of the wind turbine and it is a function of ω_r . Although the relationship is nonlinear because of $C_p(\omega_r)$, the linearization at a given operation point can be achieved with the methods introduced in [37, 38]. After the linearization, the DC-link voltage can be controlled by controlling the rotor speed in the GSC control scheme as it is shown in Fig. 30.

For the GSC, the rotor speed reference is derived from the DC-voltage reference by means of linearization, instead of MPPT control in normal situation, and the rest of the control scheme is similar to that in the normal operation.

For the LSC, the output active power P and reactive power Q is controlled in the outer loop instead of the DC-link voltage. The reactive power support can be achieved by controlling Q . If the LSC still has enough power capacity after the reactive power demand is satisfied, the MPPT control can be applied to generate active power reference P^* . Under unbalanced voltage dips, different control strategies can be applied on the LSC, which are similar to those control strategies for three-phase PV inverters and have also been discussed in Sect. 2.2.2.

3.3.3 LSC Control Under Unbalanced Faults

As for the LSC, the performance under voltage dips is similar to the three-phase PV systems under grid faults. The negative-sequence grid voltage will introduce unbalanced output current, and thus the output active and reactive power and the DC-link voltage will be fluctuated. An advanced control strategy can be used in the LSC. With different current references, desirable control effects can be achieved [16].

4 Control of Doubly-Fed Induction Generators Based Wind Turbine Systems

Although there is a trend to use full-scale power converters in WTS in recent years, the Doubly Fed Induction Generator (DFIG) based WTS with partly scale power converter is still the most widely used variable speed wind turbine until now [34]. The topology is shown in Fig. 31. The stator side of the DFIG is directly connected to the grid, while a partial-scale power converter is responsible for the control of the rotor frequency as well as the rotor speed. The power rating of the partial-scale converter settles the speed range (typically $\pm 30\%$ around the synchronous speed). Moreover, the converter performs as a reactive power compensator and a smooth grid interconnection. Smaller power converters have been the benefits of this concept from economic point of view. However, the main drawbacks are the use of slip rings, some protection schemes, and the controllability under grid faults, which will be discussed in this chapter.

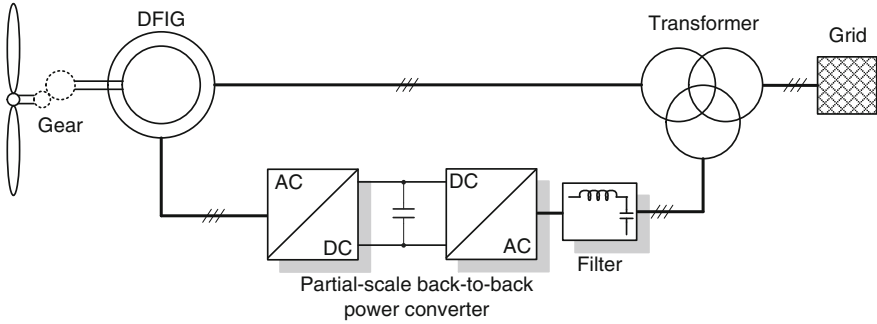
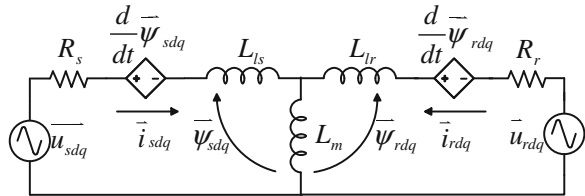


Fig. 31 DFIG based WTS configuration with partial-scale back-to-back power converters

Fig. 32 Equivalent circuit of the DFIG in the dq -reference frame



4.1 Basic Control of DFIG WTS Under Normal Situations

The control of the DFIG is achieved by regulating the partial-scale back-to-back converter. The Rotor Side Converter (RSC) controls the DFIG’s rotor speed and power, while the Grid Side Converter (GSC) controls the DC-bus voltage and performs reactive power compensation as well [39].

4.1.1 Control of the Rotor Side Converter

Vector control is one of the most widely used control schemes for the DFIG based WTS. The dq -reference frames in a vector control can be aligned either to the grid voltage or to the stator flux. The dynamic model of the DFIG under grid voltage oriented dq -reference frames can be expressed as,

$$\begin{cases} \bar{u}_{sdq} = R_s \bar{i}_{sdq} + \frac{d}{dt} \bar{\psi}_{sdq} + j\omega_0 \bar{\psi}_{sdq} \\ \bar{u}_{rdq} = R_r \bar{i}_{rdq} + \frac{d}{dt} \bar{\psi}_{rdq} + j\omega_s \bar{\psi}_{rdq} \end{cases} \quad (12)$$

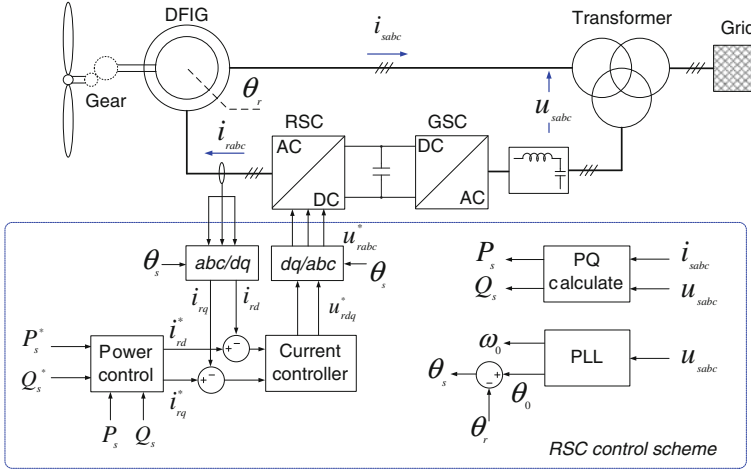


Fig. 33 Voltage oriented vector control scheme for the RSC of a DFIG based WTS

$$\begin{cases} \bar{\psi}_{sdq} = L_s \bar{i}_{sdq} + L_m \bar{i}_{rdq} \\ \bar{\psi}_{rdq} = L_r \bar{i}_{rdq} + L_m \bar{i}_{sdq} \end{cases} \quad (13)$$

where $\bar{u}_{sdq} = u_{sd} + ju_{sq}$ and $\bar{u}_{rdq} = u_{rd} + ju_{rq}$ are the stator and rotor voltages, \bar{i}_{sdq} and \bar{i}_{rdq} are the stator and rotor currents, $\bar{\psi}_{sdq}$ and $\bar{\psi}_{rdq}$ are the stator and rotor flux linkage, respectively, L_m , L_s , and L_r are the magnetizing inductance, stator inductance and rotor inductance, R_s , and R_r are the stator and rotor resistances, respectively. Since the d -axis is aligned with stator (grid) voltage vector, the following is valid,

$$u_{sd} = U_g \text{ and } u_{sq} = 0. \quad (14)$$

Based on (12) and (13), a T-shaped equivalent circuit of the DFIG can be obtained, as it is shown in Fig. 32 where L_{ls} and L_{lr} are the stator and rotor leakage inductances and $L_s = L_m + L_{ls}$, $L_r = L_m + L_{lr}$.

The active power and reactive power output from the stator side of DFIG can be derived from (12) and (13), and can be expressed as (15). It can be concluded that the stator output active power is related to the rotor d -axis current and the reactive power is related to the rotor q -axis current only. As a result, the active and reactive power can be adjusted separately by controlling the rotor dq currents. The grid voltage-oriented vector control scheme for the RSC of the DFIG is shown in Fig. 33, which consists of an inner current loop and an outer power loop. PI controllers are typically used in the inner loop to regulate the dq currents, whereas the PR controllers can be used to enhance the control performance under distorted grid voltages [3].

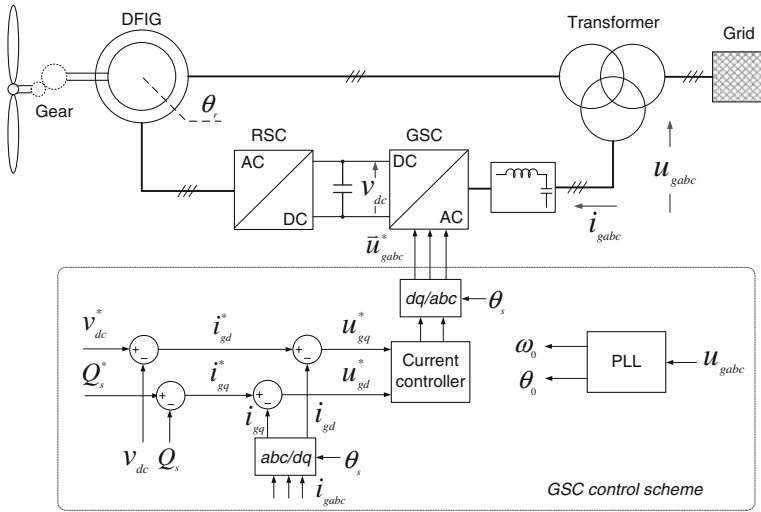


Fig. 34 Control scheme for the GSC of a DFIG based WTS

$$\begin{cases} P_s = -U_g \frac{L_m}{L_s} \cdot i_{rd} \\ Q_s = U_g \frac{L_m}{L_s} \cdot i_{rq} + \frac{U_g^2}{\omega_1 L_s} \end{cases} \quad (15)$$

4.1.2 Control of the Grid Side Converter

The control scheme of the GSC in a DFIG WTS is similar to that in a full-scale back-to-back WTS. As it is shown in Fig. 34, the GSC is controlled by regulating the DC-link voltage and the reactive power.

4.2 Challenges of the DFIG WTS Under Grid Faults

The main drawback of the DFIG WTS is its poor controllability under grid faults. As the stator of the DFIG is directly connected to the grid, the voltage dips induced by the grid faults, either balanced or unbalanced, will normally generate a natural flux, which stand still with the stator windings, resulting in large voltage and current transients. Furthermore, under unbalanced dips, a negative sequence component will also appear which makes the situation even worse [40–43].

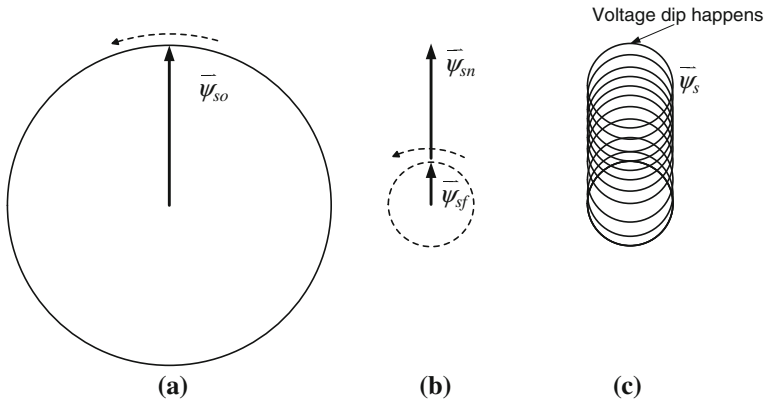


Fig. 35 Trajectory of the stator flux in the DFIG during a 80 % voltage dip: **a** before the voltage dip, **b** at the dip moment, **c** after the voltage dip

Fig. 36 The stator dq-flux of DFIG after a 50 % voltage dip

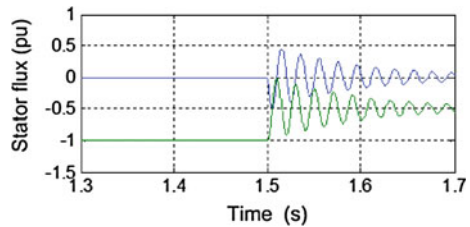
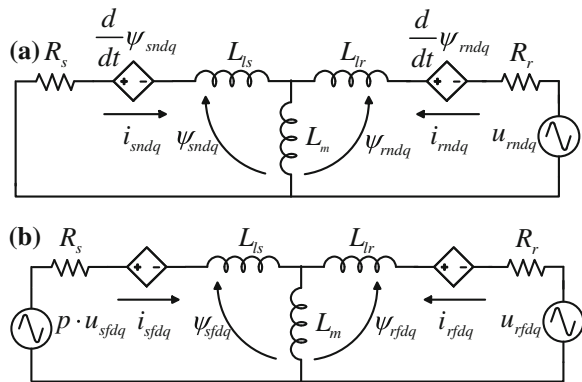


Fig. 37 Equivalent circuits of the DFIG during voltage dips: **a** the natural machine and **b** the forced machine



4.2.1 Performance of the DFIG Under Symmetrical Grid Faults

The symmetrical grid faults will normally introduce balanced voltage dips at the terminal of a DFIG WTS. The stator voltage drops instantly when a grid fault happens. According to the flux conservation principle, the stator flux cannot change

at the speed of stator voltage drop, and thus a natural flux $\bar{\psi}_{sdq}$ will hereby appear, which can be expressed as,

$$\bar{\psi}_{sn} = \frac{p \cdot \bar{u}_s}{j\omega_0} \quad (16)$$

where p is the voltage dip level.

Consequently, the stator flux after the voltage dips is the sum of two components with different frequencies. One is the stator natural flux ($\bar{\psi}_{sn}$) produced by the voltage dips, which is a DC component in the stator static reference frame, and the other is the stator forced flux ($\bar{\psi}_{sf}$) produced by the remaining grid voltage, which is rotating with the grid voltage vector and with the grid frequency. The trajectory of the stator flux after a 80 % voltage dips is shown in Fig. 35, and the stator flux in dq -reference frame is shown in Fig. 36.

According to the superposition principle, the dynamic model of DFIG under balanced voltage dips can be described with two independent equivalent circuits.

(a) The natural machine is short-circuited while the natural flux $\bar{\psi}_{sn}$ exists in the stator winding, and (b) the forced machine is the remaining grid voltage and no transient flux exists [42]. The natural and forced machine in dq reference frame is shown in Fig. 37. Where $\bar{\psi}_{sndq}$, $\bar{\psi}_{rndq}$, $\bar{\psi}_{sfdq}$ and $\bar{\psi}_{rfdq}$ are the stator and rotor flux in the natural and forced machine, respectively and $\bar{\psi}_{sndq} = \psi_{snd} + \psi_{snq}$, \bar{i}_{sndq} , \bar{i}_{rndq} , \bar{i}_{sfdq} and \bar{i}_{rfdq} are the stator and rotor current in the natural and forced machine, respectively. u_{rndq} , \bar{u}_{sfdq} and \bar{u}_{rfdq} are the rotor voltage in the natural machine and stator, rotor voltage in the forced machine, respectively.

The rotor Electro-Motive Force (EMF) in the natural machine and forced machine can be expressed as (17) and (18), respectively.

$$\bar{e}_m \approx -\frac{L_m}{L_s} j\omega_r e^{-\frac{t}{\tau_s}} \bar{\psi}_{sn} \quad (17)$$

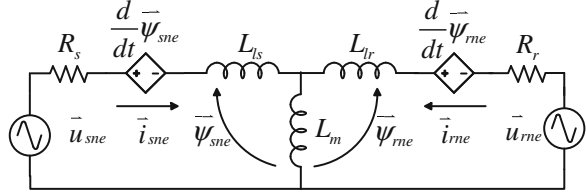
$$\bar{e}_{rf} \approx -\frac{L_m}{L_s} j\omega_s \bar{\psi}_{sf} \quad (18)$$

where τ_s is the damping time constant of the stator natural flux, if the rotor is open-circuited for the natural machine,

$$\tau_s = \frac{L_s}{R_s} \quad (19)$$

As the DFIG usually operates under the rotor speed around synchronous speed (0.7–1.2 p.u.), the rotor speed ω_r is much larger than the slip speed ω_s . As a result, the EMF produced by the stator natural flux will be much larger than the rotor EMF in the normal situations, which may result in large transient current in rotor and destroy the RSC.

Fig. 38 Equivalent negative machine model of the DFIG



4.2.2 Performance of the DFIG Under Asymmetrical Grid Faults

During asymmetrical grid faults, unbalanced voltage dips will be introduced at the terminal of the WTS, and be accompanied with phase jumps in some cases.

Besides of the stator natural and forced flux, a stator negative flux will also be introduced by the negative-sequence grid voltage. Another equivalent circuit—the negative machine, can be used to analyze the performance of DFIG, together with the natural machine and the forced machine [43]. The equivalent model is shown in Fig. 38.

The stator voltage in the negative machine is the negative-sequence grid voltage, and the rotor EMF produced by the negative-sequence stator flux is represented in (20). Compared to (17) and (18), it can be concluded that the rotor EMF produced by the stator flux with the same amplitude in the negative machine is much larger than that in the forced machine, and even larger than that in the natural machine.

$$\bar{e}_{rne} \approx \frac{L_m}{L_s} j(\omega_0 + \omega_r) \bar{\psi}_{sne} \quad (20)$$

With the existing of the forced flux and the negative-sequence flux, the steady-state stator flux trajectory after asymmetrical grid fault will be an ellipse. The stator flux trajectory under a single phase to ground fault is shown in Fig. 39a.

The stator natural flux produced during the asymmetrical grid faults not only depends on the fault types and voltage dip levels, but also depends on the time when the fault happens. If the fault happens at $t = T_0$ when the positive and negative-sequence grid voltage have the opposite directions, the sum of stator forced and negative flux after fault will be the same as the stator flux before the fault, and thus the stator natural flux will be zero, it is shown in Fig. 39b. When the fault happens at $t = T_0 + \pi/2$, the stator natural flux will be maximum, as it is shown in Fig. 39c, and in this case, it can be given as,

$$\bar{\psi}_{sn}|_{t=T_0+\frac{\pi}{2}} = \frac{2}{3} p \cdot \frac{\bar{u}_s}{j\omega_0} \quad (21)$$

The rotor EMF produced by the natural machine can be calculated by (17) as well. Under asymmetrical grid fault, the RSC has to deal with not only the natural and forced rotor EMF, but also the negative-sequence EMF. The RSC may be saturated under serious voltage dips.

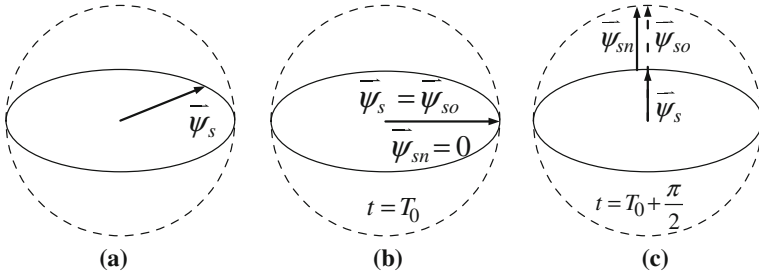


Fig. 39 Trajectory of the stator flux during asymmetrical grid faults: **a** the steady state after faults, **b** the situation with zero natural flux and **c** the situation with the maximal natural flux

Fig. 40 Grid voltage during a recurring grid fault, from the recovery of the first grid fault until the next grid fault happens

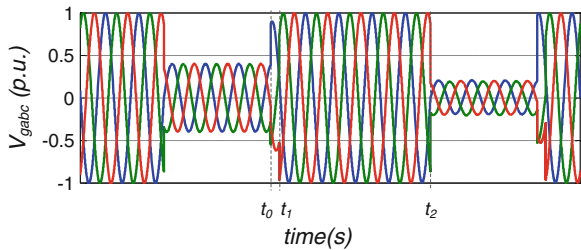


Table 2 Stator natural flux produced by the voltage recovery

θ	85°	75°	60°	45°
$\vec{\psi}_{sdqn} _{t=t_3}$	$0.124 \cdot \frac{P \cdot \vec{u}_{sdq}}{j\omega_0}$	$0.366 \cdot \frac{P \cdot \vec{u}_{sdq}}{j\omega_0}$	$0.707 \cdot \frac{P \cdot \vec{u}_{sdq}}{j\omega_0}$	$\frac{P \cdot \vec{u}_{sdq}}{j\omega_0}$

4.2.3 Performance of the DFIG Under Recurring Grid Faults

The new grid codes in some counties (e.g. Denmark) demand the WTS to ride through multiple grid faults which are happening within a certain time range, also known as recurring faults immunity. An example of two three-phase symmetrical recurring faults is shown in Fig. 40. These recurring faults last for 100 ms from the recovery of the first grid fault to the next one.

The performance of the DFIG during the first voltage dip will be the same as that in the single voltage fault. The analysis started at $t = t_0$ when the grid voltage starts recovering. The recovery of the three-phase voltage will take place gradually in most cases, as the breakers in power systems can only open at the current zero-crossing points. The grid voltage comes back to normal conditions at $t = t_1$. During t_0 and t_1 , the three-phase symmetrical fault will become a two-phase asymmetrical fault, and this period lasts for 5 ms normally.

After t_1 , the grid voltage reaches the normal condition, but a natural flux will be introduced, similar to the case of voltage dips. However, the natural flux produced

by the voltage recovery is normally smaller than that under voltage dips, depending on the angle between fault current and voltage (θ), as shown in Table 2. Moreover, since the grid voltage is normal after the grid recovery, the torque and the power fluctuations brought by the natural current with the same amplitude will be larger than that under voltage dips.

The next grid fault happens at $t = t_2$. If the natural flux produced by the voltage recovery has been decayed before t_2 , the performance of the DFIG under the next voltage dip will be the same as that under a single voltage dip. However, if the natural flux produced by the voltage recovery still exists at t_2 , it may be superposed on the natural flux produced by the next voltage dip, as it is shown in (22).

$$\bar{\psi}_{sn}|_{t=t_2} = \bar{\psi}_{sn_r} + \bar{\psi}_{sn_d} \quad (22)$$

in which $\bar{\psi}_{sn_r}$ is the remaining natural flux when the next voltage dip comes and $\bar{\psi}_{sn_d}$ is the natural flux produced by the next voltage dip. If this happens, the stator natural flux after the second grid fault may be larger than that in single dips, which will normally result in large transient current and voltage on the rotor side.

4.3 Advanced Control of the DFIG WTS in FRT Operation

The FRT of the DFIG WTS can be achieved by applying the advanced control strategies to the RSC. However, since the rotor EMF produced by the stator natural and negative flux is higher than that in normal situation, the RSC may be saturated when the voltage dip level is high. In that case, a breaking chopper is required on the DC-link in order to prevent the over-voltage.

The advanced control strategies for the DFIG WTS under grid faults aim at accelerating the damping of the natural flux as well as limiting the rotor current. Nonetheless, normally, a trade-off has to be made between the two control objectives. Two advanced control strategies are introduced in this section. One is the demagnetizing current control, which focuses on accelerating the damping of natural flux, and the other is the stator and rotor current control, which aims at limiting the stator and rotor current.

4.3.1 Demagnetizing Current Control

The demagnetizing current control proposed by D. Xiang et al. [44, 45] uses the rotor current to accelerate the damping of the stator natural flux. The relationship between rotor natural current and stator natural flux in the natural machine can be derived from (12), (13) and Fig. 37a. It can be given as,

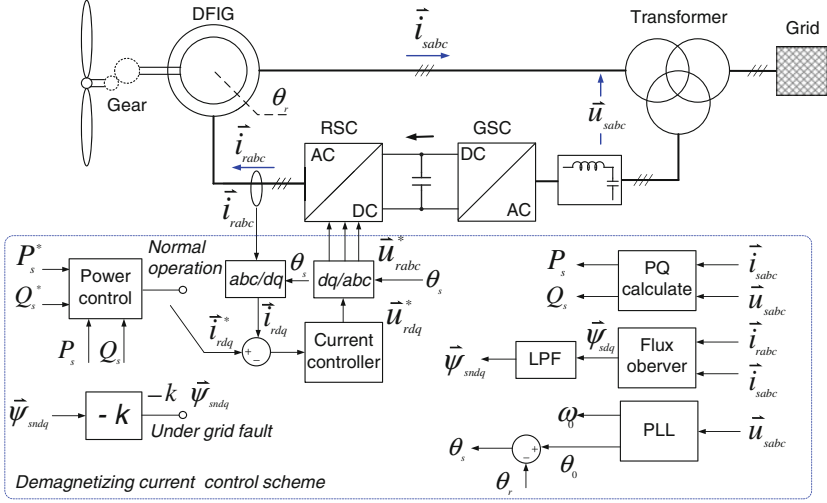


Fig. 41 Control scheme of demagnetizing control for a DFIG WTS

$$\frac{d}{dt} \bar{\psi}_{sn} = -\frac{R_s}{L_s} \bar{\psi}_{sn} + \frac{L_m}{L_s} R_s \bar{i}_{rm}. \quad (23)$$

From (23), it can be concluded that if the rotor current \bar{i}_{rm} is in the opposite direction with the stator natural flux $\bar{\psi}_{sn}$ as shown in (24), the damping of $\bar{\psi}_{sn}$ will be accelerated. The demagnetizing control is set based on (24), with the control scheme shown in Fig. 41.

$$\bar{i}_{rm} = -k \bar{\psi}_{sn} \quad (24)$$

The stator flux in the dq -reference frame $\bar{\psi}_{sdq}$ is obtained from the flux observer; the stator natural flux in dq -reference frame is with the frequency of ω_0 , while the forced flux is the DC-component. Therefore, the stator natural flux $\bar{\psi}_{sdq}$ can be separated through a Low Pass Filter (LPF). Under grid faults, the current reference is calculated based on (24) and the damping of the stator flux will be accelerated. Noticed that the larger the rotor demagnetizing current is, the faster the damping of stator natural flux becomes. A simulation in a 1.5 MW DFIG WTS under a 50 % symmetrical voltage dip is shown in Fig. 42. The parameters of the DFIG used in the simulations are listed in Table 3. Compared with the normal vector control, it can be seen how the damping of the stator flux is accelerated. However, in order to achieve better damping performance on the stator natural flux, a large rotor current cannot be avoided. At the same time, the demagnetizing current may introduce torque fluctuations with the stator flux, as shown in Fig. 42a.

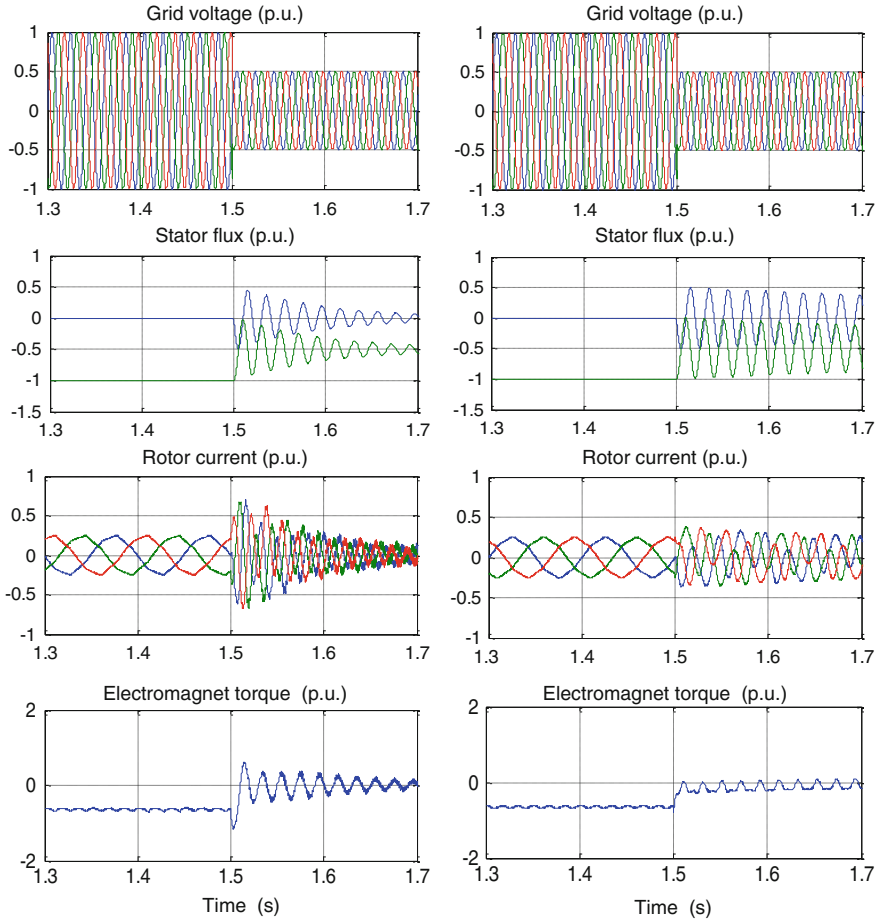


Fig. 42 Simulation results of a 1.5 MW DFIG WTS under 50 % symmetrical voltage dips: **a** with demagnetizing current control and **b** with normal vector control

Table 3 Parameters of the 1.5 MW DFIG used in the simulations

Rated power	1.5 MW	Mutual inductance L_m	4.00 mH
Rated line-to-line voltage	690 V	Stator inductance L_s	4.05 mH
Stator resistance R_s	2.139 mΩ	Rotor inductance L_r	4.09 mH
Rotor resistance R_r	2.139 mΩ	Stator-rotor ratio n_{sr}	0.369

4.3.2 Stator and Rotor Current Control

Besides accelerating the damping of the stator natural flux, limiting the rotor and stator current is another major task for the DFIG systems under grid faults. A simple control strategy is proposed F.K.A. Lima et al. [46] to limit the stator and

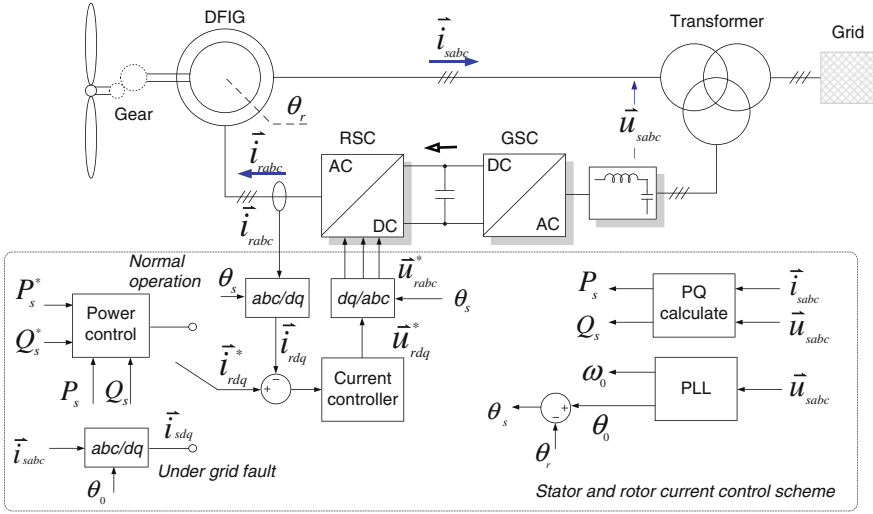


Fig. 43 Control scheme of the stator and rotor current control for a DFIG WTS

rotor currents, by applying the stator current as the rotor current reference under grid faults, which is shown in (25).

$$\vec{i}_r^* = \vec{i}_s \quad (25)$$

Therefore, the rotor current in the natural and forced machine models may be derived from (25) and (13), and expressed as (26).

$$\vec{i}_{rm} = \frac{\vec{\psi}_{sn}}{L_s + L_m} \quad \text{and} \quad \vec{i}_{rf} = \frac{\vec{\psi}_{sf}}{L_s + L_m} \quad (26)$$

If the voltage rate of the RSC is large enough to control the rotor current as expressed in (26), the rotor current during grid fault can be limited. However, since the rotor natural current here has the same direction with the stator natural flux, the damping ability on the stator natural flux may not be as good as that in demagnetizing current control. The control scheme of this control strategy is shown in Fig. 43. During the voltage dips, the rotor current reference is switched from the output of the outer power control loop to the stator current. The control structure is simple and the flux observer is not needed.

The simulation results of a 1.5 MW DFIG WTS with stator and rotor current control is shown in Fig. 44a, and also compared with the normal vector control (Fig. 44b). The rotor current is significantly reduced by the stator and rotor current control. However, the damping of the natural flux is not accelerated. The torque fluctuation is smaller than that in the demagnetizing current control, and almost the same as that in the normal vector control.

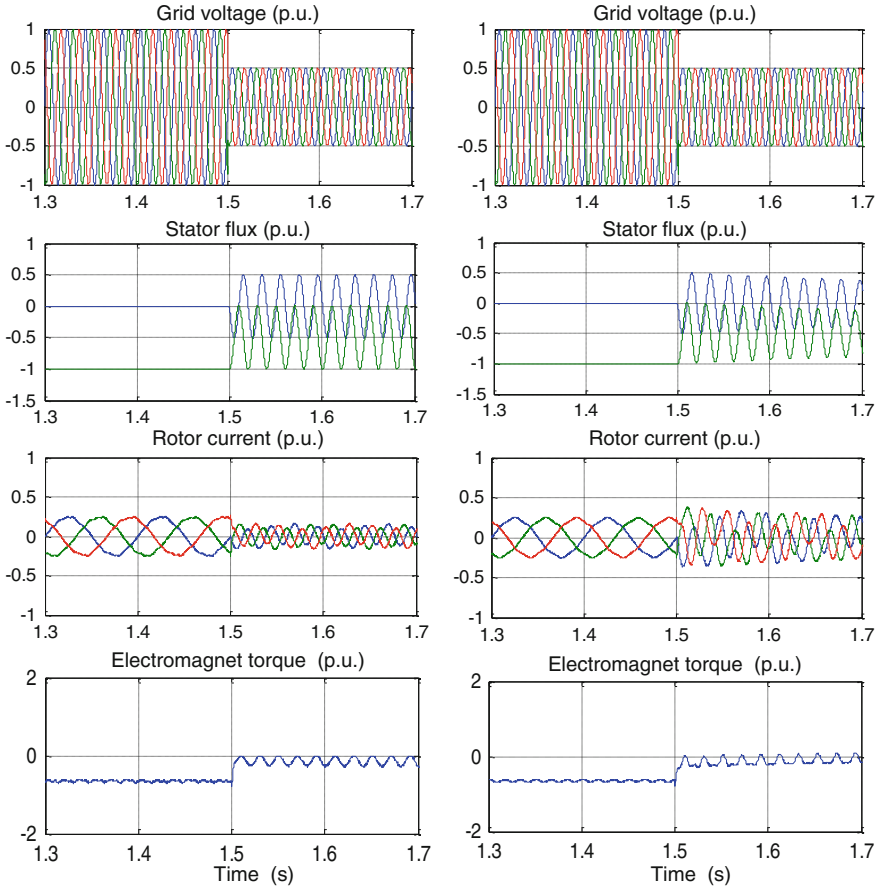


Fig. 44 Simulation results of a 1.5 MW DFIG WTS under 50 % symmetrical voltage dips: **a** with stator and rotor current control and **b** with normal vector control

4.4 Hardware Protections for the DFIG Under Grid Faults

Although it is a cost-efficient way to ride through the grid fault by applying advanced control strategies, the hardware protection is still necessary under serious voltage sags. Since the rotor EMF produced by the stator natural and negative-sequence flux may be much larger than the maximum output voltage of the RSC, the RSC may be saturated and the generator might be out of control. On the other hand, the extra power in the rotor circuit need to be dissipated as the power delivery ability of the GSC is reduced with the voltage dips. In this case, hardware solutions are necessary to protect the RSC and help the DFIG ride through grid faults.

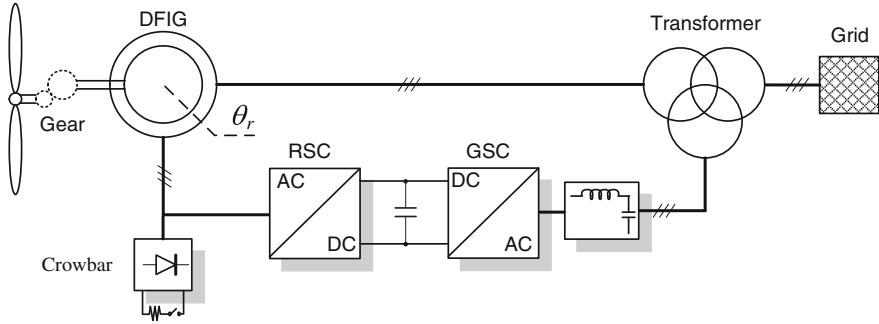


Fig. 45 A DFIG WTS with rotor side crowbar

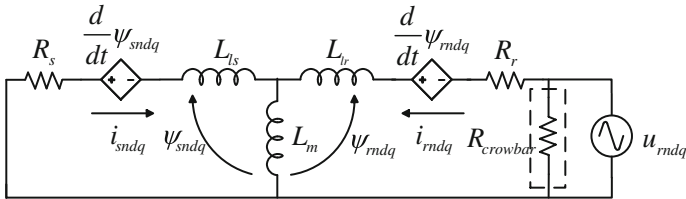


Fig. 46 Equivalent circuit of the natural machine with rotor side crowbar

4.4.1 Rotor Side Crowbar

A rotor side crowbar can short-circuit the rotor side of DFIG under grid faults with a resistance, so the rotor transient current will flow through the crowbar instead of the RSC, as shown in Fig. 45 [41]. The equivalent circuit of the natural machine in a DFIG with the rotor side crowbar is shown in Fig. 46. With the application of the rotor side crowbar, the rotor current and stator current are limited, and the damping of the stator natural flux can be accelerated.

The value of the crowbar resistance must be designed carefully to meet the FRT requirements. If the crowbar resistance is too small, the rotor and stator current will still be very large. If the crowbar resistance is too large, the voltage on the crowbar will be too high and it may give a rise to the DC-link voltage of the RSC. This may cause over-voltage on the switching devices.

Besides the additional cost, the major drawback of the crowbar is that the rotor side is short-circuited, when the crowbar is enabled. Thus, in this case, the DFIG works as a caged generator and the DFIG is out of the RSC control. Since the magnetizing current cannot be provided by the RSC, the stator will absorb reactive power from the grid, which is against the grid requirements.

To overcome these drawbacks, the rotor side crowbar can be enabled only for a short-period after the voltage dips, and then cut off from the rotor side as long as

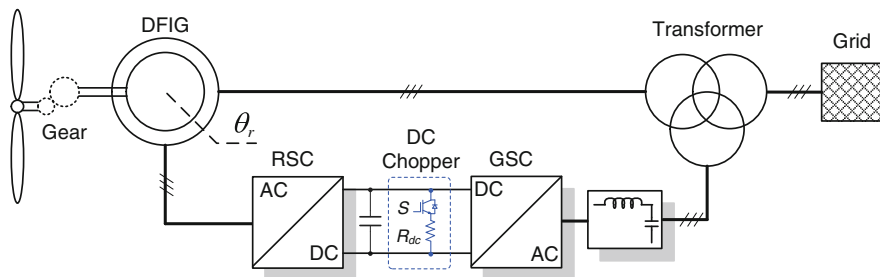


Fig. 47 A DFIG WTS with DC-chopper

the natural flux is damped. By doing so, the output voltage of RSC is large enough to control the DFIG. Advanced control schemes can be cooperated with the crowbar to shorten its operating time. However, for the asymmetrical faults, as the rotor EMF brought by the stator negative-sequence flux is so large, the crowbar has to be enabled all the time during the voltage dips.

4.4.2 DC-Chopper

In order to avoid the overvoltage on the DC-link of the RSC, a breaking chopper is usually added on the DC-link. When the DC-link voltage surpasses the limit, the DC-chopper can be connected in order to consume the energy, as it is shown in Fig. 47 [47].

If the RSC is disabled when the DC-chopper is activated at the DC-link, the DC-chopper will act as the rotor side crowbar from the rotor side point of view. The DFIG will be out of control and the stator side will absorb a large amount of reactive power from the grid. However, the DC-chopper is usually cooperated with the advanced control strategies. When the RSC is saturated and/or when the rotor EMF is too large for the RSC to handle, the DC-chopper can consume the power fed to the DC-link and thus avoid over-voltage on the DC capacitor. The safety operation is guaranteed under serious voltage dips.

The DC-chopper can also be used together with a crowbar. In this case, the rotor current can be shared between the DC-chopper and the rotor-side crowbar. The activating time of the rotor side crowbar can somehow be reduced.

4.4.3 Series Dynamic Breaking Resistor

The rotor side crowbar uses a resistor, which is parallel connected to the RSC in order to limit the rotor current. Another approach is to connect the resistor in series with the RSC in the rotor side, or with the DFIG in the stator side, or both, as it is shown in Fig. 48 [48].

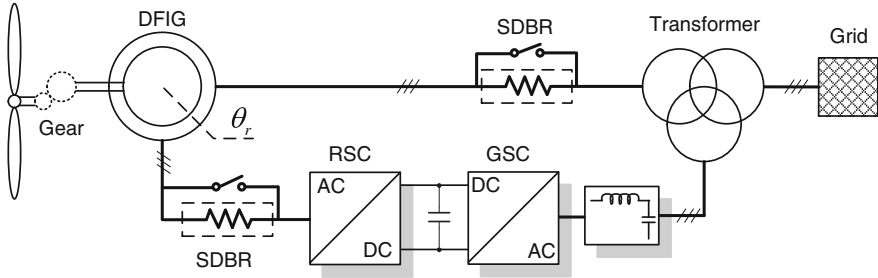


Fig. 48 A DFIG WTS with the series dynamic breaking resistor

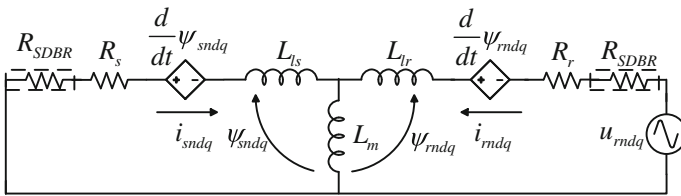


Fig. 49 Equivalent circuit of the natural machine with stator and rotor SDBR

This so-called Series Dynamic Breaking Resistor (SDBR) can limit the rotor current, and accelerate the damping of the stator natural flux at the same time. The equivalent circuit of the natural machine with stator and rotor SDBR is shown in Fig. 49. The stator and rotor resistance is increased by the SDBR, so the rotor and stator current can be significantly limited. Moreover, the voltage drop across the SDBR will reduce the output voltage demand of the RSC. Further, the increase of the stator resistance will accelerate the damping of the natural flux.

4.4.4 Dynamic Voltage Restorer and Other Wind Farm Solutions

The Dynamic Voltage Restorer (DVR) uses a converter in series connected with the stator side of the DFIG in order to compensate voltage dips, as shown in Fig. 50. In normal situation, the output voltage of the DVR is controlled to be zero. When the grid voltage drops, the DVR will generate a voltage to compensate the voltage dips, so the stator side will not “see” the voltage dips and no stator natural or negative sequence flux will be introduced [49, 50]. The DVR can also be placed between the transformer and the grid, so that the GSC will not influenced by the voltage dip either.

Since the stator voltage of the DFIG will not decrease with the compensation of the DVR, no special control strategies are needed for the RSC. However, the major drawback of the DVR is its high cost. An additional converter is required together

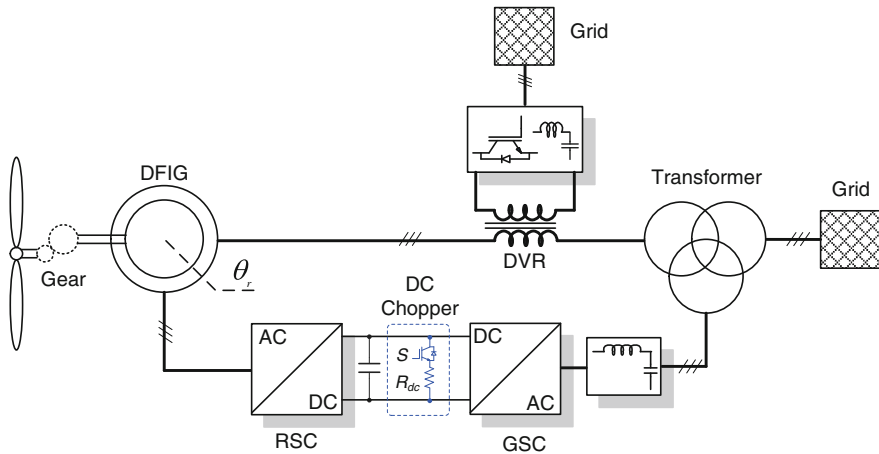


Fig. 50 A DFIG WTS with a dynamic voltage restorer

with a transformer of large power rating, which is connected to the stator side. The DVR can also be connected to the AC-bus of wind farms, known as Static Synchronous Series Compensator (SSSC). With an accurate control, all the WTSs in a wind farm will experience only a very short time of voltage dips, and the stator voltage remains in normal during the operation.

Moreover, the STATCOM has been widely used in modern wind farms, since it can provide reactive power support during the voltage dips. It can also rise the line voltage, and compensate the reactive power absorbed by the DFIG when the crowbar is activated.

5 Summary

To meet the imperative demand of a clean and reliable electricity generation, more efforts have been made on the integration of solar and wind energies. In this case, the grid stability and robustness may be violated due to the intermittency and interaction of the solar and wind renewables. Advanced and intelligent control solutions applied to the power electronics systems, discussed in this chapter, can enable the power conversion efficiently and reliably. As shown in this chapter, the power ratings range from several kilowatts to few megawatts, which covers residential PV applications and megawatts wind power plants. Related grid demands, which will be more stringent, have been presented firstly.

In respect to single-phase applications, mostly residential PV systems, advanced and intelligent control strategies have been discussed considering a wide-scale adoption of photovoltaic energy. For instance, the LVRT, which has been a basic requirement for wind turbine systems, has been investigated for

low-voltage PV systems. Three possible reactive power injection strategies can be adopted for a single-phase PV system under grid faults: (a) constant peak current control, (b) constant active current control and (c) constant average active power control strategy. In order to further increase the PV penetration level, a constant power generation control strategy has been developed in this chapter.

For commercial applications, the PV systems also include central inverters with high power ratings (e.g. tens to hundreds of kilowatts), forming three-phase systems. The control strategies for such systems are similar to those for the grid-side converter in WTs. The differences lie in the control of the rotating machines, e.g. two commonly used generators—PMSG and DFIG, and the injection of the positive- and/or negative-sequence currents under grid faults. Four major strategies are available for such systems: (a) unity power factor control, (b) positive sequence control, (c) constant active power control and (d) constant reactive power control. The implementations of such control strategies can be done in dq -, $\alpha\beta$ -, and abc -reference frames. Improvements of LVRT for DFIG based WTs by means of hardware protection solutions have also been discussed in this chapter, like using the rotor side crowbar, the DC-chopper, the SDBR and the DVR.

References

1. IEEE Std 929-2000, *IEEE Recommended practice for utility interface of photovoltaic (PV) systems*, Apr 2000, ISBN 0-7381-1934-2 SH94811
2. F. Blaabjerg, Z. Chen, S.B. Kjaer, Power electronics as efficient interface in dispersed power generation systems. *IEEE Trans. Power Electron.* **19**(5), 1184–1194 (2004)
3. F. Blaabjerg, R. Teodorescu, M. Liserre, A.V. Timbus, Overview of control and grid synchronization for distributed power generation systems. *IEEE Trans. Ind. Electron.* **53**(5), 1398–1409 (2006)
4. Y. Xue, K.C. Divya, G. Griepentrog, M. Liviu, S. Suresh, M. Manjrekar, Towards next generation photovoltaic inverters, in *Proceedings of ECCE'11*, pp. 2467–2474, 17–22 Sept 2011
5. Y. Yang, P. Enjeti, F. Blaabjerg, H. Wang, Suggested grid code modifications to ensure wide-scale adoption of photovoltaic energy in distributed power generation systems, in *Proceedings of IEEE IAS Annual Meeting*, pp. 1–8, 6–11 Oct 2013
6. Comitato Elettrotecnico Italiano, CEI 0-21: Reference technical rules for connecting users to the active and passive LV distribution companies of electricity. <http://www.ceiweb.it/>
7. E. ON GmbH, Grid Code—High and extra high voltage. <http://www.eon-netz.com/>
8. H. Kobayashi, Fault ride through requirements and measures of distributed PV systems in Japan, in *Proceedings of IEEE-PES General Meeting*, pp.1–6, 22–26 Jul 2012
9. D. Rosenwirth, K. Strubbe, Integrating variable renewables as Germany expands its grid, 2013. <http://www.renewableenergyworld.com/>
10. Technical Regulation 3.2.5, Technical regulation 3.2.5 for wind power plants with a power output greater than 11 kW, *Energinet*, 2011. <http://www.energinet.dk>
11. GB/T-19963-2011, Technical rule for connecting wind farm to power system, *The National Standard of China*, 2012. <http://www.sac.gov.cn/>
12. Transmission Code 2007, Networks and system rules of the german transmission system operators, *VDN-e.v. beim VDEW*, Aug 2007. <http://www.vdn-berlin.de>

13. Resolution P.O. 12.3, Response requirements against voltage dips in wind installations, *Red Electrical*, Mar 2006. <http://www.ree.es>
14. Requirements for offshore grid connections in the E.ON nets network, *E.ON*, 2008. <http://www.eon-netz.com>
15. S.B. Kjaer, J.K. Pedersen, F. Blaabjerg, A review of single-phase grid-connected inverters for photovoltaic modules. *IEEE Trans. Ind. Appl.* **41**(5), 1292–1306 (2005)
16. R. Teodorescu, M. Liserre, P. Rodriguez, *Grid Converters for Photovoltaic and Wind Power Systems*. (Wiley, Chichester, 2011)
17. A. Timbus, M. Liserre, R. Teodorescu, P. Rodriguez, F. Blaabjerg, Evaluation of current controller for distributed power generation systems. *IEEE Trans. Power Electron.* **24**(3), 654–664 (2009)
18. S.A. Khajehoddin, M. Karimi-Ghartemani, A. Bakhshai, P. Jain, A power control method with simple structure and fast dynamic response for single-phase grid-connected DG systems. *IEEE Trans. Power Electron.* **28**(1), 221–233 (2013)
19. S. Xu, J. Wang, J. Xu, A current decoupling parallel control strategy of single-phase inverter with voltage and current dual closed-loop feedback. *IEEE Trans. Ind. Electron.* **60**(4), 1306–1313 (2013)
20. M. Ciobotaru, R. Teodorescu, F. Blaabjerg, Control of single-stage single-phase PV inverter, in *Proceedings of EPE'05*, pp. P.1–P.10, 2005
21. Y. Yang, F. Blaabjerg, Z. Zou, Benchmarking of grid fault modes in single-phase grid-connected photovoltaic systems. *IEEE Trans. Ind. Appl.* **49**(5), 2167–2176 (2013)
22. Y. Yang, F. Blaabjerg, Low voltage ride-through capability of a single-stage single-phase photovoltaic system connected to the low-voltage grid. *Int. J. Photoenergy* **2013**, 9 (2013). Open Access. <http://dx.doi.org/10.1155/2013/257487>
23. Y. Yang, F. Blaabjerg, H. Wang, Low voltage ride-through of single-phase transformerless photovoltaic inverters. *IEEE Trans. Ind. Appl.*, May/June 2014 <http://dx.doi.org/10.1109/TIA.2013.2282966>
24. O.C. Montero-Hernandez, P.N. Enjeti, A fast detection algorithm suitable for mitigation of numerous power quality disturbances. *IEEE Trans. Ind. Appl.* **41**(6), 1684–1690 (2005)
25. Y. Yang, F. Blaabjerg, H. Wang, Constant power generation of photovoltaic systems considering the distributed grid capacity, in *Proceedings of IEEE APEC'14*, Mar 2014
26. A. Ahmed, L. Ran, S. Moon, J.-H. Park, A fast PV power tracking control algorithm with reduced power mode. *IEEE Trans. Energy Conversion.* **28**(3), 565–575 (2013)
27. H. Beltran, E. Bilbao, E. Belenguer, I. Etxeberria-Otadui, P. Rodriguez, Evaluation of storage energy requirements for constant production in PV power plants. *IEEE Trans. Ind. Electron.* **60**(3), 1225–1234 (2013)
28. C. Fitzer, M. Barnes, P. Green, Voltage sag detection technique for a dynamic voltage restorer. *IEEE Trans. Ind. Appl.* **40**(1), 203–212 (2004)
29. E. Twining, D.G. Holmes, Grid current regulation of a three-phase voltage source inverter with an *LCL* input filter. *IEEE Trans. Power Electron.* **18**(3), 888–895 (2003)
30. A.G. Yepes, F.D. Freijedo, O. Lopez, J. Doval-Gandoy, Analysis and design of resonant current controllers for voltage-source converters by means of Nyquist diagrams and sensitivity function. *IEEE Trans. Ind. Electron.* **58**(11), 5231–5250 (2011)
31. K. Ma, M. Liserre, F. Blaabjerg, Power controllability of three-phase converter with unbalanced AC source, in *Proceedings of IEEE APEC'13*, pp. 342–350, Mar 2013
32. Z. Chen, J.M. Guerrero, F. Blaabjerg, A review of the state of the art of power electronic for wind turbines. *IEEE Trans. Power Electron.* **24**(8), 1859–1875 (2009)
33. M. Liserre, R. Cardenas, M. Molinas, J. Rodriguez, Overview of multi-MW wind turbine and wind parks. *IEEE Trans. Ind. Electron.* **58**(4), 1081–1095 (2011)
34. F. Blaabjerg, M. Liserre, K. Ma, Power electronics converters for wind turbine systems. *IEEE Trans. Ind. Appl.* **48**(2), 708–719 (2012)
35. M. Chinchilla, S. Arnaltes, J.C. Burgos, Control of permanent-magnet generators applied to variable-speed wind-energy systems connected to the grid. *IEEE Trans. Energy Convers.* **21**(1), 130–135 (2006)

36. J.F. Conroy, R. Watson, Low-voltage ride-through of a full converter wind turbine with permanent magnet generator. *IET Renew. Power Gener.* **1**(3), 182–189 (2007)
37. X. Yuan, F. Wang, D. Boroyevich, Y. Li, R. Burgos, DC-link voltage control of a full power converter for wind generator operating in weak-grid systems. *IEEE Trans. Power Electron.* **24**(9), 2178–2192 (2009)
38. K.H. Kim, Y.C. Jeung, D.C. Lee, H.G. Kim, LVRT scheme of PMSG wind power system based on feedback linearization. *IEEE Trans. Power Electron.* **27**(5), 2376–2384 (2012)
39. R. Pena, J.C. Clare, G.M. Asher, Doubly fed induction generator using back-to-back PWM converters and its application to variable speed wind-energy generation. *Proc. Inst. Elect. Eng.—Elect. Power Appl.* **143**(3), 231–241 (1996)
40. G. Abad, J. Lopez, M.A. Rodriguez, L. Marroyo, G. Iwanski, *Doubly Fed Induction Machine, Modeling and Control for Wind Energy Generation*, (Wiley, Hoboken, 2011)
41. J. Morren, S.W.H. De Haan, Ride through of wind turbines with doubly-fed induction generator during a voltage dip. *IEEE Trans. Energy Convers.* **20**(2), 435–441 (2005)
42. J. Lopez, E. Gubia, P. Sanchis, X. Roboam, L. Marroyo, Wind turbines based on doubly fed induction generator under asymmetrical voltage dips. *IEEE Trans. Energy Convers.* **23**(1), 321–330 (2008)
43. J. Lopez, P. Sanchis, X. Roboam, L. Marroyo, Dynamic behavior of the doubly fed induction generator during three-phase voltage dips. *IEEE Trans. Energy Convers.* **22**(3), 709–718 (2007)
44. D. Xiang, L. Ran, P.J. Tavner, S. Yang, Control of a doubly-fed induction generator in a wind turbine during grid fault ride-through. *IEEE Trans. Energy Convers.* **21**(3), 652–662 (2006)
45. S. Hu, X. Lin, Y. Kong, X. Zhou, An improved low-voltage ride-through control strategy of doubly fed induction generator during grid faults. *IEEE Trans. Power Electron.* **26**(12), 3653–3665 (2011)
46. F.K.A. Lima, A. Luna, P. Rodriguez, E.H. Watanabe, F. Blaabjerg, Rotor voltage dynamics in the doubly fed induction generator during grid faults. *IEEE Trans. Power Electron.* **25**(1), 118–130 (2010)
47. I. Erlich, J. Kretschmann, J. Fortmann, S.M. Engelhardt, H. Wrede, Modeling of wind turbines based on doubly-fed induction generators for power system stability studies. *IEEE Trans. Power System* **22**(3), 909–919 (2007)
48. M. Rahimi, M. Parniani, Coordinate control approaches for low-voltage ride-through enhancement in wind turbines with doubly fed induction generators. *IEEE Trans. Energy Convers.* **25**(3), 873–883 (2010)
49. O. Abdel-Baqi, A.R. Nasiri, A dynamic LVRT solution for doubly fed induction generators. *IEEE Trans. Power Electron.* **25**(1), 193–196 (2010)
50. S. Zhou, J. Liu, L. Zhou, Y. Zhu, X. Yang, Sag detection algorithm for dynamic voltage restorer used in wind farms under unbalanced and distorted grid voltage conditions, in *Proceedings of ECCE Asia*, pp. 601–606, 3–6 June 2013

Chapter 3

Control of Grid Connected Converter (GCC) Under Grid Voltage Disturbances

Marek Jasiński, Grzegorz Wrona and Szymon Piasecki

Abstract In this chapter operation of a reliable control method of a Grid Connected Converter (GCC) under grid voltage disturbances is presented. As a GCC authors understand power electronic AC-DC converter with AC side filter and DC-link capacitor operating as an interface between the electrical grid and Active Loads (AL). At the beginning short introduction to selected grid voltage disturbances is given. Afterwards, the chosen modeling approach of a GCC is discussed and the example of passive components calculation are provided. In the next sections a brief review of a basic GCC control methods is described. A control method: Direct Power Control with Space Vector Modulation (DPC-SVM) is chosen for further development process. For the basic scheme of DPC-SVM special control modules for voltage dips and higher harmonics compensation are presented. Due to the development of new control modules and its integration with the classical DPC-SVM a new reliable (robust to selected grid voltage disturbances such as dips, higher harmonics) control method is proposed: Robust Direct Power Control with Space Vector Modulation (RDPC-SVM). The term “*robust*” in the name of proposed control refers to the fact that the RDPC-SVM method is expected to operate in an uncertain environment with respect to the system dynamics. This new control method can assure sinusoidal like and balanced AC current in extremely distorted grid voltage. Based on the case study from series 5–400 kVA of Voltage Source Converters (VSCs) it was verified that the control dynamic and features of the RDPC-SVM fulfill requirements of sinusoidal and balanced currents under uncertain grid voltage distortions. Moreover, the quality

M. Jasiński (✉) · G. Wrona · S. Piasecki
Institute of Control and Industrial Electronics, Warsaw University of Technology,
Warsaw, Poland

e-mail: marek.jasinski@ee.pw.edu.plmja@isep.pw.edu.pl

G. Wrona
e-mail: grzegorz.wrona@ee.pw.edu.pl

S. Piasecki
e-mail: szymon.piasecki@ee.pw.edu.pl

of current and power is significantly improved in comparison to classical methods. Hence, the negative impact of the GCC on the grid voltage (through its inner impedance) is significantly reduced i.e.: lower Total Harmonics Distortion (THD) factor of a grid current, control of active and reactive power flow assure good quality of integration with a grid even in case of increased impedance within operation limits.

1 Grid Voltage Disturbances: Introduction

In this chapter, based on particular example, is presented how to design and control the Grid Connected Converter (GCC) under distorted grid voltage conditions to keep the currents always as close to sinusoidal shape as possible (low THD) and balanced. GCC is defined as grid friendly, modern power electronic converter operating as an interface between the grid and distributed sources. It gives also possibility of energy saving because provides inverting mode useful in renewable energy application and in case of Adjustable Speed Drives (ASD) regenerative braking with energy saving capability [1]. Due to, systematical cost reduction of the semiconductor devices and digital control platforms, GCCs are serially produced from range of few kVA up to MVA.

There are a lot of different aspects related with power quality (especially with grid voltage disturbances), it is impossible to address all of them in one short chapter. In this section only short introduction to the problem of the grid voltage disturbances is given. Therefore, for more information the best source of knowledge related to power quality issues are standards, recommendations [2–18], and excellent references like Bollen, Strzelecki, Hanzelka [2, 19].

There are several regulations (standards, scientific papers, and recommendations) with information about power quality, reliability and allowed voltage disturbances that have to be taken into account while power electronics GCC is going to be connected to the utility grid.

One of them is SEMI F47-0706 standard completely rewritten in 2006. This standard is devoted to semiconductors industry. It takes into account power quality aspects, especially voltage sags (dips) [2–19]. The main aim of the document is to give information about voltage dips immunity of a device needed in semiconductor processing, metrology, and automated test equipment. There are some requirements and recommendation according to immunity of the device in case of using it under voltage dips in semiconductor mass production process. It helps to make a trade of decision between voltage dips immunity and higher costs of power electronics devices. The SEMI F47 is related to another standards: a IEC 61000-4-11 [11], related to dips phenomena. This is convenient because helps to meet both standards under one similar assumptions and grid voltage dips electronics devices immunity tests. However, it should be noted that the IEC 61000 (EN 61000) (developed by national experts) standards are unceasing updated and changed. There is also

CENELEC EN 50160 [5] standard which has been also updated very often during recent 10 years. At this point, some IEEE recommendations, practices and requirements i.e. IEEE 519-1992 or IEEE 1159 (developed by volunteers) has to be mentioned [3, 4]. These recommendations should also be taken into account in the development process of a GCC features. Moreover, there are also several local regulations of a grid operators so called “*grid codes*”. These grid codes usually are very precise and more strict than standards as in case of Wales, Germany, Denmark [17, 20]. In a grid code detailed information about integration with local power system can be found.

Taking into account dynamic changes of the power quality requirements and development of power electronics devices it is worth to focus on control methods of power electronic converters and its reliability in case of grid voltage dips, higher harmonics etc. In the literature can be found a relations between disturbance levels [19]: immunity level, emission level, compatibility level, planning level, design level versus probability density function of equipment performance degradation. For novel, environment friendly power electronics devices requirements according to power layer and control layer should be systematically updated to fulfill standards and reduce a negative influence on supply network. It would be convenient to think about GCC hardware like about power electronics building block (PEBB) that is unified and ready for programming of different sophisticated functionalities. The software (control methods) should be designed in modular way, allows to update and add new needed/expected by customer functionalities (e.g. grid voltage dips compensations module, higher harmonics compensation module or standalone operation mode module etc.).

There are two main groups of grid voltage disturbances: dips and higher harmonics. The terminology of grid voltage disturbances in literature is not unified, therefore some clarification is needed. In North America market the term sags is understanding as:

- voltage sag depth—the value in percent of nominal voltage remaining during the sag,
- and voltage sag duration—measured in cycles or in seconds.

In case of European EN 60160 voltage dip is:

- a temporary reduction of the one RMS voltage at a Point of Common Coupling (PCC) below specified start threshold (equals to 90 % of the reference voltage),
- voltage dip duration—is a time between the instant at which the one RMS voltage in the PCC falls below the start threshold value and the instant at which the one voltage rises the end threshold (time is from 10 ms up to including 1 min),
- voltage dip residual voltage—is a minimum value of the one RMS voltage occurred during a voltage dip (expressed as a percentage of the reference voltage) [5].

Harmonics distortion is defined by a Total Harmonic Distortion (THD) factor. The THD can be also calculated in different ways:

- in North America up to 50th higher harmonic,
- in Europe up to 40th higher harmonics.

Both mentioned groups of grid voltage distortions are described below.

1.1 Grid Voltage Dips

Generally, dips are temporary reduction in one, two or three phases of the RMS voltage. During dips a phase shift between each phases can also be changed. Dips can be caused by intentional changing of a power system configuration or by unpredicted short circuits. Dips can occur symmetrically (voltages in each phases are equal—Fig. 1c) and asymmetrically (as presented in Fig. 1a, b).

As it was mentioned in the introduction that dips (sags) can be described in different manner like in IEEE recommendations (493-1998, 1159-1995, 1346-1998): 70 % dip from 230 V means that voltage falls to the value equals to $230\text{ V} \times 0.7 = 161\text{ V}$. Hence, there is a possibility to make a mistake easily, because 70 % dip can be understand that voltage RMS value falls to 30 % of nominal RMS value. To avoid confusion in the literature reader can find a recommendation that when the dip is described it is better to write: “dip to 70 % of nominal voltage” [2–4]. Fortunately, in IEC standards this problem was solved by dip definition as an actual percentage voltage falls in respect to nominal RMS voltage value [5].

To summarize, in this chapter dip will be described as RMS voltage value reduction between 90 and 1 % of declared RMS voltage value. After a short period of time (from 10 ms up to including 1 min) the RMS voltage value returns to declared RMS voltage value [5]. In Fig. 1a different types of voltage dips are presented.

Dip is quite similar to short circuit, however the voltage drop is higher than 1 % of declared value. According to the EN 50160 standard dips can be classified as [5]:

- short (below few second) and weak ($\leq 60\%$),
- short (below few second) and deep ($\geq 60\%$),
- long (more than few second) and weak ($\leq 60\%$),
- long (more than few second) and deep ($\geq 60\%$).

It has to be stressed that change in grid voltage RMS value can cause a number of problems in control of grid connected converters e.g. DC-link voltage oscillations, distortion of the phase currents (like unbalance), active and reactive powers oscillations [21].

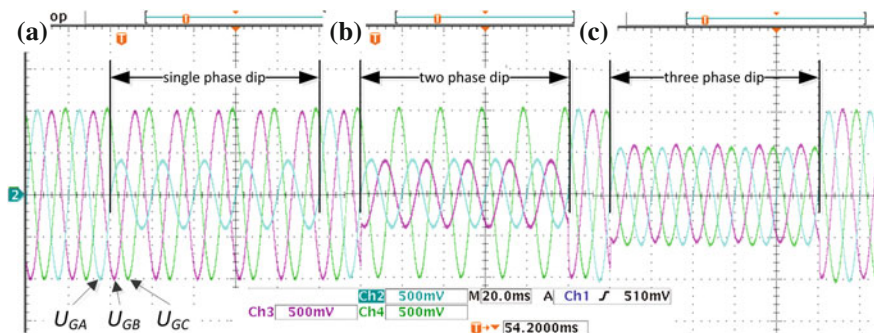


Fig. 1 Different voltage dips: **a** single-phase, **b** two-phase, **c** three-phase

1.2 Grid Voltage Harmonics

Higher harmonics are components which frequencies are being multiple of the fundamental frequency. Therefore, in Europe (50 Hz grid frequency) second harmonic frequency equals to 100 Hz, etc. Voltage harmonics are produced by nonlinear loads like: diode rectifiers, traction rectifiers, thyristor-based industrial drives etc., connected to the PCC. Because of large number of nonlinear loads the amount of higher harmonics is growing. Harmonics can cause a serious problems or even damage of electrical or electronics devices.

Several different definitions of higher harmonics distortion can be found in the literature. According to the EN 50160 standard higher harmonics are measured under normal operation conditions, during each period of week, 95 % of the 10 min mean RMS values of each individual harmonic voltage shall be less or equal to the values given in Tables 1 and 2. Note that harmonics higher than $h = 25$ is difficult to predict because it mainly depends on resonances. The THD factor of the grid voltage for considered voltage level (taking into account all harmonics up to 40) shall be less or equal to 8 % [5] or to 4 % [17] (taking into account all harmonics up to 50). Other recommended limit of the voltage disturbances given by IEEE 519-1992 is 5 % for the THD and below 3 % for each individual frequency. In this case the limit for individual harmonics is determined by number of loads at PCC (e.g. 10) and grid nominal voltage level (e.g. <69 kV).

Moreover, according to IEEE 519-1992 and EN 50160 the THD factor can be calculated as:

$$THD_{IEEE} = \sqrt{\frac{\sum_{h=2}^{50} U_{G(h)}^2}{U_{G(1)}^2}} 100\% \quad THD_{EN} = \sqrt{\sum_{h=2}^{40} U_{G(h)}^2} \quad (1)$$

It has to be remembered that computers and associated equipment such as programmable controllers frequently require AC sources that have voltage harmonics distortion lower than the 5 % of the THD, with the largest single harmonic

Table 1 Odd voltage harmonics in different standards and grid codes [4, 5, 17]

Odd harmonics						
Not multiples of 3			Any h of harmonics, Uh (%)	Multiples of 3		
Order h	Relative Amplitude, Uh (%)			Order h	Relative Amplitude, Uh (%)	
	EN50160	Wales	IEEE519-1992		EN50160	Wales
5	6	3	< 3	3	5	3
7	5	3	< 3	9	1.5	1.5
11	3.5	2	< 3	15	0.5	0.3
13	3	2	< 3	21	0.5	0.2
17	2	1.6	< 3			
19	1.5	1.2	< 3			
23	1.5	1.2	< 3			
25	1.5	0.7	< 3			
> 25	na	0.2 + 0.5(25/h)	< 3			

Table 2 Even voltage harmonics in different standards and grid codes [4, 5, 17]

Even harmonics			
Not multiples of 3			
Order h	Relative Amplitude, Uh (%)		
	EN50160	Wales	IEEE519-1992
2	2	1.5	< 3
4	1	1	< 3
6...24	0.5	na	< 3
6		0.5	
8		0.4	
10		0.4	
12		0.2	
> 12		0.2	

being lower than 3 % of the fundamental component. Higher levels of harmonics result in erratic, malfunctions of the equipment that can, in some cases, have serious consequences (e.g. costly brakes in mass production process) [22]. Also, instruments can be affected similarly. Perhaps the most serious malfunctions are in medical instruments. Consequently, many medical instruments are provided with special power electronics devices (line-conditioners). Here is a wide application field, mainly for AC-DC-AC converters, operating as uninterruptible power supplies systems.

Therefore, a lot of methods for elimination of harmonics distortion in the power system are developed and implemented [19, 23]. Moreover, several blackouts in recent years (USA and Canada (New York, Detroit, Toronto) in 08.2003, Russia (Moscow) in 05.2005, USA (Los Angeles) 09.2005) and in 2008, Poland (Szczecin

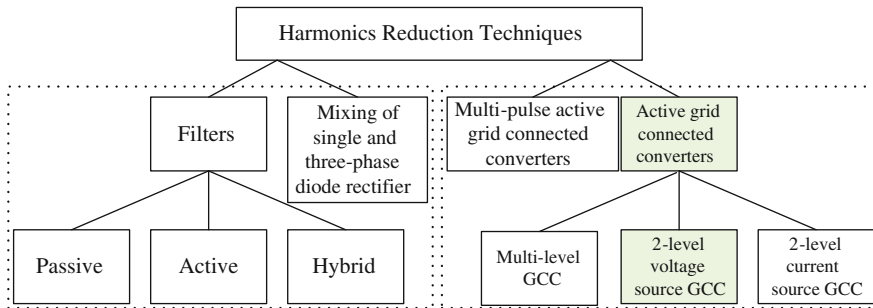


Fig. 2 Selected higher harmonics compensation method

area), shows that the power quality and reliability improvement are serious and important problems.

Methods of harmonics reduction can be divided into two main groups (Fig. 2):

- passive and active filters—harmonics reduction of the already installed non-linear loads,
- multi-pulse rectifiers and GCC—power-grid friendly converters (with limited THD index) [21].

Because the grid friendly GCC and its control methods are a scope of this chapter here it will be described the harmonics reduction method realized by the GCC. After modification an active filtering function can be introduced into a GCC control structure [24–28]. Moreover, the GCC can compensate the current of a non-linear load connected in parallel to the PCC.

It should be stressed that in a real power system a voltage is usually distorted by higher harmonics as shown in Fig. 3. This distortion has a negative impact on the grid current formed by a power electronics converter.

2 Modeling and Basic Control Methods of Grid Connected Converter

In this section mathematical modeling of the GCC is described. As can be seen from literature precise mathematical modeling of the controlled object is very important in the control process [29–44]. Here we will focus on VSC modeling operating as a GCC. This description is significantly shortened but more detailed information can be found in [45–48].

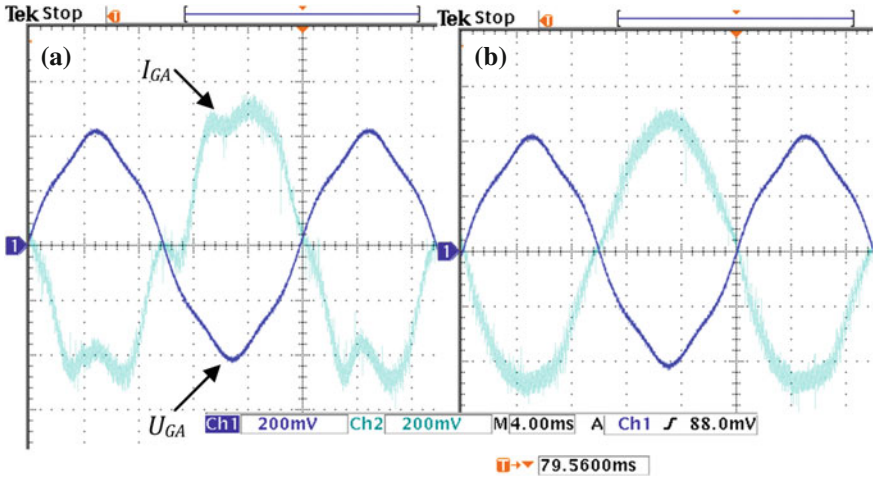
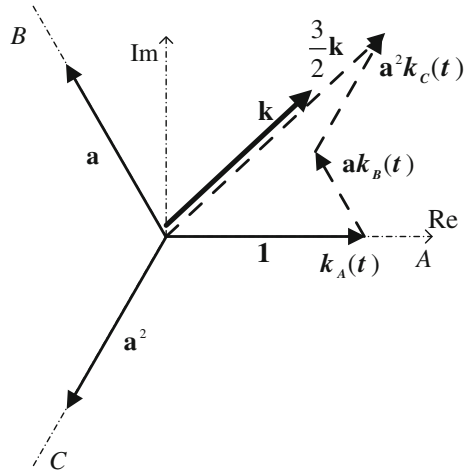


Fig. 3 Distorted grid voltage by 5th harmonic and grid current for applied control method: **a** without higher harmonics compensation, **b** with higher harmonics compensation feature

Fig. 4 Graphical representation of a Space Vector (SV) described by Eq. (2)



2.1 Space Vector Description Used in Modeling of a Voltage Source Converter

Considered, symmetric three-phase system is described by phase quantities in natural coordinate system, such as voltages, currents and fluxes or Virtual Fluxes (VF) [45, 48]. Due to Space Vector (SV) representation this system can be expressed by one SV of voltage and current respectively [49, 50]. In Fig. 4 the SV graphical representation is given.

$$\mathbf{k} \stackrel{\text{def}}{=} \frac{2}{3} (k_A(t) + \mathbf{a}k_B(t) + \mathbf{a}^2k_C(t)) \quad (2)$$

where $2/3$ is normalization factor, $1, \mathbf{a} = -1/2 + j\sqrt{3}/2, \mathbf{a}^2 = -1/2 - j\sqrt{3}/2$ are complex unity vectors, with phase shift, $k_A(t), k_B(t), k_C(t)$ denote phase quantities in a system of natural coordinates satisfying the condition:

$$k_A(t) + k_B(t) + k_C(t) = 0 \quad (3)$$

An advantage of SV is possibility of their representation in various coordinates. Therefore, space vectors are very flexible and comfortable tool to describe a three-phase objects.

2.2 Voltage Source Converter (VSC): Basic Constrains

Let consider a 2-level VSC as presented in Fig. 5. Main circuit of the three-phase bridge converter consists of three legs with two controllable power-electronics devices (e.g. Insulated Gate Bipolar Transistors (IGBT), Metal-Oxide Semiconductor Field-Effect Transistor (MOSFET), and other transistors based on Silicon Carbide (SiC)). Under consideration in this chapter the IGBT will be selected. When transistor is in conducting mode the gate signal is “1” and when transistor is in blocking mode the gate signal is “0”.

This circuit can be treated as a PEBB which may be adopted to any personal (custom) needs compatible with assumption presented in this chapter. Pre-implemented classical control method may be simple extended by additional modules to meet evolving power quality standards [51, 52].

The converter AC voltage can be obtained by eight possible switching states as shown in Fig. 6. For simplicity of the converter structure, each VSC leg is represented by an ideal switch. Six switching states construct active vectors and two switching states are related with zero vectors states. The converter AC voltage can be represented as a complex SV as follows (Fig. 7):

$$\underline{\mathbf{u}}_{c(n)} = \frac{2}{3} U_{dc} e^{j(n-1)\pi/3}, \quad n = 1, \dots, 6 \quad (4)$$

$$\underline{\mathbf{u}}_{c(n)} = 0, \quad n = 0, 7 \quad (5)$$

Active states correspond to phase voltage equal $1/3$ and $2/3$ of the DC voltage U_{DC} . Zero vectors apply zero voltage to the converter AC side (all AC side phases are connected to “+” (1, 1, 1) or “-” (0, 0, 0) DC bar). Hereafter, please consider the case that a VSC is connected to the grid and operates as a GCC. As it was mentioned the GCC can be described in different coordinate system by SV equations. Basic scheme of the GCC with small AC passive filter (usually *LCL* or

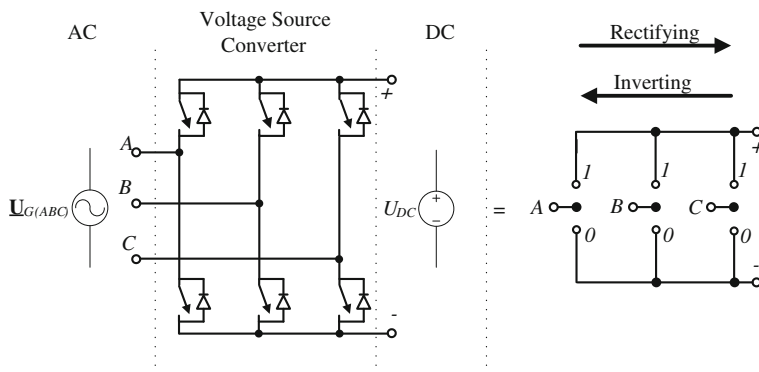


Fig. 5 Voltage Source Converter (VSC) equivalent circuit. Two operating modes are available: rectifying—energy flows from AC to DC circuit and inverting—energy flow direction is from DC to AC circuit

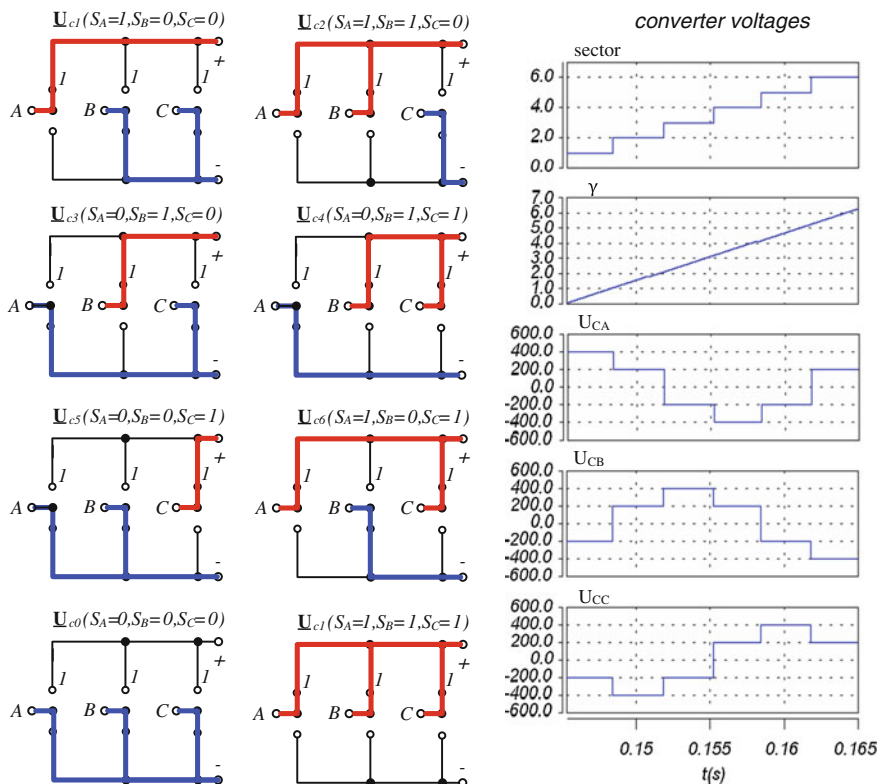
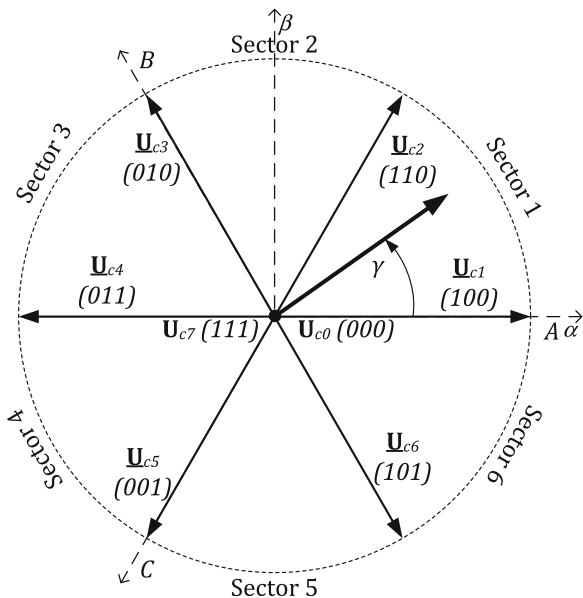


Fig. 6 Three-phase 2-level VSC switching states, modulator signals and phases voltages

Fig. 7 Voltage source converter AC voltage represented as a SV states



in simplest solution L) and output DC filter C is presented in Fig. 8a, while Fig. 8b shows its single phase representation. Where \underline{U}_G —grid voltage SV, \underline{I}_G —AC current SV, \underline{U}_C —GCC AC terminals voltage SV, and $\underline{U}_i = \underline{U}_{LC} + \underline{U}_{LG}$ —a SV of voltage drop on the AC filter (L or LCL). In case of LCL \underline{U}_{LC} —a SV of voltage drop on the converter side inductance L_C , \underline{U}_{LG} —a SV of voltage drop on the grid side inductance L_G , R —equivalent resistance of the input filter inductances.

The converter voltage \underline{U}_C is controllable and depends on switching states and DC voltage level. Through magnitude and phase control of the converter voltage \underline{U}_C , the line current can be controlled by changing the voltage drop on the input filter inductance \underline{U}_i . Therefore, inductances between grid and AC terminals of the GCC are mandatory and important. They create a current source and provide boost feature of the GCC. Through controlling the converter AC voltage \underline{U}_C , the phase and amplitude of the grid current vector \underline{I}_G is controlled indirectly.

Hence, in Fig. 9 phasor diagrams of GCC are shown in both inverting and rectifying operation. From this figure can be seen that the magnitude of converter voltage \underline{U}_C is higher during inverting than in rectifying mode. With assumption of a stiff grid (i.e., \underline{U}_G is an ideal voltage source without internal impedance) terminal voltage of GCC \underline{U}_C can be higher up to 3 % between rectifying and inverting operation [53, 54].

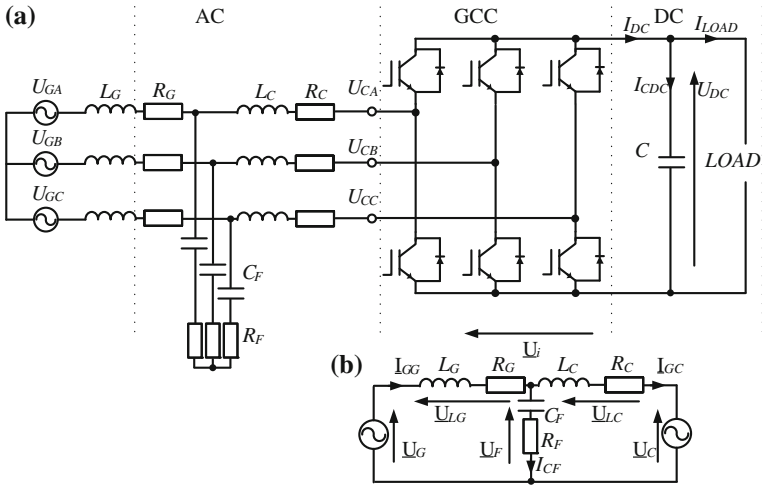


Fig. 8 The GCC: **a** three-phase 2-level circuit, **b** single phase equivalent circuit

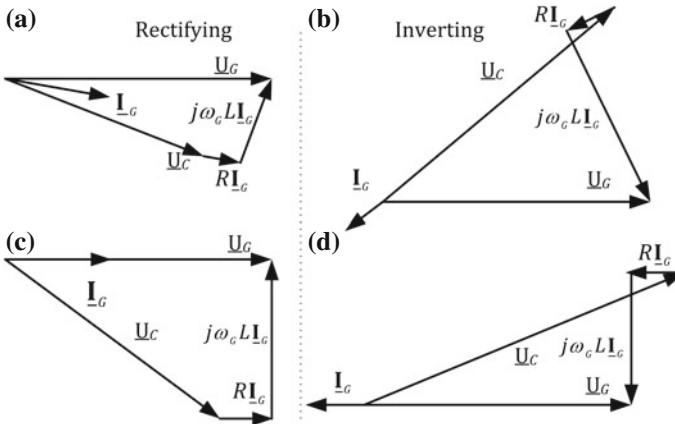


Fig. 9 Phasors diagrams of the GCC: **a, b** non-unity power factor in rectifying operation; **c, d** unity power factor operation in inverting operation

2.3 Operation Limits of the Grid Converter

From Fig. 9 it can be concluded that for the GCC load current a limit exist with assumption of constant AC grid and DC voltages. The value of AC filter inductance has to be taken into account in this consideration. Below that limit, the GCC is not able to operate and maintain a unity power factor requirement. Low value of the filter inductance and higher voltage reserve (a difference between the AC RMS

voltage and the DC voltage) can increase that limit. The consideration has to be started from the lowest limit of the DC voltage level:

$$U_{DC} > \sqrt{3}\sqrt{2}U_{GRMS} \quad (6)$$

(Example: if $U_{GRMS} = 230V \rightarrow U_{DC} = 2.45 \times 230V = 564V$)

This limitation is introduced by freewheeling diodes in the GCC which operate as an ordinary diode rectifier. This limitation is rather theoretical value. In the literature exists other limitation [45, 48, 53, 54] which takes into account the AC power (value of the AC current) of the GCC.

For simplicity it can be assumed at this stage that $\mathbf{I}_G = \mathbf{I}_{GG} + \mathbf{I}_{GC}$ if $\mathbf{I}_{CF} = 0$ for first harmonic of the grid current. Moreover, consider that referenced value of the grid current differ from actual grid current by $\Delta\mathbf{I}_G$ and its equals to difference between referenced and actual value of the grid current:

$$\Delta\mathbf{I}_G = \mathbf{I}_{Gref} - \mathbf{I}_G \quad (7)$$

Direction and velocity of the grid current SV changes are described by derivative of that grid current $L\frac{d\mathbf{I}_G}{dt}$. It can be represented in synchronous dq coordinates as follows:

$$L\frac{d\mathbf{I}_G}{dt} + R(\mathbf{I}_{Gref} - \Delta\mathbf{I}_G) = \underline{\mathbf{U}}_G - U_{DC}\mathbf{S} + j\omega_G L(\mathbf{I}_{Gref} - \Delta\mathbf{I}_G) \quad (8)$$

Assuming resistance of the input inductances $R \cong 0$ and actual grid current is very close to referenced one ($\Delta\mathbf{I}_G \approx 0$), Eq. (8) can be rewritten:

$$L\frac{d\mathbf{I}_G}{dt} = \underline{\mathbf{U}}_G - U_{DC}\mathbf{S} + j\omega_G L\mathbf{I}_{Gref} \quad (9)$$

According to Eq. (9) the direction and velocity of the actual grid current SV changes depends on: L —values of filter inductance, $\underline{\mathbf{U}}_G$ —grid voltage SV, \mathbf{I}_{Gref} —grid current reference SV, U_{DC} —value of the DC voltage level, \mathbf{S} —switching signals of the GCC.

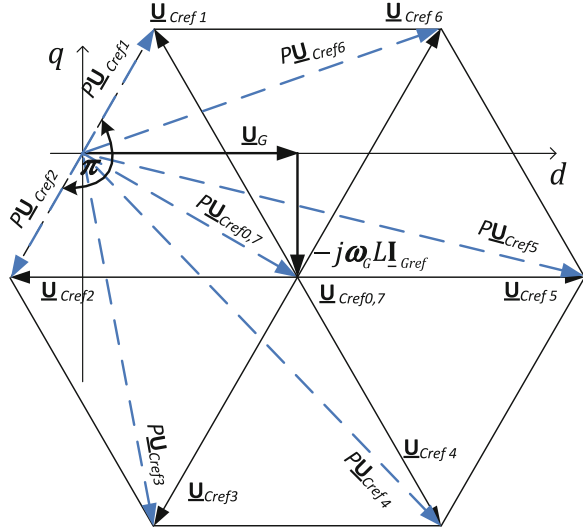
Let us consider that six active vectors ($\underline{\mathbf{U}}_{Cref(1...6)}$) of the GCC rotate clockwise in synchronous dq coordinates. For each voltage vector ($\underline{\mathbf{U}}_{Cref(0...7)}$) the current derivatives multiplied by L are denoted as ($P\underline{\mathbf{U}}_{Cref(0...7)}$) [53, 54]. Graphical illustration of Eq. (9) is shown in Fig. 10.

Referenced current \mathbf{I}_{Gref} is in phase with line voltage vector $\underline{\mathbf{U}}_G$ and it lies on the axis d . The difference between actual current \mathbf{I}_G and referenced \mathbf{I}_{Gref} is defined by Eq. (7). Based on the above equations the boundary condition can be given:

$$|U_{DC}\mathbf{S}| = \frac{\sqrt{3}}{2}|\underline{\mathbf{U}}_C| = |\underline{\mathbf{U}}_G + j\omega_G L\mathbf{I}_{Gref}| \quad (10)$$

Assuming that: $\underline{\mathbf{U}}_G = U_{Gmax}$, $\mathbf{I}_{Gref} = I_{Gmaxref}$ and $\underline{\mathbf{U}}_C = \frac{2}{3}U_{DC}$ the following expression can be derived:

Fig. 10 Graphical illustration of Eq. (9)—instantaneous position of SV and its derivatives [53, 54]



$$\frac{\sqrt{3}}{2} \frac{2}{3} U_{DC} = \sqrt{U_{Gmax}^2 + (\omega_G L I_{Gmaxref})^2} \tag{11}$$

Rearranging the equation for minimum DC voltage is obtained:

$$U_{DCmin} = \sqrt{3U_{Gmax}^2 + 3(\omega_G L I_{Gmaxref})^2} \tag{12}$$

Example: $U_{Gmax} = 230\sqrt{2} \text{ V}$, $\omega_G = 100\pi \frac{\text{rad}}{\text{s}}$, $L = 0.01 \text{ H}$, $I_{Gmaxref} = 10 \text{ A}$; than $U_{DCmin} \geq 566 \text{ V}$

Based on this relation the maximum value of the filter inductance can be derived:

$$L_{max} = \frac{\sqrt{\frac{1}{3} U_{DC}^2 - U_{Gmax}^2}}{\omega_G I_{Gmaxref}} \tag{13}$$

Example:

$U_{Gmax} = 325 \text{ V}$, $\omega_G = 100\pi \frac{\text{rad}}{\text{s}}$, $I_{Gmaxref} = 10 \text{ A}$, $U_{DCmin} = 566 \text{ V}$, than $L_{max} = 0.01 \text{ H}$

2.4 Design of LCL Filter

The AC side of grid connected converters has to be installed with L or LCL filters (Fig. 11). The purpose of the AC filter is to reduce higher harmonics distortion caused by switching process of a power electronics devices. The filtration

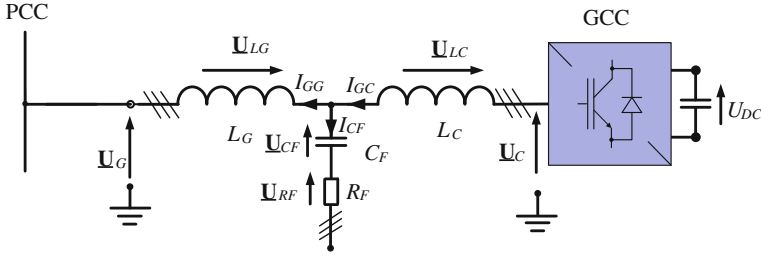


Fig. 11 A LCL filter scheme (L_C —converter side inductance, C_F —filter capacitance, R_F —resonance damping resistor, L_G —grid inductance, PCC —Point of Common Coupling)

capability of LCL filters are significantly higher than simple L filter. Therefore, the previous one are more popular in practice. LCL filters allows to reduce volume of the filter and assures more effective higher harmonics current filtration in respect to L filter. The proper calculation of LCL filter parameters are important to obtain stable operation of the GCC. There are several methods to obtain these parameters [46, 55, 56], all of them have to take into account: maximal reduction of higher harmonics caused by switching process with minimum filter volume and reactive power consumption.

For the propose of presented control method the selection of LCL filter parameters can be done according to following steps [56]:

1. Define base values

Base impedance, capacitance and inductance:

$$Z_B = \frac{U_N^2}{P_N}, \quad L_B = \frac{Z_B}{\omega_N}, \quad C_B = \frac{1}{\omega_N Z_B} \quad (14)$$

where $\omega_N = \omega_G = 2\pi 50$ —nominal converter pulsation, $U_N = U_{GL-L} = 230\sqrt{3}$ —nominal phase to phase converter voltage. Nominal RMS converter phase current can be calculated as:

$$I_N = \frac{P_N}{\sqrt{3}U_N} \quad (15)$$

2. Converter side inductance L_C calculation

The maximum ripple current $I_{maxripref}$ can be selected between 10 and 25 % of nominal phase current I_N . Let assume that $I_{maxripref} = 0.23$. Than maximum converter side ripple current can be calculated as:

$$I_{maxrip} = \sqrt{2}I_{maxripref} \times I_N \quad (16)$$

According to this the converter side inductance can be derived from:

$$L_C \geq \frac{U_{DC}}{6f_{sw}I_{maxrip}} \quad (17)$$

where, f_{sw} is a switching frequency. From the other hand Eq. (13) has to be fulfilled.

3. Filter capacitance C_F calculation

As a next step the AC filter capacitance C_F evaluation is needed. The filter capacitance should be less than 5 % of the base capacitance C_B . Therefore, after assumption that per unit capacitance is 4 % i.e. $C_{Fref} = 0.04C_B$ the filter capacitance can be derived from:

$$C_F = C_{Fref}C_B = C_{Fref} \frac{1}{\omega_N Z_B} = C_{Fref} \frac{P_N}{\omega_N U_N^2} = 0.04 \frac{P_N}{\omega_N U_N^2} \quad (18)$$

4. Grid side inductance L_G calculation

The grid side AC filter inductance can be derived from:

$$L_G = r_a L_C \quad (19)$$

where, r_a is a ratio between grid and converter side inductances.

The r_a factor can be calculated as:

$$r_a = \left| \frac{1 - HA}{HA(1 - L_C C_F \omega_{sw}^2)} \right| \quad (20)$$

where, HA is the harmonics attenuation of the phase currents for the switching frequency components ($HA = \frac{I_{GC}(h_{sw})}{I_{GG}(h_{sw})}$). In this work $HA = 0.08$ has been chosen.

5. Resonance phenomenon verification

To avoid unexpected and unwonted resonances from grid or converter frequencies active or passive damping should be provided [57, 58]. In case of passive damping a resistance R_F should not be too high because its increase losses of the filter and has strong impact on the efficiency of the GCC. The resonant frequency calculated from:

$$f_{res} = \frac{1}{2\pi} \sqrt{\frac{L_G + L_C}{L_G L_C C_F}} \quad (21)$$

should meets following border conditions:

$$10f_G \leq f_{res} \leq \frac{f_{sw}}{2} \quad (22)$$

where, f_G is a grid first harmonic frequency i.e. 50 Hz in Europe.

Table 3 Example of *LCL* filter calculation for power series (5–400 kVA), $U_{DC} = 700$ V, $f_{sw} = 5$ kHz, $U_{Grms} = 230$ V

P_N (kW)	L_C (mH)	C_F (μ F)	L_G (mH)	C (mH)	I_N (A)	I_{DC} (A)
5	9.9	3.98	2.97	0.25	7.22	7.14
15	3.3	11.9	0.99	0.74	21.65	21.43
55	0.9	43.7	0.27	2.73	79.71	78.57
150	0.33	119.4	0.099	7.45	216.5	214.3
250	0.198	199	0.059	12.39	360.8	357.1
400	0.124	318.3	0.037	19.8	577.3	571.4

In Table 3 some *LCL* filter calculation examples for power series (5–400 kVA) are presented. If the control of the GCC has a module of a grid impedance estimator the grid impedance can be taken into account in calculation process, what allows to select filter parameters with higher accuracy [59].

2.5 Choosing of DC Capacitor Parameters

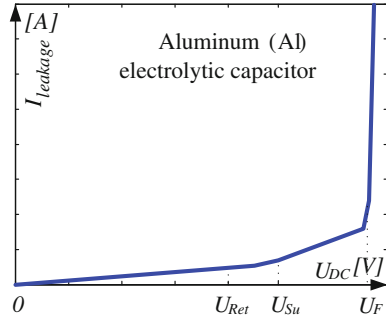
Another step of the GCC design is a DC capacitor parameters selection. The most important parameters of the DC-link capacitor are: rated voltage, leakage current, allowed ripple current and as a results life time. The main factors that have to be taken into account in case of capacitor selection are listed below.

1. DC voltage rated value

The voltage ratio of the DC capacitor is a main parameter that has to be carefully chosen. A stable and predictable DC voltage value should be assured by applied control in the GCC. Relationship between the leakage current and the voltage applied under constant temperature conditions shown in Fig. 12. It can be seen that stability of the DC voltage at desired level is very important for a capacitor life time. In Fig. 12 U_{Ret} (rated voltage) is the DC-link voltage value for which the capacitor has been designed; U_{Su} (surge voltage) is the maximum voltage which can be applied to the capacitor for short periods of time, i.e. up to five times for 1 min per hour.

The standard IEC 60384-4 specifies the above voltages as follows: for $U_{Ret} \leq 315V \rightarrow U_{Su} = 1.15U_{Ret}$ and for $U_{Ret} \geq 315V \rightarrow U_{Su} = 1.1U_{Ret}$ and higher U_F forming voltage. When the DC voltage is equals to forming voltage U_F , the forming process starts. Here large amounts of gas and heat are appear. The DC capacitor is designed to surge voltages U_{Su} for short periods only. High over-anodization (high difference between rated voltage and forming voltage) offers the possibility of producing especially reliable capacitors designed as long-life grade “LL” capacitors in accordance with IEC 60384-1 [60, 61].

Fig. 12 Current-voltage characteristic of an aluminum (Al) electrolytic capacitor [60, 61]



2. Consideration of ripple current

The term ripple current is used for the RMS value of the AC current that flows through the device as a result of any pulsating or ripple voltage. In Fig. 13 ripple current waveforms for different cases in DC of the GCC connected with AL by DC-link (AC-DC-AC converter) are shown: (a) classical old-fashion AC-DC-AC converter with diode rectifier, (b) AC-DC-AC converter with GCC without information about power consumed by AL (without Active Power Feed-Forward (APFF) which will be discussed further in this chapter), (c) AC-DC-AC converter with GCC with energy flow dynamic improvement between GCC and AL (with APFF).

The maximal permissible ripple in DC current value depends on the ambient temperature, the surface area of the capacitor (i.e. heat dissipation area), the dissipation factor (or Equivalent Series Resistance (ESR)) and on the AC frequency.

Thermal stress has a strong impact on the capacitor's life. Therefore, the dissipation heat generated by the ripple current is an important factor affecting the useful life. Thermal considerations imply that, under certain circumstances, it may be necessary to select a capacitor with a higher voltage or capacitance rating than would be required. The ripple current is a function of the switching frequency. The term useful life or—service life, operational life, or life time is defined as the life achieved by the capacitor without exceeding a specified failure rate. This time can be extended by operating the capacitor at loads below the rating value, lower voltage, current, or temperature and by appropriate cooling system [48, 60].

The ripple in the DC voltage is a function of the ripple current in the DC-link. The capacitor current I_{CDC} is difference between the current I_{DC} (DC current of the GCC) and I_{LOAD} (DC current of a load) as shown in Eq. (23).

A minimum occurs when the DC currents I_{DC} and I_{LOAD} pulses from the both converters overlap (Fig. 14b, c). It can occur when the pulses are centered on the same time instant. To obtain this conditions a modulation with symmetric zero vector placement can be implemented [62, 63]. PWM pulses are always centered on the half period of the switching state. Fig. 14 shows simulated DC voltage and DC currents I_{DC} , I_{LOAD} , and capacitors current I_{CDC} , I_{CLOAD} over sampling period. It should be noticed that there are a lot of modulation techniques and the problem of modulation and its impact on the controlled system performance (switching

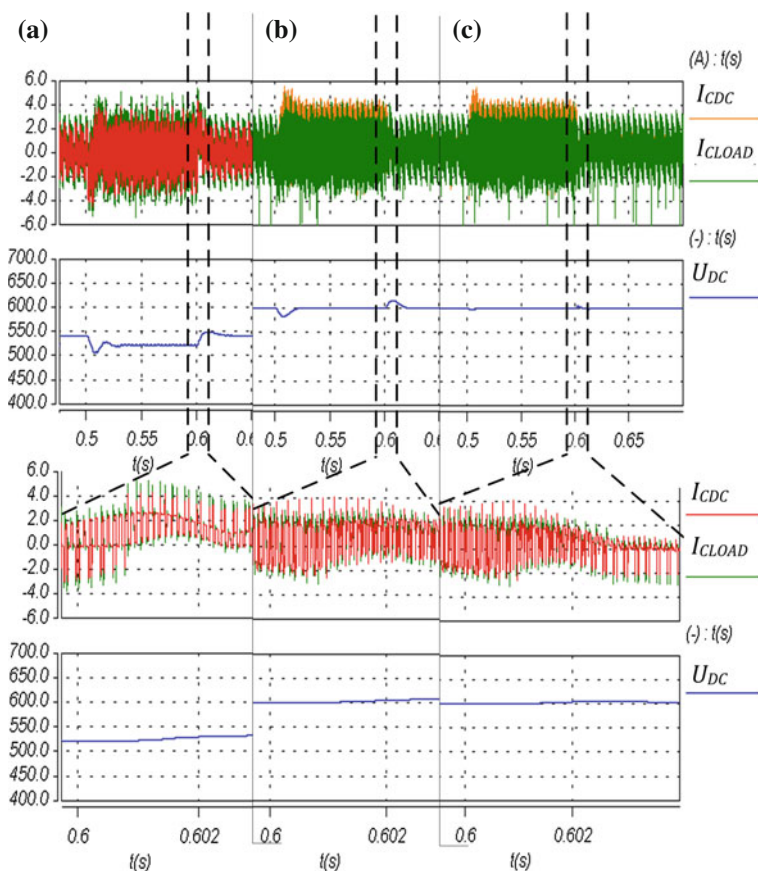


Fig. 13 Ripple current in DC-link capacitors. **a** Classical AC-DC-AC converter with diode rectifier, **b** AC-DC-AC converter with GCC without information about energy flow at AL converter side (without APFF), **c** AC-DC-AC converter with GCC, with information about energy flow at AL side in active power control loop (with APFF). DC-link capacitor $C = 470 \mu\text{F}$, $S_n = 5 \text{ kVA}$. From the *top* capacitor currents, DC voltages and zoom of them

losses, current or voltage shapes, and noise level etc.) are presented in many valuable publications [62–71] and will not be discussed in this chapter.

Summarizing when DC capacitor is under selection all mentioned points has to be determine: the DC voltage rated value, switching frequencies (both AC-DC converters in AC-DC-AC back-to-back converter), topology of an AC-DC converter, and if appropriate, dynamics and accuracy of applied control methods [48, 72]. In novel, environment friendly solution a diode rectifier in AC-DC-AC converters should be avoided because of: single direction energy flow, higher DC voltage fluctuation and ripples (Fig. 13). Therefore, in this chapter only GCC will be described. Its controllability provides more degree of freedom in DC voltage regulation process. The control dynamic and accuracy is higher than in the case of a

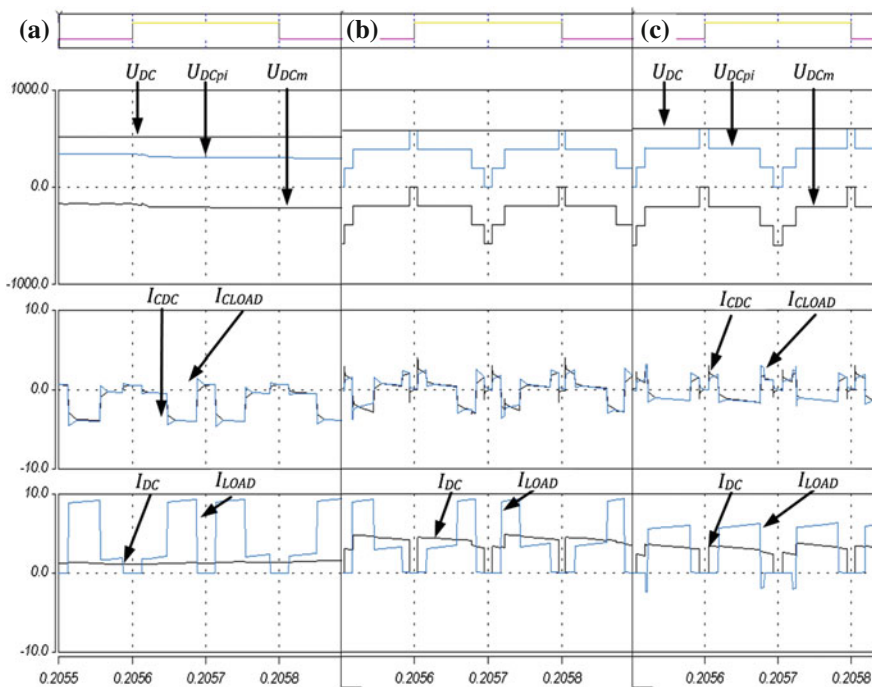


Fig. 14 Simulated ripple in DC currents. **a** Classical AC-DC-AC converter with diode rectifier, **b** AC-DC-AC converter with GCC without information about energy flow at AL converter side (without APFF), **c** AC-DC-AC converter with GCC, with information about energy flow at AL converter side (with APFF); $C = 470 \mu\text{F}$, $S_n = 5 \text{ kVA}$. From the *top* period of sampling, DC voltage and its potentials (positive and negative), capacitors current, DC currents I_{DC} , I_{LOAD}

diode grid side rectifier as shown in Fig. 13b, c. Please take a look also at the waveforms in Fig. 14 over one sampling period during operation just after load step (from 0 to 85 %). It can clearly be seen that the highest current flows from the DC capacitor in the case presented in Fig. 14a. The average value is negative. It means the energy is transferred from the capacitor to the load. In Fig. 14b the capacitor current is significantly reduced. Finally further reduction of the current I_{CDC} is observed in Fig. 14c, here information about the energy at a load side is taken into account in control of the GCC (see APFF description further in this chapter).

3. Calculation of DC capacitance value

Beside variety design criteria [72–74] of the DC-link capacitor, the minimum capacitance value is designed to limit the DC ripple voltage at a specified level, typically ΔU_{DCrip} is 1 or 2 % of U_{DC} . Therefore, peak-to-peak ripple voltage in DC-link is adopted as the design criterion for the DC capacitance determination.

With assumption of a balanced tree-phase grid and neglecting the power losses in the power switches, the GCC's DC part can be derived:

$$C \frac{dU_{DC}}{dt} = I_{DC} - I_{LOAD} \approx \sum_{k=A}^C I_{Lk} S_k - \frac{P_{LOAD}}{U_{DC}} \quad (23)$$

For given allowable peak ripple voltage and switching frequency, the minimum capacitor for the GCC converter can be calculated as [26]:

$$C_{min1GC} = P_{maxLOAD} \frac{\sqrt{2} + \frac{\sqrt{3}U_{L-L}}{U_{DC}}}{2\sqrt{3}\Delta U_{DCrip} f_{sw} U_{L-L}} \quad (24)$$

where U_{L-L} is a line-to-line voltage, $P_{maxLOAD}$ —maximal load power, ΔU_{DCrip} —specified peak-to-peak ripple voltage in DC voltage under steady states operation. This capacitance can be calculated based on different equations. An alternative approach of the DC capacitance determination, takes into account energy exchange between capacitance and load:

$$\Delta W_{DC} = T_{UT} \Delta P_{maxLOAD} \quad (25)$$

where T_{UT} is a sum of small time constant. From this equation the maximum DC voltage fluctuation under maximal load power step is proportional to energy variation:

$$\Delta U_{maxDC} = \frac{\Delta W_{DC}}{U_{DC} C_{min2GC}} \quad (26)$$

where ΔU_{maxDC} denotes maximum DC voltage fluctuation under maximal load step, C_{min2GC} —minimal DC capacitance. Transforming Eq. (25), the capacitance can be calculated [48]:

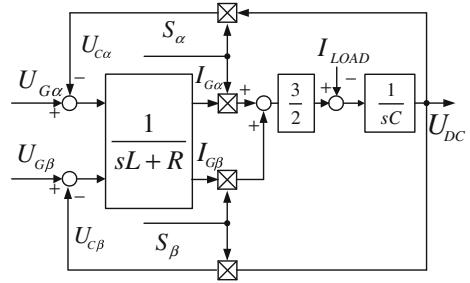
$$C_{min2GC} = \frac{T_{UT} \Delta P_{maxLOAD}}{U_{DC} \Delta U_{maxDC}} \quad (27)$$

Please take into your consideration that C_{min1GC} capacitance value is lower than C_{min2GC} . The one among other reason is that in T_{UT} time constant not only sampling (equals to switching frequency) is taken into account but also DC voltage filter measurement time delay. It depends on developer which formula will be taken within the process of capacitor sizing. For more details see also [48, 72].

2.6 Modeling of a Grid Connected Converter

There are several publication about modeling of the GCC mentioned above. However, for a reader convenience one of them in stationary $\alpha\beta$ coordinates is presented below. It is useful for description of a vector control method further in this chapter. So, the GCC can be presented as:

Fig. 15 Model of a three-phase GCC in stationary $\alpha\beta$ coordinates



AC side related with AC filter:

$$L \frac{d\mathbf{I}_G}{dt} + R\mathbf{I}_G = \mathbf{U}_G - U_{DC}\mathbf{S} \quad (28)$$

and, DC side related with DC filter:

$$C \frac{dU_{DC}}{dt} = \frac{3}{2} \text{Re}[\mathbf{I}_G \mathbf{S}^*] - I_{LOAD} \quad (29)$$

After decomposition into α and β components:

$$L \frac{dI_{G\alpha}}{dt} + RI_{G\alpha} = I_{G\alpha} - U_{DC}S_\alpha \quad (30)$$

$$L \frac{dI_{G\beta}}{dt} + RI_{G\beta} = I_{G\beta} - U_{DC}S_\beta \quad (31)$$

$$C \frac{dU_{DC}}{dt} = \frac{3}{2} (I_{G\alpha}S_\alpha + I_{G\beta}S_\beta) - I_{LOAD} \quad (32)$$

where,

$$S_\alpha = \left\{ S_A - \frac{1}{3}(S_A + S_B + S_C) \right\}, S_\beta = \frac{1}{\sqrt{3}}(S_B - S_C). \quad (33)$$

The graphical representation of Eqs. (30)–(33) are presented in Fig. 15.

The model in Fig. 15 is simple and give a sufficient basic for further consideration. Presented in this chapter RDPC-SVM control method of the GCC uses this model for calculations of system variables in algorithm.

2.7 Selected Control Methods for Grid Converter

Under control methods authors mean a way of currents regulation based on sensor or sensor-less operation of the considered GCC system.

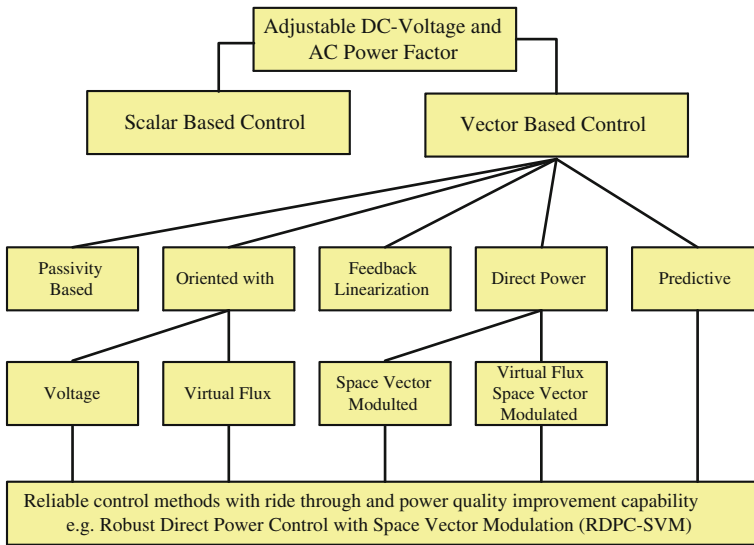


Fig. 16 Classification of a GCC control methods

With above knowledge the control methods can be classified as is presented in Fig. 16. The simplest scalar control method is based on current regulation in three-phase system (AC waveforms) [75, 76]. However, the unceasing development in the DSP platforms give better possibilities for implementation of more and more demanding control methods like model predictive control [77, 78], or additional sophisticated control modules devote to ride-through different problems in power system i.e. voltage distortion e.g. dips, and higher harmonics etc. [51, 52, 79–89].

Similar to ASD, the vector control of the GCC is a general control philosophy that can be implemented in many different ways. The most popular method, known as *Voltage Oriented Control* (VOC) [21, 45, 57, 58, 79, 80] gives high dynamic and static performances via internal current control loops. In the VOC the GCC equations are transformed from stationary to rotating synchronously with the grid voltage coordinates. To improve the robustness of VOC scheme a *Virtual Flux* (VF) concept was introduced by Duarte, Malinowski [45]. However, from the theoretical point of view, other types of mathematical coordinates transformations can be defined to achieve decoupling and linearization of the GCC equations. This has originated the methods known as nonlinear control. Jung and Lee proposed a nonlinear transformation of GCC state variables so that, in the new coordinates, the DC voltage and grid current are decoupled by feedback; this method is called also *Feedback Linearization Control* (FLC). Moreover, a *Passivity Based Control* (PBC), was also investigated in respect to the GCC [90–94].

In the 1990s have been expanded the idea of *Direct Torque Control* (DTC) for the GCC called *Direct Power Control* (DPC) [95–98]. From that time it has been continuously improved [45, 93]. However, these control principles are very similar to DTC schemes and have the same drawbacks. Therefore, to overcome that

disadvantages a *Space Vector Modulator* (SVM) [99] was introduced into DPC structure giving new DPC-SVM control scheme [100]. In recent years a novel *Predictive Control* (PrC) methods has been also implemented in GCC. Moreover, to increase reliability (ride-through) of control and finally total immunity of power electronics equipment in case of power systems disturbances a special function for classical, basic control methods can be implemented [51, 85].

2.8 Basic Control Methods

Many interesting control methods are proposed in the literature (see above). However, in this chapter we will focus on DPC-SVM investigated by research group of Kazmierkowski [32]. In this method instead of hysteresis controllers the classical PI controllers was used and the switching table was replaced by SVM. This improvement assures constant switching frequency and join the advantage of VOC (modulator i.e. low switching frequency is needed) and DPC (active and reactive power closed control loops) in one control scheme. Hence, it is quite comfortable for DSP implementation (for industry) [101]. The DPC-SVM has a simple structure, low number of coordinates transformation and assure good steady states and dynamic properties. The block diagram is presented in Fig. 17. It has to be stressed that in case of distorted grid voltage the DPC-SVM with Phase Lock Loop (PLL) cannot guarantee sinusoidal shape and balanced AC grid phase currents.

The DPC-SVM control algorithm consist of: active and reactive instantaneous power estimator, two inner powers control loops and one outer DC voltage control loop. Estimated powers are compared with referenced values, the differences (errors) are delivered to the PI controllers. Reference value of the reactive power is set by user, while reference value of the active power is calculated based on measured DC voltage of the converter and its reference value set by user. Output signals from powers PI controllers determine GCC referenced voltage in dq coordinates. After transformation to stationary $\alpha\beta$ coordinates signals are given to SVM input. The output SVM signals determinates current states of the transistors. There is a possibility to control both active and reactive powers independently (reactive power compensation realized by the GCC). In fact there are a little coupling between each other however it can be omitted in further consideration [48]. Reactive power can vary according to grid demand for reactive power while active power is varying according to DC voltage output PI controller signal. The instantaneous power estimator can be constructed in stationary $\alpha\beta$ coordinates as follows:

$$P = (U_{G\alpha}I_{G\alpha} + U_{G\beta}I_{G\beta}) \quad (34)$$

$$Q = (U_{G\alpha}I_{G\beta} - U_{G\beta}I_{G\alpha}) \quad (35)$$

where $U_{G\alpha}, U_{G\beta}, I_{G\alpha}, I_{G\beta}$ are components of the grid voltage and the grid current in stationary $\alpha\beta$ coordinates.

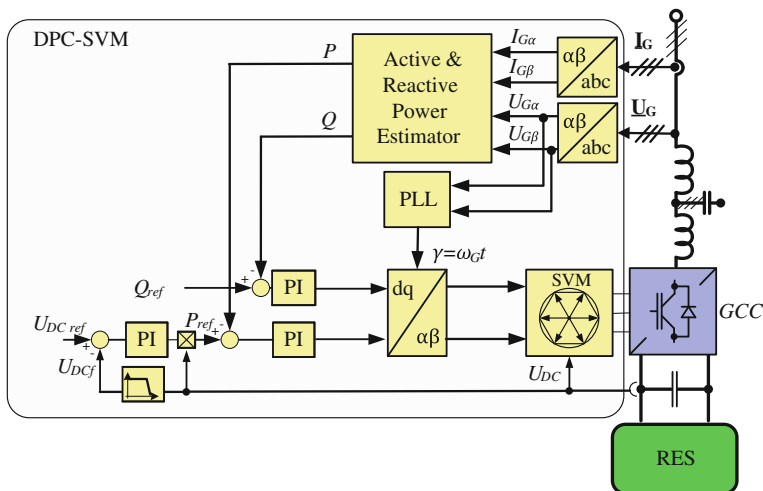
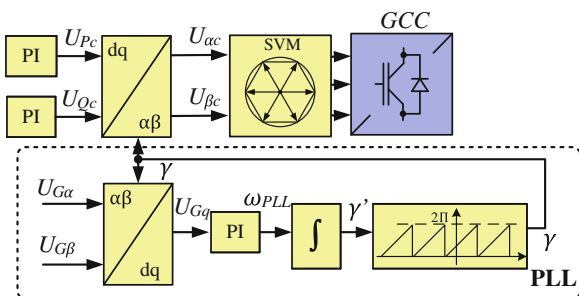


Fig. 17 Block scheme of Direct Power Control with Space Vector Modulation (DPC-SVM) and Phase Lock Loop (PLL)

Fig. 18 Phase Lock Loop (PLL) block scheme

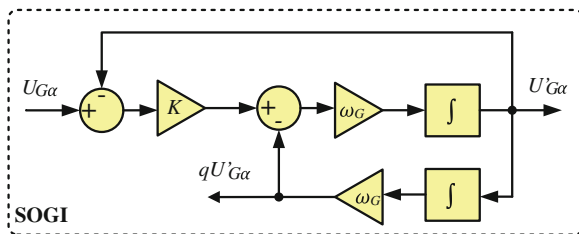


Important part of the control method is a PLL block (Fig. 18). In the PLL measured grid voltage components in stationary $\alpha\beta$ coordinates are transformed to synchronously rotating dq coordinates. Then, PI controller is minimizing of the q axis component which is responsible for the grid voltage SV angle. This angle is used for coordinates transformation in DPC-SVM control structure.

2.9 Voltage Dips Compensation Module

Hereafter, it is assumed that reader knows the GCC converter with basic control structure like DPC-SVM. Now, it is possible to implement a special functionalities

Fig. 19 Block scheme of a Second Order Generalized Integrator (SOGI) [85]



realized by additional control modules dedicated specially for standards and requirements needs. This sophisticated functions can be longer and more complicated than main algorithm itself. But let us focus only on selected, mature methods. The function should be simple in implementation and work in any operation conditions [85].

Voltage dips can appear in power systems quite often because e.g. of short circuits or intentionally on/off process of heavy loads. Usually sudden voltage changes can disturb operation of a power electronics converters control. In this case a converter can produce unsymmetrical and non-sinusoidal current. Moreover, in a DC voltage significant 100 Hz fluctuation can appears.

Additional control module designed for dips compensation provides symmetrical currents processed by the GCC in each phases for any kind of dips. The dips compensation module split unsymmetrical voltage into positive and negative sequence voltage components. In this case the negative voltage component is a main source of information about appearing voltage distortion. Separated voltage components can be used in DPC-SVM control structure with following rules and modifications:

- Implementation of the additional module of the AC voltage components extraction.
- New power estimator based on positive voltage components and actual AC grid current.
- DC voltage band-stop filter (notch filter) to eliminate fluctuation caused by negative voltage component.
- Grid voltage negative component feed-forward to referenced the SVM's input signals.

According to a definition, each asymmetry in three phase system can be represented by sum of a voltage components: positive, negative and zero sequence signals. By analogy it is possible to describe the three-phase system in stationary $\alpha\beta$ coordinates by two components: positive (rotating with grid frequency) and negative (rotating with grid frequency but in opposite direction), e.g. (36):

$$\underline{U}_G = \underline{U}_{Gp}e^{j\omega t} + \underline{U}_{Gn}e^{-j\omega t} \tag{36}$$

where $\underline{U}_{Gp}, \underline{U}_{Gn}$ —complex value of positive and negative voltage components respectively.

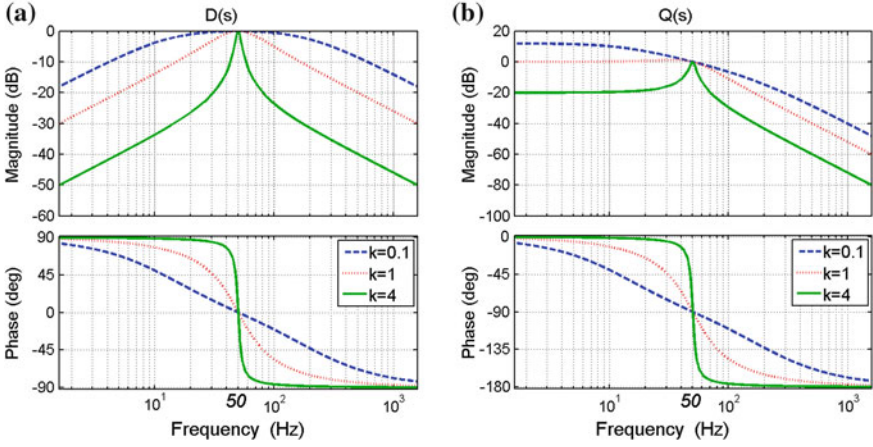
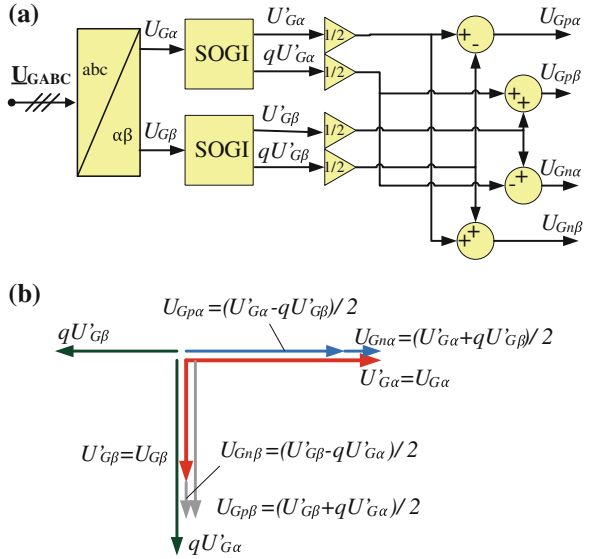


Fig. 20 Bode diagram for transmittances: **a** $D(s)$, **b** $Q(s)$

Fig. 21 Positive and negative components extraction from $U_{G\alpha}$, $U_{G\beta}$ actual grid voltage in the stationary $\alpha\beta$ coordinates: **a** block scheme for negative and positive voltage components separation, **b** vector diagram of the component separation process



The extraction and separation process of these components is realized by Second Order Generalized Integrator (SOGI) [85]. The SOGI block scheme is presented in Fig. 19. The SOGI transmittances $D(s)$ and $Q(s)$ are described by Eqs. (37) and (38):

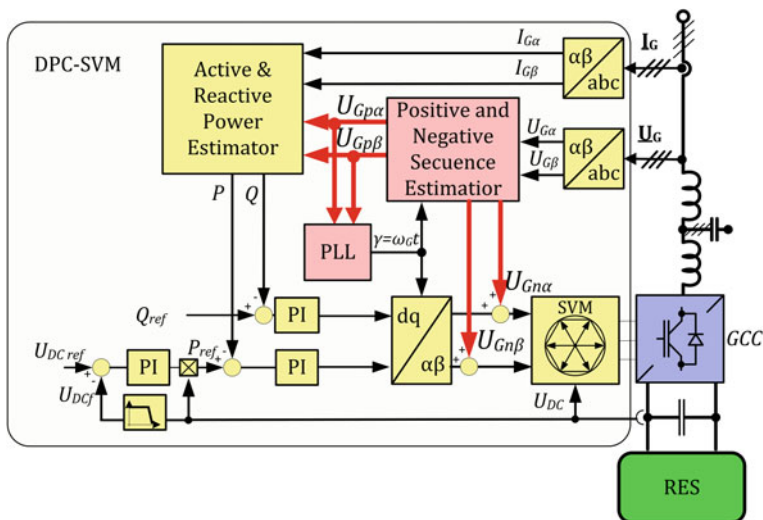


Fig. 22 Voltage Dips Compensator (VDC) module implemented in basic DPC-SVM vector control method

$$D(s) = \frac{U'_{Gz}}{U_{Gz}}(s) = \frac{k\omega_G s}{s^2 + k\omega_G s + \omega_G^2} \tag{37}$$

$$Q(s) = \frac{qU'_{Gz}}{U_{Gz}}(s) = \frac{k\omega_G^2}{s^2 + k\omega_G s + \omega_G^2} \tag{38}$$

The frequency characteristic of the SOGI are shown in Fig. 20. As can be seen the $D(s)$ transmittance operates as a low-pass filter, while $Q(s)$ transmittance provides a 90° phase shift for filtered U'_{Gz} signal.

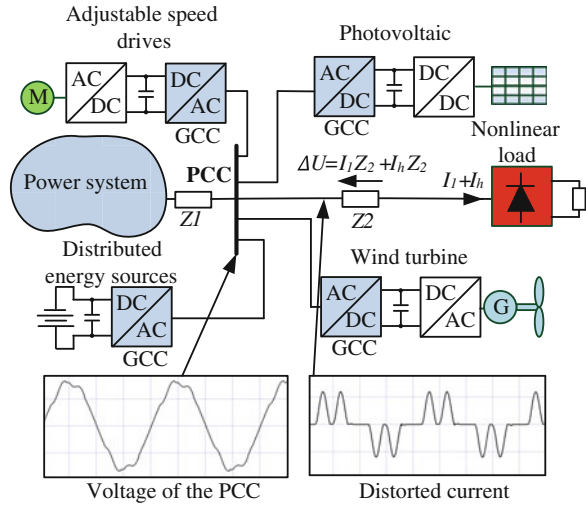
Hence, output signals of the SOGI are: filtered input signal of grid voltage component and its 90° shifted equivalent. Using the SOGI for both U_{Gz} , $U_{G\beta}$ components in $\alpha\beta$ coordinates system it is possible to extract positive and negative components of these voltages. The graphical representation of this solution is presented in Fig. 21.

Such Voltage Dips Compensator (VDC) module can be implemented in the basic vector control structure as presented in Fig. 22.

2.10 Higher Harmonics Compensation Module

Increasing number of nonlinear loads connected to the power system induce several problems mainly related with higher harmonics distortion. Undesired harmonics cause higher losses and devastation of electrical equipment connected

Fig. 23 Simplified section of a power system with a set of various devices and high power nonlinear load



to the power system. Moreover, higher harmonics can destroy power system devices e.g. transformers. Higher harmonics issues are related with both, voltage and current. Nonlinear loads (e.g. diode rectifiers) introduce to the grid hardly distorted current which can causes grid voltage distortion related to transmission line and grid impedances. All loads which are not properly secured and prepared for operation under distorted voltage conditions can work faultily or be damaged amplifying the distortion. Figure 23 presents sample power system operating with distorted voltage. The GCC which is the scope of this chapter operates as an interface between the grid and distributed active load (e.g. renewable energy sources, adjustable speed drives, and electric vehicles etc.). The modern power electronic converter should work correctly with distorted line voltage, not causing amplification of distortion, not disturbing operation of other devices and if it is possible be able to compensate harmonic distortion by rectifying/inverting sinusoidal current from/to the grid. To achieve this functionalities it is necessary to extend control algorithm by additional harmonics compensation control module described below.

Presented harmonics compensation algorithm operates based on extraction of higher harmonics from measured grid current. The extracted signal is gained and finally added to referenced voltage at the input of the SVM. Block scheme of control algorithm with additional function—current Higher Harmonic Compensation (HHC) module is presented in Fig. 24.

Grid voltage distorted by higher harmonics can be described as follows:

$$\underline{U}_G = U_1 e^{j\gamma} + U_5 e^{-j5\gamma} + U_7 e^{j7\gamma} + \dots + U_{(6k\mp 1)} e^{\mp j(6k\mp 1)\gamma} \quad (39)$$

where, $\gamma = \omega_G t$; $k = 1, 2, \dots$

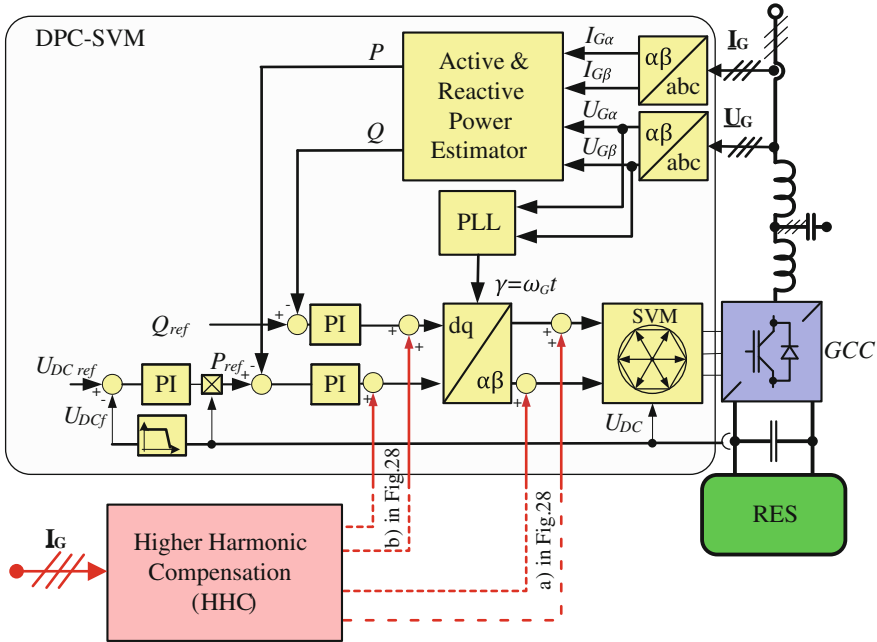


Fig. 24 Block scheme of the control method with Higher Harmonic currents Compensation (HHC) module

The most significant and frequently occur harmonics in the grid are: 250, 350, 550 and 650 Hz. There is simple relation between harmonics order and their rotating direction:

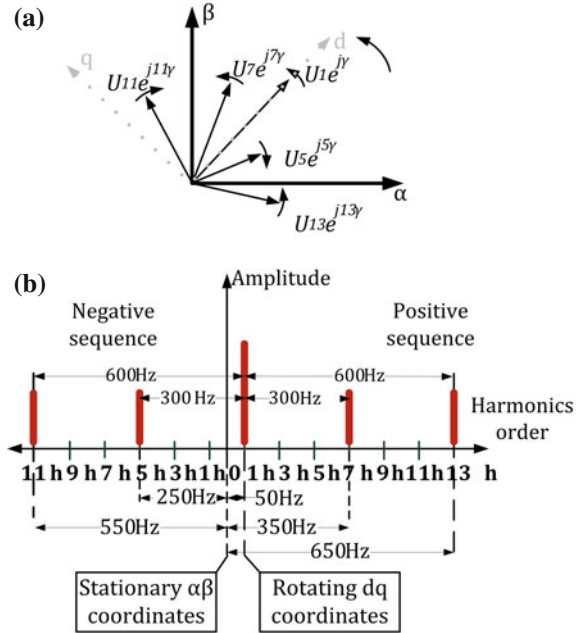
- positive harmonics, rotating in the same direction as fundamental one and can be expressed as: $3k + 1$ (1, 4, 7, 10...),
- negative harmonics, rotating in the opposite direction to the fundamental and can be expressed as: $3k + 2$ (2, 5, 8, 11...),
- zero harmonics, with no phase shift between themselves can be expressed as: $3k + 3$ (3, 6, 9, 12...).

The idea of harmonics description rotating in positive and negative direction can be seen in the SV diagram (Fig. 25a) or harmonics spectrum in different coordinates (Fig. 25b) (stationary $\alpha\beta$ coordinates and dq coordinates rotating synchronously with grid voltage fundamental component vector (i.e. with frequency 50 or 60 Hz)).

Higher harmonics extraction from measured signal can be realized by the GCC control as follows:

- In synchronous coordinates—measured values of the currents are transformed into rotating coordinates system dq [82]. As a reference signal (angle) multiplication of the fundamental harmonic phase angle is used. Respectively for 5th

Fig. 25 Illustration of positive and negative sequence harmonics based on 5th, 7th, 11th and 13th harmonics: **a** space vector diagram in stationary $\alpha\beta$ coordinates, **b** harmonics spectrum



harmonic multiplication by 5 of the fundamental phase angle, 7th is multiplication by seven, etc. After transformation each harmonics are represented by DC components. It gives possibility for extraction constant signal (voltage) which level gives information about each harmonics contend in measured current. To avoid distortion and oscillations in measured signal proper filters should be used. Compensation signal with opposite sign and tuned gain is given as an additional element (HHC block) to the reference values for the SVM.

- Filtration in stationary $\alpha\beta$ coordinates with a Resonant Controllers (RC). The RCs are used as a high-band tuned band-pass filters applied in closed control loops [83]. Transfer function of an ideal band-pass filter is as follows:

$$U_h(s) = K_i \frac{s}{s^2 + (h\omega)^2} \tag{40}$$

where K_i is a gain of the filter, ω is a resonant frequency and h is an order of the harmonics.

Bode diagram of an ideal resonant filter expressed by Eq. (40) for different gain values (K_i) are presented in Fig. 26a.

The resonant frequency is set to 250 Hz. For ideal band-pass filter the gain is infinity. Because of very narrow pass-band the frequency characteristic of the filter has to be exactly matched to frequency of the compensated harmonics. Any difference between measured and assumed frequency can cause improper operation and even lost stability of the control algorithm. To avoid this disadvantage

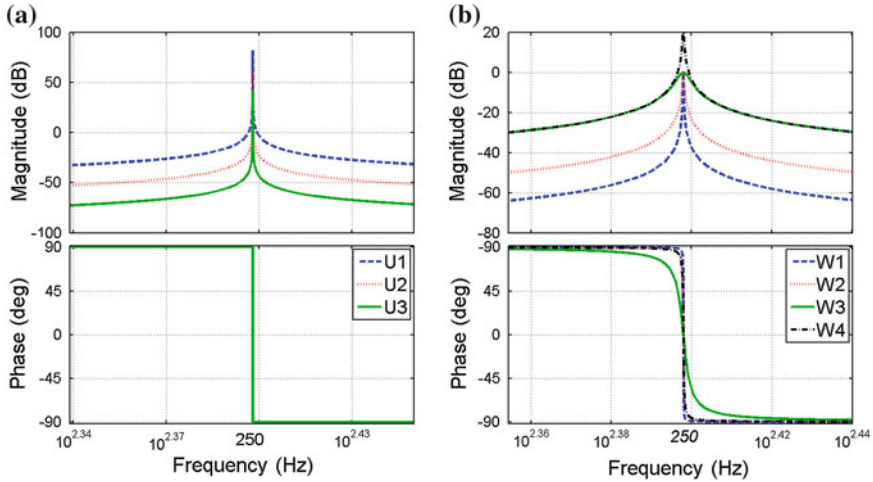


Fig. 26 Bode diagram of the resonant controllers tuned to 250 Hz frequency: **a** ideal RC with different filter gains: $K_{i(U1)} = 0.01$, $K_{i(U2)} = 1$, $K_{i(U3)} = 100$; **b** non-ideal RC with different filter gains (K_i) and pass-band width (ω_c): K_i ($K_{i(W1)} = K_{i(W2)} = K_{i(W3)} = 1$, $K_{i(W4)} = 10$) and ω_c ($\omega_{c(W1)} = 0.1$, $\omega_{c(W2)} = 1$, $\omega_{c(W3)} = 10$, $\omega_{c(W4)} = 1$)

structure of non-ideal band-pass filter should be used. The transfer function of non-ideal resonant band-pass filter is as follows:

$$W_{hN}(s) = K_i \frac{\omega_c s}{s^2 + \omega_c s + (h\omega)^2} \quad (41)$$

where K_i is a gain of the controller, ω_c defines width of the pass-band and slope steepness of the filter, h is an order of the harmonic.

Bode diagram of the non-ideal resonant filter for different gain values (K_i) are shown in Fig. 26b.

It can be observed that extending the pass-band results in reduction of the filter slope steepness what gives worse selectivity of the filter. It is the reason why the balance between filter accuracy and width of the pass-band need to be kept.

To separate particular harmonics in stationary $\alpha\beta$ coordinates system a single filter tuned for each frequency is required. But taking into consideration fact that rotating directions are easy to observe and harmonics are symmetrical in terms of rotating coordinates dq it is possible to extract two harmonics using only one RC, what is shown in Fig. 25b. It can be noticed that for control algorithm both 5th and 7th harmonics are observed as 300 Hz frequency harmonic.

Block diagrams of both presented harmonics compensation methods are presented in Fig. 27.

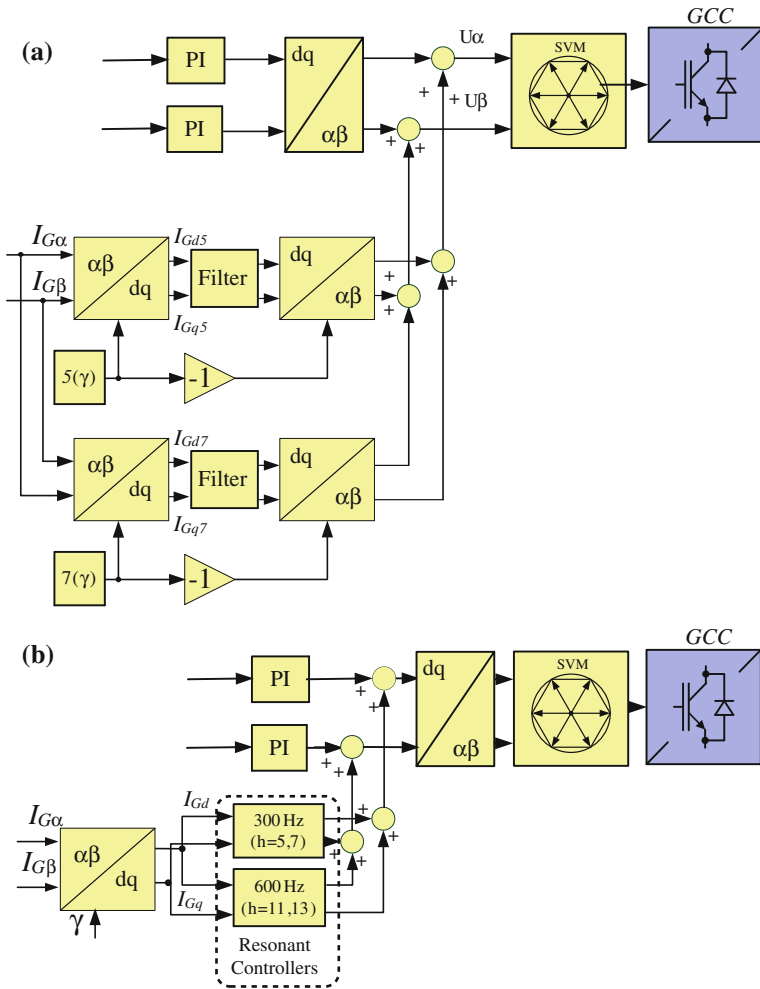


Fig. 27 Block diagram of Higher Harmonic Compensation (HHC) module realized by using: **a** Synchronous Coordinates, **b** Resonant Controllers (RES)

2.11 Active Power Feed-Forward (APFF) Module

The GCC connected to the power system should operate as an universal interface between the grid and different electrical devices (Fig. 23), providing high dynamics and stability of the control algorithm independently from the type of connected device. To achieve this functionality another control module: Active Power Feed-Forward (APFF) is introduced.

The APFF which gives information about the active power flow between the GCC and the grid can be applied as an additional module to the main control

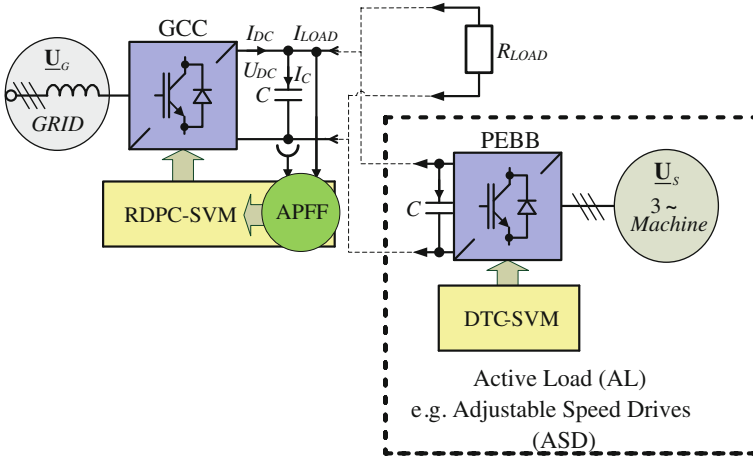


Fig. 28 Block diagram of the GCC system with the Active Power Feed-Forward (APFF) control module based on instantaneous values of DC voltage and current

algorithm of the GCC. To get an information about instantaneous value of the active power exchanged between the converter system and the grid, without need of implementation additional current and voltage sensors following method is proposed. Estimated active power is product of instantaneous DC voltage and current, as is shown in Eq. (42).

$$P_{GC} = U_{DC} \times I_{DC} \quad (42)$$

Block diagram of the GCC system with additional Active Power Feed-Forward control module is presented in Fig. 28

To achieve stable operation of the control algorithm with the APFF control module some additional filters on the measured DC current are needed. Figure 29 shows selected voltages and currents waveforms in the grid converter system interconnecting AL (e.g. consisted of an ASD) within transient responds to step changes of the machine load torque without (Fig. 29a) and with APFF (Fig. 29b) control module. It can be observed that implementation of the proposed APFF allows for significant reduction of the DC voltage fluctuations during load transients.

2.12 Impact of Grid Impedance

In this subsection impact of an increased grid impedance on a GCC with LCL filter is presented. Figure 30 shows block scheme of the considered system with additional high value of the grid impedance L_{GS} .

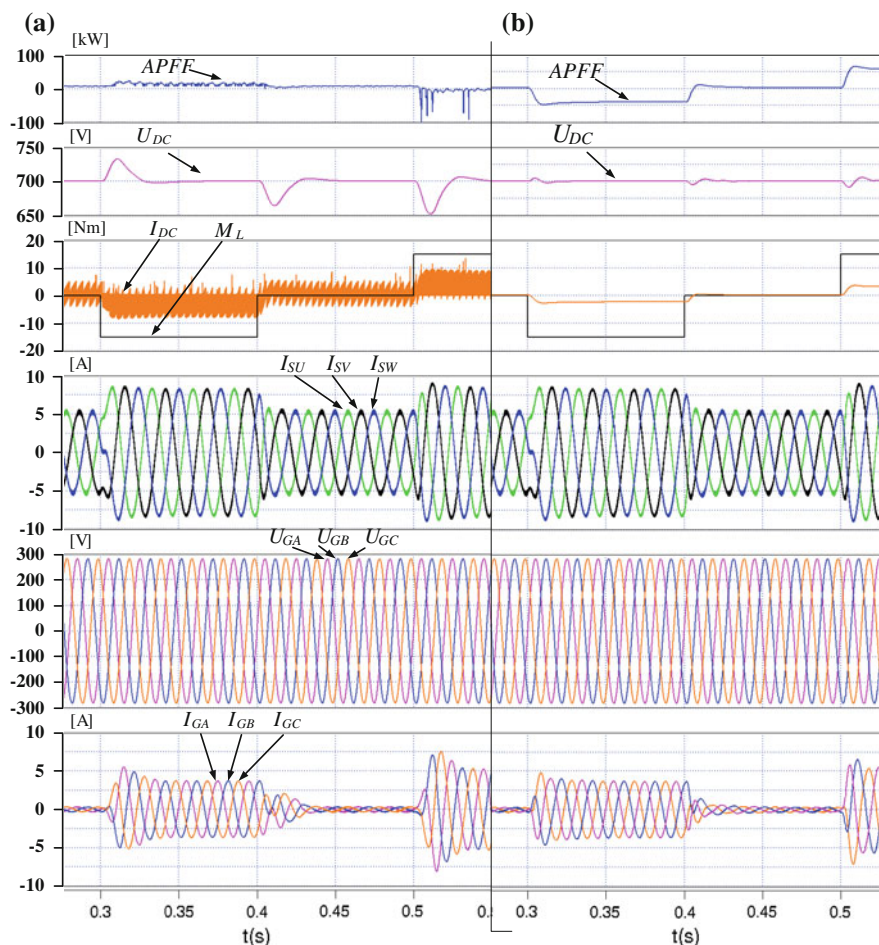


Fig. 29 Influence of Active Power Feed-Forward (APFF) applied in the GCC system interconnecting AL (e.g. ASD). System operates: **a** without APFF; **b** with APFF. From the top APFF—estimated active power (kW); U_{DC} —DC voltage (V); I_{DC} —DC current (A); M_L —machine load torque (Nm); I_{S1} , I_{S2} , I_{S3} —machine stator currents (A); U_{GA} , U_{GB} , U_{GC} —grid voltage (V); I_{GA} , I_{GB} , I_{GC} —grid currents (A)

2.13 Rectifying Operation of the Grid Connected Converter

Behavior of the system during rectifying operation of the GCC has been verified. A borderline values of the grid impedance for rectifying operation of the GCC have been found for different nominal powers of the system and collected in Table 4. Figure 31 presents voltages and currents of the system while the grid

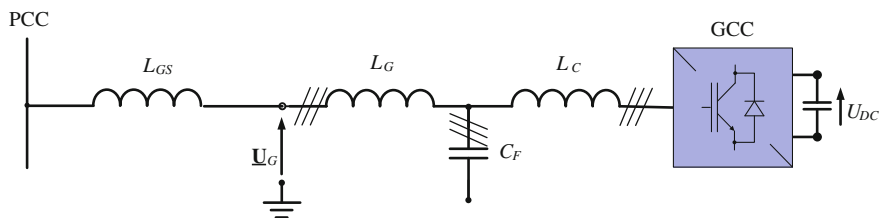


Fig. 30 Block diagram of GCC and LCL filter system with additional high grid impedance L_{GS}

Table 4 Parameters of the LCL filter for selected power ranges of the system during rectifier operation with DC load (*DC LOAD*)

GCC rated power (kW)	L_C (mH)	C_F (μ F)	L_G (mH)	L_{MGS} (mH)	<i>DC LOAD</i> (Ω)
5	9.9	3.98	2.97	60	147
15	3.3	11.9	0.99	20	49
55	0.9	43.7	0.27	4	13.36
400	0.124	318.3	0.037	0.125	1.84

Estimated borderline values of grid impedance for stable operation of the system (L_{MGS})

impedance (L_{GS}) is increasing. As it can be seen above the maximal value of the grid impedance (L_{MGS}) system loses its control stability.

2.14 Inverting Operation of the Grid Connected Converter

Behavior of the system during inverting operation of the GCC has been also tested. A borderline values of grid impedance under inverting operation have been found for selected power ranges of the system and collected in Table 5. In Fig. 32 voltages and currents of GCC system are presented while grid impedance (L_{GS}) is increasing. As it can be notice again after exceed maximum value of the grid impedance (L_{MGS}) system lose stability. Obtained value of the grid impedance is higher than in case of rectifying operation. Moreover it should be noticed that DC voltage is suddenly increasing while in case of rectifying operation the DC voltage is decreasing or is more unstable (Fig. 31d).

Based on presented simulation and experimental study following conclusion can be formulated: before connecting GCC to the electrical network to provide efficient and stable operation of the system a grid impedance should be known. It can be estimated by GCC itself by use of additional grid impedance estimation module. For further information please refer to [51, 52, 59, 87].

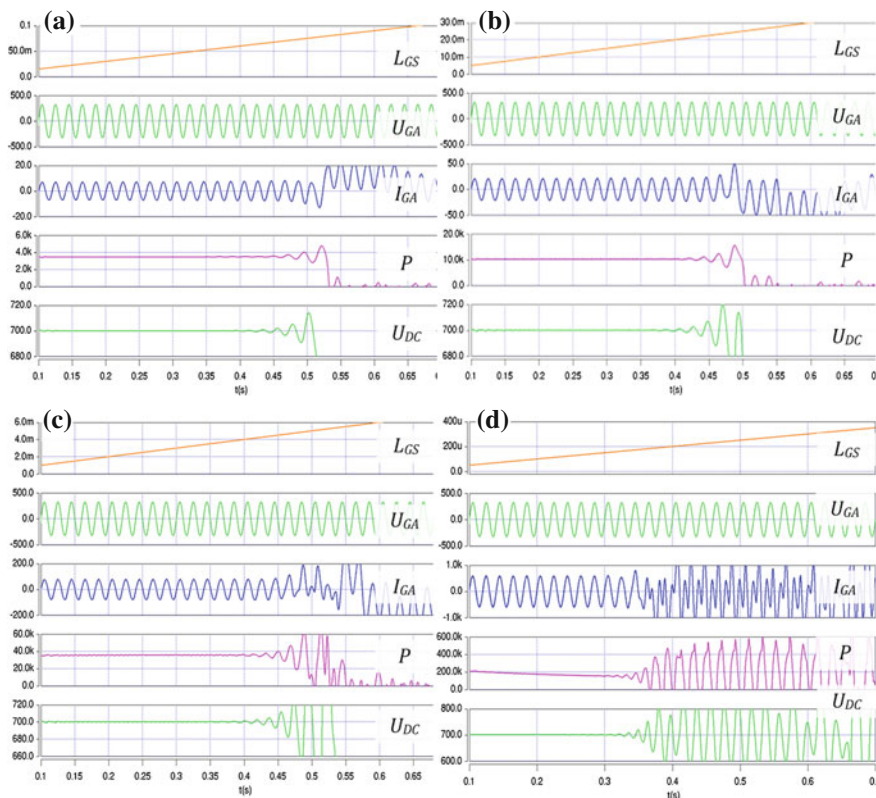


Fig. 31 Grid voltage and current waveforms during rectifying operation of the GCC with increasing grid impedance (L_{GS}). For different nominal power values of the GCC: **a** 5 kW; **b** 15 kW; **c** 55 kW; **d** 400 kW. From the *top* grid impedance (mH, μ H), U_{GA} grid voltage in phase A (V), I_{GA} grid current in phase A (A), P estimated active power (kW), U_{DC} DC voltage of the GCC (V)

Table 5 Parameters of the LCL filter for selected power ranges of the system during inverting operation with DC current source I_{DC}

GCC rated power (kW)	L_C (mH)	C_F (μ F)	L_G (mH)	L_{MGS} (mH)	I_{DC} (A)
5	9.9	3.98	2.97	70	5.3
15	3.3	11.9	0.99	22	15
55	0.9	43.7	0.27	5.5	70
400	0.124	318.3	0.037	0.3	550

Estimated borderline values of grid impedance for stable operation of the system L_{MGS}

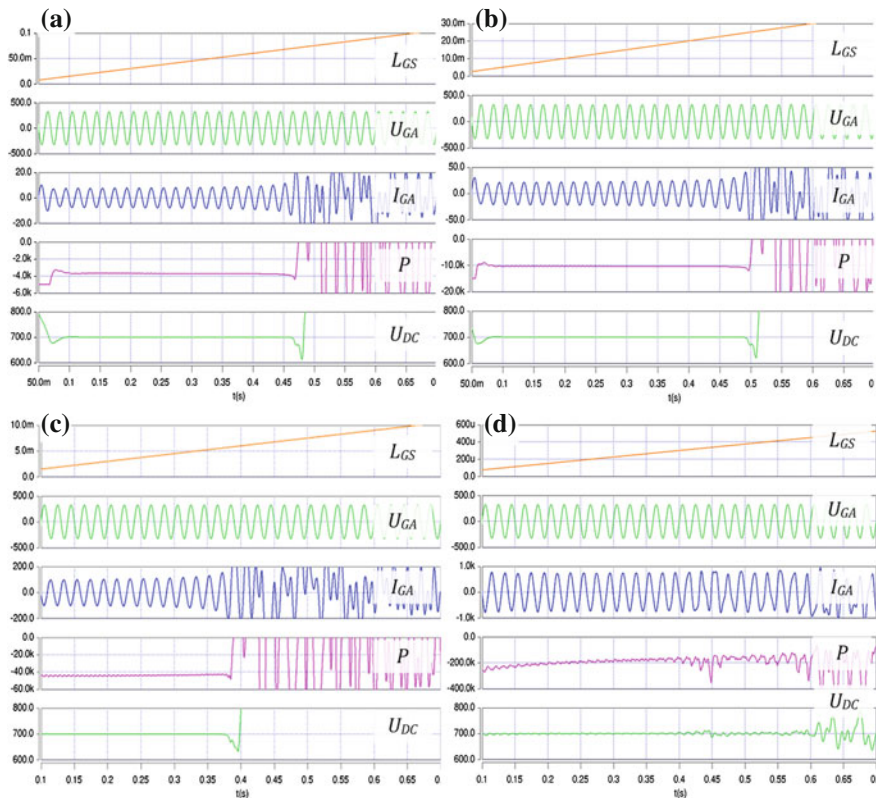


Fig. 32 Grid voltage and current waveforms during rectifier operation of the GCC with increasing grid impedance (L_{GS}). For different nominal power values of the GCC: **a** 5 kW, **b** 15 kW, **c** 55 kW, **d** 400 kW. From the *top* L_{GS} grid impedance (mH, μ H), U_{GA} grid voltage in one phase (V), converter current in one phase (A), estimated active power (kW), DC voltage of the GCC (V)

2.15 Reliable Control Method to Grid Voltage Disturbances

As it has been mentioned all presented control modules can be integrated in final control method of the GCC operating in distributed energy system. Thanks to additional modules developed control method is reliable in respect to grid voltage dips and higher harmonics. Hereafter, this new control algorithm can be presented as Robust Direct Power Control with Space Vector Modulation (RDPC-SVM). The term “*robust*” in the name of proposed control refers to the fact that the RDPC-SVM method is expected to operate in an uncertain environment with respect to the system dynamic. In the literature it can be found that:

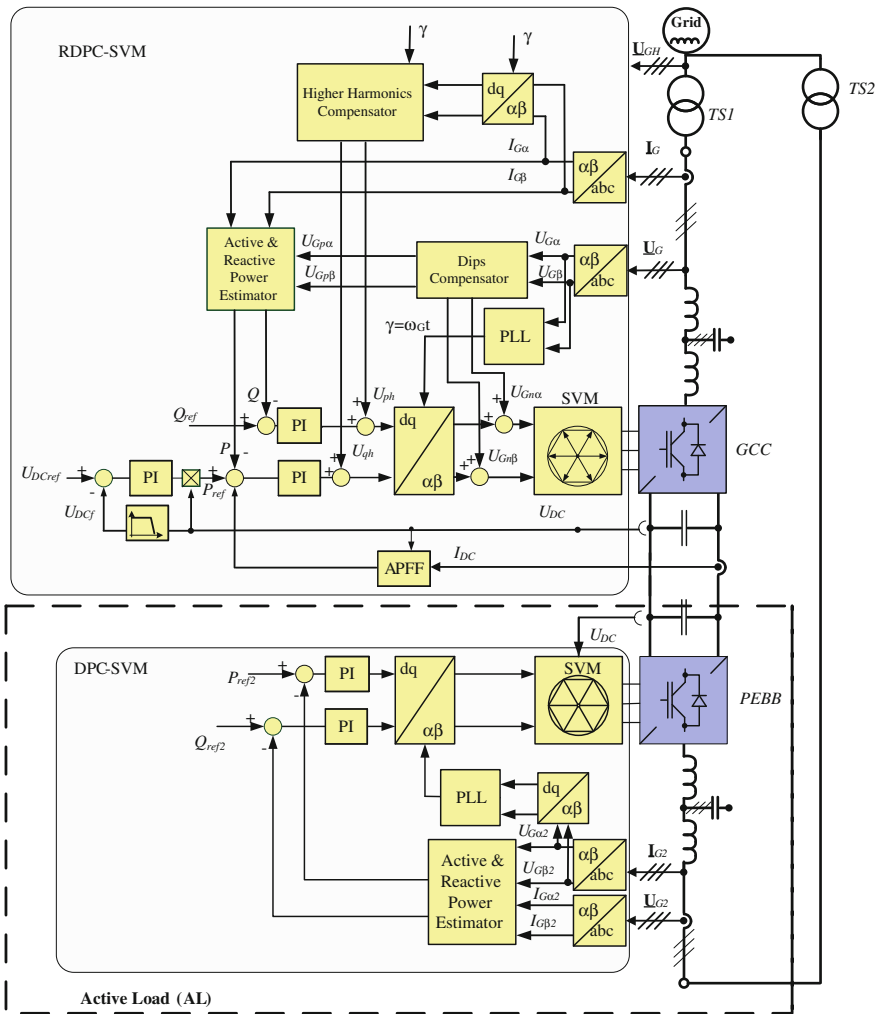


Fig. 33 Block diagram of developed Robust Direct Power Control Space with Space Vector Modulation (RDPC-SVM) applied for control the GCC in an AC-DC-AC system interconnecting energy sources

There are several ways in which systems can be uncertain, and in this course we will target the main three: (1) The initial conditions of a system may not be accurately specified or completely known; (2) Systems experience disturbances from their environment, and system commands are typically not known a priori. (3) Uncertainty in the accuracy of a system model itself is a central source. Any dynamical model of a system will neglect some physical phenomena, and this means that any analytical control approach based solely on this model will neglect some regimes of operation [102].

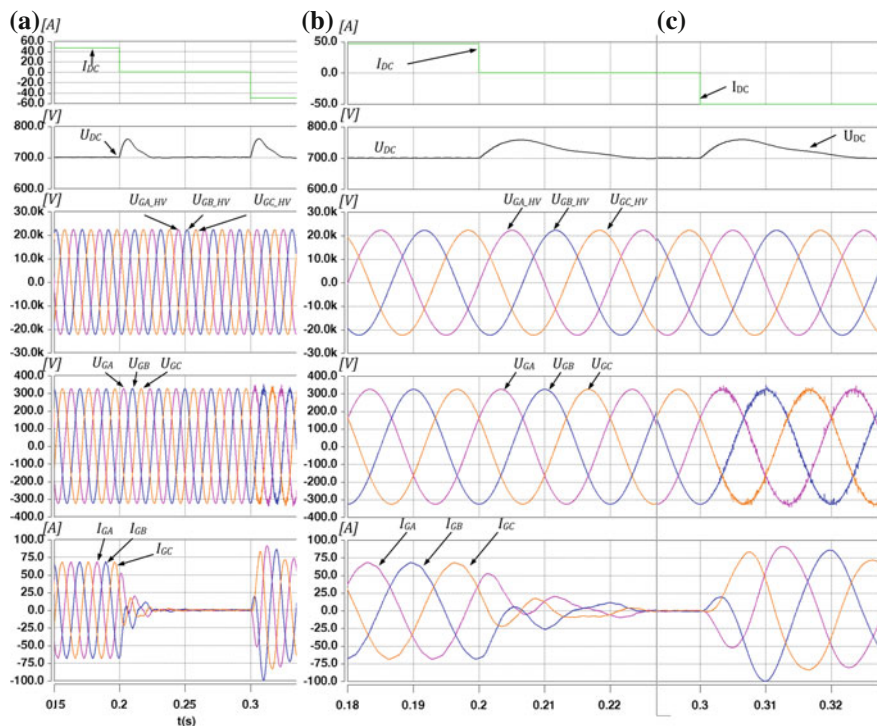


Fig. 34 Operation of the 55 kW the GCC with the RDPC-SVM under different operation modes. The GCC operation mode change: **a** from rectifying to no-load operation and to inverting mode; **b** zoomed step change from rectifying to no-load operation; **c** zoomed step change from no-load to inverting operation. From the top I_{DC} —DC-link current (A); U_{DC} —DC-link voltage (V); U_{GA_HV} , U_{GB_HV} , U_{GC_HV} —voltage on the high side of the grid transformer (V); U_{GA} , U_{GB} , U_{GC} —voltage on the low side of the transformer (V); I_{GA} , I_{GB} , I_{GC} —phase grid currents (A)

In our case all three mentioned points can be somehow found in the real power system and the GCC operation. Therefore, the reliable RDPC-SVM control algorithm is consisted of following control modules:

- Direct Power Control with Space Vector Modulation (DPC-SVM) for control converter currents and DC voltage of the GCC, with Active and Reactive Power Estimators.
- Grid angle synchronization using Phase Locked Loop (PLL) for grid angle estimation.
- Voltage Dips Compensation (VDC).
 - Voltage positive and negative component extraction using Dual Second Order Generalize Integrator (DSOGI). Negative Component Voltage Feed-Forward.
 - 100 Hz DC voltage notch filter.

- Active Power Feed-Forward control using active power estimation based on instantaneous values of DC voltage and current.
- Higher Harmonic Compensation (HHC) (based on Resonant Controllers).

The block diagram of the presented RDPC-SVM control method applied to the GCC in an AC-DC-AC interconnecting energy sources is shown in Fig. 33. Further, some selected simulation results showing operation of the RDPC-SVM control algorithm are presented. To achieve operation conditions like in a typical power system the model of 3-phase 15 kV/400 V grid transformer has been used with parameters based on producers datasheet [103].

As it can be seen in Fig. 34 the GCC operates properly during different operation modes. Applied additional control modules have no negative impact on dynamic of the control system.

Figure 35 presents operation of the GCC with RDPC-SVM scheme supplied by distorted grid voltage (high order harmonics and voltage dips). It can be observed that due to additional control modules the grid currents are controlled to be sinusoidal like and symmetrical in spite of grid voltage disturbances. Good results are obtained in steady and in transient states.

Finally Fig. 36 shows operation of the GCC with RDPC-SVM supplied by significantly distorted voltage (high order harmonics and voltage dips).

3 Experimental Test Bench

In this subsection the behavior of discussed system and control method is presented under experimental conditions, similar to these which can appear in the real power system. To verify proper operation of described control method an experimental test bench has been developed for selected power of the GCC (3, 5, 15, 55 kW). Laboratory setup is composed of the GCC (scope of interest) and another DC-AC (treat as a PEBB). To reflect operation in real power system following configuration of the test bench has been proposed:

- The AC-DC-AC system interconnecting two different AC voltage sources—scheme of the system is presented in Fig. 37. This configuration allows to model connection of two different power systems (e.g. with different frequencies or voltage levels) with bidirectional energy flow. The GCC has been controlled by RDPC-SVM control algorithm.
- The AC-DC-AC system operates in closed loop of power circuit—scheme of the system is presented in Fig. 38. This system configuration allows for bidirectional power flow as well as arranging different operating conditions for the GCC with AL. It gives also ability for operation of both converters under nominal power while from the grid only energy covering the system losses are used. As in previous case in the grid side converter the RDPC-SVM control method has been implemented and verified by series of experimental tests.

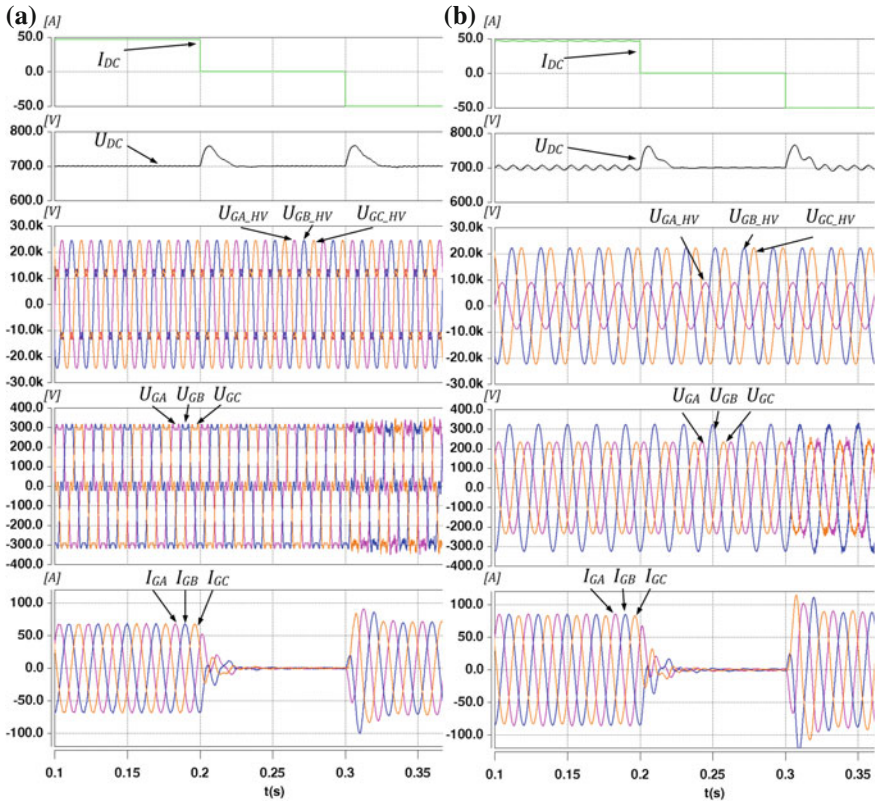


Fig. 35 Operation of 55 kW the GCC with the RDPC-SVM during transients with grid voltage disturbances. The GCC operation mode step change: **a** from rectifying, to no-load operation and to inverting operation, grid voltage distorted by high order harmonics (20 % of 5th and 10 % of 7th harmonics); **b** from rectifying to no-load operation and to inverting operation, grid voltage distorted by 60 % dip in phase A. From the *top* I_{DC} —DC-link current (A); U_{DC} —DC-link voltage (V); U_{GA_HV} , U_{GB_HV} , U_{GC_HV} —voltage on the high side of the grid transformer (V); U_{GA} , U_{GB} , U_{GC} —voltage on the low side of the transformer (V); I_{GA} , I_{GB} , I_{GC} —phase grid currents (A)

Figure 39 shows voltages and currents of the GCC with implemented basic DPC-SVM algorithm. The converter is working under distorted grid voltage (30 % voltage dip in one phase) condition. As it can be noticed: without dips compensation module the converter currents are unbalanced and non-sinusoidal. The current the THD factor is around 20 %.

Similar situation is shown in Fig. 40 (50 % voltage dip in one phase) but with proposed the RDPC-SVM control algorithm. It can be seen that converter currents are kept sinusoidal and symmetrical. In spite of high grid voltage disturbances, the current the THD factor is below 1.0 %. This feature of the GCC significantly reduce the negative impact of power electronics converter on the grid voltage, especially under distorted voltage and high grid impedance.

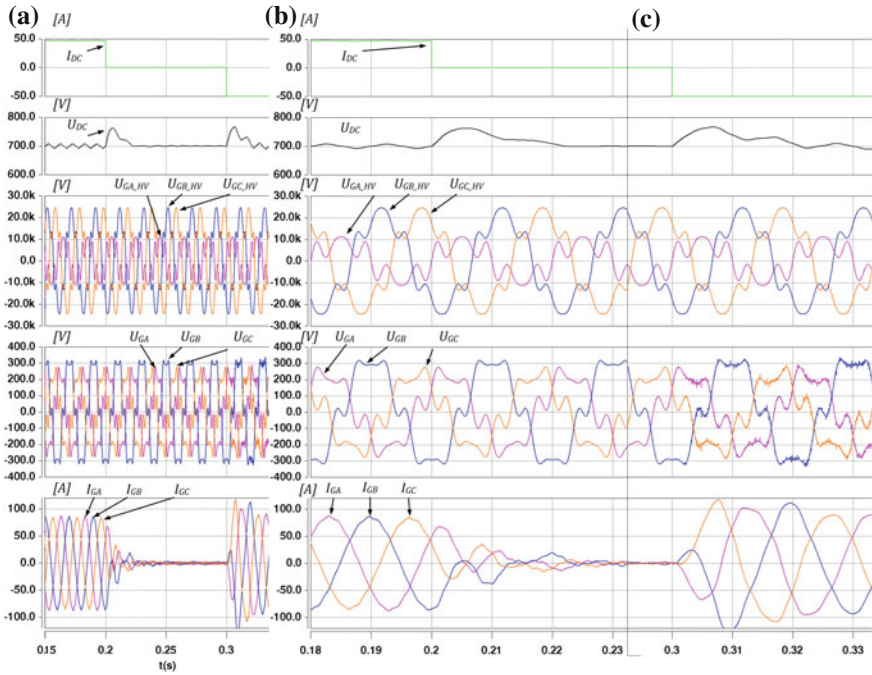


Fig. 36 Operation of 55 kW the GCC with the RDPC-SVM during transients with grid voltage disturbances: dips and harmonics (40 % dip in one phase, 20 % of 5th and 10 % of 7th harmonics). The GCC operation mode transients: **a** from rectifying, to no-load operation and to inverting operation; **b** Zoomed rectifying to no-load operation; **c** Zoomed from no-load to inverting operation. From the *top* I_{DC} —DC-link current (A); U_{DC} —DC-link voltage (V); U_{GA_HV} , U_{GB_HV} , U_{GC_HV} —voltage in high side of the grid transformer (V); U_{GA} , U_{GB} , U_{GC} —voltage in the low side of the transformer (V); I_{GA} , I_{GB} , I_{GC} —phase grid currents (A)

4 Summary and Conclusion

Grid Connected AC-DC Converters (GCC) are used for interfacing distributed energy sources, storages or loads. In recent years there is a strong trend to provide GCCs which assure bidirectional energy flow with as high power quality as possible. To obtain such features of the GCC an advanced control methodology is required. It can be observed an analogy to fast and never ending development of Adjustable Speed Drives (ASD) control methods since last 50 years. In case of ASD researcher wants to obtain the best accuracy, efficiency, dynamic, steady states operation parameters and finally power quality. The list of goals for control methods are rather open and instead to be shorter is longer every years. A control of the GCC can be treated as a dual problem to this defined in case of drives in previous years. Moreover, the important issue in case of the GCC control has to be taken into account i.e. constantly changing and updating an IEC, IEEE, SEMI, or “grid codes” standards and regulations.

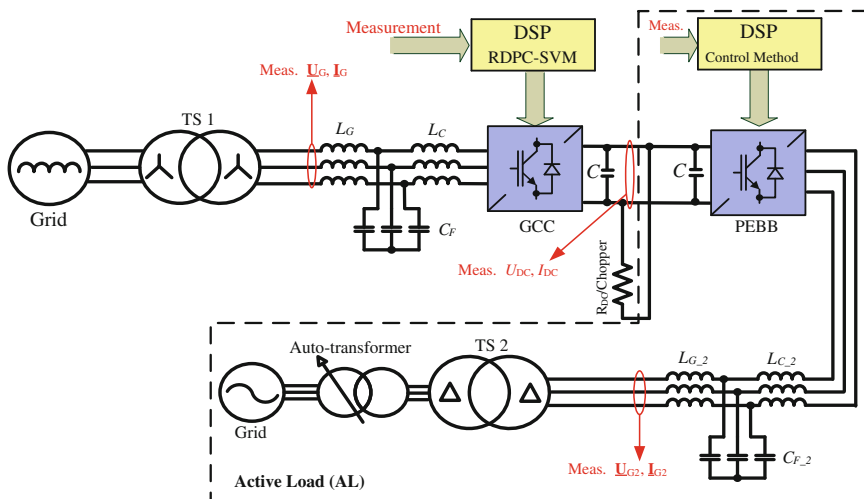


Fig. 37 Configuration of the AC-DC-AC system interconnecting two different voltage sources; model of two different power systems

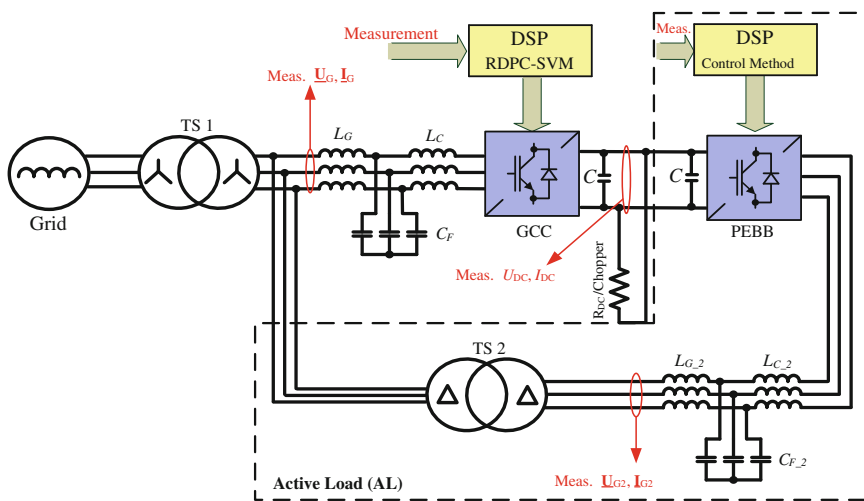


Fig. 38 Configuration of the AC-DC-AC system operating in closed loop of power flow. Setup allows to test the GCC under grid faults with rated power

To fulfill all above mentioned requirements a very flexible software (estimation and control algorithms) has to be developed, tested and implemented. In this chapter the idea of the GCC, treated as Power Electronics Building Block (PEBB) that is unified and ready for programming of different sophisticated functionalities, is given. Authors tried to show that the software (control methods) should be

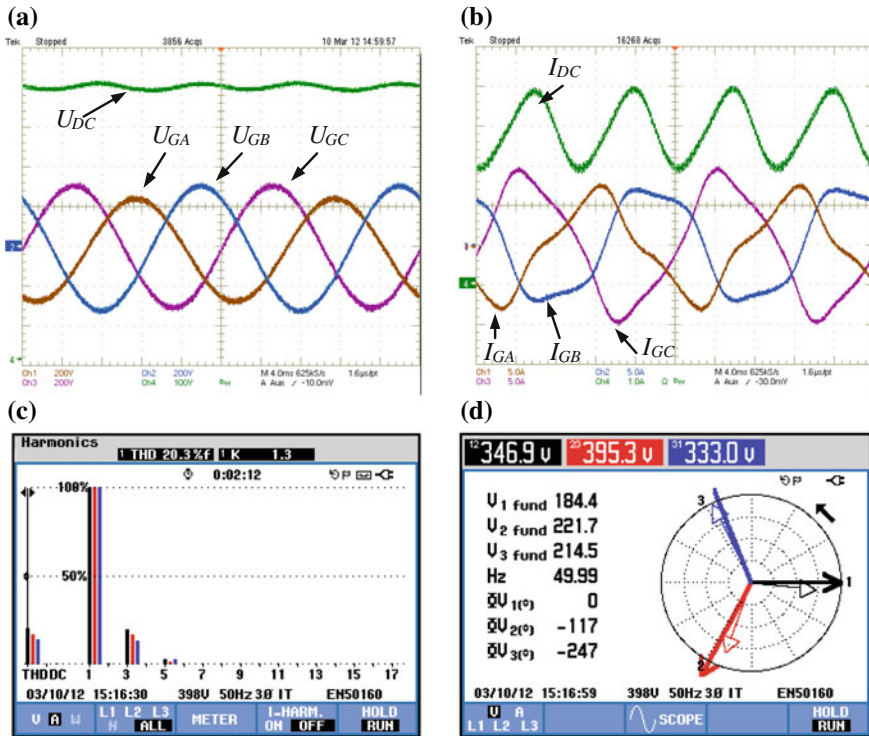


Fig. 39 Operation of the GCC with basic DPC-SVM algorithm under distorted grid voltage conditions (30 % dip in one phase of supplying voltage). **a** U_{AG} , U_{BG} , U_{GC} —grid voltage, U_{DC} —DC-link voltage (V); **b** I_{GA} , I_{GB} , I_{GC} —grid currents, I_{DC} —DC current (A); **c** grid current spectrum and the THD factor (20.3 %); **d** grid voltage and currents vector diagram

designed in modularity way allows to update and add new demanded functions (e.g. dips compensations module, higher harmonics compensation module or standalone operation mode module, etc.). Based on this assumption a new, reliable for grid voltage faults condition control method is proposed: a Robust Direct Power Control with Space Vector Modulation (RDPC-SVM). This control methods joins years of experiences and ideas developed in the research team of prof. Kazmierkowski the Institute of Control and Industrial Electronics, Warsaw University of Technology. The RDPC-SVM is based on generic structure of DPC-SVM extended by implementing several additional control modules assures a new capabilities. Obtained features are verified and tested by simulations and experimental power system [51].

Summarizing, modules of the RDPC-SVM control algorithm gives ability for:

- higher harmonics compensation,
- stable and proper operation even with higher grid impedance,
- stable and proper operation during voltage dips,

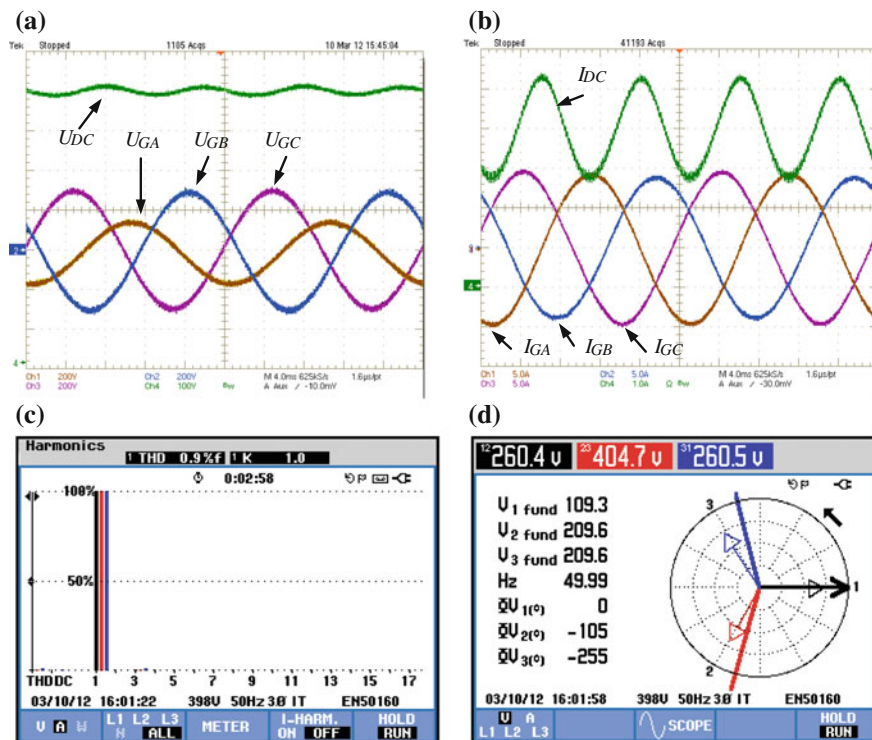


Fig. 40 Operation of the GCC with proposed RDPC-SVM algorithm supplied under distorted grid voltage conditions (50 % dip in one phase of supplying voltage). **a** U_{AG} , U_{BG} , U_{GC} —grid voltage, U_{DC} —DC voltage (V); **b** I_{GA} , I_{GB} , I_{GC} —grid currents, I_{DC} —DC current (A); **c** grid current spectrum and the THD factor (0.9 %); **d** grid voltage and currents vector diagram

- decreased negative impact on the grid voltage, hence reduction of flicker phenomenon (e.g. observed as light blinking) is reduced.

The presented control algorithm is promising for growing number of power electronic converters operating as an interface between the grid and *Renewable Energy Sources* (RES) or *Active Loads* (AL). In the future sustainable AC or DC grids an asymmetrical higher harmonics can appear even more often than symmetrical because the number of single phase loads is higher than three phase loads. Hence, the compensation of asymmetrical harmonics should be taken into account in research process for the GCC. This aspect is not described in the chapter, however, more information can be found in [52]. Moreover, there are many other problems that should be solved in the nearest future by intelligent PEBB.

Authors would like to stress that problems presented in this chapter are just a small part in the field of issues related to integration a GCC with the grid.

The RDPC-SVM control method are going to be used in a TWERD company in Torun, Poland for grid connected converters [101]. It is believed that due to continuous development in power electronics, digital signal processing and intelligent control techniques the newest solution in power electronics will have a strong impact on power quality and reliability improvements in coming decades.

Acknowledgments This work has been partially supported by the National Center for Research and Development, Poland, developing grant no. NR01 0014 06/2009 and also by the European Union in the framework of European Social Fund through the Warsaw University of Technology Development Program, realized by Center for Advanced Studies.

References

1. W. Koczara, Compensation in demand for drive power, in *Proceedings of the PEMC 1990 Conference*, pp. 354–358
2. M.H.J. Bollen, in *Understanding Power Quality Problems—Voltage Sags and Interruptions*. The Institute of Electrical and Electronics Engineers INC (IEEE), Nowy Jork, NY, 10016-5997, John Wiley & Sons Inc (2000)
3. IEEE recommended practice for monitoring electric Power quality, IEEE, Std. 1159-1995, Nowy Jork (1995)
4. IEEE Std 519-1992, IEEE Recommended Practices and Requirements for Harmonic Control in Electrical Power Systems, The Institute of Electrical and Electronics Engineers, Inc., USA (1993)
5. EN 50160, Voltage characteristics of electricity supplied by public electricity networks
6. IEC 61000-2-2 Electromagnetic Compatibility (EMC), Part 2: Environment, Section 2: Compatibility levels for low-frequency conducted disturbances and signaling In public low-voltage Power supply systems
7. IEC 61000-2-4, Electromagnetic compatibility (EMC)—Part 2-4: Environment—Compatibility levels in industrial plants for low-frequency conducted disturbances
8. IEC 61000-3-2 Electromagnetic compatibility (EMC)—Part 3-2: Limits—Limits for harmonic current emissions (equipment input current ≤ 16 A per phase)
9. IEC 61000-3-3, Electromagnetic compatibility (EMC)—Part 3-3: Limits—Limitation of voltage changes, voltage fluctuations and flicker in public low-voltage supply systems, for equipment with rated current ≤ 16 A per phase and not subject to conditional connection
10. IEC 61000-4-7 „Electromagnetic compatibility (EMC)—Part 4-7: Testing and measurement techniques—General guide on harmonics and interharmonics measurements and instrumentation, for power supply systems and equipment connected thereto
11. IEC 61000-4-11, Electromagnetic compatibility (EMC)—Part 4-11: Testing and measurement techniques—Voltage dips, short interruptions and voltage variations immunity tests
12. IEC 61000-4-14, Electromagnetic compatibility (EMC)—Part 4-14: Testing and measurement techniques—Voltage fluctuation immunity test for equipment with input current not exceeding 16 A per phase
13. IEC 61000-4-15, Electromagnetic compatibility (EMC)—Part 4-15: Testing and measurement techniques—Flickermeter—Functional and design specifications
14. SEMI F47-0706 Specification for Semiconductor Processing Equipment Voltage Sag Immunity
15. PSE Operator S.A., IRiESP—operational instruction in power distribution systems (in Polish)

16. J.A. Oliver, R. Lawrence, B.B. Banerjee, How to specify power-quality-tolerant process equipment, in *IEEE Industrial Applications Magazine*, September/October 2002, pp. 21–30
17. Planning levels for harmonic voltages, Engineering Recommendation G5/4-1
18. V. Ajodhia, B. Franken, in *Regulation of Voltage Quality* (Kema Consulting, Bonn, 2007)
19. R. Strzelecki, G. Benysek, in *Power Electronics in Smart Electrical Energy Networks* (Springer, Berlin, 2008), p. 414
20. M. Jasinski, M.P. Kazmierkowski, H.Ch. Soerensen, E. Friis-Madsen, Direct power and torque control of AC/DC/AC converter-generator subset in wave-to-wire power train for renewable energy system-wave dragon MW. *WSEAS Trans. Power Syst.* **1**(10), 1681–1688, October 2006, ISSN1790-5060
21. J.W. Kolar, H. Ertl, K. Edelmoser, F.C. Zach, Analysis of the control behavior of a bidirectional three-phase PWM rectifier system, in *Proceedings of the EPE 1991 Conference*, 1991, pp. (2-095)–(2-100)
22. J.A. Oliver, R. Lawrence, B.B. Banerjee, How to specify power-quality-tolerant process equipment, *IEEE Industrial Applications Magazine*, September/October 2002, pp. 21–30
23. N. Mohan, T.M. Undeland, W.P. Robbins, in *Power Electronics: Converters, Applications, and Design* (Wiley, New York, 1989), p. 667
24. F. Abrahamsen, A. David, Adjustable speed drive with active filtering capability for harmonic current compensation, in *Proceedings of the PESC 1995 Conference*, pp. 1137–1143
25. H. Akagi, New trends in active filters for power conditioning. *IEEE Trans. Ind. Appl.* **32**, 1312–1332 (1996)
26. M. Cichowlas, PWM Rectifier with Active Filtering, Warsaw University of Technology, Ph.D. Thesis, Warsaw, Poland, 2004
27. D. Zhou, D. Rouaud, Regulation and design issues of a PWM three-phase rectifier, in *Proceedings of the 25th Annual Conference on IECON'99*, vol. 1, pp. 485–489 (1999)
28. S. Piasecki, M. Jasinski, A. Milicua, Brief view on control of grid-interfacing AC-DC-AC converter and active filter under unbalanced and distorted voltage conditions, *Int. J. Comput. Math. Electr. Electron. Eng. (COMPEL) on EVER'09*, Emerald **30**(1), 351–373 (2011)
29. V. Blasko, V. Kaura, A new mathematical model and control of a three-phase AC-DC voltage source converter. *IEEE Trans. Power Electron.* **12**(1), 116–123 (1997)
30. R.P. Burgos, E.P. Wiechmann, J. Holtz, Complex state variables modeling and nonlinear control of PWM voltage- and current-source rectifiers, in *28th Annual Conference on IECON 02, Industrial Electronics Society, IEEE 2002*, Vol. 1, 5–8 Nov. 2002, pp. 187–192
31. G.F. Franklin, J. David Powell, A. Emami-Naeini, in *Feedback Control of Dynamic Systems*, 3rd edn (Addison-Wesley, Reading, 1994)
32. M. Malinowski, M. Jasinski, M.P. Kazmierkowski, Simple direct power control of three-phase PWM rectifier using space-vector modulation (DPC-SVM). *IEEE Trans. Ind. Electron.* **51**(2), 447–454 (2004)
33. Spagnuolo, G., Petrone, G., Araujo, S.V., Cecati, C., Friis-Madsen, E., Gubia, E., Hissel, D., Jasinski, M., Knapp, W., Liserre, M., Rodriguez, P., Teodorescu, R., Zacharias, P., Renewable energy operation and conversion schemes: a summary of discussions during the seminar on renewable energy systems. *IEEE Ind. Electron. Mag.* **4**(1), 38–51 (2010)
34. G. Joos, N.R. Zargari, P.D. Ziogas, A new class of current-controlled suppressed-link ac to ac frequency changers, in *Proceedings of Power Electronics Specialists Conference, 22nd Annual IEEE*, 24–27 June 1991, pp. 830–837
35. M.P. Kazmierkowski, L. Malesani, Current control techniques for three-phase voltage-source PWM converters: a survey. *IEEE Trans. Ind. Electron.* **45**(5), 691–703 (1998)
36. B.-K. Lee, M. Ehsani, A simplified functional simulation model for three-phase voltage-source inverter using switching function concept. *IEEE Trans. Ind. Electron.* **48**(2), 209–321 (2001)

37. H. Mao, D. Boroyevich, F.C.Y. Lee, Novel reduced-order small-signal model of a three-phase PWM rectifier and its application in control design and system analysis. *IEEE Trans. Power Electron.* **13**(3), 511–521 (1998)
38. E.P. Weichmann, P.D. Ziogas, V.R. Stefanovic, Generalized functional model for three-phase PWM inverter/rectifier converters, *IEEE Trans. Ind. Appl.* **IA-23**(2), 236–246, (1987)
39. R. Wu, S.B. Dewan, G.L. Slemon, Analysis of a PWM AC to DC voltage source converter under the predicted current control with fixed switching frequency. *IEEE Trans. Ind. Appl.* **27**(4), 756–764 (1991)
40. R. Wu, S.B. Dewan, G.R. Slemon, A PWM AC-to-DC converter with fixed switching frequency, *IEEE Trans. Ind. Appl.* **26**(5), 880–885, (1990)
41. R. Wu, S.B. Dewan, G.R. Slemon, Analysis of an ac-to-dc voltage source converter using PWM with phase and amplitude control. *IEEE Trans. Ind. Appl.* **27**(2), 355–364 (1991)
42. K. Xing, F.C. Lee, J.S. Lai, Y. Gurjit, D. Borjevic, Adjustable speed drive neutral voltage shift and grounding issues in a DC distributed system, in *Proceedings of the Annual Meeting of the IEEE-IAS*, 1997, pp. 517–524
43. Y. Xue, X. Xu, T.G. Habatler, D.M. Divan, A low cost stator flux oriented voltage source variable speed drive, in *Industry Applications Society Annual Meeting, 1990., Conference Record of the 1990 IEEE*, 7–12 Oct. 1990, pp. 410–415
44. N.R. Zargari, G. Joós, Performance investigation of a current-controlled voltage-regulated PWM rectifier in rotating and stationary frames. *IEEE Trans. Ind. Electron.* **42**(4), 396–401 (1995)
45. M. Malinowski, Sensorless Control Strategies for Three-Phase PWM Rectifiers, Warsaw University of Technology, Ph.D. Thesis, Warszawa, 2001
46. M. Liserre, Innovative control techniques of power converters for industrial automation, Politecnico di Bari, Ph.D. Thesis, Italy, 2001
47. P. Rodriguez, R. Teodorescu, I. Candela, A.V. Timbus, M. Liserre, F. Blaabjerg, New positive-sequence voltage detector for grid synchronization of power converters under faulty grid conditions, in *Power Electronics Specialists Conference, 2006. PESC '06. 37th IEEE*, pp. 1–7, 18–22 June 2006
48. M. Jasinski, Direct power and torque control of AC-DC-AC converter-fed induction motor drives, Ph.D. Thesis, Warsaw University of Technology, Warsaw, Poland, 2005
49. M.P. Kazmierkowski, H. Tunia, *Automatic Control of Converter-Fed Drives* (Elsevier, Amsterdam, 1994), p. 559
50. K. Mikołajuk, Principles of Power Electronics Circuits, Wydawnictwo Naukowe PWN, 1998, p. 525, (in Polish)
51. S. Piasecki, M. Jasinski, G. Wrona, W. Chmielak, Robust Control of Grid Connected AC-DC Converter for Distributed Generation, in *IECON 2012*, Montreal, Canada, pp. 5844–5849
52. G. Wrona, M. Jasinski, Asymmetrical Higher harmonics compensation in grid connected AC-DC converter control, in *13th International Symposium Typical Problems in the Field of Electrical and Power Engineering*, Doctoral School of Energy and Geotechnology II, Parnu, Estonia 14-19.01.2013, pp. 126–131. ISBN978-9985-69-054-3
53. A. Sikorski, Problems related with switching losses minimization in PWM AC/DC/AC fed induction machine, *Politechnika Białostocka, Rozprawy Naukowe nr. 58*, Białystok 1998, p. 217 (in Polish)
54. A. Sikorski, Current control conditions control for AC/DC, Nonsinusoidal Currents, EPN' 2000, Zielona Gora, 2000 (in Polish)
55. K. Jalili, Investigation of Control Concepts for High-Speed Induction Machine Drives and Grid Side Pulse-Width Modulation Voltage Source Converters, PhD Thesis, Technischen Universität Dresden, p. 174, 2009
56. M. Liserre, F. Blaabjerg, A. Dell'Aquila, Step-by-step design procedure for a grid-connected three-phase PWM voltage source converter. *Int. J. Electron.* **91**(8), 445–460 (2004)

57. M. Liserre, A. Dell'Aquila, F. Blaabjerg, Genetic algorithm-based design of the active damping for an LCL-filter three-phase active rectifier. *IEEE Trans. Power Electron.* **19**(1), 76–86 (2004)
58. M. Liserre, A. Dell'Aquila, F. Blaabjerg, Stability improvements of an LCL-filter based three-phase active rectifier, *IEEE*, 2002, pp. 1195–1201
59. K.A. Rothenhagen, M. Jasinski, M.P. Kazmierkowski, Grid connection of multi-megawatt clean wave energy power plant under weak grid condition, in *EPE-PEMC'08*, 1–3 September 2008, Poznan, Poland, on CD
60. EPCOS, Aluminium Electrolic Capacitors-Genera Technical Information, DataSheet, www.epcos.com
61. EPCOS, Aluminium Electrolic Capacitors-Applications, DataSheet, www.epcos.com
62. D.G. Holmes, T.A. Lipo, *Pulse Width Modulation for Power Converters, Principles and Practice* (Wiley-Interscience and IEEE Press, New York, 2003)
63. M. Alakula, J.E. Persson, Vector controlled ac/ac converters with a minimum of energy storage, in *Proceedings of the IEEE Conference*, 1994, pp. 1130–1134
64. M.M. Bech, F. Blaabjerg, J.-K. Pedersen, Random modulation techniques with fixed switching frequency for three-phase power converters. *IEEE Trans. Power Electron.* **15**(4), 753–761 (2000)
65. V. Blasko, Analysis of a hybrid PWM based on modified space-vector and triangle-comparison methods, *IEEE Trans. Ind. Appl.* **33**(3), 756–764 (1997)
66. A. Boglietti, G. Griva, M. Pasterelli, F. Profumo, T. Adam, Different PWM modulation techniques indexes performance evaluation, in *Proceedings of the IEEE Conference*, 1993, pp.193–199
67. A.M. Hava, S.-K. Sul, R.J. Kerkman, Dynamic overmodulation characteristics of triangle intersection PWM methods. *IEEE Trans. Ind. Appl.* **35**(4), 896–907 (1999)
68. A.M. Hava, R.J. Karkman, T.A. Lipo, A high-performance generalized discontinuous PWM algorithm. *IEEE Trans. Ind. Appl.* **34**(5), 059–1071 (1998)
69. J.W. Kolar, H. Ertl, F.C. Zach, Influence of the modulation method on the conduction and switching losses of a PWM converter system. *IEEE Trans. Ind. Appl.* **27**(6), 1063–1075 (1991)
70. D.-C. Lee, G.-M. Lee, A novel overmodulation technique for space-vector PWM inverters. *IEEE Trans. Power Electron.* **13**(6), 1144–1151 (1998)
71. H.W. Van Der Broeck, H.C. Skudelny, Analysis and realization of a pulsewidth modulator based on voltage space vectors. *IEEE Trans. Ind. Appl.* **24**(1), 142–150 (1988)
72. M. Winkelkemper, S. Bernet, Design and optimization of the DC-link capacitor of PWM voltage source inverter with active frontend for low-voltage drives, in *Proceedings of the EPE 2003 Conference*, 2003
73. A. Carlsson, The back-to-back converter control and design, Lund Institute of Technology, Ph.D. Thesis, Lund, 1998
74. L. Moran, P.D. Ziogas, G. Joos, Design aspects of synchronous PWM rectifier-inverter systems under unbalanced input voltage conditions. *IEEE Trans. Ind. Appl.* **28**(6), 1286–1293 (1992)
75. B.K. Bose, *Modern Power Electronics and AC Drives* (Prentice-Hall, Upper Saddle River, 2002)
76. B.T. Ooi, J.W. Dixon, A.B. Kulkarni, M. Nishimoto, An integrated AC drive system using a controlled-current PWM Rectifier/Inverter link. *IEEE Trans. Power Electron.* **3**(1), 64–71 (1988)
77. P. Cortes, J. Rodriguez, P. Antoniewicz, M. Kazmierkowski, Direct power control of an AFE using predictive control. *IEEE Trans. Power Electron.* **23**(5), 2516–2523 (2008)
78. J.C.R. Martinez, R. Kennel, A.L. Sheakh Ameen, Comparative analysis of on-line and off-line explicit solutions, applied in predictive direct current, in *5th IET International Conference on Power Electronics, Machines and Drives (PEMD 2010)*, April 2010, pp.1,6, 19–21

79. M. Liserre, C. Klumpner, F. Blaabjerg, V.G. Monopoli, A. Dell'Aquila, Evaluation of the ride-through capability of an active-front-end adjustable speed drive under real grid conditions, in *Proceedings of the Annual Conference of the IEEE-IES*, 2004
80. M. Liserre, F. Blaabjerg, S. Hansen, Design and control of an LCL-filter based three-phase active rectifier. *IEEE Trans. Ind. Appl.* **41**(5), 1281–1291 (2005)
81. J.A. Suul, A. Luna, P. Rodriguez, T. Undeland, Voltage-sensor-less synchronization to unbalanced grids by frequency-adaptive virtual flux estimation. *IEEE Trans. Ind. Electron.* **59**(7), 2910–2923 (2012)
82. N. Zaveri, A. Mehta, A. Chudasama, Performance analysis of various SRF methods in three phase shunt active filters, in *2009 International Conference. on Industrial and Information Systems (ICIIS)*, pp. 442–447, 28–31 Dec. 2009
83. R. Teodorescu, F. Blaabjerg, M. Liserre, P.C. Loh, Proportional resonant controllers and filters for grid-connected voltage-source converters. *IEE Proc. Electr. Power Appl.* **153**(5), 750–762 (2006)
84. H. Song, K. Nam, Dual current control scheme for PWM converter under unbalanced input voltage conditions. *IEEE Trans. Energy Conv.* **46**(5), October 1999
85. R. Teodorescu, M. Liserre, P. Rodríguez, *Grid Converters for Photovoltaic and Wind Power Systems* (Wiley-IEEE, New York, 2011), p. 416
86. M.P. Kazmierkowski, M. Jasiński, Power electronic grid-interface for renewable ocean wave energy, in *International Conference-Workshop Compatibility and Power Electronics*, 1–3 June 2011-CPE 2011, Tallinn, Estonia, pp. 457–463
87. M. Jasinski, K. Rafal, M. Bobrowska-Rafal, S. Piasecki, Grid interfacing of distributed energy sources by three-level BtB NPC converter under distorted grid voltage, in *2011 Workshop on Predictive Control of Electrical Drives and Power Electronics (PRECEDE)*, pp. 30–35, 14–15 Oct. 2011
88. G.D. Marques, J.F. Silva, Direct voltage control of a PWM AC/DC voltage converter, in *Proceedings of the EPE 1997 Conference*, 1997, pp. (3.222)–(3.227)
89. H. Hur, J. Jung, K. Nam, A fast dynamics DC-link power-balancing scheme for a PWM converter-inverter system. *IEEE Trans. Ind. Electron.* **48**(4), 794–803 (2001)
90. J. Jung, S. Lim, K. Nam, A feedback linearizing control scheme for a PWM converter-inverter having a very small DC-link capacitor. *IEEE Trans. Ind. Appl.* **35**(5), 1124–1131 (1999)
91. F. Kamran, T.G. Habetler, An improved deadbeat rectifier regulator using a neural net predictor. *IEEE Trans. Power Electron.* **10**(4), 504–510 (1995)
92. D.-C. Lee, K.-D. Lee, G.- M. Lee, Voltage control of PWM converters using Feedback Linearization, in *Proceedings of Thirty-Third IAS Annual Meeting. The 1998 IEEE*, Vol. 2, 12–15 Oct. 1998, pp. 1491–1496
93. M.P. Kazmierkowski, R. Krishnan, F. Blaabjerg (Eds.), in *Control in Power Electronics* (Academic Press, New York, 2002), p. 579
94. R. Ottersten, J. Svensson, Vector current controlled voltage source converter-deadbeat control and saturation strategies. *IEEE Trans. Power Electron.* **17**(2), 279–285 (2002)
95. T. Ohnishi, Three-phase PWM converter/inverter by means of instantaneous active and reactive power control, in *Proceedings of the IEEE-IECON Conference*, 1991, pp. 819–824
96. V. Manninen, Application of direct torque control modulation technology to a line converter, in *Proceedings of the EPE 1995 Conference*, 1995, pp. 1.292–1.296
97. T. Noguchi, H. Tomiki, S. Kondo, I. Takahashi, Direct power control of PWM converter without power-source voltage sensors. *IEEE Trans. Ind. Appl.* **34**(3), 473–479 (1998)
98. H. Kim, H. Akagi, The instantaneous power theory on the rotating p-q-r reference frames, in *Proceedings of the IEEE 1999 International Conference on Power Electronics and Drive Systems, 1999. PEDS '99*, Vol. 1, 27–29 July 1999, pp. 422–427
99. J. Holtz, Pulsewidth modulation for electronics power conversion. *Proc. IEEE* **82**(8), 1194–1214 (1994)

100. M. Malinowski, M.P. Kazmierkowski, M. Jasiński, Virtual flux based direct power control of tree-phase PWM rectifiers, *Electrical Power Quality and Utilization*, Vol. VII, Sheet 1, 2001, pp. 129–138
101. www.twerd.pl
102. G.E. Dullerud, F.G. Paganini, *A course in robust control theory a convex approach*, University of Illinois Urbana-Champaign and University of California Los Angeles, Springer, 2005, p. 383
103. www.nowaplus.com.pl

Chapter 4

Faults and Diagnosis Systems in Power Converters

Kyo-Beum Lee and Ui-Min Choi

Abstract A power converter is needed in almost all kinds of renewable energy systems and drive systems. It is used both for controlling the renewable source and for interfacing with the load, which can be grid-connected or working in stand-alone mode. Further, it drives the motors efficiently. Increasing efforts have been put into making these systems better in terms of reliability in order to achieve high power source availability, reduce the cost of energy and also increase the reliability of overall systems. Among the components used in power converters, a power device and a capacitor fault occurs most frequently. Therefore, it is important to monitor the power device and capacitor fault to increase the reliability of power electronics. In this chapter, the diagnosis methods for power device fault will be discussed by dividing into open- and short-circuit faults. Then, the condition monitoring methods of DC-link electrolytic capacitor will be introduced.

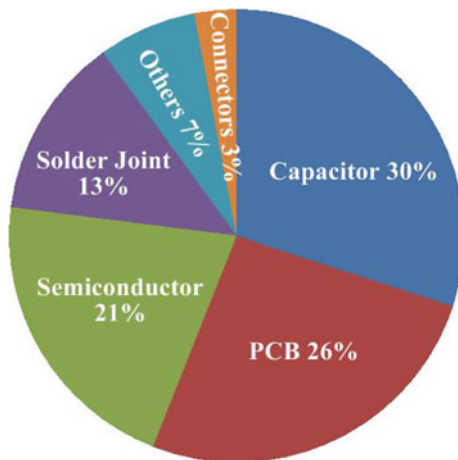
1 Introduction

The increasing use of renewable energy systems requires new strategies for the operation and management of the electricity grid in order to maintain or to improve power-supply reliability and quality. Additionally, regulations of the grid lead to new management structures in which trading of energy and power is

K.-B. Lee
Ajou University, Suwon, Korea

U.-M. Choi (✉)
University of Aalborg, Aalborg, Denmark
e-mail: uch@et.aau.dk

Fig. 1 Distribution of faults in power converters



becoming increasingly important. Power electronics, the technology to convert electric power efficiently from one stage to another, is essential for distributed renewable energy systems to achieve high efficiency and performance. The power electronics field has grown during last decades for two main reasons:

- (1) The development of fast semiconductor switches that are capable of switching quickly and handling high power.
- (2) The production of micro-controllers that can implement advanced and complex control algorithms.

These factors have led to the development of cost-effective and grid-friendly converters.

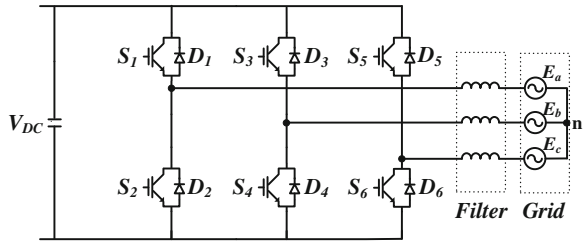
As converters perform the important role in the renewable energy systems, so does the interest in the reliability of power electronics, which can directly affect the reliability, efficiency and cost of renewable energy systems. Therefore, many researches about the reliability of power converter systems have been conducted especially for the fault diagnosis.

There are many kinds of faults in power converters such as a power semiconductor device, DC-link capacitor, PCB, solder, sensor, and etc. The distribution of faults in power converters is illustrated in Fig. 1.

As shown in Fig. 1, power semiconductor devices and DC-link capacitors are the factors that most frequently provoke faults among the components of power electronic converters. Semiconductor and soldering failures in power device modules compose 34 % of power converter failures. The DC-link capacitor fault makes 30 % of the faults in power converters [1, 2].

In this chapter, the diagnostic methods for power device faults are discussed by dividing into open- and short-circuit faults. Then, the condition monitoring methods of DC-link electrolytic capacitors are introduced.

Fig. 2 Simplified circuit diagram of a grid-connected converter system



2 Power Device Fault

The power device fault can be divided into two cases: a short-circuit fault and an open-switch fault.

A short-circuit fault can occur due to several reasons, such as the wrong gate voltage, overvoltage, avalanche stress, or temperature overshoot. The short-circuit faults are difficult to handle because an abnormal over-current which can cause serious damage to other parts is produced within a very short time. In addition, the period between the fault initiation and failure is very short. Therefore, most diagnostic methods of a short-circuit fault are based on hardware circuits [3].

An open-switch fault occurs due to the lifting of a bonding wire caused by thermal cycling. An extremely high collector current may also cause open-switch faults. The open-switch fault leads to a current distortion. It can cause secondary problems in other components through induced noise and vibrations. The open-switch fault does not cause serious damages, compared to short-circuit faults, but does degrade the performance of overall converter systems. Therefore, diagnostic methods of power device faults are needed to improve the reliability of the converter system. The diagnostic methods based on the 2-level converter are introduced. Figure 2 shows the simplified circuit diagram of grid-connected converter systems.

2.1 Diagnostic Method of Open-Switch Fault

2.1.1 Current Pattern Method

If the open-switch fault occurs, the switching state does not reach the desired state and the current flow path is also changed [4, 5]. These are caused by a distortion of phase currents. According to the faulty switch, the distortion of phase currents is differed and, therefore, the differed current patterns are formed. Hence, it is possible to detect an open-switch fault and identify the location of a faulty switch using its current patterns. The measured three-phase currents can be transformed into stationary reference frame currents as follows:

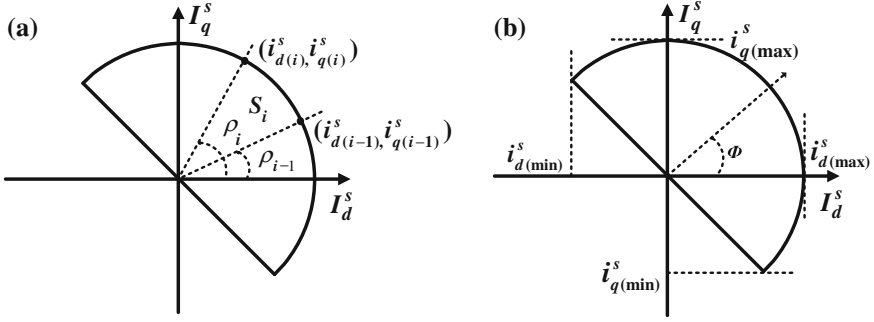


Fig. 3 Fault diagnosis parameters. **a** Surface. **b** Current pattern angle

$$\begin{aligned}
 i_d^s &= \frac{2}{3}i_a - \frac{1}{3}i_b - \frac{1}{3}i_c \\
 i_q^s &= \frac{1}{\sqrt{3}}(i_b - i_c).
 \end{aligned} \tag{1}$$

The currents expressed in (1) can be observed in the d–q frame, on which the horizontal axis is signified by i_d^s and the vertical axis is signified by i_q^s . Current patterns shown in this frame have a specific shape and angle that depend on the faulty switch. Therefore, a change in the current pattern shape and angle represents the occurrence of an open fault condition in the converter and it is an indicator of the location of the faulty switch. The change of current pattern's shape is obtained by calculating the surface (S) of the current pattern. It is illustrated in Fig. 3a and calculated as

$$S = \sum_{i=0}^n S_i = \sum_{i=0}^n \frac{\pi r_i^2 \rho}{360} \tag{2}$$

where $\rho = \rho_i - \rho_{i-1}$ is a central angle and $r_i = \sqrt{(i_{di}^s)^2 + (i_{qi}^s)^2}$ is a radius. Thus, the total surface can be obtained by the summation of S_i during the one fundamental period of measured currents.

The vector angle of a current pattern is defined as the angle between the horizontal-axis (i_d^s -axis) and the center of the current pattern as shown in Fig. 3b. The center of the current pattern can be obtained by the maximum and minimum values of stationary currents as shown below:

$$\begin{aligned}
 i_{d(\text{center})}^s &= \frac{1}{2} \left(i_{d(\text{max})}^s + i_{d(\text{min})}^s \right) \\
 i_{q(\text{center})}^s &= \frac{1}{2} \left(i_{q(\text{max})}^s + i_{q(\text{min})}^s \right).
 \end{aligned} \tag{3}$$

Using these, the angle of the current pattern is calculated by

Fig. 4 Current patterns according to faulty switches in the 2-level converter

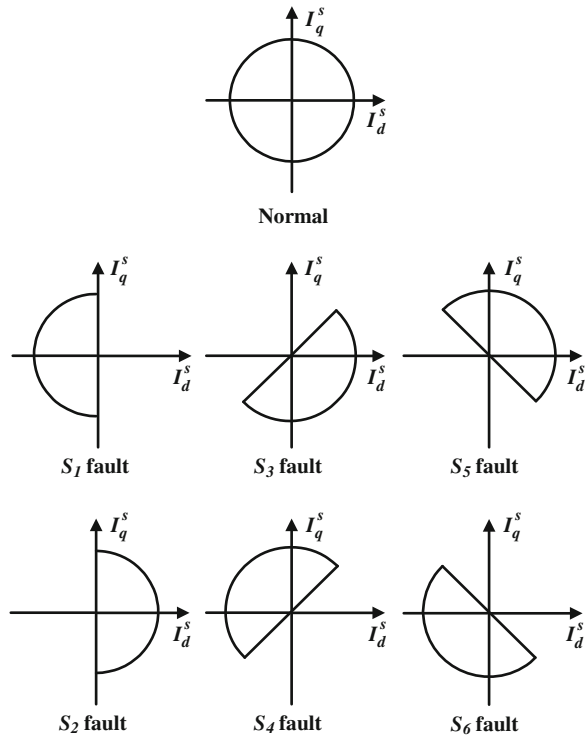


Table 1 Angles of current patterns according to faulty switch

Switch	θ
S_1	150–210°
S_2	330–30°
S_3	270–330°
S_4	90–150°
S_5	30–90°
S_6	210–270°

$$\phi = \tan^{-1} \left(\frac{i_{d(cm)}^s}{i_{q(cm)}^s} \right). \tag{4}$$

Figure 4 shows shapes of current patterns according to the faulty switch and angles of current patterns are arranged in Table 1.

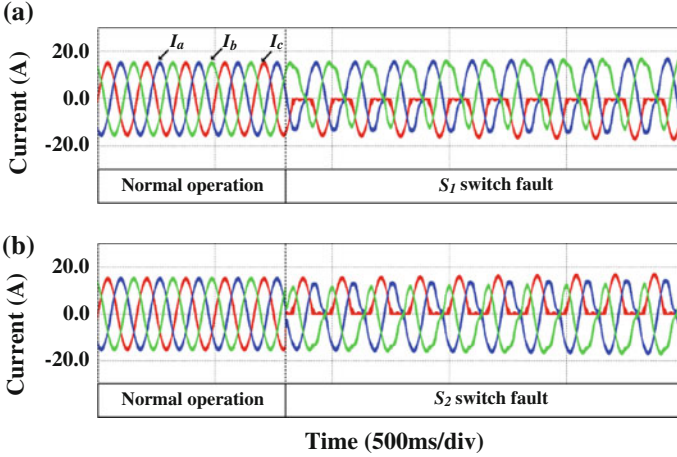


Fig. 5 Three-phase currents of the 2-level inverter. a S_1 switch fault. b S_2 switch fault

Table 2 Identification of faulty switch with direct current method

Switch	I_{a_avg}	I_{b_avg}	I_{c_avg}
S_1	$< -\delta$		
S_3		$< -\delta$	
S_5			$< -\delta$
S_2	$> \delta$		
S_4		$> \delta$	
S_6			$> \delta$

2.1.2 Direct Current Method

This method directly uses the average three-phase currents calculated by

$$I_{x_avg}(x = a, b, c) = \frac{1}{N} \sum_{j=k-N+1}^k I_x(j). \tag{5}$$

During the normal operation, the average phase current is zero [2, 6]. However, if an open-switch fault occurs, the average of phase currents has a positive or negative value. Figure 5a, b show the output phase currents when the open switch fault occurs in switches S_1 and S_2 , respectively. In this method, the faulty switch is identified by comparing the current with a threshold value, δ . The identification of faulty switches using this method is described in Table 2.

Table 3 Identification of fault switch with modified normalized DC method

Switch	d_{1a}	d_{1b}	d_{1c}	d_{2a}	d_{2b}	d_{2c}
S_1	0			1		
S_3		0			1	
S_5			0			1
S_2	1			1		
S_4		1			1	
S_6			1			1

2.1.3 Modified and Normalized DC Current Method

As mentioned above, under the normal operating condition, the average of phase currents are zero [6]. If an open switch fault occurs, the average phase current has a positive or negative value. However, this method is very simple but it can lead to false alarms. This is because it tends to be highly unreliable under varying operating conditions, especially during fast transient conditions.

To avoid false alarms and improve the accuracy, the normalized DC current method has been introduced. The normalized DC current is calculated by

$$\gamma_{x(=a,b,c)} = \frac{I_{x_avg}}{\sqrt{(a_{1x})^2 + (b_{1x})^2}} \quad (6)$$

$$a_{1x} = \frac{1}{N} \sum_{k=1}^N I_x(k\tau) \cos\left(\frac{2\pi k}{N}\right) \quad (7)$$

$$b_{1x} = \frac{1}{N} \sum_{k=1}^N I_x(k\tau) \sin\left(\frac{2\pi k}{N}\right)$$

where a_{1x} and a_{x2} are the first order harmonic coefficients of the output currents. The I_{x_avg} can be calculated from (5). For identification of the faulty switch, the largest absolute value of resulting residuals γ_a , γ_b and γ_c is compared with thresholds given in (8) and (9):

$$d_{1x} = \begin{cases} 1 : \gamma_x > 0 \\ 0 : \gamma_x \leq 0 \end{cases} \quad (8)$$

$$d_{2x} = \begin{cases} 1 : |\gamma_x| > 0.45 \\ 0 : |\gamma_x| \leq 0.45 \end{cases} \quad (9)$$

The threshold value is 0.45 which has been reported to be a universal value derived from the experience. Using Table 3, the faulty switch can be identified.

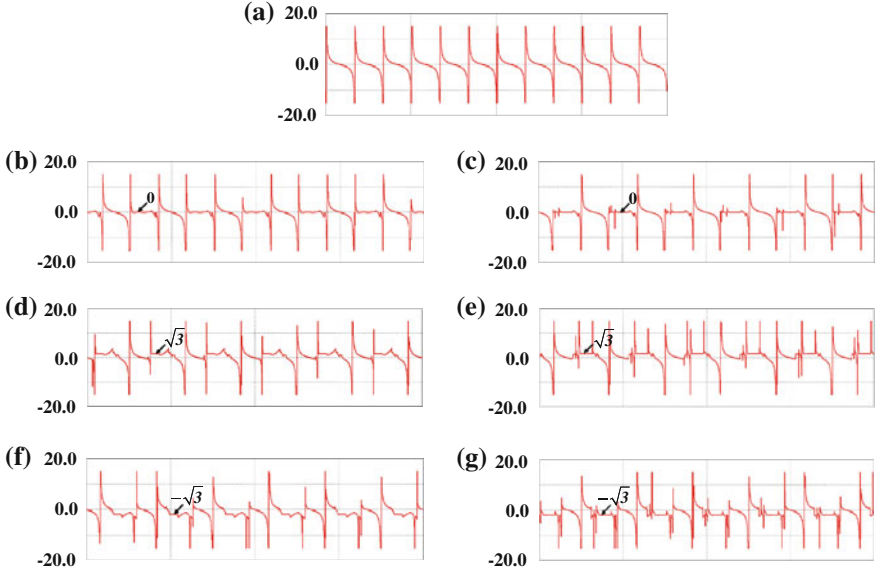


Fig. 6 Slope of the current vector's trajectory. **a** Normal condition. **b** S_1 switch fault. **c** S_2 switch fault. **d** S_3 switch fault. **e** S_4 switch fault. **f** S_5 switch fault. **g** S_6 switch fault

Table 4 Identification of faulty switch with slope method

Faulty switch	Slope Ψ	Polarity
S_1	0	-
S_2	0	+
S_3	$\sqrt{3}$	-
S_4	$\sqrt{3}$	+
S_5	$-\sqrt{3}$	-
S_6	$-\sqrt{3}$	+

2.1.4 Slope Method

The slope of the current space vector's trajectory can be also used to diagnose the open-switch fault in power converters [7, 8]. The slope Ψ is defined as

$$\psi = \frac{i_{dk}^s - i_{d(k-1)}^s}{i_{qk}^s - i_{q(k-1)}^s} \quad (10)$$

where i_{dk}^s and i_{qk}^s are the sampled current transformed into the stationary reference frame. $i_{d(k-1)}^s$ and $i_{q(k-1)}^s$ are the previous values of the sampled current. During the normal condition, the slope Ψ always varies because the trajectory of the current space vector is a circle. However, if the open-switch fault occurs, the slope has the

Fig. 7 Current path. **a** S_2 fault condition when $SW_{a+} = 0, SW_{a-} = 1$. **b** S_1 fault condition when $SW_{a+} = 1, SW_{a-} = 0$

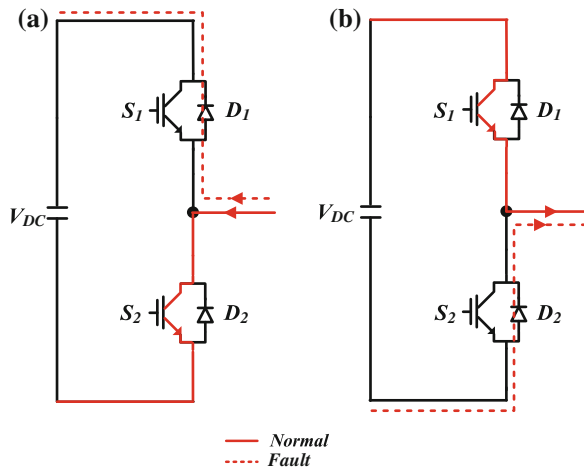


Table 5 Switch voltage when the open-switch fault occurs in S_2

I_a	S_{a+}	S_{a-}	Normal		Open fault occurs in S_2	
			V_{S1}	V_{S2}	V'_{S1}	V'_{S2}
+	1	0	0	V_{DC}	0	V_{DC}
+	0	0	V_{DC}	0	V_{DC}	0
+	0	1	0	V_{DC}	0	V_{DC}
-	1	0	0	V_{DC}	0	V_{DC}
-	0	0	0	V_{DC}	0	V_{DC}
-	0	1	V_{DC}	0	0	V_{DC}

specific value according to the faulty leg. Figure 6 shows the slope of the current vector’s trajectory according to a faulty switch. To identify the faulty switch, it is necessary to detect whether the current of the faulty phase is positive or negative. If the faulty phase current is positive, an open-switch fault occurs in the lower switch. Conversely, if the faulty phase current is negative, the open-switch fault occurs in the upper switch. The slope of the current vector’s trajectory and polarity of the phase current are described in Table 4.

2.1.5 Switching Function Model Based Method

Suppose that the power switches are ideal and ignoring the dead-time effect, under the normal operating condition, the relationship between the collector-emitter voltage of the IGBTs and the binary variables are expressed as

Table 6 Switch voltage when the open-switch fault occurs in S_1

I_a	S_{a+}	S_{a-}	Normal		Open fault occurs in S_2	
			V_{s1}	V_{s2}	V'_{s1}	V'_{s2}
+	1	0	0	V_{DC}	V_{DC}	0
+	0	0	V_{DC}	0	V_{DC}	0
+	0	1	V_{DC}	0	V_{DC}	0
-	1	0	0	V_{DC}	0	V_{DC}
-	0	0	0	V_{DC}	0	V_{DC}
-	0	1	V_{DC}	0	V_{DC}	0

$$\begin{cases} V_{s1} = (1 - SW_a)V_{DC} \\ V_{s2} = SW_a V_{DC} \\ V_{s3} = (1 - SW_b)V_{DC} \\ V_{s4} = SW_b V_{DC} \\ V_{s5} = (1 - SW_c)V_{DC} \\ V_{s6} = SW_c V_{DC} \end{cases} \quad (11)$$

where V_{DC} is the DC-link voltage, and SW_a – SW_c represent the switching states, which are set to “1” when the switch is closed and “0” when the switch is open [9]. V_{s1} – V_{s6} indicate the collector-emitter voltages of the six respective IGBTs.

Open-Switch Fault of Lower Switch

The current paths and switch voltages when an open-switch fault occurs in S_2 are shown in Fig. 7a and arranged in Table 5. When the current is negative and an open-switch fault occurs in S_2 , under lower switching signal mode ($SW_{a+} = 0$, $SW_{a-} = 1$), the current flows only through D_1 because S_2 breaks down. At this moment, S_2 carries the voltage V_{DC} , and the output pole voltage of S_1 is null, which disagree with the calculated values from the switching function model in (11). Hence, the open-switch fault in S_2 is detected using errors between the real-switch voltage values (V_{s1} and V_{s2}) and the calculated values (V'_{s1} and V'_{s2}).

Open-Switch Fault of Upper Switch

An overall analysis using this method is similar to the one above. When $SW_{a+} = 1$, $SW_{a-} = 0$, and the current is positive, the fault is identified using the voltage errors.

Figure 7b shows the current path when an open-switch fault occurs in S_1 , and the corresponding switch voltages are arranged as given in Table 5.

The simple and fast-diagnostic circuit for open-switch faults is illustrated in Fig. 8, which includes the diagnostic photocoupler, the time-delay circuit of the

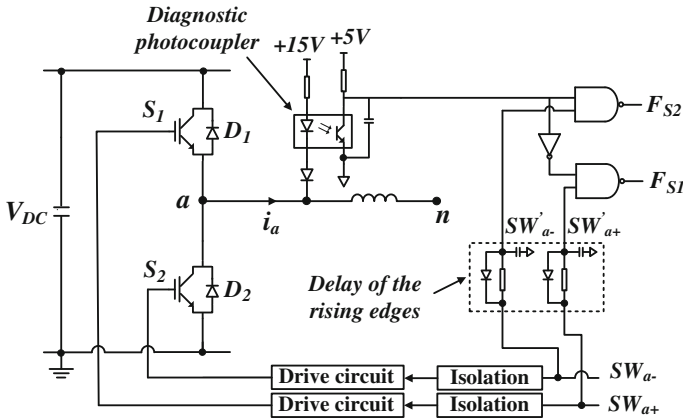
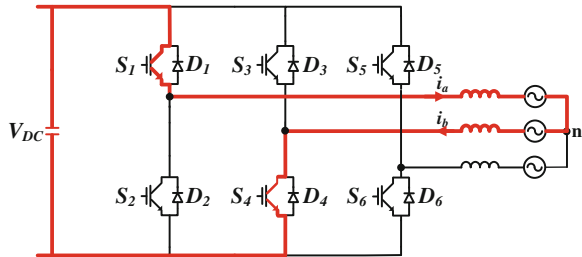


Fig. 8 Simple and fast-diagnostic circuit for open-switch faults

Fig. 9 Low switch voltage of S_6 switch fault when the switching state is [100]



signal rising edges, and the logical gate circuit. The voltage of the lower switch is sensed indirectly by the diagnostic photocoupler. The F_{S1} and F_{S2} are the diagnostic signals of S_1 and S_2 faults. The diagnostic signal is generated by comparing the switching signal with indirectly sensed voltage of the lower switch. The IGBTs have the turn-on delay because these are not ideal. Hence, the turn-on time delay can cause a misdiagnosis. To avoid misdiagnosis due to the delay, a rising edge delay circuit is used on the switching signal. Because of the rising edge delay circuit, the switching signals SW_{a+} and SW_{a-} are changed to the delayed switching signals SW'_{a+} and SW'_{a-} as shown in Fig. 8.

2.1.6 Lower Switch Voltage Method

Under the normal operating condition, the voltage across the lower switch has V_{DC} or 0 and changes complementarily [10]. However, if an open-switch fault occurs, the voltage across the lower switch in the faulty phase has $V_{DC}/2$, despite the upper or lower switch fault. For example, when the open-switch fault occurs in S_6 and the switching state is [100] as shown in Fig. 9, the voltage across S_6 becomes $V_{DC}/2$.

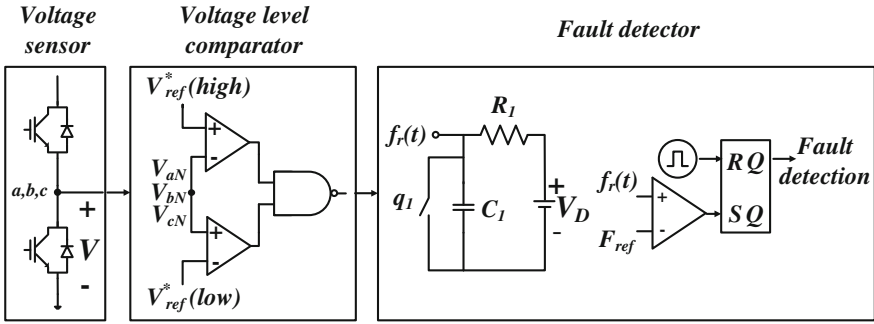
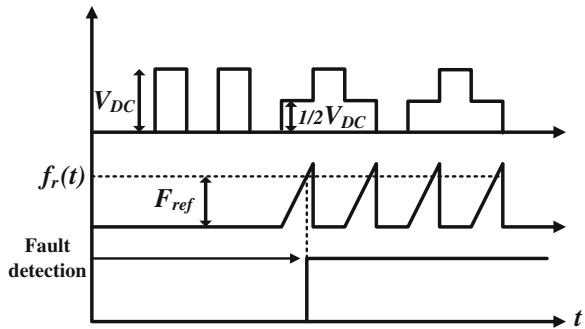


Fig. 10 Block diagram of the fault detection method using the lower switch voltage

Fig. 11 Procedure of the fault detection with the lower switch voltage method



The switching state [100] indicates that S_1 , S_4 and S_6 are on. The measured voltages are compared with the reference voltages ($V_{ref}^*(low)$, $V_{ref}^*(high)$) using an op-amp based voltage level comparator. In the normal operation mode, the comparator’s output has a high value. In the faulty mode, the comparator’s output is low and these values are maintained for a while. The comparator’s output is applied to the gate of the switch q_1 .

The middle voltage ($V_{DC}/2$) is detected by changing the ramp function

$$f_r(t) = (1 - q_1)V_D(1 - e^{-\frac{t}{R_1C_1}}) \tag{12}$$

where q_1 is the switching function and is “1” for on state and “0” for off state. The ramp function $f_r(t)$ is compared with the threshold value F_{ref} to detect the fault. If $f_r(t)$ is smaller than F_{ref} , the system is considered to be operating in the normal condition. If $f_r(t)$ is larger than F_{ref} , it is considered that the open fault occurs in the system and a fault signal is produced.

Figure 10 shows the block diagram of the fault detection method using the lower switch voltage. Figure 11 shows the procedure where the ramp function $f_r(t)$ is compared to F_{ref} to detect the open-switch fault.

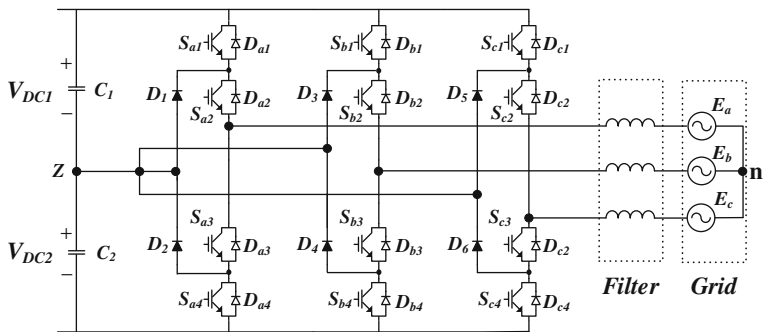


Fig. 12 Simplified circuit diagram of a grid-connected NPC inverter

2.1.7 Detection Method for NPC Inverter

Figure 12 shows the simplified circuit diagram of the grid-connected NPC inverter system [11]. In the NPC inverter system, it is impossible to identify the faulty switch between the upper two switches (S_{x1} , S_{x2}) or between the lower two switches (S_{x3} , S_{x4}) using the previously introduced method based on the output phase current. This is because the output phase currents are the same when the open-switch fault occurs in upper switches (S_{x1} and S_{x2}) or lower switches (S_{x3} and S_{x4}). Therefore, the current patterns are also the same between upper switches or between lower switches.

Figure 13 shows the output phase currents when the open-switch fault occurs in leg A. Figure 14 shows the current patterns according to the faulty switches.

The remarkable difference between the S_{x1} fault and S_{x2} fault or between the S_{x3} fault and S_{x4} fault is the possibility of the switching state [O]. However, the grid voltage nullifies the positive phase current or negative phase current, regardless of the possibility of the switching state [O]. It is difficult to determine the effect of the switching state [O] on the current patterns as shown in Fig. 14. The location of the fault switch either between the two upper switches or between two lower switches in the grid-connected NPC inverter system can be identified by adding a simple switching scheme to the conventional method. The switching scheme can be divided into two cases.

Case1. Open-switch fault occurs in one of the two upper switches; when the grid voltage of faulty leg is negative, the switching state [O] is applied for a very short period of time. If the open-switch fault occurs in S_{x1} , the positive current flows for a very short period of time, because the switching state [O] is possible. If the open-switch fault occurs in S_{x2} , the phase current path is opened and the positive phase current does not flow.

Case 2. Open-switch fault occurs in one of the two lower switches; in contrast to the case 1, the switching state [O] is applied for a very short period of time when the grid voltage of faulty leg is positive. If the open-switch fault occurs in S_{x3} , the phase current does not flow, because the phase current path is opened. If the open-

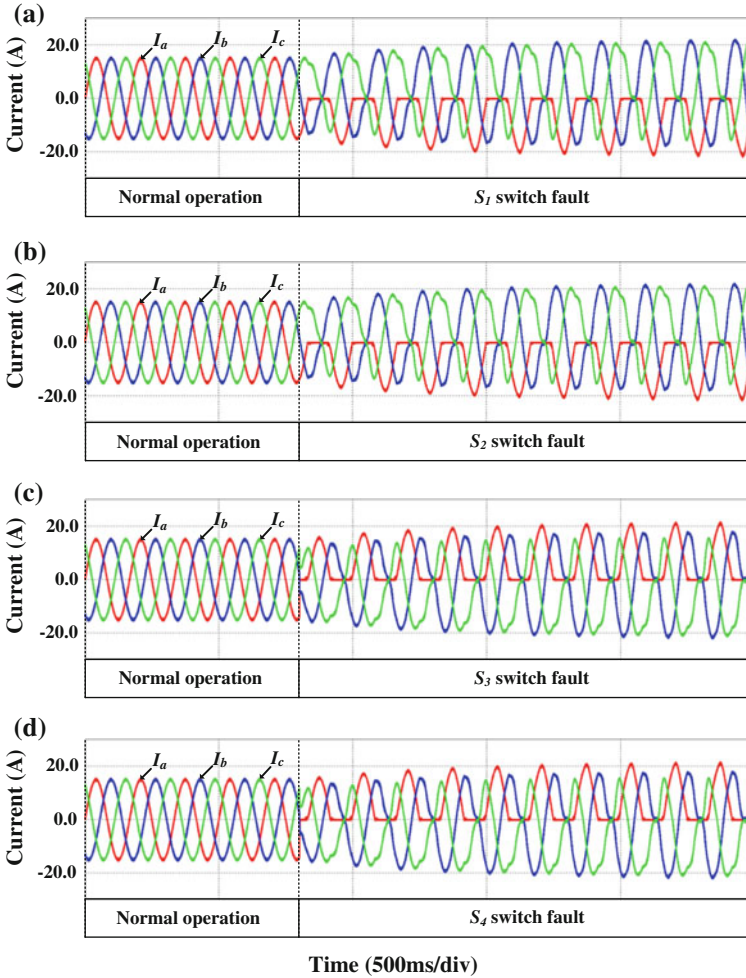


Fig. 13 Three-phase currents of an NPC inverter. **a** S_1 switch fault. **b** S_2 switch fault. **c** S_3 switch fault. **d** S_4 switch fault

switch fault occurs in S_{x4} , the negative current flows for a very short period of time, because the switching state [O] is possible.

The grid voltage state (positive or negative) is determined on the basis of the PLL angle in this proposed method. The peak magnitude of current is changed according to the period that allows for the switching state to change to the switching state [O]. If this period is long, the phase current increases above the rated current. The period can be determined by $t_2 - t_1$ in the following equation:

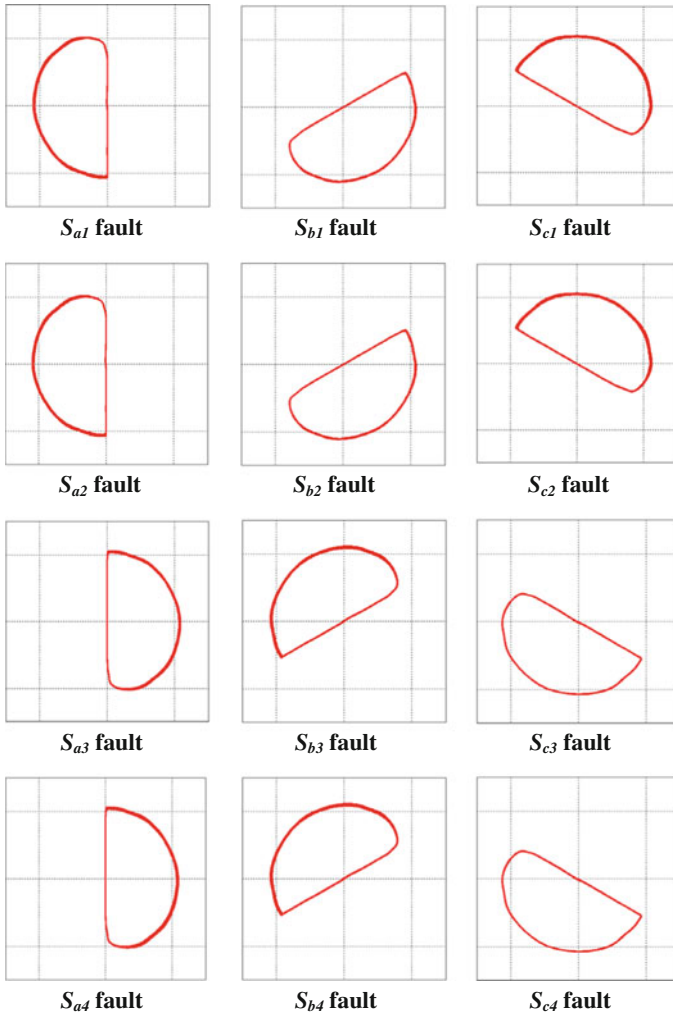


Fig. 14 Current patterns according to a faulty switch in a 3-level NPC inverter

$$I = \frac{1}{L} \int_{t1}^{t2} -E(t) dt \leq I_{rate}. \tag{13}$$

The procedure for open-switch fault detection in the grid-connected NPC inverter system is as follows:

- (1) Detect the open-switch fault on the basis of previous method using the output phase currents.

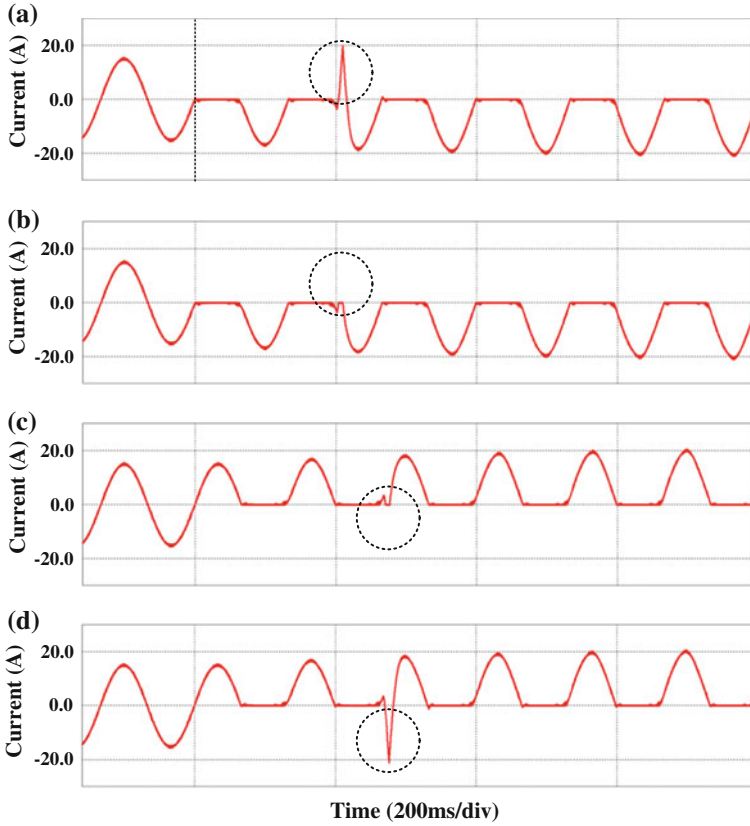


Fig. 15 Results of fault diagnosis method for NPC inverter **a** S_{a1} switch fault **b** S_{a2} switch fault **c** S_{a3} switch fault **d** S_{a4} switch fault

- (2) If the open-switch fault occurs, estimate the angle of the current patterns. It is possible to identify the leg that includes the faulty switch and to identify whether the open-switch fault occurs in one of the two upper switches (S_{x1} , S_{x2}) or in one of the two lower switches (S_{x3} , S_{x4}) using Table 1.
- (3) If the open-switch fault occurs in one of the two upper switches, then the switching state [O] is applied for a very short period of time when the grid voltage of the faulty leg is negative. If the positive phase current flows for a short period, then it can be inferred that the open-switch fault has occurred in S_{x1} . If the positive current does not flow, then it can be inferred that the open-switch fault has occurred in S_{x2} .
- (4) If the open-switch fault occurs in one of the two lower switches, then the switching state [O] is applied for a very short period of time when the grid voltage of the faulty leg is positive. If the negative phase current flows for a short period, then it can be inferred that the open-switch fault has occurred in

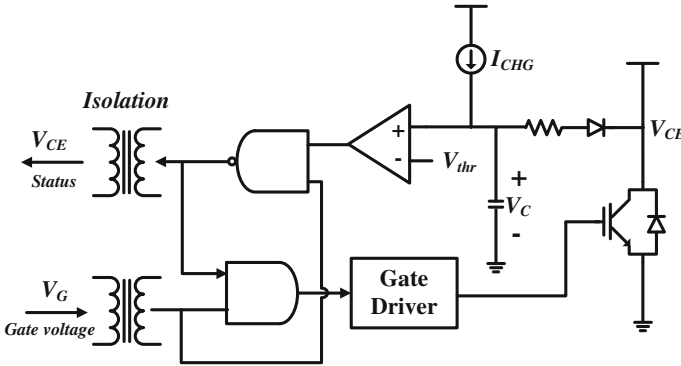


Fig. 16 Fault diagnosis circuit for the de-saturation detection method

S_{x4} . If the negative current does not flow, then it can be inferred that the open-switch fault has occurred in S_{x3} .

Figure 15 shows the results of the open-switch fault detection method for the grid-connected NPC inverter when the open switch fault occurs in leg A.

2.2 Diagnostic Method of Short-Circuit Fault

2.2.1 De-Saturation Detection Method

If a short fault occurs in an IGBT, the voltage between the collector and emitter increases [3, 12]. A protection circuit is used to generate a control signal to suppress the gate pulses when the voltage V_{CE} reaches the threshold value which is typically 7 V. The V_{CE} is sensed by the following procedures: when the gate pulse is on, the protection circuit provides a small current. The capacitance voltage V_C is increased by the provided current and the sensing diode becomes forward biased. Under normal operating conditions, the capacitance voltage V_C is very small when the IGBT is on because V_{CE} is very small. However, if a short-circuit fault occurs, V_{CE} and the capacitance voltage V_C increase when the gate pulse is on. The protection circuit determines whether a fault has occurred or not by detecting V_C . This method uses only a simple sensing diode. However, it is not suitable for the high-speed IGBT switching, because it requires a blanking time which is about 1–5 μ s. The blanking time means that the time taken to charge the capacitor by the internal charge current (I_{CHG}) and it rejects the noise from normal switching transient. Also, the dynamic feedback information is not provided. Figure 16 shows an example of a fault diagnosis circuit for the de-saturation detection method.

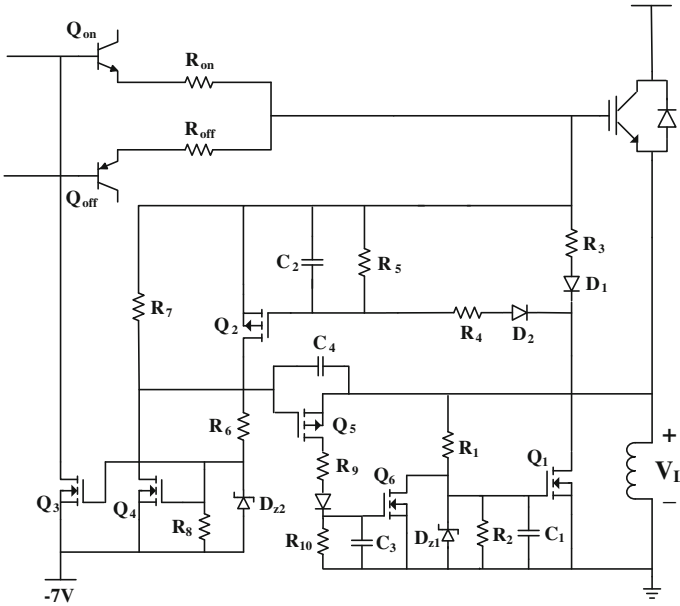


Fig. 17 Fault diagnosis circuit for the di/dt measuring method

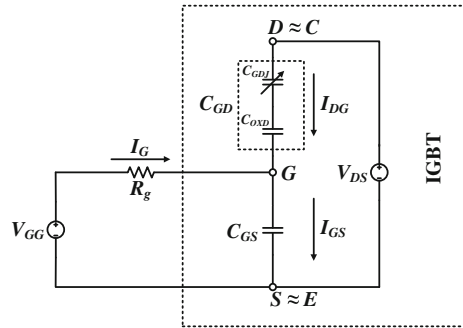
2.2.2 di/dt Measuring Method

In this method, the fault detection is implemented by measuring the voltage across the internal inductor of the module between the control emitter and main emitter [3, 12]. The voltage across the inductor is expressed by

$$V_L = L \frac{di}{dt}. \tag{14}$$

When a fault occurs, there is a large change in the current through the inherent inductance. This large change in the current (di/dt) will generate a large V_L across the inductor. V_L is compared with a reference voltage to determine whether a fault has occurred. This method does not require any blanking time nor has any issues with noise. Therefore, the control is of an open loop type and dynamically responds to a fault condition immediately after a fault is detected. This is extremely important for high-performance IGBTs, which are operated at very high switching speed and where the margins for current and voltage ratings are designed at its minimum. Figure 17 shows the fault diagnosis circuit for the di/dt measuring method. This circuit provides four functions.

Fig. 18 IGBT equivalent circuit



di/dt Dynamic Control

The induced voltage across the stray inductance V_L is measured by the voltage divider R_1 and R_2 . The values of R_1 and R_2 are set so that the minimum voltage across R_2 is higher than the threshold value of Q_1 under the fault condition. Under the normal condition, the switch on transient time is set in the range of 100–200 ns. The time constant $(R_1//R_2 * C_1)$ should be set so that the voltage charged to C_1 is less than the threshold value of Q_1 during normal switching transient state. If V_L is positive and lasts for more than 250 ns, the charged voltage at C_1 will be more than the threshold value of Q_1 . Hence, Q_1 is turned on and the path to control the gate voltage of an IGBT is formed through R_3 , D_1 , and Q_1 . The information of active state of the di/dt control is indicated with the voltage across R_3 . D_1 is used to block the reverse current flow when V_L is negative. D_{z1} is used to prevent the gate Q_1 from over voltage.

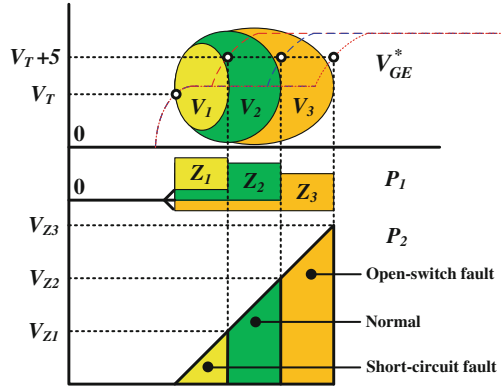
di/dt Control Sensing and Hold

The active state of the di/dt control is latched with the RC circuit (R_4, C_2) . The voltage across R_3 charges up C_2 above the threshold value of Q_2 . C_2 is charged to the same voltage of R_3 before the di/dt control process is over. D_2 blocks the discharge path formed through R_4 and C_2 when the voltage V_{R3} drops below the charged voltage V_{C2} . The discharge time of C_2 through R_5 is much longer than the whole process of the fault protection. As soon as C_2 is charged to the threshold of Q_2 , Q_2 will be conducted. The conduction of Q_2 provides a current path for the next function of the circuit.

di/dt Control Sensing and Hold

The current through Q_2 make Q_3 and Q_4 to be turned on with a current limit resistor R_6 . Then, Q_3 (turned on) disables the command signal by pulling down the base of Q_{on} . Q_4 activates the soft turn-off process through R_7 . The conduction of

Fig. 19 Time diagram to determine the P_1 width and P_2 amplitude



Q_4 provides a trigger signal for the di/dt control shutdown function. The function of R_8 is to keep the gates Q_3 and Q_4 discharged during the normal operation. D_{z2} clamps the gates Q_3 and Q_4 to prevent the transient over voltage.

di/dt Control Shunt Down

The time required for the di/dt control process to complete is about 0.5 μ s. As mentioned earlier, di/dt control is used to limit the fault current at a safe level. In this case, it is limited at 4 kA in the worst case of a shoot through fault. The signal from Q_4 is inverted from active low with the reference to -7 V to active high with the reference to the power emitter by Q_5 . The time constant of the RC circuit (R_9 , R_{10} , C_3) is set such that the time for C_3 charging to the threshold of Q_6 is the same as the required time that the di/dt control process is completed. The conduction of Q_6 discharges the gate voltage of Q_1 and terminates the di/dt control process. The slow discharge of V_{C3} through R_{10} holds Q_6 in the conduction mode to prevent Q_1 from getting into the active di/dt control mode again.

2.2.3 Gate Voltage Sensing Method

The region between the gate and drain of the IGBT is modeled by C_{GD} [13]. This region has great mobility during the turn-on transient, and is formed by the variable capacitance C_{GDJ} which models the depletion zone, and the fixed capacitance C_{OXD} which models the oxide zone. The capacitances involved in the IGBT gate charge signal are shown in Fig. 18. The variable capacitance C_{GDJ} is defined by

$$C_{GD} = A_{GD} \sqrt{\left(\frac{q \cdot N_B \cdot \epsilon_{si}}{2(V_{DS} - V_{GS})} \right)} \quad (15)$$

where N_B is n-layer doping concentration and q is an electron charge.

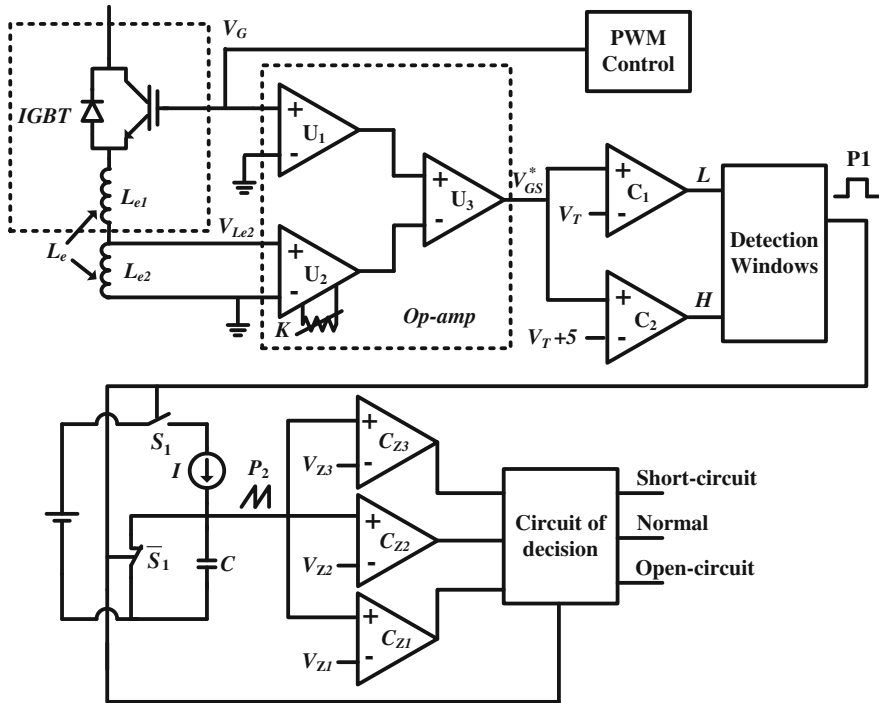


Fig. 20 Fault diagnosis circuit for the gate voltage sensing method

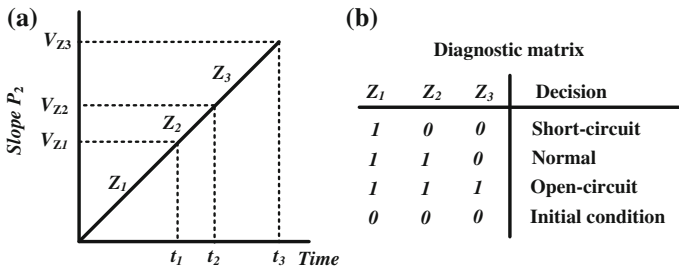


Fig. 21 Decision criterion. a Threshold voltage level. b Diagnostic matrix

In the above expression, the variation of several designs and semiconductor-material parameters such as gate-drain area A_{GD} and dielectric constant ϵ_{si} can cause a significant change of C_{GDJ} . The variation of these parameters can appear in the IGBT with the destructive effect. C_{GD} is affected by the change of C_{GDJ} because C_{GD} is expressed as

$$C_{GD} = \frac{C_{OXD} \cdot C_{GDJ}}{C_{OXD} + C_{GDJ}} \quad (V_{DS} > V_{GS}). \quad (16)$$

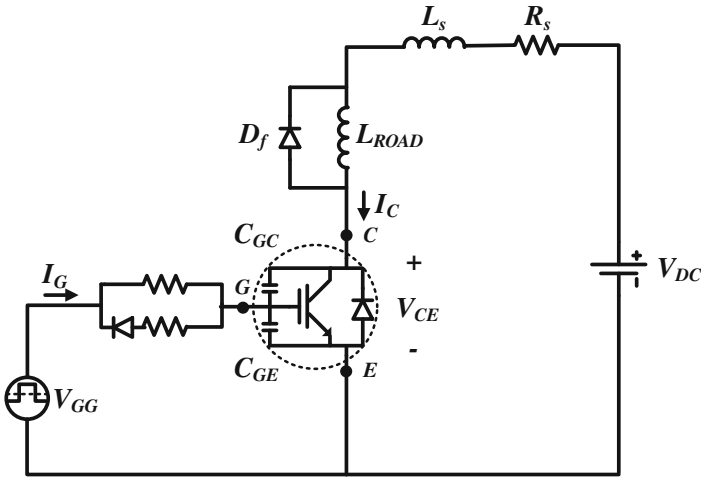


Fig. 22 Diode clamped inductive loads

The gate current I_G is derived from the equivalent circuit shown in Fig. 18 and defined by

$$I_G(t) = C_{GS} \frac{dV_{GS}(t)}{dt} - C_{GD} \frac{dV_{DS}(t)}{dt} + C_{GD} \frac{dV_{GS}(t)}{dt}. \tag{17}$$

As shown in this equation, the change of C_{GD} directly affects the gate current and leads to a significant change in the gate voltage. Therefore, changes in the gate voltage can be analyzed to identify a faulty condition. IGBT failures due to rupture in the isolated gate zone can be detected and proactive action can be taken to avoid major damages in the inverter.

This method is simple, but requires a complicated protection circuitry in order to interpret the gate voltage information and protect the IGBT effectively.

The detection-circuit design is based on the measurement of the gate signal. The principle of the design consists of measuring the energy of the IGBT gate charge during the turn on, from V_T up to $V_T + 5$ V, giving an output signal P_1 , which is evaluated by using detection thresholds V_{Z1} , V_{Z2} , and V_{Z3} in order to determine the IGBT short circuit or open circuit fault. Figure 19 shows detection windows V_1 , V_2 , and V_3 for hysteresis zones of the fault-free and faulty cases.

Figure 20 shows the fault diagnosis circuit for the gate voltage sensing method and Fig. 21 shows the decision criterion.

2.2.4 Gate Voltage Comparing Method

This method detects the short-circuit fault by comparing the gate input voltage V_{GG} and gate voltage V_{GE} [14, 15]. Figure 22 shows the diode clamped inductive

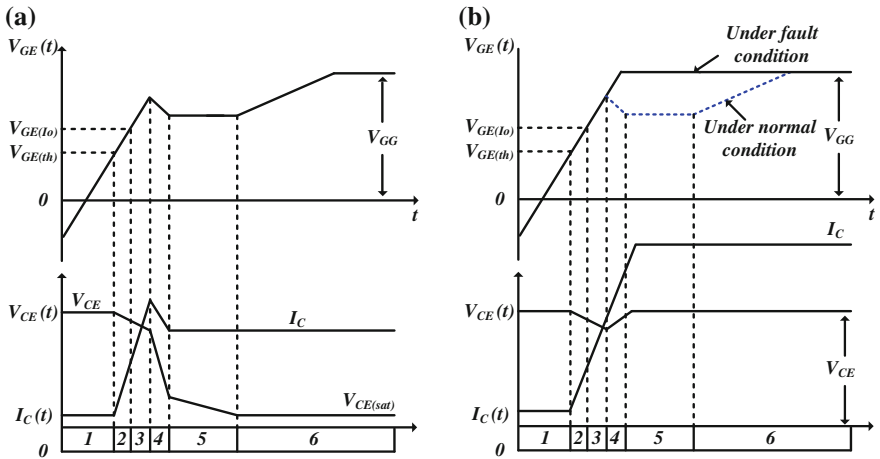


Fig. 23 Turn-on characteristic of IGBT. **a** Under normal condition. **b** Under hard switching fault condition

load circuit to examine the switching transient state characteristic of an IGBT. L_S and R_S represent stray inductance and resistance respectively.

Figure 23 shows the turn-on switching characteristic of the IGBT under the normal condition. The turn-on transient state can be divided into six regions.

Region 1 The gate current I_G charges the parasitic input capacitance C_{GE} and C_{GC} . Then, the gate voltage V_{GE} is increased to $V_{GE(th)}$. V_{GE} is increased exponentially with the time constant of $R_G(C_{GE} + C_{GC})$ as shown below

$$V_{GE}(t) = V_{GE(th)}(1 - e^{[-t/R_G(C_{GE}+C_{GC})]}). \tag{18}$$

In this region, V_{GE} , the voltage between the gate and emitter, maintains to the same level at the input voltage V_{GG} because the collector current I_C does not flow through the IGBT.

Region 2 V_{GE} increases continuously. I_C begins to increase and reaches the full load current I_0 . In this region, V_{CE} decreases due to the induced voltage which is the value related to L_S and di_c/dt . On the other hand, I_C rises continuously due to a reverse recovery current of freewheeling diode.

Region 3–Region 4 The reverse recovery current starts to decrease at region 4. At this time, the voltage across the freewheeling diode increases, while V_{CE} falls. In region3, C_{GC} absorbs and discharges the current from the gate drive and the current from C_{GE} . At the end of region 4, the reverse recovery time of the diode is ended.

Region 5 C_{GC} is charged by I_G , and V_{GE} is maintained at $V_{GE(I_0)}$, and I_C is maintained at full load current I_0 , while V_{CE} falls at a rate $(V_{CG} - V_{GE(I_0)})/(R_G C_{GC})$.

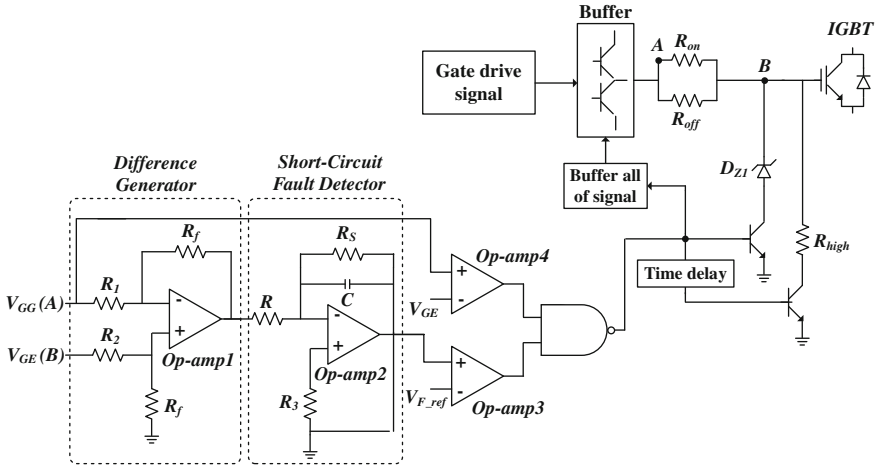


Fig. 24 Fault diagnosis circuit for the gate voltage comparing method

Region 6 V_{GE} increases to V_{GG} with the time constant of $R_G(C_{GE} + C_{GC(miller)})$. $C_{GC(miller)}$ is the C_{GC} that rose from low V_{CE} due to the Miller effect. In this region, V_{CE} slowly diminishes to the collector-to-emitter on-state voltage and becomes completely saturated.

As explained above and shown in Fig. 23, V_{GE} is kept to constant because of the Miller effect in *Region 3–Region 4*. However, under the hard switching fault condition, V_{GE} is increased in *Region 3–Region 4*. There is no Miller effect because V_{CE} is not changed under the hard switching fault condition. V_{GE} with the slope of the initially charged C_{GE} rises to V_{GG} . Consequently, the hard switching fault of the IGBT is detected by comparing V_{GG} and V_{GE} .

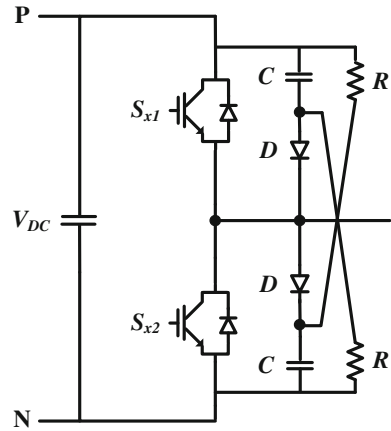
Figure 24 shows the fault detection circuit of the gate voltage comparing method. V_{GG} and V_{GE} are compared by the differential generator and the output of the differential generator is defined by

$$V_O = \frac{R_f}{R_1} (V_{GG} - V_{GE}). \quad (19)$$

The output V_O becomes the input of the short-circuit fault detector which consists of an integrator using an op-amp, resistor and capacitor. In order to identify V_O of the differential generator, the short-circuit fault detector has an integral circuit which detects the difference between V_{GG} and V_{GE} . The output V_{FO} of the short-circuit fault is given by

$$V_{FO} = -\frac{1}{CR} \int_0^t V_O dt. \quad (20)$$

Fig. 25 RCD voltage clamp for the IGBT bridge



If the short-circuit fault occurs, the time that the voltage is applied across the differential generator is short. Thus, the output voltage V_{FO} of the integrator becomes lower than that of the normal condition. V_{FO} is compared with the fault reference voltage by the op-amp 3 and the V_{GG} is compared with V_{GE} by the op-amp 4 to measure the rise of V_{GE} to V_{GG} . If the short-circuit fault occurs, the output of the fault detection circuit is high, gate voltage is clamped by zener diode and, at that time, the both switches of the buffer are turned off. After the short time delay, the gate voltage is softly turned off by a high resistor.

2.2.5 Protection Using Snubber and Clamped-Circuit

The resistor–capacitor diode (RCD) clamp, shown in Fig. 25, acts as a voltage clamp [16]. During the IGBT conduction period, the snubber capacitors are charged to the bus voltage. As the IGBT is turned-off, V_{CE} , voltage across it, rises rapidly. The stray inductance L_S in the circuit “dc loop” may cause V_{CE} to rise above the bus voltage. As this occurs, the snubber diode is forward biased, and the snubber is activated. The energy trapped in the stray inductance is then diverted to the snubber capacitor, which absorbs this incremental energy without the substantial rise in its voltage. The voltage overshoot is, thereby, substantially reduced. Additionally, the higher the inductance L_S within the snubber circuitry, the higher the final voltage peak V_{PK} the snubber circuit has because there is more trapped energy $L_S \cdot I^2/2$ diverted to the same snubber capacitor. Adjusting this for hard switching applications, the trapped energy in the circuit stray inductance caused by abrupt interruptions of the device current appears as a voltage overshoot across the device. Snubber and clamp circuits offer optimized protection against these transients. However, the use of these circuits for the protection against turnoff transients caused by the rapid suppression of the gate drive is not optimal, because it requires high-capacity, high-voltage snubber capacitors that are bulky and costly.

Fig. 26 Circuit for the resistive short circuit protection method

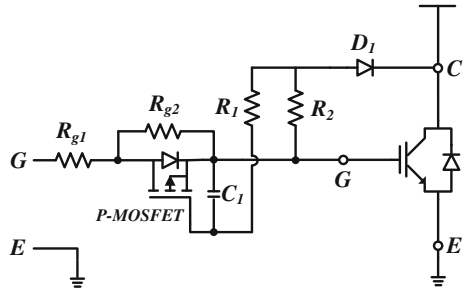
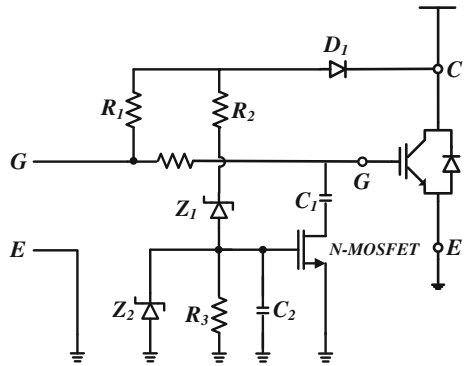


Fig. 27 Circuit for the capacitive short circuit detective method



2.2.6 Protection by Slow Turn-Off of IGBT

If a short-circuit fault occurs, the resulting high current can produce extremely high di/dt [16]. The IGBT fault current rate can be reduced by slowing the turn-off time. This can be achieved by increasing the gate turn-on resistor, but this is inefficient because it also increases the switching losses. To solve the problem above, two novel circuits are introduced to decrease the V_{GE} fall rate, only when a fault current is sensed.

Resistive Method

The fault protection circuit shown in Fig. 26 is composed of a de-saturation sensing diode D_1 and a P-channel MOSFET, to switch in a higher value of resistor R_{g2} when a short-switch fault occurs. In normal turn-on conditions, this circuit does not affect the system. During the normal turnoff operation, the gate driver output voltage is switched to a low state and the capacitance of the P-MOSFET starts to discharge. The values of C_1 , R_1 and R_2 are adjusted so that the MOSFET is kept turned-on at least until the IGBT turns-off.

If a fault occurs, D_1 is reverse biased and the P-MOSFET input starts to discharge through R_1 and R_2 . The MOSFET is then turned-off because its gate voltage

Fig. 28 Equivalent circuit of an electrolytic capacitor



drops below the threshold value, and V_{GE} fall rate is reduced significantly as the discharge is now forced to take place through R_{g2} . The fault current fall rate decreases accordingly.

Capacitive Method

The circuit in Fig. 27 is composed of the de-saturation diode D_I , used to sense a fault condition, and an N-channel MOSFET, to switch in a higher value of the capacitor C_I in parallel with the IGBT input capacitance upon occurrence of a fault. The small switching operation is not affected by this protection circuit. If a fault occurs, the sensor diode becomes reverse biased and the MOSFET gate input capacitance C_2 is charged by the gate drive power. When the MOSFET is turned on, the capacitor C_I is switched on, in parallel with the IGBT input capacitance. A drop in the IGBT gate voltage is then observed because some charges are removed to charge the capacitor C_I , which was initially charged to the off-bias voltage. This, in turn, lowers the value of I_{sc} momentarily, reducing the energy losses during short-circuit periods. The IGBT discharge time constant increases because it now includes the capacitor C_I in parallel with the IGBT input capacitance. Therefore, the fault current di/dt is increased and the transient is brought down substantially.

3 DC-Link Electrolytic Capacitor Fault

In many power converter applications, the electrolytic capacitors are dominantly used for DC-links because of their low cost. However, they have some undesirable properties such as sensitivity to temperature, frequency and low reliability. The main disadvantage of electrolytic capacitors is their finite lifetime and high failure rate due to wear-out degradation failure. Due to the aging effects such as the electrolytic reaction and the effects of temperature, frequency and humidity, the capacitor banks lose their initial operating characteristics. The increase of equivalent series resistor (ESR) is usually more pronounced than the decrease of the capacitance. It has been a standard that the lifetime of the capacitor ends if ESR of the capacitor increases by more than two times its initial value. Therefore, the variations in the ESR value can be regarded as a key parameter for diagnosing electrolytic capacitor failure.

In this chapter, the condition monitoring methods for electrolytic capacitors are introduced.

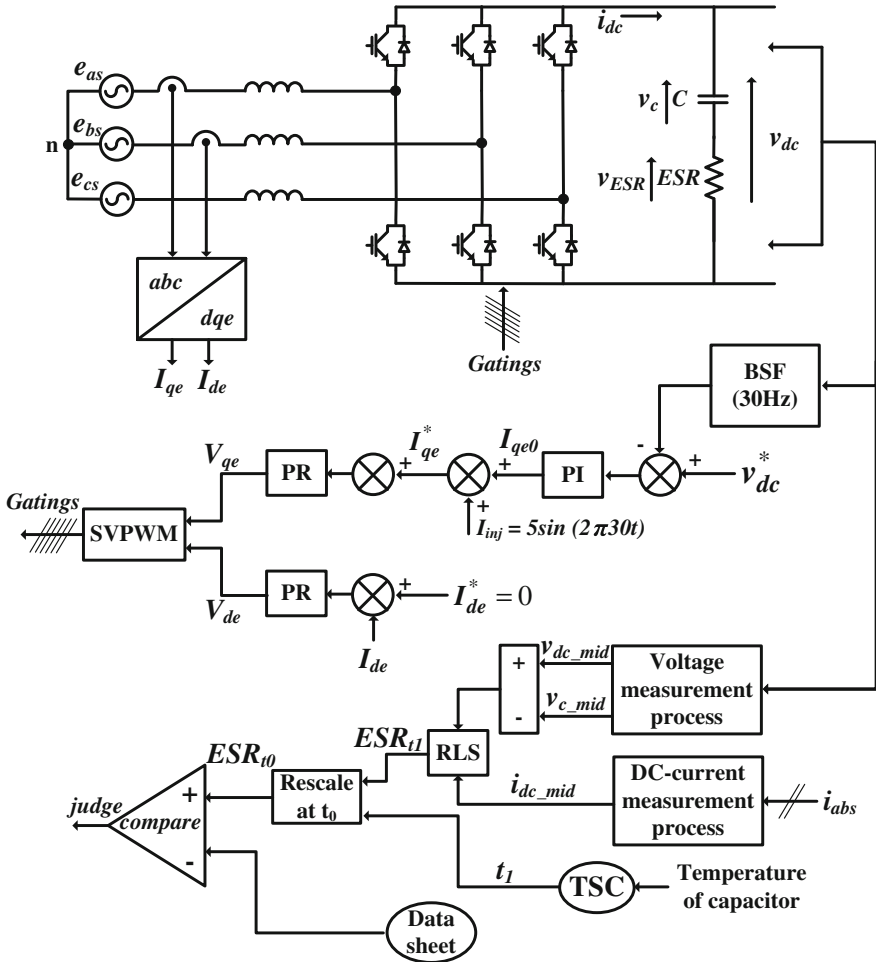


Fig. 29 Control block diagram of the three phase AC/DC converter with condition monitoring of the DC-link capacitor

3.1 Online Estimation of Equivalent Series Resistance

The capacitor is usually modeled as a capacitance in series with a resistance as shown in Fig. 28 [17].

The ESR value of the capacitor can be found from the voltage across the ESR and the current through the ESR. The ESR of the capacitor is expressed by

$$ESR = \frac{V_{ESR}}{i_{dc}}. \tag{21}$$

Since the ESR value of the capacitor varies depending on the operating temperature, the temperature effect has to be considered. The information of the ESR voltage and the current for (21) is obtained as described in the following sections.

3.1.1 AC Current Injection

Figure 29 shows the control block diagram of a three-phase AC/DC converter involving the ESR estimation and temperature detection. To obtain the meaningful information from the converter, a regulated AC component is injected to the q -axis input current component which is the real power component. The injected current reference is expressed as

$$\dot{i}_{inj}^* = I_{inj} \sin(2\pi \times f_{in}t) \quad (22)$$

where I_{inj} is the magnitude of the injected current and f_{in} is the frequency of the injected current.

This current induces a ripple voltage of the same frequency in the DC-link. In this work, $f_{in} = 30$ Hz and $I_{inj} = 5$ A. These AC voltage and current components estimate the ESR value. There are no effects of the injected current on the converter because the test current is injected for a short time at no load.

A band-stop filter (BSF) with a 30 Hz cut-off frequency is applied to the measured DC-link voltage. The proportional-integral (PI) controller are employed for the outer DC-link voltage loop. The proportional-resonance (PR) regulators are used to control the dq -axis components of the source currents.

The DC-link voltage can be expressed as the summation of the capacitance voltage and the ESR voltage as illustrated in Fig. 28.

$$v_{dc} = v_c + v_{ESR} \quad (23)$$

3.1.2 Indirect Measurement of the DC-Link Capacitor Currents

The estimation of the ESR is carried out at every sampling period using its voltage and current. However, the current in the ESR is zero at the normal sampling instants because the current does not flow through the capacitor during the zero switching states. Therefore, the quantities at the mid-point of every sampling period are used for the estimation, obtained from (21) and (23) as

$$ESR = \frac{v_{dc} - v_c}{\dot{i}_{dc}} = \frac{v_{dc_mid} - v_{c_mid}}{\dot{i}_{dc_mid}}. \quad (24)$$

Figure 30 shows the relationship between the phase currents, instantaneous DC-link current and voltage according to the switching state where A+, B+ and C+ and T_{ga} , T_{gb} and T_{gc} represent the switching states and gating signals.

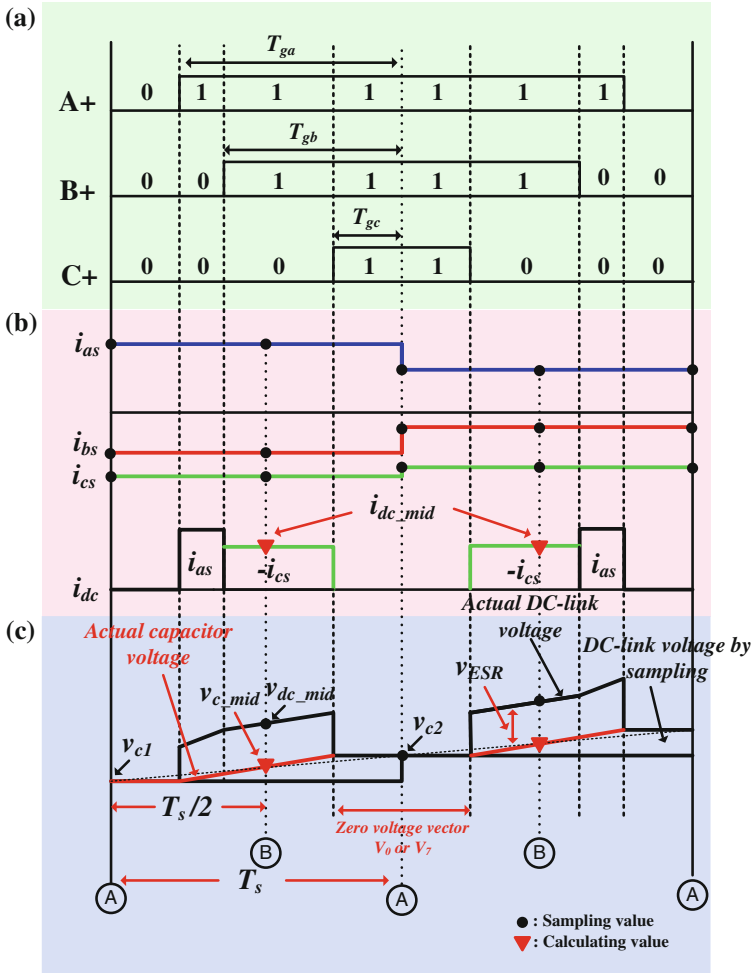


Fig. 30 Behavior of the DC-link current and voltages according to gating pulses. **a** Switching state of upper switches. **b** Relation of phase currents and DC-link current. **c** DC-link capacitor voltage

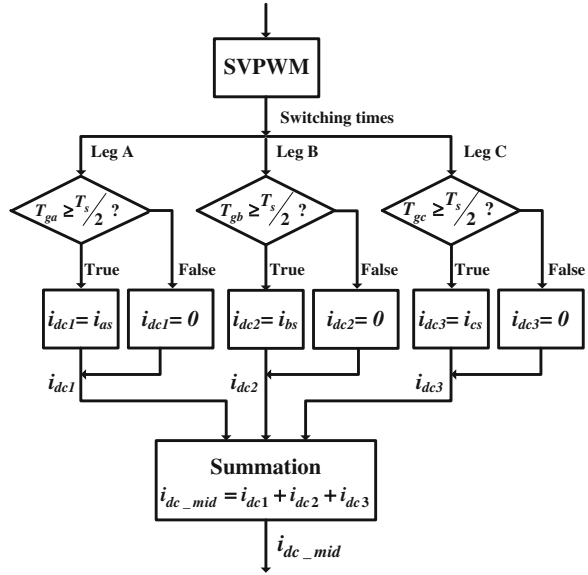
The instantaneous DC-link current can be expressed from the phase currents and switching functions as follow:

$$i_{dc} = S_{A+}i_{as} + S_{B+}i_{bs} + S_{C+}i_{cs} \tag{25}$$

where switching functions are “1” or “0” when the upper switches of inverter legs turn on or off, respectively.

Figure 31 shows the flow chart used to calculate the mid-point value of the DC-link current which can be expressed as

Fig. 31 Flowchart for calculating the mid-point value of DC-link current



$$i_{dc_mid} = i_{dc1} + i_{dc2} + i_{dc3} \tag{26}$$

where $i_{dc1} = S_{A+}i_{as}$, $i_{dc2} = S_{B+}i_{bs}$ and $i_{dc3} = S_{C+}i_{cs}$.

3.1.3 Measurement of the DC-Link and Capacitor Voltages

Figure 30c shows DC-link and capacitor voltages. For the ESR estimation, the mid-point value of the DC-link voltage is needed. The mid-point voltage value of the DC-link voltage is illustrated at ② in Fig. 30c. The capacitance voltage is equal to the DC-link voltage at the normal sampling instant. Therefore, the mid-point value of the capacitance voltage, v_{c_mid} can be calculated as the average value of the two consecutive DC-link voltages v_{c1} and v_{c2} measured at the zero switching state that is

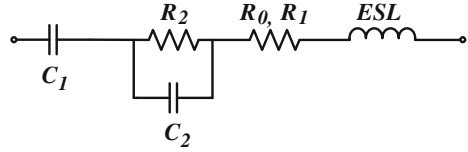
$$v_{c_mid} = \frac{v_{c1} + v_{c2}}{2}. \tag{27}$$

This measurement technique is depicted in Fig. 30c. The ESR voltage can be expressed as

$$v_{ESR} = v_{dc_mid} - v_{c_mid}. \tag{28}$$

It is noted that at ① in Fig. 30, the voltages and currents are sampled not only for the control but also for the calculation of the mid-point value of the capacitor voltage. Meanwhile, at ②, the mid-point values of the DC-link voltage are measured for the estimation only.

Fig. 32 Aluminum-electrolytic-capacitor model



3.1.4 Calculation of the ESR

A recursive least squares (RLS) method can be minimized as a least-square cost function iteratively. It allows the estimated parameter of the system to be updated at every sampling period with fast convergence and tracking capabilities. Since the ESR value calculated in (24) usually has ripple components, the RLS method can be applied for a more reliable estimation.

The RLS update of parameter, $E\hat{S}R(n)$, is given by

$$E\hat{S}R(n+1) = E\hat{S}R(n) + \mu(n)i_{dc_mid}(n) \times [\{v_{dc_mid}(n) - v_{c_mid}(n)\} - E\hat{S}R(n) + i_{dc_mid}(n)] \quad (29)$$

where $\mu(n)$ is an adjustment gain which was chosen by trial and error as a constant ($8 * 10^{-5}$).

3.2 A Simple Offline Technique

3.2.1 Capacitor Model

Figure 31 shows the equivalent circuit of an aluminum electrolytic-capacitor [18]. Using this model, the impedance of the capacitor can be represented as

$$Z_{cap} = R_1 + R_0 + \frac{1}{\left(\frac{1}{R_2} + j(\omega C_2)\right)} + \frac{1}{j(\omega C_1)} + (\omega ESL)j \quad (30)$$

where

- f frequency;
- ω radian frequency ($\omega = 2\pi f$);
- R_0 resistance of the foils, tabs, and terminals (in ohms);
- R_1 resistance of electrolyte (in ohms);
- R_2 dielectric loss resistance (in ohms);
- C_1 terminal capacitance (in farads);
- C_2 dielectric loss capacitance (in farads);
- ESL equivalent series inductance

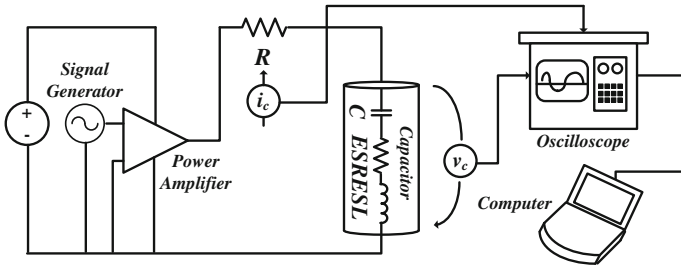


Fig. 33 Experimental setup

The most significant contributor to the ESL of capacitor is the loop formed by the terminals and tabs, and its typical value for radial and screw-terminal capacitor is about 1–2 nH/mm for terminal spacing. The resistance R_2 accounts for the leakage current of the capacitor and decrease with increasing capacitance, temperature, voltage, and time. Its typical value is on the order of $100/C \text{ M}\Omega$, with C in microfarads (Fig. 32).

The impedance of capacitance expressed in (31) can be simplified by

$$Z_{cap} = ESR + \left(-\frac{1}{\omega C} + \omega ESL \right) j \tag{31}$$

where C represents the series of C_1 and C_2

$$ESR \cong R_1 + R_0 + \frac{1}{(\omega C_2)^2 R_2} \tag{32}$$

3.2.2 Estimation ESR

To implement the estimation of ESR, the experimental setup as shown in Fig. 33 is required which is composed of a function generator, a class AB audio power amplifier, a non-inductive thick film resistor soldered to the capacitor, a digital oscilloscope, and a microcomputer with Matlab software. This method uses the discrete fourier transform algorithm (DFT).

The capacitor is connected to non-inductive resistor and exposed both components to a sinusoidal voltage waveform. After capturing the input and capacitor voltages, it is necessary to represent the second waveform as a function of the first one. Since both waveforms are sinusoidal, it is possible to automatically obtain both the phase and modulus of the fundamental component using the DFT.

$$f_{1st} \cong \sum_{n=1}^{NPP} \frac{f(n) \times e^{j\omega_0 n}}{0.5NPP} \quad (33)$$

where

NPP total number of points per period;
 ω_0 radian frequency ($\omega = 2\pi/NPP$);
 $f(n)$ waveforms;
 f_{1st} first harmonic of $f(n)$

It is possible to compute the real and imaginary parts of the impedance of the capacitor as

$$ESR \cong \frac{|v_c|}{|i_c|} \cos(|v_c| - |i_c|) \quad (34)$$

$$X_C \cong \frac{|v_c|}{|i_c|} \sin(|v_c| - |i_c|) \quad (35)$$

where

$|v_c|$ modulus of the capacitor voltage;
 $|i_c|$ modulus of the capacitor current;
 $\angle v_c$ phase angle of the capacitor voltage;
 $\angle i_c$ phase angle of the capacitor current

In order to obtain a higher level of accuracy, its value should be estimated at high frequency about 1 kHz whereas the capacitance value should be obtained at lower frequency (120 Hz) to neglect the ESL effect. Thus, the proposed method is based on the estimation of the ESR at 1 kHz and of C at 120 Hz.

After obtaining the capacitor current and voltage, it is necessary to deal with the data in order for them to be processed in Matlab. Two m files were developed: one to obtain both the modulus and phase of each waveform and the other one to compute C , DF, and ESR.

4 Summary

This chapter provides a comprehensive study about the fault and diagnosis systems in power converters. Among the components of the power converters, the power switching devices and the electrolytic capacitors which cause the most frequent failures in power converters are discussed. The diagnosis methods of the switching device are discussed by dividing into open- and short- switch faults. Further, the online and offline methods for monitoring the condition of the electrolytic capacitors are introduced.

References

1. S. Yang, A. Bryant, P. Mawby, D. Xiang, L. Ran, P. Tavner, An industry-based survey of reliability in power electronic converter. *IEEE Trans. Ind. Appl.* **47**(3), 1441–1451 (2011)
2. S. Yang, D. Xiang, A. Bryant, P. Mawby, L. Ran, P. Tavner, Condition monitoring for device reliability in power electronic converters: a review. *IEEE Trans. Power Electron.* **25**(11), 2734–2752 (2010)
3. B. Lu, S. Sharma, A literature review of IGBT fault diagnostic and protection methods for power inverters. *IEEE Trans. Ind. Appl.* **45**(5), 1770–1777 (2009)
4. Y.J. Ko, K.B. Lee, Fault diagnosis of a voltage-fed PWM inverter for a three-parallel power conversion system in a wind turbine. *J. Power Electron* **10**(6), 686–693 (2010)
5. Y.J. Ko, K.B. Lee, D.C. Lee, J.M. Kim, Fault diagnosis of three-parallel voltage-source converter for high-power wind turbine. *IET Power Electron* **5**(7), 1058–1067 (2012)
6. W. Sleszynski, J. Nieznanski, A. Cichowski, Open-transistor fault diagnosis in voltage-source inverter by analyzing the load currents. *IEEE Trans. Indus. Electron* **56**(11), 4681–4688 (2009)
7. M. Trabelsi, M. Boussak, M. Gossa, Multiple IGBTs open circuit faults diagnosis in voltage source inverter fed induction motor using modified slope method. in *Proceedings of ICEM'10 Conference*, pp. 1–6, Sept 2010
8. R. Peugot, S. Courtine, J.P. Rognon, Fault detection and isolation on a PWM inverter by knowledge-based model. *IEEE Trans. Ind. Appl.* **34**(6), 1318–1326 (1998)
9. Q.T. An, L.Z. Sun, K. Zhao, L. Sun, Switching function model-based fast-diagnostic method of open-switch faults in inverters without sensors. *IEEE Trans. Power Electron* **26**(1), 119–126 (2011)
10. O.S. Yu, N.J. Park, D.S. Hyun, A novel fault detection scheme for voltage fed PWM inverter, in *Proceedings of IECON'06 Conference*, pp. 2654–2659, Nov 2006
11. U.M. Choi, H.G. Jung, K.B. Lee, F. Blaabjerg, Method for detecting an open-switch fault in a grid-connected NPC inverter system. *IEEE Trans. Power Electron* **27**(6), 2726–2739 (2012)
12. F. Huang, F. Flett, IGBT fault protection based on di/dt feedback control, in *Proceeding of PESC'07 Conference*, pp. 1478–1484, 2007
13. M.A.R. Blanco, A.C. Sanchez, D. Theilliol, L.G.V. Valdes, P.S.Teran, L.H. Gonzalez, J.A. Alquicira, A failure-detection strategy for IGBT based on gate-voltage behavior applied to a motor drive system. *IEEE Trans. Indus. Electron.* **58**(5), 1625–1633 (2011)
14. M.S. Kim, B.G. Park, R.Y. Kim, D.S. Hyun, A novel fault detection circuit for short-circuit faults of IGBT, in *Proceedings of APEC'11 Conference*, pp. 359–363, March 2011
15. M.A. Rodriguez, A. Claudio, D. Theilliol, L.G. Vela, A new fault detection technique for IGBT based on gate voltage monitoring, in *Proceedings of PESC'07 Conference*, pp. 1001–1005, 2007
16. R.S. Chokhawala, S. Sobhani, Switching voltage transient protection schemes for high-current IGBT modules. *IEEE Trans. Ind. Appl.* **33**(6), 1601–1610 (1997)
17. X. Pu, T.H. Nguyen, D.C. Lee, K.B. Lee, J.M. Kim, Fault diagnosis of DC-link capacitors in three-phase AC/DC PWM converters by online estimation of equivalent series resistance. *IEEE Trans. Indus. Electron.* **60**(9), 4118–4127, Sep. 2013
18. A.M.R. Amaral, A.J.M. Cardoso, A simple offline technique for evaluating the condition of aluminum-electrolytic-capacitors. *IEEE Trans. Industr. Electron* **56**(8), 3230–3237 (2009)

Author Biographies

Kyo-Beum Lee He received the B.S. and M.S. degrees in electrical and electronic engineering from the Ajou University, Korea, in 1997 and 1999, respectively. He received the Ph.D. degree in electrical engineering from the Korea University, Korea in 2003. From 2003 to 2006, he was with the Institute of Energy Technology, Aalborg University, Aalborg, Denmark. From 2006 to 2007, he was with the Division of Electronics and Information Engineering, Chonbuk National University, Jeonju, Korea. In 2007 he joined the School of Electrical and Computer Engineering, Ajou University, Suwon, Korea. He is an Associate Editor of the *IEEE TRANSACTIONS ON POWER ELECTRONICS*, *IEEE TRANSACTIONS ON INDUSTRIAL ELECTRONICS* and the *Journal of Power Electronics*.

Ui-Min Choi He received the B.S. and M.S. degrees in electrical and computer engineering from Ajou University, Suwon, Korea, in 2011 and 2013, respectively. He is currently working toward the Ph.D. degree at Aalborg University, Aalborg, Denmark.

Part II
Predictive Control of Power Converters
and Drives

Chapter 5

Predictive Control in Power Electronics and Drives: Basic Concepts, Theory, and Methods

Daniel E. Quevedo, Ricardo P. Aguilera and Tobias Geyer

Abstract In this chapter we revise basic principles and methods of model predictive control with a view towards applications in power electronics and drives. The simplest predictive control formulations use horizon-one cost functions, which can be related to well-established dead-beat controllers. Model predictive control using larger horizons has the potential to give significant performance benefits, but requires more computations at each sampling instant to solve the associated optimization problems. For particular classes of system models, we discuss practical algorithms, which make long-horizon predictive control suitable for power electronics applications.

1 Introduction

Model predictive control (MPC), also referred to as *receding horizon control*, has received significant attention. Applications and theoretical results abound, see, e.g., the books [17, 50, 51, 76, 107] and survey papers [83, 97]. An attractive feature of MPC is that it can handle general constrained nonlinear systems with multiple inputs and outputs in a unified and clear manner.

D. E. Quevedo (✉) · R. P. Aguilera
School of Electrical Engineering and Computer Science, The University of Newcastle,
Callaghan, NSW 2308, Australia
e-mail: dquevedo@ieee.org

R. P. Aguilera
e-mail: raguilera@ieee.org

T. Geyer
ABB Corporate Research, ABB Switzerland Ltd, Power Electronic Systems,
Segelhofstrasse 1 K 5405 Baden-Dättwil, Switzerland
e-mail: t.geyer@ieee.org

Particularly, in the field of power electronics, various embodiments of MPC principles have emerged as a promising control alternative for power converters and electrical drives [20, 65, 110, 111]. This is due to the fact that predictive control algorithms present several advantages that make it suitable for the control of power converters:

1. Concepts are intuitive and easy to understand;
2. MPC can handle converters with multiple switches and states, e.g., current, voltage, power, torque, etc.;
3. constraints and nonlinearities can be easily included; and
4. the resulting controller is, in general, easy to implement.

The aim of this chapter is to provide an overview of the basic theoretical underpinnings of MPC and to illustrate their use in power converters. For that purpose, in Sect. 2, we begin by presenting the key element underlying MPC, namely, that of moving horizon optimization. In Sect. 3 we analyze, in detail, the special case of MPC with horizon one. These simple formulations often give good results and only require little computations, leading to their immense popularity in power electronics applications [111]. In particular, we establish relationships between dead-beat control and horizon-one MPC strategies. For implementations without a modulator, dealt with by so called *Finite Control-Set MPC* with a quadratic cost function, we derive the optimal control input by exploring the geometry of the underlying optimization problem. Section 4 focuses on the general case of MPC with longer horizons. In general, using long horizons yields better closed-loop performance than MPC with horizon one [34, 52]. However, solving the underlying on-line optimization problems can be highly demanding. To overcome these issues, we examine special purpose optimization algorithms, which allow one to implement long-horizon optimal solutions in practical power electronics and drive systems.

2 Basic Concepts

Various model predictive control methods have been proposed for controlling power electronics and drives. Here, one can distinguish between formulations that use system models governed by linear time invariant dynamics, and those that incorporate nonlinearities. Most MPC strategies are formulated in a discrete-time setting with a fixed sampling interval, say $h > 0$. System inputs are restricted to change their values only at the discrete sampling instants, i.e., at times $t = kh$, where $k \in \mathbb{N} \triangleq \{0, 1, 2, \dots\}$ denotes the sampling instants.

Since power electronics applications are often governed by nonlinear dynamic relations, it is convenient to represent the system to be controlled in discrete-time state space form via:

$$x(k+1) = f(x(k), u(k)), \quad k \in \mathbb{N}, \quad (1)$$

where $x(k) \in \mathbb{R}^n$ denotes the state value at time k and $u(k) \in \mathbb{R}^m$ is the plant input. Depending on the application at hand, the system state is a vector, which may contain capacitor voltages, inductor and load currents, and fluxes.

2.1 System Constraints

An interesting feature of the MPC framework is that it allows one to incorporate state and input constraints, say:

$$\begin{aligned} x(k) &\in \mathbb{X} \subseteq \mathbb{R}^n, & k &\in \{0, 1, 2, \dots\}, \\ u(k) &\in \mathbb{U} \subseteq \mathbb{R}^m, & k &\in \{0, 1, 2, \dots\}. \end{aligned} \quad (2)$$

State constraints can, for example, correspond to constraints on capacitor voltages in flying capacitor converters or neutral point clamped converters. Constraints on load currents can also be modeled as state constraints. Throughout this chapter we will focus on input constraints, since their form is peculiar to the nature of power converters.

Input constraints, $u(k) \in \mathbb{U}$, are related to the switch positions during the interval $(kh, (k+1)h]$. If the converter uses a modulator, then $u(k)$ will be constrained to belong to a bounded continuous set. For example, the components of $u(k)$ could correspond to duty cycles, $d(k)$, or PWM reference signals. In this case, the control input is constrained by

$$u(k) = d(k) \in \mathbb{U} \triangleq [-1, 1]^m \subset \mathbb{R}^m, \quad k \in \{0, 1, 2, \dots\}, \quad (3)$$

where m denotes the number of phases, see Fig. 1. Clearly, the above model can only approximate switching effects, see also [72]. Nevertheless, as we will see, several interesting and powerful controllers for power electronics and drives have been developed by using this simple setting.

On the other hand, in direct control-applications, where no modulator is used, $u(k)$ is constrained to belong to a finite set describing the available switch combinations. Such approaches have attracted significant attention in the power electronics community, often under term Finite Control Set MPC [111]. The main advantage of this predictive control strategy comes from the fact that switching actions, say $S(k)$, are directly taken into account in the optimization as constraints on the system inputs, see Fig. 2. Thus, the control input is restricted to belong to a finite set represented by

$$u(k) = S(k) \in \mathbb{U} \triangleq \{0, 1\}^m \subset \mathbb{R}^m, \quad k \in \{0, 1, 2, \dots\}, \quad (4)$$

where \mathbb{U} is a boolean set obtained by combining the m switch values. For the control of some multi-level topologies, it is at times convenient to consider the resultant voltage level as the control input, without making the distinction at a

Fig. 1 MPC with continuous control set

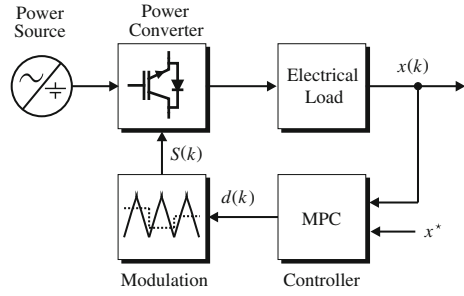
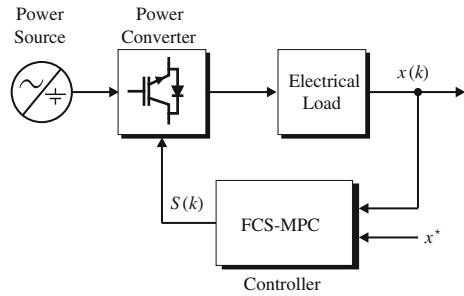


Fig. 2 MPC with finite control set



switch level. For example, for a 5-level inverter, one would have $\{-2, -1, 0, 1, 2\}^m$.

2.2 Cost Function

A distinguishing element of MPC, when compared to other control algorithms, is that at each time instant k and for a given (measured or estimated) plant state $x(k)$, a cost function over a finite horizon of length N is minimized. The following choice encompasses many alternatives documented in the literature:

$$V(x(k), \mathbf{u}'(k)) \triangleq F(x'(k+N)) + \sum_{\ell=k}^{k+N-1} L(x'(\ell), \mathbf{u}'(\ell)). \quad (5)$$

Here, $L(\cdot, \cdot)$ and $F(\cdot)$ are weighting functions, which serve to penalize predicted system behaviour, e.g., differences between voltage references and predicted values, see Sect. 2.4. Predicted plant state values, $x'(\ell)$, are formed using the system model (1):

$$x'(\ell+1) = f(x'(\ell), \mathbf{u}'(\ell)), \quad \ell \in \{k, k+1, \dots, k+N-1\} \quad (6)$$

where

$$u'(\ell) \in \mathbb{U}, \quad \ell \in \{k, k+1, \dots, k+N-1\}$$

refers to tentative plant inputs (to be decided). The recursion (6) is initialized with the current plant state measurement (or estimate), i.e.:

$$x'(k) \leftarrow x(k).$$

Thus, (6) refers to predictions of the plant states that would result if the plant inputs at the update times $\{k, k+1, \dots, k+N-1\}$ were set equal to the corresponding values in

$$\mathbf{u}'(k) \triangleq \{u'(k), u'(k+1), \dots, u'(k+N-1)\}. \quad (7)$$

Both, the predicted plant state trajectory and the plant inputs are constrained in accordance with (2), i.e., we have:

$$\begin{aligned} u'(\ell) &\in \mathbb{U}, & \forall \ell \in \{k, k+1, \dots, k+N-1\} \\ x'(\ell) &\in \mathbb{X}, & \forall \ell \in \{k+1, k+2, \dots, k+N\}. \end{aligned}$$

Constrained minimization of $V(\cdot, \cdot)$ in (5) gives the optimizing control sequence at time k and for state $x(k)$:

$$\mathbf{u}^{\text{opt}}(k) \triangleq \{u^{\text{opt}}(k), u^{\text{opt}}(k+1; k), \dots, u^{\text{opt}}(k+N-1; k)\}. \quad (8)$$

It is worth emphasizing here that, in general, plant state predictions, $x'(\ell)$, will differ from actual plant state trajectories, $x(\ell)$. This is a consequence of possible model inaccuracies and the moving horizon optimization paradigm described next.

2.3 Moving Horizon Optimization

Despite the fact that the optimizer $\mathbf{u}^{\text{opt}}(k)$ in (8) contains feasible plant inputs over the entire horizon, $(kh, (k+N-1)h]$, in most MPC approaches, only the first element is used, i.e., the system input is set to

$$u(k) \leftarrow u^{\text{opt}}(k).$$

At the next sampling step, i.e., at discrete-time $k+1$, the system state $x(k+1)$ is measured (or estimated), the horizon is shifted by one step, and another optimization is carried out. This yields $\mathbf{u}^{\text{opt}}(k+1)$ and its first element provides $u(k+1) = u^{\text{opt}}(k+1)$, etc. As illustrated in Fig. 3 for a horizon length $N=3$, the horizon taken into account in the minimization of V slides forward as k increases. The design of observers for the system state lies outside the scope of the present chapter. The interested reader is referred to [2, 29, 40], which illustrate the use of Kalman filters for MPC formulations in power electronics.

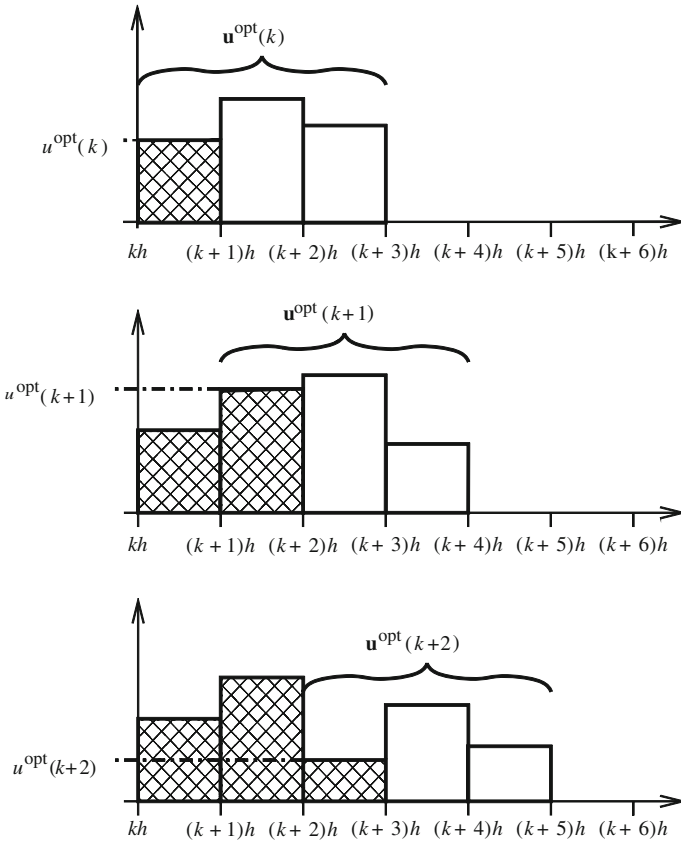


Fig. 3 Moving horizon principle with horizon $N = 3$

2.4 Design Parameters

As seen above, MPC allows one to treat multi-variable nonlinear systems in an, at least conceptually, simple way. In addition to choosing the sampling interval h (which, amongst other things, determines the system model (1)), MPC design essentially amounts to selecting the cost function, i.e., the weighting functions $F(\cdot)$ and $L(\cdot, \cdot)$, and the horizon length N .

The design of the weighting functions $F(\cdot)$ and $L(\cdot, \cdot)$ should take into account the actual control objectives and may also consider stability issues [3, 4, 83].¹ For example, tracking of desired output and internal voltages and currents can be accommodated into the MPC framework by choosing weights which penalize a measure of the difference between predicted and reference values.

¹ Note that the weighting functions should be chosen such that $V(\cdot, \cdot)$ depends on the decision variables contained in $\mathbf{u}^i(k)$, see (7).

For a given sampling frequency $1/h$ and, especially for systems with inverse response, larger values for the horizon length N will in general provide better performance, as quantified by the weighting functions $F(\cdot)$ and $L(\cdot, \cdot)$. Indeed, one can expect that, for large enough N , the effect of $u(k)$ on $x'(\ell)$ for $\ell > k + N$ will be negligible and, consequently, MPC will approximate the performance of an infinite horizon optimal controller [52]. On the other hand, the constrained optimization problem which, in principle, needs to be solved on-line to find the controller output, has computational complexity which, in general, increases with the horizon length. As a consequence, the optimization horizon parameter N allows the designer to trade-off performance versus on-line computational effort. Fortunately, excellent performance can often be achieved with relatively small horizons. In fact, in most applications of MPC to power electronics and electrical drives a horizon $N = 1$ is chosen. We will next present key aspects of *horizon-one MPC*. In Sect. 4, we will then discuss specific optimization algorithms which allow MPC with larger horizons to be implemented in practical power electronics and drive applications.

3 Horizon-One Predictive Control

In the academic field of power electronics, it is most common to focus on one-step horizon formulations when using predictive controllers. This comes from the fact that horizon-one solutions are easy to obtain and often give satisfactory results.

In this section, we present some basic concepts underlying horizon-one predictive control formulations used in power electronics. Our focus is on power converters and electrical drive systems, which can be modeled in discrete-time as

$$x(k+1) = Ax(k) + Bu(k), \quad (9)$$

where $x \in \mathbb{R}^n$ stands for the n -system states (e.g., voltages and currents) and $u \in \mathbb{R}^m$ stands for the m -control inputs (e.g., duty cycles or power switches).

For our subsequent analysis, it is convenient to focus on regulation problems with a constant reference, say $x^\star \in \mathbb{R}^n$. By setting

$$x(k+1) = x(k) = x^\star,$$

it follows that

$$x^\star = Ax^\star + Bu^\star \Rightarrow x^\star = (I - A)^{-1}Bu^\star,$$

where $u^\star \in \mathbb{R}^m$ is the required input to maintain x^\star .

If we now introduce the system state and input tracking errors as

$$\begin{aligned} \hat{x} &\triangleq x - x^\star, & \text{and} \\ \hat{u} &\triangleq u - u^\star, \end{aligned} \quad (10)$$

respectively, then it is easy to see that

$$\hat{x}(k+1) = x(k+1) - x^{\star} = A(\hat{x}(k) + x^{\star}) + B(\hat{u}(k) + u^{\star}) - x^{\star}.$$

Since $x^{\star} = Ax^{\star} + Bu^{\star}$, we obtain the system model:

$$\hat{x}(k+1) = A\hat{x}(k) + B\hat{u}(k), \quad (11)$$

In the sequel, we shall refer to $\hat{x} \in \mathbb{R}^n$ as the system state, whereas $\hat{u} \in \mathbb{R}^m$ is the control input. Consequently, the control goal becomes one of leading the system (11) to the origin. This is equivalent to leading the original system (9) to the desired reference, x^{\star} .

3.1 Deadbeat Control with a Modulator

One of the earliest control strategies referred to as “predictive control” in the power electronics community are deadbeat controllers. These use a discrete-time system model to calculate, at each sampling instant, the required control input to lead the system output to some desired value in a finite number of time steps. Generally, this input is in the form of a voltage reference, which is then modulated as described in Sect. 2.1. Deadbeat control has been applied to current control in three-phase inverters [69, 124, 126], rectifiers [77, 90], active filters [58, 86], DC-DC converters [113], and torque control of induction machines [19].

This control technique is normally used to govern power converters and electrical drives by obtaining the required input to achieve the desired system reference in only one sampling instant. Nevertheless, for some class of power converters, it is not possible to achieve the control target in just one sampling instant and more time-steps need to be considered. A useful concept to understand this issue is called reachability, which is defined as follows.

Definition 1 (Reachability [5]) The system (11) is reachable if it is possible to find a control sequence, say

$$\mathbf{u} = \begin{bmatrix} u(0) \\ u(1) \\ \vdots \\ u(\ell-1) \end{bmatrix}, \quad \ell \in \mathbb{N}$$

such that an arbitrary state, x^{\star} , can be reached from an initial state, $x(0)$, in a finite time, i.e., ℓ -sampling steps. ■

Now, we introduce the so-called reachability matrix, used to determine the system reachability, which is represented via

$$W_{\ell} = [A^{\ell-1}B \quad \dots \quad AB \quad B]. \quad (12)$$

The following theorem follows from the preceding definition.

Theorem 1 (Reachability [5]) *The system (11) is reachable in ℓ sampling steps if and only if the reachability matrix W_ℓ has rank n , where n is the number of system states. ■*

Assuming that the initial state, $x(0)$, is known, the system state at the sampling time ℓ is given by

$$x(\ell) = A^\ell x(0) + W_\ell \mathbf{u}. \quad (13)$$

As stated in Theorem 1 above, if W_ℓ has rank n , then it is possible to obtain \mathbf{u} by solving a system of n linearly independent equations. This sequence leads the initial system state, $x(0)$, to the desired final state value, x^\star .

It is important to emphasize that, based on Theorem 1, for the one-step case, where $\ell = 1$, we have that

$$W_1 = B.$$

Thus, if one wants to lead the system state from $x(0)$ to an arbitrary value x^\star in only one sampling instant, then the number of control inputs must be equal or larger than the number of system states, i.e., $m \geq n$. Notice that if there are more control inputs than system states, i.e., $m > n$, then the solution to $Ax(0) + W_1 \mathbf{u} = 0$, see (13), is not unique.

Following, based on the above discussion, two particular cases are analyzed.

Invertible Matrix B

In this case, we focus on power converters which present the same number of system states as control inputs, i.e., $n = m$. This occurs for several converter topologies, e.g., a three-phase inverter in $\alpha\beta$ coordinates with an RL-load, which has 2-inputs and 2-outputs [112].

Here, B is a square matrix which, if nonsingular, is invertible. Moreover, the one-step reachability matrix, $W_1 = B$, has rank n . Therefore, it is possible to lead the system (11) to x^\star in one sampling instant. The one-step deadbeat control law for this case is expressed by:

$$\begin{aligned} \hat{u}(k) &= -B^{-1}A\hat{x}(k), \\ u(k) &= -B^{-1}A(x(k) - x^\star) + u^\star. \end{aligned} \quad (14)$$

Non-Invertible Matrix B

Here, we consider the case where the system (11) has less control inputs than system states, e.g., a three-phase inverter with an LC-filter [21]. Thus, matrix $B \in \mathbb{R}^{n \times m}$, with $n > m$, is not invertible. Moreover, the one-step reachability matrix $W_1 = B$ has rank smaller than n . However, if matrix B has rank m , then $B^T B \in \mathbb{R}^{m \times m}$ is invertible. Therefore, one can obtain the, so called, Moore–Penrose pseudoinverse matrix, which is given by

$$B^\dagger = (B^T B)^{-1} B^T;$$

see, e.g., [5]. Thus, the minimum time deadbeat control law can be expressed via:

$$\begin{aligned}\hat{u}(k) &= -B^\dagger A \hat{x}(k) = -(B^T B)^{-1} B^T A \hat{x}(k), \\ u(k) &= -(B^T B)^{-1} B^T A (x(k) - x^\star) + u^\star.\end{aligned}\tag{15}$$

The minimum number of sampling steps required to achieve a desired reference can be determined by adding terms of the form $A^\ell B$, until the reachability matrix W_ℓ in (12) has full rank n .²

Notice that if the system inputs are constrained to a bounded set, e.g., $u(k) \in [-1, 1]^m$, then it is necessary to saturate the control input when the system is far from the reference yielding:

$$\begin{aligned}\hat{u}(k) &= \text{sat} \left[-B^\dagger A \hat{x}(k) \right], & \hat{u} &\in [u_{\min} - u^\star, u_{\max} - u^\star] \\ u(k) &= \text{sat} \left[-B^\dagger A (x(k) - x^\star) + u^\star \right], & u &\in [u_{\min}, u_{\max}]\end{aligned}$$

Thus, the desired system reference may not be reached in one sampling instant whenever the control input is saturated.

While this method has been used when a fast dynamic response is required, being deadbeat-based, it is often fragile. Indeed, uncertainties such as model errors, unmodeled delays, and external disturbances may often deteriorate the closed-loop performance. In the literature, there exist some works addressing these issues. For example, in [85] an adaptive self tuning deadbeat controller has been proposed to deal with system parameter uncertainties and compensate the calculation delay. On the other hand, in [82] a disturbance observer has been included to improve the disturbance rejection of the closed-loop system.

3.2 Horizon-One MPC with a Finite Control Set

One of the most popular predictive control strategies for power converters and drives is FCS-MPC [20, 111]. This predictive control strategy explicitly considers the power switches, $S(k)$ in the optimization by means of a finite control set constraint. Modulation stages are not needed.

In general, large prediction horizons are preferable when using MPC. However, finding the optimal input sequence for the finite control set case typically requires one to solve a combinatorial optimization problem. Interestingly, for some topologies, one-step horizon MPC provides good closed-loop performance [65, 110]. In this subsection, we discuss the optimal solution to this predictive control strategy.

² It is important to remark that in the case that $B \in \mathbb{R}^{n \times n}$, with B nonsingular, we have that $B^\dagger = B^{-1}$. Thus, the control law (14) is a particular case of (15).

3.2.1 Cost Function

When using MPC for power electronics, it is often desirable to minimize the tracking error of the system state, which includes variables of different physical nature and order of magnitude, e.g., currents, voltages, torques, power. It is therefore convenient to adopt a cost function, which considers a weighted positive sum of the tracking errors of the controlled variables, see, e.g., [111]. This particular class of cost function can, in general, be expressed via:

$$V = \lambda_1(x_1(k+1) - x_1^{\star})^2 + \lambda_2(x_2(k+1) - x_2^{\star})^2 + \cdots + \lambda_n(x_n(k+1) - x_n^{\star})^2, \quad (16)$$

where λ_i are the weighting factors, which allow the designer to trade-off among the different system state tracking errors. For example, for a two-level three-phase inverter, in $\alpha\beta$ orthogonal coordinates, one can use (see [112])

$$V_{2LI} = \lambda_1(i_\alpha(k+1) - i_\alpha^{\star})^2 + \lambda_2(i_\beta(k+1) - i_\beta^{\star})^2,$$

where $\lambda_1 = \lambda_2 = 1$. For a one-phase three-cell Flying Capacitor Converter (FCC) one can choose (see, e.g., [73])

$$V_{FCC} = \lambda_1(i_a(k+1) - i_a^{\star})^2 + \lambda_2(v_{c1}(k+1) - v_{c1}^{\star})^2 + \lambda_3(v_{c2}(k+1) - v_{c2}^{\star})^2.$$

The above cost functions can be expressed as

$$V(x(k), u(k)) = \hat{x}^T(k+1)P\hat{x}(k+1) \quad (17)$$

where $\hat{x}(k) = x(k) - x^{\star}$ represents the state tracking errors of system (11), and $P = \text{diag}\{\lambda_1, \dots, \lambda_n\}$ is the weighting matrix.

In this case, it is also assumed that the power converter to be controlled is modeled as per (9), i.e.,

$$x(k+1) = Ax(k) + Bu(k), \quad (18)$$

where u represents the m -control inputs, which belong to a finite set of p elements, i.e.,

$$u \in \mathbb{U} \triangleq \{u_1, \dots, u_p\} \subset \mathbb{R}^m. \quad (19)$$

3.2.2 Unconstrained Optimum

To derive a closed form solution for FCS-MPC with horizon $N = 1$, we note that given (9), the quadratic cost function (17) can be expanded via

$$V(x(k), u(k)) = \hat{x}^T(k)A^T P A \hat{x}(k) + \hat{u}^T(k)B^T P B \hat{u}(k) + 2\hat{u}^T(k)B^T P A \hat{x}(k), \quad (20)$$

where $\hat{u}(k) = u(k) - u^{\star}$, as before. If there were no control constraints, i.e., $\hat{u}(k) \in \mathbb{R}^m$, then the unconstrained optimal solution can be obtained as follows:

$$\frac{\partial V(\hat{x}(k), \hat{u}(k))}{\partial \hat{u}(k)} = 2B^T PB\hat{u}(k) + 2B^T PA\hat{x}(k) = 0$$

Thus, the minimizer to (17), without taking into account any system constraints, is given by

$$\begin{aligned} \hat{u}_{uc}^{\text{opt}}(k) &= -K\hat{x}(k), \\ u_{uc}^{\text{opt}}(k) &= -K(x(k) - x^{\star}) + u^{\star}, \end{aligned} \quad (21)$$

where

$$K = (B^T PB)^{-1} B^T PA. \quad (22)$$

It is worth noting that this unconstrained solution will normally not belong to the finite set (19).

To obtain the constrained optimal solution, $u^{\text{opt}}(k) \in \mathbb{U}$, it is convenient to introduce the following auxiliary variable:

$$z(k) \triangleq u(k) - u_{uc}^{\text{opt}}(k) = \hat{u}(k) - \hat{u}_{uc}^{\text{opt}}(k). \quad (23)$$

In terms of $z(k)$, the cost function in (20) can be expressed via:

$$V(x(k), u(k)) = g(x(k)) + z^T(k)Hz(k), \quad (24)$$

where the term $g(x(k))$ is independent of $u(k)$ and

$$H \triangleq B^T PB. \quad (25)$$

3.2.3 Closed-Form Solution

To obtain the optimal finite set constrained solution, one must find the control input which minimizes $V(x(k), u(k))$. From (24), it follows that level sets of the cost function are ellipsoids, where the eigenvectors of H define the principal directions of the ellipsoid. Thus, the constrained optimizer $u^{\text{opt}}(k)$ does not necessarily correspond to the nearest neighbour of $u_{uc}^{\text{opt}}(k)$ within the constraint set \mathbb{U} .

Example 1 Consider the case where a power converter, modeled as per (18), has 2 power switches, which can take only two values, i.e., $u_1, u_2 \in \{0, 1\}$. Thus, the control input belongs to the following finite set:

$$u \in \mathbb{U} \triangleq \left\{ \begin{bmatrix} 0 \\ 0 \end{bmatrix}, \begin{bmatrix} 0 \\ 1 \end{bmatrix}, \begin{bmatrix} 1 \\ 0 \end{bmatrix}, \begin{bmatrix} 1 \\ 1 \end{bmatrix} \right\} \subset \mathbb{R}^2. \quad (26)$$

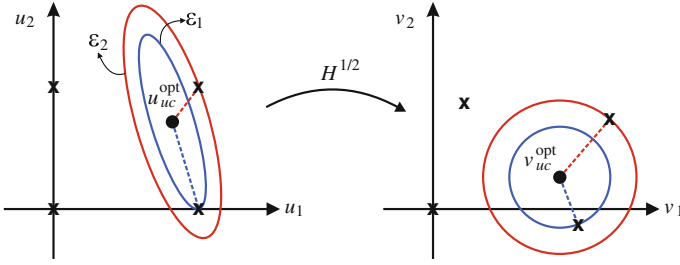


Fig. 4 Geometrical representation of FCS-MPC optimal solution; $u_1, u_2 \in \{0, 1\}$

The vectorial representation of the optimal solution is depicted in Fig. 4. Here, the ellipses, ε_i centered in u_{uc}^{opt} , represent all the points that lead to the same cost. Formally, if $a, b \in \varepsilon_i$ then, $V(x(k), a) = V(x(k), b)$.

As we move away from the centre, the ellipses become larger, increasing the cost function value, i.e., if $a \in \varepsilon_1$ and $b \in \varepsilon_2$ then, $V(x(k), a) < V(x(k), b)$. Thus, in this example, the optimal solution, which produces the minimum cost function value is $u^{opt} = [1 \ 0]^T$, despite the nearest vector to the unconstrained solution being $u = [1 \ 1]^T$. Clearly, the optimal solution is, in general, not the nearest neighbour to the unconstrained solution. ■

To obtain the optimal solution, we use the following transformation [103]:

$$v = H^{1/2}u, \quad v \in \mathbb{V} \triangleq H^{1/2}\mathbb{U}.$$

Now, the cost function (24) can be expressed as:

$$V(x(k), v(k)) \triangleq g(x(k)) + (v(k) - v_{uc}^{opt}(k))^T (v(k) - v_{uc}^{opt}(k)), \quad (27)$$

where

$$v_{uc}^{opt}(k) \triangleq H^{1/2}u_{uc}^{opt}(k).$$

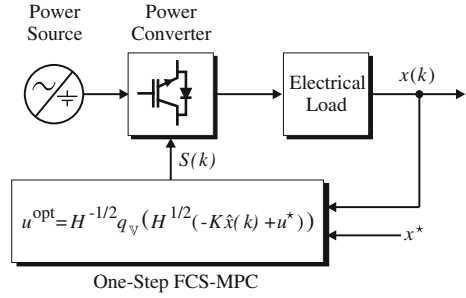
Thus, using this transformation, the level sets of the cost function describe spheres centered in v_{uc}^{opt} , as depicted in Fig. 4. Therefore, in terms of these transformed variables, the nearest vector to the unconstrained solution, $v_{uc}^{opt}(k)$, is indeed the (constrained) optimal solution.

Definition 2 (*Vector Quantizer* (see e.g. [31])) Consider a set $\mathcal{A} \subseteq \mathbb{R}^n$ and a finite set $\mathcal{B} \triangleq \{b_1, \dots, b_p\} \subset \mathbb{R}^n$. A function $q_{\mathcal{B}}(\cdot) : \mathcal{A} \rightarrow \mathcal{B}$ is an Euclidean vector quantizer if $q_{\mathcal{B}}(a) = b_i \in \mathcal{B}$ if and only if b_i satisfies that $|a - b_i| \leq |a - b_j|$, for all $b_j \neq b_i$, where $b_j \in \mathcal{B}$. ■

Using the vector quantizer presented in Definition 4, it follows that

$$v^{opt}(k) = q_{\mathbb{V}}\left(H^{1/2}u_{uc}^{opt}(k)\right), \quad v^{opt}(k) \in \mathbb{V}.$$

Fig. 5 One-step FCS-MPC closed-loop



Finally, the actual optimal solution, which minimizes the cost function (17), is given by:

$$u^{\text{opt}}(k) = H^{-1/2} v^{\text{opt}}(k) = H^{-1/2} q_{\mathbb{V}}\left(H^{1/2} u_{uc}^{\text{opt}}(k)\right), \quad u^{\text{opt}}(k) \in \mathbb{U}. \quad (28)$$

A block diagram of the resulting one-step FCS-MPC closed-loop is depicted in Fig. 5. Notice that $q_{\mathbb{V}}(\cdot)$ in (28) implies that the quantization considers the vectors from the finite set $\mathbb{V} = H^{1/2}\mathbb{U}$, i.e., $q_{\mathbb{V}}(a) \in \mathbb{V}$.

3.2.4 Relationship to Deadbeat Control and Embellishments

It is interesting and instructive, to compare horizon-one predictive control with deadbeat control. Here, we first notice that (21) is a weighted version of (15). In fact, when $P = I$, where I denotes the identity matrix, both control values are the same. Thus, horizon-one FCS-MPC, with the simple cost function presented in (16) and (17), is a class of quantized deadbeat controller. Intuitively, such a predictive control methodology presents features akin to those of a deadbeat controller, i.e., a fast dynamic response but poor robustness.

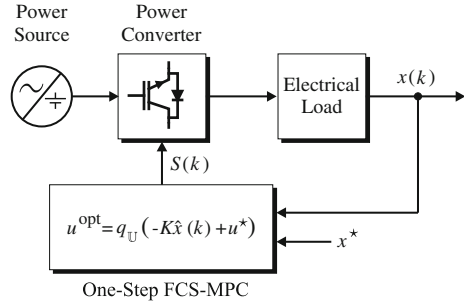
To mitigate this problem, it is convenient to include control weighting in the cost function. This will lead to a less aggressive, more cautious, controller. In this case, the cost function can be formulated as³

$$V(x(k), u(k)) = \hat{u}^T(k) R \hat{u}(k) + \hat{x}^T(k+1) P \hat{x}(k+1), \quad (29)$$

see (10) and where R is a positive definite matrix, which can be used as a tuning parameter. With a larger matrix R we are seeking to apply an input close to u^{\star} . This allows one to reduce the control action that is applied to the system, leading to a slower dynamic response with often better robustness properties.

³ Alternatively, one can also penalize the size of the increments of the control input via a term of the form $(u(k) - u(k-1))^T R (u(k) - u(k-1))$.

Fig. 6 One-step FCS-MPC closed-loop with a diagonal matrix H



To obtain the optimal solution of this embellished horizon-one FCS-MPC formulation, one can roughly follow the analysis presented in Sect. 3.2.3. The optimal solution has the same structure as presented in (28) (see also (21)), but where

$$H = B^T P B + R, \quad (30)$$

and

$$K = H^{-1} B^T P A, \quad (31)$$

see also [103]. Notice that, the control gain matrix K is reduced as R is increased. Thus, for the same system tracking error, $\hat{x}(k)$, this new formulation produces a less aggressive actuation.

Example 2 If H is diagonal, i.e., $H = \alpha I$, with $\alpha \in \mathbb{R}$, then the cost in (24) becomes

$$\begin{aligned} V(x(k), u(k)) &= g(x(k)) + z^T(k) H z(k), \\ &= g(x(k)) + \alpha^2 (u(k) - u_{uc}^{opt}(k))^T (u(k) - u_{uc}^{opt}(k)). \end{aligned} \quad (32)$$

The level sets of this cost function are spheres centered in $u_{uc}^{opt}(k)$. Therefore, one can directly quantize the unconstrained solution $u_{uc}^{opt}(k)$, to obtain the finite optimal solution without performing any transformation, i.e.,

$$u^{opt}(k) = q_{\mathbb{U}}(u_{uc}^{opt}(k)) = q_{\mathbb{U}}(-K\hat{x}(k) + u^{\star}) \in \mathbb{U}.$$

Figure 6 illustrates a block diagram for this particular horizon-one FCS-MPC closed-loop when $H = \alpha I$.

4 Predictive Control with Long Horizons

In the context of MPC, long prediction horizons yield in general a better closed-loop performance than short horizons. In particular, extending the length of the prediction horizons typically reduces the cost associated with the objective

function in closed-loop operation [52, 102]. The infinite horizon case often ensures closed-loop stability, provided that a solution with a finite cost exists [76, 107].

In the field of power electronics and electrical drives, the benefits of long prediction horizons can be highlighted using the following three examples. First, for the direct MPC formulation outlined in Sect. 4.5.2, very long prediction horizons of 100 and more time-steps yield a superior steady-state performance, in the sense that current THDs similar to the ones obtained by employing optimized pulse patterns (OPPs) can be achieved, when assuming the same device switching losses. In contrast to that, very short horizons tend to lead to steady-state performance results that are inferior to carrier-based PWM [34, 114].

Second, for systems with an inverse behavior,⁴ long prediction horizons are required during transient operation to ensure the tracking of the reference signals and to avoid closed-loop instability. This was illustrated in [60] for a boost converter with a single voltage control loop (without an underlying current control loop) that directly manipulates the switch position.

Third, and as already mentioned in Sect. 3, very short horizons lead to a closed-loop behavior similar to the one typically obtained by deadbeat control, particularly when the penalty on the manipulated variable is small or set to zero. Deadbeat control is known to be highly sensitive to measurement and estimation noise, as well as parameter uncertainties of the system model. Long prediction horizons, on the other hand, significantly reduce the sensitivity of the controller to noise and—as a result—improve the performance during steady-state operation [38].

Unfortunately, the computational burden associated with solving most of the the optimization problems underlying MPC increases exponentially with the length of the prediction horizon. At the same time, the sampling intervals typically required in power electronic systems are very short, often amounting to a few tens of μs . From a computational point of view, this makes the solution of MPC problems with long prediction horizons very challenging. Indeed, the belief in the power electronics community is widespread that MPC problems with long horizons cannot be solved in real time. Nevertheless, control and optimization techniques are available that reduce the computational burden to a level, which allows the solution of MPC problems on today's available computational platforms within sampling intervals of less than 100 μs . In this section, several such techniques will be presented along with corresponding power electronics examples, for which they have been applied to. Selected experimental results are highlighted as well.

⁴ When considering linear time-invariant (LTI) systems, *inverse behavior* is equivalent to non-minimum phase behavior, i.e. systems with zeros in the right half-plane of the Laplace domain.

4.1 Linear Quadratic MPC for Converters with a Modulator

A particularly simple case of (5)–(6) arises when the cost function is quadratic and the system model is linear, i.e.:

$$\begin{aligned}
 V(x(k), \mathbf{u}(k)) &= x'^T(k+N)Px'(k+N) \\
 &\quad + \sum_{\ell=k}^{k+N-1} \{x'^T(\ell)Qx'(\ell) + u'^T(\ell)Ru'(\ell)\}, \\
 x'(\ell+1) &= Ax'(\ell) + Bu'(\ell), \\
 x'(\ell) &\in \mathbb{X} \subseteq \mathbb{R}^n, u'(\ell) \in \mathbb{U} \subseteq \mathbb{R}^m, \quad \ell \in \{0, 1, \dots, N\},
 \end{aligned} \tag{33}$$

where A and B denote the state-update matrices of a linear time-invariant system, and P , Q and R are penalty matrices of appropriate dimensions. More specifically, P and Q are positive semi-definite matrices and R is a positive definite matrix. The constraint sets \mathbb{X} and \mathbb{U} are polyhedra, given by the intersection of a finite number of half-spaces, which are defined by hyperplanes. In such a setup, a PWM is typically used.

By successively using the state-update equation in (33) and assuming a finite N , the state vector at time-step $\ell+1$ can be represented as a function of the state vector at time-step k and the control sequence as follows:

$$\begin{bmatrix} x'(k) \\ x'(k+1) \\ \vdots \\ x'(k+N) \end{bmatrix} = \begin{bmatrix} I \\ A \\ \vdots \\ A^N \end{bmatrix} x(k) + \begin{bmatrix} 0 & \dots & \dots & 0 \\ B & 0 & \dots & 0 \\ AB & B & \dots & 0 \\ \vdots & \vdots & \ddots & \vdots \\ A^{N-1}B & A^{N-2}B & \dots & B \end{bmatrix} \begin{bmatrix} u'(k) \\ u'(k+1) \\ \vdots \\ u'(k+N-1) \end{bmatrix}. \tag{34}$$

We rewrite this expression in compact form as

$$\mathbf{x}(k) = \mathbf{S}x(k) + \mathbf{T}\mathbf{u}(k), \tag{35}$$

with \mathbf{S} and \mathbf{T} appropriately defined. Introducing $\mathbf{Q} \triangleq \text{diag}(Q, \dots, Q, P)$ and $\mathbf{R} \triangleq \text{diag}(R, \dots, R)$, the cost function in (33) can be rewritten as

$$V(x(k), \mathbf{u}(k)) = \mathbf{x}^T(k)\mathbf{Q}\mathbf{x}(k) + \mathbf{u}^T(k)\mathbf{R}\mathbf{u}(k). \tag{36}$$

Substituting (35) into (36) leads to⁵

$$V(x(k), \mathbf{u}(k)) = \mathbf{u}^T(k)\mathbf{H}\mathbf{u}(k) + 2x^T(k)\mathbf{F}\mathbf{u}(k), \tag{37}$$

⁵ Note that (37) contains the third term $x^T(k)\mathbf{S}^T\mathbf{S}x(k)$. Since this term is constant and independent of $\mathbf{u}(k)$, it can be omitted in the cost function without affecting the result of the optimization problem.

with

$$\begin{aligned} H &= \mathbf{T}^T \mathbf{Q} \mathbf{T} + \mathbf{R} \\ F &= \mathbf{S}^T \mathbf{Q} \mathbf{T}. \end{aligned}$$

Note that $\mathbf{u}(k)$ is the real-valued optimization variable and $H = H^T$ is the positive definite Hessian matrix.

4.1.1 Unconstrained Solution

Similar to the horizon-one case treated in Sect. 3.2.2, if the system inputs and states in (33) are unconstrained, i.e. $\mathbb{X} = \mathbb{R}^n$ and $\mathbb{U} = \mathbb{R}^m$, then the finite horizon optimization problem (33) with the reformulated cost function (37) can be solved algebraically. This yields the control sequence as a linear function of the state vector according to $\mathbf{u}(k) = -\mathbf{K}x(k)$ with $\mathbf{K} = -H^{-1}F^T$. The control input at time-step k is obtained by taking the first element of this sequence, i.e. the linear state-feedback controller is of the form

$$u(k) = -K_0 x(k) \quad (38)$$

with $\mathbf{K} = [K_0^T, K_1^T, \dots, K_{N-1}^T]^T$. Directly related to this is the concept of generalized predictive control (GPC) [18]. The unconstrained finite-horizon approach was investigated in [63, 75] for use in electrical drive applications.

Optimality, however, does not ensure stability, motivating the use of an infinite horizon N . The problem (33) is then referred to as the *linear quadratic regulator* (LQR), and $K = K_0 = \dots = K_{N-1}$ is the solution of an algebraic Riccati equation. LQR controllers have been proposed for a number of power electronics applications; early examples of such applications include dc-dc converters [30] and electrical drives [87].

4.1.2 Constrained Solution

On the other hand, if the inputs and states are constrained to belong to polyhedra, then (33) can be rewritten⁶ in the form

$$\begin{aligned} \min_{\mathbf{u}(k)} V(x(k), \mathbf{u}(k)) &= \mathbf{u}^T(k) H \mathbf{u}(k) + 2x^T(k) F \mathbf{u}(k) \\ \text{subj. to } G \mathbf{u}(k) &\leq w + E x(k). \end{aligned} \quad (39)$$

⁶ For the cost function the constant term in (37) has been neglected. The inequality constraints can be derived by substituting (35) into the state constraints and adding the input constraints.

with G and E being matrices of appropriate dimensions and w denoting a column vector. For a given state vector $x(k)$, (39) can be simplified to

$$\begin{aligned} \min_{\mathbf{u}(k)} V(\mathbf{u}(k)) &= \mathbf{u}^T(k)H\mathbf{u}(k) + 2c^T\mathbf{u}(k) \\ \text{subj. to } G\mathbf{u}(k) &\leq g, \end{aligned} \quad (40)$$

with $c = F^T x(k)$ and $g = w + Ex(k)$.

If $\mathbf{u}(k)$ satisfies the constraints $G\mathbf{u}(k) \leq g$ in (40), then $\mathbf{u}(k)$ is said to be a *feasible* solution. The problem (40) is feasible, if there exists at least one such feasible solution, else the problem is *infeasible*. Assuming feasibility, the optimization variable, for which the minimal (i.e. the optimal) value of the cost function is obtained, is the *optimizer* $\mathbf{u}^{\text{opt}}(k)$.

The form (40) is a convex mathematical optimization problem with a quadratic objective function and linear constraints, a so called *quadratic program* (QP) [50]. Such problems can be solved efficiently. Specifically, with H being positive definite, (40) can be solved in polynomial time [66].

QPs are typically solved using the interior point method [61, 89]. Other solution approaches include the active set [28] and gradient methods [88]. Examples of QP solvers include SeDuMi [118], CPLEX [57] and IpOpt [123]. Recently, first efforts have been reported in the literature to solve QPs in embedded systems, particularly when running on field-programmable gate arrays (FPGAs), see e.g. [24, 59, 108, 109]. Moreover, a simplified QP is solved algebraically in [75] to derive a position controller for a brushless dc drive.

Another example is model predictive pulse pattern control (MP³C), which manipulates online the switching instants of pre-computed optimized pulse patterns (OPPs) [14, 96] to achieve very fast closed-loop control. The underlying QP can be solved easily using a variation of the active set method [38]. First experimental results on a 1.1 MVA five-level inverter with a 6 kV medium-voltage induction machine can be found in [91].

4.2 The Explicit State-Feedback Control Law for Linear Quadratic MPC with a Modulator

Despite the ever growing computational power available and recent advances in implementing QP solvers on embedded system architectures, solving the QP in real-time for power electronics applications poses a highly challenging problem. When using sampling intervals in the μs range, the computation times needed to solve the QP typically exceed the sampling interval—often by one or two orders of magnitude. Rather than solving the mathematical optimization problem in real-time for the given state vector at the current time-step, the optimization problem can be solved offline for *all possible* states. Specifically, the so-called (explicit) *state-feedback control law* can be computed for all states $x(k) \in \mathbb{X}$ [9]. The

explicit control law can be stored in a look-up table and the optimal control input can be read from the look-up table in a computationally efficient manner. We refer to this methodology as *explicit MPC*, in contrast to MPC, which has traditionally been solved entirely online.

4.2.1 The State-Feedback Control Law

Using the coordinate transformation

$$\mathbf{z}(k) = \mathbf{u}(k) + H^{-1}F^T x(k), \quad (41)$$

(39) can be rewritten as

$$\min_{\mathbf{z}(k)} V(\mathbf{z}(k)) = \mathbf{z}^T(k)H\mathbf{z}(k) \quad (42a)$$

$$\text{subj. to } G\mathbf{z}(k) \leq w + Sx(k) \quad (42b)$$

with $S = E + GH^{-1}F^T$. Note that the optimization variable $\mathbf{z}(k)$ includes, in a linear manner, the control sequence $\mathbf{u}(k)$ and the state vector $x(k)$. Moreover, the constraints in (42b) depend linearly on the state vector $x(k)$.

As previously, for a given $x(k)$, the optimizer $\mathbf{z}^{\text{opt}}(k)$ can be computed. Using the notion of *sensitivity analysis*, we are interested in exploring the sensitivity of $\mathbf{z}^{\text{opt}}(k)$ to small perturbation in $x(k)$. In general, unless the set of active constraints changes in (42b), a small perturbation in $x(k)$ will lead to a small variation in $\mathbf{z}^{\text{opt}}(k)$. Because of the linear dependency in (41), in a small neighborhood around $x(k)$, the variation in $\mathbf{z}^{\text{opt}}(k)$ depends linearly on the modification in $x(k)$. As a result, in this neighborhood, $\mathbf{z}^{\text{opt}}(k)$ is a linear function of $x(k)$ plus an offset, a so called *affine* function. Rewriting (41) to express $\mathbf{u}^{\text{opt}}(k)$ as a function of the optimizer and the state vector, we conclude that the control sequence is also affine in the state vector.

We refer to the neighborhood around $x(k)$, in which $\mathbf{z}^{\text{opt}}(k)$ is an affine function of $x(k)$, as a *critical region*. Using the Karush-Kuhn-Tucker (KKT) conditions for optimality [62, 68], the critical region and its shape can be computed. Due to the linearity of (42b), the boundaries of the critical region are hyperplanes. More specifically, it can be shown that the critical region is a polyhedron, with its facets being defined by the active constraints. An algorithm can be constructed, which iteratively explores the whole set of states, \mathbb{X} , computes all critical regions and the associated affine control laws. By doing so, we treat the state vector as a parameter, which gives rise to *multi-parametric programming* and yields the state-feedback control law. In particular, (42) is a *multi-parametric quadratic program* (mp-QP).

Hereafter, the main results of mp-QP are recapitulated. For this, a number of definitions are required.

Definition 3 (*Polyhedron*) A polyhedron \mathcal{P} is a set that is equal to the intersection of a finite number of half-spaces defined by hyperplanes. ■

Definition 4 (*Polyhedral Partition*) A collection of polyhedra

$$\mathcal{P}_i \subseteq \mathbb{X}, \quad i \in \{1, 2, \dots, n\},$$

is a *polyhedral partition* of the polyhedron \mathbb{X} , if and only if $\bigcup_{i=1}^n \mathcal{P}_i = \mathbb{X}$ and $\mathcal{P}_i \cap \mathcal{P}_j$ is lower dimensional $\forall i \neq j$. ■

Theorem 2 *The solution to the mp-QP in (42a, b) is a state-feedback control law $u^{\text{opt}}(k)$ that is a continuous and piecewise affine function of the state vector $x(k)$ defined on a polyhedral partition of the feasible state-space \mathbb{X} . ■*

More specifically, the feasible state-space is partitioned into polyhedra, and for each polyhedron the optimal control law $u^{\text{opt}}(k)$ is given as an affine function of the state. Note that $u^{\text{opt}}(k)$ is the first element in $\mathbf{u}^{\text{opt}}(k)$, as defined in (7).

Theorem 3 *The value function $V^{\text{opt}}(x(k)) = V(x(k), \mathbf{u}^{\text{opt}}(k))$ of the mp-QP (42a, 42b) is continuous, convex and piecewise quadratic in the state. ■*

More details about multi-parametric programming for QPs and the proofs of the above theorems can be found in [9, 120]. Related results were obtained in [115]. When the cost function in (42a) is linear, a *multi-parametric linear program* (mp-LP) results. The state-feedback control law is, as in the mp-QP case, continuous and piecewise affine in the state. The value function, on the other hand, is convex and piecewise affine. For more details on mp-LPs, the reader is referred to [7, 13]. Multi-parametric programs can be solved efficiently using the multi-parametric toolbox (MPT) [70]. This versatile and numerically robust toolbox is available for free on <http://control.ee.ethz.ch/~mpt/>.

4.2.2 Implementation Aspects

The state-feedback control law, which is the result of mp-LP or mp-QP, is of the form

$$u^{\text{opt}}(k) = \begin{cases} K_1 x(k) + f_1 & \text{if } G_1 x(k) \leq g_1 \\ \vdots & \vdots \\ K_n x(k) + f_n & \text{if } G_n x(k) \leq g_n \end{cases} \quad (43)$$

with $K_i x(k) + f_i$ denoting the i th affine control law and $G_i x(k) \leq g_i$ the corresponding polyhedron. Such a state-feedback controller can be easily implemented and evaluated online. In a first step, given the state vector $x(k)$, the polyhedron needs to be determined, in which the estimated or measured state lies. The brute force approach is to go through all polyhedra and to check the corresponding inequalities. An alternative approach is to build a binary search tree as proposed in [121]. Such a search tree reduces the online computational demand at the expense of an increased memory requirement. In a second step, after the correct polyhedron has been identified, the affine control law is read out and the optimal control input $u^{\text{opt}}(k)$ is computed using [42].

In general, polyhedra with the same control law form convex unions and can thus be merged and replaced by their unions. This leads to an equivalent piecewise affine control law that features a lower number of polyhedra and thus a reduced complexity. From an implementation point of view, such a representation is highly desirable, since it relaxes the memory requirements and reduces the computational burden. Indeed, by adopting the notion of hyperplane arrangements, an equivalent piecewise affine control law can be derived that is *minimal* in the number of polyhedra [47]. We refer to this concept as *optimal complexity reduction*. For control laws with hundreds of polyhedra, the number of polyhedra can often be reduced by an order of magnitude.

4.2.3 An Illustrative Example of the State-Feedback Control Law

To further illustrate the derivation and properties of the explicit state-feedback control law of MPC, consider a dc-dc buck converter, as shown in Fig. 7. Using the classic technique of averaging between the on and off modes of the circuit, the discrete-time system model

$$x(k+1) = Ax(k) + Bv_s d(k) \quad (44)$$

can be obtained, where v_s denotes the unregulated input voltage and $d(k)$ the duty cycle. The state vector contains the inductor current i_ℓ and the output voltage v_o , i.e. $x = [i_\ell \ v_o]^T$. The continuous-time system matrices are

$$F = \begin{bmatrix} -\frac{R_\ell}{L} & -\frac{1}{L} \\ \frac{R_o}{R_o+R_c} \frac{L-R_c R_\ell C}{LC} & -\frac{1}{R_o+R_c} \frac{L+R_c R_o C}{LC} \end{bmatrix}, \quad G = \begin{bmatrix} \frac{1}{L} \\ \frac{R_o}{R_o+R_c} \frac{R_c}{L} \end{bmatrix} \quad (45)$$

and their discrete-time representations are given by

$$A = e^{Fh}, \quad B = \int_0^h e^{F\tau} G d\tau, \quad (46)$$

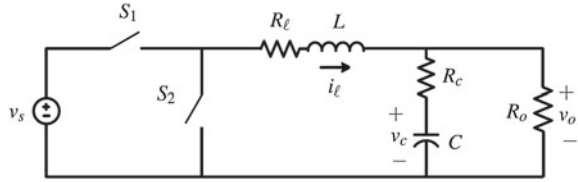
where h denotes the sampling interval. Adopting the per unit (pu) system, the parameters in (45) are the inductor $L = 3$ pu, capacitor $C = 20$ pu and output resistor $R_o = 1$ pu. The internal resistor of the inductor is $R_\ell = 0.05$ pu and the equivalent series resistance of the capacitor is $R_c = 0.005$ pu. The nominal input voltage is assumed to be $v_s = 1.8$ pu.

To allow for variations in the input voltage, it is convenient to scale the system equations by v_s , as proposed in [41]. To this end, we define $\tilde{i}_\ell = i_\ell/v_s$, $\tilde{v}_o = v_o/v_s$ and $\tilde{x} = [\tilde{i}_\ell \ \tilde{v}_o]^T$, and rewrite (44) as

$$\tilde{x}(k+1) = A\tilde{x}(k) + Bd(k) \quad (47)$$

Note that, unlike (44), (47) is linear in the state vector and the duty cycle.

Fig. 7 Topology of the step-down synchronous converter



The control objective is to regulate the output voltage to its reference v_o^* and to maintain the inductor current below its maximal allowed limit $i_{\ell,max}$ by manipulating the duty cycle. The latter is bounded between zero and one. This control problem can be captured by the optimization problem (cf., (29))

$$\begin{aligned}
 V(\tilde{x}(k), \mathbf{u}(k)) &= \sum_{\ell=k}^{k+N-1} \left\{ (\tilde{x}'(\ell) - \tilde{x}^*)^T Q (\tilde{x}'(\ell) - \tilde{x}^*) + R(u'(\ell))^2 \right\}, \\
 \tilde{x}'(\ell + 1) &= A\tilde{x}'(\ell) + B u'(\ell), \\
 \tilde{x}'(\ell) &\in \mathbb{X}, u'(\ell) \in \mathbb{U}, \quad \ell \in \{0, 1, \dots, N\},
 \end{aligned} \tag{48}$$

where we set $Q = \text{diag}(0, 1)$, $R = 0.1$, $\mathbb{X} = [-\tilde{i}_{\ell,max}, \tilde{i}_{\ell,max}] \times [-10, 10]$ and $\mathbb{U} = [0, 1]$. Note that $\tilde{i}_{\ell,max} = i_{\ell,max}/v_s$ and $u = d$. To facilitate the regulation of the output voltage to a non-zero reference, we define $\tilde{x}^* = [0, \tilde{v}_o^*]^T$ with $\tilde{v}_o^* = v_o^*/v_s$. We assume $\tilde{v}_o^* = 0.5$ and choose the horizon $N = 3$.

The explicit control law can be computed using the MPT toolbox [70]. The two-dimensional state-space is partitioned into 20 polyhedra. Using optimal complexity reduction [47], an equivalent control law with 11 polyhedra can be derived, as shown in Fig. 8a. The corresponding state-feedback controller $u^{opt}(k)$ is shown in Fig. 8b. Note that the duty cycle is limited by zero and one as a result of the design procedure. An additional patch, such as an anti-windup scheme, is not required.

A similar MPC scheme was proposed in [79]. This basic controller can be enhanced in various ways. In the context of dc-dc converters, it is usually preferred to penalize the *change* in the duty cycle rather than the duty cycle as such, by introducing $\Delta u(k) = u(k) - u(k-1)$ and penalizing $R(\Delta u(\ell))^2$ rather than $R(u(\ell))^2$ in (48). To enhance the voltage regulation at steady-state by removing any dc offset, an integrator state can be added [79]. Load variations can be addressed by a Kalman filter, see [42].

4.2.4 Application Examples of the State-Feedback Control Law

In the context of power electronics and drives applications, the notion of the state-feedback control law of MPC formulations has been studied extensively. One of the earliest references is [74], which proposes an explicit MPC controller in a field-oriented controller setting for an electrical drive. These initial results are extended in [80]. In [10], the speed and current control problem of a permanent-magnet

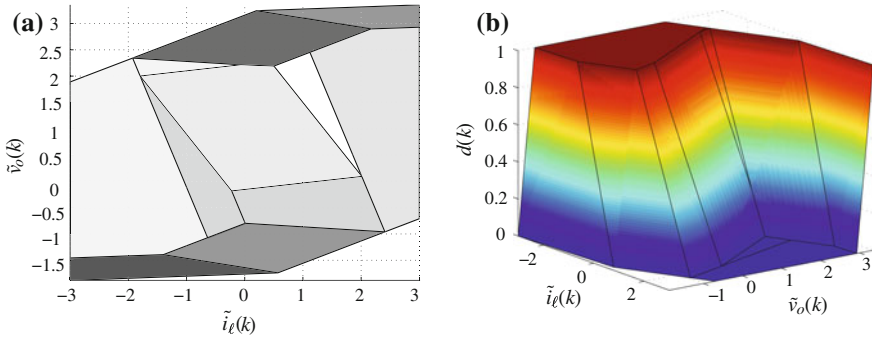


Fig. 8 Explicit state-feedback control law for the dc-dc buck converter over the state-space \mathbb{X} spanned by the scaled inductor current $\tilde{i}_l(k)$ and the scaled output voltage $\tilde{v}_o(k)$. **a** Polyhedral partition of the state-space \mathbb{X} . **b** Control law $u^{\text{opt}}(k)$

synchronous machine is solved using MPC. Drives with flexible shafts are considered in [22] and active rectifier units with LC filters in [81].

4.3 Linear Quadratic MPC with a Finite Control Set

As for the continuous control set case studied above, when the control set is constrained to a finite set, the use of horizons larger than one will often give significant performance gains. This is well known in other application areas, where the use of MPC with finite decision variables has been examined; see, e.g., [56, 92, 99, 101, 104–106]. However, only few results have been documented in the literature regarding power converters, see [22, 44, 45, 100, 117].

We will next examine how to use prediction horizons longer than one for MPC formulations where the plant inputs are constrained to belong to a finite set \mathbb{U} . As in (48), we will focus on linear plant models and quadratic cost functions with reference tracking. To address computational issues, we will exploit the geometrical structure of the underlying MPC optimization problem and presents a practical optimization algorithm. The algorithm uses elements of sphere decoding [53] to provide optimal switching sequences, requiring only little computational resources, thus, enabling the use of longer prediction horizons [44, 45]. We will illustrate the ideas on a variable speed drive application consisting of a three-level neutral point clamped voltage source inverter driving an induction machine. Our results show that using prediction horizons larger than one does, in fact, provide significant performance benefits. In particular, at steady-state operation the current distortions and/or the switching frequency can be reduced considerably with respect to direct MPC with horizon one, as presented in Sect. 3.

The methods proposed and results obtained are directly applicable to both the machine-side inverter in an ac drive setting, as well as to grid-side converters. The

ideas can also be used for other converter topology and are particularly promising for topologies with a high number of voltage levels.

4.3.1 Physical Model

As an illustrative example of a medium-voltage power electronic system, we consider a variable speed drive consisting of a three-level neutral point clamped (NPC) voltage source inverter (VSI) driving an induction machine (IM), as depicted in Fig. 9. The total dc-link voltage V_{dc} is assumed constant and the neutral point potential N is fixed.

Let the integer variables $u_a, u_b, u_c \in \{-1, 0, 1\}$ denote the switch positions in the three phase legs, corresponding to the phase voltages $-\frac{V_{dc}}{2}, 0, \frac{V_{dc}}{2}$, respectively.

Thus, the voltage applied to the machine terminals in orthogonal coordinates is

$$v_{s,\alpha\beta} = \frac{1}{2} V_{dc} u_{\alpha\beta} = \frac{1}{2} V_{dc} \mathbf{P} \mathbf{u}$$

with

$$\mathbf{P} \triangleq \frac{2}{3} \begin{bmatrix} 1 & -\frac{1}{2} & -\frac{1}{2} \\ 0 & \frac{\sqrt{3}}{2} & -\frac{\sqrt{3}}{2} \end{bmatrix}, \quad \mathbf{u} \triangleq \begin{bmatrix} u_a \\ u_b \\ u_c \end{bmatrix} \in \mathbb{U}, \quad \mathbb{U} \triangleq \{-1, 0, 1\}^3. \quad (49)$$

The state-space model of a squirrel-cage induction machine in the stationary $\alpha\beta$ reference frame is summarized hereafter. For the current control problem at hand, it is convenient to choose the stator currents $i_{s\alpha}$ and $i_{s\beta}$ as state variables. The state vector is complemented by the rotor flux linkages $\psi_{r\alpha}$ and $\psi_{r\beta}$, and the rotor's angular velocity ω_r . The model input are the stator voltages $v_{s\alpha}$ and $v_{s\beta}$. The model parameters are the stator and rotor resistances R_s and R_r , the stator, rotor and mutual reactances X_{ls} , X_{lr} and X_m , respectively, the inertia J , and the mechanical load torque T_ℓ . All rotor quantities are referred to the stator circuit. In terms of the above quantities, the continuous-time state equations are [55, 67]

$$\frac{di_s}{dt} = -\frac{1}{\tau_s} i_s + \left(\frac{1}{\tau_r} - \omega_r \begin{bmatrix} 0 & -1 \\ 1 & 0 \end{bmatrix} \right) \frac{X_m}{D} \psi_r + \frac{X_r}{D} v_s \quad (50a)$$

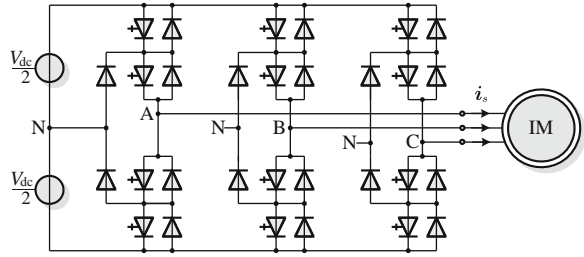
$$\frac{d\psi_r}{dt} = \frac{X_m}{\tau_r} i_s - \frac{1}{\tau_r} \psi_r + \omega_r \begin{bmatrix} 0 & -1 \\ 1 & 0 \end{bmatrix} \psi_r \quad (50b)$$

$$\frac{d\omega_r}{dt} = \frac{1}{J} (T_e - T_\ell), \quad (50c)$$

where we have used⁷

⁷ To simplify the notation, in (50, 50b, 50c) we dropped $\alpha\beta$ from the vectors i_s , ψ_r and v_s .

Fig. 9 Three-level three-phase neutral point clamped voltage source inverter driving an induction motor with a fixed neutral point potential



$$\begin{aligned}
 X_s &\triangleq X_{ls} + X_m \\
 X_r &\triangleq X_{lr} + X_m \\
 D &\triangleq X_s X_r - X_m^2.
 \end{aligned} \tag{51}$$

The transient stator time constant and the rotor time constant are equal to

$$\tau_s \triangleq \frac{X_r D}{R_s X_r^2 + R_r X_m^2} \quad \text{and} \quad \tau_r \triangleq \frac{X_r}{R_r},$$

whereas the electromagnetic torque is given by

$$T_e = \frac{X_m}{X_r} (\psi_{rx} i_{s\beta} - \psi_{r\beta} i_{s\alpha}). \tag{52}$$

4.3.2 MPC Formulation

The control problem is formulated in the $\alpha\beta$ reference frame. Let

$$i_s^{\star} \triangleq \begin{bmatrix} i_{s\alpha}^{\star} \\ i_{s\beta}^{\star} \end{bmatrix}$$

denote the reference of the instantaneous stator current. The objective of the current controller is to manipulate the three-phase switch position u , by synthesizing a switching sequence, such that the stator current i_s closely tracks its reference. At the same time, the switching effort, i.e., the switching frequency or the switching losses, are to be kept small.

It is convenient to describe the system by introducing the following state vector of the drive model:

$$x \triangleq \begin{bmatrix} i_{s\alpha} \\ i_{s\beta} \\ \psi_{rx} \\ \psi_{r\beta} \end{bmatrix}. \tag{53}$$

The stator current is taken as the system output vector, i.e., $y = i_s$. The switch position $u_{\alpha\beta}$ in the orthogonal coordinate system constitutes the input vector,

which is provided by the controller. Discretization of (50a, 50b, 50c) yields a linear system model of the form

$$x(k+1) = Ax(k) + Bu(k).$$

To penalise current errors and the control effort, we adopt the cost function:

$$V(x(k), \mathbf{u}(k)) = \sum_{\ell=k}^{k+N-1} (i'_{e,\alpha\beta}(\ell+1))^T (i'_{e,\alpha\beta}(\ell+1)) + \lambda_u (\Delta u'(\ell))^T \Delta u'(\ell), \quad (54)$$

where

$$i'_{e,\alpha\beta} \triangleq i_{s,\alpha\beta}^{\star} - i'_{s,\alpha\beta}$$

$$\Delta u'(\ell) \triangleq u'(\ell) - u'(\ell-1)$$

and subject to (see (49))

$$\mathbf{u}(k) \in \mathbb{U}^N$$

$$\|\Delta u'(\ell)\|_{\infty} \leq 1, \quad \forall \ell \in \{k, k+1, \dots, k+N-1\}. \quad (55)$$

The latter constraint is imposed since in each phase switching is only possible by one step up or down.

4.3.3 Obtaining the Switch Positions via Exhaustive Search

Due to the discrete nature of the decision variable \mathbf{u} , minimizing (54) subject to (55) is difficult, except for short horizons. In fact, as the prediction horizon is enlarged and the number of decision variables is increased, the (worst-case) computational complexity grows exponentially, thus, cannot be bounded by a polynomial, see also [103]. The difficulties associated with minimizing J become apparent when using exhaustive search. With this method, the set of admissible switching sequences $\mathbf{u}(k)$ is enumerated and the cost function evaluated for each such sequence. The switching sequence with the smallest cost is (by definition) the optimal one and its first element is chosen as the control input. At every time-step k , exhaustive search entails the following procedure:

1. Given the previously applied switch position $u(k-1)$ and taking into account (55), determine the set of admissible switching sequences over the horizon.
2. For each of these switching sequences, compute the cost V according to (54).
3. Choose the switching sequence, $\mathbf{u}^{\text{opt}}(k)$, which minimizes the cost. Apply its first element, $u^{\text{opt}}(k)$, to the converter.

It is easy to see that exhaustive search is computationally feasible only for very small horizons N , such as one or two. For $N = 5$, assuming a three-level converter, the number of switching sequences amounts to 1.4×10^7 .

Techniques from vector quantization [31] and from mathematical programming, such as branch and bound [35, 71, 84], can be used to reduce the computational burden. In particular, following akin to the method described in Sect. 3.2, an explicit state-feedback control law for FCS-MPC can be obtained which, as for the convex case in Sect. 4.2, induces a partition of the state-space [103]. In addition, off-the-shelf solvers such as CPLEX [57], include a wealth of smart heuristics and methods. However, none of the general methods take advantage of the particular structure of (54) and the fact that in MPC the solution is implemented in a moving horizon manner.

4.4 An Efficient Algorithm for Finite-Control Set MPC

We will next present a method for calculating the optimal switching sequences in FCS-MPC. The algorithm requires only little computations and is thereby attractive for applications in power electronics and drives.

4.4.1 Modified Sphere Decoding Algorithm

Direct algebraic manipulations akin to those mentioned in Sects. 4.1 and 4.2 (see also [49, 103]), give that minimization of (54) amounts to finding

$$\mathbf{u}^{\text{opt}}(k) = \arg \min_{\mathbf{u}} (\mathbf{z} - \mathbf{H}\mathbf{u})^T (\mathbf{z} - \mathbf{H}\mathbf{u}), \quad (56)$$

subject to (55), and where \mathbf{H} is an invertible lower-triangular matrix. In (56),

$$\mathbf{z} = \mathbf{H}\mathbf{u}^{\text{uc}},$$

where \mathbf{u}^{uc} is the sequence obtained from optimizing (54) *without constraints*, i.e., with $\mathbb{U} = \mathbb{R}^3$. Thus, we have rewritten the MPC optimization problem as a (truncated) *integer least-squares* problem. Interestingly, various efficient solution algorithms for (56) subject to finite-set constraints have been developed in recent years; see, e.g. [1, 53], and references therein. We will next show how to adapt the sphere decoding algorithm [27, 53] to find the optimal switching sequence $\mathbf{u}^{\text{opt}}(k)$.

The basic idea of the algorithm is to iteratively consider candidate sequences, say $\mathbf{u} \in \mathbb{U}^N$, which belong to a sphere of radius $\rho(k) > 0$ centered in \mathbf{z} ,

$$(\mathbf{z} - \mathbf{H}\mathbf{u})^T (\mathbf{z} - \mathbf{H}\mathbf{u}) \leq \rho(k). \quad (57)$$

Especially in the case of multi-level converters (where \mathbb{U} has many elements; see, e.g. [73].), the set of candidate sequences satisfying the above conditions is much smaller than the original constraint set \mathbb{U}^N . Not surprisingly, computation times can be drastically reduced compared to exhaustive search.

A key property used in sphere decoding is that, since \mathbf{H} is triangular, for a given radius, identifying candidate sequences which satisfy (57) is very simple. In particular, for the present case, \mathbf{H} is lower triangular, thus (57) can be rewritten as

$$\rho^2(k) \geq (z_1 - H_{(1,1)}u_1)^2 + (z_2 - H_{(2,1)}u_1 - H_{(2,2)}u_2)^2 + \dots \quad (58)$$

where z_i denotes the i -th element of \mathbf{z} , u_i is the i -th element of \mathbf{u} , and $H_{(i,j)}$ refers to the (i,j) -th entry of \mathbf{H} . Therefore, the solution set of (57) can be found by proceeding in a sequential manner akin to Gaussian elimination, in the sense that at each step only a one-dimension problem needs to be solved; for details, see [53].

The algorithm requires an initial value for the radius used at time k to determine \mathbf{u} . On the one hand, the radius $\rho(k)$ should be as small as possible, enabling us to remove as many candidate solutions a priori as possible. On the other hand, $\rho(k)$ must not be too small, to ensure that the solution set is non-empty. We propose to choose the initial radius by using the following *educated guess* for the optimal solution:

$$\mathbf{u}^{\text{sub}}(k) = \begin{bmatrix} 0 & I & 0 & \dots & 0 \\ 0 & 0 & I & \ddots & \vdots \\ \vdots & & \ddots & \ddots & 0 \\ 0 & \dots & \dots & 0 & I \\ 0 & \dots & \dots & 0 & I \end{bmatrix} \mathbf{u}^{\text{opt}}(k-1), \quad (59)$$

which is obtained by shifting the previous solution by one time-step and repeating the last switch position. This is in accordance with the moving horizon optimization paradigm described in Sect. 2. Since the optimal solution at the previous time-step satisfies the constraint, $\mathbf{u}^{\text{sub}}(k)$ is a feasible solution candidate of (54). Given (59), the initial value of $\rho(k)$ is then set to:

$$\rho(k) = (\mathbf{z} - \mathbf{H}\mathbf{u}^{\text{sub}}(k))^T (\mathbf{z} - \mathbf{H}\mathbf{u}^{\text{sub}}(k)). \quad (60)$$

At each time-step k , the controller first uses the current system state $\mathbf{x}(k)$, the future reference values, the previous switch position $\mathbf{u}(k-1)$ and the previous optimizer $\mathbf{u}^{\text{opt}}(k-1)$ to calculate $\mathbf{u}^{\text{sub}}(k)$, $\rho(k)$ and \mathbf{z} . The optimal switching sequence $\mathbf{u}^{\text{opt}}(k)$ is then obtained by invoking Algorithm 1:

$$\mathbf{u}^{\text{opt}}(k) = \text{MSPHDEC}(\emptyset, 0, 1, \rho^2(k), \mathbf{z}), \quad (61)$$

where \emptyset is the empty set.⁸

As can be seen in Algorithm 1, the proposed modification to sphere decoding operates in a recursive manner. Starting with the first component, the switching

⁸ The notation $\mathbf{H}_{(i,1:i)}$ refers to the first i entries of the i -th row of \mathbf{H} ; similarly, $\mathbf{u}_{1:i}$ are the first i elements of the vector \mathbf{u} . Note that the matrix \mathbf{H} is time-invariant and does not change when running the algorithm. Therefore, \mathbf{H} can be computed once offline before the execution of the algorithm.

sequence \mathbf{u} is built component by component, by considering the admissible single-phase switch positions in the constraint set $\{-1, 0, 1\}$. If the associated squared distance is smaller than the current value of ρ^2 , then we proceed to the next component. If the last component, i.e., u_{3N} , has been reached, meaning that \mathbf{u} is of full dimension $3N$, then \mathbf{u} is a candidate solution. If \mathbf{u} meets the switching constraint (55) and if the distance is smaller than the current optimum, then we update the incumbent optimal solution \mathbf{u}^{opt} and also the radius ρ .

Algorithm 1 Modified sphere decoding algorithm

```

function  $\mathbf{u}^{\text{OPT}}(k) = \text{MSPHDEC}(\mathbf{u}, d^2, i, \rho^2, \mathbf{z})$ 
  for each  $u \in \{-1, 0, 1\}$  do
     $u_i \leftarrow u$ 
     $d'^2 \leftarrow (\mathbf{z}_i - \mathbf{H}_{(i,1:i)} \mathbf{u}_{1:i})^T (\mathbf{z}_i - \mathbf{H}_{(i,1:i)} \mathbf{u}_{1:i}) + d^2$ 
    if  $d'^2 \leq \rho^2$  then
      if  $i < 3N$  then
         $\text{MSPHDEC}(\mathbf{u}, d'^2, i + 1, \rho^2, \mathbf{z})$ 
      else
        if  $\mathbf{u}$  meets (55) then
           $\mathbf{u}^{\text{opt}} \leftarrow \mathbf{u}$ 
           $\rho^2 \leftarrow d'^2$ 
        end if
      end if
    end if
  end for
end function

```

The computational advantages of this algorithm stem from adopting the notion of branch and bound [71, 84]. Branching is done over the set of single-phase switch positions $\{-1, 0, 1\}$; bounding is achieved by considering solutions only within the sphere of current radius. If the distance d' exceeds the radius, a certificate has been found that the branch (and all its associated switching sequences) provides only solutions worse than the incumbent optimum. Therefore, this branch can be pruned, i.e., removed from further consideration without exploring it. During the optimization procedure, whenever a better incumbent solution is found, the radius is reduced and the sphere thus tightened, so that the set of candidate sequences is as small as possible, but non-empty. The majority of the computational burden relates to the computation of d' via evaluating the terms $\mathbf{H}_{(i,1:i)} \mathbf{u}_{1:i}$. Thanks to (58), d' can be computed sequentially, by computing only the squared addition due to the i th component of \mathbf{u} . In particular, the sum of squares in d , accumulated over the layers 1 to $i - 1$, does not need to be recomputed.

4.4.2 Performance Evaluation

Whilst the main advantages of using MPC, when compared to other methods such as optimized pulse patterns (OPPs), see e.g. [14], lie in the handling of transients,

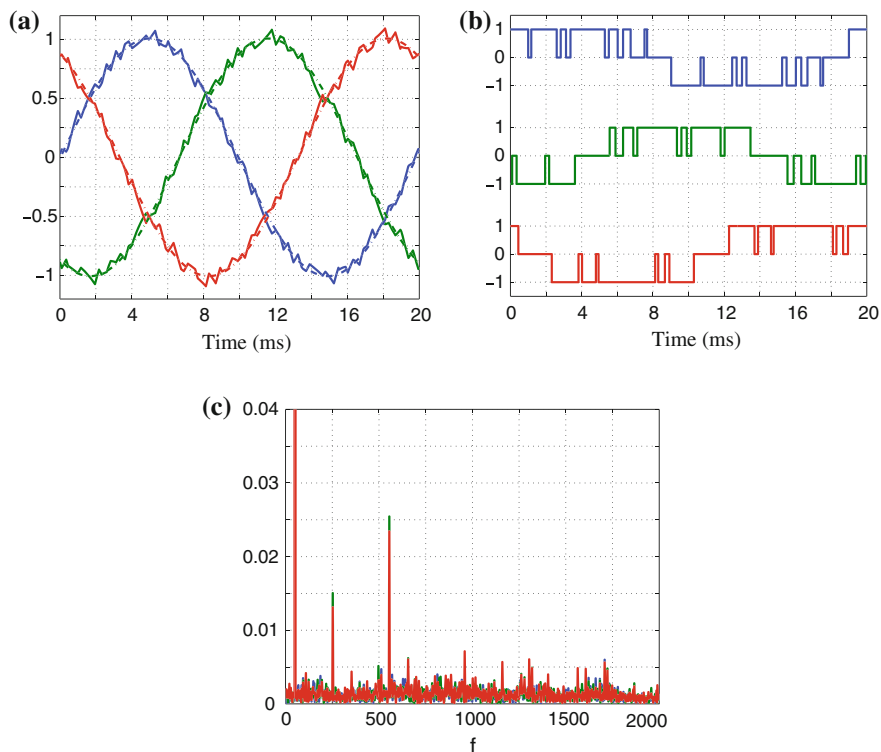


Fig. 10 Simulated waveforms for MPC with horizon $N = 10$ and the weight $\lambda_u = 103 \times 10^{-3}$. **a** Stator currents i_s , **b** Switch positions u , **c** Stator current spectrum

we will focus on the steady-state behaviour. We consider a three-level voltage source inverter driving an induction machine with a constant mechanical load. A 3.3 kV and 50 Hz squirrel-cage induction machine rated at 2MVA with a total leakage inductance of 0.25 pu is used as an example of a typical medium-voltage induction machine. The dc-link voltage is $V_{dc} = 5.2$ kV and assumed to be constant.

The key control performance criteria are the device switching frequency f_{sw} and the current THD I_{THD} . In addition, we will also investigate the empirical *closed-loop* cost, V_{cl} , which in accordance with (54) captures the squared RMS current error plus the weighted averaged and squared switching effort. In a first step, the steady-state performance of MPC tracking the current reference is illustrated, using the sampling interval $h = 25 \mu s$. The controller uses the cost function J with prediction horizon $N = 10$ and weighting factor $\lambda_u = 103 \times 10^{-3}$. This results in an average device switching frequency of $f_{sw} = 300$ Hz, which is typical for medium-voltage applications, and a current THD of $I_{THD} = 5.03$ %. Figure 10a illustrates three-phase stator current waveforms along with their (dash-dotted) references over one fundamental period. The colours blue, green and red correspond to phase a ,

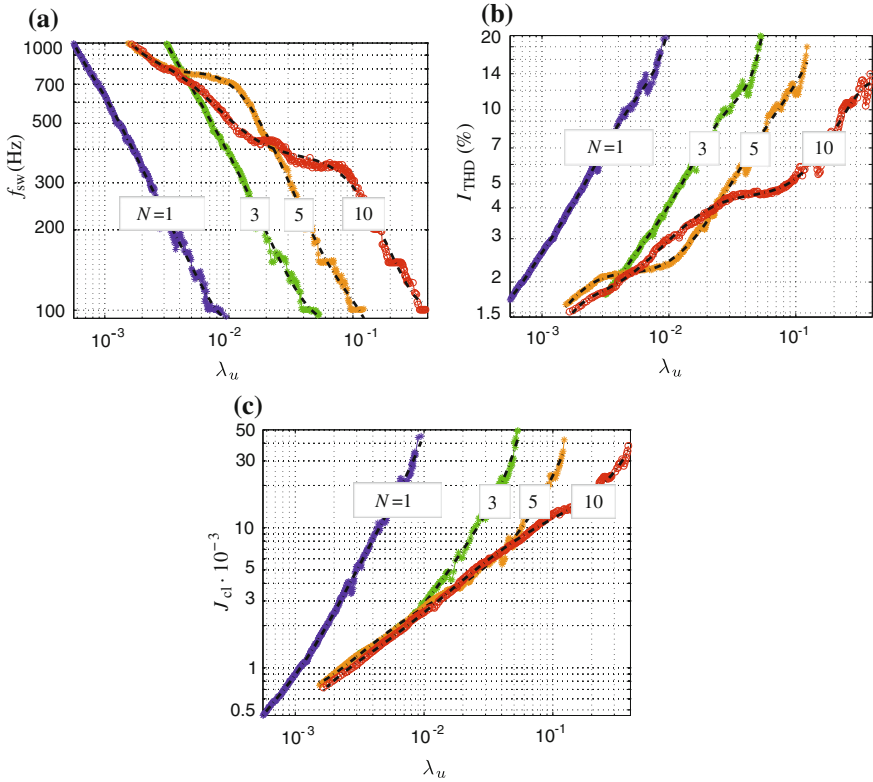


Fig. 11 Key performance criteria of MPC for the prediction horizons $N = 1, 3, 5, 10$. The switching frequency, current THD and closed-loop cost are shown as a function of the tuning parameter λ_u , using a double logarithmic scaling. The individual simulations are indicated using dots, their overall trend is approximated using dash-dotted polynomials. **a** Average switching frequency f_{sw} . **b** Current THD I_{THD} . **c** Closed-loop cost

b and *c*, respectively. The spectrum of the stator current, computed with a Fourier transformation, is shown in Fig. 10c. The three-phase switching sequence is depicted in Fig. 10b. As can be seen, unlike PWM, the switching pattern lacks symmetry and repetitiveness, resulting in a non-discrete and predominantly flat spectrum. Nevertheless, non-tripled odd-order current harmonics such as the 5th, 7th, 11th, 13th and 19th harmonics are clearly identifiable.

Next, the influence of λ_u on the switching frequency, the current THD and the cost is investigated. For each of the horizons $N = 1, 3, 5$ and 10 and for more than 1,000 different values of λ_u , ranging between 0 and 0.5, steady-state simulations were run. Focusing on switching frequencies between 100 Hz and 1 kHz, and current THDs below 20 %, the results are shown in Fig. 11, using a double logarithmic scale. Each simulation corresponds to a data point. Polynomial functions are overlaid, which approximate the individual data points. Figure 11a, b suggest that, for small prediction horizons, the relationship between λ_u and the performance

Table 1 Average and maximal number of switching sequences that need to be considered by the sphere decoding and exhaustive search algorithms to obtain the optimal result, depending on the length of the prediction horizon

Prediction horizon N	Sphere decoding		Exhaustive search	
	Average	Maximal	Average	Maximal
1	1.18	5	11.8	18
2	1.39	8	171	343
3	1.72	14	2350	4910
5	2.54	35	4,67,000	9,70,000
10	8.10	220		

variables is approximately linear in double logarithmic scale; for larger values of N , the relationship is more complicated, but still monotonic. Fig. 11c illustrates the empirical closed-loop costs obtained. Clearly, the cost is reduced as the prediction horizon is increased, suggesting the use of horizons larger than one. For example, with $\lambda_u = 0.01$ and $N = 1$, we have $J_{cl} \approx 50$, whereas with horizon $N = 3$, the closed-loop cost can be reduced to $J_{cl} \approx 3$! We note that, for this value of λ_u , the empirical closed-loop cost achieved is almost optimal.

4.4.3 Computational Burden

We next compare the computational burden of the algorithm presented in Sect. 4.4 with that of exhaustive search, see Sect. 4.3.3. The weight λ_u is tuned such that approximately the same switching frequency of $f_{sw} = 300$ Hz is obtained, irrespective of the chosen prediction horizon. As a measure of the computational burden, the number of switching sequences, which are investigated by the algorithm at each time-step when computing the optimum, is considered. Over multiple fundamental periods, the average as well as the maximal number of sequences is monitored, as summarized in Table 1. The table shows that, as the prediction horizon is increased, initially, the computational burden associated with Algorithm 1 grows slowly, despite being exponential, whilst exhaustive search becomes computationally intractable already for horizons of five and longer.

4.5 MPC for Switched Systems

Power electronic systems are hybrid systems, featuring different dynamics for different sets of binary switch positions. When considering currents, fluxes and voltages, power electronic systems constitute switched linear systems. However, when an electromagnetic torque, flux magnitude, or real and reactive power expression is used, the system turns into a switched nonlinear system. The switched linear behavior of power electronic systems can be directly captured by

polyhedral piecewise affine (PWA) systems as described below. PWA systems also allow the approximation of switched nonlinear behavior with an arbitrary accuracy. Alternatively, solution approaches are available that directly address the switched nonlinear optimization problem, albeit in an approximate manner, as shown at the end of this section.

4.5.1 Piecewise Affine Systems

Polyhedral PWA systems [54, 116] are defined by partitioning the state-input space into polyhedra and associating with each polyhedron an affine state-update and output function

$$x(k+1) = A_{i(k)}x(k) + B_{i(k)}u(k) + f_{i(k)} \quad (62a)$$

$$y(k) = C_{i(k)}x(k) + D_{i(k)}u(k) + g_{i(k)} \quad (62b)$$

$$\text{with } i(k) \text{ such that } [x^T(k)u^T(k)]^T \in \mathcal{P}_{i(k)}, \quad (62c)$$

where $x \in \mathbb{X}$, $u \in \mathbb{U}$, $y \in \mathbb{Y}$ denote the state, input and output vectors, respectively. The state vector $x = [x_r^T x_b^T]^T$ encompasses, in general, real-valued components $x_r \in \mathbb{X}_r \subseteq \mathbb{R}^{n_r}$ as well as binary components $x_b \in \mathbb{X}_b \subseteq \{0, 1\}^{n_b}$. The same applies to the inputs and outputs.

The polyhedra $\mathcal{P}_{i(k)}$ define a set of polyhedra $\{\mathcal{P}_i\}_{i \in I}$ on $\mathbb{X} \times \mathbb{U}$, and the real matrices $A_{i(k)}$, $B_{i(k)}$, $C_{i(k)}$, $D_{i(k)}$ and real vectors $f_{i(k)}$, $g_{i(k)}$ with $i(k) \in I$, I finite, are constant and have suitable dimensions. We refer to $i(k)$ as the *mode* of the system, which is associated with a binary state and a binary input.

PWA systems are so called *linear hybrid* systems. These are heterogeneous systems that incorporate both continuous-valued components governed by difference equations, as well as discrete-valued components, such as finite state machines, if-then-else rules and on/off switches. PWA systems switch between different operating modes, with each mode being governed by a discrete-time affine dynamical law. Mode transitions are triggered by inputs or states crossing specific affine thresholds. PWA constraints can be imposed on states and inputs.

Modelling complex hybrid systems in PWA form is, in general, a tedious and highly non-trivial task. To facilitate the modelling process, the HYbrid Systems DEscription Language (HYSDEL) has been developed, which allows the designer to describe a hybrid system on a textual basis [122]. The HYSDEL modelling language is an integral part of the MPT toolbox. Tools, such as the mode enumeration algorithm, are available to translate hysdel code into PWA form [48].

Within the class of linear hybrid systems, a number of modelling frameworks are available, which are equivalent to each other [54]. Apart from PWA systems, another major representative is the *mixed logical dynamical* (MLD) framework [8]. The MLD framework extends linear discrete-time systems by augmenting the state and output equations by auxiliary real and binary variables and a mixed-

integer linear inequality constraint. MLD models are very suitable for online MPC, since the equality and inequality constraints of the MLD model can be easily included in the optimization problem. Depending on whether the cost function is linear or quadratic, the optimization problem is either a *mixed-integer* linear or quadratic program (MILP or MIQP).

The State-Feedback Control Law

PWA models are the starting point to derive off-line the state-feedback control law [11]. Indeed, the notion of multi-parametric programming mentioned in Sect 4.2 can be extended to PWA systems. Specifically, the formulation of a linear cost function subject to a PWA model gives rise to a *multi-parametric mixed-integer linear program* (mp-MILP). As proposed in [11, 12], the state-feedback control law can be computed, by augmenting mp-LP with dynamic programming, i.e. by moving backwards in time using mp-LP.

Theorem 4 *The solution to mp-MILP is a state-feedback control law $u^{opt}(k)$ that is a piecewise affine function of the state vector $x(k)$ defined on a polyhedral partition of the feasible state-space \mathbb{X} .* ■

Theorem 5 *The value function $V^{opt}(x(k)) = V(x(k), u^{opt}(k))$ of the mp-MILP is convex and piecewise affine in the state.* ■

The related proofs and additional details can be found in [26] for mp-MILPs, and in [11, 25] for mp-MIQPs. Furthermore, [12] provides an in-depth analysis and description of multi-parametric programming for MILPs and MIQPs.

Application Examples

Consider the direct torque control (DTC) problem of ac machines, first addressed in [119]. In DTC, the electromagnetic torque T and the stator flux magnitude Ψ are directly controlled without using a modulator. A suitable voltage vector is selected that keeps the torque and flux magnitude within upper and lower bounds, which are imposed around their references. For a neutral point (NP) clamped three-level inverter, also the NP potential is to be balanced around zero. By approximating the nonlinearities relating to the torque, flux magnitude, machine rotation and NP potential by PWA functions, the DTC problem can be cast in the MLD framework using hysdel, as shown in [93], and then translated into PWA form.

Let Ψ_{\max} and Ψ_{\min} denote the upper and lower flux magnitude bounds, respectively, and Ψ^{\star} its reference. We introduce the non-negative term

$$\varepsilon_{\Psi}(\ell) = \begin{cases} q_F(\Psi(\ell) - \Psi_{\max}) & \text{if } \Psi(\ell) \geq \Psi_{\max} \\ q_F(\Psi_{\min} - \Psi(\ell)) & \text{if } \Psi(\ell) \leq \Psi_{\min} \\ q_f|\Psi(\ell) - \Psi^{\star}(\ell)| & \text{else} \end{cases} \quad (63)$$

that uses soft constraints with the weight q_F to heavily penalize violations of the bounds. A small penalty q_f , with $q_f \ll q_F$, is added to penalize deviations from the reference. Similarly, for the torque and the NP potential, the terms ε_T and ε_v can be defined. The switching transitions are penalized by

$$\varepsilon_u(\ell) = q_u(\ell) \|u(\ell) - u(\ell - 1)\|_1, \quad (64)$$

where $q_f < q_u(\ell) < q_F$ is a time-varying weight that decays exponentially within the prediction horizon, providing an incentive to further reduce the switching frequency by postponing switching until at least one soft constraint is about to be violated.

Aggregating these terms results in the piecewise linear cost function

$$V(x(k), \mathbf{u}(k), u(k-1)) = \sum_{\ell=k}^{k+N-1} \left\| \begin{bmatrix} \varepsilon'_T(\ell+1) & \varepsilon'_\varphi(\ell+1) & \varepsilon'_v(\ell+1) & \varepsilon'_u(\ell) \end{bmatrix}^T \right\|_1. \quad (65)$$

The state vector includes the stator flux components in a rotating dq reference frame, the angular position of the reference frame and the NP potential. Minimizing (65) subject to the integer constraints on the switch positions and the PWA model results in an MILP, which can be solved off-line by computing the state-feedback control [94]. A move blocking strategy [16] reduces the complexity of the solution, albeit it remains high. Considering a two-level inverter for the ease of visualization, Fig. 12 depicts the state-feedback control law in the stator flux plane for a specific angular position and for $u(k-1) = [+1 -1 -1]^T$. The colours refer to distinct switch positions $u(k)$, as explained in detail in [94]. In particular, the large (yellow) region refers to $u(k) = u(k-1)$. In this region, to maintain the controlled variables within their bounds, switching is not required and thus avoided.

Recognizing that the DTC problem of keeping the torque and stator flux magnitude within given bounds strongly relates to feasibility, by computing a semi-explicit control law a controller of lower complexity can be derived [39].

Similarly, also dc-dc converters can be modelled as PWA systems, and an MPC problem with a linear cost function can be formulated for the buck converter [41]. A Kalman filter can be used to account for load changes, and closed-loop stability can be proven by deriving a piecewise quadratic Lyapunov function [42]. The state-feedback control law can be easily computed and implemented on a DSP to obtain experimental results [40]. Similar results are available for boost converters [6, 78].

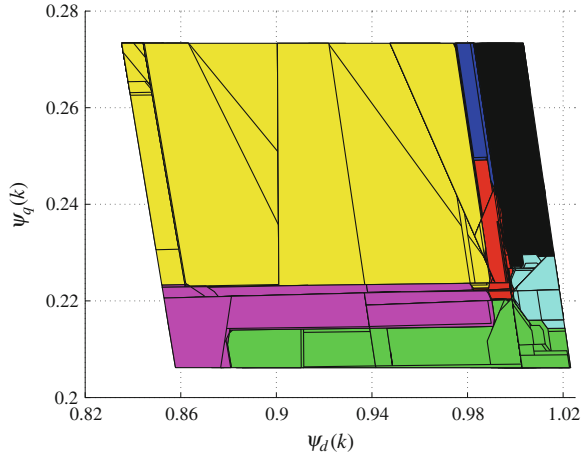
4.5.2 Switched Nonlinear Systems

Solving MPC problems involving switched *nonlinear* systems in real-time is a highly challenging task, since this amounts to solving a *mixed-integer nonlinear program*. Computing an explicit solution for such problems remains largely an open problem.

Optimization Problem

Nevertheless, for a subclass of MPC problems with switched nonlinear systems, an optimization algorithm can be constructed, which features a computational

Fig. 12 The explicit state-feedback control law for the DTC drive with a two-level inverter for $u(k-1) = [+1 -1 -1]^T$ and a given angular position of the dq reference frame, where the colours correspond to the unique switch positions



complexity that is suitable for implementation, albeit it solves the MPC problem only in an approximative manner. More specifically, consider a nonlinear system with integer inputs, whose output variables are to be regulated along given trajectories, by keeping the outputs within upper and lower bounds around their references. The second control objective is to minimize the switching effort, i.e. the switching frequency or the switching losses.

The (short-term) switching frequency is captured by the objective function

$$V(x(k), \mathbf{u}(k), u(k-1)) = \frac{1}{N} \sum_{\ell=k}^{k+N-1} \|\Delta u'(\ell)\|_1, \quad (66)$$

which represents the sum of the switching transitions (number of commutations) over the prediction horizon divided by the length of the horizon. Alternatively, the switching (power) losses can be directly represented through

$$V(x(k), \mathbf{u}(k), u(k-1)) = \frac{1}{N} \sum_{\ell=k}^{k+N-1} E_{sw}(x'(\ell), u'(\ell), u'(\ell-1)), \quad (67)$$

which is the sum of the instantaneous switching (energy) losses E_{sw} over the prediction horizon.⁹

For a drive system as in the previous section, for example, the optimization problem can be stated as

$$\mathbf{u}^{\text{opt}}(k) = \arg \min_{\mathbf{u}(k)} V(x(k), \mathbf{u}(k), u(k-1)) \quad (68a)$$

⁹ Note that, E_{sw} is a function of the inverter current i , which in turn is either a state variable or a linear combination of the state vector x .

$$\text{s.t. } x'(\ell + 1) = Ax'(\ell) + Bu'(\ell) \quad (68b)$$

$$y'(\ell + 1) = g(x'(\ell + 1)) \quad (68c)$$

$$y'(\ell + 1) \in \mathcal{Y} \text{ or } \varepsilon'_y(\ell + 1) < \varepsilon'_y(\ell) \quad (68d)$$

$$u'(\ell) \in \mathbb{U}, \|\Delta u'(\ell)\|_\infty \leq 1 \quad (68e)$$

$$\forall \ell = k, \dots, k + N - 1, \quad (68d)$$

When using inductor currents, fluxes or capacitor voltages as states, the state-update equation is typically linear in power electronic systems, while the outputs y , such as the torque, stator flux magnitude and the NP potential, are a nonlinear function $g(\cdot)$ of the state vector. The outputs are to be maintained within their bounds, described by the set \mathcal{Y} or, if a bound is violated, brought closer to this set at every time-step within the horizon.

An Algorithm based on Enumeration and Extrapolation

Attempting to solve the optimization problem (68) for a long horizon, say 80, leads for a three-level inverter to as many possible switching sequences as there are atoms in the observable universe, which is clearly a futile endeavour. By considering switching transitions only when one of the output variables is close to one of its bounds, the number of switching sequences to be considered can be greatly reduced. Depending on the horizon length, a few tens to a few thousand sequences are to be investigated. Since the switching effort is to be minimized, this heuristic turns out to have only a minor effect on the solution. Indeed, as shown in [34], optimality is only mildly affected, which is evidenced by the fact that the closed-loop performance in terms of the current THD and switching losses is, at least for very long prediction horizons, effectively equal to the one obtained by offline computed optimized pulse patterns [14]. The latter are widely considered to provide steady-state operating conditions that upper bound achievable performance.

Between switching instants, the concept of extrapolation is used, which is similar to an adaptive move blocking scheme. The notion of *linear* extrapolation is highlighted in Fig. 13, where two output variables are considered along with their—in this case—constant bounds. At time-step k , the model (68b)–(68c) is used to compute $y(k + 1)$ for three different switching inputs $u(k)$. For each $u(k)$, based on $y(k)$ and $y(k + 1)$, extrapolation is used to compute the number of steps a switch position can be applied to the inverter before a bound is violated. This operation is computationally very cheap.

Using enumeration of all possible switching transitions, an algorithm using extrapolation can be easily constructed, which relies on three key concepts:

1. The optimization problem is formulated in an open, rather than in a closed, form. The set of admissible switching sequences is constructed sequentially, and the corresponding output trajectories are computed forward in time.

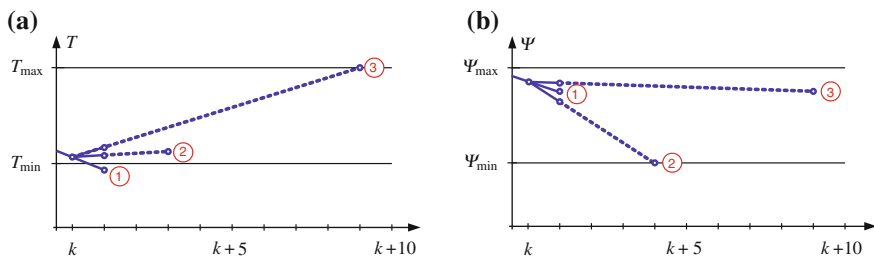


Fig. 13 Linear extrapolation of the torque and stator flux trajectories using the samples at time-steps k and $k + 1$. For each of the three switch positions $u(k)$ the trajectories are extrapolated until one of them hits a bound. **a** Electromagnetic torque. **b** Stator flux magnitude

2. In between of the switching events, the output trajectories are either computed using a model of the drive system or by extrapolating them. Typically, quadratic extrapolation is used, even though linear extrapolation is often sufficiently accurate.
3. The set of admissible switching sequences is controlled by the so-called switching horizon, which is composed of the elements “S” and “E” that stand for switch and extrapolate (or more generally extend), respectively.

It is important to distinguish between the switching horizon (number of switching instants within the horizon, i.e., the degrees of freedom) and the prediction horizon (number of time steps MPC looks into the future). Between the switching instants, the switch positions are frozen and the drive behavior is extrapolated until a bound is hit. The concept of extrapolation gives rise to long prediction horizons (typically, 30–200 time steps), while the switching horizon is short (usually one to three). Note that the prediction horizon directly relates to the steady-state performance, which, in this case, is the ratio between the switching effort and the current THD. The switching horizon, on the other hand, is proportional to the computational burden.

For an in-depth description and analysis of this algorithm, the reader is referred to [43] and [33]. Its roots can be traced back to the 1980s [114]. Branch and bound techniques can be used to reduce the computation time by an order of magnitude [35]. Smart extrapolation methods can be used to increase the accuracy of the predictions [125]. Infeasible states, so called deadlocks, can be largely avoided, by adding terminal weights and terminal constraints [15]. A deadlock resolution strategy was proposed in [95]. Closed-loop and robust stability can be shown [37].

Application Examples

The algorithm described above was first proposed as model predictive direct torque control (MPDTC) to address the DTC problem of medium-voltage induction motor drives. During the past few years, MPDTC has been extended into the *model predictive direct control* family (MPD x C) with $x \in \{T, C, P, B\}$, representing the torque, current, power and balancing control problem, respectively.

More specifically, model predictive direct torque (MPDTC) was proposed in 2005 [32, 43] as a successor of DTC, tested on a 2.5 MVA drive in 2007 [95] and generalized in 2009 to arbitrary switching horizons [33]. At steady-state operating conditions, MPDTC provides switching losses and current distortions similar to the ones typically achieved by optimized pulse patterns [14], while during transients, its dynamic response is as fast as the one of DTC [34]. Model predictive direct current control (MPDCC) is a derivative of MPDTC [36], while model predictive direct power control (MPDPC) is the adaptation of MPDTC to grid-connected converters [46, 114]. Model predictive direct balancing control (MPDBC) is the most recent member of the family, being used to control the internal voltages of multi-level converters [64].

A control approach similar to MPDTC can be also applied to dc-dc boost converters. As shown in [60], the voltage control problem can be tackled with one control loop, by adopting the concepts of enumeration, move blocking as well as penalties on the tracking error and switching effort.

5 Conclusions

In this chapter, basic aspects and methods underlying model predictive control have been discussed. To clarify the concepts, horizon-one controllers have been analyzed in detail, including a derivation of the optimal solution and establishing relationships to dead-beat controllers. For MPC formulations with longer horizons, we have presented optimization algorithms, which allow one to implement long-horizon MPC in practical applications in power electronics and drives.

The presentation in this chapter has been kept at a basic system-theoretic level and illustrated on simple converter topologies. Some configurations like, e.g., Active-Front-End converters [98], require a more careful consideration of both control theoretic tools and also physical system knowledge for the design of high-performance model predictive controllers. Subsequent chapters in this book will serve to illustrate the synergy required.

Acknowledgments Research supported under Australian Research Council's Discovery Projects funding scheme (project number DP 110103074).

References

1. E. Agrell, T. Eriksson, A. Vardy, K. Zeger, Closest point search in lattices. *IEEE Trans. Inform. Theory* **48**(8), 2201–2214 (2002)
2. R.P. Aguilera, D.E. Quevedo, Capacitor voltage estimation for predictive control algorithm of flying capacitor converters, in *IEEE International Conference on Industrial Technology* (Melbourne, 2009)

3. R.P. Aguilera, D.E. Quevedo, On stability and performance of finite control set MPC for power converters, in *Workshop on Predictive Control of Electrical Drives and Power Electronics (PRECEDE)* (2011), pp. 55–62
4. R.P. Aguilera, D.E. Quevedo, Stability analysis of quadratic MPC with a discrete input alphabet. *IEEE Trans. Autom. Control* (2013), **58**(12), pp. 3190–3196
5. K.J. Åström, B. Wittenmark, *Computer-Controlled Systems: Theory and Design*, 3rd edn. (Prentice Hall, Upper Saddle River, 1997)
6. A.G. Beccuti, G. Papafotiou, M. Morari, Explicit model predictive control of the boost dc-dc converter, in *Proceedings of the 2nd IFAC Conference on Analysis and Design of Hybrid Systems* (Alghero, 2006)
7. A. Bemporad, F. Borrelli, M. Morari, Model predictive control based on linear programming—the explicit solution. *IEEE Trans. Autom. Control* **47**(12), 1974–1985 (2002)
8. A. Bemporad, M. Morari, Control of systems integrating logic, dynamics and constraints. *Automatica* **35**(3), 407–427 (1999)
9. A. Bemporad, M. Morari, V. Dua, E.N. Pistikopoulos, The explicit linear quadratic regulator for constrained systems. *Automatica* **38**(1), 3–20 (2002)
10. S. Bolognani, S. Bolognani, L. Peretti, M. Zigliotto, Design and implementation of model predictive control for electrical motor drives. *IEEE Trans. Industr. Electron.* **56**(6), 1925–1936 (2009)
11. F. Borrelli, *Constrained OPTIMAL Control of Linear and Hybrid Systems*, LNCIS, vol. 290 (Springer, Berlin, 2003)
12. F. Borrelli, M. Baotić, A. Bemporad, M. Morari, Dynamic programming for constrained optimal control of discrete-time linear hybrid systems. *Automatica* **41**(10), 1709–1721 (2005)
13. F. Borrelli, A. Bemporad, M. Morari, Geometric algorithm for multiparametric linear programming. *J. Optim. Theory Appl.* **118**(3), 515–540 (2003)
14. G.S. Buja, Optimum output waveforms in PWM inverters. *IEEE Trans. Ind. Appl.* **16**(6), 830–836 (1980)
15. T. Burtcher, T. Geyer, Deadlock avoidance in model predictive direct torque control. *IEEE Trans. Ind. Appl.* **49**(5), 2126–2135 (Raleigh, 2013)
16. R. Cagienard, P. Grieder, E. Kerrigan, M. Morari, Move blocking strategies in receding horizon control. *J. Process Control* **17**, 563–570 (2007)
17. E.F. Camacho, C. Bordons, *Model Predictive Control* (Springer, New York, 1999)
18. D.W. Clarke, C. Mohtadi, P.S. Tuffs, Generalized predictive control—part I. The basic algorithm. *Automatica* **23**(2), 137–148 (1987)
19. P. Correa, M. Pacas, J. Rodriguez, Predictive torque control for inverter-fed induction machines. *IEEE Trans. Industr. Electron.* **54**(2), 1073–1079 (2007)
20. P. Cortés, M.P. Kazmierkowski, R.M. Kennel, D.E. Quevedo, J. Rodríguez, Predictive control in power electronics and drives. *IEEE Trans. Industr. Electron.* **55**(12), 4312–4324 (2008)
21. P. Cortés, G. Ortiz, J.I. Yuz, J. Rodríguez, S. Vazquez, L. Franquelo, Model predictive control of an inverter with output filter for UPS applications. *IEEE Trans. Industr. Electron.* **56**(6), 1875–1883 (2009)
22. P. Cortés, J. Rodríguez, S. Vazquez, L. Franquelo, Predictive control of a three-phase UPS inverter using two steps prediction horizon, in *Proceedings IEEE International Conference Industrial Technology* (Viña del Mar, 2010), pp. 1283–1288
23. M. Cychowski, K. Szabat, T. Orłowska-Kowalska, Constrained model predictive control of the drive system with mechanical elasticity. *IEEE Trans. Industr. Electron.* **56**(6), 1963–1973 (2009)
24. A. Domahidi, A. Zgraggen, M. Zeilinger, M. Morari, C. Jones, Efficient interior point methods for multistage problems arising in receding horizon control, in *IEEE Conference on Decision and Control* (Maui, 2010), pp. 668–674

25. V. Dua, N.A. Bozinis, E.N. Pistikopoulos, A multiparametric programming approach for mixed-integer quadratic engineering problems. *Comput. Chemical Eng.* **26**(4–5), 715–733 (2002)
26. V. Dua, E.N. Pistikopoulos, An algorithm for the solution of multiparametric mixed integer linear programming problems. *Ann. Oper. Res.* 123–139 (2000)
27. U. Fincke, M. Pohst, Improved methods for calculating vectors of short length in a lattice, including a complexity analysis. *Math. Comput.* **44**(170), 463–471 (1985)
28. R. Fletcher, A general quadratic programming algorithm. *IMA J. Appl. Math.* **7**(1), 76–91 (1971)
29. E.J. Fuentes, C.A. Silva, J.I. Yuz, Predictive speed control of a two-mass system driven by a permanent magnet synchronous motor. *IEEE Trans. Industr. Electron.* **59**(7), 2840–2848 (2012)
30. F. Garofalo, P. Marino, S. Scala, F. Vasca, Control of DC/DC converters with linear optimal feedback and nonlinear feed forward. *IEEE Trans. Power Electron.* **9**(6), 607–615 (1994)
31. A. Gersho, R.M. Gray, *Vector Quantization and Signal Compression* (Kluwer Academic, Boston, 1992)
32. T. Geyer, Low complexity model predictive control in power electronics and power systems. Ph.D. Thesis, Automatic Control Laboratory ETH Zurich (2005)
33. T. Geyer, Generalized model predictive direct torque control: long prediction horizons and minimization of switching losses, in *IEEE Conference on Decision and Control* (Shanghai, 2009), pp. 6799–6804
34. T. Geyer, A comparison of control and modulation schemes for medium-voltage drives: emerging predictive control concepts versus PWM-based schemes. *IEEE Trans. Ind. Appl.* **47**(47), 1380–1389 (2011)
35. T. Geyer, Computationally efficient model predictive direct torque control. *IEEE Trans. Power Electron.* **26**(10), 2804–2816 (2011)
36. T. Geyer, Model predictive direct current control: formulation of the stator current bounds and the concept of the switching horizon. *IEEE Ind. Appl. Mag.* **18**(2), 47–59 (2012)
37. T. Geyer, R.P. Aguilera, D.E. Quevedo, On the stability and robustness of model predictive direct current control, in *Proceedings of the IEEE International Conference on Industrial Technology*, Cape Town, South Africa (2013)
38. T. Geyer, N. Oikonomou, G. Papafotiou, F. Kieferndorf, Model predictive pulse pattern control. *IEEE Trans. Ind. Appl.* **48**(2), 663–676 (2012)
39. T. Geyer, G. Papafotiou, Direct torque control for induction motor drives: A model predictive control approach based on feasibility, in *Hybrid Systems: Computation and Control*, ed. by M. Morari, L. Thiele, LNCS, vol. 3414 (Springer, New York, 2005), pp. 274–290
40. T. Geyer, G. Papafotiou, R. Frasca, M. Morari, Constrained optimal control of the step-down dc-dc converter. *IEEE Trans. Power Electron.* **23**(5), 2454–2464 (2008)
41. T. Geyer, G. Papafotiou, M. Morari, On the optimal control of switch-mode dc-dc converters, in *Hybrid Systems: Computation and Control*, ed. by R. Alur, G. Pappas, LNCS, vol. 2993 (Springer, New York, 2004), pp. 342–356
42. T. Geyer, G. Papafotiou, M. Morari, Hybrid model predictive control of the step-down dc-dc converter. *IEEE Trans. Control Syst. Technol.* **16**(6), 1112–1124 (2008)
43. T. Geyer, G. Papafotiou, M. Morari, Model predictive direct torque control—Part I: Concept, algorithm and analysis. *IEEE Trans. Industr. Electron.* **56**(6), 1894–1905 (2009)
44. T. Geyer, D.E. Quevedo, Multistep direct model predictive control for power electronics – Part 1: Algorithm, in *Proceedings of the Energy Conversion Congress and Exposition (ECCE)* (2013)
45. T. Geyer, D.E. Quevedo, Multistep direct model predictive control for power electronics – Part 2: Analysis, in *Proceedings of the Energy Conversion Congress and Exposition (ECCE)* (2013)
46. T. Geyer, J. Scoltock, U. Madawala, Model predictive direct power control for grid-connected converters, in *Proceedings of the IEEE Industrial Electronics Society Annual Conference*, Melbourne, Australia (2011)

47. T. Geyer, F. Torrisi, M. Morari, Optimal complexity reduction of polyhedral piecewise affine systems. *Automatica* **44**(7), 1728–1740 (2008)
48. T. Geyer, F. Torrisi, M. Morari, Efficient mode enumeration of compositional hybrid systems. *Int. J. Control* **83**(2), 313–329 (2010)
49. G. Goodwin, D. Mayne, K.Y. Chen, C. Coates, G. Mirzaeva, D. Quevedo, An introduction to the control of switching electronic systems. *Ann. Rev. Control* **34**(2), 209–220 (2010)
50. G.C. Goodwin, M.M. Serón, J.A. De Doná, *Constrained Control & Estimation – An Optimization Perspective* (Springer, London, 2005)
51. L. Grüne, J. Panne, *Nonlinear Model Predictive Control: Theory and Algorithms* (Springer, New York, 2011)
52. L. Grüne, A. Rantzer, On the infinite horizon performance of receding horizon controllers. *IEEE Trans. Autom. Control* **53**(9), 2100–2111 (2008)
53. B. Hassibi, H. Vikalo, On the sphere-decoding algorithm I. Expected complexity. *IEEE Trans. Signal Process.* **53**(8), 2806–2818 (2005)
54. W.P.M.H. Heemels, B. De Schutter, A. Bemporad, Equivalence of hybrid dynamical models. *Automatica* **37**(7), 1085–1091 (2001)
55. J. Holtz, The representation of AC machine dynamics by complex signal graphs. *IEEE Trans. Industr. Electron.* **42**(3), 263–271 (1995)
56. J.S. Hu, K.Y. Chen, Analysis and design of the receding horizon constrained optimization for class-D amplifier driving signals. *Digital Signal Process.* **20**, 1511–1525 (2010)
57. IBM ILOG, Inc., CPLEX 12.5 User Manual. Somers, NY, USA (2012)
58. S.G. Jeong, M.H. Woo, DSP-based active power filter with predictive current control. *IEEE Trans. Industr. Electron.* **44**(3), 329–336 (1997)
59. J. Jerez, G. Constantinides, E. Kerrigan, An FPGA implementation of a sparse quadratic programming solver for constrained predictive control, in *Proceedings of the ACM/SIGDA International Symposium FPGA*, pp. 209–218 (2011)
60. P. Karamanakos, T. Geyer, S. Manias, Direct voltage control of DC-DC boost converters using model predictive control based on enumeration, in *Proceedings of the International Power Electronics and Motion Control Conference*, Novi Sad, Serbia (2012)
61. N. Karmarkar, A new polynomial-time algorithm for linear programming, in *Proceedings of the ACM Symposium Theory Computing*, pp. 302–311 (1984)
62. W. Karush, Minima of functions of several variables with inequalities as side constraints. Master’s thesis, University of Chicago, Chicago, IL, USA (1939)
63. R. Kennel, A. Linder, M. Linke, Generalized predictive control (GPC) – ready for use in drive applications ? in *Proceedings of the IEEE Power Electronics Specialists Conference (PESC)*, pp. 1839–1844. Vancouver, Canada (2001)
64. F. Kieferndorf, P. Karamanakos, P. Bader, N. Oikonomou, T. Geyer, Model predictive control of the internal voltages of a five-level active neutral point clamped converter, in *Proceedings of the IEEE Energy Conversion Congress and Exposition*, Raleigh, NC, USA (2012)
65. S. Kouro, P. Cortés, R. Vargas, U. Ammann, J. Rodriguez, Model Predictive Control—A Simple and Powerful Method to Control Power Converters. *IEEE Trans. Industr. Electron.* **56**(6), 1826–1838 (2009)
66. M. Kozlov, S. Tarasov, L. Khachiyan, The polynomial solvability of convex quadratic programming. *USSR Comput. Math. Math. Physics* **20**(5), 223–228 (1980)
67. P.C. Krause, O. Wasynczuk, S.D. Sudhoff, *Analysis of Electric Machinery and Drive Systems*, 2nd edn. (John Wiley & Sons Inc, New York, 2002)
68. H. Kuhn, A. Tucker, Nonlinear programming, in *Proceedings of the 2nd Berkeley Symposium Mathematical Statistics and Probability*, pp. 481–492 (1951)
69. O. Kukrer, Discrete-time current control of voltage-fed three-phase PWM inverters. *IEEE Trans. Power Electron.* **11**(2), 260–269 (1996)
70. M. Kvasnica, P. Grieder, M. Baotić, M. Morari, Multi parametric toolbox (MPT), in *Hybrid Systems: Computation and Control, LNCS*, ed. by R. Alur, G. Pappas, vol. 2993 (Springer, 2004), pp. 448–462. <http://control.ee.ethz.ch/~mpt>

71. E.L. Lawler, D.E. Wood, Branch and bound methods: A survey. *Op. Res.* **14**(4), 699–719 (1966)
72. B. Lehman, R.M. Bass, Extensions of averaging theory for power electronic systems. *IEEE Trans. Power Electron.* **11**(4), 542–553 (1996)
73. P. Lezana, R.P. Aguilera, D.E. Quevedo, Model predictive control of an asymmetric flying capacitor converter. *IEEE Trans. Industr. Electron.* **56**(6), 1839–1846 (2009)
74. A. Linder, R. Kennel, Model predictive control for electrical drives, in *Proceedings of the IEEE Power Electronics Specialists Conference (PESC)*, (Recife, Brazil, 2005), pp. 1793–1799
75. K.S. Low, X. Zhuang, Robust model predictive control and observer for direct drive applications. *IEEE Trans. Power Electron.* **15**(6), 1018–1028 (2000)
76. J.M. Maciejowski, *Predictive Control with Constraints* (Prentice-Hall, Englewood Cliffs, 2002)
77. L. Malesani, P. Mattavelli, S. Buso, Robust dead-beat current control for PWM rectifiers and active filters. *IEEE Trans. Ind. Appl.* **35**(3), 613–620 (1999)
78. S. Mariéthoz, S. Almér, M. Bâja, A. Beccuti, D. Patino, A. Wernrud, J. Buisson, H. Cormerais, H. Fujioka, T. Geyer, U. Jönsson, C.Y. Kao, M. Morari, G. Papafotiou, A. Rantzer, P. Riedinger, Comparison of hybrid control techniques for buck and boost DC-DC converters. *IEEE Trans. Control Syst. Technol.* **18**(5), 1126–1145 (2010)
79. S. Mariéthoz, A. Beccuti, G. Papafotiou, M. Morari, Sensorless explicit model predictive control of the dc-dc buck converter with inductor current limitation, in *Proceedings of the Applied Power Electronics Conference and Exposition* (2008), pp. 1710–1715
80. S. Mariéthoz, A. Domahidi, M. Morari, High-bandwidth explicit model predictive control of electrical drives. *IEEE Trans. Ind. Appl.* **48**(6), 1980–1992 (2012)
81. S. Mariéthoz, M. Morari, Explicit model predictive control of a PWM inverter with an LCL filter. *IEEE Trans. Industr. Electron.* **56**(2), 389–399 (2009)
82. P. Mattavelli, An improved deadbeat control for UPS using disturbance observers. *IEEE Trans. Industr. Electron.* **52**(1), 206–212 (2005)
83. D.Q. Mayne, J.B. Rawlings, C.V. Rao, P.O.M. Scokaert, Constrained model predictive control: Optimality and stability. *Automatica* **36**(6), 789–814 (2000)
84. L.G. Mitten, Branch-and-bound methods: General formulation and properties. *Op. Res.* **18**(1), 24–34 (1970)
85. Y.A.R.I. Mohamed, E.F. El-Saadany, An improved deadbeat current control scheme with a novel adaptive self-tuning load model for a three-phase PWM voltage-source inverter. *IEEE Trans. Industr. Electron.* **54**(2), 747–759 (2007)
86. J. Mossoba, P.W. Lehn, A controller architecture for high bandwidth active power filters. *IEEE Trans. Power Electron.* **18**(1), 317–325 (2003)
87. T. Murata, T. Tsuchiya, I. Takeda, Vector control for induction machine on the application of optimal control theory. *IEEE Trans. Industr. Electron.* **37**(4), 283–290 (1990)
88. Y. Nesterov, A method of solving a convex programming problem with convergence rate $O(1/k^2)$. *Soviet Math. Dokl.* **27**(2), 372–386 (1983)
89. Y. Nesterov, A. Nemirovskii, Interior-point polynomial algorithms in convex programming. *SIAM* (1994)
90. Y. Nishida, O. Miyashita, T. Haneyoshi, H. Tomita, A. Maeda, A predictive instantaneous-current PWM controlled rectifier with AC-side harmonic current reduction. *IEEE Trans. Industr. Electron.* **44**(3), 337–343 (1997)
91. N. Oikonomou, C. Gutscher, P. Karamanakos, F. Kieferndorf, T. Geyer, Model predictive pulse pattern control for the five-level active neutral point clamped inverter. *IEEE Trans. Ind. Appl.* **49**(6), 2583–2592, Raleigh, NC, USA (2013)
92. J. Østergaard, D.E. Quevedo, J. Jensen, Real-time perceptual moving-horizon multiple-description audio coding. *IEEE Trans. Signal Process.* **59**(9), 4286–4299 (2011)
93. G. Papafotiou, T. Geyer, M. Morari, Optimal direct torque control of three-phase symmetric induction motors, in *Proceedings of the IEEE Conference on Decision and Control*, Atlantis, Bahamas (2004)

94. G. Papafotiou, T. Geyer, M. Morari, A hybrid model predictive control approach to the direct torque control problem of induction motors (invited paper). *Int. J. Robust Nonlinear Control* **17**(17), 1572–1589 (2007)
95. G. Papafotiou, J. Kley, K.G. Papadopoulos, P. Böhren, M. Morari, Model predictive direct torque control—Part II: Implementation and experimental evaluation. *IEEE Trans. Industr. Electron.* **56**(6), 1906–1915 (2009)
96. H.S. Patel, R.G. Hoft, Generalized techniques of harmonic elimination and voltage control in thyristor inverters: Part I—Harmonic elimination. *IEEE Trans. Ind. Appl.* **9**(3), 310–317 (1973)
97. S.J. Qin, T.A. Badgwell, A survey of industrial model predictive control technology. *Contr. Eng. Pract.* **11**, 733–764 (2003)
98. D.E. Quevedo, R.P. Aguilera, M.A. Pérez, P. Cortés, R. Lizana, Model predictive control of an AFE rectifier with dynamic references. *IEEE Trans. Power Electron.* **27**(7), 3128–3136 (2012)
99. D.E. Quevedo, H. Bölskei, G.C. Goodwin, Quantization of filter bank frame expansions through moving horizon optimization. *IEEE Trans. Signal Process.* **57**(2), 503–515 (2009)
100. D.E. Quevedo, G.C. Goodwin, Control of EMI from switch-mode power supplies via multi-step optimization, in *Proceedings of the American Control Conference*, vol. 1, pp. 390–395. Boston, MA (2004)
101. D.E. Quevedo, G.C. Goodwin, Moving horizon design of discrete coefficient FIR filters. *IEEE Trans. Signal Process.* **53**(6), 2262–2267 (2005)
102. D.E. Quevedo, G.C. Goodwin, Multistep optimal analog-to-digital conversion. *IEEE Trans. Circuits Syst. I* **52**(4), 503–515 (2005)
103. D.E. Quevedo, G.C. Goodwin, J.A. De Doná, Finite constraint set receding horizon quadratic control. *Int. J. Robust Nonlin. Contr.* **14**(4), 355–377 (2004)
104. D.E. Quevedo, G.C. Goodwin, J.A. De Doná, Multistep detector for linear ISI-channels incorporating degrees of belief in past estimates. *IEEE Trans. Commun.* **55**(11), 2092–2103 (2007)
105. D.E. Quevedo, D. Nešić, Robust stability of packetized predictive control of nonlinear systems with disturbances and Markovian packet losses. *Automatica* **48**(8), 1803–1811 (2012)
106. D.E. Quevedo, J. Østergaard, D. Nešić, Packetized predictive control of stochastic systems over bit-rate limited channels with packet loss. *IEEE Trans. Autom. Control* **56**(12), 2854–2868 (2011)
107. J.B. Rawlings, D.Q. Mayne, *Model Predictive Control: Theory and Design* (Nob Hill Publishing, Madison, 2009)
108. S. Richter, C. Jones, M. Morari, Real-time input-constrained MPC using fast gradient methods, in *Proceedings of the IEEE Conference on Decision and Control*, pp. 7387–7393. Shanghai, China (2009)
109. S. Richter, S. Mariéthoz, M. Morari, High-speed online MPC based on fast gradient method applied to power converter control, in *Proceedings of the American Control Conference*, Baltimore, MD, USA (2010)
110. J. Rodríguez, P. Cortés, *Predictive Control of Power Converters and Electrical Drives*, 1 edn. (Wiley-IEEE Press, Chichester, 2012)
111. J. Rodríguez, M.P. Kazmierkowski, J. Espinoza, P. Zanchetta, H. Abu-Rub, H.A. Young, C.A. Rojas, State of the art of finite control set model predictive control in power electronics. *IEEE Trans. Industr. Inf.* **9**(2), 1003–1016 (2013)
112. J. Rodríguez, J. Pontt, C. Silva, P. Correa, P. Lezana, P. Cortés, U. Ammann, Predictive current control of a voltage source inverter. *IEEE Trans. Industr. Electron.* **54**(1), 495–503 (2007)
113. S. Saggini, W. Stefanutti, E. Tedeschi, P. Mattavelli, Digital deadbeat control tuning for dc-dc converters using error correlation. *IEEE Trans. Power Electron.* **22**(4), 1566–1570 (2007)
114. J. Scoltock, T. Geyer, U. Madawala, A comparison of model predictive control schemes for MV induction motor drives. *IEEE Trans. Industr. Inf.* **9**(2), 909–919 (2013)

115. M. Serón, G.C. Goodwin, J.A. De Doná, Characterisation of receding horizon control for constrained linear systems. *Asian J. Contr.* **5**(2), 271–286 (2003)
116. E. Sontag, Nonlinear regulation: The piecewise linear approach. *IEEE Trans. Autom. Control* **26**(2), 346–358 (1981)
117. P. Stolze, P. Landsmann, R. Kennel, T. Mouton, Finite-set model predictive control of a flying capacitor converter with heuristic voltage vector preselection, in *Proceedings of the IEEE International Conference on Power Electronics and ECCE Asia* (2011)
118. J. Sturm, Using SeDuMi 1.02, a MATLAB toolbox for optimization over symmetric cones (1998)
119. I. Takahashi, T. Noguchi, A new quick response and high efficiency control strategy for the induction motor. *IEEE Trans. Ind. Appl.* **22**(2), 820–827 (1986)
120. P. Tøndel, T.A. Johansen, A. Bemporad, An algorithm for multi-parametric quadratic programming and explicit MPC solutions, in *Proceedings of the IEEE Conference on Decision and Control*, Orlando, Florida (2001)
121. P. Tøndel, T.A. Johansen, A. Bemporad, Evaluation of piecewise affine control via binary search tree. *Automatica* **39**(5), 945–950 (2003)
122. F.D. Torrisi, A. Bemporad, Hysdel – a tool for generating computational hybrid models for analysis and synthesis problems. *IEEE Trans. Control Syst. Technol.* **12**(2), 235–249 (2004)
123. A. Wächter, L. Biegler, On the implementation of a primal-dual interior point filter line search algorithm for large-scale nonlinear programming. *Math. Program.* **106**(1), 25–57 (2006)
124. S.M. Yang, C.H. Lee, A deadbeat current controller for field oriented induction motor drives. *IEEE Trans. Power Electron.* **17**(5), 772–778 (2002)
125. Y. Zeinaly, T. Geyer, B. Egardt, Trajectory extension methods for model predictive direct torque control, in *Proceedings of the Applied Power Electronics Conference and Exposition*, pp. 1667–1674. Fort Worth, TX, USA (2011)
126. Q. Zeng, L. Chang, An advanced svpwm-based predictive current controller for three-phase inverters in distributed generation systems. *IEEE Trans. Industr. Electron.* **55**(3), 1235–1246 (2008)

Chapter 6

Application of Predictive Control in Power Electronics: An AC-DC-AC Converter System

José Rodríguez, Haitham Abu-Rub, Marcelo A. Perez
and Samir Kouro

Abstract This chapter presents an application of predictive control in power electronics. The analyzed application is an energy conversion system from alternate current (AC) to direct current (DC) and to alternate current (AC) again. This example has been carefully selected because a number of predictive control principles can be clearly explained using this topology and later expanded to a wide variety of converter topologies. The chapter includes the mathematical models and a clear presentation of the control strategies. The results show that the use of predictive control introduces a conceptually different solution which allows for the control of electrical energy without using pulse-width modulation and linear controllers.

1 Introduction

After years of development, predictive control has found increasing acceptance, particularly in the process industry [1], being considered as one of the major advances during the last two decades in the field of control theory [2].

J. Rodríguez · M. A. Perez (✉) · S. Kouro
Universidad Técnica Federico Santa María, Valparaiso, Chile
e-mail: marcelo.perez@usm.cl

J. Rodríguez
e-mail: jose.rodriguez@usm.cl

S. Kouro
e-mail: samir.kouro@usm.cl

H. Abu-Rub
Texas A and M University at Qatar, Doha, Qatar
e-mail: haitham.abu-rub@qatar.tamu.edu

Now, the scientific community is observing an increasing application of predictive control to control and transform electrical energy using power semiconductors.

The main driving forces behind this development are:

The maturity of the control theory

The field of control theory has developed a firm theoretical basis that allows for a good prediction of the behaviour for different physical systems with a high degree of accuracy and certainty.

The existence of very good models in electrical engineering

In the field of electrical engineering there are very good mathematical models to describe the behaviour of all variables of interest. By using these models it is possible to predict very precisely the future behaviour of variables like voltage, current, power, etc.

The same situation is valid for mechanical systems. In addition, the interaction of electrical variables with mechanical variables is also very well known and established through the theory of electrical machine and drives [3].

The existence of powerful microprocessors

Microprocessors are the tool that allows the calculation of the variables prediction. Today it is possible to find very powerful microprocessors in the market, that can perform a large amount of calculations at very reduced cost. In addition, these calculations can be fast enough to predict the behaviour of variables like electrical currents or voltages in real time without affecting negatively the performance of the system under control .

The attractive features of predictive control

The control community has already established several attractive features of predictive control such as: it is easy to implement and simple to understand, it works in an intuitive and logical way, it can deal very easily with non-linearities and finally, it can easily include sophisticated and diverse control laws.

About the selected example

The major part of electrical energy is generated, transmitted, distributed and finally consumed in the form of three-phase AC voltages and currents. For this reason, the control and transformation of electrical energy from a three-phase source with voltage at fixed amplitude and frequency to a three-phase load with voltages of variable amplitude and frequency is a topic of high interest.

Figure 1 presents the main structure of an indirect conversion system. This system includes the grid side converter which transforms the three-phase alternate voltages of fixed frequency and amplitude into controlled direct voltage when a capacitive DC link is used as shown in the figure. Machine side converter transforms the DC voltage into three-phase alternate voltages of variable amplitude and frequency.

This conversion system has a wide variety of applications in different productive areas like:

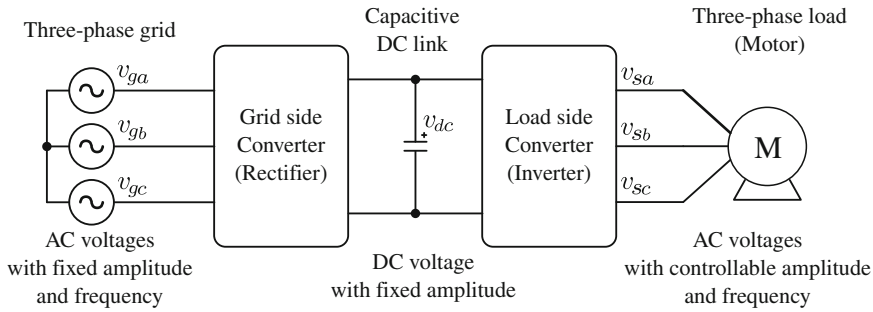


Fig. 1 Basic structure of an AC-DC-AC power converter

Energy	Energy transmission, renewable energies (wind and photovoltaic), etc.
Transportation	Trains, conveyor belts, electric trucks, cars, etc.
General industries	Pumps, shovels, laminators, industrial robots, etc.

This converter system was carefully selected to present the predictive control application due to its very general nature. In effect, the analysis, design procedures and conclusions obtained from this converter can be easily extended and used in a wide variety of different converter topologies.

2 The AC-DC-AC Conversion System

There are different ways to achieve the transformation from alternating current into direct current and to alternating current again. In Figs. 2 and 3 two conversion systems with diode and thyristor bridges respectively as grid side converter are shown.

The grid side converter presented in Fig. 2 allows for power flow exclusively from the AC source to the DC link, in consequence this converter system is suitable for applications where the energy flows only from the three-phase source to the three-phase load. If regenerative braking is required a DC-DC chopper with a resistive load is added to the DC link. In spite of this restriction, this topology is widely used in a number of industrial applications with unidirectional power flow: fans, blowers, pumps, etc. Among its main characteristics are the simple and reliable structure and the fixed, but not controllable, DC voltage. The main disadvantage is the high harmonic content of the input current requiring large input filters or multi-pulse configurations to reduce current harmonics and comply with standards. Additionally, although the fundamental component of the current is in phase with the input voltage the distortion factor produced by the harmonic content reduces the power factor.

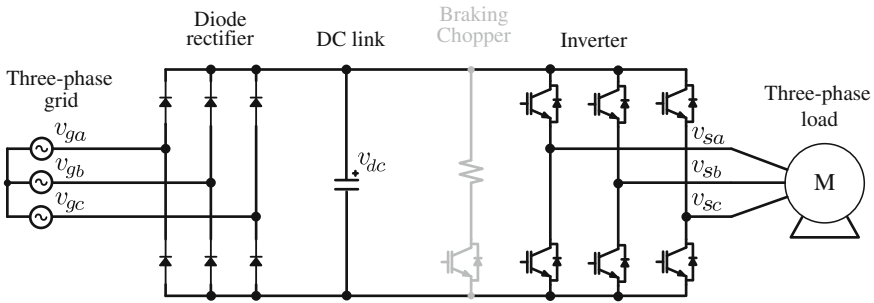


Fig. 2 Topologies for AC-DC-AC conversion: diode rectifier at the input

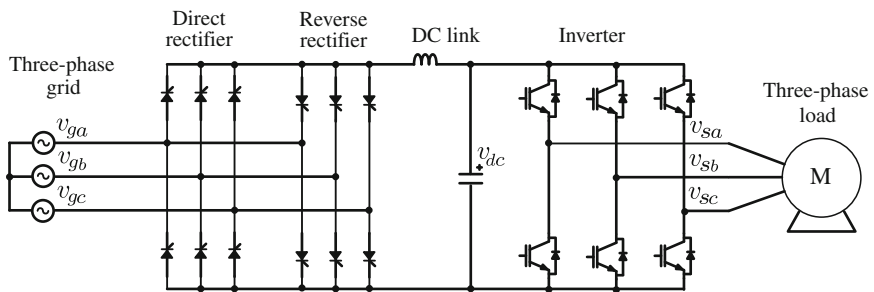


Fig. 3 Topologies for AC-DC-AC conversion: thyristor rectifier at the input

The topology presented in Fig. 3 uses two thyristor rectifiers in anti-parallel connection at the grid side. The direct rectifier transfers energy from the three phase-source to the load, while the reverse rectifier permits the flow of energy from the load to the three-phase source, what is called regenerative operation. This converter topology is suited for loads with regenerative capability such as shovels, trucks, mills, downhill conveyors, etc. This topology is much more complex than the diode bridge and is prone to failure during its operation, particularly in the regenerative mode. The thyristor rectifier provides control over the DC voltage, but the harmonic content is higher than diode bridge. The power factor is usually lower than the diode bridge because the DC voltage control is performed changing the firing angle and consequently modifying the angle between the current and voltage.

2.1 General Description of the Back-to-Back Converter

Although the two grid side topologies shown in the previous section have been used for years in machine drives, a third alternative called back-to-back converter has been increasing its industrial application. This converter has reduced input

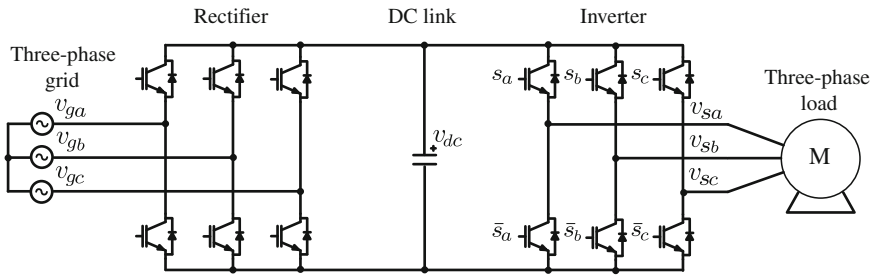


Fig. 4 Back-to-back topology for AC-DC-AC conversion

current harmonics, bidirectional power flow, operation with variable input power factor and controllable DC voltage.

The back to back converter topology is shown in Fig. 4. The output stage is composed, as usual, by a six fully controlled semiconductors arranged to form a three phase bridge but, in this case, the rectifier has the same topology of the inverter resulting in a completely symmetrical topology.

The inverter generates an output voltage whose fundamental component is variable in frequency and amplitude. To provide this output voltage the inverter assumes a regulated DC voltage. The rectifier must provide this regulated DC voltage and take care of the input active and reactive power. The control system must manage all these control objectives.

The predictive control of this back-to-back topology will be presented, analysed and designed in this chapter.

2.2 Classical Control of Power Converters

There are several linear control methods to control the back-to-back converter proposed in the literature, where usually the control of the inverter is considered separately from the control of the rectifier. In this section some of the classical methods to control back-to-back converters are reviewed.

2.2.1 Field Oriented Control

The inverter must control the output voltages and currents in terms of amplitude and frequency. When the load is a machine the control objective is the flux and torque and, usually in an external loop, the speed. One of the fundamental methods to control machines is the flux oriented control. In this control scheme, the currents are controlled in a rotating frame aligned with the flux. Therefore, the flux amplitude and torque are decoupled and can be controlled independently by the direct and quadrature current components.

The dynamical equation of the stator of an electrical machine is

$$\mathbf{v}_s = r_s \mathbf{i}_s + \frac{d\boldsymbol{\Psi}_s}{dt} \quad (1)$$

The dynamical equation of the rotor of an squirrel cage induction machine is

$$0 = r_r \mathbf{i}_r + \frac{d\boldsymbol{\Psi}_r}{dt} \quad (2)$$

The flux linkages are defined as

$$\boldsymbol{\Psi}_s = l_s \mathbf{i}_s + l_m \mathbf{i}_r \quad (3)$$

$$\boldsymbol{\Psi}_r = l_m \mathbf{i}_s + l_r \mathbf{i}_r \quad (4)$$

Expressing the rotor equation in terms of rotor flux and stator current and using a rotating coordinate transformation, the rotor flux equations can be written as

$$\frac{r_r}{l_r} l_m i_d = \frac{r_r}{l_r} \psi_{rd} - \omega_r \psi_{rq} + \frac{d\psi_{rd}}{dt} \quad (5)$$

Aligning this system with the rotor flux $\psi_{rq} = 0$, $\psi_{rd} = \Psi_r$, the dynamical equation of the rotor flux becomes

$$\frac{d\Psi_r}{dt} + \frac{r_r}{l_r} \Psi_r = \frac{r_r}{l_r} l_m i_d \quad (6)$$

The electromagnetic torque can be expressed as

$$T_e = \frac{p l_m}{2 l_r} \mathbf{i}_s \times \boldsymbol{\Psi}_r \quad (7)$$

Expressing the torque equation in the coordinate transformation

$$T_e = \frac{p l_m}{2 l_r} (i_q \psi_{rd} - i_d \psi_{rq}) \quad (8)$$

Aligning this system to the rotor flux, the torque can be expressed as

$$T_e = \frac{p l_m}{2 l_r} \Psi_r i_q \quad (9)$$

It is clear from expressions (6) and (9) that the flux amplitude can be controlled by the direct component of the stator current i_d and, if the rotor flux dynamics is considered slower than the current, the torque can be controlled by the quadrature component i_q of the same current. Figure 5 shows the FOC scheme where, after a coordinate rotation, the direct and quadrature component of the stator currents are controlled by two independent PI controllers. The reference of the torque (quadrature current component) is given by an external speed controller. The stator voltage reference generated by the current controllers is transformed to the original

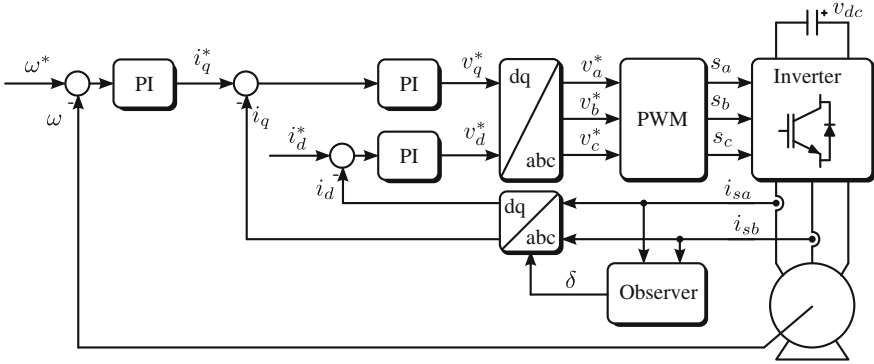


Fig. 5 Classical control of inverters: field oriented control

coordinate system, then they are modulated and sent as gating signals to the inverter. It can be noticed that an observer is required to obtain the angle for the coordinate transformation.

There are two main pulse width modulation (PWM) schemes used in industrial drives: the carrier based modulation and space vector modulation. The carrier based modulation uses a high frequency triangular carrier which is compared to the reference and directly generates the gating signals. The references must be in three-phase coordinates and the frequency of the carrier defines the frequency of the output harmonics. This modulation is very simple to implement both in analogical or digital technology.

The space vector modulation uses a vector representation of the reference voltage and the possible voltages generated by the converter. In each sample time the reference voltage is synthesized by the three nearest vectors the inverter can generate. The time in which each vector must be applied is calculated using geometric relationships between these vectors. The gating signals are generated combining the selected vector and the time each one must be applied in a given sequence. This sequence can be arbitrary defined, for example, to reduce switching frequency or to keep the symmetry of the pulse pattern. This modulation technique is more complex than carried based modulation, requiring digital implementation, but it brings better utilization factor and more control over the pulse pattern.

2.2.2 Direct Torque Control

Another well establish drive control method is direct torque control. This control scheme uses the model of the rotor dynamics Eq. (2), but in this case the rotor equation is expressed in terms of stator flux amplitudes as

$$r_r \frac{l_s \Psi_r}{l_s l_r - l_m^2} + \frac{d\Psi_r}{dt} = r_r \frac{l_m \Psi_s}{l_s l_r - l_m^2} \tag{10}$$

The torque can be expressed in terms of flux amplitudes as

$$T_e = \frac{p}{2} \frac{l_m}{l_s l_r - l_m^2} \Psi_s \Psi_r \sin(\delta) \quad (11)$$

From the previous expressions (10) and (11), the rotor flux amplitude can be controlled by the stator flux amplitude and, considering that rotor flux has slower dynamic than stator flux, the torque can be controlled by the angle of the stator flux vector. From the stator equation, neglecting the stator losses, the stator flux can be approximated in one sample time T_s by

$$\Delta \Psi_s \approx \mathbf{v}_s T_s \quad (12)$$

where \mathbf{v}_s is the voltage vector generated by the converter which can have only a finite number a possibilities. Each one of these switching states will have a different effect in both, the amplitude and angle of the stator flux and, therefore, generates a different combination of changes in rotor flux and torque. All these combinations can be listed in a table and, depending on the errors in torque and flux amplitude, and the angle of the rotor flux, they can be addressed to generate the proper switching signals.

The complete scheme of DTC is shown in Fig. 6. To generate the errors of torque and flux hysteresis controllers are used. It is worth to note that torque has a double-band hysteresis block in order to minimize the torque ripple. The torque reference, as well as FOC is generated by an external speed controller. The main advantage of this scheme is that it does not require the parameters of the drive. Its main drawback is the variable switching frequency. However, it is possible to keep the switching frequency in a defined range by changing the width of the hysteresis bands.

2.2.3 Voltage Oriented Control

The rectifier control schemes are closely related to the inverter control schemes. The control must regulate the DC voltage adjusting the input current reference. The active rectifier can provide independent active and reactive power, therefore, this reference must be also modified to control the reactive power. The main difference between the grid side and the load side converter is the operation at constant frequency, which is fixed by the grid voltage.

The model of the grid side converter is

$$\mathbf{v}_g = r_s \mathbf{i}_g + L_s \frac{d\mathbf{i}_g}{dt} + \mathbf{v}_r \quad (13)$$

where \mathbf{v}_g is the grid voltage, \mathbf{i}_g is the grid current and \mathbf{v}_r is the rectifier voltage.

Using a coordinate transformation the dynamic model becomes

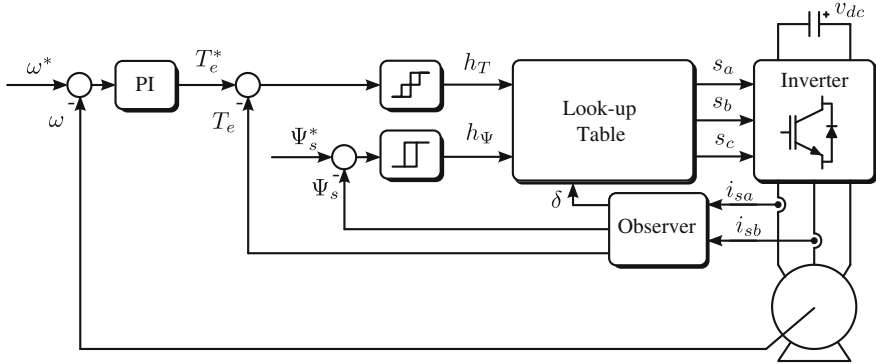


Fig. 6 Classical control of inverters: direct torque control

$$v_{gd} = r_s i_d + L_s \omega_s i_q + L_s \frac{di_d}{dt} + \mathbf{v}_{rd} \quad (14)$$

$$v_{gq} = r_s i_q - L_s \omega_s i_d + L_s \frac{di_q}{dt} + \mathbf{v}_{rq} \quad (15)$$

Since the amplitude and frequency of the input voltage can be considered constant, a compensation of the input voltage and the coupled terms can be added as feed-forward terms, resulting

$$L_s \frac{di_d}{dt} + r_s i_d = -v_{rd} \quad (16)$$

$$L_s \frac{di_q}{dt} + r_s i_q = -v_{rq} \quad (17)$$

The instantaneous active and reactive power in the rotating frame can be written as

$$p_s = v_{gd} i_d + v_{gq} i_q \quad (18)$$

$$q_s = v_{gd} i_q - v_{gq} i_d \quad (19)$$

Considering the coordinate transformation aligned with the input voltage $v_{gd} = V_g$ and $v_{gq} = 0$ these powers can be written

$$p_s = V_g i_d \quad (20)$$

$$q_s = V_g i_q \quad (21)$$

Therefore, from the previous expressions, the active and reactive power can be controlled by the direct and quadrature components of the grid current. This control technique is called VOC and can be seen that is very similar to FOC, where each current component controls one output variable - torque and flux in FOC and

replacing with the definition of active and reactive power

$$L_s \frac{dp_s}{dt} + r_s p_s + L_s \omega_s q_s = \mathbf{v}_g^T \mathbf{v}_g - \mathbf{v}_g^T \mathbf{v}_r \quad (26)$$

$$L_s \frac{dq_s}{dt} + r_s q_s - L_s \omega_s p_s = -\mathbf{v}_g^T \mathbf{J} \mathbf{v}_r \quad (27)$$

Applying a compensation of the input voltage and coupled terms and writing in terms of amplitudes gives

$$L_s \frac{dp_s}{dt} + r_s p_s = -V_g V_r \cos(\delta) \quad (28)$$

$$L_s \frac{dq_s}{dt} + r_s q_s = -V_g V_r \sin(\delta) \quad (29)$$

From the previous expressions it is possible to note that both active and reactive power change depending on the angle between the input voltage and the rectifier voltage. The rectifier can generate only a finite number of voltages, and each voltage has a different effect on both powers. In this case, just like in DTC, it is possible to store all the switching states in a table and, depending on the error in active and reactive power, to apply the switching state that makes the power to follow the references. This method is called Direct Power Control (DPC) [4] and is very similar to DTC as shown in Fig. 8. The active and reactive power errors are obtained by hysteresis blocks. The active power reference, as well as in VOC, is obtained from an external DC voltage PI controller. An observer is required to obtain the angle reference to perform the coordinate transformation.

3 Principle of Predictive Control in Power Electronics

Model predictive control has several advantages when it is applied in power electronics applications. The well known models, the finite number of the converter states and the flexibility of the cost function, make this control strategy very well suited for power electronics.

In this section the predictive control principle, its algorithm and how to include it into the converter control scheme will be explained.

3.1 The Basic Idea

The basic idea behind predictive control is to predict the behaviour of the complete drive using a mathematical model of it. The predicted variables are calculated for each one of the possible switching states of the converter and evaluated in a cost

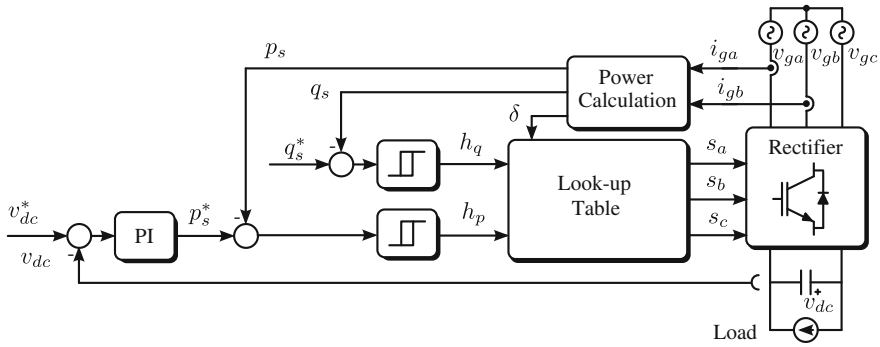


Fig. 8 Classical control of rectifiers: direct power control

function which describes the control objectives. The switching state that minimize this cost function is selected and applied to the converter in the next sample time.

Predictive control can be used to control inner variables such as currents, directly replacing the linear or hysteresis controllers as shown in Fig. 9. In the next sections this example will be developed and more advanced predictive control schemes will be discussed.

3.2 Why Predictive Control is Suitable for Power Electronics

As stated in the introduction, predictive control has been already used in the process industry. However its introduction to power electronics, although recent, seems to have high impact. There are several reasons for this effect:

Established and well known models

The models in power electronics are basically electrical machines (induction, synchronous, permanent magnets, etc.) whose physical models have been widely studied. Other loads correspond to combinations of resistive, inductive and capacitive elements.

Finite set of input variables

Power converters are composed by semiconductors operating in short-circuit and open-circuit. Therefore, it always exists a finite number of possible combination of these switching states. This characteristic greatly simplifies the application of predictive control because a direct evaluation is used instead of continuous optimization.

Cost function definition

The cost function directly represents the control objective of the system, which is usually to follow the currents, voltages, power, torque, flux or another reference. However, additional aspects such as commutation losses, common mode voltages,

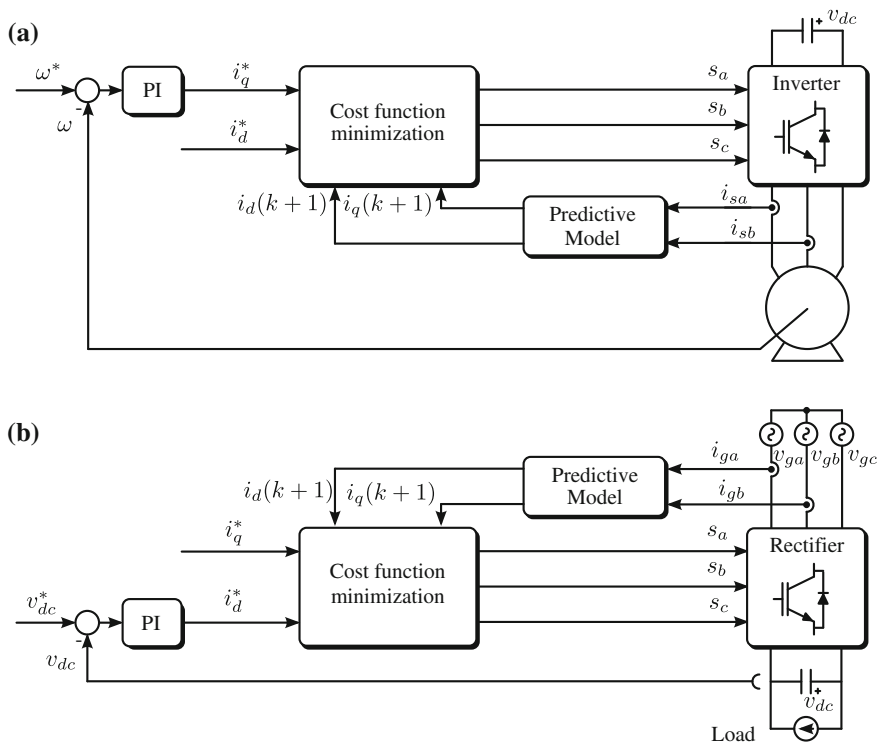


Fig. 9 Model predictive control **a** Inverter, **b** Rectifier

switching frequency and others, can be included. Furthermore, non-linear operation, such as restrictions can be easily added.

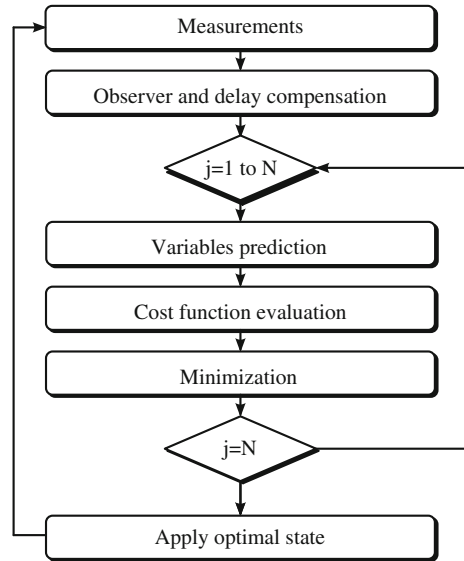
Processing capability

New digital processors have increased their calculation capability to afford high demanding tasks such as video processing. This huge calculation capability allows the implementation of sophisticated control strategies such as predictive control, without any negative effect on the performance.

3.3 Predictive Algorithm

The algorithm of predictive control is shown in Fig. 10. This algorithm is the same in all the predictive control schemes, because if the plant changes only the model must be adjusted, if the converter changes, just the switching states evaluation must be adjusted and, if the control objective changes, only the cost function must be modified accordingly.

Fig. 10 Model Predictive Control algorithm



The algorithm starts with the measurements of variables at the beginning of the sampling time. Then, if it necessary, delay compensation and observers to obtain non measured variables are implemented. Once all the variables are available, the model is evaluated for the first switching state. The predicted variables are used in the cost function whose resulting value is kept if it is minimum or dropped if not. The loop is repeated for all the switching states. Once all the switching states were evaluated the optimal one is selected and applied to the load. This implementation is well suited for processors that work sequentially. If the hardware is capable of parallel processing, the model evaluation, cost function and minimization can be performed in parallel.

4 Mathematical Models for Predictive Control

The majority of the models used in predictive control are based on physical phenomena with well developed mathematical models. Among the variables used in predictive control can be mentioned electrical and mechanical variables such as electrical charges, magnetic fluxes, currents, voltages, power, torque, speed, heat and temperature.

In this section, different models to control the back-to-back converter by means of predictive algorithm will be presented.

4.1 Load Side Model

From the stator Eq. (1), neglecting the derivative of the rotor current and using the coordinate transformation, the dynamic equation of the stator current is given by

$$l_s \frac{d\mathbf{i}_s}{dt} + r_s \mathbf{i}_s + \omega l_s \mathbf{J}_{dq} \mathbf{i}_s = \mathbf{v}_s \quad (30)$$

From the rotor flux expression, the dynamic behaviour of the rotor flux is

$$\frac{d\Psi_r}{dt} + \frac{r_r}{l_r} \Psi_r = \frac{r_r}{l_r} l_m i_{sd} \quad (31)$$

and the torque is

$$T_e = \frac{p}{2} \frac{l_m}{l_r} \Psi_r i_{sq} \quad (32)$$

Using a forward Euler discretization gives

$$i_{sd}(k+1) = \left(1 - T_s \frac{r_s}{l_s}\right) i_{sd}(k) - T_s \omega(k) i_{sq}(k) + \frac{T_s}{l_s} v_{sd}(k) \quad (33)$$

$$i_{sq}(k+1) = \left(1 - T_s \frac{r_s}{l_s}\right) i_{sq}(k) + T_s \omega(k) i_{sd}(k) + \frac{T_s}{l_s} v_{sq}(k) \quad (34)$$

$$\Psi_r(k+1) = \left(1 - \frac{r_r}{l_r} T_s\right) \Psi_r(k) + T_s \frac{r_r}{l_r} l_m i_{sd}(k+1) \quad (35)$$

$$T_e(k+1) = \frac{p}{2} \frac{l_m}{l_r} \Psi_r(k+1) i_{sq}(k+1) \quad (36)$$

These four last discrete equations are used to model the complete drive. The first two equations predict the stator current requiring the measurement of the actual current. The third equation calculates the prediction of the rotor flux. It is worth to note that this prediction requires an observer of the rotor flux. The last equation is the evaluation of the torque prediction.

4.2 Grid Side Model

The active and reactive instantaneous power are calculated as

$$p_s = \mathbf{v}_g^T \mathbf{i}_g \quad (37)$$

$$q_s = \mathbf{v}_g^T \mathbf{J} \mathbf{i}_g \quad (38)$$

This calculation can be performed in three-phase stationary frame, as well as, in the rotating frame. The matrix used to calculate the cross product must be modified accordingly. The dynamic model of the current is

$$L_s \frac{d\mathbf{i}_g}{dt} + r_s \mathbf{i}_g = \mathbf{v}_g - \mathbf{M} \mathbf{s} v_{dc} \quad (39)$$

where \mathbf{M} is a matrix used to calculate the common mode voltage generated by the rectifier. Using a forward Euler discretization gives

$$\mathbf{i}_g(k+1) = \left(1 - T_s \frac{r_s}{L_s}\right) \mathbf{i}_g(k) + \frac{T_s}{L_s} (\mathbf{v}_g(k) - \mathbf{M} \mathbf{s}(k) v_{dc}) \quad (40)$$

$$p_s(k+1) = \mathbf{v}_g^T(k) \mathbf{i}_g(k+1) \quad (41)$$

$$q_s(k+1) = \mathbf{v}_g^T(k) \mathbf{J} \mathbf{i}_g(k+1) \quad (42)$$

From the first equation, the current prediction is calculated. The last two equations calculate the predictions of the powers.

4.3 Power Converter Model

The converter structure will influence the calculation of the predictive algorithm defining the switching states in which the model must be evaluated.

This is one of the most attractive characteristics of model predictive control because, if in a given application the converter is changed, the model is still the same but it must be now evaluated in the switching states the new converter generates. No matter how complex the converter could be, always there will be a finite number of switching states associated with it.

The back-to-back converter is composed by two three-phase two-level converters which have the switching states given in the Table 1. From this table it is possible to obtain the converter voltages applied to the AC side v_{ra} , v_{rb} and v_{rc} and the converter current injected to the DC side i_r . The predictive models of load side and grid side obtained in the previous sections must be evaluated at these switching states.

5 Control Objectives

There are several control objectives in the back-to-back converter depending on the control implementation. For example, if the predictive control is designed to replace the linear controllers, current error minimization will be the control objective. However, if the model of the torque and flux are directly included in the

Table 1 Switching states of three-phase two-level converters

Switching state	s_a	s_b	s_c	v_{ra}	v_{rb}	v_{rc}	v_0	i_r
s_0	0	0	0	0	0	0	v_0	0
s_1	0	0	1	0	0	v_{dc}	v_1	i_{sc}
s_2	0	1	0	0	v_{dc}	0	v_2	i_{sb}
s_3	0	1	1	0	v_{dc}	v_{dc}	v_3	$i_{sb} + i_{sc}$
s_4	1	0	0	v_{dc}	0	0	v_4	i_{sa}
s_5	1	0	1	v_{dc}	0	v_{dc}	v_5	$i_{sa} + i_{sc}$
s_6	1	1	0	v_{dc}	v_{dc}	0	v_6	$i_{sa} + i_{sb}$
s_7	1	1	1	v_{dc}	v_{dc}	v_{dc}	v_7	$i_{sa} + i_{sb} + i_{sc}$

control strategy, then the control objective will be the error minimization of these two variables. Moreover, if the speed is modelled, then the speed error and the current-to-torque ratio must be minimized.

The cost function in predictive control can contain not only the main control objective, but other operational aspects can be included. For example, to minimize the common mode voltage, to reduce or to fix the switching frequency, to minimize the losses, to reduce THD, etc., giving a high flexibility in this aspect.

In this section a comprehensive review of different control objectives applied in the back to back converter are shown.

5.1 Machine Current Controllers

The simplest form to include predictive control in machine drives is to control the stator currents. The model of currents is a first order model and, if no compensation is required, it does not require observers. The cost function to reach this control objective is

$$G = (i_{d,\text{pred}} - i_{d,\text{ref}})^2 + (i_{q,\text{pred}} - i_{q,\text{ref}})^2 \quad (43)$$

where $i_{d,\text{pred}}$ is the predicted value of i_d .

5.2 Torque and Flux Controllers

If predictive control is used to control the torque and flux, the cost function is

$$G = (T_{\text{pred}} - T_{\text{ref}})^2 + \lambda_\psi (\psi_{\text{pred}} - \psi_{\text{ref}})^2 \quad (44)$$

where λ_ψ is a weighting factor used to give relative importance to one of the error terms. This weighting factor is a design parameter.

5.3 Grid Current Controllers

In the rectifier, just as the inverter, predictive control can be used to replace the current controllers using the following cost function

$$G = (i_{d,\text{pred}} - i_{d,\text{ref}})^2 + (i_{q,\text{pred}} - i_{q,\text{ref}})^2 \quad (45)$$

It can be noticed that this equation has the same structure of the machine current controller cost function.

5.4 Direct Power Controllers

To control the instantaneous input active and reactive power the following cost function can be used

$$G = (p_{s,\text{pred}} - p_{s,\text{ref}})^2 + (q_{s,\text{pred}} - q_{s,\text{ref}})^2 \quad (46)$$

5.5 DC Voltage Controllers

The DC voltage can be also included in the predictive algorithm using the cost function

$$G = (p_{s,\text{pred}} - p_{s,\text{ref}})^2 + (q_{s,\text{pred}} - q_{s,\text{ref}})^2 + \lambda_{dc} (v_{dc,\text{pred}} - v_{dc,\text{ref}})^2 \quad (47)$$

In this expression the terms associated with the DC voltage and the active power are heavily related. Therefore, an internal algorithm to adjust the required active power reference must be included [5].

5.6 Restrictions and Constraints

One of the aspects where predictive control shows its flexibility is in the inclusion of non linear elements in it. For example, restrictions can be added simply by using a logical function as

$$G = \lambda_{lim} (i_{d,\text{pred}} > i_{lim}) \quad (48)$$

The value of λ_{lim} must be large enough to avoid the minimization algorithm to select the state if it is higher than the limit.

5.7 Advanced Control Objectives

In predictive control it is possible to include other operational issues which are not directly related to the main control objective, but could improve another features. This is possible due to the optimization stage in which no matter what the structure is and the number of terms of the cost function, the algorithm always find the optimum value.

For example, the common mode voltage can be minimized if a suitable model of it is included and the respective term is added to the cost function [6] as

$$G = (v_{cm,pred})^2 \quad (49)$$

with

$$v_{cm,pred} = \frac{v_{sa} + v_{sb} + v_{sc}}{3} \quad (50)$$

Also the switching frequency can be controlled using [7] the following term in the cost function

$$G = (i_{de,pred})^2 + (i_{qe,pred})^2 \quad (51)$$

where $i_{de,pred}$ and $i_{qe,pred}$ are the filtered value of the currents.

Finally, it is possible to add to the cost function a term related with the total harmonic distortion, eliminating or mitigating the harmonic content [8].

$$G = \sum_{i=0}^N \lambda_i \text{SDFT} |(v_{s,pred} - v_{s,ref})| \quad (52)$$

where the function SDFT() is the Sliding Discrete Fourier Transform, calculated for each one of the harmonics that will be minimized. It is important to note that the harmonics are not simply minimized, but they are assigned with a fixed value. In this way the switching frequency is not heavily increased and the converter still comply with harmonics regulations.

5.8 Predictive Control Results

The results of a back-to-back system with an inverter using Predictive Torque Control and a rectifier using Predictive Power Control are shown in Fig. 11. The initial condition of the inverter is a speed reference of 1,500 RPM with a nominal torque of +100 Nm and a nominal output frequency of 50 Hz. At $t = 0.05$ s the speed reference is changed from 1,500 to $-1,500$ RPM. The PI controller generates a negative reference torque which is saturated at -220 Nm. At $t = 0.25$ s the speed is completely reversed and the torque is set at -100 Nm. During the complete operation

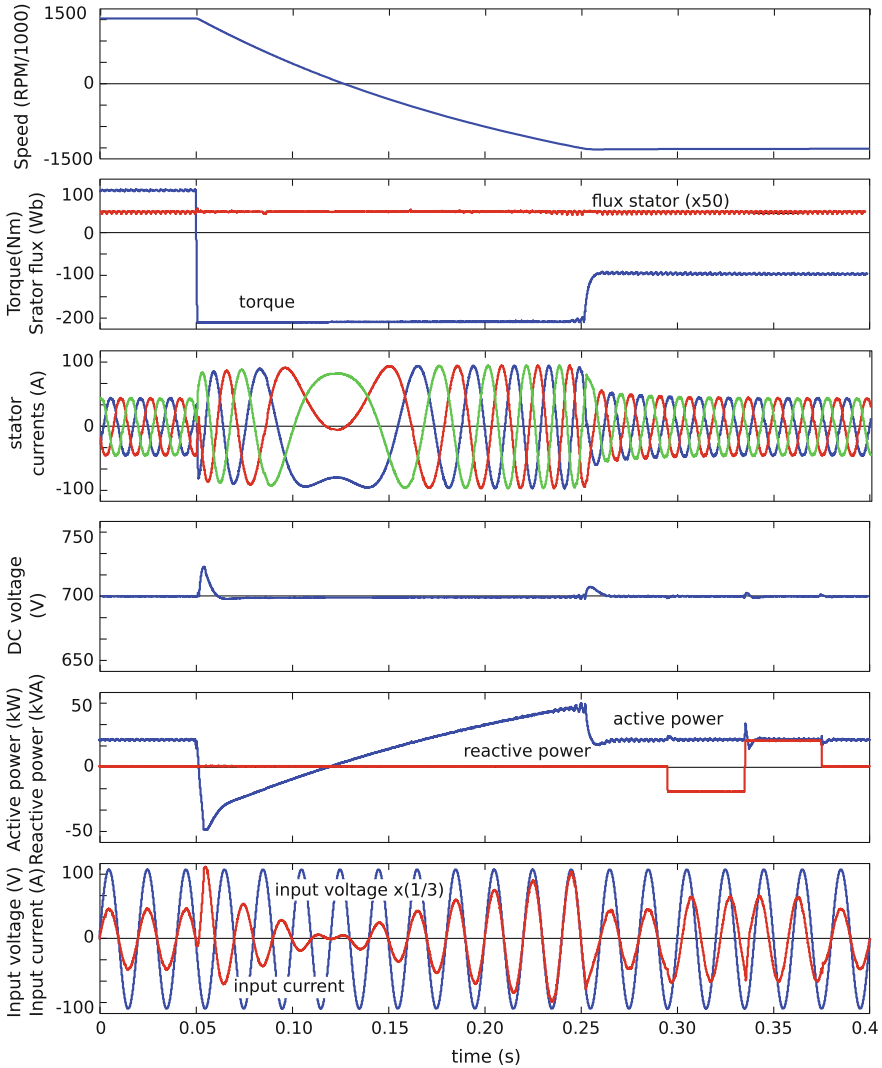


Fig. 11 Model predictive control of the inverter and the rectifier

the flux is kept constant. The DC voltage has small disturbances when the speed change starts and ends however it is kept fixed at its reference value of 700 V. The rectifier delivers initially +25 kW nominal at unity power factor. At $t = 0.05$, when the machine is braking, the power is reversed reaching a peak of -50 kW. When the machine is accelerated in the reverse direction, the power reach a positive peak of +50 kW. When the reversal speed is set the power is set again at the +25 kW. During the entire operation the reactive power reference is zero keeping the current in phase with the voltage. At $t = 0.295$ s the reactive power reference is set at -25 kVA

displacing the current in a lagging angle. At $t = 0.335$ s the reactive power reference is changed to +25 kVAr and the current is accordingly displaced to a leading angle.

6 Digital Implementation

Digital processors are used for control purposes from the early 1980s where the digital signal processors (DSP) and field programmable gate array (FPGA) appear. Their capabilities also includes analogical to digital signal conversion, digital filter implementation, sequential and parallel processing making use of an ever increasing number of mathematical and logical functions. In industrial power electronics converters, digital controllers are steadily used from the 1990s. They are in charge of tasks such as handling of signal acquisition, carrier generation and modulation, filtering and control algorithm implementation. The control algorithm includes PI controller, observers and estimators which are usually digital implementations of their linear counterpart. Nowadays, digital processors are designed to develop intense calculation tasks, such as, audio, image and video processing. Therefore, there exists a large processing capability gap between processor calculation capability and the requirements of power electronics applications. This increasing processing capability has pushed the development and implementation of more complex controller structures, such as fuzzy logic, genetic algorithms and model predictive control.

6.1 Delay Time Compensation

From the algorithm description it is clear that the optimization is performed with the variables measured in time k , but the controller sends the gating signal at time $k + 1$. This can be neglected when the dynamics of the variables are slower compared to the sample time. Unfortunately, electric variables such as currents and voltages are fast compared to the currently available processors, therefore a compensation of the time delay must be included.

This delay compensation consists on making an estimation of the predicted variables at the next sample time $k + 1$ using the switching state applied in that moment. With these estimated values the prediction is now evaluated in time $k + 2$, therefore, the optimization will give a result valid for the time in which it will be applied [9].

6.2 Forward Prediction

It is possible to perform the prediction of the states using an extended prediction horizon in order to improve the dynamic response, but more important to improve the steady state response, in particular the steady state error [10].

7 Conclusions

The advances in modern control theory and in microprocessors have made it possible to apply MPC in power electronics and drives in a natural and simple way. The results shown in this chapter demonstrate that, in principle, MPC allows for high quality control of AC-DC-AC converters. This method shows a behaviour similar to well established linear controllers. However, there are a number of aspects that must be clarified in the near future in order to bring MPC to industrial application in drives. First, a rigorous comparison with the existing techniques must be done in order to assess the possible advantages of MPC in terms of performance and simplicity. In addition, the design procedure for MPC must be improved to a more simple and systematic form, as other standard control strategies typically are. In particular, a simpler and more systematic procedure must be found to calculate the weighting factors used in the cost functions. With the research results obtained so far, MPC has proved to be a modern, attractive and competitive alternative for the control of electrical energy using power semiconductors.

Acknowledgment Part of this work was supported by NPRP grant No. 4-077-2-028 from the Qatar National Research Fund (a member of Qatar Foundation). In addition, we also acknowledge support from Universidad Técnica Federico Santa María. The statements made herein are solely the responsibility of the authors.

References

1. M. Morari, J.H. Lee, Model predictive control: past, present and future. *Comput. Chem. Eng.* **23**, 667–682 (1999)
2. J.H. Lee, Model predictive control: review of the three decades of development. *Int. J. Control Autom. Syst.* **9**(3), 415–424 (2011)
3. E. Fuentes, R. Kennel, Finite-set model predictive control of the two-mass-system, in *2011 Workshop on Predictive Control of Electrical Drives and Power Electronics (PRECEDE)*, pp. 82–87 (2011)
4. M. Malinowski, M. Kazmierkowski, S. Hansen, F. Blaabjerg, G. Marques, Virtual-flux based direct power control of three-phase pwm rectifiers. *IEEE Trans. Ind. Appl.* **37**(4), 1019–1027 (2001)
5. D. Quevedo, R. Aguilera, M. Perez, P. Cortes, R. Lizana, Model predictive control of an afc rectifier with dynamic references. *IEEE Trans. Power Electron.* **27**(7), 3128–3136 (2012)
6. R. Vargas, U. Ammann, J. Rodríguez, J. Pontt, Predictive strategy to control commonmode voltage in loads fed by matrix converters. *IEEE Trans. Ind. Electron.* **55**(12), 4372–4380 (2008)
7. P. Cortes, J. Rodríguez, D. Quevedo, C. Silva, Predictive current control strategy with imposed load current spectrum. *IEEE Trans. Power Electron.* **23**(2), 612–618 (2008)
8. H. Aggrawal, J. Leon, L. Franquelo, S. Kouro, P. Garg, J. Rodríguez, Model predictive control based selective harmonic mitigation technique for multilevel cascaded h-bridge converters. in *IECON 2011—37th Annual Conference on IEEE Industrial Electronics Society*, pp. 4427–4432 (2011)
9. P. Cortes, J. Rodríguez, C. Silva, A. Flores, Delay compensation in model predictive current control of a three-phase inverter. *IEEE Trans. Ind. Electron.* **59**(2), 1323–1325 (2012)
10. T. Geyer, Model predictive direct current control: formulation of the stator current bounds and the concept of the switching horizon. *IEEE Ind. Appl. Mag.* **18**(2), 47–59 (2012)

Chapter 7

Application of the Long-Horizon Predictive Control to the Drive System with Elastic Joint

Krzysztof Szabat, Piotr Serkies and Teresa Orłowska-Kowalska

Abstract In the paper a robust Model Predictive Control structure for speed regulation of a drive system with an elastic transmission is proposed. A methodology for robust design based on suitable selection of the explicit form of MPC which enables the drive's safety and physical limitations to be directly incorporated into control synthesis is presented. The simulation results show that the controller is very effective in regulating load speed for a wide-range of the changes of the load side inertia. The simulation studies are confirmed through a variety of experimental tests.

1 Introduction

Torsional vibrations are evident in many industrial drive systems: starting from traditional rolling-mill drives, conveyer belt drives, machines for paper and textile industry, deep space antenna drives, the wind-mill generator and modern servo drives and robotic applications (including space robots) [1–11, 12]. The flexible modes affect the performances of the drive, and in some situations can even lead to the failure of the entire drive system. There are many control structures designated for drive systems with an elastic coupling. Structures with the simplest PI/PID controllers, systems with additional feedback(s) from the internal state variable(s), Resonance Ratio Control, state controller structures, sliding-mode, fuzzy logic, adaptive control and model predictive control structure and many more have been successfully used [1–11, 12].

Recently, the MPC control techniques have attracted a lot of attention [13–19]. The MPC algorithm adapts to the current operation point of the process generating

K. Szabat (✉) · P. Serkies · T. Orłowska-Kowalska
Institute of Electrical Machines Drives and Measurements, Wrocław University
of Technology, Wybrzeże Wyspiańskiego 27, Wrocław, Poland
e-mail: krzysztof.szabat@pwr.wroc.pl

an optimal control signal. The biggest advantage of the model predictive control strategy is that the physical and safety constraints of the drive can be directly and systematically incorporated into the control problem formulation so that future constraint violations are anticipated and prevented. There are two common ways of implementation of MPC algorithms. The direct framework relies on the on-line solving of optimization problems. This strategy can be computationally intensive for systems with fast sampling requirements, especially for a relatively long prediction horizon. In another possible approach optimization problems are solved off-line using multi-parametric programming. Since the controller in its explicit form is defined as a piecewise affine function of the initial state, the implementation can be performed via a simple look up table without the complex and computationally demanding numerical optimization [14–19].

The state-of-the-art of currently employed predictive control methods in power electronics and motion control sector is given in [19]. In general they can be divided into two groups: short- and long- horizon MPC [19–26]. The first framework is much less complicated, as the prediction horizon is set to be between 1 or 3 samples. This reduces the calculation complexity significantly, yet it decreases the performance of the controller. It is usually applied in power electronics and sometimes in motion control. The long-horizon MPC is more useful in speed and position control of the drive as shown in [26, 26]. In this case, the suitable dynamic and constrain fulfillment is ensured.

The main contribution of this chapter is designing and real-time validation of an explicit model predictive controller for an uncertain two-mass elastic drive system. The explicit version of the MPC algorithm is used in the chapter. The chapter is divided into seven sections. After a short introduction the mathematical model of the drive is presented. Then the MPC algorithm in its explicit form is described in detail. Next the optimization procedure based on genetic and pattern search algorithms is presented. In the fourth section Kalman Filter used in the control structure to reconstruct of the plant states and parameters is described. Next the results concerning the chapter goal are presented. The chapter ends with some concluding remarks.

2 Mathematical Model of the Drive and the Control Structure

Usually multi-mass models are used to analyze the performance of a drives with a flexible load. A more complicated model allows obtaining better accuracy of the calculation, but it increases the computational complexity. The right choice of the model order is especially important in sensor less drives, where special estimation methods have to be applied so as to reconstruct the non-measurable state variables. For this reason, the influence of an additional degree of freedom on the drive system dynamics is usually neglected and the simplest two-mass system model is considered.

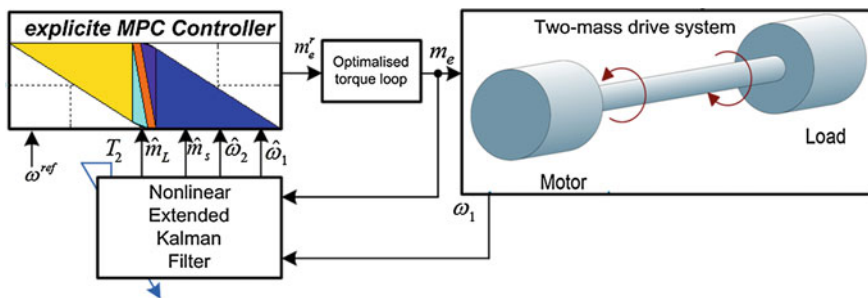


Fig. 1 Block diagram of the considered control structure

$$\frac{d}{dt} \underbrace{\begin{bmatrix} \omega_1(t) \\ \omega_2(t) \\ m_s(t) \end{bmatrix}}_x = \underbrace{\begin{bmatrix} \frac{d}{T_1} & \frac{-d}{T_1} & \frac{-1}{T_1} \\ \frac{-d}{T_2} & \frac{d}{T_2} & \frac{1}{T_2} \\ \frac{1}{T_c} & \frac{-1}{T_c} & 0 \end{bmatrix}}_A \cdot \begin{bmatrix} \omega_1(t) \\ \omega_2(t) \\ m_s(t) \end{bmatrix} + \underbrace{\begin{bmatrix} \frac{1}{T_1} \\ 0 \\ 0 \end{bmatrix}}_B \cdot m_e(t) + \underbrace{\begin{bmatrix} 0 \\ \frac{-1}{T_2} \\ 0 \end{bmatrix}}_{Bd} \cdot m_L(t) \quad (1)$$

where: ω_1 —motor speed, ω_2 —load speed, m_e —electromagnetic torque, m_s —shaft—torque, m_L —load torque, T_1 —mechanical time constant of the motor, T_2 —mechanical time constant of the load machine, T_c —stiffness time constant.

The resonant and antiresonant frequency of the two-mass system are defined as follows:

$$f_r = \frac{1}{2\pi} \sqrt{T_c \frac{T_1 + T_2}{T_1 T_2}} \quad (2)$$

$$f_{ar} = \frac{1}{2\pi} \sqrt{\frac{T_c}{T_2}} \quad (3)$$

The considered control structure with MPC controller is shown in Fig. 1. The proposed control structure consists of the two main loops: inner (electromagnetic torque control) and outer (speed) loop.

The electromagnetic torque control loop consists the torque controller (usually PI), power converter, electromagnetic part of the motor and the current sensor. The parameters of the torque controller are selected to ensure the suitable fast torque regulation, usually with the help of the modulus criteria. The transfer function of the torque controller compensates the delay caused by electromagnetic part of the motor. The final delay of the optimized loop results mainly from the power converter and in the study is smaller than 2 ms.

The speed control loop consists of an MPC controller in explicit form, optimized electromagnetic torque control loop, mechanical part of the drive, speed sensor and nonlinear Kalman Filter (KF). The estimated states of the system are used by the MPC controller. The parameters T_2 is only used to update the matrices of KF. The exact description of the MPC controller and KF are presented in the subsequent sections.

3 Design of the Proposed Predictive Controller

In model predictive control, an explicit model of the plant is used to predict the effect of future actions of the manipulated variables on the process output. In recent literature, the following linear discrete-time state-space model is predominantly employed [14]:

$$\begin{aligned} \mathbf{x}(t+1) &= \mathbf{A}\mathbf{x}(t) + \mathbf{B}\mathbf{u}(t) \\ \mathbf{y}(t) &= \mathbf{C}\mathbf{x}(t) \end{aligned} \quad (4)$$

where $\mathbf{x}(t) \in \mathbb{R}^n$, $\mathbf{u}(t) \in \mathbb{R}^m$, $\mathbf{y}(t) \in \mathbb{R}^p$ are the state, input and output variables, respectively, and $\mathbf{A} \in \mathbb{R}^{n \times n}$, $\mathbf{B} \in \mathbb{R}^{n \times m}$ $\mathbf{C} \in \mathbb{R}^{p \times n}$ are known time-invariant system matrices.

The system variables in (x) are subject to the following constraints

$$\begin{aligned} u(k) \in U &:= \{u | u_{\min} \leq u(k) \leq u_{\max}\} \\ y(k) \in Y &:= \{y | y_{\min} \leq y(k) \leq y_{\max}\} \end{aligned} \quad (5)$$

for all $k \geq 0$. Here, the set U is a convex, compact subset of \mathbb{R}^m and Y is a convex, closed subset of \mathbb{R}^p , each set containing the equilibrium point of (5) in its interior. The control input bounds u_{\min} and u_{\max} arise naturally from physical restrictions of control actuators, whereas the output constraints y_{\min} and y_{\max} may be introduced due to safety concerns, environmental regulations or various consumer specifications.

System performance (whether predicted or actual) will be assessed through the cost function

$$\min_{u_0^T, \dots, u_{N_c-1}^T} \left\{ \sum_{i=0}^{N_p} \mathbf{y}_{k+i|k}^T \mathbf{Q} \mathbf{y}_{k+i|k} + \sum_{i=0}^{N_c-1} \mathbf{u}_{k+i|k}^T \mathbf{R} \mathbf{u}_{k+i|k} \right\} \quad (6)$$

where $\mathbf{Q} \geq 0$ and $\mathbf{R} > 0$ denote the weighing matrices and N_p and N_c are the prediction and control horizons, respectively.

The implementation of the MPC controller amounts to solving problem (6) on-line for a given \mathbf{x}_0 in a receding horizon fashion. This means that, at time k , only the first element u_0^* of the optimal input sequence is applied to the plant and the actions $u_1^*, \dots, u_{N_c-1}^*$ are discarded. At the next time step the whole procedure is repeated for the new measured or estimated output $y(k+1)$ [13–14]. This strategy can be computationally intensive for systems with fast sampling requirements thus greatly limiting the scope of applicability to systems with relatively slow dynamics. Therefore, an on-line MPC is not used in the presented study.

Alternatively, rather than using the initial state x_0 to “update” the optimization problem (5) at each time k , the idea is to treat the state vector as a parameter vector and then solve problem (6) *off-line* for all realizations of x_0 within a predefined set of states using multi-parametric programming [16–21]. In this strategy, the parameter space is subdivided into characteristic regions where the optimizer is given as an explicit piecewise affine (PWA) function of the parameters:

$$u_0^*(x_0) = K_r x_0 + g_r, \quad \forall x \in P_r \quad (7)$$

where P_r are polyhedral sets defined as

$$P_r = \{x \in \mathfrak{R}^n | H_r x \leq d_r\}, \quad r = 1, \dots, Nr \quad (8)$$

Here $Nr > 0$ represents the total number of polyhedral regions in the partition. The main advantage of this approach is that the optimal input u_0^* for a given initial state x_0 can be obtained by evaluating a PWA function in the control unit thus greatly simplifying the controller implementation process as numerical optimization is no longer required [16–21].

The vector \mathbf{y} (6) is defined as follows:

$$y_1 = (\omega_1 - \omega_{ref}) \quad (9a)$$

$$y_2 = (m_s - m_L) \quad (9b)$$

$$y_3 = (\omega_2 - \omega_{ref}) \quad (9c)$$

Vector \mathbf{y} defined in such a way brings about the minimization of the difference between the motor (9a), the load (9c) and the reference model. The impact of the load torque to the drive system is reduced by (9b).

In the considered problem the MPC controller requires information about the evolution of the load torque and the reference signal ω_{ref} . Since their future behaviour is usually unknown, the following assumption is made:

$$\frac{dm_L(t)}{dt} = 0 \quad (10a)$$

$$\frac{d\omega_{ref}}{dt} = 0 \quad (10b)$$

For the purpose of computing the explicit MPC control law and to guarantee offset-free control, the basic drive system model (1) needs to be augmented with additional state variables which take into account the effect of the load disturbance m_L and the reference speed ω_{ref} . This can be achieved by defining the following augmented model:

$$\frac{d}{dt} \underbrace{\begin{bmatrix} x \\ m_L \\ \omega_{ref} \end{bmatrix}}_{x_c} = \underbrace{\begin{bmatrix} A & B_d & 0 \\ 0 & 0 & 0 \\ 0 & 0 & A_\omega \end{bmatrix}}_{A_c} \cdot \underbrace{\begin{bmatrix} x_c \\ m_L \\ \omega_{ref} \end{bmatrix}}_{x_c} + \underbrace{\begin{bmatrix} B_c \\ 0 \\ 0 \end{bmatrix}}_{B_c} m_e \quad (11a)$$

where:

$$x = [\omega_1 \quad \omega_2 \quad m_s \quad m_L \quad \omega_{ref}]^T \quad (11b)$$

and \mathbf{A} , \mathbf{B}_c and \mathbf{B}_d are the state-space matrices describing the original drive system model. The weighting matrices \mathbf{Q} and \mathbf{R} have the following sizes: $\dim(\mathbf{Q}) = 3$, $\dim(\mathbf{R}) = 1$.

The matrix \mathbf{Q} is defined as follows:

$$\mathbf{Q} = \begin{bmatrix} q_{11} & 0 & 0 \\ 0 & q_{22} & 0 \\ 0 & 0 & q_{33} \end{bmatrix} \quad (12)$$

While the primary goal of the MPC controller is to provide a good load speed tracking performance, the control system must respect the physical and safety limitations of the electrical drive variables during operation. For the drive in question, the following constraints are considered: electromagnetic torque and shaft torque constrains:

$$-3 \leq m_e \leq 3 \quad (13a)$$

$$-2 \leq m_s \leq 2 \quad (13b)$$

Constraints (13) incorporate the physical limits of the drive power converter and are introduced in order to ensure that the produced motor torque (13a) does not exceed its maximum permissible value. The shaft torque constraint in (13b), which places a limit on the admissible shaft twists that are likely to occur during the drive transients, is critical for the drive safety and its long-term reliable operation. While in principle the maximum torsional stress values undertaken by a shaft must be considerably smaller than the yielded stress limit of the material, in practice, the shaft should never be exposed to stresses exceeding the metal fatigue point (in case of cycling loading) in order to maximize the lifetime of the drive system.

Taking into account the abovementioned equation, the control problem can be defined as follows:

$$\min_{u_0^T, \dots, u_{N_c-1}^T} \left\{ \sum_{p=1}^{N_p} \left(\begin{array}{c} q_{11}(\omega_1(p) - \omega_{ref}(p))^2 + \\ q_{22}(\omega_2(p) - \omega_{ref}(p))^2 + \\ q_{33}(m_s(p) - m_L(p))^2 \end{array} \right) + \sum_{k=0}^{N_u-1} \left(R \cdot m_e(k)^2 \right) \right\} \quad (14)$$

$$\begin{array}{l} |m_e| \leq m_e^{\max} \\ |m_s| \leq m_s^{\max} \end{array}$$

The state and control prediction horizon are set to $N_p = 10$, $N_u = 2$ respectively.

The values of \mathbf{Q} matrix define the dynamic properties of the system. The main subject of the work is to obtain the same shape of the load speed when of the mechanical time constant of the load machine changes. At the same time oscillations cannot appear in the transients of the system variables. The cost function used in the optimization algorithm is as follows:

$$F = \min_{q11; q22; q33; R} \left[\prod_{i=1}^3 (f_i(e_1, e_2, K_1, K_2)) \cdot f_4(e_3) \right] \quad (15)$$

where: e_1 —tracking error of motor speed ω_1 , e_2 —tracking error of load speed ω_2 , K_1 —penalty coefficient for exceeds of the limit of the shaft torque, K_2 —penalty coefficient for overshoot in the load speed, e_3 —coefficient in the cost function responsible for minimization of the tracking error of the speed for the systems with a different value of the parameter T_2 .

The factors of the cost function can be expressed as follows:

$$\begin{aligned} f_1^{T_2 = T_{2N}} &= \frac{1}{n} \left\{ \sum_1^n (|\omega^{ref} - \omega_1|) + \sum_1^n (|\omega^{ref} - \omega_2|) + K_1 + K_2 \right\} \\ f_2^{T_2 = 0.5 \cdot T_{2N}} &= \frac{1}{n} \left\{ \sum_1^n (|\omega^{ref} - \omega_1|) + \sum_1^n (|\omega^{ref} - \omega_2|) + K_1 + K_2 \right\} \\ f_3^{T_2 = 2 \cdot T_{2N}} &= \frac{1}{n} \left\{ \sum_1^n (|\omega^{ref} - \omega_1|) + \sum_1^n (|\omega^{ref} - \omega_2|) + K_1 + K_2 \right\} \\ f_4 &= \frac{1}{n} \left\{ \begin{aligned} &\sum_1^n (|\omega_2^{T_2 = T_{2N}} - \omega_2^{T_2 = 0.5 T_{2N}}|) + \sum_1^n (|\omega_2^{T_2 = T_{2N}} - \omega_2^{T_2 = 2 T_{2N}}|) \\ &+ \sum_1^n (|\omega_2^{T_2 = 0.5 T_{2N}} - \omega_2^{T_2 = 2 T_{2N}}|) \end{aligned} \right\} \quad (16) \end{aligned}$$

Penalty coefficient K_1 and K_2 are defined as:

$$\begin{aligned} K_1 &= \begin{cases} 0 \Rightarrow \text{when } m_s \leq m_s^{\max} \\ k_1 \cdot (m_s - m_s^{\max}) \Rightarrow \text{when } m_s > m_s^{\max} \end{cases} \\ K_2 &= \begin{cases} 0 \Rightarrow \text{when } \omega_2 \leq \omega^{ref} \\ k_2 \cdot (\omega_2 - \omega^{ref}) \Rightarrow \text{when } \omega_2 > \omega^{ref} \end{cases} \end{aligned} \quad (17)$$

where k_1 and k_2 are positive defined numbers.

The dynamics of the reference value is described by the second order term:

$$G = \frac{\omega_r^2}{s^2 + 2\zeta\omega_r s + \omega_r^2} \quad (18)$$

where ω_o is a reference frequency and the ζ is the damping coefficient of the reference model.

4 Nonlinear Extended Kalman Filter

In the presence of the time-varying load machine inertia T_2 , there is a need to extend the two-mass system state vector (1) with the additional element $1/T_2$ and non-measurable load torque m_L [12]:

$$\mathbf{x}_R(t) = \left[\omega_1(t) \quad \omega_2(t) \quad m_s(t) \quad m_L(t) \quad \frac{1}{T_2}(t) \right]^T. \quad (19)$$

The extended, nonlinear state and output equations can be written in the following form:

$$\frac{d}{dt} \mathbf{x}_R(t) = \mathbf{A}_R \left(\frac{1}{T_2}(t) \right) \mathbf{x}_R(t) + \mathbf{B}_R \mathbf{u}(t) + \mathbf{w}(t) = \mathbf{f}_R(\mathbf{x}_R(t), \mathbf{u}(t)) + \mathbf{w}(t) \quad (20a)$$

$$\mathbf{y}_R(t) = \mathbf{C}_R \mathbf{x}_R(t) + \mathbf{v}(t) \quad (20b)$$

where the matrices of the system are defined as follows (in [p.u.]):

$$\mathbf{A}_R \left(\frac{1}{T_2}(t) \right) = \begin{bmatrix} 0 & 0 & \frac{-1}{T_1} & 0 & 0 \\ 0 & 0 & \frac{1}{T_2}(t) & \frac{-1}{T_2}(t) & 0 \\ \frac{1}{T_c} & \frac{-1}{T_c} & 0 & 0 & 0 \\ 0 & 0 & 0 & 0 & 0 \\ 0 & 0 & 0 & 0 & 0 \end{bmatrix}, \mathbf{B}_R = \begin{bmatrix} \frac{1}{T_1} \\ 0 \\ 0 \\ 0 \\ 0 \end{bmatrix}, \mathbf{C}_R = \begin{bmatrix} 1 \\ 0 \\ 0 \\ 0 \\ 0 \end{bmatrix}^T \quad (21)$$

and $\mathbf{w}(t)$, $\mathbf{v}(t)$ —represent process and measurement errors (Gaussian white noise), according to the Kalman Filter (KF) theory.

Matrix \mathbf{A}_R depends on the changeable parameter T_2 . It means that in every calculation step this matrix must be updated due to the estimated value of T_2 . The input and the output vectors of the drive system (and NEKF) are electromagnetic torque and motor speed, respectively:

$$\mathbf{u} = m_e, \mathbf{y} = \omega_1 \quad (22)$$

After the discretization of Eq. (8) with T_p sampling step, the state estimation using Nonlinear Extended Kalman Filter (NEKF) algorithm is calculated (23):

$$\hat{\mathbf{x}}_R(k+1/k+1) = \hat{\mathbf{x}}_R(k+1/k) + \mathbf{K}(k+1)[\mathbf{y}_R(k+1) - \mathbf{C}_R(k+1)\hat{\mathbf{x}}_R(k+1/k)] \quad (23)$$

where the gain matrix \mathbf{K} is obtained by the suitable numerical procedure. In the first step the estimation of the filter covariance matrix is calculated:

$$\mathbf{P}(k+1/k) = \mathbf{F}_R(k)\mathbf{P}(k)\mathbf{F}_R^T(k) + \mathbf{Q}_{KF}(k) \quad (24)$$

where:

$$\mathbf{F}_R(k) = \left. \frac{\partial \mathbf{f}_R(\mathbf{x}_R(k/k), \mathbf{u}(k), k)}{\partial \mathbf{x}_P(k/k)} \right|_{\mathbf{x}_R = \hat{\mathbf{x}}_R(k/k)} \quad (25)$$

and \mathbf{Q}_{KF} is a state noise covariance matrix.

\mathbf{F}_R is the state matrix of the nonlinear dynamical system after its linearization in the actual operating point, which must be updated in every calculation step:

$$\mathbf{F}_R(k) = \begin{bmatrix} 1 & 0 & \frac{-1}{T_1} T_p & 0 & 0 \\ 0 & 1 & \frac{1}{T_2}(k) T_p & \frac{-1}{T_2}(k) T_p & T_p(m_s(k) - m_L(k)) \\ \frac{1}{T_c} T_p & \frac{-1}{T_c} T_p & 1 & 0 & 0 \\ 0 & 0 & 0 & 1 & 0 \\ 0 & 0 & 0 & 0 & 1 \end{bmatrix} \quad (26)$$

The filter gain matrix \mathbf{K} of the NEKF and the update of the covariance matrix of the state estimation error \mathbf{P} are calculated using the following Eq. (27):

$$\mathbf{K}(k+1) = \mathbf{P}(k+1/k) \mathbf{C}_R^T(k+1) [\mathbf{C}_R(k+1) \mathbf{P}(k+1/k) \mathbf{C}_R^T(k+1) + \mathbf{R}_{KF}(k)]^{-1}$$

$$\mathbf{P}(k+1/k+1) = [\mathbf{I} - \mathbf{K}(k+1) \mathbf{C}_R(k+1)] \mathbf{P}(k+1/k), \quad (27)$$

where: \mathbf{Q}_{KF} and \mathbf{R}_{KF} —are the covariance matrix.

It should be emphasized that the estimated value of T_2 is used only to update the state matrix of KF. This ensure the good estimation accuracy of the original state vector of the system which is crucial for proper work of the proposed control structure. Due to the explicit form of the MPC algorithm it is not possible to used estimate the value of T_2 to change the controller gain. Despite this, the control structure has good dynamic properties which is shown in the next session.

5 Results of the Optimization

Due to the complexity of the cost function (15), in order to select optimal values of the \mathbf{Q} and \mathbf{R} matrices, the hybrid optimization procedure ais applied. First the genetic algorithm (GA) is utilized. Then the pattern search optimization procedure is used taking for the starting point the values selected by GA.

The optimization procedure can be implemented in two ways. The first methodology assures that the state vector of the system is directly accessible. It means that the dynamics of the KF is neglected. In the second approach the complete system is analyzed, including the dynamics of the KF.

Firstly, the optimization procedure for the simplify control structure (without KF) is done. The characteristic values of the optimization procedure are presented in Fig. 2: mean and the best individual in GA (a, d, g), value of the pattern search

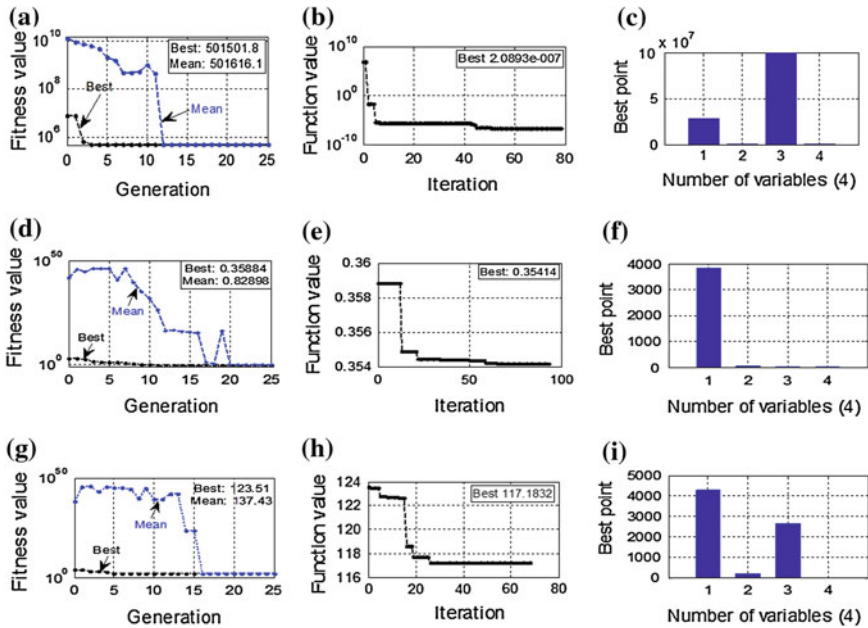


Fig. 2 Selected values of the optimization procedure: best and mean values for the GA (a, d, g), fitness function for the pattern search procedure (b, e, h) and selected values (c, f, i) for the system with direct feedbacks from state variables (a–c), system with KF for $\omega_r = 15 \text{ s}^{-1}$ (d–f) and system with KF for $\omega_r = 25 \text{ s}^{-1}$ (g–i)

algorithm (b, e, h) and final points (c, f, i). The resonant frequency of the reference model is set to 15 s^{-1} . As can be concluded from Fig. 2c, the coefficient q_{33} responsible for minimization the difference between the load and reference speed has the biggest value. The same procedure is repeated for the resonant frequency $\omega_r = 25 \text{ s}^{-1}$ and similar, as previously, values are obtained.

Next, the optimization procedure is done for the complete model of the system including KF. The characteristic values of the system are presented in Fig. 2d–i for the following values of the resonant frequency of the reference model: $\omega_r = 15 \text{ s}^{-1}$ (Fig. 2d–f) and $\omega_r = 25 \text{ s}^{-1}$ (Fig. 2g–i). As can be seen from the obtained results, the optimal values of the coefficients are different than in the first approach and they depend on the set resonant frequency ω_r . For the smaller value of the resonant frequency the coefficient q_{11} has predominant values. Increasing the values of ω_r results in the increase of the rest coefficients. The value q_{33} goes up the most. In Fig. 3a the selected fragments of the $\omega_1 - m_s$ controller regions are presented. The graph of the cost function (15) plots for the change of the motor speed versus shaft torque (the rest of the variables are keep constant) is demonstrated in Fig. 3b. It can be concluded that this relationship has one global minimum.

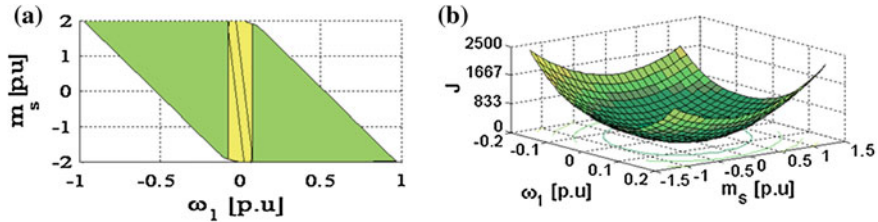


Fig. 3 Explicit MPC controller: a fragment of the controller polyhedral regions (a), cost function (15) in dependence of the motor speed and shaft torque (b)

6 Results

The parameters of the simulated and real control structure are as follows. The sampling time of the optimized torque control loop is set to 100 μs , the estimator is working with the sampling and the predictive controller with 500 μs . The prediction and the control horizon of the predictive controller have been set to $N_u = 2$, $N_p = 10$ samples. In the simulation study the electromagnetic torque and the motor speed (there are only two measured signals) has been disrupted by additional noises.

At the beginning the performance of the control system is evaluated through the simulation study. The transients of the system states are presented in Fig. 4: electromagnetic, shaft and load torques (a), motor, load and reference speeds motor torques (b) and enlarged error between the reference and load speeds (c). The drive system starts with the nominal value of the time constant of the load machine $T_2 = 203$ ms. Then, at time $t = 8, 16$ and 24 s, the time constant of the load machine T_2 varied rapidly to the values 101, 406 and 609 ms respectively. The nominal load torque is switched on at the times 3, 11, 19 and 27 s. After one second it is switched off.

As it can be concluded from the transients presented in Fig. 4, the system is working correctly. The load speed follows the reference signal without noticeable errors (Fig. 4a) through the first 20 s of work. The remarkable tracking error is evident during reversal in the last 10 s of the system work. It results from the limitation of the control signal (electromagnetic torque). It should be stressed that for the smaller value of the reference speed the system follows the reference value accurately. Despite the variation of the time constant of the load machine, the constrains of the system are not validated. The maximal value of the shaft torque is keep in set interval $\langle -2, 2 \rangle$. The enlarged values of the errors between the system speed and reference model is presented in Fig. 4c. Also the electromagnetic torque does not exceed its limit.

Then the performance of the control structure is examined through experimental tests. The laboratory set-up is composed of a 0.5 kW DC motor driven by a static converter. The motor is coupled to a load machine by an elastic shaft (a steel shaft of 5 mm diameter and 600 mm length). The speed and position of the driven

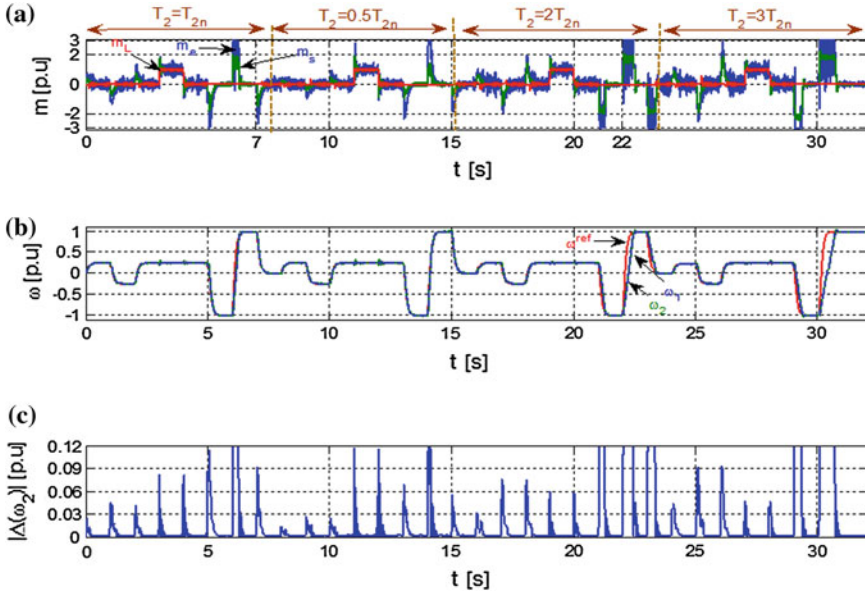


Fig. 4 Simulation transients for $\omega_r = 15 \text{ s}^{-1}$: (a) electromagnetic, shaft and load torques transients (b) module of the error between the load and reference signal (c)

and loading motors have been measured by incremental encoders (36,000 pulses per rotation). The control and estimation algorithms are implemented in a digital signal processor using the dSPACE 1103 control hardware. The implementation of the explicit MPC control law involves evaluation of a PWA function at each sampling instant in the control unit. This process requires the storage of all polyhedral regions and the associated affine control laws.

Firstly, the drive working in the low speed region is examined. The system is tested for the two resonant frequency of the reference model $\omega_r = 15 \text{ s}^{-1}$ (Fig. 5) and $\omega_r = 25 \text{ s}^{-1}$ (Fig. 6). At the time $t = 0 \text{ s}$ the system starts to the reference speed $\omega_{ref} = 0.25$. Then at the time $t_2 = 0.5 \text{ s}$ and $t_3 = 1.5 \text{ s}$ the nominal load torque is switched on and off, respectively. Then at the time $t_4 = 2 \text{ s}$ the reference speed is changing to contrary the value $\omega_{ref} = -0.25$. The cycle of work is repeated after 4 s. This test is done for the system with three values of the time constant of the load machines approximately $T_2 = 200, 400$ and 600 ms . As can be concluded from presented transients, the robust control structure is working correctly. Despite the different values of T_2 , the load speed transients have almost similar shapes (Figs. 5a and 6a.). The electromagnetic and shaft torques are far below its set limits—so the constrains are not validated. The increase of T_2 results in the bigger value of the torques during transients which is clearly visible in Figs. 5b, d and 6b, d. In every case the KF starts with misidentified time constant of T_2 . Then, as can be concluded from Figs. 5e and 6e, KF identifies the correct

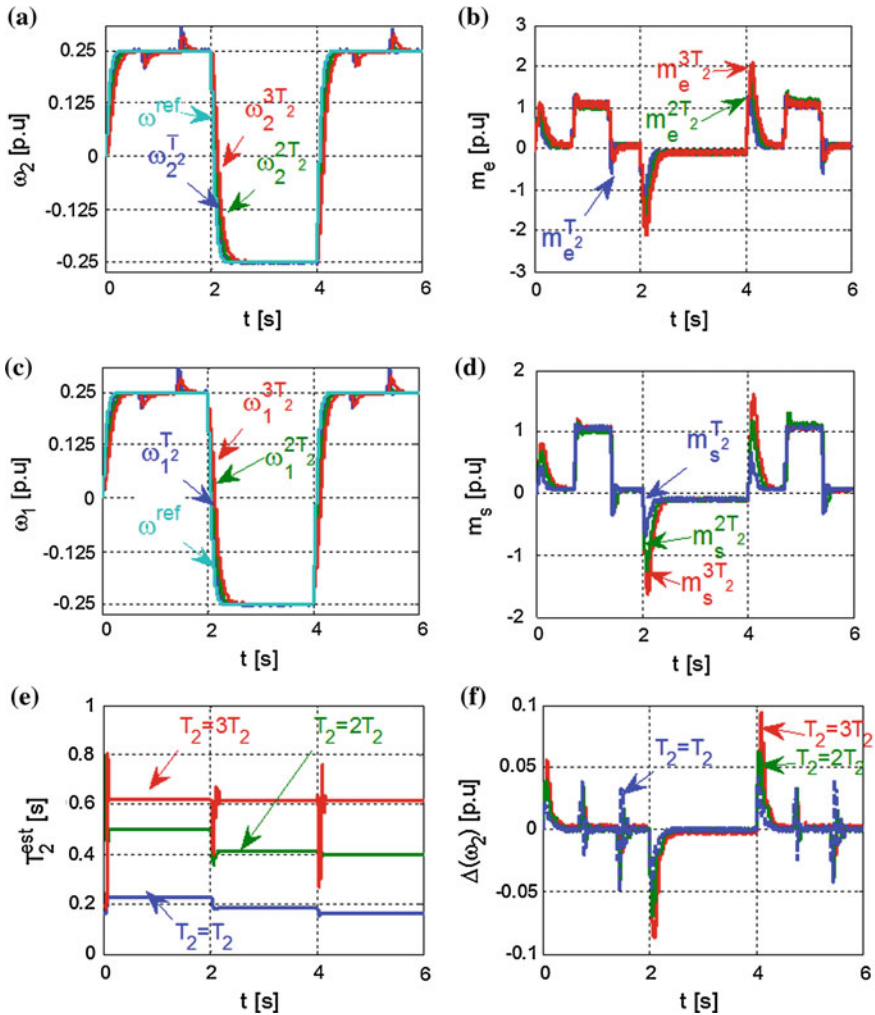


Fig. 5 Experimental transients for the $\omega_r = 0.25$ and the resonant frequency of the reference model 15 s^{-1} : **a** load speed, **b** electromagnetic torque, **c** motor speed, **d** shaft torque, **e** estimate time constant of the load machine, **f** error between the load and reference speed

value of the T_2 after the start-up with small errors. These errors increase its value after next reversal.

Next the performance of the system for the nominal reference value is examined. For this condition the system is working within the limit values of the electromagnetic and shaft torque. The selected transients of the system variables are shown in Fig. 7.

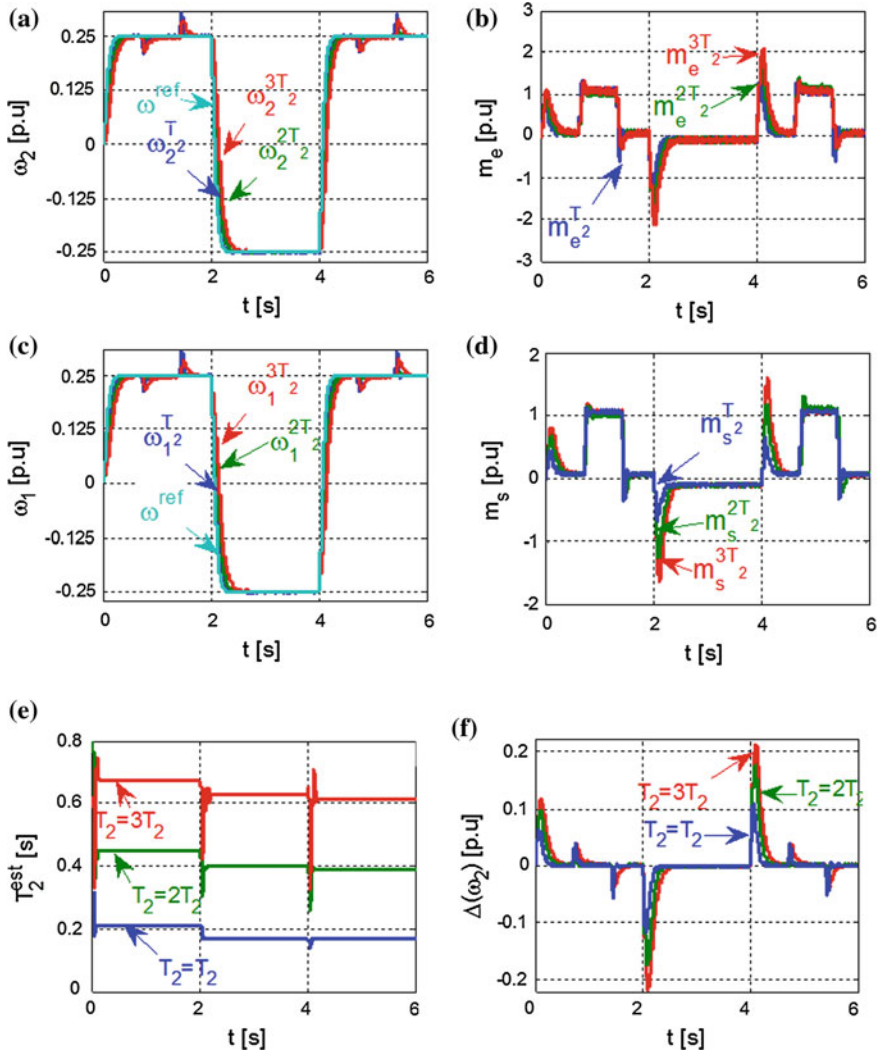


Fig. 6 Experimental transients for the $\omega_r = 0.25$ and the resonant frequency of the reference model 25 s^{-1} : **a** load speed, **b** electromagnetic torque, **c** motor speed, **d** shaft torque, **e** estimate time constant of the load machine, **f** error between the load and reference speed

As can be expected, due to the limitation of the control signal, the speed transients are different from each other. However, the shaft torque is kept within the set limit (Fig. 7c, d). The control structure is working correctly.

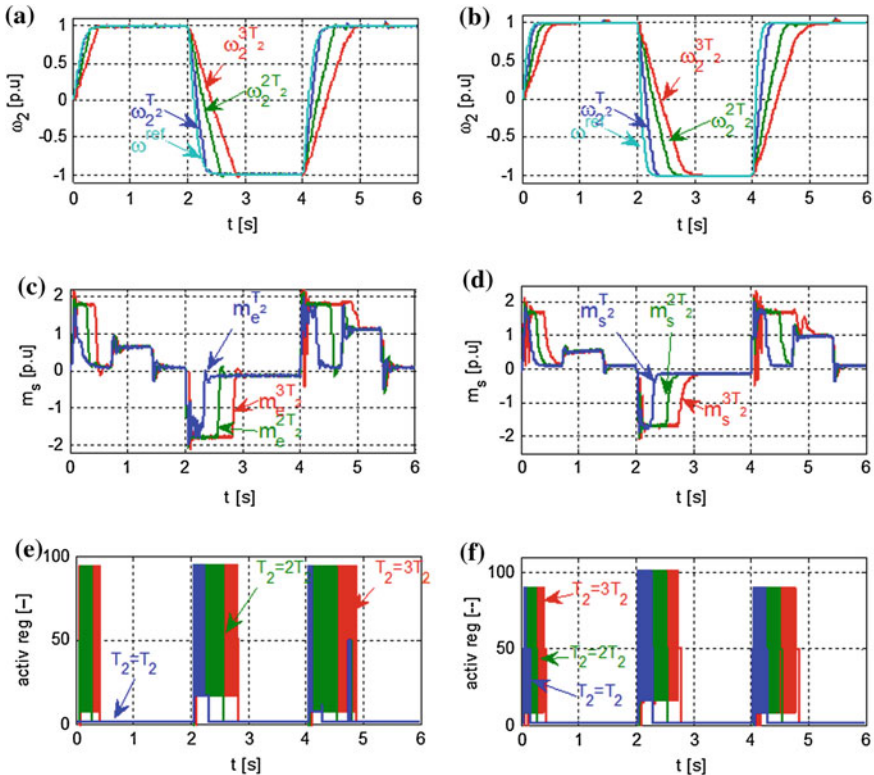


Fig. 7 Experimental transients for the nominal speed of the system for the resonant frequency of the reference 15 s^{-1} (a, c, e) and 25 s^{-1} (b, d, f), load speed (a, b), shaft torque (c, d) active region (e, f) for different values of the time constant T_2

7 Conclusion

In the chapter some issues related to the application of the MPC in the position control structure for the drive system with an elastic joint are presented. The following remarks can be formulated on the basis of the presented study:

- It is possible to implement in practice the MPC strategy with the help of the multiparametric programming. This enables implementation of the MPC controller on a standard microprocessor.
- The robust response of the speed can be obtained through suitable selections of the values of the MPC **Q** and **R** matrices.
- The constraints of the system state variables are not validated under nominal and changed parameters.

- The performance of the system depends on the quality of the estimation states. Therefore, the nonlinear KF which estimates the state and the time constant of the load machine is applied.
- The estimated value of T_2 is used only to update the matrices of the KF. It can not change the parameters of the MPC controller in explicit form.
- The system correctly works for very small as well as big values of the reference speed.

Acknowledgements This work has been founded by Polish National Science Centre under project UMO-2011/01/B/ST7/103500 (2011-2014).

References

1. M.A. Valenzuela, J.M. Bentley, R.D. Lorenz, Computer-aided controller setting procedure for paper machine drive systems. *IEEE Trans. Ind. Electron.* **45**(2), 638–650 (2009)
2. M. Molinas, J.A. Suul, T. Undeland, Extending the life of gear box in wind generators by smoothing transient torque with STATCOM. *IEEE Trans. Ind. Electron.* **57**(2), 476–484 (2010)
3. Y. Hori, H. Sawada, Y. Chun, Slow resonance ratio control for vibration suppression and disturbance rejection in torsional system. *IEEE Trans. Ind. Electron.* **46**(1), 162–168 (1999)
4. R. Muszynski, J. Deskur, Damping of torsional vibrations in high-dynamic industrial drives. *IEEE Trans. Ind. Electron.* **57**(2), 544–552 (2010)
5. S. Villwock, M. Pacas, Application of the Welch-method for the identification of two- and three-mass-systems. *IEEE Trans. Ind. Electron.* **55**(1), 457–466 (2008)
6. J. Guzinski, H. Abu-Rub, M. Diguët, Z. Krzeminski, A. Lewicki, Speed and load torque observer application in high-speed train electric drive. *IEEE Trans. Ind. Electron.* **57**(2), 565–574 (2010)
7. P.K.W. Abeygunawardhana, T. Murakami, Vibration suppression of two-wheel mobile manipulator using resonance-ratio-control-based null-space control. *IEEE Trans. Ind. Electron.* **57**(12), 4137–4146 (2010)
8. M. Vasak, M. Baotic, I. Petrovic, N. Peric, Hybrid theory-based time-optimal control of an electronic throttle. *IEEE Trans. Ind. Electron.* **54**(3), 1483–1494 (2007)
9. K. Szabat, T. Orłowska-Kowalska, Vibration suppression in a two-mass drive system using pi speed controller and additional feedbacks—comparative study. *IEEE Trans. Ind. Electron.* **54**(2), 1193–1206 (2007)
10. K. Szabat, T. Orłowska-Kowalska, Application of the Kalman filters to the high performance drive system with elastic coupling. *IEEE Trans. Ind. Electron.* **59**(11), 4226–4235 (2012)
11. A. Hacı, K. Jezernik, A. Sabanovic, SMC with disturbance observer for a linear belt drive. *IEEE Trans. Ind. Electron.* **54**(6), 3402–3412 (2007)
12. K. Szabat, T. Orłowska-Kowalska, Performance improvement of industrial drives with mechanical elasticity using nonlinear adaptive Kalman filter. *IEEE Trans. Ind. Electron.* **55**(3), 1075–1084 (2008)
13. M. Cychowski, K. Szabat, T. Orłowska-Kowalska, Constrained model predictive control of the drive system with mechanical elasticity. *IEEE Trans. Ind. Electron.* **56**(6), 1963–1973 (2009)
14. J.M. Maciejowski, in *Predictive Control With Constraints* (Prentice-Hall, Harlow, 2002)
15. A. Bemporad, M. Morari, V. Dua, E.N. Pistikopoulos, The explicit linear quadratic regulator for constrained systems. *Automatica* **38**(1), 3–20 (2002)

16. E.N. Pistikopoulos, V. Dua, N.A. Bozinis, A. Bemporad, M. Morari, On-line optimization via off-line parametric optimization tools. *Comput. Chem. Eng.* **24**(2), 183–188 (2000)
17. P. Trndel, T.A. Johansen, A. Bemporad, An algorithm for multi-parametric quadratic programming and explicit MPC solutions. *Automatica* **39**(3), 489–497 (2003)
18. M. Kvasnica, P. Grieder, M. Baotic, M. Morari, in ‘*Multiparametric toolbox (MPT)*’, in eds. by R. Alur, G.J. Pappas. ‘*Hybrid Systems: Computation and Control*’ (LNCS, 2993), (Springer, Heidelberg, 2004), pp. 448–462
19. J. Rodriguez, M. Kazmierkowski, J. Espinoza, P. Zanchetta, H. Abu-Rub, H. Young, C. Rojas, State of the art of finite control set model predictive control in power electronics. *IEEE Trans. Ind. Inf.* **9**(2), 1003–1016 (2013)
20. M. Preindl, S. Bolognani, Model predictive direct torque control with finite control set for pmsm drive systems, Part 2: field weakening operation. *IEEE Trans. Ind. Inf.* **9**(2), 648–657 (2013)
21. J. Scoltock, T. Geyer, U. Madawala, A comparison of model predictive control schemes for MV induction motor drives. *IEEE Trans. Ind. Inf.* **9**(2), 909–919 (2013)
22. M. Stephens, C. Manzie, M. Good, Model predictive control for reference tracking on an industrial machine tool servo drive. *IEEE Trans. Ind. Inf.* **9**(2), 808–816 (2013)
23. R.P. Aguilera, P. Lezana, D.E. Quevedo, Finite-control-set model predictive control with improved steady-state performance. *IEEE Trans. Ind. Inf.* **9**(2), 658–667 (2013)
24. R. Morales-Caporal, E. Bonilla-Huerta, C. Hernandez, M.A. Arjona, M. Pacas, Transducerless acquisition of the rotor position for predictive torque controlled pm synchronous machines based on a DSP-FPGA digital system. *IEEE Trans. Ind. Inf.* **9**(2), 799–807 (2013)
25. E.J. Fuentes, C.A. Silva, J.I. Yuz, Predictive speed control of a two-mass system driven by a permanent magnet synchronous motor. *IEEE Trans. Ind. Electron.* **59**(7), 2840–2848 (2012)
26. E. Fuentes, R. Kennel, Finite-set model predictive control of the two-mass-system, in *Workshop on Predictive Control of Electrical Drives and Power Electronics (PRECEDE)* (2011)
27. P. Serkies, K. Szabat, Application of the MPC controller to the position control of the two-mass drive system. *IEEE Trans. Ind. Electron.* **60**(9), 3679–3688 (2013)

Part III
Neuro and Nonlinear Control of Power
Converters and Drives

Chapter 8

Adaptive Neurocontrollers for Drive Systems: Basic Concepts, Theory and Applications

Teresa Orłowska-Kowalska and Marcin Kamiński

Abstract In this chapter basic principles of neurocontrol are revised and discussed from the point of view of applications in converter-fed drive systems. The main neural network structures used as neural controllers are presented and classified into two groups: off-line and on-line trained controllers. From the point of view of drive system uncertainties, caused by simplifying assumptions under mathematical model formulation, errors in drive parameters identification and changes of the models and their parameters under different operation conditions, on-line adaptive neural controllers are proposed. Various neural structures and their on-line training methods are discussed. The chosen neurocontrollers were verified in simulation and experimental tests for converter-fed drives with rigid and resilient mechanical connections between the driving motor and loading machine.

1 Introduction

In the last few decades there has been a significant evolution of traditional control techniques in parallel with the appearance of modern tools associated with artificial intelligence. It should be noticed that most of classical model-based control methods, including nonlinear ones, require the knowledge of the controlled system by means of set of algebraic and differential equations, which relate inputs and outputs analytically. Moreover, complete mathematical models describing the systems are often very complex and their parameters need to be known. In real applications some parameters may be hard to measure or their identification is very

T. Orłowska-Kowalska (✉) · M. Kamiński
Institute of Electrical Machines Drives and Measurements, Wrocław University
of Technology, ul. Wybrzeże Wyspiańskiego 27 50-370 Wrocław, Poland
e-mail: teresa.orłowska-kowalska@pwr.wroc.pl

M. Kamiński
e-mail: marcin.kaminski@pwr.wroc.pl

complicated. In order to overcome these problems, it is beneficial to use artificial intelligence techniques, such as neural networks, fuzzy logic and genetic algorithms [1, 2], which do not need the controlled system models and use expert knowledge or experimental data for controller training.

Artificial neural networks (NN), are models with structure and mode of data processing based on human nerve cells. The history of NN theory is not new, the theory (neural models and training algorithms) has been gradually evolving since the 1950s. Possibility of data approximation, learning and generalization ability, robustness, parallel processing, belong to the main NN features, which determined their wide application to control of dynamical plants. The development of modern digital computer as well as programmable electronic elements force hardware implementations of neural networks during the last two decades. Thus nowadays, the number of industrial applications of neural models is increasing, also in power electronics and electrical drives—for control, identification, state estimation and diagnostics [1, 3].

This chapter is focused on the on-line trained NN application in electrical drives, however, off-line solutions are also described shortly. After a short introduction, the general control structure of the AC motor drive is discussed and control issues generated by the drive system uncertainties and nonlinearities, including nonlinearities caused by complex mechanical connection between driving motor and loading machine are presented. Next an overview of the application of NN-based controllers in electrical drives, chosen neural network structures and their training algorithms are described. Then the results of simulations and experimental tests are shown for the drive systems with rigid and resilient connections between the driving motor and loading machine. Some issues connected with practical implementation of NN controllers are presented in the last part of this chapter.

2 Main Control Concepts for Uncertain Electrical Drives

The AC machines, like induction motors (IM) and permanent magnet synchronous motors (PMSM) are actually the most commonly used systems in electrical drives in many industrial processes and applications. Especially the IM, which is a low cost, versatile and maintenance-free motor, and due to its torque-speed characteristic and relatively high starting torque it is widely used in simple drives of pumps, compressors and fans. However, when the IM fed by an inverter is controlled using vector methods, like field-oriented (FOC) or direct torque control (DTC), it can be also applied in high-performance applications like cranes, elevators, rolling mills, electric and hybrid vehicles, machine tools, spindles, servo drives, etc., similarly to PMSM, which has the advantages of high efficiency (no rotor loss), high reliability, and high torque/power density. Vector control provides excellent dynamic torque and speed response and is suitable for applications which require precise acceleration and braking, including operation at high speed.

The most popular vector control method for the IM is based on rotor field orientation [4, 5]. In this control, stator current is oriented towards the rotor flux vector, rotating with a synchronous reference frame, and thus its real component is responsible for the exciting rotor flux value, while the second (imaginary) current component gives the possibility of independent motor torque control. The precision of such decoupled control depends a lot on the proper coordinate transformation based on the estimated position of the rotor flux vector.

On the other hand, the field-oriented control of PMSM is based on the assumption, that stator current components are oriented to the exciting flux from permanent magnets placed in the rotor, thus the rotor field orientation is also used, based on the information on actual rotor position.

Thus, for proper coordinate transformation and stator current orientation towards the rotor flux vector, the electromagnetic torque of AC motors, controlled by FOC concept, can be expressed in a general way as a vector product of rotor flux and stator current vectors:

$$T_e^{AC} = k^{AC} |\Psi_r^{AC} \times \mathbf{i}_s^{AC}|. \quad (1)$$

Hence for the IM we have:

$$T_e^{IM} = \frac{3}{2} p_b \frac{L_m}{L_r} |\Psi_r^{xy} \times \mathbf{i}_s^{xy}| = k_{IM} (\Psi_r i_{sy}) \quad (2)$$

where: L_m , L_r —magnetizing and rotor winding inductances, p_b —number of pole pairs, Ψ_r —rotor flux magnitude (in real x axis of field-oriented coordinate system), i_{sy} —stator current component in y axis.

Respectively for the PMSM, for constant torque region, we obtain the following torque expression:

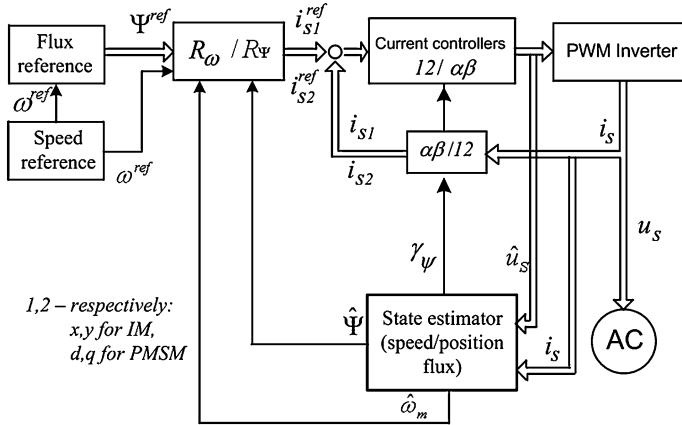
$$T_e^{PMSM} = \frac{3}{2} p_b |\Psi_{pm}^{d-q} \times \mathbf{i}_s^{d-q}| = k_{PM} (\Psi_{pm} i_{sq}) \quad (3)$$

where: Ψ_{pm} —permanent magnet (rotor) flux value (in real d axis of rotor-oriented coordinate system), i_{sq} —stator current component in q axis.

The general scheme of such control concept for AC motors is shown in Fig. 1.

With such control approach, the dynamic behavior of the IM or PMSM is rather similar to that of a separately excited DC motor. It can be seen that internal, parallel control paths for stator current components, responsible for the flux excitation and torque control, are subordinated to the external control paths for the rotor flux and speed control, respectively. Due to the difference in dynamics of the stator current and speed control loops, sometimes it is reasonable to replace the internal torque generation loop by small inertia dynamics. Such approach is usually used for drive systems of robots or machine tools, with more complicated mechanical part, which can be replaced by multi-mass systems with elastic connections.

However, in the FOC method, the decoupled relationship is obtained by means of a proper selection of state coordinates, under the hypothesis that the rotor flux is kept constant. Therefore, the rotor speed is only asymptotically decoupled from the



1,2 – respectively:
x,y for IM,
d,q for PMSM

Fig. 1 The block diagram of the FOC structure for AC motor

rotor flux, and is linearly related to the torque current after the rotor flux becomes steady-state value. This issue is not so critical in the case of PMSM, because the rotor flux is given by permanent magnets and can be assumed constant. However, the control performance of the AC motors is still influenced by the uncertainties of the drive, such as mechanical parameter uncertainty, external load disturbance, and unmodeled dynamics in practical applications.

The influence of the load is much more complicated in the case of systems, where mechanical part of the driving machine is more expanded, and contains long shaft with elasticity, backlash, hysteresis and hardly modeled friction. In such systems torsional vibrations occur, which significantly deteriorate control performance obtained with vector methods and in consequence different control concepts are required [6–11]. Such problems exist in high-power drives of heavy industry, like rolling-mill drives, textile machines, conveyers [6, 7], however, due to the progress in power electronics and microprocessor systems, which allows to control the electromagnetic torque almost without delay, they are acknowledged also in medium and small power applications, like: servo-drives, throttle drives, robot arm drives including space applications, and others [8–11].

This more advanced mechanical construction of control objects makes it significantly more difficult to precisely control the drive speed or position. In most cases, for analysis purposes, it is possible to model such complicated mechanical connection using the two-mass model [10] on the assumption, that motor torque is generated in the torque control loop (with stabilized motor flux value in the separate parallel control loop) almost without delay (first order dynamics) and is cascaded to the speed controller, as in Fig. 1. Such concept is presented in Fig. 2.

In Fig. 2 the following notation is used: ω_1 —motor speed, ω_2 —load speed, m_e —electromagnetic torque, m_s —shaft torque, m_L —load torque, τ_1 —mechanical time constant of the motor, τ_2 —mechanical time constant of the load machine, τ_c —stiffness time constant [10].

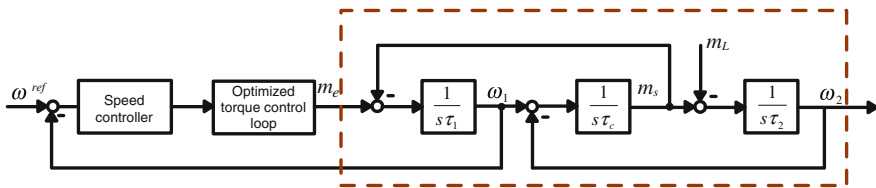


Fig. 2 Speed control structure of the drive system with a complicated mechanical part (simplified to a two-mass system)

The mechanical time constants τ_1 , τ_c , τ_2 of the mechanical part of the drive are usually much bigger than the time constant of the inner torque loop, therefore the delay of the inner torque control loop is often neglected. However, in drive systems with high resonant frequency (like servo drives or robot drives), this torque control delay causes some problems and applied control structures should take it into account at the design stage or should be robust to such unmodeled dynamics.

As it was said, the control performance of the AC motor drives with stiff and elastic mechanical connections are influenced by the uncertainties of the drive, such as electrical and mechanical parameters uncertainty, external load disturbance, unmodeled dynamics and measurement noise and delays in practical applications.

To deal with the above mentioned problems of system uncertainty, a lot of research has been done in recent years to apply various approaches known from the control theory [12–14], which can replace the well-known and widely used in industry PID-type controllers for systems with nonlinearities and uncertainties.

In the case of bounded uncertainties with known structure, the robust and adaptive techniques have been developed [13, 14]. However, to obtain the stability of these solutions, some constraint conditions and detailed prior knowledge of the controlled object are usually required in the controller design process.

In the past several years, active research has been carried out on the application of neural network and neuro-fuzzy control of electrical drives [15–18]. The learning ability, fault tolerance and parallelism suggest that such solutions may be good candidates for implementing real-time adaptive control for nonlinear and uncertain drive systems.

3 Neural Controllers with Off-Line and On-Line Training

3.1 The Main Types of Neural Networks Used in Control Systems

In most of research related to the NN implementation in power electronics and electrical drives, the *Multi Layer Perceptron* (MLP) neural networks are used. The characteristic features of such structures are as follows [19]:

- MLP are essentially feedforward structures where the information is passed from inputs to outputs, through hidden layers. This is a very convenient structure for control engineers, who get used to work with systems represented by blocks with inputs and outputs clearly defined and separated;
- according to the NN theory, MLP with one or maximum two hidden layers, using neurons with nonlinear (e.g. sigmoidal) activation functions, are able to realize any nonlinear mapping between two finite-dimensional spaces to any degree of accuracy, provided that there is a sufficient number of the hidden neurons;
- the basic learning algorithm for MLPs is the back propagation algorithm, which belongs to the class of gradient methods widely applied in optimal control, and therefore it is familiar to control engineers.

However, over time also *Radial Basis Function* (RBF) neural networks became popular, especially due to their specific structure with only one hidden layer, with neurons containing the same radial activation functions. These types of NN and their modifications are often the fundamental part of the controllers applied in dynamical systems. Due to different structures and calculations inside these NN, the learning process of RBF networks often differs from MLP networks.

3.2 Neural Controllers Trained Off-Line

For neural controllers trained off-line, the trained and testing data sets should be available. They should be specially prepared for each type of drive system, to take into account the most characteristic features and operation conditions of the drive. Training data for representation of the given task are prepared in advance, next training process is realized using special software, and then NN model (or controller) is tested. Sometimes, during the training process NN structure optimization is carried out simultaneously [19], using tools mentioned below.

In the case of the MLP structure the learning process is focused on the selection of the weights coefficients. In some solutions extensions of training process can be introduced, like structure optimization [20], application of regularization methods [21], supervision of the number of iterations during training process [22].

In RBF networks, weights factors in the hidden layer and centers of the radial function must be chosen. Often for this purpose special algorithms, such as clustering are used [23], different from those used in the optimization of weights. The analyzed data are divided into groups according to their properties, and the centers of these groups are next determined. Based on this information, center of radial function is selected. There are clustering algorithms, which enable the automatic selection of the number of clusters, thus partly optimization of the NN structure complexity is obtained [24–26].

In the training process of a MLP network it is possible to optimize the structure of a neural model. For reduction of the number of connections between neurons a prior definition of the maximum number of nodes should be defined. Then based

on a properly appointed criteria, some connections are deleted (usually based on the calculation of the sensitivity of the network during removing of the connections; it is related to determining of the influence of weighting factors removal on the value of the cost function) [27, 28]. Similar algorithms are also used in case of RBF networks [29, 30]. In order to optimize the RBF models, genetic algorithms can be also applied [31].

The mentioned above solutions, introduced during training process, are designed to optimize the generalization properties of NNs. However, this type of action is particularly important in applications of neural models designed using the off-line training process.

3.3 Neural Controllers Trained On-Line

In many applications off-line trained NN controllers are difficult for realization, as they require training data, which can be obtained by simulations of the mathematical model of a plant or by real experiments. In the case of complex industrial processes, also converter-fed drives, NN-based controllers trained on-line, are the main interest. In such solutions, parameters of NN are calculated during the operation of the electric drive, based on the actual value of the control error. Therefore, there is no necessity to use the complex optimization algorithms mentioned above. These several iterations of the learning algorithm correspond to one step of the control algorithm of the whole structure [32]. Such an approach allows for the implementation of an adaptive neural controller which reacts dynamically to the operation conditions of the drive system and its uncertainties, caused by changes of the parameters, delays in torque control loop, nonlinearities, etc.

Additional, important advantage of neural controllers with on-line weights adaptation, is the possibility to use the same design process, without parameters identification, for drives with different types of electric motors (DC, AC) and also for electrical drives with rigid and elastic mechanical connections between the driving motor and load machine. The number of parameters/features of the controllers selected during the design process, which affect the operation of the drive system is significantly reduced. These are mostly: number of hidden neurons, type of activation functions, time constants in the block shaping the input vector of NN, and coefficients of the adaptive algorithm.

The structure of the NN with on-line weights adaptation, implemented in the control system, is not so important as in the case of the off-line training strategy, therefore the problem of NN structure selection is almost neglected. Generally, we can say that activation functions of nodes depend on selected network type. Mostly the neurons of the input layer are linear and thus pre-scaling of input signals is achieved. The hidden layer, in most of the reported cases has sigmoidal neurons (mainly MLP networks), or radial (RBF) neurons. The neurons in the output layer realize calculations which form the output signal, thus usually a linear activation function is used.

In the design process of neural controllers a selection of elements of the input vector should be made. For this purpose, the properties of NN and practical implementation aspects should be taken into account. Excessive expansion of the input vector requires increasing the neural structure, which may hinder its practical implementation in a digital signal processor or FPGA (computation times, the consumption of resources). At the same time the effect (operation of the NN controller) may be only slightly improved or may even become worse. From the engineering point of view, the input vector should contain signals with important information about process changes and at the same time easily accessible for measurements. It should be noted that MLP or RBF networks, often applied in application related to the drive systems, do not have any internal feedbacks. So naturally these networks do not include dynamic calculation in the processing. Therefore, in order to take into account the dynamics of the control system signals, delayed samples of the variables used in the input vector are introduced. However, such a solution causes a dependence on numerical calculation step. Thus, it is preferred to use input preprocessing (for example, low-pass filters) with a defined time constant. The choice of the time constants should be performed during the design of the neural controller, and this is often done experimentally. The most important aspect of the design process of neural controllers trained on-line is the selection of the adaptation algorithms and the suitable coefficients of these algorithms (learning factors). The assumed values influence directly the dynamics of the obtained transients in control structure. In the case of electrical drives, these values significantly depend on the delays in the electromagnetic torque control loop and the mechanical time constants of the drive systems.

3.4 Application of Off-Line and On-Line Trained Neural Controllers in Electrical Drives

Applications of neural networks in control structures of electrical drives are widely described in scientific publications. It can be observed that the differences in applications consist of:

- the role fulfilled in the control structure,
- applied neural network topology (not only classical MLP networks, but also many modifications),
- weights adaptation methods (used training algorithm),
- mode of weights update (on-line, off-line),
- hardware implementation of neural networks.

Most of the tasks performed by neural networks in electric drives is associated with: control [33–38], parameters identification [39], state variables estimation [40–44] and diagnostics of electrical machines [45–47].

In this chapter the neural models trained on-line, for control of servomechanisms, are the main field of interest. In most of motion control systems DC or AC motors are used as actuators. In such systems the adaptive neural controllers based on model reference adaptive control concept are most often found in literature, like [33, 34]. In the Direct Torque Control structure neural networks can perform two main tasks. The first one is their application as a speed controller in the external speed control loop. The NN controller is trained on-line based on an error signal and historical samples, and thus the control signal is calculated [35]. The second task of NN in DTC structure is its operation as a voltage vector selector based on output signals of the hysteresis flux and torque controllers [37]. Moreover, these two tasks can be combined in one controller as it was proposed in [38].

A vast majority of the above mentioned applications are based on MLP neural networks and backpropagation algorithm. This training method is one of the most popular for implementation of neural networks in electrical drives. Analyzed data are processed twice in the neural model. Firstly signal is propagated through network and then the output error is propagated to all nodes in a model. Based on this calculation values of weights can be adapted. It should be mentioned that BP algorithm is effective, however, it can be time consuming (e.g. due to few cycles of calculation of each iteration of adaptation algorithm). This way of calculation may be a drawback for hardware implementation, especially for neural controller trained on-line. Alternative method for backpropagation, applied in control of electrical drive, is Resilient Backpropagation [38]. This method has two important features (particularly from the perspective of hardware implementation): update of weights is based on sign of derivative of the cost function according to weights, magnitude of changes can be selected individually for each weight. These characteristic properties give: simplicity of calculations and finally shorter time needed for realization. In application in neural controllers it can lead to better reaction to changes of input speed error and robustness against parameter fluctuations. In papers related to neural networks, one can find descriptions of different training algorithms. In our review of the literature, we want to draw attention to the adaptive interaction method applied in neural networks. It is described in literature as equivalent for BP algorithm [48]. However there is an important advantage because of the simplicity of the analysis of the influence of weight changes on a cost function. As a result feedback propagation of error can be omitted.

One of the most common topics related to neural controllers is stability analysis. In the case of neural models it is hard to observe the placement of the poles of the whole control structure. Moreover, neural networks should be considered as nonlinear systems. The most popular way of stability analysis applied for neural controllers with on-line training is the Lyapunov method [49–51]. The main problem of this method is the definition of the Lyapunov function, which should satisfy the conditions of Lyapunov stability theory. It can provide a limitation of weights or training coefficients which guarantee stability of the system. It is possible to use a combination of neural networks with fuzzy model for stable control, however, this method is less common [52]. Stability analysis of neural

controller can be carried out using methods which are different from the control theory related to nonlinear systems. An interesting application is Harmonic Balance Method for analysis of closed neural control loop. Based on this method the description of neural controller function can be designed. Then speed control structure can be examined using Nyquist stability criterion [53].

Numerous papers are related to electrical drives with a specific, complex mechanical part. The mathematical model used in this analysis takes into account the elements that represent a long flexible shaft connecting the motor with the load. This construction makes it significantly more difficult to precisely control speed or position. One of the solutions used in such a situation are controllers based on elements of artificial intelligence, implementing fuzzy logic, neural networks and genetic algorithms. For systems with a flexible connection application of the neural networks, it is not presented very frequently. One of the first descriptions related to the application of MLP neural networks and back propagation algorithm was presented in [54]. The presented simulation studies are related to medical equipment control (used in laparoscopy). It was assumed that it would be possible to achieve a control structure for a drive with an elastic shaft, robust against nonlinearities like friction and backlash. Neural networks can also cooperate with linear controllers. In the control system of a manipulator two neural networks were applied to compensate disturbances [55]. Moreover, the original implementation of neural speed controller is described in [56]. Calculations of neural network are realized on a PC computer while the two-mass model is made as an electronic circuit (analogue). In publication [50] theoretical analysis, stability proof and simulations of control systems with RBF neural network is presented. Besides the full topology of neural networks, like MLP or RBF, much simpler structures using ADALINE (linear neuron) models with adaptation of weights can be used for speed control of electrical drives [57]. The advantage of this type of application is its significantly simplified structure; this argument is especially important for hardware implementation.

4 Description of the Analyzed Neural Models with On-Line Training Capability

4.1 Adaptive Linear Neuron (ADALINE)-Based Controller with the Delta Training Rule

One of the simplest adaptive models based on neural networks theory is an ADALINE [15, 58, 59]. It is a simple node with adaptive coefficients. These parameters are introduced for calibration of input signals and have a significant influence on the output/control signal. The mathematical model of the ADALINE is represented by formulas:

$$y(k) = f(u(k)) \tag{4}$$

$$u(k) = b(k) + \sum_{i=1}^N x_i(k)w_i(k). \tag{5}$$

where: f —activation function, w_i —weights coefficients, x_i —input signals, u —argument of the activation function, b —bias value, N —number of input signals.

In the application of the ADALINE model for speed control of electrical drives, the bias input is omitted, moreover linear activation function is assumed. So the ADALINE based controller can be thus generally described using following equation:

$$y(k) = \sum_{i=1}^N x_i(k) w_i(k). \tag{6}$$

The block diagram of such ADALINE structure is presented in Fig. 3.

In the case of the on-line ADALINE training process, in several iteration k of the training algorithm, weights are recalculated:

$$\mathbf{w}(k + 1) = \mathbf{w}(k) + \Delta\mathbf{w}(k), \quad k = 0, 1, 2, \dots \tag{7}$$

In minimization of the cost function, its expansion in Taylor series is used, and can be written as follows:

$$E(\mathbf{w}(k + 1)) = E(\mathbf{w}(k) + \Delta\mathbf{w}(k)) \approx E(\mathbf{w}(k)) + \mathbf{g}(k)\Delta\mathbf{w}(k), \tag{8}$$

where $\mathbf{g}(k)$ is a gradient matrix that contains first derivatives of cost function according to the weights:

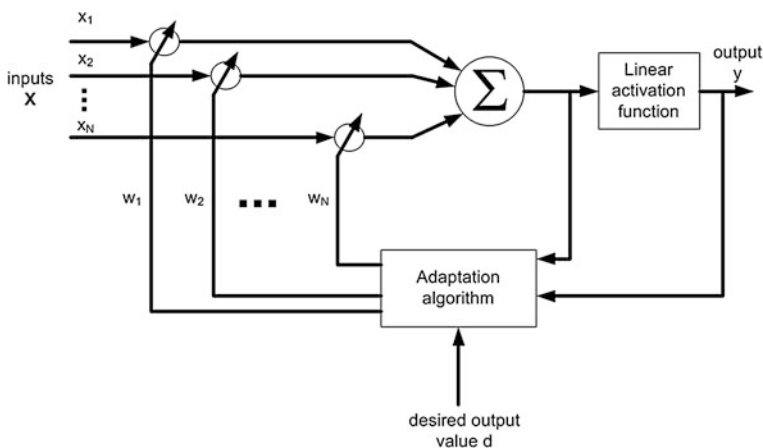


Fig. 3 The structure of the ADALINE model

$$\mathbf{g}(k) = \frac{\partial \mathbf{E}}{\partial \mathbf{w}}. \quad (9)$$

Adaptation algorithm must lead to the cost function minimization:

$$E(\mathbf{w}(k+1)) < E(\mathbf{w}(k)), \quad (10)$$

so, following condition should be satisfied:

$$\mathbf{g}(k) \Delta \mathbf{w}(k) < 0, \quad (11)$$

and changes of weights factors in (5) should be done according to the formula:

$$\mathbf{w}(k+1) = \mathbf{w}(k) - \lambda \mathbf{g}(k), \quad k = 0, 1, 2, \dots \quad (12)$$

where: λ —positive value—adaptation coefficient.

For the linear activation function of the ADALINE, the cost function, defined usually as a square of the error between NN output and its desired value, will take the following form:

$$E(\mathbf{w}(k)) = (y(k) - d(k))^2 = \left(\sum_{i=1}^N x_i(k) w_i(k) - d(k) \right)^2, \quad (13)$$

where: $y(k)$ —output value in each iteration, $d(k)$ —desired value in each iteration. Gradient matrix of the cost function is thus described by following equation:

$$\mathbf{g}(k) = \frac{\partial \mathbf{E}}{\partial \mathbf{w}} = 2 \left(\sum_{i=1}^N x_i(k) w_i(k) - d(k) \right) \mathbf{x}_i(k). \quad (14)$$

Connection of the Eqs. (9) and (11) leads to the expression for weights calculation in each training epoch [58, 59]:

$$\mathbf{w}(k+1) = \mathbf{w}(k) - 2\lambda \left(\sum_{i=1}^N x_i(k) w_i(k) - d(k) \right) \mathbf{x}_i(k). \quad (15)$$

On-line adaptation of weights can be very effective in control applications of the ADALINE. It is possible to design an adaptive controller, giving better results than classical PI/PID controllers especially for time-varying systems [60, 61].

4.2 Multi-Layer Perceptron-Based Neural Controller with Backpropagation Training Algorithm

Structures based on MLP networks are highly configurable adaptive models (containing potentially multiple changeable parameters). Configurability means here a possible modification of the NN structure. In the presented analysis MLP networks are applied as speed controllers of electrical drives. Values of weight

factors are changed on-line. The general topology of the used NNs contains one hidden layer (Fig. 4).

In the hidden layer nonlinear sigmoidal activation functions are used, in the output layer (controller output) a linear neuron is implemented. Several steps of the signal processing in such MLP-based controller are presented below:

- input signals are initially scaled using input weights w_{ij} ,
- input signals of each hidden neuron are next summed and recalculated using activation function,
- output, linear neuron is introduced for summation of scaled signals from hidden layer.

Each iteration of the training process introduces changes of weights:

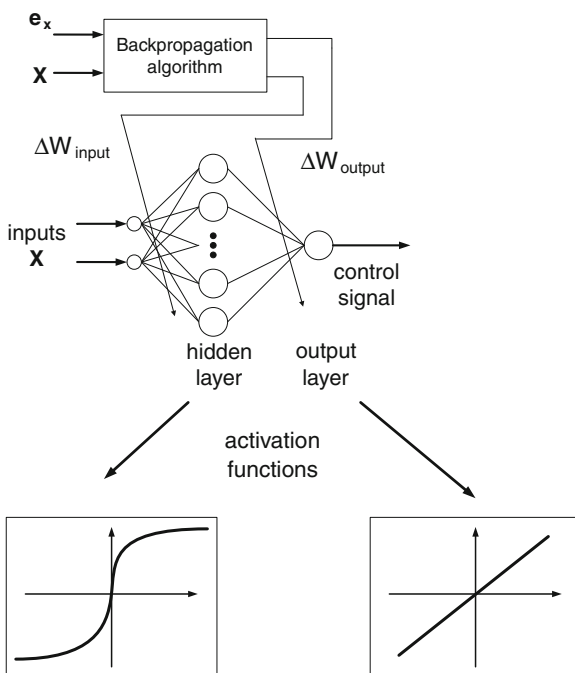
$$w_{ij}(k + 1) = w_{ij}(k) + \Delta w_{ij} \tag{16}$$

where: w_{ij} —weights between node i and j in k th iteration.

Corrections of weight values Δw_{ij} are calculated according to the backpropagation algorithm [62]. An update of each weight value can be described using the following expression:

$$\Delta w_{ij} = -\alpha \delta_j x_{ij} \tag{17}$$

Fig. 4 Structure of the one-output MLP neural network trained on-line



where: α —learning rate, x_{ij} — i th input of j th neuron, δ_j —propagated error and derivative of the activation function (described below).

Parameter α in (17) determines intensity of the adaptation algorithm. Increasing this coefficient during off-line training can make it difficult to find a minimum of the objective function. In the case of neural controllers trained on-line, the value of α can shape the dynamics of the controlled object in the control structure.

The analyzed controller contains only one hidden layer with sigmoidal neurons and one output. The values δ_j from Eq. (17), for weights between inputs and hidden layer, can be described by the following equation:

$$\delta_j = f'_j \delta_o w_{jo}, \quad (18)$$

f'_j —derivative of the activation function of the j th neuron in the hidden layer, w_{jo} —weights between hidden layer and output neuron.

For the output layer with a single linear neuron $\delta_j = \delta_o$:

$$\delta_o = d - y, \quad (19)$$

where: d —desired value of the output signal, y —actual value of the output signal.

4.3 Radial Basis Function-Based Adaptive Neural Controller

Another commonly applied neural network structure is the Radial Basis Function network. RBF neural network differs from the classical MLP structure in the idea of neural processing and learning methodology. Input data of the RBF network are transformed using local mapping carried out in radial neurons, the final result is obtained by calculating the sum of the weights of each hidden layer neurons. The structure of RBF neural network is presented in Fig. 5.

The layers are arranged inside the structure of the neural network, relative to each other, in series, and the radial neurons are arranged in parallel. Data inside the network are processed from input to output, without internal connections in a layer, therefore these models are called 'feedforward'. In the structure of the analyzed NN the following calculation stages can be extracted [62, 63]:

- in the input layer distances between inputs elements and centers of radial neurons are calculated (the most often—Euclidean norm),
- scaling with σ coefficient,
- in the hidden layer calculation of radial functions for arguments obtained in the previous stage are realized (hidden neurons do not have the connections to external signals and internal feedbacks),
- in the output layer, containing a linear neuron, values obtained at the output of radial neurons are multiplied by weight factors and then summed).

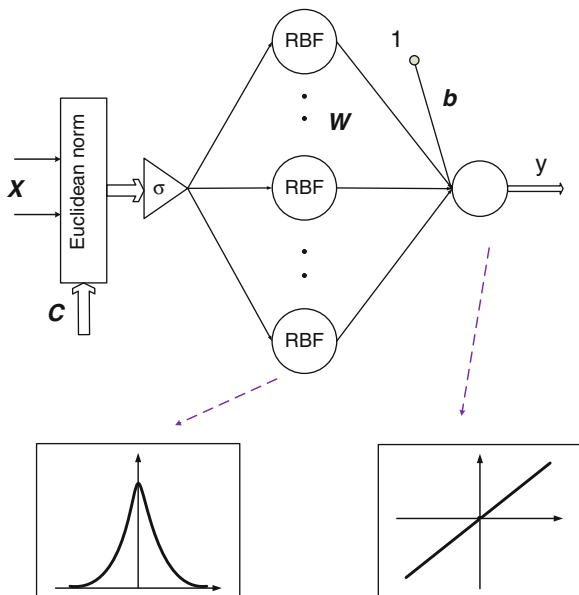


Fig. 5 The topology of RBF network

Outputs of hidden layer are usually determined using Gaussian function:

$$f_g(\mathbf{X}, \mathbf{C}, \sigma) = \exp\left(-\frac{v^2}{\sigma^2}\right), \tag{20}$$

where: σ scaling parameter, shaping the radial function, v is the difference between center of neuron and inputs elements, \mathbf{X} -input vector of NN.

Usually the difference between the center of a neuron and input elements is calculated using an Euclidean norm:

$$v(\mathbf{X}) = \|\mathbf{X} - \mathbf{C}\| = \sqrt{\sum_{i=1}^N (x_i - c)^2}, \quad i = 1, 2, 3, \dots, N \tag{21}$$

where: x_i — k th element of the input vector \mathbf{X} , c —one of center of the RBF function.

Calculations in the output layer with one input are described using the following equation:

$$y = b + \sum_{h=1}^H w_h f_{g_h} \tag{22}$$

where: h -number of hidden radial nodes, y -actual value of the neural network output, w_h -weight coefficient between h th RBF neuron (with Gaussian-type activation function f_g) and output, b -bias.

In the case of the RBF-based neural controller with one output ($j = 1$), the output value of the network can be represented as follows, using matrix notation:

$$y = b + \mathbf{W}\mathbf{f}_g(\mathbf{X}, \mathbf{C}, \sigma) \quad (23)$$

In the RBF network applied as a neural controller, the weights and centers of radial neurons are updated simultaneously. For this purpose, a gradient algorithm can be selected. This type of optimization method is described as the most efficient and the most sensitive to the changes of the input signals [64, 65].

For this purpose the quadratic cost function can be selected [66]:

$$E(\mathbf{W}) = \frac{1}{2} \sum_{j=1}^M [e(\mathbf{W}_j)]^2 = \frac{1}{2} \sum_{j=1}^M (d_j - y_j)^2, \quad (24)$$

where j —number of NN outputs.

For the described above structure of RBF controller with one output ($j = 1$), this cost function takes the following form:

$$E = \frac{1}{2} (e(\mathbf{W}))^2 = \frac{1}{2} [d - (b + \mathbf{W}\mathbf{f}_g(\mathbf{X}, \mathbf{C}, \sigma))]^2. \quad (25)$$

The gradient of the cost function against the optimized weight coefficients is given by the following equation:

$$\frac{\partial E}{\partial \mathbf{W}} = \frac{1}{2} \left(2e \frac{\partial e}{\partial \mathbf{W}} \right), \quad (26)$$

where partial derivatives calculated from the Eq. (25):

$$\frac{\partial e}{\partial \mathbf{W}} = -\mathbf{f}_g(\mathbf{X}, \mathbf{C}, \sigma). \quad (27)$$

Thus the gradient value (26) takes the form:

$$\frac{\partial E}{\partial \mathbf{W}} = -[d - (b + \mathbf{W}\mathbf{f}_g(\mathbf{X}, \mathbf{C}, \sigma))] \mathbf{f}_g(\mathbf{X}, \mathbf{C}, \sigma) = -e \mathbf{f}_g(\mathbf{X}, \mathbf{C}, \sigma) \quad (28)$$

Therefore, the update of the weights in the output layer of the analyzed RBF controller, in each iteration of the algorithm is described by the following formula, according to the gradient method:

$$\mathbf{W}(k) = \mathbf{W}(k-1) - \eta_w \frac{\partial E}{\partial \mathbf{W}}. \quad (29)$$

Substituting gradient value (28) in the Eq. (29) we obtain:

$$\mathbf{W}(k) = \mathbf{W}(k - 1) + \eta_w e \mathbf{f}_g(\mathbf{X}, \mathbf{C}, \sigma). \quad (30)$$

A similar calculation was carried out in order to obtain an equation describing the update of the centers of the RBF neural controller. For the same form of the cost function (25), the gradient calculated according to RBF neuron centers takes the form:

$$\frac{\partial e}{\partial \mathbf{C}} = \frac{1}{2} \left(2e \frac{\partial e}{\partial \mathbf{C}} \right), \quad (31)$$

where:

$$\frac{\partial e}{\partial \mathbf{C}} = -\mathbf{W} \frac{(\mathbf{X} - \mathbf{C})}{\sigma^2} \mathbf{f}_g(\mathbf{X}, \mathbf{C}, \sigma), \quad (32)$$

and thus:

$$\frac{\partial E}{\partial \mathbf{C}} = -e \mathbf{W} \frac{(\mathbf{X} - \mathbf{C})}{\sigma^2} \mathbf{f}_g(\mathbf{X}, \mathbf{C}, \sigma) \quad (33)$$

According to the gradient algorithm the relationship for RBF centers updating is presented below:

$$\mathbf{C}(k) = \mathbf{C}(k - 1) - \eta_c \frac{\partial E}{\partial \mathbf{C}}. \quad (34)$$

Combining Eqs. (34) and (33) this updating algorithm takes the form:

$$\mathbf{C}(k) = \mathbf{C}(k - 1) + \eta_c e \mathbf{W} \frac{\mathbf{X} - \mathbf{C}}{\sigma^2} \mathbf{f}_g(\mathbf{X}, \mathbf{C}, \sigma). \quad (35)$$

Equations (30) and (35) describe the calculations realized for weight and center vectors in the training process of the of the RBF neural controller. In the presented application the update process is performed *on-line*. Coefficients η_w and η_c are constant and they have influence on the dynamics of control structure based on RBF neural controller.

4.4 Neural Controller with an Adaptive Interaction Algorithm

The most popular method for weight adaptation in NN is the backpropagation algorithm. This algorithm is realized in two steps: first the input signals are processed through the network structure, and next—the error between the desired and actual output is back propagated through the net. This second part of this algorithm

constitutes the main drawback of the MLP-based neural networks, and can be troublesome for real applications, especially for on-line implementations. In paper [48] the adaptation algorithm of weight factors, similar to backpropagation was presented, however, it does not need propagation of the error thorough the net. This algorithm is equivalent to the gradient descent method, but is much simpler in the case of a hardware realization.

The output of each neuron in the hidden layer is calculated according to the following equation:

$$y_n = f_n(u_n) = f_n\left(\sum_{i=1}^N w_i x_i + b_n\right), \quad (36)$$

where: y_n —output of n th neuron, b_n —value of bias of n th neuron, w_i —weight for i th input of neuron, f_n —activation function of n th neuron.

In this application external input (bias) is neglected. During the training process the cost function, is defined in a classical way:

$$E = \frac{1}{2} \left(\sum_{n=1}^M e_n^2 \right), \quad (37)$$

is minimized. In the above equation:

$$e_n = \begin{cases} y_n - d_n & \text{for output neuron} \\ 0 & \text{otherwise} \end{cases}, \quad (38)$$

where: d_n —desired output value of n th output node and M is a number of all output neurons.

Update of weights can be calculated using the following expression:

$$\Delta w_i = f'_n(u_n) \frac{x_i}{y_n} \sum_{j=1}^p w_{oj} w'_{oj} - \gamma f'_n(u_n) x_i e_n, \quad (39)$$

where: p —is a number of neurons in next layer, $\gamma > 0$.

In the case of neurons with sigmoidal activation functions:

$$f_n(u_n) = \frac{1}{1 + e^{-u_n}}, \quad (40)$$

where: u_n —input of the activation function, derivative of (40) can be calculated as:

$$f'_n(u_n) = f_n(u_n)(1 - f_n(u_n)) \Rightarrow f'_n(u_n) = f_n(u_n)f_n(-u_n) = y_n f_n(-u_n). \quad (41)$$

Then Eq. (39) can be rewritten as follows:

$$\begin{aligned} \Delta w_i &= y_n f_n(-u_n) \frac{x_i}{y_n} \sum_{j=1}^p w_{oj} w'_{oj} - \gamma y_n f_n(-u_n) x_i e_n \\ &= x_i f_n(-u_n) \sum_{j=1}^p w_{oj} \Delta w_{oj} - \gamma y_n f_n(-u_n) x_i e_n \end{aligned} \tag{42}$$

Based on the Eq. (42) the neural controller can be designed [67], with topology presented in Fig. 6.

In the structure of the tested controller two main subsystems can be specified: the first one with processing of signals in neural controller and the other one with realization of adaptation law. The coefficient is selected experimentally.

5 The Chosen Application of the On-Line Trained Neural Controllers in Electrical Drives

5.1 Adaptive Neural Controllers in the Induction Motor Drive with Vector Control

This part of the chapter presents selected applications of neurocontrollers trained-on-line, described in previous section, in speed control of electrical drives. The main advantages, design problems and specific features are presented.

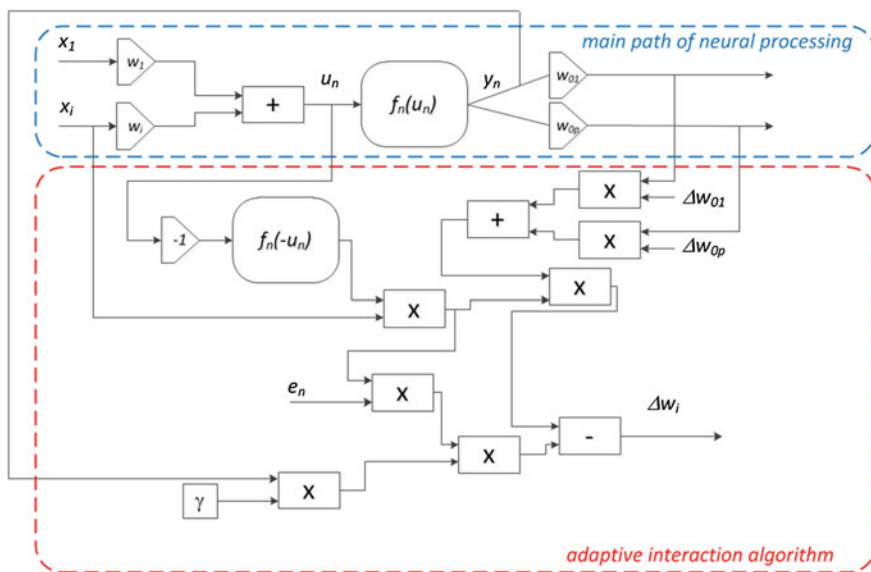


Fig. 6 The structure of NN controller with Adaptive Interaction Algorithm

First of all, the MLP-based controller was applied in the Direct Rotor Field Oriented Control (DRFOC) structure of the induction motor drive with a stiff connection between the motor and the loading machine. In most of IM drives, design process of the rotor speed and flux requires adjustment of the PI/PID controllers based on preliminary identification of the drive, which is rather complicated. The application of neural speed controllers leads to simplification of the control structure synthesis. Parameters inside the neural speed controller are recalculated on-line, according to the backpropagation algorithm (16–18), based on the speed error. In most applications only selection of adaptation coefficient in the on-line training algorithm is needed. In the control structure presented in Fig. 7, the classical PI rotor speed and flux controllers in the outer loops are replaced by NN-based controllers.

The speed error is defined as the difference between the desired and actual value of controlled state variable (rotor flux magnitude and rotor speed, respectively). This information is used in the backpropagation algorithm for calculation of new values of weights. The input vector of MLP network contains a speed or flux error and the filtered value of this signal (using first order low-pass filter). In the structure of a neural controller two parts can be extracted, the first one is related to calculation of neural network and the other one is connected with adaptation algorithm, based on Eq. (17). Weight values of the MLP networks are calculated in parallel to the main processing path. Neural controllers are applied directly in

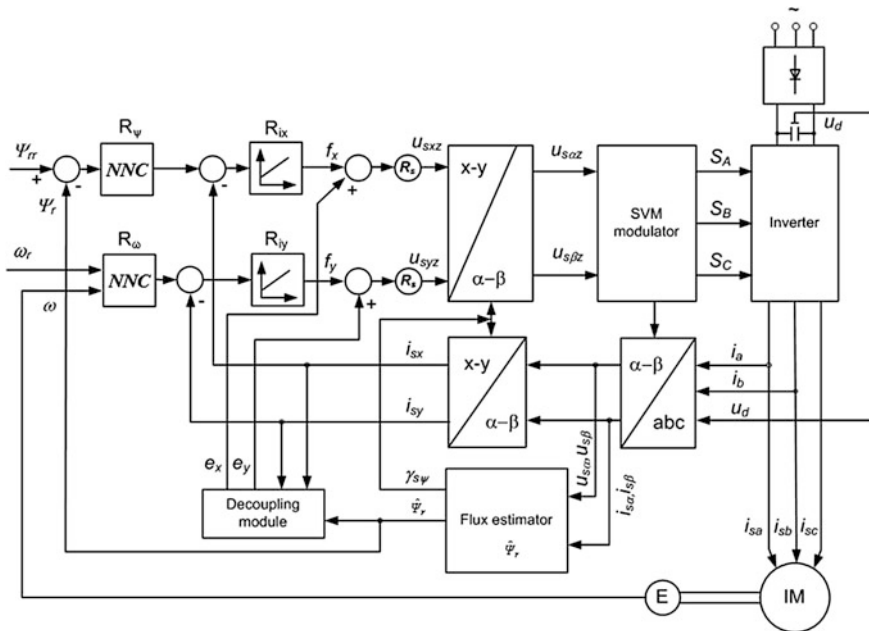


Fig. 7 An induction motor drive with DRFOC structure and MLP-based neural adaptive controllers

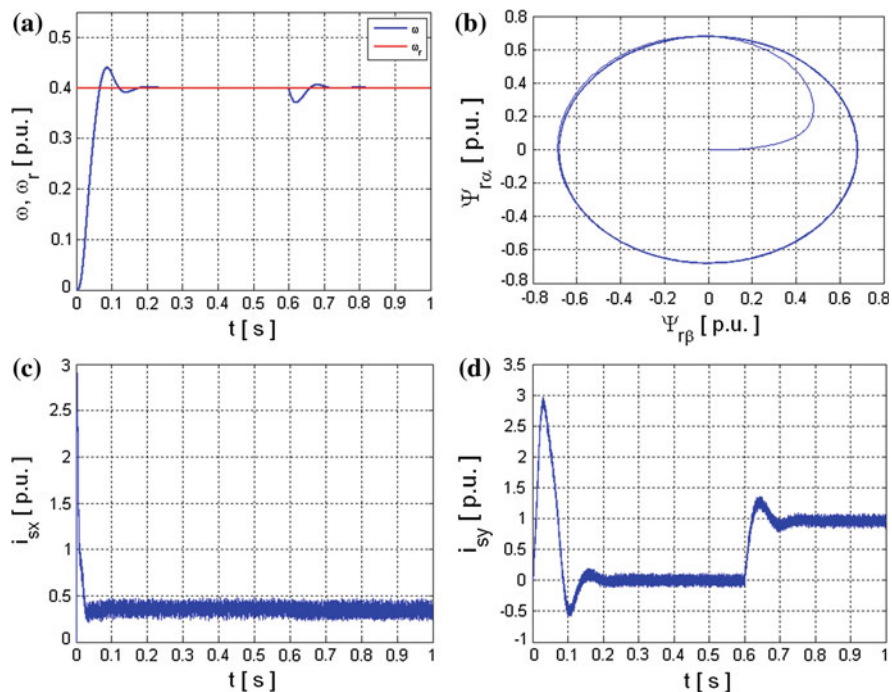


Fig. 8 Transients of state variables in DRFOC drive: the actual and reference speeds (a), rotor flux hodograph (b), components of the stator current vector (c, d)

control loops of the rotor speed and flux. It can be said that in the control structure presented in Fig. 7 the neural networks and adaptation algorithms are applied for errors (in the speed and flux control path) minimization. It is realized on-line during the drive system operation, so controller reaction to state variables changes is ensured.

In Fig. 8 simulation results for speed and flux controllers applied in the DRFOC structure are presented. The chosen state variables present the correct work of this drive system. Transients of rotor speed, rotor flux and stator current in the structure present a response of the drive to step change of reference speed, which is taken to be equal to 40 % of the nominal speed. Training coefficients in both NN controllers are equal to 0.03. The speed of the induction motor is set to the reference level very quickly (Fig. 8a). At time $t = 0.6$ s the load torque is applied. It leads to an increase of the torque current i_{sy} (Fig. 8d). Effective decoupling of electromagnetic torque and rotor flux control circuits is observed (Fig. 8c).

As it was said before, in the case of MLP controller, the application of only one externally tuned parameter (at the design stage)—the training coefficient, instead of four parameters in two PI controllers, as in the classical solution, means that the drive system parameters are not required for the controller design.

5.2 Adaptive Neural Controllers in a Drive System with Resilient Coupling

As it is known from the literature, the effective damping of torsional vibrations in such drive systems can be obtained with the application of different control structures, like PI controllers with additional feedbacks from mechanical variables (load side speed, ω_2 , shaft torque m_s and their combinations [10]) or more advanced controllers, like adaptive—including neuro-fuzzy controllers [17] or predictive controllers [68]. The last ones control algorithms are rather complicated and thus require fast microcontrollers with high computation power.

As it was shown before, the ADALINE or RBF-based neurocontrollers have a large number of adaptive coefficients, but only one design factor (learning rate), thus their application in the drive system with elastic coupling can be a competitive solution. So the on-line trained neural controllers presented in Sect. 4, were tested also as speed controllers of the drive system with resilient coupling.

The general scheme of the analyzed control structure with a neural speed controller, based on the one feedback from easily measured (or estimated—in the case of the speed sensorless drive) driven motor speed ω_1 , is presented in Fig. 9.

First, the ADALINE-type speed controller is applied in the speed control loop. In Fig. 10 state variables of a two-mass drive system controlled by such NN controller are presented. Adaptation was realized on-line according to the adaptation algorithm (15). The influence of the learning coefficient λ on speed response dynamics is demonstrated.

Transients of speeds in control structure: of motor and load have higher dynamics for bigger value of λ parameter, reference value is achieved faster, reaction to the load torque change is faster too. It should be noticed that the transients of both speeds, ω_1 , ω_2 , are very similar to the control structure realized without additional feedbacks. During transients, the electromagnetic torque reaches bigger values in order to force the higher dynamics of the drive. So, values of training factor λ in this neural controller determine the dynamics of all state variables of the electrical drive. It should be highlighted, that a neurocontroller starts with weights values equal to zero and adapts its weights on-line, during drive transients.

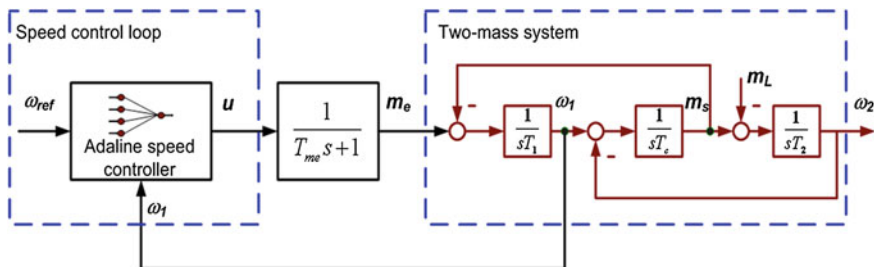


Fig. 9 Neural speed control structure of two-mass system

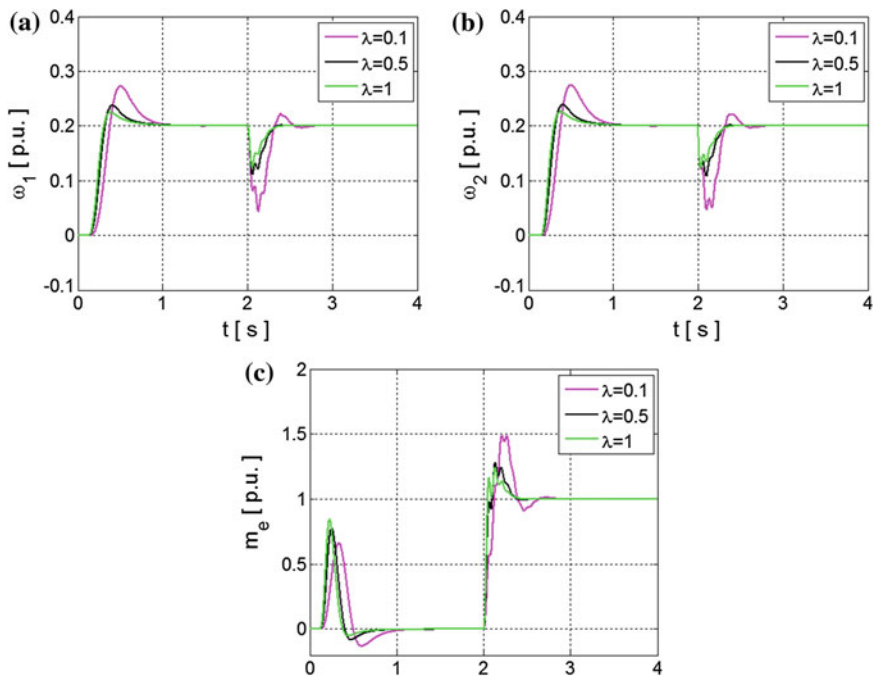


Fig. 10 Influence of the learning coefficient λ of the ADALINE speed controller on the transients of motor speed ω_1 (a), load speed ω_2 (b) and electromagnetic torque m_e (c)

Adaptive controllers based on artificial intelligence have a very important advantage. These models can ensure very high precision of control for a drive with time-varying parameters. The adaptation of internal weights shapes the control signal and interacts with the object to dynamically follow the reference trajectory.

Next the effectiveness of the RBF-based neurocontroller is tested in a two-mass system. The tested controller has five radial nodes with Gaussian-type activation function in the structure. Sample transients of chosen state variables for cyclic reverse operation are presented in Fig. 11. The drive starts work without load and for random initial values of the RBF controller. After a very short time (about 1 s) weights are adapted to the correct level, and motor and load side speed trajectories are almost identical with the reference trajectory. Additionally in subsequent reversions, the reduction of overshoot is observed. After some time (about 15.5 s) load torque is applied; the drive still works properly and both speeds track the reference speed.

In Figs. 12 and 13, the influence of training coefficients on weights and state variables transients is presented. These tests were realized for the step response of the control system. It is more interesting than in ADALINE controller case, because in the case of RBF neural network not only weight are adjusted. During the operation of the drive, values of centers are simultaneously recalculated. Changes of the learning rate η_c were introduced for $\eta_w = \text{const} = 0.01$, while tests for different value of η_w were realized for $\eta_c = \text{const} = 0.01$. Higher values of

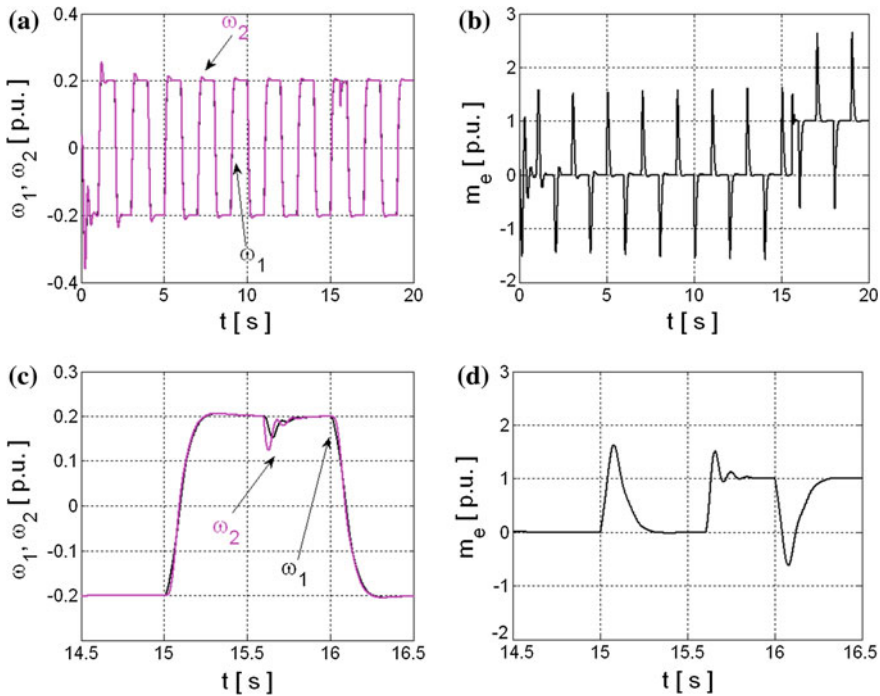


Fig. 11 Transients of speeds (a, c) and electromagnetic torque (b, d) in two-mass system with RBF-based speed controller

these parameters lead to faster changes of weights. Parameter η_w has more significant influence on dynamics of the weights reaction. Values of the above mentioned training parameters have direct influence on weights in neural controller and indirect on state variables of whole drive.

Next the robustness of RBF-based speed controller of drive with elastic connection is tested. In Fig. 14 state variables for nominal values and additionally for changes of stiffness time constant T_c are presented.

It should be noted that most of adaptation algorithms used in neural controllers require selection of initial values of weights. Training methods are sensitive to initial condition. Selection of initial values of weights is important for correct calculation and stability. Most often these parameters are selected randomly. It can give different results during start of the drive for each test. It should be remembered that for objective comparison of the results achieved by one controller, tests should be prepared for the same initial weights.

The tested neurocontrollers, together with whole control structure of electromagnetic torque control of the driving motor fed from the converter, were implemented in a digital signal processor (using dSPACE card) and the selected results are presented in Figs. 14 and 15. The practical implementation of neural networks in DSP was realized using the high-level programming language.

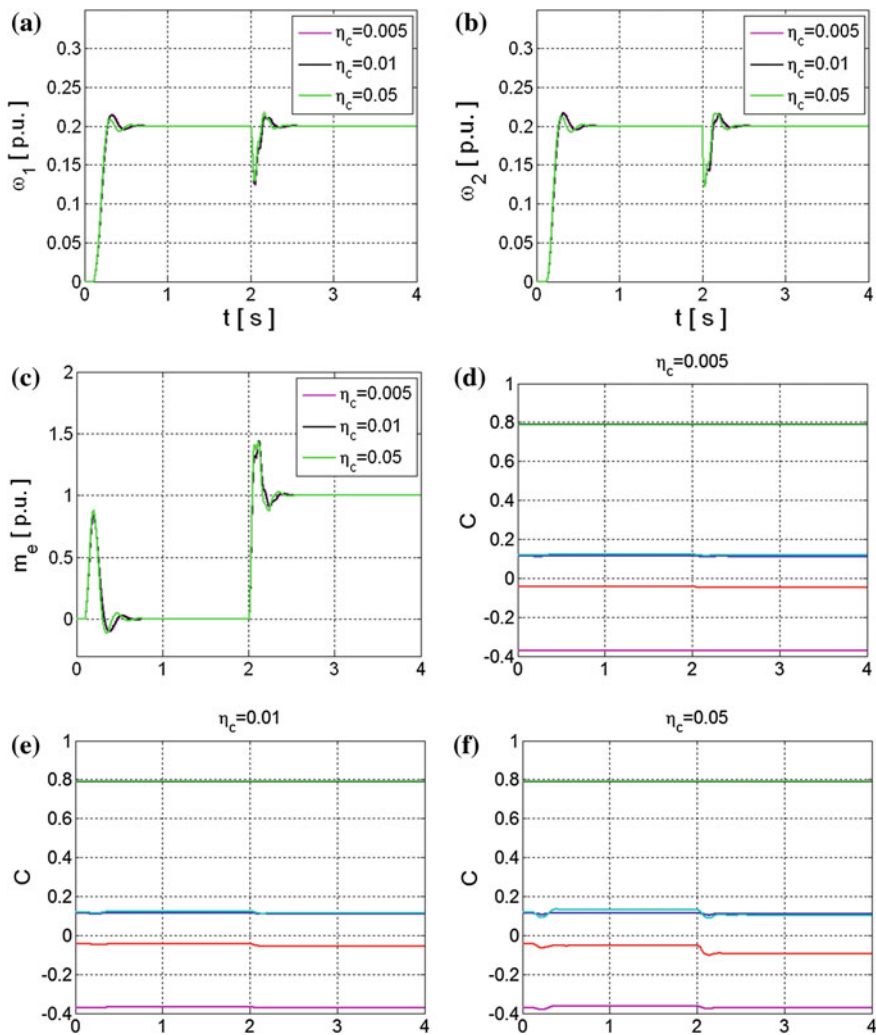


Fig. 12 Influence of the η_c coefficient of RBF controller on state variables and centers' transients: motor (a) and load (b) speeds, electromagnetic torque (c) and changes of neurons centers (d–f); $\eta_w=0.01$

Simulink was used for this purpose. It leads to the simplification of the implementation procedure (the same programming language is used in simulation, which means that implementation is easier comparing to the low-level languages, e.g. C++, simple support for input/output signals). Data from motor speed and current sensors are read, NN-based control algorithm is calculated and then each of switches of the power converter is suitably controlled. The loading machine can be also controlled from dSPACE, trough power electronics elements.

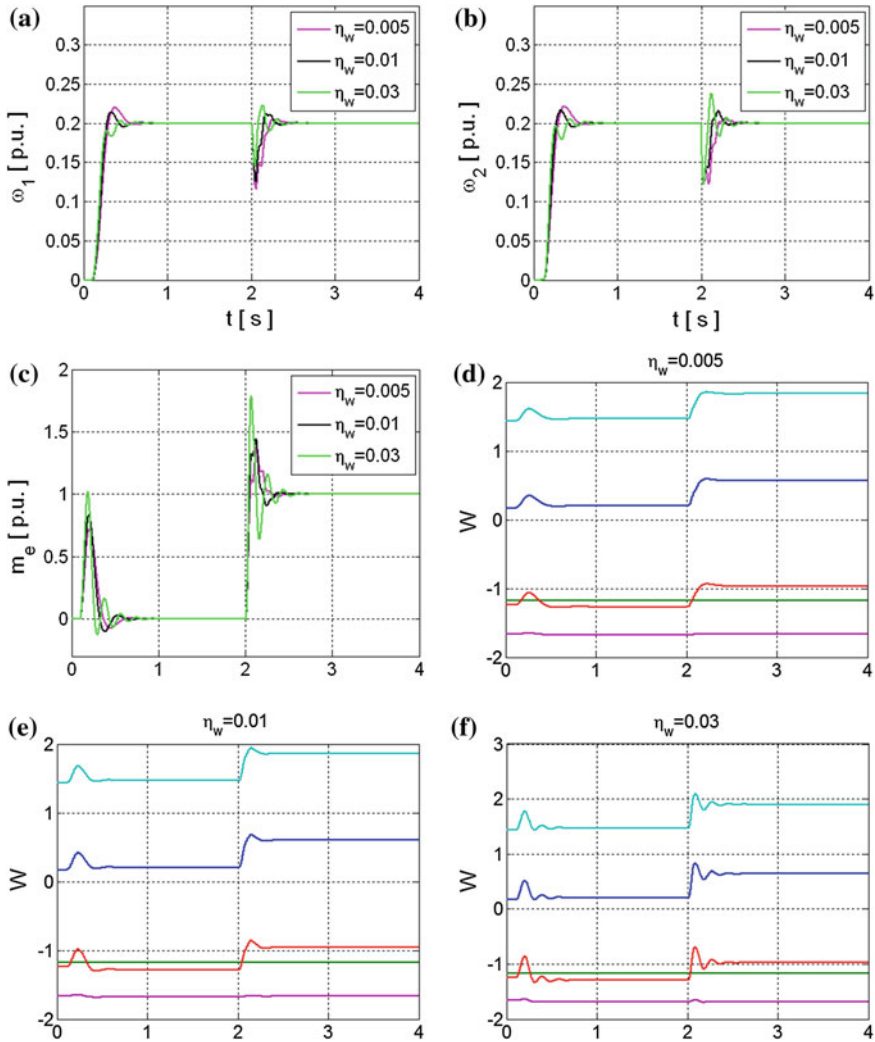


Fig. 13 Influence of the η_w coefficient of RBF controller on state variables and weights transients: motor (a) and load (b) speeds, electromagnetic torque (c) and changes of neurons weights (d-f); $\eta_c=0.01$

In Fig. 16 the experimental results of MLP-based speed controllers trained with the backpropagation method and using Adaptive Interaction algorithm for the drive system with elastic shaft are presented, respectively.

Transients measured in a real laboratory drive, are obtained for $\alpha = 0.5$ and $\gamma = 500$, respectively. Tests were realized for reference speed set to 20 % of nominal value and after $t = 2.5$ s reverse of the drive is realized. Load torque is changed in $t_1 = 1$ s and $t_2 = 3.5$ s. The presented transients are confirmation of

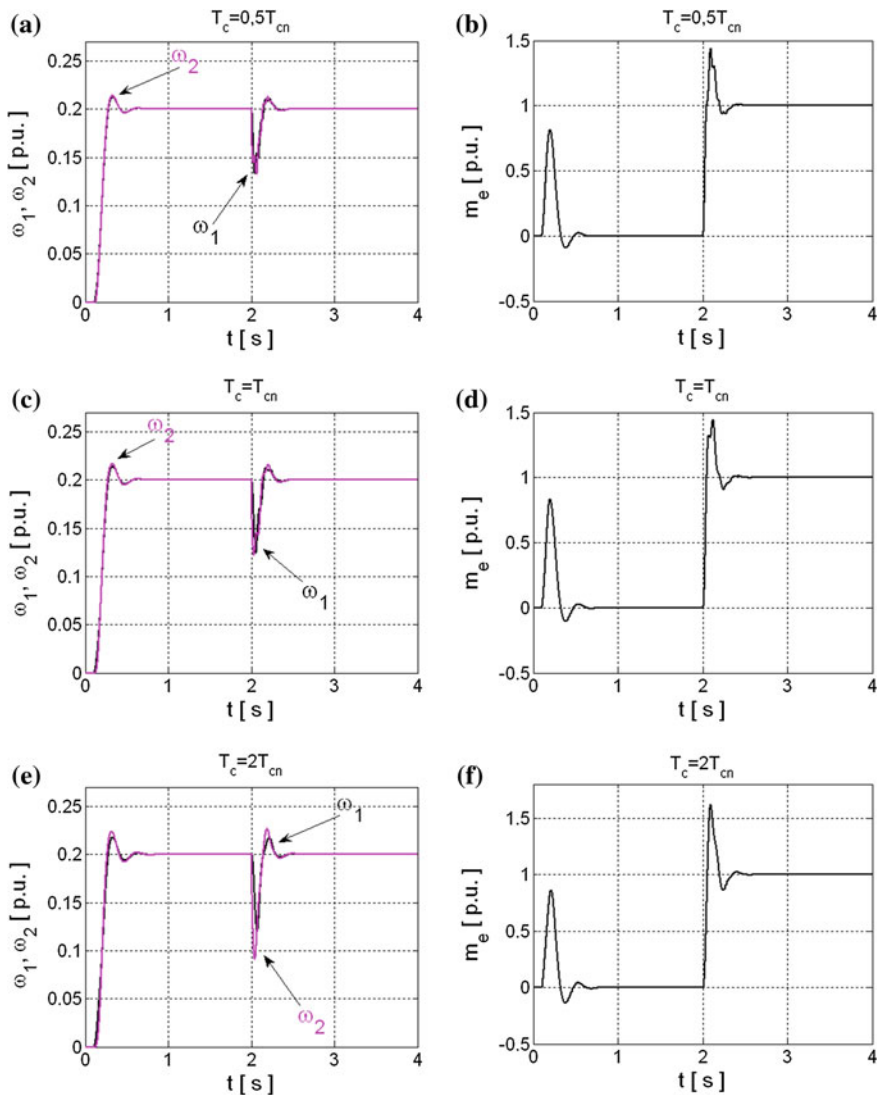


Fig. 14 Transients of state variables in control structure with RBF based neurocontroller: motor ω_1 and load ω_2 speeds (a, c, e) and electromagnetic torque m_e (b, d, f) for different values of time constant T_c

properties observed earlier in simulation tests. The second of the neural controllers is the simplest realization for hardware and gives slightly better results (see Fig. 16c, d). Adaptive interaction is equivalent to backpropagation algorithm, but it is much easier in implementation from the data processing point of view (it does not need two steps of data processing through the network).

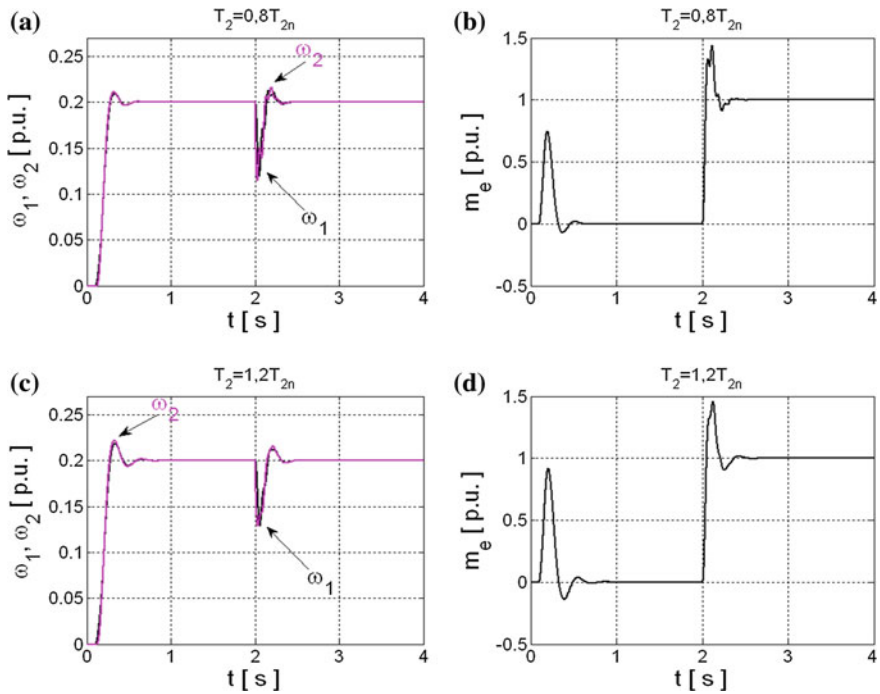


Fig. 15 Transients in the drive system with RBF-based speed controller: motor ω_1 and load ω_2 speeds (a, c) and electromagnetic torque m_e (b, d) for different values of time constant T_2

6 Hardware Implementations of Neural Controllers

Artificial neural networks are mathematical models which realize calculations inspired by human brain operation. Neural networks are a useful tool for computing implemented in many fields of science and technology. This is due to a lot of advantageous properties, such as data generalization and the ease of the description of complicated uncertain phenomena. In the last decades of previous century researches were concentrated on theoretical analysis. Nowadays their work is more related to practical implementations in different areas. Opportunities for practical applications of artificial neural networks have increased with the development of electronics. Elementary operations in processing of neural networks are simple, however, often a huge number of such calculations are preformed. These models can be implemented in hardware or simulated using software. One of the special features of neural networks is the parallel performance of mathematical operations. In standard structure (without internal feedbacks) calculations in several layers (between nodes) are realized in parallel with processing between layers which is made in series. In fact, this property is difficult to obtain using software, where steps of the code are executed sequentially [69]. In the case of hardware

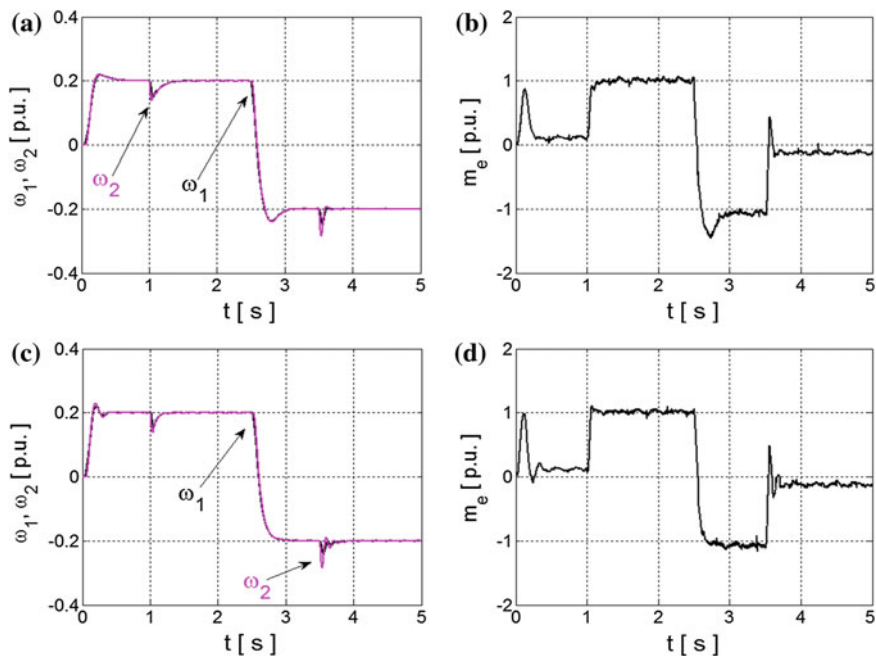


Fig. 16 Experimental transients of state variables in control system: motor speed ω_1 , load speed ω_2 (a, c) and electromagnetic torque m_e (b, d) for MLP-based speed controller trained with backpropagation (a, b) and with adaptive interaction (c, d) algorithms

implementation of neural networks in analog technology, there is a problem with a relatively low degree of configurability of the neural model. This is particularly important for a practical use of a neural network, where during the design process a frequent reconfiguration of the structure and its parameters is needed. Implementation of neural network in digital technology is not easy either because of the needed computational power. Two main solutions are dominant:

- implementation in Field Programmable Gate Arrays [70],
- using Digital Signal Processors [71].

Analyzing the FPGA possibilities and the construction of neural network models, advantages of combining both of these issues can be seen. They result from the following aspects [72]:

- the possibility of the real realization of many calculations in parallel,
- FPGA hardware resources contain a large number of logic blocks allowing to perform many mathematical operations, which is typical for NN,
- configurability of hardware is essential in the implementation of neural networks,

- availability of specialized components that can be used for an example in the implementation of an activation function,
- user-friendly developed environment shortening implementation time (this may be important, for example due to the external network training in other programs, which is time consuming).

However, very often the implementation process of neural network in FPGA is very complicated. During the programming the complexity of the code with respect to the computation time and the consumption of FPGA logic elements should be taken into account. In addition, there is the problem of digital realization of the activation function, which usually is the hyperbolic tangent or its different variations [73]. Moreover, modern DSP chip allows obtain a high frequency of calculation even for complex structures. Implementation using a high level of programming languages is easy and enables rapid tests. Concluding, it is preferable to perform preliminary tests using Digital Signal Processors placed on dSPACE cards. Then, for specific implementations, involving the high-speed calculations or mass production, it is better to use FPGAs.

7 Conclusions

In this chapter neural network controllers applied for electrical drives are described. Selected neural models and training algorithms are described and used in the speed control structure. Weights of neural networks are updated on-line. Neural network controllers can be used in control structures in various combinations (e.g. with a reference model, as a predictive neural controller). The presented examples of applications are related to neural networks implemented directly as the main speed controller. This helps to observe the influence of each neural model and training algorithm on drive properties.

The design procedure of the presented controllers is simple, it is necessary to select only one parameter. This coefficient is selected experimentally, however, it is easy to designate the correct value. In fact, it is obvious that this factor depends on time constants of the drive. It is important that in the case of neural controllers with weights recalculated on-line the size of the structure has insignificant influence on the achieved results. It is an important simplification contrary to neural models applied in control structures with off-line training (there topology of neural network determines generalization abilities). The above mentioned parameter, when inflicted externally, has an important influence on the dynamics of the control structure. Neural controllers can be applied in electrical drives with different configurations of control structure and various motors (f.e. DC, AC).

The results presented in this chapter show fast stabilization of electrical drive speed at the reference level. Application of neural network controllers is also very advantageous when parameters of electrical drives are not precisely identified. During the drive operation, the error of controlled state variable gives information

for adaptation algorithm, which changes parameters in the main processing path of the controller. As a result the control signal for error correction is generated. This leads also to robustness against parameter changes.

Experimental results confirm the properties of the control structure observed in simulation. Neural network based controllers ensure high precision of speed control even in the case of inaccuracies of construction appearing in a real drive. Some nonlinearities of mechanical connections, like friction, natural backlash do not have any influence on the achieved results. Moreover, hardware implementation of these models using modern programmable devices is easy.

Acknowledgment This work was partly supported by the National Science Centre Poland, under project 2011/01/B/ST7/04632 (2011–2014).

References

1. M. Cirstea, A. Dinu, M. McCormick, J. Ghee Khor, *Neural and Fuzzy Logic Control of Drives and Power Systems* (Newnes, Jordan Hill, 2002)
2. M.R.G. Meireles, P.E.M. Almeida, M.G. Simões, A comprehensive review for industrial applicability of artificial neural networks. *IEEE Trans. Ind. Electron.* **50**(3), 585–601 (2003)
3. B.K. Bose, Neural network applications in power electronics and motor drives—an introduction and perspective. *IEEE Trans. Ind. Electron.* **54**(1), 14–33 (2007)
4. P. Vas, *Sensorless Vector and Direct Torque Control* (Oxford University Press, New York, 1998)
5. M.P. Kazmierkowski, F. Blaabjerg, R. Krishnan, *Control in Power Electronic—Selected Problems* (Academic Press, Boston, 2002)
6. J. Pittner, M.A. Simaan, Control of a continuous tandem cold metal rolling process. *Control Eng. Pract.* **16**(11), 1379–1390 (2008)
7. M.A. Valenzuela, J.M. Bentley, A. Villablanca, R.D. Lorenz, Dynamic compensation of torsional oscillation in paper machine sections. *IEEE Trans. Ind. Appl.* **41**(6), 1458–1466 (2005)
8. A. Hace, K. Jezernik, A. Sabanovic, A. SMC with disturbance observer for a linear belt drive. *IEEE Trans. Ind. Electron.* **53**(6), 3402–3412 (2007)
9. Y. Hori, H. Sawada, Y. Chun, Slow resonance ratio control for vibration suppression and disturbance rejection in torsional system. *IEEE Trans. Ind. Electron.* **46**(1), 162–168 (1999)
10. K. Szabat, T. Orłowska-Kowalska, Vibration suppression in two-mass drive system using PI speed controller and additional feedbacks—comparative study. *IEEE Trans. Ind. Electron.* **54**(2), 1193–1206 (2007)
11. K. Hamamoto, T. Fukuda, T. Sugie, Iterative feedback tuning of controllers for a two-mass-spring system with friction. *Control Eng. Pract.* **11**(9), 1061–1068 (2003)
12. K.J. Åström, T. Hagglund, *PID Controller: Theory, Design and Tuning* (Instrument Society of America, Research Triangle Park, 1995)
13. J.J.E. Slotine, W. Li, *Applied Nonlinear Control* (Prentice-Hall, Englewood Cliffs, 1991)
14. K.J. Åström, B. Wittenmark, *Adaptive Control*, 2nd edn. (Addison-Wesley, New York, 1995)
15. J.R. Noriega, H. Wang, A direct adaptive neural-network control for unknown nonlinear systems and its application. *IEEE Trans. Neural Networks* **9**(1), 27–34 (1998)
16. F.J. Lin, R.F. Fung, R.J. Wai, Comparison of sliding-mode and fuzzy neural network control for motor-toggle servomechanism. *IEEE Trans. Mechatron.* **3**(4), 302–318 (1998)
17. T. Orłowska-Kowalska, K. Szabat, Control of the drive system with stiff and elastic couplings using adaptive neuro-fuzzy approach. *IEEE Trans. Ind. Electron.* **54**(1), 228–240 (2007)

18. M.P. Kazmierkowski, T. Orłowska-Kowalska, *NN State Estimation and Control in Converter-Fed Induction Motor Drives, Chapter 2 in a Book: Soft Computing in Industrial Electronics* (Physica-Verlag, Springer, Heilderlberg, 2002), pp. 45–94
19. M. Norgaard, O. Ravn, N.K. Poulsen, L.K. Hansen, *Neural Networks for Modeling and Control of Dynamic Systems* (Springer, London, 2000)
20. D.R. Hush, B.G. Horne, Progress in supervised neural networks. *IEEE Signal Process. Mag.* **10**(1), 8–39 (1993)
21. F. Dan Foresee, M.T. Hagan, Gauss-Newton approximation to Bayesian learning. in *IEEE International Conference on Neural Networks*, vol. 3, pp. 1930–1935 (1993)
22. Y. Shao, G.N. Taff, S.J. Walsh, Comparison of early stopping criteria for neural-network-based subpixel classification. *IEEE Geosci. Remote Sens. Lett.* **8**(1), 113–117 (2011)
23. L.E. Aik, Z. Zainuddin, An improved fast training algorithm for RBF networks using symmetry-based fuzzy C-means clustering. *Matematika* **24**(2), 141–148 (2008)
24. P. Yang, Q. Zhu, X. Zhong, Subtractive clustering based RBF neural network model for outlier detection. *J. Comput.* **4**(8), 755–762 (2009)
25. H. Sarimveis, A. Alexandridis, G. Bafas, A fast training algorithm for RBF networks based on subtractive clustering. *Neurocomputing* **51**, 501–505 (2003)
26. M. Kaminski, T. Orłowska-Kowalska, Clustering in optimization of RBF-based neural estimators for the drive system with elastic joint. in *IEEE International Symposium on Industrial Electronics (ISIE)*, pp. 1907–1912 (2011)
27. Y. Le Cun, J.S. Denker, S.A. Solla, *Optimal Brain Damage* (AT&T Bell Laboratories, Holmdel, 1990)
28. B. Hassibi, D.G. Stork, Second order derivatives for network pruning: optimal brain surgeon, in *Advances in Neural Information Processing Systems*, vol. 5, ed. by D.S. Lippman, J.E. Moody, D.S. Touretzky (Morgan Kaufmann, San Mateo, 1993)
29. T.-S. Quah, K.-C. Wong, Utilizing generalized growing and pruning algorithm for radial basis function (GGAP-RBF) network in predicting IPOs performance. in *Proceedings of IEEE International Joint Conference on Neural Networks*, pp. 3007–3012 (2006)
30. J. Ni, Q. Song, Sequential neuron pruning algorithm for RBF network with guaranteed stability. in *Proceedings of IEEE International Joint Conference on Neural Networks*, vol. 2, pp. 1069–1074 (2005)
31. H. Jiang, Y. Yuan, Y. Huang, G. Li, RBF Neural network based on genetic algorithm used in line loss calculation for distribution network. in *Proceedings of Third International Conference on Natural Computation*, vol. 3, pp. 338–342 (2007)
32. D. Saad, *On-Line Learning in Neural Networks* (Cambridge University Press, Cambridge, 2009)
33. K.K. Shyu, H.J. Shieh, S.S. Fu, Model reference adaptive speed control for induction motor drive using neural networks. *IEEE Trans. Industr. Electron.* **45**(1), 180–182 (1998)
34. T.C. Chen, T.T. Sheu, Model reference neural network controller for induction motor speed control. *IEEE Trans. Energy Convers.* **17**(2), 157–163 (2002)
35. L.M. Grzesiak, V. Megnack, J. Sobolewski, B. Ufnalski, Genetic algorithm for parameters optimization of ANN-based speed controller. in *Proceedings of the International Conference on Computer as a Tool*, pp. 1700–1705. Warsaw, Poland (2007)
36. F. Perez Hidalgo, J.L. Duran Paz, Sensorless control of induction motors by artificial neural networks. *IEEE Trans. Ind. Electron.* **48**(5), 1038–1040 (2001)
37. R. Toufouti, S. Meziane, H. Benalla, Direct torque control for induction motor using intelligent techniques. *J. Theor. Appl. Inf. Technol.* **3**(3), 35–44 (2007)
38. L.M. Grzesiak, G. Gabka, Neural network controller of AC induction motor based on direct torque control. *Przegl. Elektrotechniczny* **86**(12), 280–287 (2010)
39. H.A. Toliyat, M. Wlas, Z. Krzeminski, Neural-network-based parameter estimations of induction motors. *IEEE Trans. Ind. Electron.* **55**(4), 1783–1794 (2008)
40. M. Godoy Simoes, B.K. Bose, Neural network based estimation of feedback signals for a vector controlled induction motor drive. *IEEE Trans. Ind. Appl.* **31**(3), 620–629 (1995)

41. V.P.B. Aguiar, R.S. Thepontes, A.P.S. Braga, S. De Aguiar, A strategy for induction motor stator flux estimation using neural networks. in *Proceedings of International Conference on Electrical Machines and Systems (ICEMS)*, pp. 1923–1927 (2007)
42. T. Orłowska-Kowalska, K. Szabat, Neural-network application for mechanical variables estimation of a two-mass drive system. *IEEE Trans. Ind. Electron.* **54**(3), 1352–1364 (2007)
43. M. Cirrincione, M. Pucci, An MRAS-based sensorless high-performance induction motor drive with a predictive adaptive model. *IEEE Trans. Ind. Electron.* **52**(2), 532–551 (2005)
44. S.M. Gadoue, D. Giaouris, J.W. Finch, Sensorless control of induction motor drives at very low and zero speeds using neural network flux observers. *IEEE Trans. Ind. Electron.* **56**(8), 3029–3039 (2009)
45. F. Filippetti, G. Franceschini, C. Tassoni, P. Vas, Recent developments of induction motor drives fault diagnosis using AI techniques. *IEEE Trans. Ind. Electron.* **47**(5), 994–1004 (2000)
46. M.A. Awadallah, Application of AI tools in fault diagnosis of electrical machines and drives—an overview. *IEEE Trans. Energy Convers.* **18**(2), 245–251 (2003)
47. C.T. Kowalski, T. Orłowska-Kowalska, Application of neural networks for the induction motor faults detection. *Trans. Math. Comput. Simul.* **63**(3–5), 435–448 (2003)
48. R.D. Brandt, F. Lin, Adaptive interaction and its application to neural networks. *Inf. Sci.* **121**(3–4), 201–215 (1999)
49. J. Restrepo, J. Viola, R. Harley, T. Habetler, Induction machine current loop neuro controller employing a Lyapunov based training algorithm. in *IEEE Power Engineering Society General Meeting*, pp. 1–8 (2007)
50. K.-B. Lee, F. Blaabjerg, An improvement of speed control performances of a two-mass system using a universal approximator. *Electr. Eng.* **89**(5), 389–396 (2007)
51. X.-L. Wei, J. Wang, Z.-X. Yang, Robust smooth-trajectory control of nonlinear servo systems based on neural networks. *IEEE Trans. Ind. Electron.* **54**(1), 208–217 (2007)
52. T. Feuring, J.J. Buckleyb, W.M. Lippea, A. Tenhagena, Stability analysis of neural net controllers using fuzzy neural networks. *Fuzzy Sets Syst.* **101**(2), 303–313 (1999)
53. F. de Canete, S. Gonzales-Perez, P. De Saz-Orozco, Robust neural network control using harmonic analysis. *Int. J. Comput. Inf. Syst. Sci. Eng.* **3**(1), 47–51 (2009)
54. M. Englert, R. Trapp, R. de Klerk, Neural control of a nonlinear elastic two-mass system. in *Computational Intelligence, Theory and Applications, International Conference, 5th Fuzzy Days*, vol. 1226, pp. 553–553 (1997)
55. Z. Su, K. Khorasani, A neural-network-based controller for a single-link flexible manipulator using the inverse dynamics approach. *IEEE Trans. Ind. Electron.* **48**(6), 1074–1086 (2001)
56. R. Dhaouadi, K. Nouri, Neural network-based speed control of a two-mass-model system. *J. Adv. Comput. Intell. Inform.* **3**(5), 427–430 (1999)
57. M. Kaminski, T. Orłowska-Kowalska, Adaline-based speed controller of the drive system with elastic joint. in *13th International Conference on Optimization of Electrical and Electronic Equipment*, pp. 1052–1057 (2012)
58. L.V. Fausett, *Fundamentals of Neural Networks: Architectures, Algorithms and Applications* (Prentice Hall, Englewood Cliffs, 1993)
59. B. Widrow, M.A. Lehr, Perceptrons, adalines, and backpropagation, in *Handbook of Brain Theory and Neural Networks*, pp. 719–724, ed. by M.A. Arbib (MIT Press, Cambridge, 1995)
60. P. Ryckaert, B. Salaets, A.S. White, M. Stoker, A comparison of classical, state-space and neural network control to avoid slip. *Mechatronics* **15**(10), 1273–1288 (2005)
61. A. Olatunbosun, Comparison of neural network and PID control techniques based on a case study. *Res. J. Appl. Sci.* **6**(6), 349–353 (2011)
62. M.C. Bishop, *Neural Networks for Pattern Recognition* (Oxford University Press, Oxford, 1996)
63. H. Yu, T. Xie, S. Paszczynski, B.M. Wilamowski, Advantages of radial basis function networks for dynamic system design. *IEEE Trans. Ind. Electron.* **58**(12), 5438–5450 (2011)
64. W. Sun, Y. Yuan, *Optimization Theory and Methods: Nonlinear Programming*, 1st edn. (Springer, New York, 2006)

65. K.S. Narendra, K. Parthasarathy, Gradient methods for the optimization of dynamical systems containing neural networks. *IEEE Trans. Neural Networks* **2**(2), 252–262 (1991)
66. M.E.A. Farrag, G.A. Putrus, An on-line training radial basis function neural network for optimum operation of the UPFC. *Eur. Trans. Electr. Power* **21**(1), 27–39 (2011)
67. G. Saikalis, F. Lin, A neural network controller by adaptive interaction. in *Proceedings of the American Control Conference*, vol. 2, pp. 1247–1252 (2001)
68. M. Cychowski, K. Szabat, T. Orłowska-Kowalska, Constrained model predictive control of the drive system with mechanical elasticity. *Trans. Ind. Electron.* **56**(6), 1963–1973 (2009)
69. J. Liu, D. Liang, A survey of FPGA-based hardware implementation of ANNs. in *International Conference on Neural Networks and Brain ICNN&B '05*, vol. 2, pp. 915–918 (2005)
70. E. Monmasson, M.N. Cirstea, FPGA design methodology for industrial control systems—a review. *IEEE Trans. Industr. Electron.* **54**(4), 1824–1842 (2007)
71. M. Mohamadian, E.P. Nowicki, A. Chu, F. Ashrafzadeh, J.C. Salmon, DSP implementation of an artificial neural network for induction motor control. in *IEEE Canadian Conference on Electrical and Computer Engineering, Engineering Innovation: Voyage of Discovery*, vol. 2, pp. 435–437 (1997)
72. N. Sulaiman, Z.A. Obaid, M.H. Marhaban, M.N. Hamidon, Design and implementation of FPGA-based systems—a review. *Aust. J. Basic Appl. Sci.* **3**(4), 3575–3596 (2009)
73. T. Orłowska-Kowalska, M. Kamiński, FPGA implementation of the multilayer neural network for speed estimation of the two-mass drive system. *IEEE Trans. Ind. Inform.* **7**(3), 436–445 (2011)

Chapter 9

Advanced Control and Optimization Techniques in AC Drives and DC/AC Sine Wave Voltage Inverters: Selected Problems

Barłomiej Ufnalski, Lech M. Grzesiak and Arkadiusz Kaszewski

Abstract This chapter presents the application of a particle swarm optimization (PSO) to a controller tuning in selected power electronic and drive systems. The chapter starts with a relatively simple tuning of a cascaded PI speed and position control system for a BLDC servo drive. This example serves as the background for a discussion on selecting the objective function for the PSO. Then the PSO is used in two challenging controller tuning tasks. This includes optimizing selected learning parameters in the adaptive artificial neural network (ANN) based online trained speed controller for an urban vehicle (3D problem) and selecting penalty factors in the LQR with augmented state (i.e. with oscillatory terms) for a three-phase four-leg sine wave inverter (15D problem). It is demonstrated with the help of these case studies why and where the PSO, or any other similar population based stochastic search algorithm, can be beneficial. Engineers encounter many non-straightforward controller tuning problems in power electronic systems and this chapter illustrates that in some cases it is relatively easy to reduce these tasks into the objective function selection problem. The relevant controller parameters are then determined automatically by the PSO.

B. Ufnalski (✉) · L. M. Grzesiak · A. Kaszewski
Institute of Control and Industrial Electronics, Warsaw University of Technology,
75 Koszykowa Str., Warsaw 00-662, Poland
e-mail: bartlomiej.ufnalski@ee.pw.edu.pl
URL: <http://www.isep.pw.edu.pl>

L. M. Grzesiak
e-mail: lech.grzesiak@ee.pw.edu.pl

A. Kaszewski
e-mail: arkadiusz.kaszewski@ee.pw.edu.pl

1 Particle Swarm Optimization

Particle swarm optimization is attributed to Kennedy, Eberhart and Shi [1]. It is an iterative gradient-free search algorithm inspired by biological swarming such as bird flocking, fish schooling, herding of land animals or collective behavior of insects. The search starts with a random set (here called swarm) of solutions (here called particles). The particles travel through a search space and are rated according to a user defined objective function. Their movements are a function of the individual experience and information acquired from other particles. However, the velocity vectors are not deterministic. The instantaneous strength of social and individual behavior varies randomly for each particle in each iteration. In a basic version of the algorithm the only piece of information shared among the particles is the global best solution found so far. Each particle stores also its best solution found so far. The velocity and position update rules are as follows

$$\mathbf{v}_j(i+1) = c_1 \mathbf{v}_j(i) + c_2 \text{rand}() (\mathbf{p}_j^{pbest} - \mathbf{p}_j(i)) + c_3 \text{rand}() (\mathbf{p}_j^{gbest} - \mathbf{p}_j(i)) \quad (1)$$

$$\mathbf{p}_j(i+1) = \mathbf{p}_j(i) + \mathbf{v}_j(i+1), \quad (2)$$

where: j is the particle identification number, i denotes the iteration number, \mathbf{v}_j and \mathbf{p}_j are speed and position of the j -th particle, \mathbf{p}_j^{pbest} stores the best solution proposed so far by the j -th particle ($pbest$), \mathbf{p}^{gbest} denotes the best solution found so far by the swarm ($gbest$), c_1 , c_2 and c_3 are the explorative factor (inertia weight), the individuality factor and the social factor, respectively. It is to note that the speed $\mathbf{v}_j(i+1)$ in the rule (2) should be multiplied by time to represent physical velocity. However, it is common practice to set the time increment to 1 and thereafter neglect it in (2). An introduction of a different time increment does not influence a behavior of the swarm because coefficients present in (1) have to be divided by this increment. The search path is not deterministic because of the last two terms in (1) that include multiplication by the random numbers $\text{rand}()$ generated for each particle in each iteration. The random numbers are uniformly distributed in the unit interval. In all experiments described in this chapter, the c_1 , c_2 and c_3 factors have been calculated using the constricted PSO formula [1] and are 0.73, $0.73 \cdot 2.05$ and $0.73 \cdot 2.05$, respectively. If the basic velocity update rule does not manifest satisfactory search abilities, numerous refinements are available. A fairly representative survey can be found in [2, 3]. Taking into account the no free lunch theorem for optimization [4] one can conclude that there is no ultimate version of the PSO. The set of modifications should be selected individually, usually by trials and errors, to suit a given optimization problem. These modifications range from simple velocity clamping to substantial adjustments of particle communication principles like, e.g., in the fully-informed PSO [5]. Additionally, there are certain

modifications dedicated to online optimization in non-stationary environments [6]. The rules of swarm movements can be rearranged to handle multi-objective [7] and/or multi-modal [8] problems. Various neighborhood topologies are proposed to serve these purposes [9]. Our main goal is to keep the swarm as simple as possible and still effective in the controller tuning tasks encountered in power electronic or drive systems. This chapter deals with offline optimization in such systems, hence the environment is assumed to be stationary even if a measurement noise is included in the model. Moreover, all optimizations are performed on numerical models of the plants, therefore the search space does not need to be bounded to specific territory resulting from safety requirements for the given plant. The numerical model should include all nonlinearities, noises and other parasitic effects crucial from control point of view. No information on gradient is harnessed by the PSO. This gives a lot of freedom to the designer at problem formulation stage—the mathematical model of the system being optimized can include, e.g., discontinuities. From the same reason, the objective function chosen by the designer can be of any type and one can focus on formulating this function to be aligned with the desired behavior of the system without bothering about its mathematical properties in terms of complexity and differentiability.

In the case of all discussed problems no special measures have been taken regarding swarm movements. The very basic formula (1) tends to produce implementable solutions. All problems have been handled as single-modal and no explicit multi-objectivity has been introduced. It is common among control practitioners to reduce problems with contradictory objectives to single-objective ones with the help of weighted terms in the objective function. This methodology has been employed also here. The simplest communication topology has been used, i.e. the *gbest* attracts all particles and no neighborhood operator is present. However, it has been decided to introduce absorbing walls [10] if clear physical or theoretical constraints are identifiable. This means that the speed of a particle is reset to zero if known boundaries are crossed. No other modifications to the standard PSO have been identified as necessary to effectively tune the below discussed controllers.

2 Objective Function

The objective function (also called cost function, energy function, performance index or fitness function) determines the behavior of the optimal controller. There are some commonly used performance measures as the integral of squared error (ISE)

$$J_{\text{ISE}} = \int_0^{\infty} e^2(t) dt, \quad (3)$$

where $e(t)$ denotes control error, or the generalized ISE

$$J_{\text{IGSE}} = \int_0^{\infty} (e^2(t) + \alpha \dot{e}^2(t)) dt, \quad (4)$$

where α is a subjective weighting factor, or the integral of squared error and derivative of control effort

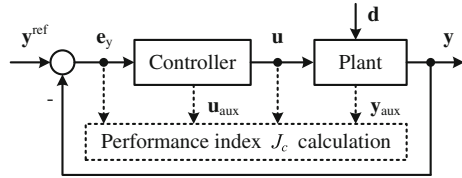
$$J_{\text{ISEDCE}} = \int_0^{\infty} (e^2(t) + \beta \dot{u}^2(t)) dt, \quad (5)$$

where $u(t)$ denotes control effort (control signal) and β is again a subjective weighting factor. Especially (3) earns its popularity by producing problems that are easy to approach analytically for some classes of control systems ([11] might serve as the example). However, in a gradient free optimization the performance index can be chosen freely to reflect in the best possible way the desired behavior of the system. It has been decided that for all studied cases the performance indices will be positive definite and the optimization problem will be of the minimization type. The philosophy of signals contributing to the performance index its mean squared value has been kept in all discussed tuning procedures. Nevertheless, to promote sometimes contradictory behaviors like fast transients and no chattering at steady state, additional functions are introduced into the performance index definition allowing for selective contribution to the overall value. For example, the dynamics of the control effort is not penalized during the specific time interval after the change in the reference signal whereas this penalty is non-zero at the steady state. These time windows have to be carefully chosen for each term in the performance index according to physical limitations of the plant. Also, it is common practice to add terms that take into account overshooting or crossing acceptable levels for control signal. The nature of the PSO enables the designer to work with any form of performance index. However, our main goal is to keep this stage simple without sacrificing the performance of the resulting system. All proposed here performance measures have the form of

$$J_c = \frac{T_s}{t_{\text{stop}}} \sum_{k=1}^{\frac{t_{\text{stop}}}{T_s}} (f_1(k) \mathbf{e}_y^T(k) \mathbf{e}_y(k) + f_2(k) \Delta \mathbf{u}^T(k) \Delta \mathbf{u}(k) + f_3(k) \mathbf{u}_{\text{aux}}^T(k) \mathbf{u}_{\text{aux}}(k) + f_4(k) \mathbf{y}_{\text{aux}}^T(k) \mathbf{y}_{\text{aux}}(k)), \quad (6)$$

where \mathbf{e}_y , \mathbf{u} , \mathbf{u}_{aux} and \mathbf{y}_{aux} are vectors (in the MIMO case, e.g. as in three-phase converters) containing control errors, control signals, auxiliary signals from the controller and auxiliary signals from the plant, respectively (as depicted in Fig. 1). The discrete representation of the performance measure has been chosen to correspond to the assumed digital implementation of a control system. All signals are sampled at the rate of T_s . The t_{stop} denotes the assessment test time for the particle

Fig. 1 Selected signals for performance calculation



(equal for all particles). It is to note that the infinite integration limit commonly used in the analytical approach has to be changed to finite test time if the performance evaluation is done by using signal samples recorded during a numerical simulation or a physical experiment. The functions f_1, f_2, f_3 and f_4 are bivalent functions with zero value for intervals with no penalty for a given behavior and positive value, usually different for each function with one of them set to 1, for intervals with a penalty for this behavior. These intervals are correlated with the reference test signal(s) and the test disturbance(s). In some designs they depend on states of a system when, e.g., additional penalty for overshooting is needed. It should be stressed that the bivalency is assumed here to make the design process more intuitive. From now onward the bivalent functions will be referred to as switching functions. The resulting system is optimal for a given shape of the reference and disturbance signals. That is why it is crucial to design the test scenario that includes representative set of anticipated system states. The scaling by the reciprocal of the number of samples present in (6) does not influence the optimization process and is introduced solely to make the value of the performance index easier in interpretation as the mean value of the sum of squares. The test reference signal(s) should take into account physical limits of a plant, e.g. the available acceleration. Otherwise, a dominant contribution to the cost function value coming from demanded behavior outside the physical limits makes determining upper values for switching functions significantly more difficult. It is common practice to implement ramps and s-ramps as reference models for speed or position in electric drive systems. This limits first and second derivative of the reference signal, respectively. It is also practical to use first and second order lag elements if these derivatives are expected to be limited. An example is shown in Figs. 2 and 3. The step reference signal should be avoided in such performance index based assessment tests because this does not reflect most real-life applications. For example, the s-ramp speed reference model is frequently used in drivetrain systems to limit the jerk which is important for a lifetime of a mechanical part of the system and for a comfort of its users, e.g. passengers of a vehicle.

It is common that in the early stage of the search many particles cannot be rated using (6) because the simulation stops before reaching the assumed t_{stop} due to numerical problems. The simulation is also stopped intentionally before t_{stop} if states of a plant reach unacceptable levels from the physical implementation point of view. For some search problems the particles do not carry directly values of parameters of the model but those values are calculated using the values stored in

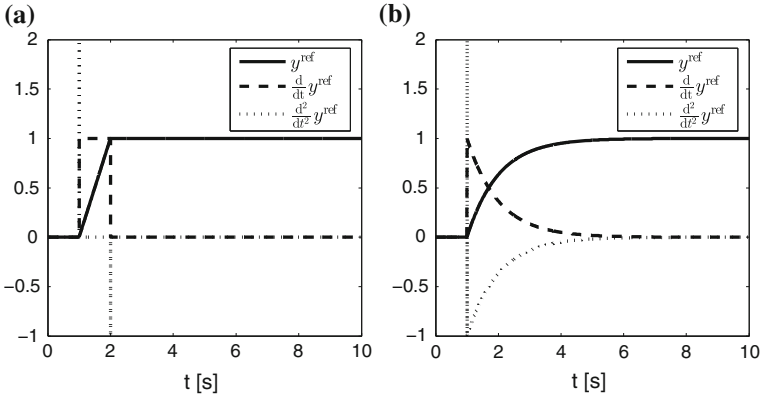


Fig. 2 Reference signal shaped by using rate limiter (a) and first order lag element $G(s) = \frac{1}{s\tau+1}$ with $\tau = 1$ s fed by the step signal (b)

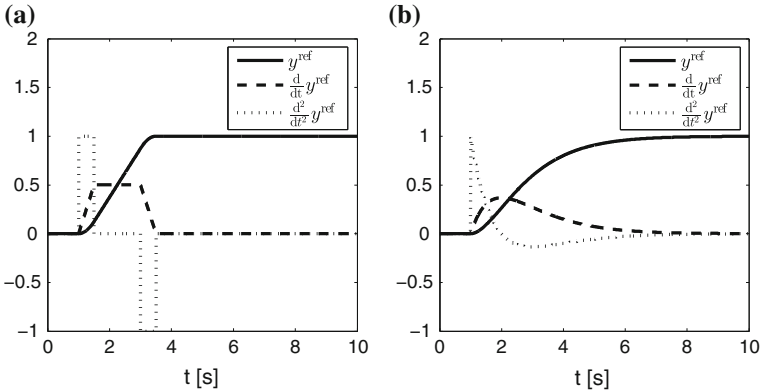


Fig. 3 Reference signal shaped directly as a quadratic spline (a) and generated using second order lag element $G(s) = \frac{1}{(s\tau_1+1)(s\tau_2+1)}$ with $\tau_1 = \tau_2 = 1$ s fed by the step signal (b)

the particle (see Sect. 6). It is possible then that the identification of poor solutions may takes place even before running the numerical model of the system. It has been tested that rating all such particles as equally poor may impair swarm’s capability to keep a good balance between exploration and exploitation. Any functions can be used to rate particles in the event that (6) is not applicable as far as they preserve logical order and their codomains do not overlap. The idea is illustrated in Fig. 4.

The PSO itself puts a minor computational burden on the optimization procedure. The time needed to complete the optimization is dictated by the wall clock time required by the numerical model of the system to be simulated. Non surprisingly, the number of needed simulations depends highly on the form of the objective function. Some guidelines on choosing a good number of particles and

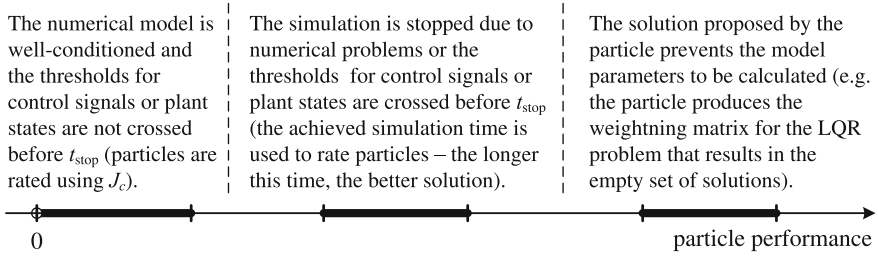


Fig. 4 The methodology of distinguishing particles' performance outside the area covered by the definition of J_c

iterations are given in [12]. It has been verified that 50 particles and 100 swarm iterations would suffice in most of the discussed here problems. However, this implies up to 5,000 runs of the model. It could be problematic if the performance of, e.g., a drive with a pulse width modulated (PWM) converter is to be assessed. Usually, a simulation step size two orders of magnitude lower than the controller sampling time is required to obtain trustworthy numerical results. In order to tackle such problems in a reasonable wall clock time, one will need processing capacity extending far beyond the one offered by today's personal computers. On the other hand, many controller tuning tasks encountered in power electronics and drives deal with plant natural frequencies significantly lower than the used PWM frequencies. In such cases it is reasonable to neglect discontinuities introduced by the modulator and simplify the converter to a linear amplifier with a delay. Obtained model usually produces reliable numerical results for a simulation step size equal to the controller sample time. This has helped to reduce computational complexity of the below presented experiments to levels resulting in several-hour-long tuning procedures. The number of swarm iterations is always a subjective choice. Even though there are various indices elaborated for assessing a search progress, none of them is free from subjective choice of thresholds. A fairly representative set of stopping criteria has been described in [13]. The thresholds are usually determined using the guess and check method. For all following optimization problems the number of swarm iterations has been set arbitrary to meet assumed wall-clock time constraints. However, it is advisable to monitor swarm diversity variations which can be helpful in detection of ill-posed problems. A well-established measure of diversity incorporates Euclidean distance of particles to the mean and is defined, see e.g. [14], as follows

$$D_{\text{dist}} = \frac{1}{N_p \sqrt{N_d}} \sum_{j=1}^{N_p} \sqrt{\sum_{n=1}^{N_d} (p_{jn} - \bar{p}_n)^2}, \tag{7}$$

where N_p is the swarm size, N_d is the dimensionality of the problem and \bar{p} is the average point. Originally this diversity measure uses the length of the longest diagonal in the search space instead of $\sqrt{N_d}$. However, the original definition

cannot be applied to swarms with at least one unbounded search direction which is the case in all discussed here systems. If more insight into separate dimensions is needed, a slightly different diversity measure could be used. It contains standard deviations of proposed solutions that can also be merged into a single formula by calculating their mean value per dimension

$$D_{\text{std}} = \frac{1}{N_d} \sum_{n=1}^{N_d} \sqrt{\frac{1}{N_p} \sum_{j=1}^{N_p} (p_{jn} - \bar{p}_n)^2}. \quad (8)$$

By monitoring the evolution of inner sums in (8) one can detect dimensions with poor convergence. If the swarm does not calm down in selected dimensions, it could suggest that the problem is ill-posed for these dimensions. Such a lack of convergence in selected dimensions can also be intensified by measurement and system noises. Possible solutions are rethinking parameters to be optimized and/or redefining the fitness function.

3 Simultaneous Tuning of Cascaded PI Position and Speed Controllers

There exist numerous analytical and experimental methods for effective PID tuning in a cascaded position, speed and torque control system frequently used in servo drives. Just to mention some of them: modulus and symmetrical optimum methods (Kessler's criteria) [15], Ziegler-Nichols method [16] with different tuning charts, e.g. Pessen recipe, Seborg et al. recipes (some-overshoot rule, no-overshoot rule), Tyreus-Luyben tuning chart. In most cases the resulting control quality is sufficient and there is no need for more elaborated tuning procedures. The example of PSO for a BLDC servo drive serves here only illustrative purposes. However, some easily identifiable advantages of the evolutionary gradientless optimization are present in contrast to the abovementioned methods: the optimizer can work with any user-defined performance index and simultaneous tuning of more than one out of the cascaded controllers is possible. These principles have already been used in [17] for optimizing a cascaded PI control structure with respect to the H_∞ norm. Moreover, the process and the control system can be modeled in any drag-and-drop environment and can include all crucial nonlinearities, i.e. controller saturation and anti-windup, and parasitic effects as the measurement noise.

The dynamics of a three-phase brushless DC machine can be numerically modeled using following mathematical description

$$\begin{cases} u_a(t) = L \frac{di_a(t)}{dt} + Ri_a(t) + e_a(\alpha_e(t), \omega_m(t)) \\ u_b(t) = L \frac{di_b(t)}{dt} + Ri_b(t) + e_b(\alpha_e(t), \omega_m(t)) \\ u_c(t) = L \frac{di_c(t)}{dt} + Ri_c(t) + e_c(\alpha_e(t), \omega_m(t)), \end{cases} \quad (9)$$

where

$$e_x(\alpha_e(t), \omega_m(t)) = K_{\text{BLDC}} k_{ex}(\alpha_e(t)) \omega_m(t) \Big|_{x=a,b,c}. \quad (10)$$

The electromagnetic torque produced in the machine can be calculated using formula

$$T_e(t) = \frac{\sum_{x=a,b,c} e_x(\alpha_e(t), \omega_m(t)) i_x(t)}{\omega_m(t)}, \quad (11)$$

where $e_x(x = a, b, c)$ is the phase back-EMF voltage, K_{BLDC} is the back-EMF constant, $k_{ex}(x = a, b, c)$ is the ideal trapezoidal shape function, L and R denote the stator inductance and resistance, $\alpha_e = p\alpha_m$ is the electrical rotor angle equal to the mechanical rotor angle α_m multiplied by the number of pole pairs, ω_m is the rotor angular speed. If the motor is electronically commutated in such a way that the current flows only through two phases, its dynamics can be modeled using equations similar to the ones describing a brushed DC machine

$$u_{\text{BLDC}}(t) = 2L \frac{di_{\text{BLDC}}(t)}{dt} + 2Ri_{\text{BLDC}}(t) + 2K_{\text{BLDC}}\omega_m(t) \quad (12)$$

$$T_e(t) = 2K_{\text{BLDC}}i_{\text{BLDC}}(t) \quad (13)$$

accompanied by the Newton's law for rotation

$$T_e(t) = J \frac{d\omega(t)}{dt} + T_{\text{load}}(t) + F_v \omega_m(t), \quad (14)$$

where T_{load} is the load torque and F_v is the viscous friction coefficient. The BLDC servo drive considered here consists of a hypothetical converter-fed motor equipped with a torque/current PI control loop, tuned with the help of the modulus optimum method, and a cascaded speed and position PI controllers. Parameters of the drive are given in Table 1. All controllers include standard anti-windup algorithm depicted in Fig. 5. Input signals of the speed and torque controllers have per-unit values with the motor nominal values as the base ones. The input of the position controller is left unscaled. The model of the servo drive is then connected to the PSO (Fig. 6) and a performance index is defined as follows

$$J_c^{\text{BLDC}} = \frac{T_s}{t_{\text{stop}}} \sum_{k=1}^{t_{\text{stop}}/T_s} (f_1^{\text{BLDC}}(k) e_x^2(k) + f_2^{\text{BLDC}}(k) (\Delta T_e^{\text{ref}}(k))^2 + f_3^{\text{BLDC}}(k) e_x^2(k)), \quad (15)$$

Table 1 Parameters of the torque controlled BLDC drive

Parameter	Value	Units
Nominal angular speed	15	$\text{rad} \cdot \text{s}^{-1}$
Nominal voltage	24.6	V
Nominal current	3.33	A
Nominal torque	4	$\text{N} \cdot \text{m}$
Back-EMF constant K_{BLDC}	0.6	Wb
Resistance R	1	Ω
Inductance L	2.5	mH
Moment of inertia J	0.0075 ^a	$\text{kg} \cdot \text{m}^2$
Viscous friction F_v	0.0133 ^b	$\text{N} \cdot \text{m} \cdot \text{s} \cdot \text{rad}^{-1}$
Converter gain	32	V
Switching frequency	2	kHz
Delay introduced by the modulator	250 ^c	μs
Controller sampling time	500 ^c	μs
Current acquisition delay	125 ^c	μs

^a including some hypothetical driven machine

^b 20 % of the nominal torque at the nominal speed (incl. some hypothetical driven machine)

^c delays discussed in [18] and taken into account when applying the modulus optimum method

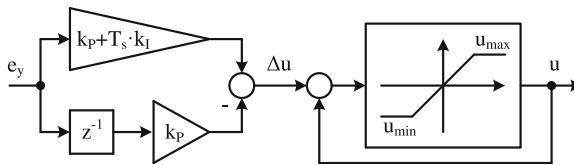


Fig. 5 Discrete implementation of a PI controller with saturation and anti-windup (conditional integration algorithm): k_p —proportional path gain, k_i —integral path gain, T_s —controller sampling time, u_{\min} and u_{\max} are minimal and maximal control signal levels

where the function f_1^{BLDC} introduces penalty for position control error after the time equal to a theoretical time needed to travel a test angle under assumption that the only physical limits are these related to maximal absolute values of electromagnetic torque and angular speed, the function f_2^{BLDC} switches off the penalty for reference torque variations during transients forced by the test reference speed and test disturbance torque, and the function f_3^{BLDC} penalizes for an overshoot.

For the discussed PI controllers tuning task, each particle is a vector of candidate settings for both controllers. These settings can be explicitly stored as the vector components. However, it has been tested that in some tuning problems it is easier and sometimes also more effective to perform the search in an exponential scale. For the purpose of this search, the particle is a vector

$$\mathbf{p}^{\text{BLDC}} = [\log_{10} k_{p\omega}, \log_{10} k_{i\omega}, \log_{10} k_{p\alpha}, \log_{10} k_{i\alpha}], \quad (16)$$

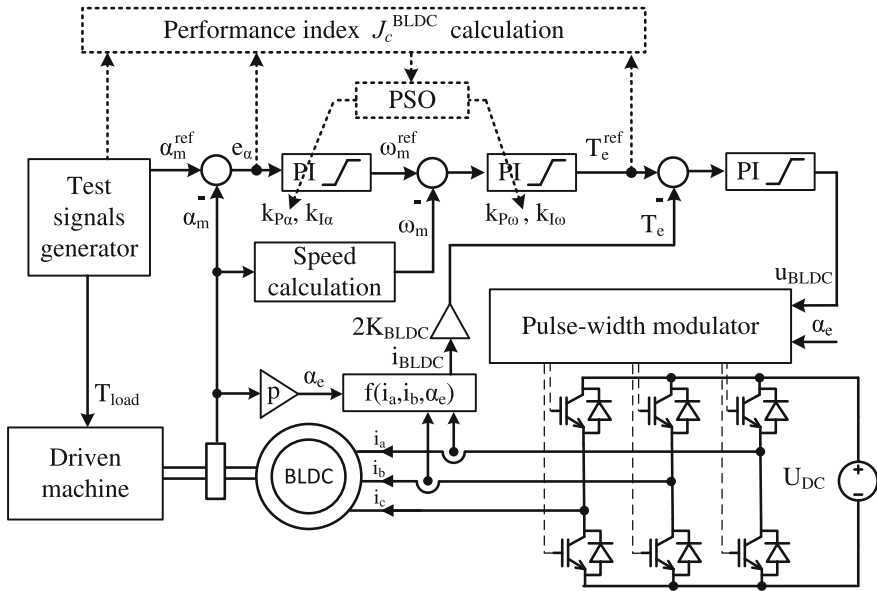
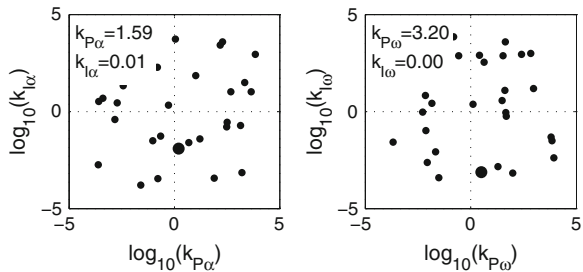


Fig. 6 The BLDC servo drive connected to the PSO system

Fig. 7 Initial particles position—the bigger in diameter black dot denotes g_{best}



where $k_{P\omega}$, $k_{I\omega}$, $k_{P\alpha}$ and $k_{I\alpha}$ are the controllers' gains. The swarm consists of 30 particles and is stopped arbitrary after 100 iterations. The diversity (7) and standard deviations present in (8) are inspected visually. In the case of any stochastic search algorithm each search attempt is unique due to the presence of random variables in the speed update rule (1). It is recommended to repeat several times the search, to be able to assess how conditioned the problem is. If the search process is repeatable in terms of a final position of the swarm, the optimization task is well-posed. For illustrative purposes selected iterations are shown in Figs. 7, 8, 9. The evolution of the performance index J_c^{BLDC} for the g_{best} solution is depicted in Fig. 10. However, the most informative are standard deviations shown in Fig. 11. They clearly indicate that the solutions proposed by the swarm

Fig. 8 Position of particles after five iterations

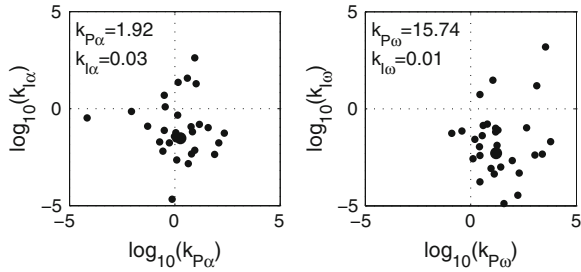


Fig. 9 Position of particles after 100 iterations—swarm near its equilibrium

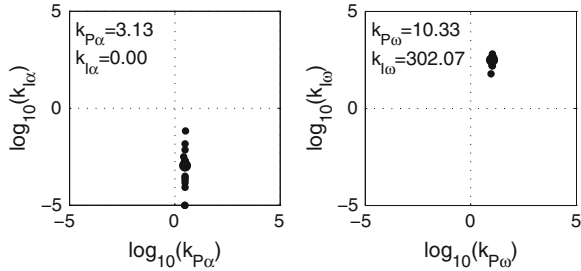
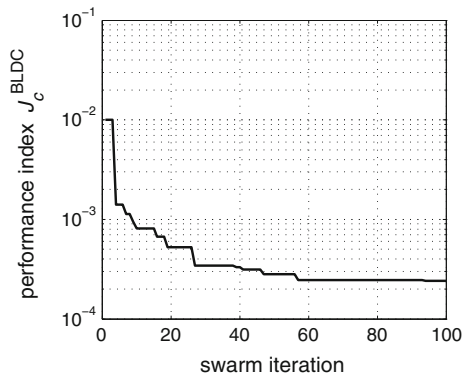


Fig. 10 Evolution of the performance index J_c^{BLDC} for *gbest* solution during the search



for the quadruple of controller gains are convergent except the gain k_{Ia} in the integral path of the position controller. The reason for this is that in the test scenario used for assessing a particle the dominant term comes from a steady state error for a constant reference. A physical integration present in the plant, since the angular position controlled in the outer loop is the integral of the speed controlled in the inner loop, is then sufficient to accomplish the objective. It should be noted that the proposed *gbest* for k_{Ia} is near zero (see Fig. 9). The dynamics of the system for the *gbest* after 100 search iterations is illustrated in Fig. 12. The swarm has identified that the assumed controller topology is excessive for this task. The behavior of the swarm illustrates its ability to prompt to the designer potential

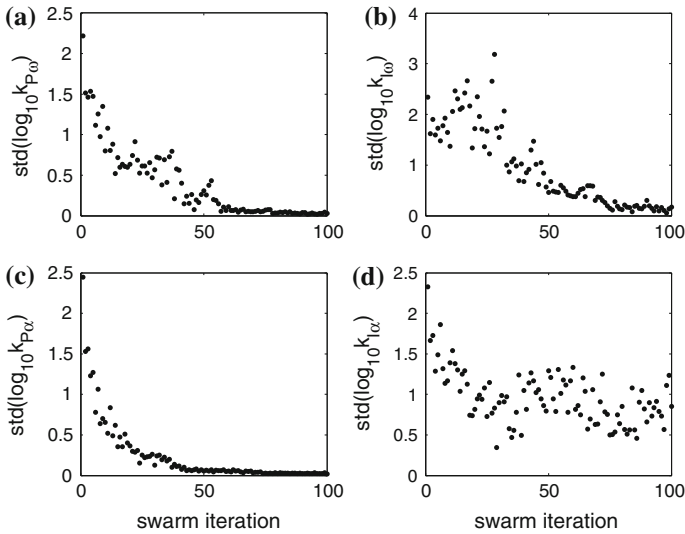


Fig. 11 Evolution of standard deviations during the BLDC servo drive tuning

further refinements of the assumed topology. This can be especially helpful when a controller for a gray-boxed or a black-boxed plant has to be designed. Obviously, there is a possibility to extend such a random search into simultaneous topology selection and gain tuning. Two typical situations could be addressed: optimization of a semi-fixed-structure controller or selecting the best fixed-structure controller from a set of predefined structures. The former refers, e.g., to determining the number of neurons in a neurocontroller. The control structure is fixed—the type of artificial neural network is assumed to be fixed—the only decision variable related to the structure is the number of hidden neurons. On the other hand, the latter refers to a situation where a set of structurally different controllers is tested by the particles, i.e. one entry of the particle vector is a pointer to a set of predefined structures. This is especially useful for black-boxed plants when little or no information about the dynamics of the process is available. The designer can then define a set of potentially applicable control structures: cascaded PIs, augmented-state feedback controllers, various neurocontrollers, iterative learning controllers, repetitive controllers, etc. The PSO will then find the most suitable one for a given black-boxed process.

4 Adaptive Online Trained Speed Neurocontroller

Nonlinear and adaptive speed controllers are often used to cope with inertia variations present in many applications. A robotic arm or an electric vehicle carrying various loads can serve as the examples. A direct method assumes

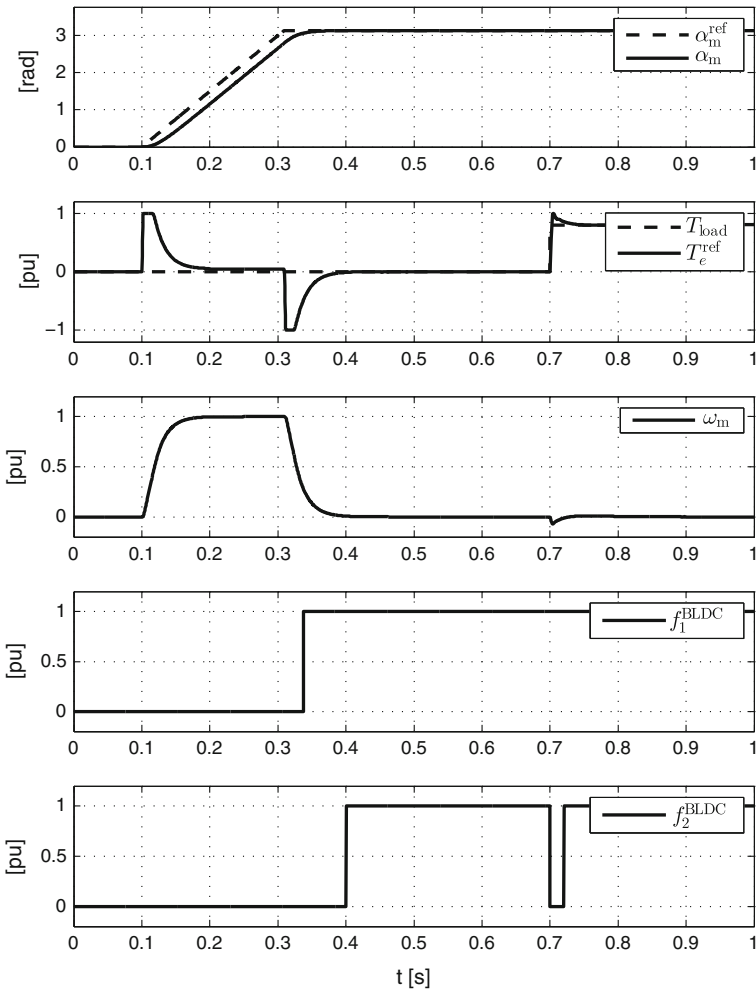


Fig. 12 Response of the BLDC servo drive tuned by the PSO

introduction of an inertia estimator into the system (see e.g. [19]). In indirect methods no inertia is estimated explicitly. These methods usually take advantage of introducing nonlinearity into the controller with the intention to reduce sensitivity to variations of plant parameters. Fuzzy logic (FL), artificial neural networks (ANN) and their combinations are commonly used for implementation of nonlinear controllers. This nonlinearity can be static, i.e. determined in an offline optimization procedure, or can be tuned continuously during the regular operation of a drive. A fairly representative examples of online and offline trained neurocontrollers can be found in [20–28]. The online trained neurocontrollers offer natural capability of adaptation. A learning algorithm is kept active during regular

operation of the drive [29, 30]. It has been already identified that the resilient backpropagation `Rprop` algorithm possesses properties that are especially useful if real-time training is considered. The algorithm is less sensitive to noise in comparison to the original backpropagation algorithm because it takes into account only a sign of the gradient. In many tests the `Rprop` outperforms other first-order training algorithms in terms of convergence [31]. An `Rprop` modification known as the `Rprop` with weight-backtracking [31] has been selected in this study. Its pseudocode is as follows:

```

for each  $w_{ij}$  do
  if  $\frac{\partial E}{\partial w_{ij}}^{(k-1)} \frac{\partial E}{\partial w_{ij}}^{(k)} > 0$ 
     $\delta_{ij}^{(k)} = \min(\delta_{ij}^{(k-1)} \eta^+, \delta_{\max})$ 
     $\Delta w_{ij}^{(k)} = -\text{sgn}\left(\frac{\partial E}{\partial w_{ij}}^{(k)}\right) \delta_{ij}^{(k)}$ 
     $w_{ij}^{(k+1)} = w_{ij}^{(k)} + \Delta w_{ij}^{(k)}$ 
  elseif  $\frac{\partial E}{\partial w_{ij}}^{(k-1)} \frac{\partial E}{\partial w_{ij}}^{(k)} < 0$ 
     $\delta_{ij}^{(k)} = \max(\delta_{ij}^{(k-1)} \eta^-, \delta_{\min})$ 
     $w_{ij}^{(k+1)} = w_{ij}^{(k)} - \Delta w_{ij}^{(k-1)}$ 
     $\frac{\partial E}{\partial w_{ij}}^{(k)} = 0$ 
  else
     $\Delta w_{ij}^{(k)} = -\text{sgn}\left(\frac{\partial E}{\partial w_{ij}}^{(k)}\right) \delta_{ij}^{(k)}$ 
     $w_{ij}^{(k+1)} = w_{ij}^{(k)} + \Delta w_{ij}^{(k)}$ 
  end
end,

```

where E is the cost function (usually MSE), w_{ij} is the weight of a neural connection, δ_{\min} and δ_{\max} are allowable minimal and maximal absolute values of Δw_{ij} , δ_{ij} is the current weight change, η^- and η^+ are decrease and increase factors for δ_{ij} .

If a speed control task is considered and no repetitiveness of this process is assumed (see [32] for more details), the cost function is as follows

$$E_{\text{ANN}}^{\text{SPEED}}(k) = \frac{1}{2} (\omega_m^{\text{ref}}(k) - \omega_m(k))^2. \quad (17)$$

It has been tested in several different systems that the most crucial settings are δ_{\max} , η^- and η^+ as far as the training process is equivalent to the control task. Other parameters as the number of neurons, the length of the tapped delay line (TDL) or δ_{\min} are easy to tune using the guess and check method. The latter can usually be set to zero or to a very small positive value. Some recommendations on δ_{\max} , η^- and η^+ potentially working settings are available in the literature (e.g. [31]). They are reported as suitable for selected offline benchmarks. It was verified that these recommendations cannot be easily extended to online tasks. This only shows that any optimization task is always problem specific (see Sect. 2) and parameters of the `Rprop` have to be adjusted for a given drive system. Some level

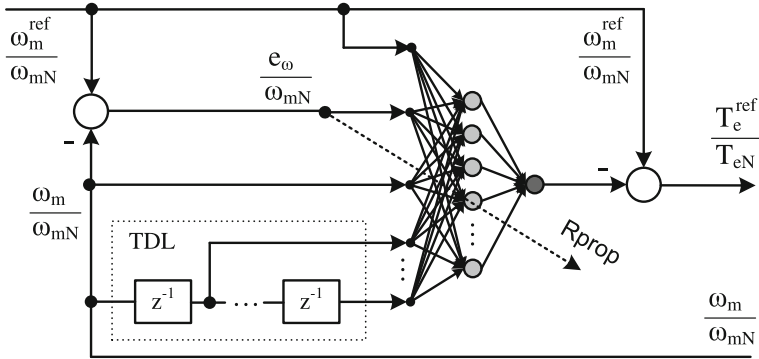


Fig. 13 Topology of the speed neurocontroller for normalized signals with ω_{mN} and T_{eN} denoting nominal speed and torque values

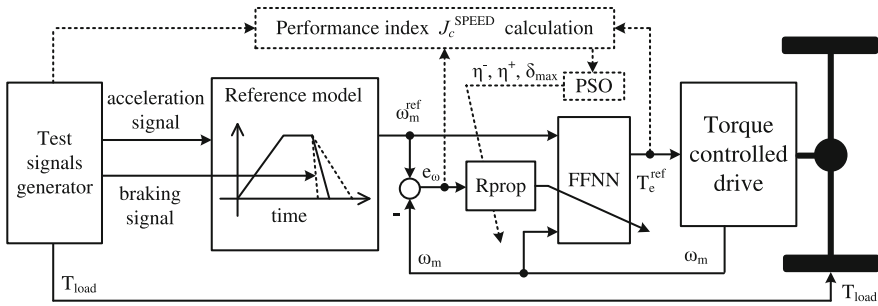


Fig. 14 Adaptive neurocontroller as a part of a vehicle’s control system (FFNN stands for the feed-forward neural network)

of automatism can be easily achieved by employing the swarm-based optimization as reported in [33].

For illustrative purposes the controller shown in Fig. 13 has been implemented in a hypothetical drive (Fig. 14) suitable for a passenger city car (of assumed total mass variations equal to $1,500 \pm 300$ kg) and then has been optimized using a user defined performance index. Each particle is a vector

$$p^{SPEED} = [\eta^-, \eta^+, \delta_{max}] \tag{18}$$

of candidate settings for the R_{prop} adaptation rule. There exist clear search boundaries resulting from the R_{prop} itself. Absorbing walls have been introduced to limit the search to acceptable regions and they are as follows

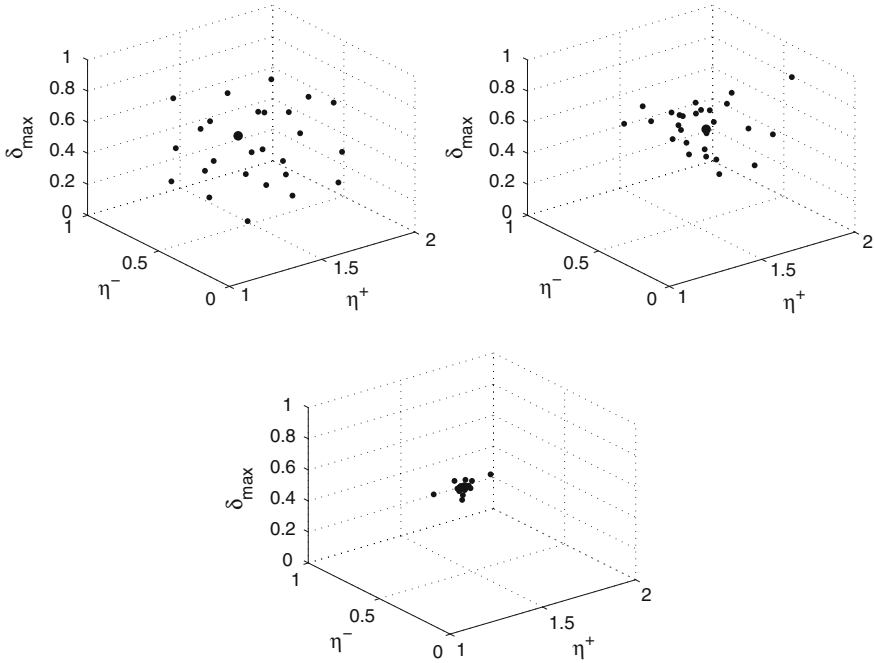


Fig. 15 Swarm position after 1st, 5th and 50th iteration—the bigger in diameter *black dot* denotes *gbest*

$$\begin{cases} 0 < \eta^- < 1 \\ \eta^+ > 1 \\ \delta_{\max} > 0 \end{cases} \quad (19)$$

The swarm consists of 27 particles rated according to the following performance index

$$J_c^{\text{SPEED}} = \frac{T_s}{t_{\text{stop}}} \sum_{k=1}^{t_{\text{stop}}/T_s} (f_1^{\text{SPEED}}(k)e_{\omega}^2(k) + f_2^{\text{SPEED}}(k)(\Delta T_e^{\text{ref}}(k))^2 + f_3^{\text{SPEED}}(k)e_{\omega}^2(k)), \quad (20)$$

where f_3^{SPEED} detects overshooting. The performance index has been changed in comparison to the one proposed in [33] so as to test whether a performance index similar to the one used in Sect. 4 can produce satisfactory results. In the previous work, an expert knowledge about the controller has been incorporated into the performance index definition. Here this knowledge is neglected, i.e. no special measures during the rating related to random initial weights of ANN are taken. The system is assumed to be black-boxed. Variations of the vehicle inertia have been included in the test scenario to optimize the controller for anticipated operating

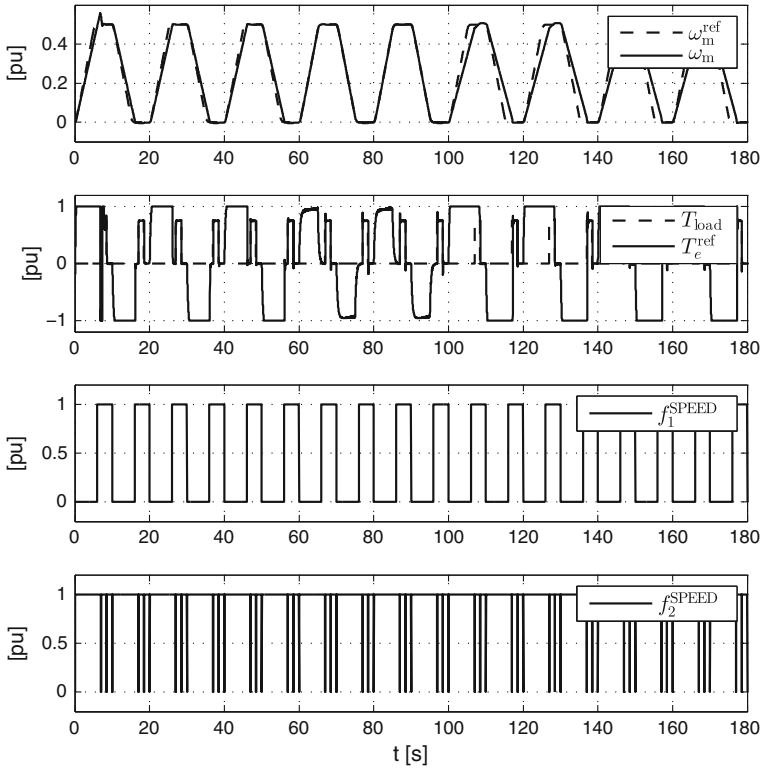


Fig. 16 Response of the drive with the speed neurocontroller tuned by the PSO—moment of inertia drops 20 % at 60 s and rises 20 % at 100 s in comparison to the value set for the first 60 s (assumed total mass variations $1,500 \pm 300$ kg)

conditions. The evolution of the swarm is illustrated in Fig. 15. The performance of the drive along with the switching functions used in (20) is shown in Fig. 16. The speed overshoot visible in Fig. 16 during the first acceleration is the result of a random initial weights of the neurocontroller. The training procedure needs some transients on speed to be able to identify the dynamics of the plant. After one vehicle braking no subsequent significant overshoots occur.

5 Augmented Full-State Feedback Controller for a Three-Phase Inverter

Oscillatory controllers have proven to be one of the highest performance alternatives for AC voltage control in many applications, including grid converters, active power filters and sine wave inverters. Examples of such solutions are

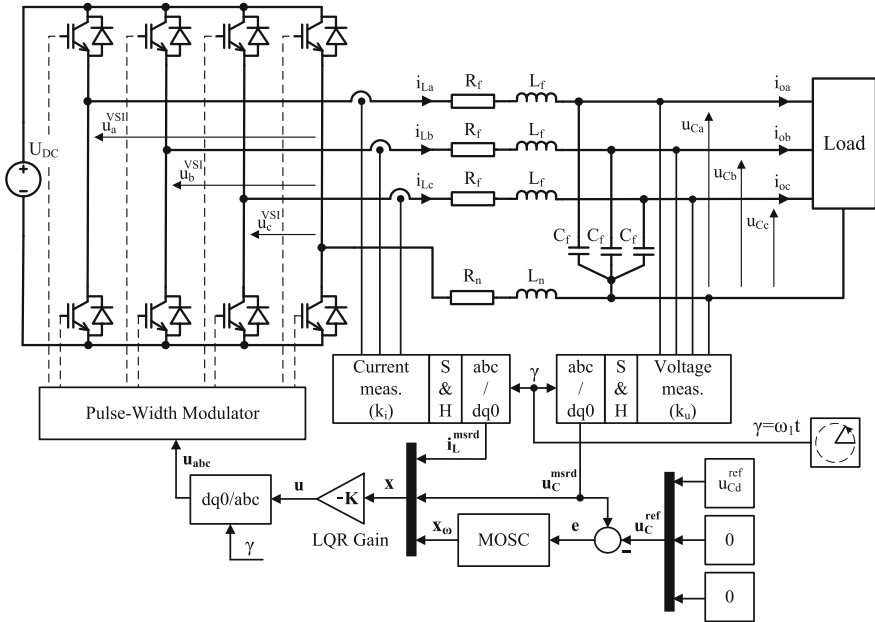


Fig. 17 Three-phase four-leg inverter with LC filter and augmented full state feedback controller

described in [34–38]. The solution considered here relies solely on the LQR design method and has been proposed in [39]. A full-state feedback controller with a state vector augmented to include integral plus multiple oscillatory actions has been implemented in the $dq0$ rotating reference frame with all its gains calculated in one pass using the LQR approach. The LQR design method is known to deliver good performance in practical systems. The resulting system is inherently stable and the controller is relatively simple in coding. The procedure comes down to preparation of a state-space description of an augmented system (plant plus auxiliary controller states), setting weighting matrices in the quadratic cost function and calling the function that solves analytically the optimization problem, known as the discrete-time algebraic Riccati equation (DARE). A three-phase four-leg inverter with an output LC filter depicted in Fig. 17 is considered as the plant to be controlled. Therefore, its mathematical model in the $dq0$ rotating reference frame is as follows

$$\frac{d}{dt} \mathbf{x}_f(t) = \mathbf{A}_f^{\text{cont}} \mathbf{x}_f(t) + \mathbf{B}_f^{\text{cont}} \mathbf{u}(t) + \mathbf{E}_f^{\text{cont}} z(t), \quad (21)$$

where

$$\mathbf{A}_f^{\text{cont}} = \begin{bmatrix} -\frac{R_f}{L_f} & \omega_1 & 0 & -\frac{k_i}{k_u L_f} & 0 & 0 \\ -\omega_1 & -\frac{R_f}{L_f} & 0 & 0 & -\frac{k_i}{k_u L_f} & 0 \\ 0 & 0 & -\frac{R_f+3R_n}{L_f+3L_n} & 0 & 0 & -\frac{k_i}{k_u(L_f+3L_n)} \\ \frac{k_u}{k_i C_f} & 0 & 0 & 0 & \omega_1 & 0 \\ 0 & \frac{k_u}{k_i C_f} & 0 & -\omega_1 & 0 & 0 \\ 0 & 0 & \frac{k_u}{k_i C_f} & 0 & 0 & 0 \end{bmatrix} \quad (22)$$

$$\mathbf{B}_f^{\text{cont}} = \begin{bmatrix} \frac{k_{dc} k_i}{L_f} & 0 & 0 \\ 0 & \frac{k_{dc} k_i}{L_f} & 0 \\ 0 & 0 & \frac{k_{dc} k_i}{L_f+3L_n} \\ 0 & 0 & 0 \\ 0 & 0 & 0 \\ 0 & 0 & 0 \end{bmatrix} \quad (23)$$

$$\mathbf{E}_f^{\text{cont}} = \begin{bmatrix} 0 & 0 & 0 \\ 0 & 0 & 0 \\ 0 & 0 & 0 \\ -\frac{k_u}{C_f} & 0 & 0 \\ 0 & -\frac{k_u}{C_f} & 0 \\ 0 & 0 & -\frac{k_u}{C_f} \end{bmatrix} \quad (24)$$

and

$$\mathbf{x}_f(t) = \left[i_{Ld}^{\text{msrd}}(t), i_{Lq}^{\text{msrd}}(t), i_{L0}^{\text{msrd}}(t), u_{Cd}^{\text{msrd}}(t), u_{Cq}^{\text{msrd}}(t), u_{C0}^{\text{msrd}}(t) \right]^T \quad (25)$$

$$\mathbf{u}(t) = \left[u_d(t), u_q(t), u_0(t) \right]^T \quad (26)$$

$$\mathbf{z}(t) = \left[i_{od}(t), i_{oq}(t), i_{o0}(t) \right]^T, \quad (27)$$

where L_f, R_f, L_n, R_n, C_f and ω_1 denote respectively inductances and resistances of phase and neutral filter legs, capacitance of the filter, and angular speed of the reference frame $dq0$ equal to the fundamental angular frequency of the desired output voltage. The load current vector $\mathbf{z}(t)$ represents the unmeasured disturbance. This description already accommodates k_u, k_i, k_{dc} gains that model current and voltage transducers, and the voltage source inverter, respectively. The superscript \bullet^{msrd} denotes the output signal of a measurement transducer. Thereafter, auxiliary states are introduced to achieve control objectives, i.e. zero steady-state error for the reference frequency and good disturbance rejection for the anticipated load current dominant harmonics. Thus, the auxiliary state variables are as follows

$$\frac{d}{dt}\mathbf{x}_0(t) = \mathbf{e}(t) \quad (28)$$

with

$$\mathbf{e}(t) = \underbrace{[u_{Cd}^{\text{msrd}}(t) - u_d^{\text{ref}}(t)]}_{e_d(t)}, \underbrace{[u_{Cq}^{\text{msrd}}(t) - u_q^{\text{ref}}(t)]}_{e_q(t)}, \underbrace{[u_{C0}^{\text{msrd}}(t) - u_0^{\text{ref}}(t)]}_{e_0(t)}^T \quad (29)$$

and

$$\begin{cases} \frac{d}{dt}x_1(t) = x_2(t) \\ \frac{d}{dt}x_2(t) = -\omega^2 x_1(t) + e(t), \end{cases} \quad (30)$$

where ω is the desired resonant angular frequency and $e(t)$ denotes a selected control error component from (29). The number and the value of resonant angular frequencies ω are selected individually for each voltage component and have to reflect anticipated load current harmonics seen in the $dq0$ reference frame. The integral term can be regarded as the special case of the oscillatory term with zero resonant frequency. As a result, the auxiliary subsystem can be categorized as a sole multi-oscillatory (MOSC) subsystem

$$\frac{d}{dt}\mathbf{x}_\omega(t) = \mathbf{A}_\omega^{\text{cont}}\mathbf{x}_\omega(t) + \mathbf{B}_\omega^{\text{cont}}\mathbf{e}(t), \quad (31)$$

where the auxiliary state vector x_ω refers to all three voltage components and accommodates any desired frequency from available bandwidth. The auxiliary states are merged with the plant states and the augmented state matrix and the input matrix are composed as follows

$$\mathbf{A}^{\text{cont}} = \begin{bmatrix} \mathbf{A}_f^{\text{cont}} & \mathbf{0} \\ [0 \quad \mathbf{B}_\omega^{\text{cont}}] & \mathbf{A}_\omega^{\text{cont}} \end{bmatrix} \quad (32)$$

$$\mathbf{B}^{\text{cont}} = [\mathbf{B}_f^{\text{cont}}, \mathbf{0}]^T. \quad (33)$$

This description is then transformed into the discrete-time domain using ZOH method and weighting matrices \mathbf{Q} and \mathbf{R} have to be determined in the quadratic cost function

$$J_{\text{LQ}} = \sum_{k=1}^{\infty} (\mathbf{x}^T(k)\mathbf{Q}\mathbf{x}(k) + \mathbf{u}^T(k)\mathbf{R}\mathbf{u}(k)) \quad (34)$$

being the part of the LQR definition. The dynamics of the non-disturbed augmented full-state feedback system

$$\mathbf{x}(k+1) = (\mathbf{A} - \mathbf{BK})\mathbf{x}(k) \quad (35)$$

Table 2 Selected parameters of the laboratory setup

Symbol	Value and units	Description
DSC	TMS320F28335	Digital signal controller (150 MHz)
U_n	325 V	Nominal output voltage amplitude
ω_1	$2\pi \cdot 50 \text{ s}^{-1}$	Output reference angular frequency
f_{PWM}, T_s	10 kHz, 100 μs	Switching frequency, sampling time
Dead-time	1.3 μs	Dead-time for IGBT gate signals
U_{DC}	620 V	DC-link voltage
L_f	250 μH	Inductance of the phase leg
R_f	165 m Ω	Series resistance of the phase leg
C_f	85 μF	Capacitance of the output filter
L_n	250 μH	Inductance of the neutral leg
R_n	165 m Ω	Series resistance of the neutral leg
k_u	$1/U_n$	Voltage transducer gain
k_i	0.01 A $^{-1}$	Current transducer gain
k_{dc}	U_{DC}	Voltage source inverter gain
Noise	1 %	Measurement noise level

for the zero reference signals is then shaped by \mathbf{K} designed using the LQR method. Selecting \mathbf{Q} and \mathbf{R} is the crucial step and in the most common approach of guessing and checking this step involves an expert knowledge combined with usually numerous trials. Moreover, the resulting controller though optimal according to (34) is not optimal according to commonly used control performance indices as (3), (4) or (5). On the other hand, with the help of a population based optimizer, a full-state feedback controller can be tuned according to a user defined cost function [40–42]. It has been verified that in the case of the discussed controller the performance index

$$J_c^{\text{LQR}} = \frac{T_s}{t_{\text{stop}}} \sum_{k=1}^{t_{\text{stop}}/T_s} (e^T(k)e(k) + \beta \Delta u^T(k) \Delta u(k)), \quad (36)$$

where β is the weighting factor that directly influences dynamics of the control signal by penalizing this dynamics, is able to produce practical controller gains applicable in the real system in the presence of a measurement noise. In the discussed system the LQR design approach has been kept. However, it should be noticed that a swarm could also perform direct search for \mathbf{K} entries [40] or closed-loop poles [41]. If no presumptions concerning the poles or the gains are available, the LQR approach seems to be the most effective if the convergence rate of the stochastic search is taken into account. This conclusion is similar if the augmented state feedback controller is tuned by the human using a trial and error method.

The optimization takes place in offline mode on numerical model of the physical converter with parameters as in Table 2. The method has been verified for the case of the auxiliary states covering 2nd, 3rd, 4th, 6th, 8th, 9th, 10th and 12th harmonic in the dq paths and 1st, 3rd, 5th, 6th, 7th, 9th, 11th and 12th harmonic for

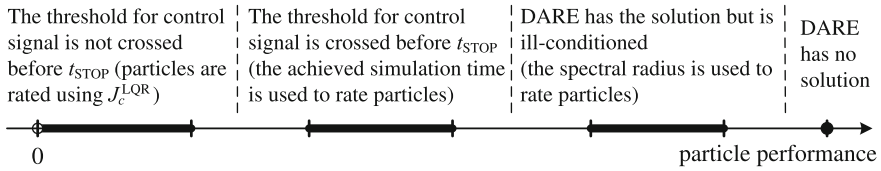


Fig. 18 The order of performance regions for the LQR

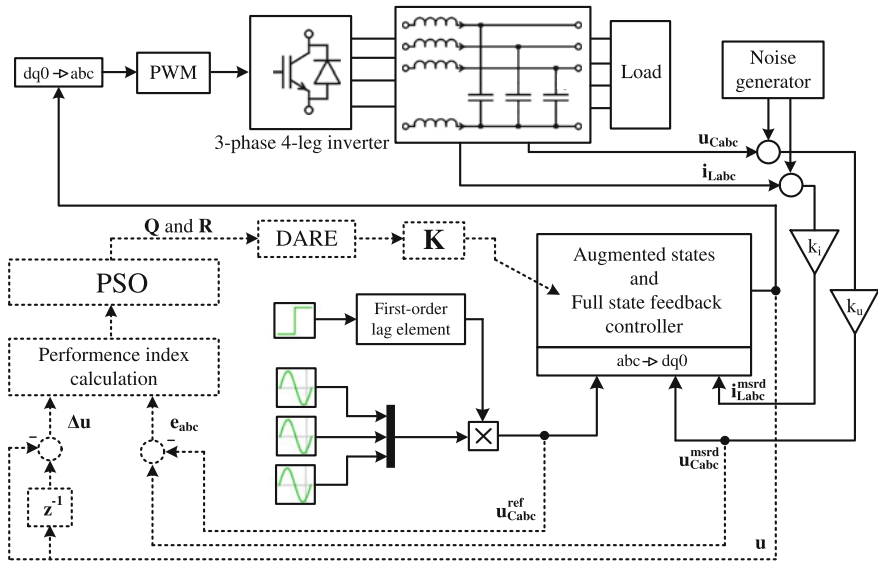


Fig. 19 PSO connected to the numerical model of the three-phase four-leg inverter with the output LC filter

the 0-component. The auxiliary states related to integral actions for all error components are also included. This produces the 59-dimensional optimization problem: 3 entries of R and 57 entries of Q with one entry set arbitrary to 1 as scaling of (34) does not influence the result. The entries in Q are related to: 6 measured state variables, 3 integral actions and $2 \cdot 3 \cdot 8$ oscillatory state variables. It has been decided to merge selected search dimensions to get less challenging problem from wall-clock time perspective. First of all, the Bryson's rule [43] has been applied to normalize the weighting entries of Q and R . Next, penalties are not varied for a given harmonic (regardless to its occurrence in the different axis). Moreover, it has been tested that the search performed in an exponential scale is more effective in comparison to the search in a linear scale. This gives entries with the decision variables as exponents, e.g. for 3rd harmonic of the form $3^2 \omega_1^{2} 10^{q_3}$ and 10^{q_3} for the two auxiliary states introduced by the oscillatory term. The optimization can then be run in 15D space. The particle is a vector

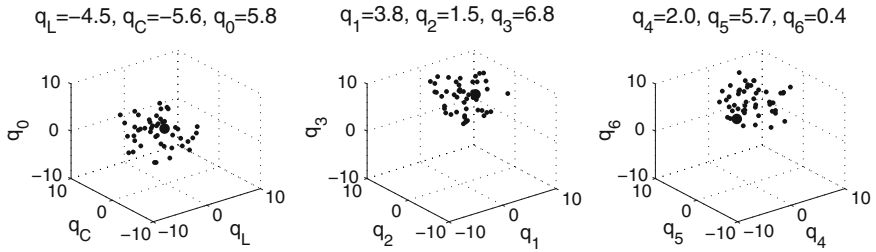


Fig. 20 Initial position of the swarm—the bigger in diameter *black dot* denotes *gbst*

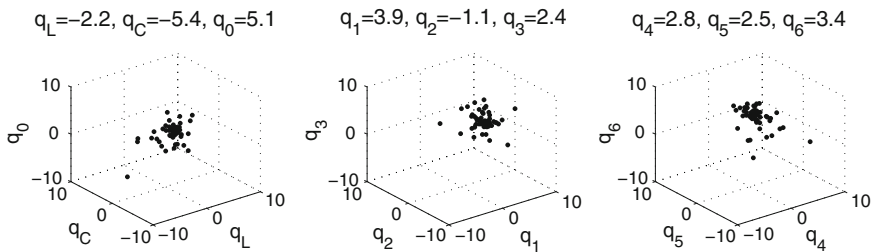


Fig. 21 Position of the particles at 15th iteration, i.e. at the early stage of the search

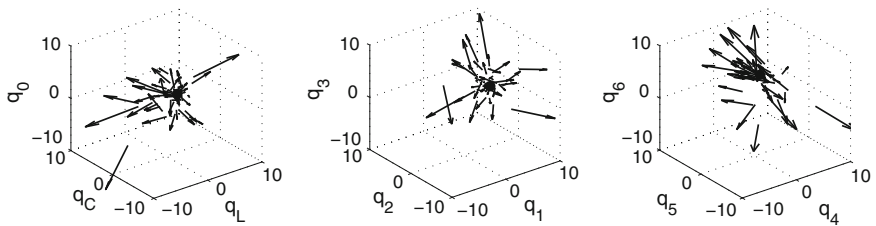


Fig. 22 Velocity vectors of the particles at 15th iteration

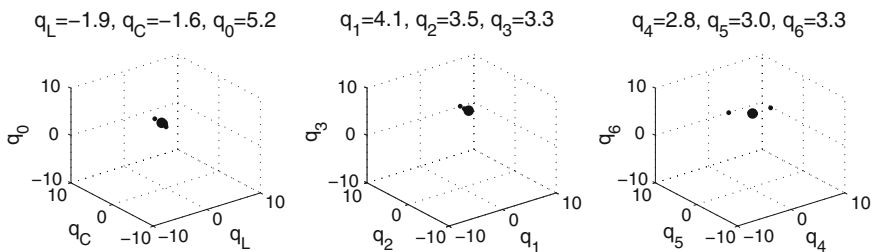


Fig. 23 Position of the swarm near its equilibrium after 75 iterations

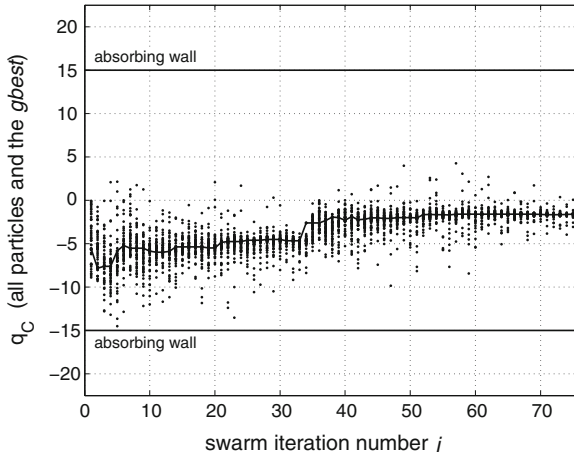


Fig. 24 The evolution of g_{best} (curved line) and the swarm position (dots) over optimization iterations for q_C

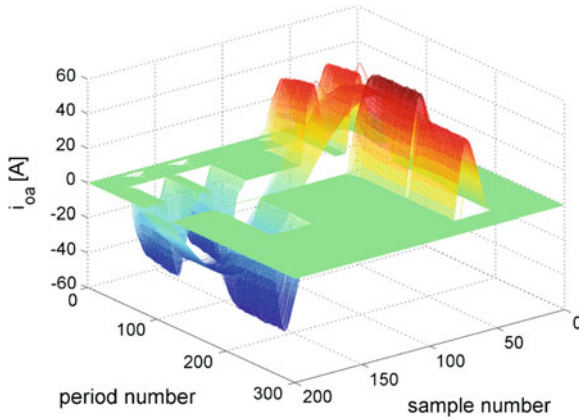


Fig. 25 The test load current (phase a)

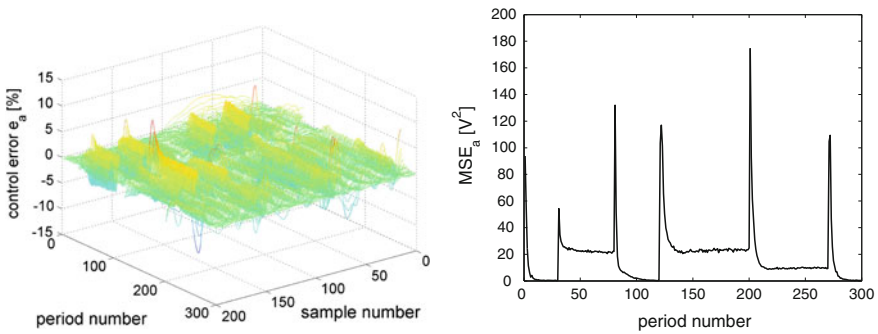


Fig. 26 The performance of the system optimized according to the performance index J_c^{LQR} —instantaneous control error (on the left) and MSE per period of the reference signal (on the right)

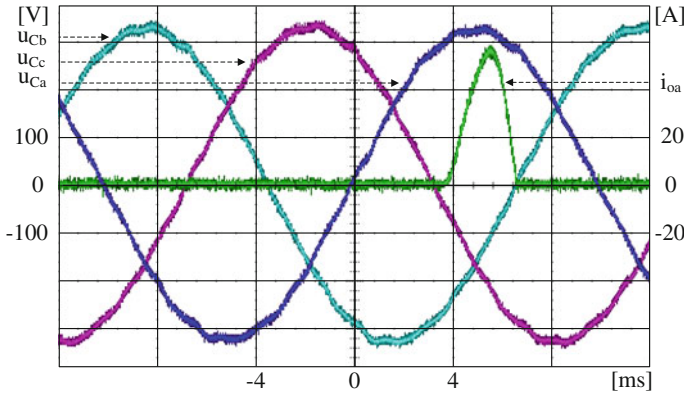


Fig. 27 Output voltage (u_{Ca} , u_{Cb} , u_{Cc}) and output current (i_{oa}) waveforms under the three-pulse diode rectifier load: $U_{Ca} = 230$ Vrms, $I_{oa} = 14.14$ Arms, $\text{THD}_{u_{Ca}} = 1.58$ %, $\text{THD}_{i_{oa}} = 179$ %

$$\mathbf{p}^{\text{LQR}} = [q_L, q_C, q_0, q_1, \dots, q_{12}] \quad (37)$$

of candidate exponents determining weighting coefficients for the LQR cost function (34). All search directions could have been left unconstrained because of lack of clear physical boundaries. The entries of \mathbf{Q} are positive for any real-valued particle (37). However, the absorbing walls have been introduced at -15 and 15 to turn the particles back to practical search regions. The walls have been set with considerable surplus according to the experience gathered during previously used trial and error tuning method. Particles that cannot be rated using (36) are handled as in Fig. 18. The swarm of 50 particles is connected to the numerical model of the system as in Fig. 19. Envelopes of the reference voltages seen in natural reference frame are shaped using a first order lag element (see Fig. 2) with a time constant of 0.05 s to avoid excessive contribution to the performance index due to zero initial conditions for the LC filter. Alternatively, a switching function could be introduced in (36) as discussed in Sect. 1.

Position and speed graphs have been broken into 3D plots. An illustrative selection of such graphs is shown in Figs. 20, 21, 22 and 23. The evolution of the swarm in one selected dimension is shown in Fig. 24. The performance of the resulting system under the load current from Fig. 25 is shown in Fig. 26. The obtained matrix \mathbf{K} is transferred to the physical controller without any further alterations. Selected parameters of the laboratory setup are given in Table 2. The tuning procedure from the designer side is only one-dimensional and finding a good β for (36) that produces desired behavior of the physical system usually takes less than five trials. The performance of the physical system under nonlinear loads is illustrated in Figs. 27 and 28. The transient state caused by the step resistive load in one phase (and no-load operation of other phases) is shown in Fig. 29. The harmonic contents are compared in Table 3.

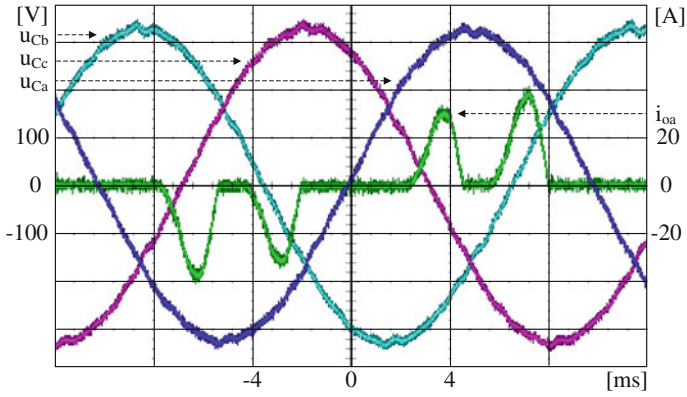


Fig. 28 Output voltage (u_{Ca} , u_{Cb} , u_{Cc}) and output current (i_{oa}) waveforms under the six-pulse diode rectifier load: $U_{Ca} = 230$ Vrms, $I_{oa} = 15.11$ Arms, $THD_{U_{Ca}} = 1.68\%$, $THD_{I_{oa}} = 105\%$

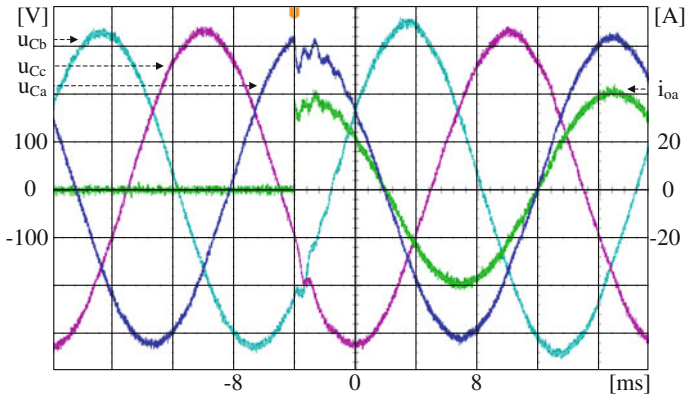


Fig. 29 Transient state on capacitor voltage and output current for the step load ($R_{step} = 8\Omega$) in phase a (phases b , c left unloaded)

Table 3 Harmonic spectra of the output voltage (u_{Ca}) and the load current (i_{oa})

	Open loop operation under 3-pulse diode rectifier load		Closed loop operation under 3-pulse diode rectifier load		Closed loop operation under 6-pulse diode rectifier load	
	$U_{rms} = 227$ Vrms		$U_{rms} = 230$ Vrms		$U_{rms} = 230$ Vrms	
	$I_{rms} = 12.24$ Arms		$I_{rms} = 14.14$ Arms		$I_{rms} = 15.11$ Arms	
	THD $_U = 4.38$ %		THD $_U = 1.58$ %		THD $_U = 1.68$ %	
	THD $_I = 152$ %		THD $_I = 179$ %		THD $_I = 105$ %	
	$U_1 = 227$ Vrms		$U_1 = 230$ Vrms		$U_1 = 230$ Vrms	
	$I_1 = 6.14$ Arms		$I_1 = 6.42$ Arms		$I_1 = 10.38$ Arms	
h	U (%)	I (%)	U (%)	I (%)	U (%)	I (%)
1	100	100	100	10	100	100
2	0.574	92	0.410	95	0.313	14
3	3.149	80	0.226	86	0.339	5
4	0.612	64	0.128	76	0.139	13
5	0.697	48	0.534	64	0.484	79
6	2.054	32	0.063	52	0.129	2
7	0.190	19	0.276	38	0.558	58
8	0.064	10	0.152	27	0.125	4
9	0.728	7	0.121	17	0.037	3
10	0.081	8	0.110	11	0.092	3
11	0.218	8	0.102	8	0.114	27
12	1.488	7	0.031	8	0.094	1
13	0.163	5	0.163	9	0.212	12

6 Conclusions

Nowadays, control systems become more and more elaborated and related tuning procedures often require theoretical insight into the system. And even then, analytical tuning procedures available for these systems usually forces a designer to guess some parameters that are needed as their input arguments. Also often these arguments do not directly shape the dynamics of the closed-loop system, and consequently achieving the desired behavior of the system is not a straightforward task. That is why still cascaded PI controllers are dominant in the industrial practice. They earn their popularity because of relatively simple tuning methods and low computational complexity. Theoretically, any controller tuning task can be redefined into a performance index optimization problem. Relevant controller settings turn into decision variables. Such an optimization problem can be solved with little or no insight into the system by using gradientless population-based optimizers. This approach can be applied to problems that do not have yet an analytical solution as well as to problems that do have one. In the case of the latter this can result in much more straightforward procedure from the designer point of view in comparison to the original analytical solution. It has been illustrated that a swarm of particles can support control engineers in a simultaneous tuning of

cascaded controllers, in identifying potential excessiveness of a control structure (as in Sect. 4), in reducing dimensionality of the problem in terms of number of parameters that have to be passed to the function by the user (as in Sect. 6). Moreover, swarms are extremely useful when a user-defined performance index should be addressed in the system and analytical solution has not been yet developed. It has been shown that swarms can help to tune adaptive neurocontrollers (as in Sect. 5) that otherwise would have to be tuned by using a time-consuming trial and error method accompanied by an expert knowledge. It should be noted that the PSO is itself a trial-and-error-like method. However, points that are to be visited in the solution space are determined by the swarm itself in the iterative manner. The visual inspection of a performance often used during human made trials is replaced by rating solutions according to a user defined real-valued performance index. In most practical engineering problems no analytical solution is expected as far as stochastic search is able to deliver good suboptimal solution and this turns out to be achievable if some basic expert knowledge is incorporated into the performance index definition.

References

1. R.C. Eberhart, Y. Shi, J. Kennedy, *Swarm Intelligence*, 1st edn. (The Morgan Kaufmann Series in Evolutionary Computation, Morgan Kaufmann Publishers, Burlington, 2001)
2. A. Banks, J. Vincent, C. Anyakoha, A review of particle swarm optimization. Part I: background and development. *Nat. Comput.* **6**(4), 467–484 (2007)
3. A. Banks, J. Vincent, C. Anyakoha, A review of particle swarm optimization. Part II: hybridisation, combinatorial, multicriteria and constrained optimization, and indicative applications. *Nat. Comput.* **7**(1), 109–124 (2008)
4. D. Wolpert, W. Macready, No free lunch theorems for optimization. *IEEE Trans. Evolut. Comput.* **1**(1), 67–82 (1997)
5. R. Mendes, J. Kennedy, J. Neves, The fully informed particle swarm: simpler, maybe better. *IEEE Trans. Evolut. Comput.* **8**(3), 204–210 (2004)
6. J. Fernandez-Marquez, J. Arcos, Adapting particle swarm optimization in dynamic and noisy environments, in *IEEE Congress on Evolutionary Computation (CEC 2010)* (2010), pp. 1–8
7. X. Hu, R. Eberhart, Multiobjective optimization using dynamic neighborhood particle swarm optimization, in *Proceedings of the 2002 Congress on Evolutionary Computation (CEC 2002)*, vol. 2, pp. 1677–1681, 2002
8. A. Röhrler, S. Chen, An analysis of sub-swarms in multi-swarm systems, in *AI 2011: Advances in Artificial Intelligence*, vol. 7106, Lecture Notes in Computer Science, ed. by D. Wang, M. Reynolds (Springer, Berlin, 2011), pp. 271–280
9. J. Kennedy, R. Mendes, Neighborhood topologies in fully informed and best-of-neighborhood particle swarms. *IEEE Trans. Syst. Man Cyber. Part C Appl. Rev.* **36**(4), 515–519 (2006)
10. J. Robinson, Y. Rahmat-Samii, Particle swarm optimization in electromagnetics. *IEEE Trans. Antennas Propag.* **52**(2), 397–407 (2004)
11. M.A. Rahimian, M.S. Tavazoei, Improving integral square error performance with implementable fractional-order PI controllers. *Optimal Control Appl. Methods* (In press) (2013)

12. I.C. Trelea, The particle swarm optimization algorithm: convergence analysis and parameter selection. *Info. Process. Lett.* **85**(6), 317–325 (2003)
13. K. Zielinski, R. Laur, Stopping criteria for a constrained single-objective particle swarm optimization algorithm. *Informatika (Slovenia)* **31**(1), 51–59 (2007)
14. J. Riget, J. Vesterstrøm, A diversity-guided particle swarm optimizer—the ARPSO. Technical report (Aarhus Universitet, Aarhus, 2002)
15. K.J. Åström, T. Hägglund, *PID Controllers: Theory, Design, and Tuning*, 2 edn. (Instrument Society of America, Research Triangle Park, Charlotte, 1995)
16. K.J. Åström, T. Hägglund, Revisiting the Ziegler–Nichols step response method for PID control. *J. Process Control* **14**(6), 635–650 (2004)
17. M. Joost, K. Zielinski, B. Orlik, R. Laur, Robust PI cascade control for a multi-mass system optimized by evolutionary algorithms, in *The 13th Power Electronics and Motion Control Conference, (EPE-PEMC 2008)* (2008), pp. 1064–1070
18. T. Nussbaumer, M. Heldwein, G. Gong, S. Round, J. Kolar, Comparison of prediction techniques to compensate time delays caused by digital control of a three-phase buck-type PWM rectifier system. *IEEE Trans. Ind. Electron.* **55**(2), 791–799 (2008)
19. J.W. Choi, S.C. Lee, H.G. Kim, Inertia identification algorithm for high-performance speed control of electric motors. *IEEE Proc. Electr. Power Appl.* **153**(3), 379–386 (2006)
20. M.O. Efe, in *Neural Network-based Control*, ed. by B.M. Wilamowski, J.D. Irwin. The Industrial Electronics Handbook: Intelligent Systems, vol. 3 (CRC Press, Boca Raton, 2011)
21. J. Sarangapani, *Neural Network Control of Nonlinear Discrete-Time Systems*, (CRC Press, Boca Raton, 2006)
22. P. Potocnik, I. Grabec, Adaptive self-tuning neurocontrol. *Math. Comput. Simulat.* **51**, 201–207 (2000)
23. Y.C. Wang, C.J. Chien, D.T. Lee, An output recurrent fuzzy neural network based iterative learning control for nonlinear systems, in *IEEE International Conference on Fuzzy Systems (FUZZ-IEEE 2008)*, *IEEE World Congress on Computational Intelligence* (2008), pp. 1563–1569
24. Q. Zhu, L. Guo, Stable adaptive neurocontrol for nonlinear discrete-time systems. *IEEE Trans. Neural Netw.* **15**(3), 653–662 (2004)
25. J.H. Park, S.H. Kim, C.J. Moon, Adaptive neural control for strict-feedback nonlinear systems without backstepping. *IEEE Trans. Neural Netw.* **20**(7), 1204–1209 (2009)
26. J. Levin, N. Perez-Arancibia, P. Ioannou, T.C. Tsao, A neural-networks-based adaptive disturbance rejection method and its application to the control of hard disk drives. *IEEE Trans. Magnet.* **45**(5), 2140–2150 (2009)
27. T. Pajchrowski, K. Zawirski, Application of artificial neural network to robust speed control of servodrive. *IEEE Trans. Ind. Electron.* **54**(1), 200–207 (2007)
28. T. Orłowska-Kowalska, K. Szabat, Control of the drive system with stiff and elastic couplings using adaptive neuro-fuzzy approach. *IEEE Trans. Ind. Electron.* **54**(1), 228–240 (2007)
29. L. Grzesiak, V. Meganck, J. Sobolewski, B. Ufnalski, On-line trained neural speed controller with variable weight update period for direct-torque-controlled AC drive, in *12th International Power Electronics and Motion Control Conference (EPE-PEMC 2006)* (2006), pp. 1127–1132
30. L. Grzesiak, V. Meganck, J. Sobolewski, B. Ufnalski, Genetic algorithm for parameters optimization of ANN-based speed controller, in *The International Conference on Computer as a Tool (EUROCON 2007)* (2007), pp. 1700–1705
31. C. Igel, M. Hüskens, Empirical evaluation of the improved Rprop learning algorithms. *Neurocomputing* **50**, 105–123 (2003)
32. B. Ufnalski, L. Grzesiak, Artificial neural network based voltage controller for the single phase true sine wave inverter—a repetitive control approach. *Electr. Rev. (Przegląd Elektrotechniczny, paper in English, open access at pe.org.pl)*, **89**(4), 14–18 (2013)
33. B. Ufnalski, L. Grzesiak, Particle swarm optimization of artificial-neural-network-based on-line trained speed controller for battery electric vehicle. *Bull. Polish Acad. Sci. Tech. Sci.* **60**(3), 661–667 (2012)

34. D. De, V. Ramanarayanan, A proportional + multiresonant controller for three-phase four-wire high-frequency link inverter. *IEEE Trans. Power Electron.* **25**(4), 899–906 (2010)
35. G. Bonan, O. Mano, L. Pereira, D. Coutinho, Robust control design of multiple resonant controllers for sinusoidal tracking and harmonic rejection in uninterruptible power supplies, in *IEEE International Symposium on Industrial Electronics (ISIE 2010)* (2010), pp. 303–308
36. M. Dai, M. Marwali, J.W. Jung, A. Keyhani, A three-phase four-wire inverter control technique for a single distributed generation unit in island mode. *IEEE Trans. Power Electron.* **23**(1), 322–331 (2008)
37. C. Liu, F. Blaabjerg, W. Chen, D. Xu, Stator current harmonic control with resonant controller for doubly fed induction generator. *IEEE Trans. Power Electron.* **27**(7), 3207–3220 (2012)
38. A. Hasanzadeh, C.S. Edrington, B. Maghsoudlou, F. Fleming, H. Mokhtari, Multi-loop linear resonant voltage source inverter controller design for distorted loads using the linear quadratic regulator method. *Power Electron. IET* **5**(6), 841–851 (2012)
39. A. Kaszewski, L. Grzesiak, B. Ufnalski, Multi-oscillatory LQR for a three-phase four-wire inverter with L3nC output filter, in *38th Annual Conference on IEEE Industrial Electronics Society (IECON 2012)* (2012), pp. 3449–3455
40. S. Karanki, M. Mishra, B. Kumar, Particle swarm optimization-based feedback controller for unified power-quality conditioner. *IEEE Trans. Power Deliv.* **25**(4), 2814–2824 (2010)
41. J. Wang, B. Brackett, R. Harley, Particle swarm-assisted state feedback control: from pole selection to state estimation, in *American Control Conference (ACC 2009)* (2009), pp. 1493–1498
42. A. Hasanzadeh, C. Edrington, J. Leonard, Y. Liu, VSI optimal controller tuning with LQR-based gain space determination and PSO finalization in LEV drive, in *IEEE Vehicle Power and Propulsion Conference (VPPC 2011)* (2011), pp. 1–6
43. F. Gene, J.D.P. Franklin, M.L. Workman, *Digital Control of Dynamic Systems*, 3rd edn. (Addison Wesley Longman, Boston, 1998)

Chapter 10

Space Vector Modulation in Three-Phase Three-Level Flying Capacitor Converter-Fed Adjustable Speed Drive

Sebastian Styński and Mariusz Malinowski

Abstract This Chapter is devoted to the Space Vector Modulation (SVM) in three-phase three-level Flying Capacitor Converter (FCC) fed adjustable speed drive (ADS). First, the classical and adaptive SVM are described. The adaptive SVM provides reduction of number of switching in the whole linear range of the converter operation because minimal number of vectors is used in each modulation region. As result, switching losses in FCC are reduced in comparison to the classical SVM and thus, the converter efficiency is increased. Next, elimination of DC sources unbalance in full range of operation of the FCC is presented. The minimization of the flying capacitors voltages pulsation is obtained by the compensation of flying capacitors voltages balancing delay based on prediction of those voltages values in next modulation period. Finally, taking to account the requirements of the demanding ASD application: low speed operation without phase current distortion and the high speed operation over the linear range of the converter with reference output voltage amplitude, the additional features for both modulation techniques: the dead-time effect and semiconductor devices voltage drop compensation as well as the overmodulation algorithm are shown.

1 Introduction

Recent advances in the energy conversion area (e.g. Distributed Power Generation systems, traction and Adjustable Speed Drives (ASD)) show a focus trend in the Voltage Source Converters (VSC) [1–5]. Generally we can distinguish two groups

S. Styński (✉) · M. Malinowski
Warsaw University of Technology, Pl. Politechniki 1, 00-661 Warsaw, Poland
e-mail: stynskis@isep.pw.edu.pl

M. Malinowski
e-mail: malin@isep.pw.edu.pl

of VSC: two-level and multilevel. Two-level converter is well known topology used for a long time by industry. Multilevel converter is also not new topology, some of converters are known since 1960s, but they were not used by industry until recently by some of technological barrier. Two technology breakthroughs of the electronic industry have enabled this remarkable development:

- the introduction of modern IGBTs on the market enabled the manufacturing of reliable, robust and low cost VSC modules which allow to construct VSC working with increased voltage and current ratings,
- the introduction of low cost digital signal microprocessors and FPGA for real time applications allowed the successful implementation of complex vector control schemes for VSC.

The idea of multilevel VSC is based on series connection of semiconductor devices with more than one DC voltage source. The multilevel VSC operation above typical semiconductor voltage limits with reduced voltage stress, lower common mode voltages, reduced harmonics distortion and lower filter requirements are some of the well known advantages that have made this topologies popular for research and industry. Lately, the multilevel VSC topologies fed three-phase ASD have become attractive for the medium and high power conversion [6, 7]. Especially two three-level topologies are now used in the three-phase ASD industrial applications: the Diode Clamped Converter (DCC), proposed in 1981 by Nabae and Takahashi [8] and the Flying Capacitor Converter (FCC), proposed in 1991 by T. A. Meynard and A. Foch [9].

The three-phase three-level DCC is most popular in the ASD industrial application. In the DCC, the DC-link capacitors voltage balancing depends on the switching states in all phases. However, many DC voltage sources causes problem of capacitors utilization in full range of the converter operation. For example, in three-phase three-level DCC for high modulation index and for higher number of levels, even with sophisticated Pulse Width Modulation (PWM) techniques, bringing DC-link capacitors voltage difference to zero is difficult [10–15]. Hardware solutions (such as passive voltage balancing with parallel resistors) or introducing additional virtual switching states may have detrimental effects on the ASD efficiency [12, 13, 16]. To solve this problem, for higher number of levels, the Active DCC topology was introduced by ABB [17, 18]. This five-level hybrid topology combines flexibility of the FCC with the robustness of the industrial DCC to generate multilevel voltages. However, it cannot be used for commonly three-level applications.

From other hand FCC topology typically is used in active filtering [19, 20] because the flying capacitors (FCs) voltage balancing in one phase is independent of switching states in other phases [9, 21–24]. It means, that each phase can be considered separately and in that case the FC's voltage balancing does not depend on the value of modulation index, only on the current flow direction. In comparison to the DCC this is an advantage of the FCC topology, because the FC's are used for output voltage generation in full converter operation range, except six step operation. Thus, the three-phase three-level FCC can be an important alternative to

the three-phase three-level DCC in ASD application especially in aspect of capacitors utilization in full range of operation.

In the typical active power filter application of the FCC, usually for each phase Carrier-Based PWM (CB-PWM) is applied [25–28]. Therefore, the SVM techniques were not developed for the FCC as widely as for the DCC, and only several works describing this issue in classical approach can be found [24, 29–33]. However it should be noted that various SVM strategies of selecting the vectors order exist for multilevel converters. Strategy selection will affect the harmonic content and the switching losses [34–36]. Especially, SVM techniques which minimize number of switching and as consequence, the switching losses were not published for the FCC—only a few works exist in this subject [24, 33].

This chapter is devoted to SVM in three-phase three-level FCC fed ASD. First, the classical and adaptive SVM, which minimizes number of switching and as consequence, reduces the switching losses in FCC are described. Next, elimination of DC sources unbalance in full range of operation of the VSC and minimization of the FCs voltages pulsation is presented. Finally, taking to account the requirements of the demanding ASD application: low speed operation without phase current distortion and the high speed operation over the linear range of the converter with reference output voltage amplitude, the additional features for both modulation techniques: the dead-time effect and semiconductor devices voltage drop compensation as well as the Overmodulation algorithm are shown.

2 Space Vector Modulation in Flying Capacitor Converter

2.1 Introduction

Modulation techniques for VSC are responsible for generation of average output (represented by different width of short voltage pulses) voltage with proper balancing of the additional DC voltage sources for multilevel converters. Depending on VSC topologies and switching frequency numerous PWM techniques can be listed [26]. Among them two kinds of PWM are used for FCC: CB-PWM [25–28, 37] and SVM [29–33].

The operation principle of CB-PWM bases for each phase on comparison of reference sinusoidal output phase voltage signal $u_{x,ref}$ where x is the phase of the system with the triangular carrier signals. As result, the width of output pulses is proportional to the reference signal and the output voltage harmonics are concentrated around doubled carrier signal frequency and their multiplication. The multilevel converter needs $n-1$ triangular carrier signals, where n is number of levels. Thus, two carrier signals are used for the three-level converter. Depending on mutual location of carrier signals two general groups of the CB-PWM can be listed: Phase Shifted [27, 38] and Level Shifted PWM [28]. The Phase Shifted PWM carrier signals are shifted in phase by $360^\circ/(n-1)$. The Level Shifted PWM

carrier signals are level shifted in mean of average voltage level value. Phase Shifted PWM is widely used in FCC due to automatic self-balancing of FC capacitors [39]. For Level Shifted PWM three modifications based on carrier signals phase shifting are known, however they do not provide automatic self-balancing of FC capacitors.

The three-phase VSC output phase voltage maximum instantaneous value is $2/3$ of DC-link voltage in so-called six step or square wave mode operation [21]. The maximum possible modulation index for six step operation is $M = n - 1$. However, the linear modulation range of the VSC for CB-PWM with sinusoidal reference output phase voltage signal $u_{x,ref}$ is limited to $M < 0.785(n - 1)$. To extend converter linear range of operation in the CB-PWM up to $M = 0.907(n - 1)$, the Zero Sequence Signal (ZSS) of 3rd harmonics frequency is added to sinusoidal reference output phase voltage signal $u_{x,ref}$ [21, 40]. If neutral point of ASD is not connected to the DC-link midpoint, the phase current depends only on phase-to-phase voltage. In such case, the ZSS does not produce phase voltage distortion, however current harmonics are changed. The most known ZSS bases on sinusoidal signal with $1/4$ and $1/6$ amplitude of the fundamental harmonics. The $1/4$ amplitude provides minimum phase current harmonics [41] while the $1/6$ amplitude provides maximal converter linear range of [42]. It should be noticed that the triangular ZSS with $1/4$ amplitude generates the same output voltage as the SVM with symmetrical vector placement.

The second kind of mostly used PWM is SVM [21, 43]. The three-phase circuit—due to space vector theory—can be described in stationary rectangular coordinate system. Thus, the three-phase VSC can be described in $\alpha\beta$ plane as switching state representation of Space Vector. As it was mentioned before, the SVM techniques were not widely developed for the FCC, usually in the typical active power filter application for each phase CB-PWM is applied [25–28]. Thus, only several works describing this SVM issue in classical approach can be found [24, 29–33]. However, recent advances and constant development of the digital signal processing systems (allowing high precision digital implementation of complex control algorithms) contributed to this, that the SVM gained superior position for research and industry. The digital implementation of SVM is characterized by its simplicity. Therefore, the SVM is a good alternative for the CB-PWM in the modern three-phase FCC fed ASD application.

For multilevel converters various SVM strategies of selecting the vectors order exist. Strategy selection can affect—in the same way as the CB-PWM—the harmonic content and the switching losses [34–36]. The SVM FC voltage balancing mostly depend on selection of redundant vectors [22, 23, 43]. Thus, to reduce switching losses with proper FC voltages balancing, only minimal number of vectors in each modulation region—typically three—can be applied to the FCC [13, 35]. The vectors selection is made adaptively to the changes of the FCC electrical parameters (currents sign and amplitude, FC voltages amplitude etc.) [13]. In this section the classical and adaptive SVM (CSVM and ASVM, respectively), which minimizes number of switching and as consequence, reduces the switching losses in FCC are described.

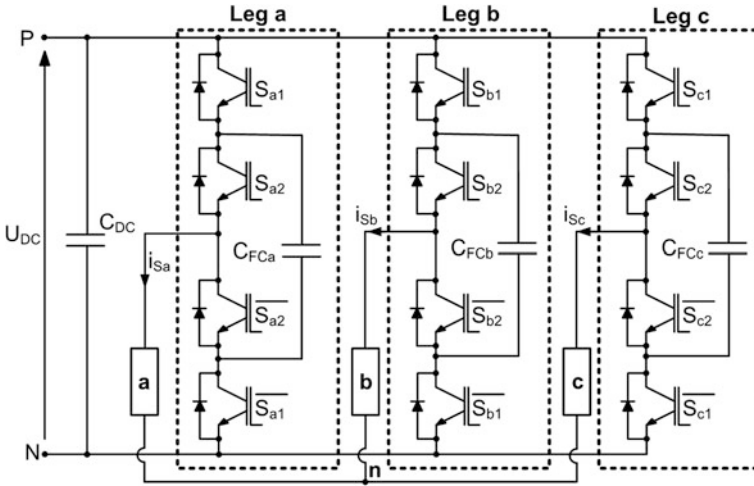


Fig. 1 Three-level three-phase FCC converter

2.2 General Description of Space Vector Modulation for Flying Capacitor Converter

Figure 1 shows the three-level three-phase FCC converter. Each leg consist of four switches and a Flying Capacitor C_{FCx} .

As far as the FCC three-phase system is assumed to be symmetric, the simplified Clarke transformation from natural abc into stationary $\alpha\beta$ coordinate system can be used. Figure 2 shows graphic representation of the Space Vector $\alpha\beta$ voltage plane with possible output voltage vectors of the three-level converter. All voltage vectors are described by three numbers, corresponding to switching states in leg a , b and c , respectively. Table 1 presents possible switching states for single inverter leg. Typically, the FC voltage for the FCC operation should be equal half of the DC-link voltage. With this condition switching state **1** can be divided into two redundant states **1A** and **1B** (highlighted in the Fig. 3) which generates the same output voltage $U_{FCx} = U_{DC}/2$. As the output voltage does not depend on the type of selected state (**1A** or **1B**), they can be used for independent control of U_{FCx} . To decrease number of commutations only one state for each phase is chosen in sampling period. Table 2 shows selection between redundant states **1A** or **1B** based on the stator current i_{Sx} sign.

For the three-phase three-level FCC the twenty-seven voltage vectors \mathbf{V} can be specified, as follows:

- 3 zero vectors (**000**, **111** and **222**),
- 12 internal small amplitude vectors (**100**, **211**, **110**, **221**, **010**, **121**, **011**, **122**, **001**, **112**, **101** and **212**),
- 6 middle medium amplitude vectors (**210**, **120**, **021**, **012**, **102** and **201**),

Fig. 2 The $\alpha\beta$ voltage plane for three-level three-phase converter

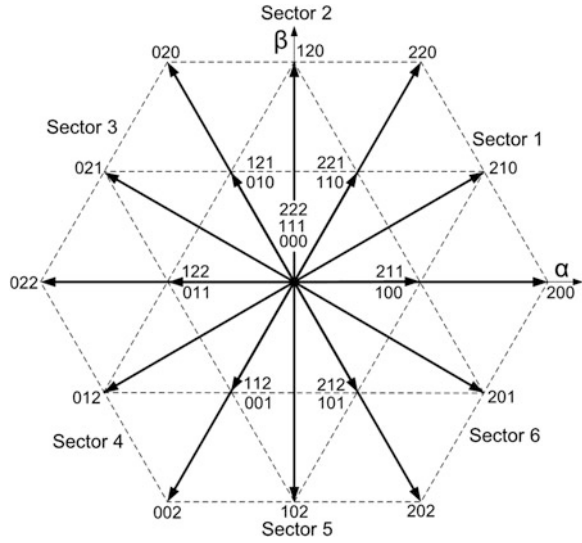


Table 1 Switching states for the three-level FCC leg

Switching states	S_{x1}	S_{x2}	$U_{a,UdcN}$
0	OFF	OFF	0
1A	ON	OFF	$U_{DC} - U_{FCx}$
1B	OFF	ON	U_{FCx}
2	ON	ON	U_{DC}

Fig. 3 Sector 1 with division into four regions and all possible switching states

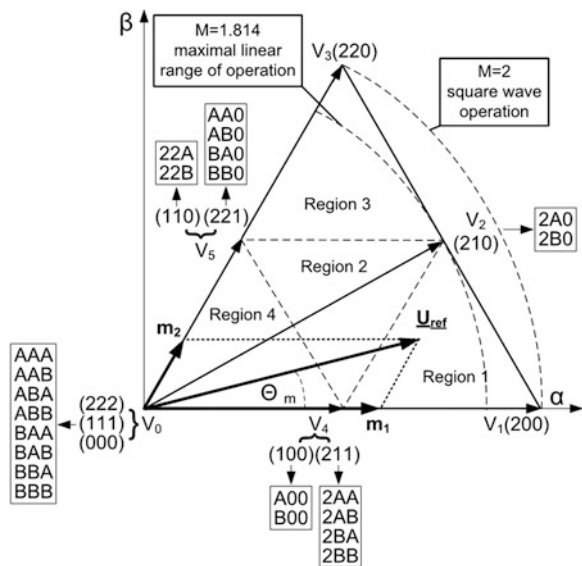


Table 2 Redundant switching state selection

Conditions	$i_{Sx} < 0$	$i_{Sx} > 0$
$U_{FCx} < U_{DC}/2$	1B	1A
$U_{FCx} > U_{DC}/2$	1A	1B

- 6 external large amplitude vectors (**200**, **220**, **020**, **022**, **002** and **022**).

External vectors divide vector plane into six sectors: 1–6 (see Fig. 2). Each sector is divided into four triangular regions. Figure 3 shows sector 1 divided into four regions with all possible switching states.

The reference Space Vector U_{ref} is described by length and its angle:

$$U_{ref} = \sqrt{u_{\alpha,ref}^2 + u_{\beta,ref}^2}, \quad \Theta_m = \arctan \frac{u_{\alpha,ref}}{u_{\beta,ref}} \quad (1)$$

Since each sector encloses in 60° , the Space Vector angle Θ_m is used to determine reference Space Vector U_{ref} sector location. To calculate region number and duration of switching states, a value of modulation index is indispensable. Modulation index M determines proportion of reference Space Vector U_{ref} length in respect to the DC-link voltage. There are a few definitions of modulation index:

$$M = \frac{\sqrt{3}U_{ref}}{U_{DC}}(n-1) \quad (2)$$

where $M = 2$ when U_{ref} trajectory lies on circumscribed circle in the hexagon,

$$M = \frac{3U_{ref}}{U_{DC}}(n-1) \quad (3)$$

where $M = 2$ when U_{ref} trajectory lies on inscribed circle in the hexagon,

$$M = \frac{\pi U_{ref}}{2U_{DC}}(n-1) \quad (4)$$

where $M = 2$ for the square wave operation (six step mode) of the VSC. In further considerations the (4) definition will be used.

Calculation of the region number of the Space Vector location and duration of switching states is based on two additional factors, so-called *small modulation indexes*. The m_1 and the m_2 are projection of the reference Space Vector U_{ref} on the sector sides, limited by external vectors (see Fig. 3) According to the trigonometric dependence, *small modulation indexes* are calculated as follows:

$$m_1 = M \left(\cos \Theta_m - \frac{\sin \Theta_m}{\sqrt{3}} \right) \quad (5)$$

$$m_2 = 2M \frac{\Theta}{\sqrt{3}} \quad (6)$$

Table 3 Region number and duty cycles calculation

Conditions	Region	Switching times
$m_1 > 1$	1st	$T_1 = (m_1 - 1)T_S, T_2 = m_2 T_S$ $T_4 = (2 - m_1 - m_2)T_S, T_0 = T_3 = T_5 = 0$
$m_1 < 1, m_2 < 1$ $m_1 + m_2 > 1$	2nd	$T_2 = (m_1 + m_2 - 1)T_S, T_4 = (1 - m_2)T_S$ $T_5 = (1 - m_1)T_S, T_0 = T_1 = T_3 = 0$
$m_2 > 1$	3rd	$T_1 = m_1 T_S, T_3 = (m_2 - 1)T_S$ $T_5 = (2 - m_1 - m_2)T_S, T_0 = T_1 = T_4 = 0$
$m_1 < 1, m_2 < 1$ $m_1 + m_2 < 1$	4th	$T_4 = m_1 T_S, T_5 = m_2 T_S$ $T_0 = (1 - m_1 - m_2)T_S, T_1 = T_2 = T_3 = 0$

In each sector calculations carried out to achieve vectors switching times are the same and the difference is only in power switch selection for the gating signal. Thus, the reference vector is normalized to the first sector and after evaluation of vectors switching times a proper transistor switching sequence, for reference position, is created. Table 3 presents calculation of region number and switching times in respect to the m_1 and the m_2 .

Depending on placement of zero and internal vectors, the CSVM and their modifications, like ASVM, can be distinguished.

2.3 Compensation of Flying Capacitor Voltage Balancing Delays

Regardless of used SVM, control algorithm introduces one period delay between switching states calculation and its hardware realization. One period delay has a significant impact on FC voltages balancing through the PWM modulator, which is based on actual measured values. When the FC balancing is delayed, the FC voltage ripples are doubled. Therefore, for compensation of the delay effect, the estimation of the FC voltages instantaneous value was introduced. In the first step, the U_{FCx} instantaneous value at the end of sampling period is calculated as:

$$U_{FCx}(t + 1) = U_{FCx}(t) + \frac{i_{Sx}(t + 0.5)dT_{Sx}}{C_{FC}} \quad (7)$$

where $U_{FCx}(t)$ is measured FC voltage and dT_{Sx} is pulse time duration influencing C_{FCx} voltage. Moreover, the $i_{Sx}(t + 0.5)$ is estimated amplitude of measured stator current $i_{Sx}(t)$ in the middle of sampling period:

$$i_{Sx}(t + 0.5) = i_{Sx}(t) + \frac{i_{Sx}(t) - i_{Sx}(t - 1)}{T_S} \quad (8)$$

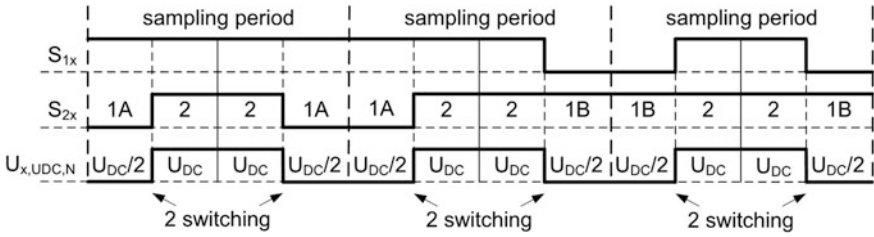


Fig. 4 Modification of switching pattern

where: $i_{Sx}(t - 1)$ measured stator current in previous sampling period. In the next step estimated $U_{FCx}(t + 1)$ instantaneous value of U_{FCx} is used for the FC voltages balancing selection. This eliminates the delay effect.

2.4 Classical Space Vector Modulation

The CSVM modulation for the FCC uses all possible nearest vectors including their redundant states (e.g. in sector 1: V_1 , V_2 and V_4 in 1st, V_2 , V_4 and V_5 in 2nd, V_2 , V_3 and V_5 in 3rd and V_0 , V_4 and V_5 in 4th region) for output voltage generation with symmetrical placement of zero and internal vectors [29–33]. It means that time T_0 dedicated for zero vector is divided by three and each of zero vectors V_0 (**000**, **111** and **222**) are selected for one-third of the T_0 . Also times T_4 and T_5 are divided by two and each of V_4 (e.g. in sector 1: **100** and **211**) and V_5 (e.g. in sector 1: **110** and **221**) vectors are selected for half of proper calculated time. The CSVM provides low phase current distortion due to high number of switching states used for the output voltage generation (all 7 possible vectors in 4th region and 5 vectors in regions 1st, 2nd and 3rd are used). The FC capacitors voltages U_{FCx} ripples are also limited—both redundant states **1A** and **1B** uses the FC for output voltage generation. However, high phase current quality results in switching losses.

When the selected redundant state **1A** or **1B** is changed, the next modulation period can contain additional switching between sampling periods: two in 2nd and four in region 1st and 3rd region. These additional switching can damage the converter—all switches are changing their state what can generate overvoltage. To eliminate this undesired effect and to provide better switching distribution between particular switches a modification of switching pattern was introduced (see Fig. 4). Modified switching patterns of the CSVM always provide 6 switching in 1st and 3rd, 8 switching in 2nd and 12 switching in 4th region.

Figures 5, 6, 7 and 8 presents switching patterns in 1st, 2nd, 3rd and 4th region in sector 1 for different switching states selected **1A** or **1B** for all phases, respectively.

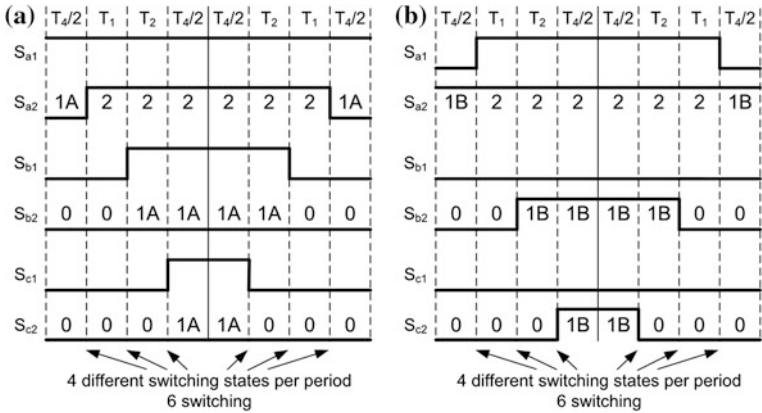


Fig. 5 Duty cycles for the 1st region in sector 1: **a** for 1A state selection in each phase, **b** for 1B state selection in each phase

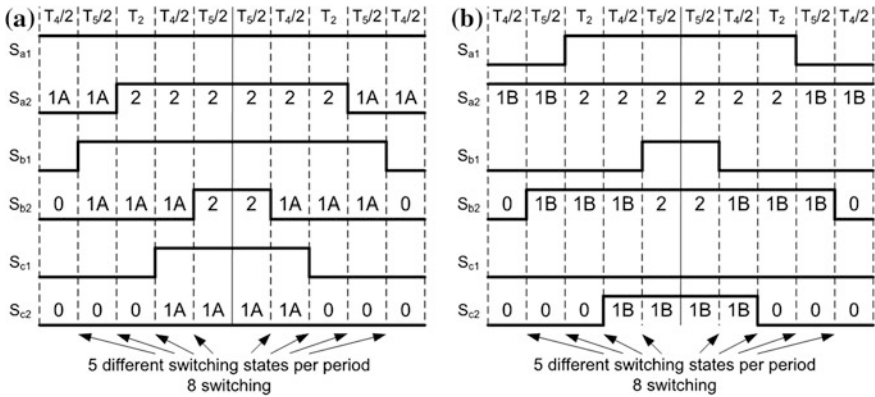


Fig. 6 Duty cycles for the 2nd region in sector 1: **a** for 1A state selection in each phase, **b** for 1B state selection in each phase

2.5 Adaptive Space Vector Modulation with Reduced Number of Switching

To reduce switching losses only three selected vectors in each operation region are applied in modulation period adaptively to the electrical parameters [13, 21, 24, 44, 45]. To achieve this goal two solutions have been used in the ASVM.

The first one—used in all regions—bases on assumption that only one instead of two states of internal vectors V_4 and V_5 is applied in each sampling period. Table 4 shows pairs of internal vectors that should be chosen in each sector.

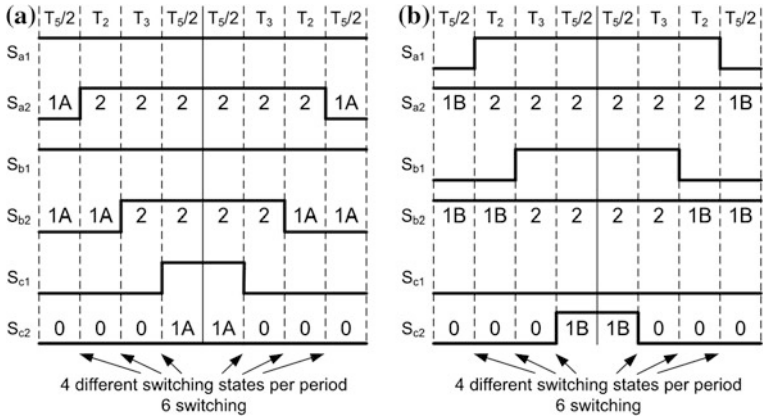


Fig. 7 Duty cycles for the 3rd region in sector 1: **a** for 1A state selection in each phase, **b** for 1B state selection in each phase

Fig. 8 Duty cycles for the 4th region in sector 1: **a** for 1A state selection in each phase, **b** for 1B state selection in each phase

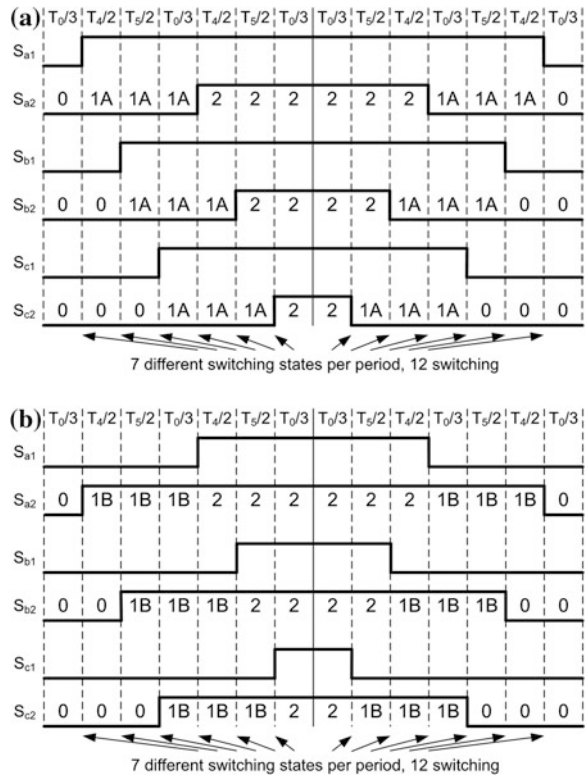


Table 4 Internal vectors \mathbf{V}_4 and \mathbf{V}_5 pairs selection

Sector	Pair P1	Pair P2
1	100 and 110	211 and 221
2	110 and 010	221 and 121
3	010 and 011	121 and 122
4	011 and 001	122 and 112
5	001 and 101	112 and 212
6	101 and 100	212 and 211

Those pairs combined with middle and external vectors provide switching losses reduction. Which pair should be selected depends on their influence on U_{FCx} values at the end of sampling period. The pair which provide smallest maximum difference between reference $U_{DC}/2$ and estimated voltage at the end of sampling period $U_{FCx}(t+1)$ for all FCs will be used. The pair selection algorithm is realized as follows:

1. For each phase the redundant state **1A** or **1B** is chosen.
2. For each pair, according to the (9) and (10) all FCs voltages at the end of sampling period are estimated:

$$U_{FCx,P1}(t+1) = U_{FCx}(t) + \frac{i_{Sx}(t+0.5)dT_{Sx,P1}}{C_{FC}} \quad (9)$$

$$U_{FCx,P2}(t+1) = U_{FCx}(t) + \frac{i_{Sx}(t+0.5)dT_{Sx,P2}}{C_{FC}} \quad (10)$$

where: $dT_{Sx,P1}$ and $dT_{Sx,P2}$ are pulse time duration respectively of pair P1 and P2 influencing C_{FCx} voltage and the $i_{Sx}(t+0.5)$ is estimated amplitude of measured stator current $i_{Sx}(t)$ in the middle of sampling period:

$$i_{Sx}(t+0.5) = i_{Sx}(t) + \frac{i_{Sx}(t) - i_{Sx}(t-1)}{T_s} \quad (11)$$

3. For each pair the modulus of the difference between estimated $U_{FCx}(t+1)$ and reference $U_{DC}/2$ voltage is calculated:

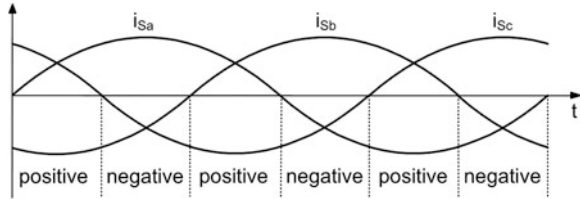
$$\Delta U_{FCx,P1} = \left| \frac{U_{DC}}{2} - U_{FCx,P1}(t+1) \right| \quad (12)$$

$$\Delta U_{FCx,P2} = \left| \frac{U_{DC}}{2} - U_{FCx,P2}(t+1) \right| \quad (13)$$

4. For each pair the maximum of above modulus for each FC is calculated:

$$U_{FC,P1,MAX} = \text{maximum}(\Delta U_{FCa,P1}, \Delta U_{FCb,P1}, \Delta U_{FCc,P1}) \quad (14)$$

Fig. 9 Peak of the current polarity



$$U_{FC,P2,MAX} = \text{maximum}(\Delta U_{FCa,P2}, \Delta U_{FCb,P2}, \Delta U_{FCc,P2}) \quad (15)$$

5. The pair for which maximum of above modulus has smaller value is chosen for better global FC voltages balancing.

In comparison to the CSVM the above solution slightly increases ripples of the FC voltages.

The second solution is used only in 4th region, where zero vectors are applied. It bases on assumption that only two phases are modulated and third phase is clamped in one of switching states: **0**, **1** or **2** during whole modulation period. As result only one zero vector is used in sampling period. This minimize switching losses, however they strongly depend on load power factor [44]. Therefore maximal reduction can be obtained, when peak of the phase current is located in the centre of clamped regions. It is necessary to observe the peak current position and select proper zero vector for this purpose. The peak current observer according to the Fig. 9 is realized by simple relation describing positive or negative peak of current polarity in each phase:

$$\text{peak of current} \begin{cases} \text{positive when } i_{sa}i_{sb}i_{sc} > 0 \\ \text{negative when } i_{sa}i_{sb}i_{sc} < 0 \end{cases} \quad (16)$$

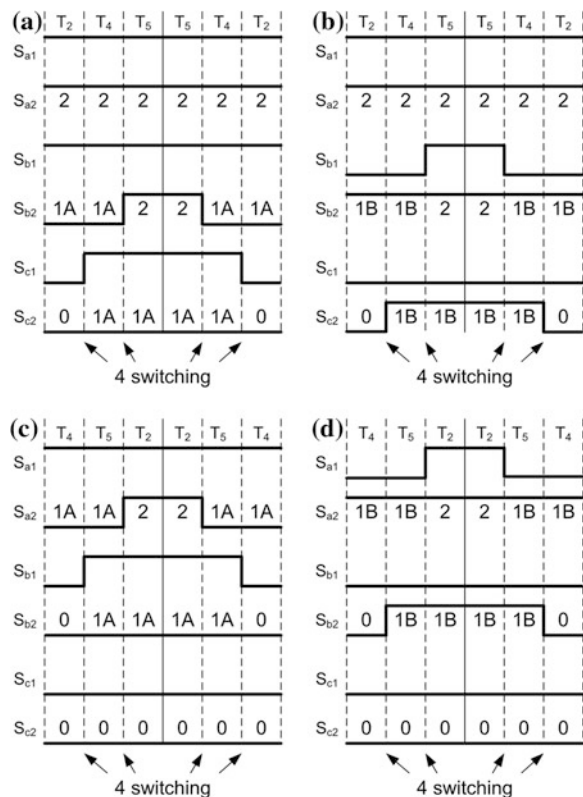
If the peak of current is positive for pair **P1** or **P2**, the zero vector **111** or **222** should be selected. If the peak of current is negative, the zero vector **000** or **111** should be selected, respectively. However, for low speed operation selection of **111** is associated with the FC's voltages change during almost whole sampling period as far as zero vector will be applied mainly. Regardless to the switching losses minimization, quality of the output voltage and as a consequence phase current is priority. Therefore, if the state **111** should be selected according to the peak current observer, the same calculation of zero vectors influence U_{FCx} values at the end of sampling period should be carried out as for the internal vectors pairs. The **111** zero vector with proper **P1** or **P2** pair can be chosen only if give smaller error between estimated and commanded FC voltage. In practice for low speed operation **111** is chosen only for high FC voltages unbalance. Final vectors selection in respect to peak of current and pair selection in sector 1 is shown in Table 5.

Figure 10 presents example of switching patterns in 2nd region for different switching states selected **1A** or **1B** as well as different pair selection **P1** or **P2** for all phases, respectively. Note that—the same as for the CSVM—next modulation

Table 5 Final vectors selection in sector 1

Selected pair	Peak of current	Region			
		1st	2nd	3rd	4th
<i>P1</i>	$i_{Sa}i_{Sb}i_{Sc} > 0$	100	100	110	100
		200	110	210	110
		210	210	220	111
	$i_{Sa}i_{Sb}i_{Sc} < 0$				000
					100
					110
<i>P2</i>	$i_{Sa}i_{Sb}i_{Sc} > 0$	200	210	210	211
		210	211	220	221
		221	221	221	222
	$i_{Sa}i_{Sb}i_{Sc} < 0$				111
					211
					221

Fig. 10 Duty cycles for the 2nd region in sector 1: **a, c** for **1A** state selection in each phase, **b, d** for **1B** state selection in each phase, **a, b** for *P1* pair selection, **c, d** for *P2* pair selection



period can contain additional switching between sampling periods, when selected redundant state **1A** or **1B** is changed. Those additional switching can be divided into two groups:

Table 6 Theroretical number of switching in modulation period

Region number	CSVM	ASVM		Switching reduction		
		Typical	Maximum	Maximum (%)	Average (%)	Minimum (%)
1st	6	4	6	33.33	16.66	0.00
2nd	8	4	6	50.00	37.50	25.00
3rd	6	4	6	33.33	16.66	0.00
4th	12	4	6	66.66	58.33	50.00

- related with different switching states selection **1A** or **1B**, that can damage the converter—all switches are changing their state what can generate overvoltage,
- related with different pair selection $P1$ or $P2$, that mean normal operation of the converter—only two of four switches are changing their state.

To eliminate additional switching that can damage the converter and to provide better switching distribution between particular switches a modification of switching pattern introduced for the CSVM is used (see Fig. 4).

The ASVM provide number of switching reduction to 4 in all regions, however with additional switching as result different pair selection $P1$ or $P2$ number of switching can be increased to 7.

2.6 Space Vector Modulation Comparative Study

Table 6 shows theoretical comparison between the CSVM and the ASVM in respect to number or switching in modulation period. As it can be observed, highest reduction can be obtained in 4th region, which corresponds to low values of modulation index $M < 0.866$. For higher values of modulation index $M > 1$, reduction depends on the value of M due to different switching number reduction in region 2nd and regions 1st and 3rd. Thus, according to reference Space Vector U_{ref} trajectory, in upper regions greater value of the M provides smaller total reduction of switching number. For modulation index $0.866 < M < 1$, reference Space Vector U_{ref} crosses between 2nd and 4th region. Thus, in this operation region—the same as for $M > 1$ —total reduction of switching number depends on M value—greater value of the M provides smaller total reduction. However, it can be assumed, that the ASD in traction application operates mainly in the low and high speed region. Thus, the further comparative study present operation of FCC for two different values of modulation index: $M < 0.866$ and $M > 1$.

Tables 7 and 8 shows THD factor of phase a stator current $THD(i_{Sa})$ and switching number reduction in simulation and experiment, respectively. In simulation, the calculation of switching number reduction is based on real, counted number of switching. In experiment, the calculation of switching number reduction is based on assumption that the changes of stator current $THD(i_{Sa})$ depends only on number of switching, and therefore shows how much the $THD(i_{Sa})$ is increased.

Table 7 Switching number reduction and stator current i_{Sa} THD factor $THD(i_{Sa})$ in CSVM and ASVM—simulation results

Modulation index	CSVM		ASVM		Switching reduction (%)
	$THD(i_{Sa})$ (%)	Switching	$THD(i_{Sa})$ (%)	Switching	
$M = 0.51$	0.96	3,000	2.08	1238	58.73
$M = 1.55$	1.28	507	1.93	336	33.73

Table 8 Switching number reduction and stator current i_{Sa} THD factor $THD(i_{Sa})$ in CSVM and ASVM—experimental results

Modulation index	CSVM $THD(i_{Sa})$ (%)	ASVM $THD(i_{Sa})$ (%)	Switching reduction (%)
$M = 0.51$	0.85	1.69	49.70
$M = 1.55$	1.45	2.15	32.56

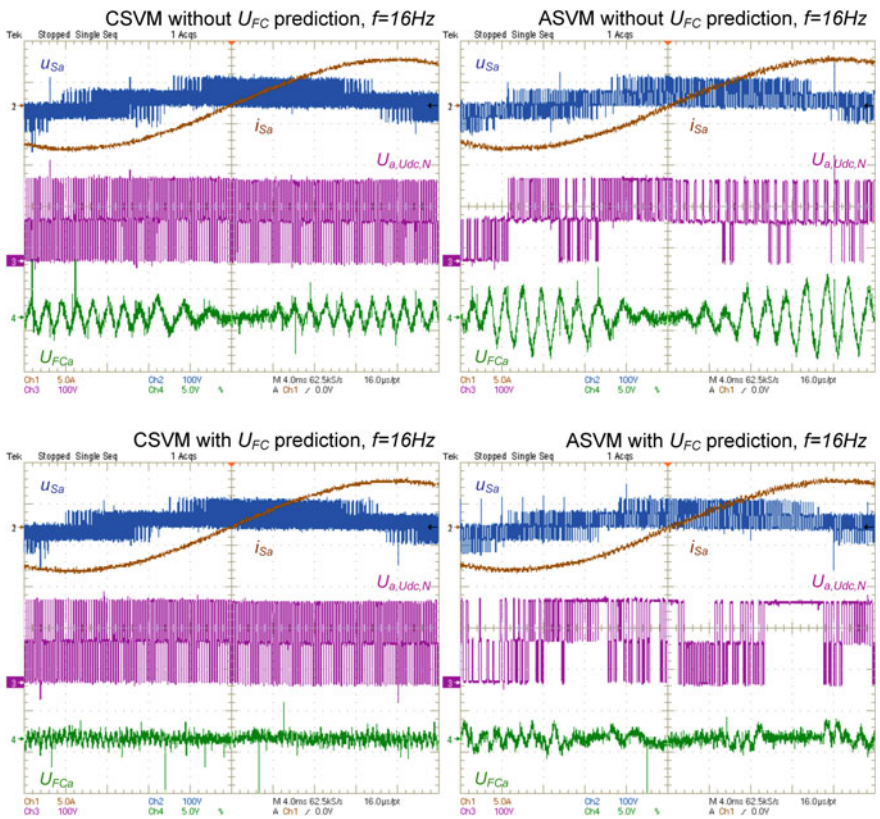


Fig. 11 Operation of the FCC (phase a) without and with the FC voltage prediction for the CSVM and the ASVM, output frequency $f = 16$ Hz (modulation index $M = 0.51$, 4th region): stator voltage u_{Sa} and current i_{Sa} , pole voltage $U_{a,Udc,N}$ and AC component of FC voltage $U_{FC,a}$

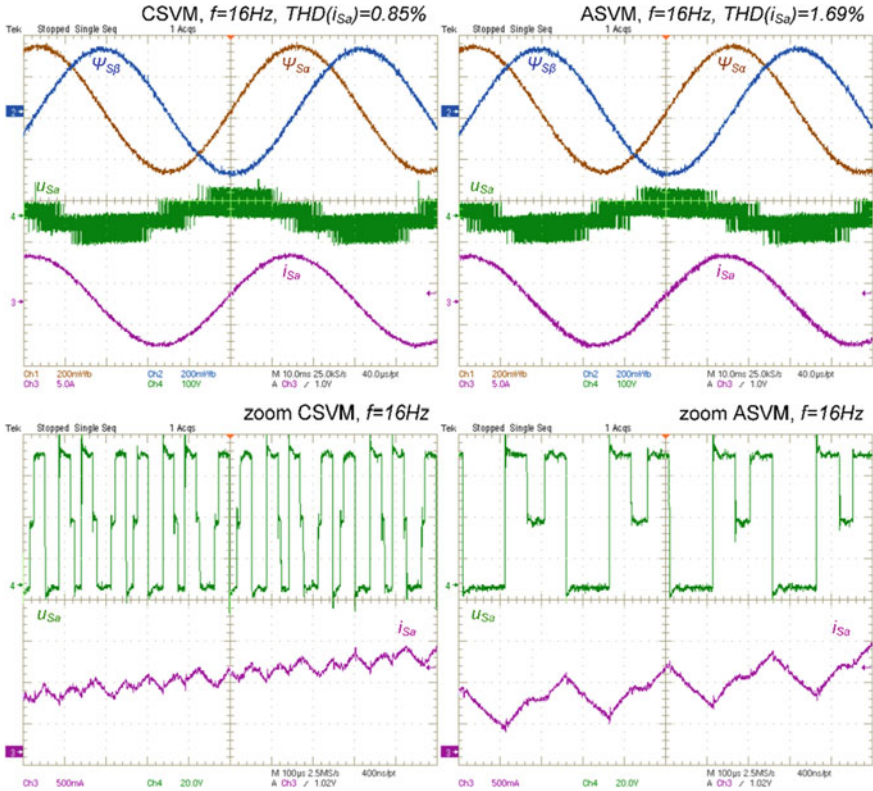


Fig. 12 Operation of the FCC (phase a) for the CSVM and the ASVM, output frequency $f = 16\text{ Hz}$ (modulation index $M = 0.51$, 4th region): stator fluxes Ψ_{Sa} and $\Psi_{S\beta}$, stator voltage u_{Sa} and current i_{Sa} , zoom of stator voltage u_{Sa} and current i_{Sa}

Average theoretical (58.33 %, Table 6) and simulation (58.33 %, Table 7) values of switching number reduction are the same for $M = 0.51$. The experimental value of switching number reduction (49.70 %, Table 8) is lower than the average theoretical however is equal minimum value of reduction in 4th region—50 %—what corresponds to the maximum number of 6 switching in ASVM. For $M = 1.51$, average theoretical value of switching number reduction depends on the reference Space Vector U_{ref} trajectory in 1st, 2nd and 3rd region. Therefore, the similar results for simulation (33.73 %, Table 7) and experimental (32.56 %, Table 8) are not equal to average theoretical value. However, for typical switching number values the maximum theoretical switching number reduction is 33.33 % in 1st and 3rd and 50.00 % in 2nd region, respectively. Thus, the simulation and experimental values of switching number reduction stays in possible range and are similar to the typical theoretical value (for $M = 1.51$ reference Space Vector U_{ref} trajectory largely lies in 1st and 3rd region).

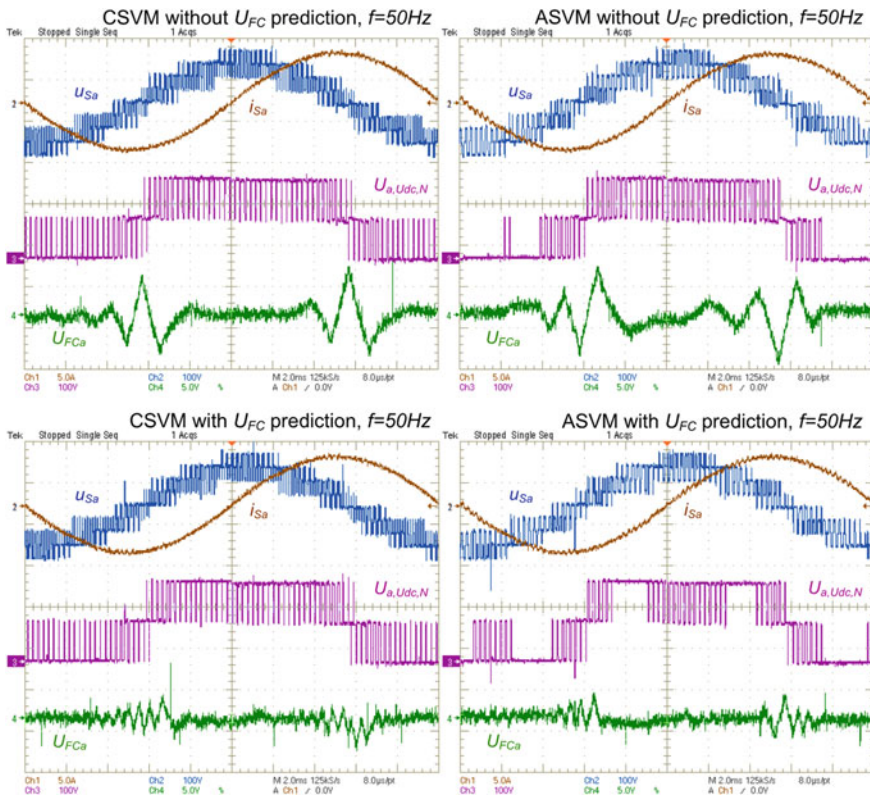


Fig. 13 Operation of the FCC (phase a) without and with the FC voltage prediction for the CSVM and the ASVM, output frequency $f = 50$ Hz (modulation index $M = 1.55$, 1st, 2nd and 3rd region): stator voltage u_{Sa} and current i_{Sa} , pole voltage $U_{a,UdcN}$ and AC component of FC voltage U_{FCa}

Figures 11 and 12 shows steady state operation of the FCC with CSVM and ASVM for the output frequency $f = 16$ Hz (modulation index $M = 0.51$, operation in 4th region).

Figure 11 presents the FCC operation without and with the FC voltage prediction U_{FCx} . As it can be observed on the AC component of FC voltage U_{FCa} , the FC voltage prediction provides significant ripples reduction. Also, Fig. 11 shows high reduction of the number of switching at the ASVM, which is visible on the pole voltage $U_{a,UdcN}$. However, this can be seen better on the zoom of stator voltage u_{Sa} and stator current i_{Sa} presented in Fig. 12. Figure 12 shows also that the modified SVM does not affect the estimated stator fluxes $\Psi_{S\alpha}$ and $\Psi_{S\beta}$.

Figures 13 and 14 shows—similarly to the previous one—steady state operation of the FCC with the CSVM and the ASVM for the output frequency $f = 50$ Hz (modulation index $M = 1.55$, operation in 1st, 2nd and 3rd region). In such conditions the reduction of the number of switching, which is visible on the

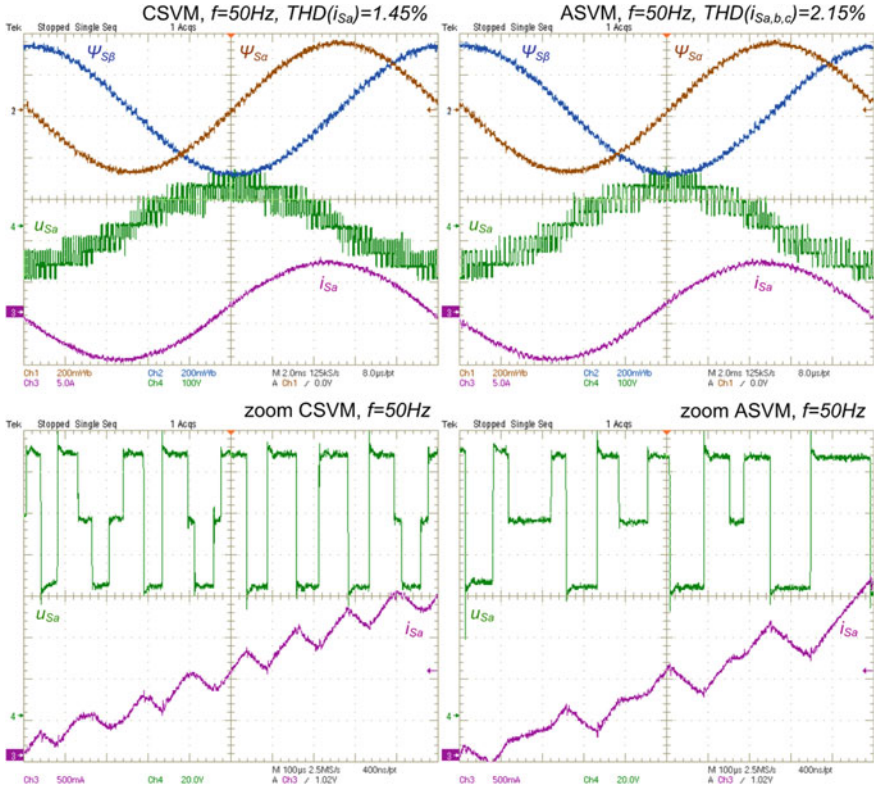


Fig. 14 Operation of the FCC (phase a) for the CSVM and the ASVM, output frequency $f = 50\text{ Hz}$ (modulation index $M = 1.55$, 1st, 2nd and 3rd region): stator fluxes $\Psi_{S\alpha}$ and $\Psi_{S\beta}$, stator voltage $u_{S\alpha}$ and current $i_{S\alpha}$, zoom of stator voltage $u_{S\alpha}$ and current $i_{S\alpha}$

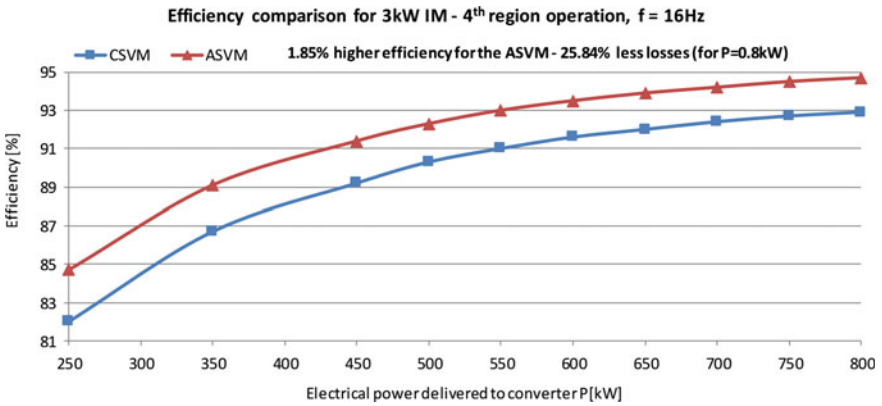


Fig. 15 The FCC efficiency comparison for the CSVM and the ASVM for 3 kW IM, output frequency $f = 16\text{ Hz}$ (modulation index $M = 0.51$, 4th region)

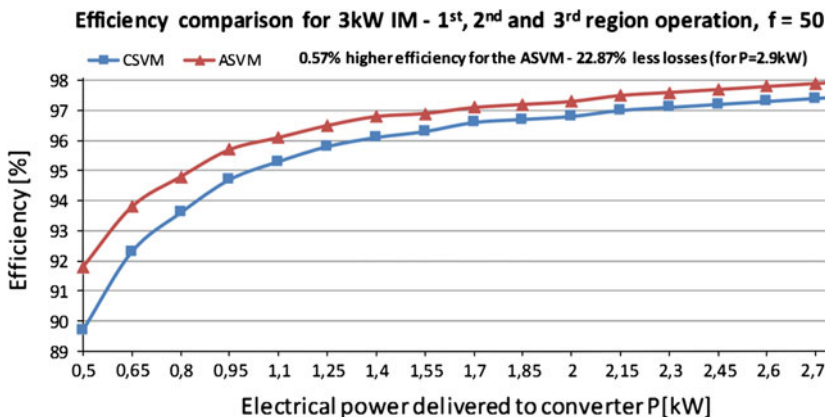


Fig. 16 The FCC efficiency comparison for the CSVM and the ASVM for 3 kW IM, output frequency $f = 50$ Hz (modulation index $M = 1.55$, 1st, 2nd and 3rd region)

pole voltage $U_{a,UdcN}$ is lower. However, similarly to previous case, the FC voltage prediction provides significant ripples reduction as well as the ASVM does not affect the estimated stator fluxes $\Psi_{S\alpha}$ and $\Psi_{S\beta}$.

Figure 15 presents the FCC efficiency comparison for the CSVM and the ASVM modulation with the 3 kW IM drive. For the FCC operation in 4th region, total efficiency of the converter (including not only switching losses) with the ASVM is 1.85 % higher than for the CSVM. It means that the FCC losses for the nominal load are reduced approximately 26 %.

Figure 16 presents the FCC efficiency comparison for the CSVM and the ASVM modulation with the 3 kW IM drive. For the operation in regions 1st, 2nd and 3rd profit of the ASVM is lower. The total efficiency of the converter with the ASVM is 0.57 % higher than for the CSVM, with the FCC losses lower for the nominal load approximately 23 %.

3 Compensation of Dead-Time Effect and Semiconductor Devices Voltage Drop

3.1 Introduction

The IGBT devices has finite switching time and they are turning off much more slower than turning on, therefore there is needed a delay in control signals between

complementary switching devices (so-called dead-time t_{DT}) in order to prevent a short-circuit across the converter voltage sources. Depending on the sign of stator current i_{Sx} , dead-time can increase or decrease the amplitude of the output voltage amplitude applied to the converter in comparison to the reference Space Vector U_{ref} , and in result stator current i_{Sx} is distorted.

The voltage drop on semiconductor devices is second nonlinearity that has significant impact on the amplitude of output voltage applied to the converter. Similarly to the dead-time effect, it can increase or decrease the amplitude of reference output voltage applied to the converter, depending on the sign of stator current i_{Sx} and in result distorts the stator current i_{Sx} . However, contrary to the dead-time depends not only on the ratio of the dead-time t_{DT} of the sampling time T_S , but also on the amplitude of the stator current i_{Sx} .

It is obvious, that frequency and amplitude of reference Space Vector U_{ref} significantly depend on reference speed of the drive. Thus, for the low speed operation the amplitude of reference Space Vector U_{ref} is also low. Therefore, in low speed operation the dead-time as well as the voltage drop on semiconductor devices has significant impact on stator current i_{Sx} on the output voltage amplitude applied to the converter due to the distortion introduced by the them is relative large to the amplitude of reference Space Vector U_{ref} . For high speed operation the distortion introduced by the them is relative small and their impact on stator current i_{Sx} is negligible. To avoid that, the dead-time effect as well as the voltage drop on semiconductor devices compensation algorithms are used. The semiconductor devices voltage drop and dead-time impact on phase current distortion have been well investigated for the two-level as well multilevel converters. These methods can be divided into two groups:

- modification of amplitude (length) of reference Space Vector U_{ref} [33, 46, 47, 50],
- modification of the duty cycles at the output of the PWM modulator [33, 46, 48, 49].

3.2 Compensation of Dead-Time Effect

Figure 17 presents the dead-time t_{DT} impact on the pole voltage $U_{x,UdcN}$ applied to the converter, depending on the stator current i_{Sx} polarity. The dead-time effect does not depend on the amplitude of the stator current i_{Sx} , only on the sampling time T_S and the amplitude of the DC-link voltage U_{DC} . However, it should be noticed, that for multilevel converter the dead-time effect on the output voltage amplitude applied to the converter is increased in comparison to the two-level converter due to increased number of switching. However, the impact of dead-time in multilevel converter depends on type of applied modulation technique. In case of three-level VSC with the CSVM in comparison to the two-level VSC is doubled. For the ASVM, where the number of switching is reduced the dead-time effect is similar to the two-level VSC.

Thus, in first step the stator voltage error δu_{Sx} should be calculated for single switching device of the n -level converter [50]:

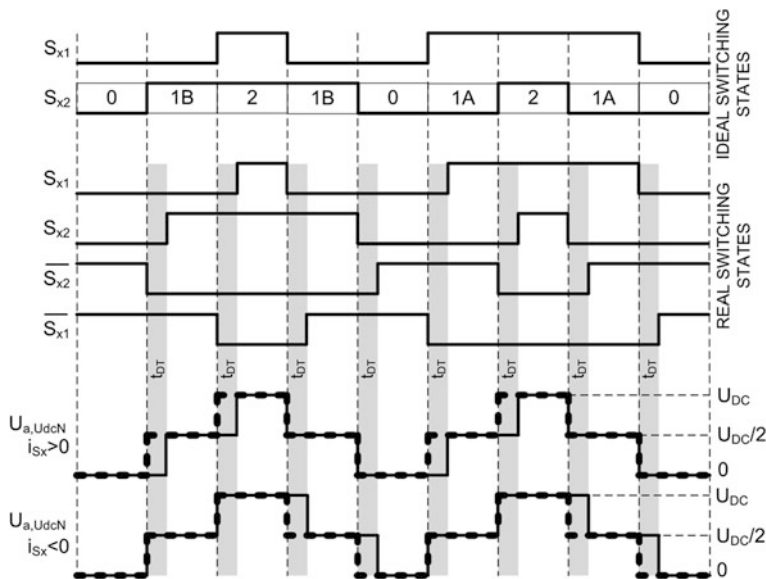


Fig. 17 Dead-time effect impact on the pole voltage $U_{a,UdcN}$ applied to the converter depending on the stator current i_{Sx} polarity—ideal (solid line) and real (dotted line) output pole voltage $U_{a,UdcN}$

$$\delta u_{Sx} = \frac{U_{DC} t_{DT}}{(n - 1) T_S} \text{sgn}(i_{Sx}) \tag{17}$$

where sign of stator current i_{Sx} is defined as:

$$\text{sgn}(i_{Sx}) \begin{cases} 1 & \text{for } i_{Sx} > 0 \\ -1 & \text{for } i_{Sx} < 0 \end{cases} \tag{18}$$

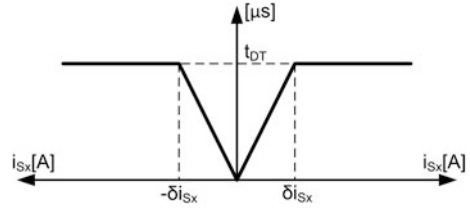
In next step, depending on the type of applied modulation, the total stator voltage error $\sum \delta u_{Sx}$ should be calculated for each leg:

$$\sum \delta u_{Sx} = k \delta u_{Sx} \tag{19}$$

where k factor denotes number of switching per phase, e.g. typically for CSVM $k = 2$ and for ASVM $k = 1$. From (17) it can be noticed that changes of the sampling time T_S has significant influence on the dead-time effect, as far as the DC-link voltage U_{DC} and dead-time t_{DT} is assumed to be constant. Dead-time effect—understood as ratio of the phase voltage error to the reference output voltage—increases linearly with increasing of the switching frequency.

One of important aspects related to the dead-time effect compensation is proper calculation of stator current i_{Sx} zero crossing. If stator current i_{Sx} polarity is not calculated properly, inadequate compensation can worsen the shape of i_{Sx} . Quality of the stator current i_{Sx} polarity calculation depends on the measurement noise level as well as on the control delays. To improve $\text{sgn}(i_{Sx})$ calculation two solutions can be

Fig. 18 Dead-time t_{DT} value limiting in assumed range δi_{Sx} of stator current i_{Sx}



used. First uses simple current estimation based on current difference which allow to eliminate one sampling control delay. Second solution uses hysteresis regulator on the estimated current to obtain $sgn(i_{Sx})$ with hysteresis width equal to measurement noise level. Taking into account that both solutions does not provide exact phase current zero crossing, total stator voltage error $\Sigma \delta u_{Sx}$ or dead-time t_{DT} should be linearly limited in assumed range of phase current i_{Sx} (Fig. 18). In industrial applications the value of δi_{Sx} is set experimentally, as far as it depends on the measurement noise level as well as on the control delays.

As it was aforementioned, the compensation of the dead-time can be realized by modification of amplitude (length) of reference Space Vector U_{ref} or by modification of the duty cycles at the output of the PWM modulator. For the dead-time effect it is recommended to use second solution. Such approach allows to decrease number of calculations due to omitting the precalculation, which switches will be modulated in sampling period. Only for each switch the switching time is increased or decreased according to Fig. 18.

3.3 Compensation of Semiconductor Devices Voltage Drop

Figure 19 presents the stator current i_{Sx} flow (bold line) in single leg of the FCC for different switching states. As it can be observed, semiconductor devices voltage drop does not only depend on the selected switching state, but also on the phase current polarity. Table 9 shows the desired $U_{x,UdcN,ref}$ and the real pole voltage $U_{x,UdcN}$ produced for all possible switching states and different direction of the current flow. The $u_{fD,x}$ denotes the voltage drop on the freewheeling diodes and $u_{CEon,x}$ denotes the voltage drop on the conducting IGBT during ON state.

Contrary to the dead-time effect, the voltage drop on semiconductor devices depends not only on the changes of the sampling time but also on the amplitude of the phase currents. Figure 20 presents example of voltage drop characteristics of the IRG4BC20UDPBF IGBT transistor, according to the International Rectifier datasheet [51]. As it can be observed on the $u_{fD,x}$ and the $u_{CEon,x}$ characteristics are strongly nonlinear functions of stator current i_{Sx} . Thus, contrary to the dead-time effect, the voltage drop on semiconductor devices depends not only on the changes of the sampling time but also on the amplitude of the phase currents. Therefore, two-straight-line approximation for each characteristic should be used (see Fig. 21). The first approximation is assumed as a linear resistance for relatively

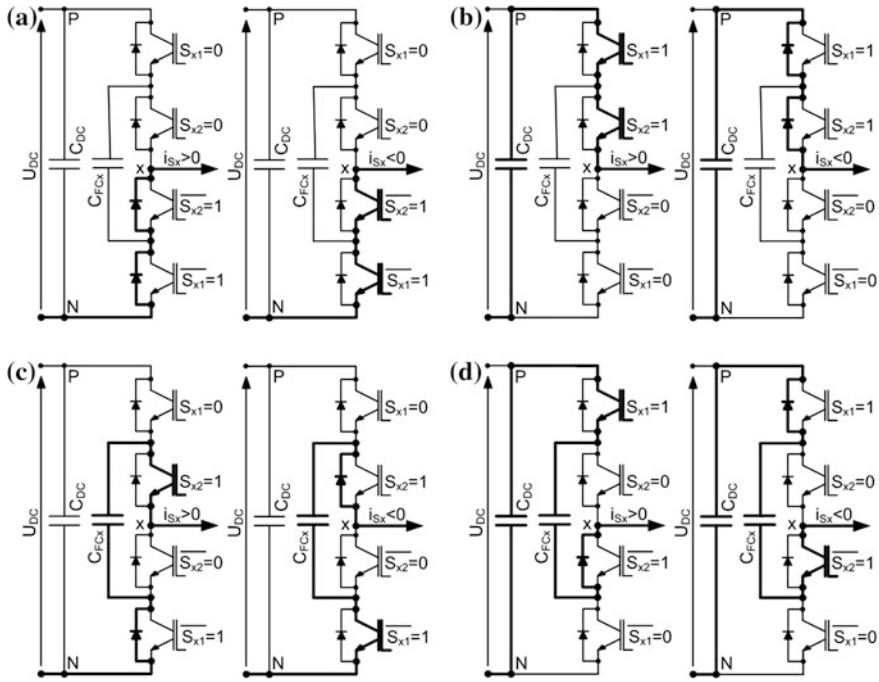


Fig. 19 Stator current i_{Sx} flow (bold line) in single leg of the FCC for different switching states: **a** 0 switching state, **b** 2 switching state, **c** 1A switching state, **d** 1B switching state

Table 9 The desired $U_{x,UdcN,ref}$ and real pole voltage $U_{x,UdcN}$ for different conditions

Switching states	Pole voltage		
	$U_{x,UdcN,ref}$	$U_{x,UdcN}$ for $i_{Sx} > 0$	$U_{x,UdcN}$ for $i_{Sx} < 0$
0	0	$U_{x,UdcN,ref} - 2u_{fD,x}$	$U_{x,UdcN,ref} + 2u_{CEon,x}$
1A	U_{FCx}	$U_{x,UdcN,ref} - u_{fD,x} - u_{CEon,x}$	$U_{x,UdcN,ref} + u_{fD,x} + u_{CEon,x}$
1B	$U_{DC} - U_{FCx}$	$U_{x,UdcN,ref} - u_{fD,x} - u_{CEon,x}$	$U_{x,UdcN,ref} + u_{fD,x} + u_{CEon,x}$
2	U_{DC}	$U_{x,UdcN,ref} - 2u_{CEon,x}$	$U_{x,UdcN,ref} + 2u_{fD,x}$

low stator currents. The second approximation is assumed as a constant voltage drop with an incremental resistance for higher stator currents.

Similarly to presented dead-time t_{DT} value limitation in assumed range δi_{Sx} of stator current (see Fig. 18), the dual slope of approximated characteristics reduces the amount of voltage drop to be compensated around the current zero crossing. Thus, voltage drop on switching devices compensation is prevented against overcompensation.

Figure 22 shows example of sector 1 with the ideal and real vectors location. For each vector and six different current directions, six different voltage drop errors can be specified (white dots). Note that single current polarity shifts all

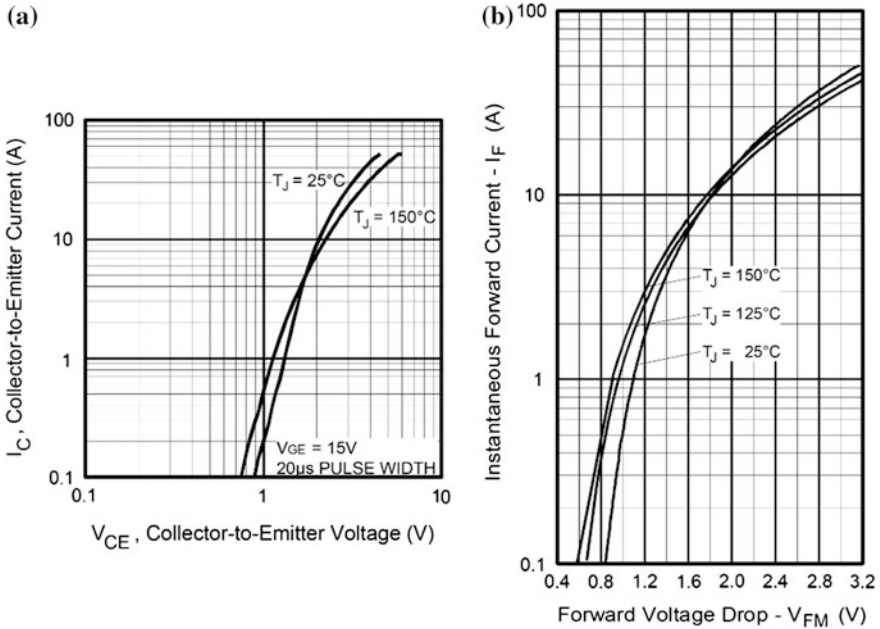


Fig. 20 Voltage drop characteristics of the IRG4BC20UDPBF IGBT [51]: **a** on the IGBT during ON state, **b** on the freewheeling diode

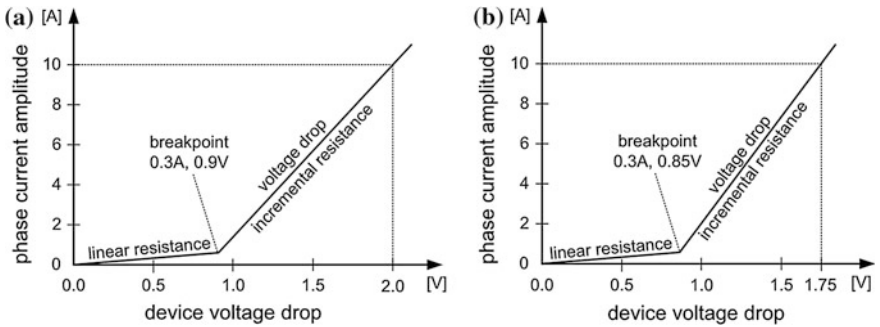
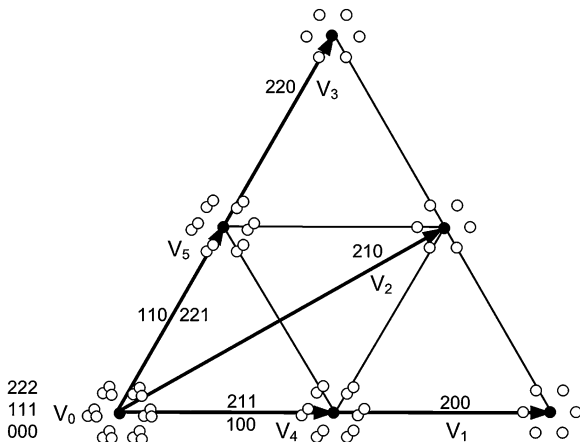


Fig. 21 Linearized voltage drop characteristics of the IRG4BC20UDPBF IGBT: **a** on the IGBT during ON state, **b** on the freewheeling diode

vectors location in the same direction, regardless of the voltage drop error amplitude [51]. It means also that redundant vectors \mathbf{V}_4 and \mathbf{V}_5 can generate two different semiconductor devices voltage drop values as well as zero vector \mathbf{V}_0 can generate three different values of voltage drop (in the one of six positions of voltage drop two or three white dots, respectively). For example, for each of \mathbf{V}_5 redundant states $\mathbf{110}$ and $\mathbf{221}$ the amplitude of the ideal pole voltage $U_{x,UdcN,ref}$ is the same, but for each of them currents flow through different semiconductor

Fig. 22 Ideal and real (taking into account semiconductor devices voltage drop) vectors location in sector 1—black and white dots, respectively



devices and as consequence, for each summary voltage drop is different. Therefore, to compensate voltage drop on semiconductor devices, the calculated value of voltage drop should be added to the reference stator voltages.

According to the Clarke transformation, three-phase system without neutral wire can be transformed from natural abc to stationary $\alpha\beta$ coordinates. As far as the voltage drop on semiconductor devices introduced by all legs of the VSC is nonlinear, it does not fulfil following condition:

$$u_{VDa} + u_{VDb} + u_{VDC} = 0 \tag{20}$$

where u_{VDx} denotes summary voltage drop in leg x . Therefore, to obtain reference converter output voltages in stationary $\alpha\beta$ coordinates: $u_{\alpha,ref}$ and $u_{\beta,ref}$, respectively, with voltage drop compensation, the full Clarke transformation has to be used:

$$\begin{bmatrix} u_{\alpha,ref} \\ u_{\beta,ref} \end{bmatrix} = \begin{bmatrix} 1 & -\frac{1}{2} & -\frac{1}{2} \\ 0 & \frac{\sqrt{3}}{2} & -\frac{\sqrt{3}}{2} \end{bmatrix} \begin{bmatrix} u_{a,ref} + u_{VDa} \\ u_{b,ref} + u_{VDb} \\ u_{c,ref} + u_{VDC} \end{bmatrix} \tag{21}$$

Thanks to that, vector plane will be shifted to the position, where the real vectors location coincides with ideal position [51].

3.4 Results of Low Speed Operation of Adjustable Speed Drive

Figures 23 and 24 presents compensation of dead-time effect and voltage drop on semiconductor devices for the CSVM and the ASVM modulation in leg a for a low speed operation.

Reference output frequency is 3 Hz. Without compensations, for both CSVM and ASVM stator current i_{sa} is strongly distorted (see Figs. 23a and 24a).

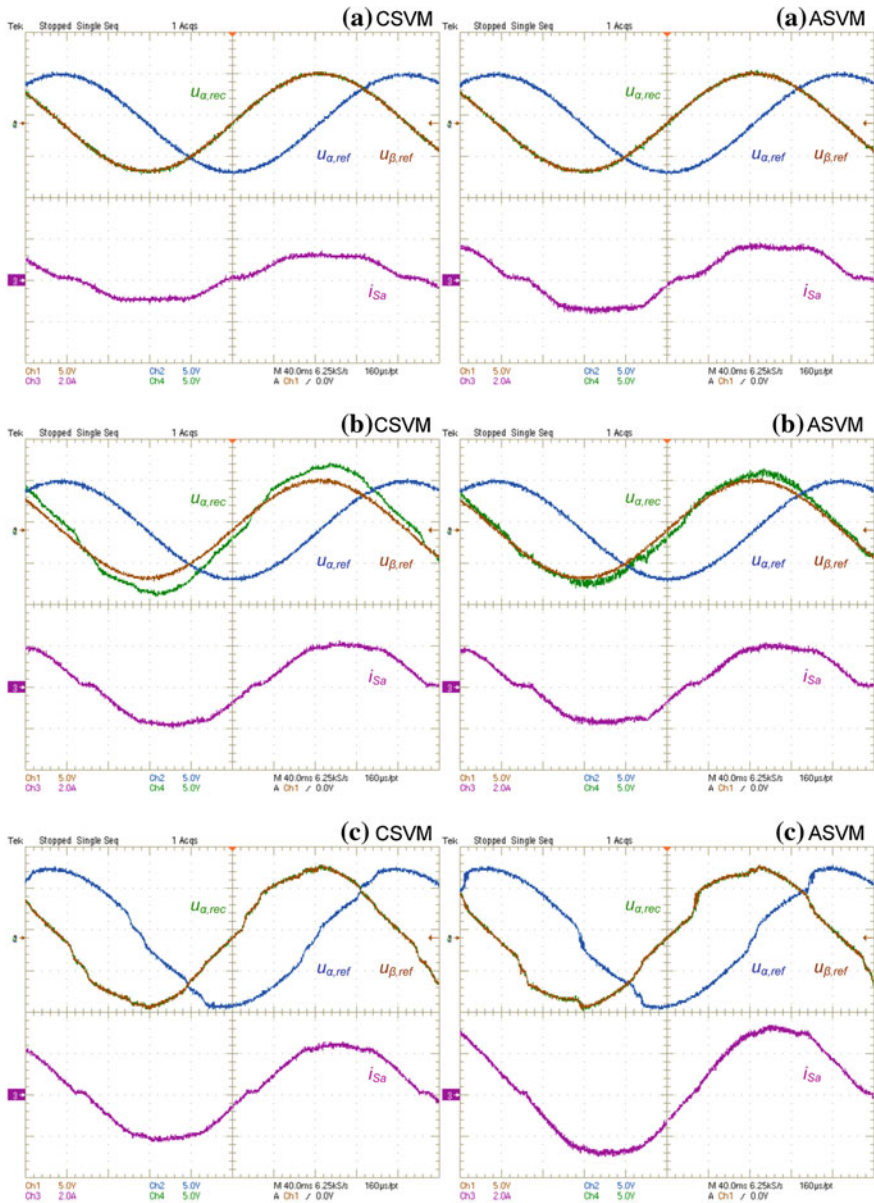


Fig. 23 Dead-time effect compensation for the CSVM and the ASVM, output frequency $f = 3$ Hz: **a** no compensation, **b** dead-time effect compensation, **c** voltage drop effect compensation. From the *top*: converter reference voltage $u_{\alpha,ref}$ and $u_{\beta,ref}$ in $\alpha\beta$ coordinates, $u_{\alpha,rec}$ which is reconstructed from switching states $u_{\alpha,ref}$ and phase a stator current i_{Sa}

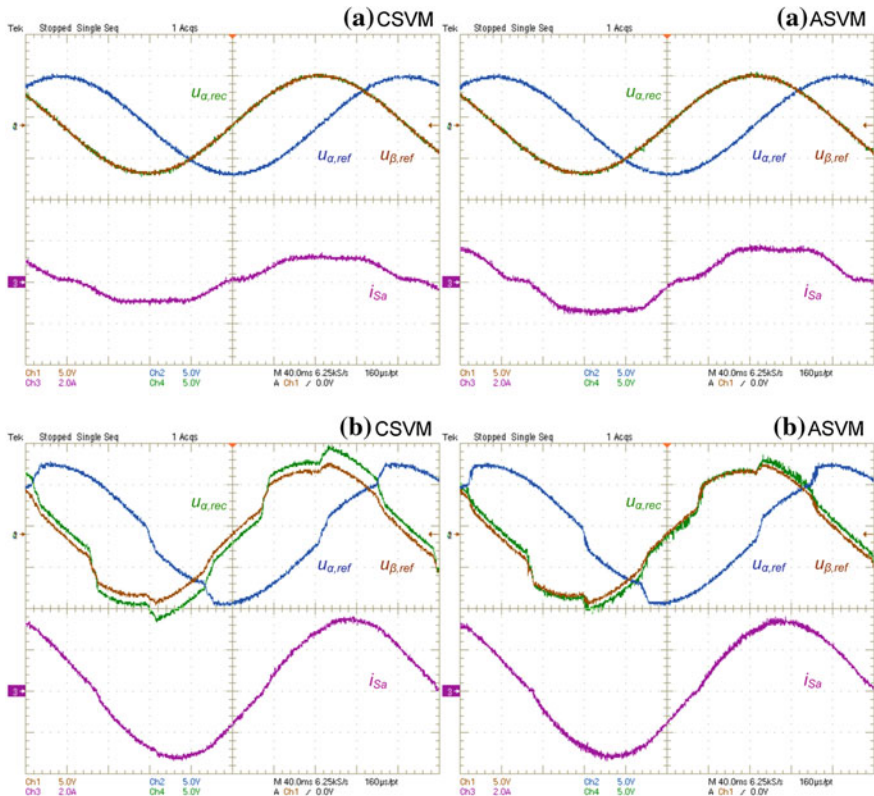


Fig. 24 Dead-time effect compensation for the CSVM and the ASVM, output frequency $f = 3$ Hz: **a** no compensation, **b** dead time and voltage drop effect compensation. From the *top*: converter reference voltage $u_{\alpha,ref}$ and $u_{\beta,ref}$ in $\alpha\beta$ coordinates, $u_{\alpha,rec}$ which is reconstructed from switching states $u_{\alpha,ref}$ and phase *a* stator current i_{Sa}

However, for the CSVM amplitude of i_{Sa} is lower. It is caused by increased dead-time effect for the CSVM, due to higher number of switching.

The dead-time compensation is realized on the output of the modulator—thus, converter reference voltages in $\alpha\beta$ coordinates $u_{\alpha,ref}$ and $u_{\beta,ref}$ are not modified. The influence of the Dead Time effect compensation can be observed on Fig. 23b, where the $u_{\alpha,rec}$ voltage is shown. The $u_{\alpha,rec}$ is the output converter voltage reconstructed from the switching states of $u_{\alpha,ref}$, and contains the dead-time effect compensation signal. As it can be observed on Fig. 23b, for the CSVM, the amplitude of the $u_{\alpha,rec}$ is higher than for the ASVM modulation. It means that the higher number of switching must be compensated.

From other hand, the voltage drop on semiconductor devices compensation signal is added directly to the $u_{\alpha,ref}$ and $u_{\beta,ref}$ reference voltages (see Fig. 23c), where for both modulation techniques voltage drop effect is similar. It manifests itself in the same amplitude of $u_{\alpha,ref}$ and $u_{\beta,ref}$ reference voltages, regardless of the type of SVM.

Figures 23c and 24b shows operation of the both compensation algorithms applied to the converter.

4 Space Vector Overmodulation in Flying Capacitor Converter

The SVM generates sinusoidal output voltages, when the trajectory of the reference Space Vector U_{ref} traces a circle inscribed into the hexagon. According to the modulation index definition (4) for the three-level VSC:

$$M = \frac{\pi U_{ref}}{U_{DC}} \quad (22)$$

where $M = 2$ for the square wave operation (six step mode) of the VSC. Thus, the trajectory of the reference Space Vector U_{ref} traces a circle inscribed into the hexagon when $M = \sqrt{3}$, which corresponds to the height of an equilateral triangle with the length of the side equal 2. As far as the external vectors generates output voltage amplitude equal $2/3 U_{DC}$ for the sinusoidal output voltage generation the maximum length of the Space Vector is:

$$U_{ref,max} = \frac{\sqrt{3} U_{ref}}{3} \quad (23)$$

Therefore, for linear operation the modulation index value is limited to:

$$M = \frac{\pi U_{ref,max}}{U_{DC}} = \frac{\sqrt{3}\pi}{3} \cong 1.814 \quad (24)$$

Above $M = 1.814$ the inverter output voltage is distorted, and the magnitude of output voltage becomes smaller than the reference output voltage. For demanding ASD high speed operation over the linear range ($M > 1.814$) of the converter is very often required. However, when output voltage does not correspond to the reference value, drive cannot work properly due to decreased stator flux amplitude. The SVM high speed operation over the linear range of the converter is possible thanks to the Space Vector Overmodulation algorithm. For the Space Vector Overmodulation output voltage and phase current is distorted, however the amplitude of first harmonic of the output voltage is equal to the reference output voltage. Thus, the Space Vector Overmodulation make possible to maximize stator flux. However, it should be noticed that for the six step operation, Flying Capacitor voltages cannot be controlled because switching states **1A** and **1B** are not used.

The Space Vector Overmodulation bases on the proper modification of the Space Vector length and angle, when the trajectory of the reference Space Vector lies partly outside a circle inscribed into the hexagon. Based upon the degree of

output voltage distortion, for the Space Vector Overmodulation two modes can be defined [13, 21, 24, 53–55]:

- Space Vector Overmodulation mode I—where the output voltage is distorted continuous reference output voltage,
- Space Vector Overmodulation mode II—where the output voltage is distorted discontinuous reference output voltage.

4.1 Space Vector Overmodulation Mode I

In the Space Vector Overmodulation mode I, the SVM algorithm changes the magnitude of the reference Space Vector U_{ref} , while the angle of Space Vector Θ_m is not changed. Figure 25 presents the trajectory of the reference and compensated (boosted) Space Vector U_{ref}^* in stationary $\alpha\beta$ coordinates.

For a given U_{ref} the output phase voltage waveform can be divided into four segments, depending on the Θ_r angle [54] The Θ_r angle denotes a reference angle of the insertion of the compensated Space Vector U_{ref}^* trajectory. The output voltage equations in each segment are expressed as:

$$f_1 = \frac{U_{DC}}{\sqrt{3}} \tan \Theta_m \text{ for } 0 \lesssim \Theta_m < \left(\frac{\pi}{6} - \Theta_r\right) \quad (25)$$

$$f_2 = \frac{U_{DC}}{\sqrt{3} \cos\left(\frac{\pi}{6} - \Theta_r\right)} \sin \Theta_m \text{ for } \left(\frac{\pi}{6} - \Theta_r\right) \lesssim \Theta_m < \left(\frac{\pi}{6} + \Theta_r\right) \quad (26)$$

$$f_3 = \frac{U_{DC}}{\sqrt{3} \cos\left(\frac{\pi}{3} - \Theta_r\right)} \sin \Theta_m \text{ for } \left(\frac{\pi}{6} + \Theta_r\right) \lesssim \Theta_m < \left(\frac{\pi}{2} - \Theta_r\right) \quad (27)$$

$$f_4 = \frac{U_{DC}}{\sqrt{3} \cos\left(\frac{\pi}{6} - \Theta_r\right)} \sin \Theta_m \text{ for } \left(\frac{\pi}{2} - \Theta_r\right) \lesssim \Theta_m < \frac{\pi}{2} \quad (28)$$

Expanding (25, 26, 27 and 28) in a Fourier series and taking only the fundamental component into consideration, the resultant equation can be expressed as [54]:

$$F(\Theta_r) = \frac{\pi}{4} \left[\int_A f_1 \sin \Theta d\Theta + \int_B f_2 \sin \Theta d\Theta + \int_C f_3 \sin \Theta d\Theta + \int_D f_4 \sin \Theta d\Theta \right] \quad (29)$$

where A , B , C and D denote integral ranges of each voltage function f_1 , f_2 , f_3 , and f_4 , respectively. Since $F(\Theta_r)$ represents the peak value of the fundamental component, the $F(\Theta_r)$ according to the definition of the modulation index (4) can be expressed as:

$$F(\Theta_r) = \frac{2}{\pi} U_{DC} M \quad (30)$$

Fig. 25 Reference U_{ref} (solid bold line) and compensated U_{ref}^* (dotted bold line) trajectory of Space Vector in the Space Vector Overmodulation mode I

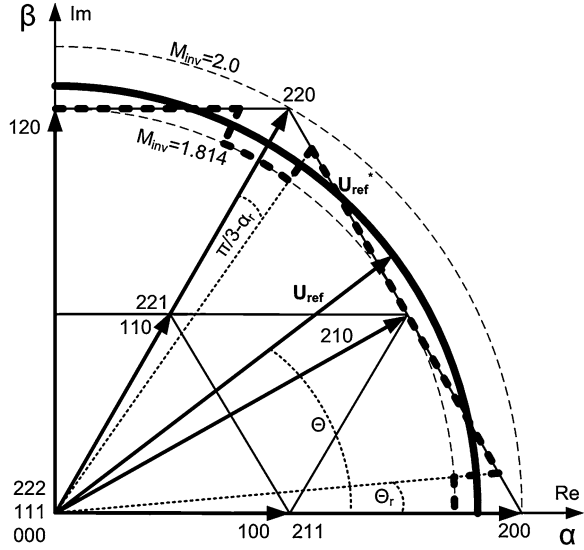
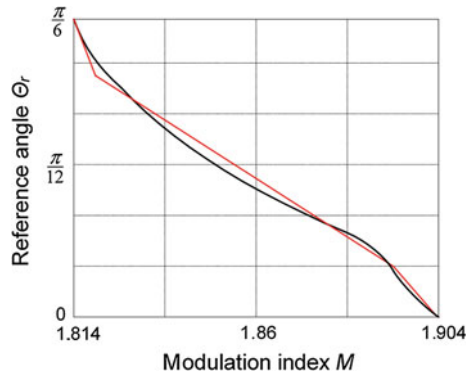


Fig. 26 Reference angle θ_r versus modulation index M and linearization of $\theta_r = f(M)$



Thus, combining the (22) with the (29) a relationship between modulation index and the angle can be determined, which gives a linearity of the reference output voltage. Because of strong nonlinearity, the linearization of (30) function was proposed [53, 54]:

$$\theta_r \begin{cases} 30^\circ \div 24.5^\circ & \Leftrightarrow M \in (1.814, 1.818) \\ 24.5^\circ \div 5.5^\circ & \Leftrightarrow M \in (1.818, 1.896) \\ 5.5^\circ \div 0^\circ & \Leftrightarrow M \in (1.896, 1.904) \end{cases} \quad (31)$$

Figure 26 presents the θ_r angle versus the modulation index. For a given angle of the reference Space Vector U_{ref} :

$$\Theta_m \in \left\langle \Theta_r, \frac{\pi}{3} - \Theta_r \right\rangle \quad (32)$$

only two vectors are used: external and middle vector. For the (22) magnitude of the reference Space Vector it changed. Thus, small modulation indexes have to be calculated as follows, where the sum of the m_1 and m_2 is always equal 2:

$$m_1 = 2 \frac{\sqrt{3} \cos \Theta_m - \sin \Theta_m}{\sqrt{3} \cos \Theta_m + \sin \Theta_m} \quad (33)$$

$$m_2 = 2 - m_1 \quad (34)$$

Outside of the region (32) the magnitude of the reference Space Vector it not changed. Thus, the CSVM or ASVM modulation is applied. From the Fig. 26 it is obvious, that for the Space Vector Overmodulation mode I, modulation index M limit is 1.904. When $M > 1.904$, the Space Vector Overmodulation mode II should be applied.

4.2 Space Vector Overmodulation Mode II

In the Space Vector Overmodulation mode II, the SVM algorithm changes the magnitude and the angle of the reference Space Vector U_{ref} . When the U_{ref} enters to the sector, the compensated Space Vector U_{ref}^* is held at a vertex for particular time. The time, in which compensated Space vector U_{ref}^* remains at the vertices is determined by the holding angle Θ_h . When the reference U_{ref} crosses the holding angle Θ_h , compensated Space Vector U_{ref}^* speeds up and moves along the side of hexagon. For the angle of the reference Space Vector $\Theta_m = \pi/6$, accelerated compensated Space Vector U_{ref}^* catches up reference U_{ref} . When the reference Space Vector U_{ref} crosses the holding angle $\Theta_m = \pi/6 - \Theta_h$, the compensated Space Vector U_{ref}^* arrives to the next vertex. Figure 27 presents the trajectory of the reference U_{ref} and compensated Space Vector U_{ref}^* in stationary $\alpha\beta$ coordinates.

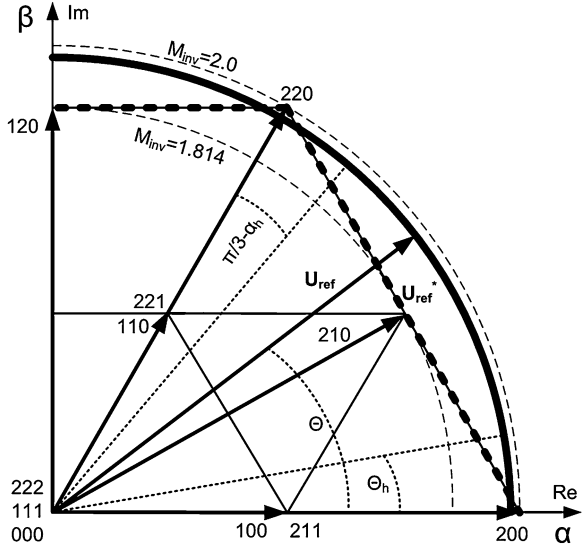
Similarly to the Space Vector Overmodulation mode I, for a given reference Space Vector, the output phase voltage waveform can be divided into four segments, depending on the Θ_h angle [54]. The output voltage equations in each segment are expressed as:

$$f_1 = \frac{U_{DC}}{\sqrt{3}} \tan \Theta_p \quad \text{for} \quad 0 \lesssim \Theta_m < \left(\frac{\pi}{6} - \Theta_h \right) \quad (35)$$

$$f_2 = \frac{U_{DC}}{3} \quad \text{for} \quad \left(\frac{\pi}{6} - \Theta_h \right) \lesssim \Theta_m < \left(\frac{\pi}{6} + \Theta_h \right) \quad (36)$$

$$f_3 = \frac{U_{DC}}{\sqrt{3} \cos \left(\frac{\pi}{3} - \Theta'_p \right)} \sin \Theta'_p \quad \text{for} \quad \left(\frac{\pi}{6} + \Theta_h \right) \lesssim \Theta_m < \left(\frac{\pi}{2} - \Theta_h \right) \quad (37)$$

Fig. 27 Reference U_{ref} (solid bold line) and compensated U_{ref}^* (dotted bold line) trajectory of space vector in the space vector overmodulation mode II



$$f_4 = \frac{2U_{DC}}{3} \text{ for } \left(\frac{\pi}{2} - \Theta_h\right) \lesssim \Theta_m < \frac{\pi}{2} \quad (38)$$

where:

$$\Theta_p = \frac{\Theta_m}{1 - \frac{\pi}{6}\Theta_h} \quad (39)$$

$$\Theta_p' = \Theta_p - \frac{\pi}{6} \quad (40)$$

are angles of compensated Space Vector U_{ref}^* for $0 \leq \Theta_m < (\pi/6 - \Theta_h)$ and $(\pi/6 - \Theta_h) \leq \Theta_m < (\pi/3)$, respectively.

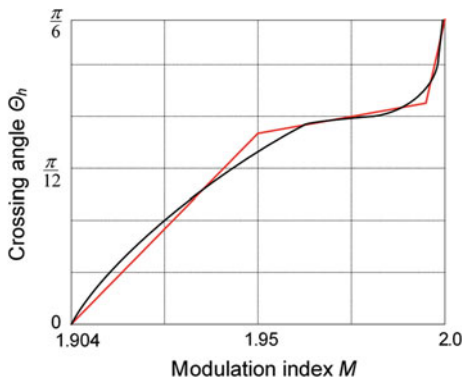
Similarly to the Space Vector Overmodulation mode I, substituting (35, 36, 37 and 38) into (29), the $F(\Theta_h)$ according to (22) can be expressed as:

$$F(\Theta_h) = \frac{2}{\pi} U_{DC} M \quad (41)$$

Figure 28 presents the Θ_h angle versus the modulation index. Because of strong nonlinearity, the linearization of (41) function was proposed [52, 53]:

$$\Theta_h \begin{cases} 0^\circ \div 17.2^\circ & \Leftrightarrow M \in (1.814, 1.818) \\ 17.2^\circ \div 19.5^\circ & \Leftrightarrow M \in (1.818, 1.896) \\ 19.5^\circ \div 30^\circ & \Leftrightarrow M \in (1.896, 1.904) \end{cases} \quad (42)$$

Fig. 28 Crossing angle Θ_h versus modulation index M and linearization of $\Theta_h = f(M)$



As far as compensated Space Vector U_{ref}^* trajectory lies on the side of hexagon, only external vectors are used in the Space Vector Overmodulation mode II. Thus, small modulation indexes are evaluated similarly like in the Space Vector Overmodulation mode I, when Space Vector magnitude is changed, where the sum of the m_1 and m_2 is always equal 2:

$$m_1 = 2 \frac{\sqrt{3} \cos \Theta_p - \sin \Theta_p}{\sqrt{3} \cos \Theta_p + \Theta_p} \tag{43}$$

$$m_2 = 2 - m_1 \tag{44}$$

4.3 Results of High Speed Operation of Adjustable Speed Drive over the Linear Range of Operation

Figure 29 presents steady state operation of the FCC in the Space Vector Overmodulation mode I ($M = 1.85$) and mode II ($M = 1.94$ and $M = 1.98$) for the CSVM and the ASVM modulation. In spite of the stator current i_{Sa} distortion, the FC voltages are properly balanced. Figure 30 shows the FCC operation in six step mode. As can be observed, in six step mode the FC voltage balancing is not possible. Thus, depending on the FCC parameters (such as dead-time value t_{DT}) modulation index should be limited.

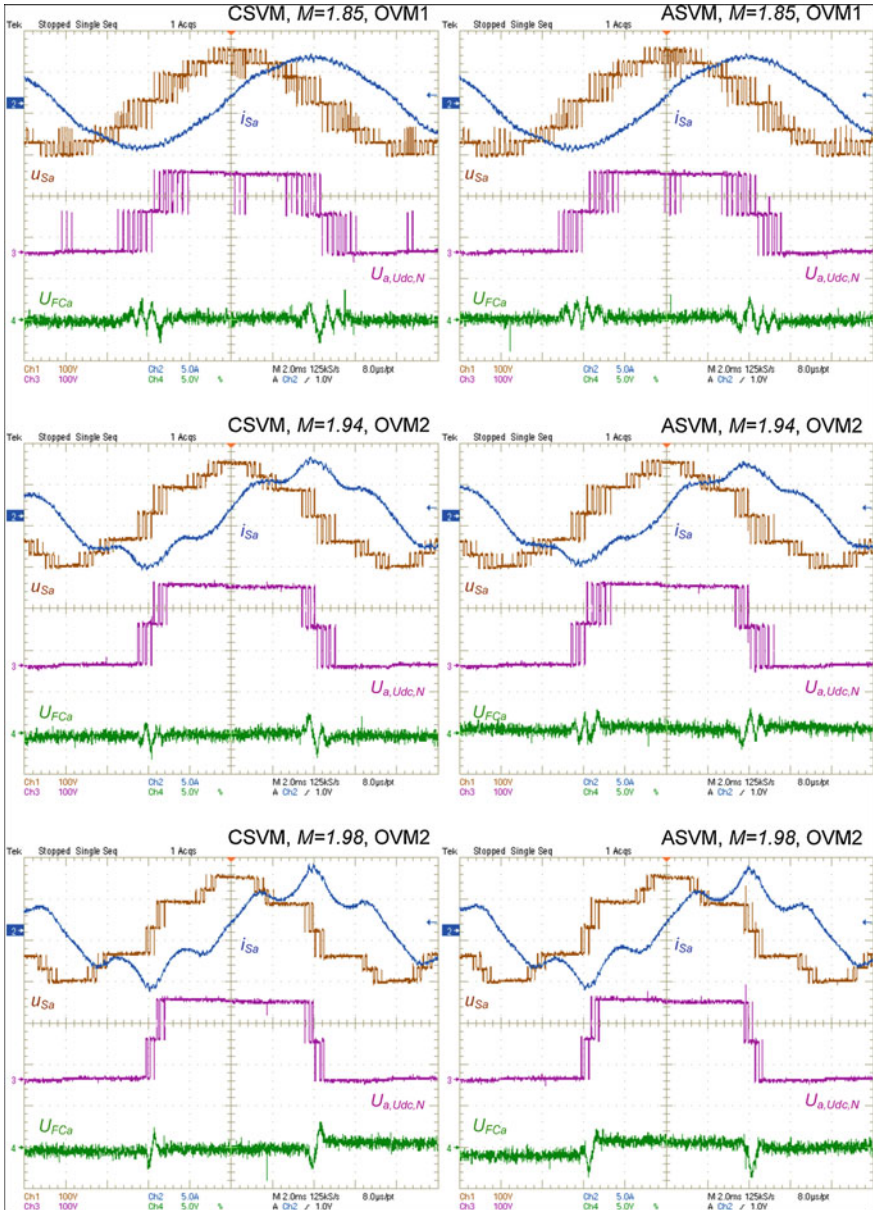


Fig. 29 Operation of the FCC in the space vector overmodulation mode I ($M = 1.85$) and mode II ($M = 1.94$ and $M = 1.98$) for the CSVM and the ASVM: stator voltage u_{Sa} and current i_{Sa} , pole voltage $U_{a,Udc,N}$ and AC component of FC voltage U_{FCa}

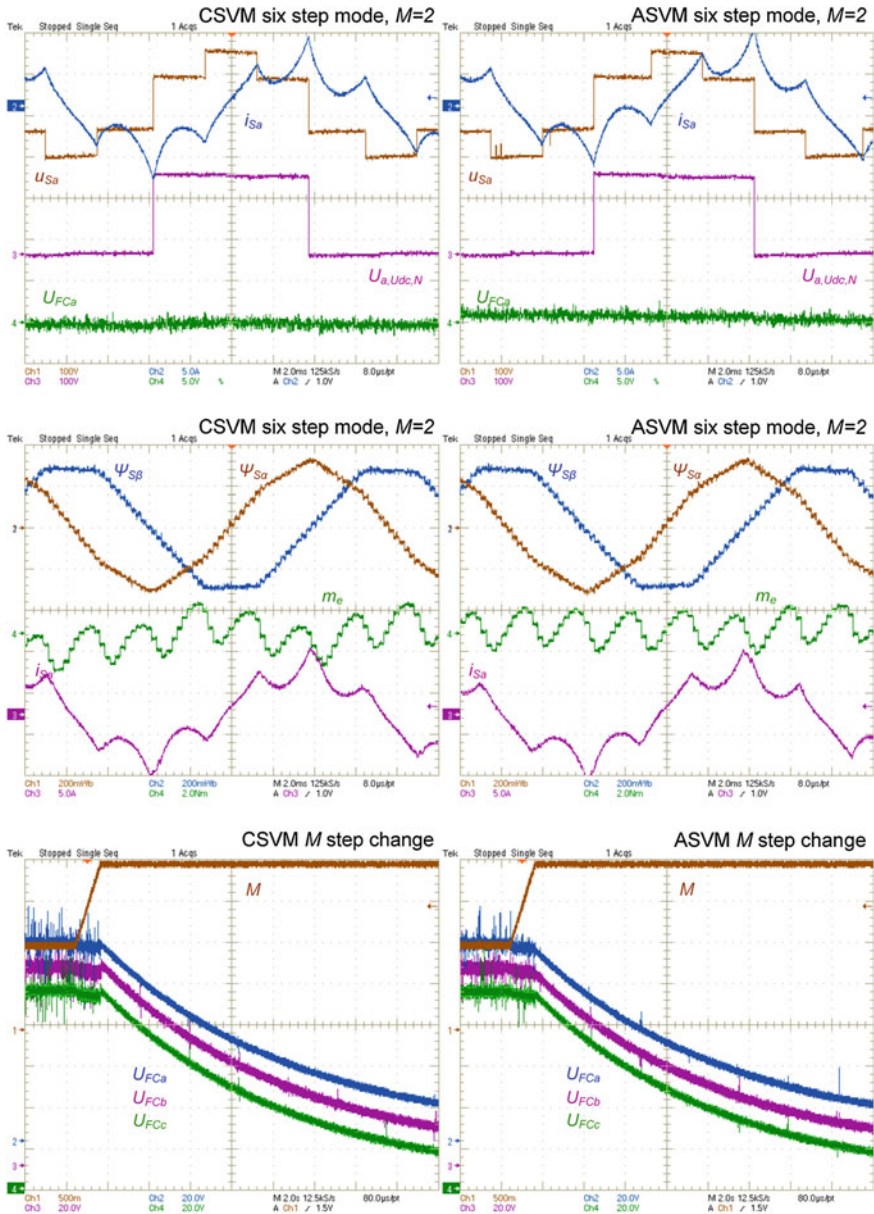


Fig. 30 Operation of the FCC in six step mode for the CSVM and the ASVM. From the top: **a** stator voltage u_{Sa} and current i_{Sa} , pole voltage $U_{a,Udc,N}$ and AC component of FC voltage U_{FCa} , **b** stator fluxes Ψ_{Sa} and Ψ_{Sb} , electromagnetic torque m_e and stator current i_{Sa} . Step change of modulation index M from 1 to 2 for CSVM and ASVM: modulation index M , FC voltages U_{FCa} , U_{FCb} and U_{FCc}

5 Summary

In this Chapter the classical (CSVM) and adaptive (ASVM) Space Vector modulation for the Flying Capacitor Converter (FCC) was shown. The ASVM provides reduction of number of switching and the switching losses (more than 20 %) in the whole linear range of the converter operation because minimal number of vectors is used in each modulation region.

Also, additional features for both the CSVM and the ASVM was shown:

- elimination of DC sources voltage unbalance in full range of the converter operation (except square wave operation—six step mode),
- compensation of the Dead Time and the effect of semiconductor devices voltage drop—possible low speed operation, without phase currents distortion,
- the non-linear Overmodulation algorithm extending the operation range of the converter—possible high speed operation over the linear voltage control range of the converter,
- compensation of FC voltages balancing delay based on prediction of the FC voltages at the end of each sampling period, which provides minimization of the FC voltages pulsations.

References

1. J. Rodriguez, J.S. Lai, F.Z. Peng, Multilevel inverters: a survey of topologies, controls, and applications. *IEEE Trans. Ind. Electron.* **49**(4), 724–738 (2002)
2. R.J. Rodriguez, S. Bernet, B. Wu, J.O. Pontt, S. Kouro, Multilevel voltage–source–converter topologies for industrial medium–voltage drives. *IEEE Trans. Ind. Electron.* **54**(6), 2930–2945 (2007)
3. L.G. Franquelo, J. Rodriguez, J.I. Leon, S. Kouro, R. Portillo, M.A.M. Prats, The age of multilevel converters arrives. *IEEE Ind. Electron. Mag.* **2**(2), 28–39 (2008)
4. J. Rodriguez, L. G. Franquelo, S. Kouro, J. I. Leon, R. C. Portillo, M. A. M. Prats, M. A. Perez, Multilevel converters: an enabling technology for high–power applications, in *Proceedings of the IEEE*, vol. 97, no. 11, pp. 1786–1817, Nov 2009
5. B.K. Bose, Power electronics and motor drives recent progress and perspective. *IEEE Trans. Ind. Electron.* **56**(2), 581–588 (2009)
6. S. Kouro, M. Malinowski, K. Gopakumar, J. Pou, L.G. Franquelo, B. Wu, J. Rodriguez, M.A. Perez, J.I. Leon, Recent advances and industrial applications of multilevel converters. *IEEE Trans. Ind. Electron.* **57**(8), 2553–2580 (2010)
7. H. Akagi, New trends in medium-voltage power converters and motor drives, in *Proceedings of IEEE (ISIE)*, pp. 5–14, Jun 2011
8. A. Nabae, I. Takahashi, H. Akagi, A new neutral–point–clamped PWM inverter. *IEEE Trans. Ind. Appl.* **17**(5), 518–523 (1981)
9. T. A. Meynard, H. Foch, Multi–level conversion: high voltage choppers and voltage–source inverters, in *Proceedings of IEEE PESC 1992*, vol. 1, pp. 397–403, Jun/Jul 1992
10. O. Alonso, L. Marroyo, P. Sanchis, E. Gubia, A. Guerrero, Analysis of neutral–point voltage balancing problem in three–level neutral–point–clamped inverters with svpwm modulation, in *Proceedings of IEEE IECON 2002*, pp. 920–925, Nov 2002

11. S. Busquets-Monge, J. Bordonau, D. Boroyevich, S. Somavilla, The nearest three virtual space vector pwm—a modulation for the comprehensive neutral-point balancing in the three-level npc inverter. *IEEE Power Electron. Lett.* **2**(1), 11–15 (2004)
12. J. Pou, R. Pindado, D. Boroyevich, P. Rodriguez, J. Vicente, Voltage balancing strategies for diode-clamped multilevel converters, in *Proceedings of IEEE PESC 2004*, pp. 3988–3993, Jun 2004
13. W. Kolomyjski, Modulation strategies for three-level pwm converter–fed induction machine drive, Ph.D. dissertation, Warsaw University of Technology, Warsaw, Poland, 2009
14. G. Zongzhi, L. Yujie, Z. Jia, L. Fei, T. Q. Zheng, Voltage utilization ratio increasing and neutral point potential balancing of npc inverter based on zero sequence voltage for linear induction motor drive, in *Proceedings of IEEE IPEMC 2009*, pp. 1045–1049, May 2009
15. K. S. Kumar, S. De, K. Gopakumar, G. Mondal, K. Corzine, Neutral–point–balancing of neutral–point–clamped three–level inverter with a front end switched rectifier dc source for the full modulation range, *IET Power Electron.*, pp. 527–234, Sept 2009
16. J. Pou, P. Rodriguez, V. Sala, S. Busquets-Monge, D. Boroyevich, Algorithm for the virtual vectors modulation in three–level inverters with a voltage–balance control loop, in *Proceedings of the European Conference on Power Electronics and Applications*, pp. 1–9, Sept 2005
17. P. Barbosa, P. Steimer, J. Steinke, L. Meysenc, M. Winkelkemper, N. Celanovic, Active neutral–point–clamped multilevel converters, in *Proceedings of IEEE PESC 1995*, pp. 2296–2301, Jul 1995
18. J. Meili, S. Ponnaluri, L. Serpa, P. K. Steimer, J. W. Kolar, Optimized pulse patterns for the 5–level anpc converter for high speed high power applications, in *Proceedings of IEEE IECON 2006*, pp. 2587–2592, Nov 2006
19. F. Defay, A.M. Llor, M. Fadel, A predictive control with flying capacitor balancing of a multicell active power filter. *IEEE Trans. Ind. Electron.* **55**(9), 3212–3220 (2008)
20. J. Hu, L. Zhang, S. J. Watkins, Active power filtering by a flying-capacitor multilevel inverter with capacitor voltage balance, in *Proceedings of IEEE ISIE 2008*, pp. 2348–2352, Jul 2008
21. D.G. Holmes, T.A. Lipo, *Pulse Width Modulation for Power Converters Principles and Practice* (Wiley-IEEE Press, New York, 2003)
22. B.P. McGrath, D.G. Holmes, Natural capacitor voltage balancing for a flying capacitor converter induction motor drive. *IEEE Trans. Power Electron. Lett.* **24**(6), 1554–1561 (2009)
23. B.P. McGrath, D.G. Holmes, Analytical determination of the capacitor voltage balancing dynamics for three phase flying capacitor converters. *IEEE Trans. Ind. Electron.* **45**(4), 1425–1433 (2009)
24. S. Stynski, Analysis and control of multilevel AC–DC–AC flying capacitor converter fed from single–phase grid, Ph.D. Dissertation, Warsaw University of Technology, Warsaw, Poland, 2011
25. S. Lee, D. Kang, Y. Lee, D. Hyun, The carrier–based pwm method for voltage balance of flying capacitor multilevel converter, in *Proceedings of IEEE PESC 2001*, pp. 126–131, Jun 2001
26. J. Rodriguez, Tutorial on multilevel converters, in *Proceedings of the International Conference PELINCEC 2005*, Oct 2005
27. C. Feng, J. Liang, V.G. Agelidis, Modified phase–shifted pwm control for flying capacitor multilevel converters. *IEEE Trans. Power Electron.* **22**(1), 178–185 (2007)
28. B. P. McGrath, D. G. Holmes, Enhanced voltage balancing of a flying capacitor multilevel converter using phase disposition (pd) modulation, in *Proceedings of IEEE ECCE 2009*, pp. 3108–3115, Nov 2009
29. M. A. S. Mendes, Z. M. A. Peixoto, P. F. Seixas, P. Donoso-Garcia, A space vector pwm method for three–level flying–capacitor inverters, in *Proceedings of IEEE PESC 2001*, pp. 182–187, Jun 2001
30. S. J. Watkins, L. Zhang, Multilevel space vector pwm control schemes for a flying–capacitor inverter, in *Proceedings of PEMD 2004*, pp. 12–17, Mar/Apr 2004

31. S. Choi, M. Saeedifard, A space vector modulation approach for capacitor voltage balancing of flying capacitor converters, in *Proceedings of IEEE APEC 2007*, pp. 1174–1179, Mar 2007
32. M. J. Waite, L. Zhang, Analysis and comparison of 3d-svm schemes for flying-capacitor multi-level inverters, in *Proceedings of EPE 2009*, pp. 1–10, Sep 2009
33. S. Stynski, Space vector pwm modulator reducing switching losses for three-level flying-capacitor inverters, in *Proceedings of IEEE ISIE 2010*, pp. 3912–3917, 4–7 July 2010
34. J. W. Kolar, H. Ertl, F. C. Zach, Influence of the modulation method on the conduction and switching losses of a pwm converter system, *IEEE Trans. Ind. Appl.*, **27**(6), pp. 1063–1075, Nov/Dec 1991
35. S. J. Watkins, L. Zhang, Influence of multilevel sinusoidal pwm schemes on the performance of a flying-capacitor inverter, in *Proceedings of PEMD 2002*, pp. 92–97, Jun 2002
36. M. Bierhoff, H. Brandenburg, F. W. Fuchs, An analysis on switching loss optimized pwm strategies for three phase pwm voltage source converters, in *33rd Annual Conference of the IEEE Industrial Electronics Society*, pp. 1512–1517, Nov 2007
37. L. Won-Kyo, K. S.-Y. Y. J.-S. Yoon, B. Doo-Hyun, A comparison of the carrier-based pwm techniques for voltage balance of flying capacitor in the flying capacitor multilevel inverter, in *Proceedings of IEEE APEC 2006*, pp. 1653–1658, Mar 2006
38. S. Thielemans, A. Ruderman, B. Reznikov, J. Melkebeek, Improved natural balancing with modified phase shifted pwm for single-leg five-level flying-capacitor converters. *IEEE Trans. Power Electron.* **27**(4), 1658–1667 (2012)
39. A. Shukla, A. Ghosh, A. Joshi, Natural balancing of flying capacitor voltages in multicell inverter under pd carrier-based pwm. *IEEE Trans. Power Electron.* **26**(6), 1682–1693 (2011)
40. E.R.C. da Silva, E.C. dos Santos, C.B. Jacobina, Pulse width modulation strategies. *IEEE Ind. Electron. Mag.* **5**(2), 37–45 (2011)
41. D.G. Holmes, The significance of zero space vector placement for carrier-based pwm schemes. *IEEE Trans. Ind. Appl.* **32**(5), 1122–1129 (1996)
42. F. Jenni and D. Wueest, The optimization parameters of space vector modulation, in *Proceedings of EPE 1993*, pp. 376–381, Sept 1993
43. R. Wilkinson, H. du Mouton, T. Meynard, Natural balance of multicell converters: the general case. *IEEE Trans. Power Electron.* **21**(6), 1658–1666 (2006)
44. M. Malinowski, Sensorless control strategies for three-phase pwm rectifiers, Ph.D. Dissertation, Warsaw University of Technology, Warsaw, Poland, 2001
45. T. Bruckner, D. G. Holmes, Optimal pulse-width modulation for three-level inverters, in *Proceedings of the IEEE Power Electronics Specialist*, vol. 20, no. 1, pp. 82–87, Jan 2005
46. S.-G. Jeong, M.-H. Park, The analysis and compensation of deadtime effects in pwm inverters. *IEEE Trans. Ind. Electron.* **38**(2), 108–114 (1991)
47. L. Ben-Brahim, On the compensation of dead time and zero-current crossing for a pwm-inverter-controlled ac servo drive. *IEEE Trans. Ind. Electron.* **51**(5), 1113–1118 (2004)
48. D. Leggate, R.J. Kerkman, Pulse-based dead-time compensator for pwm voltage inverters. *IEEE Trans. Ind. Electron.* **44**(2), 191–197 (1997)
49. A.C. Oliveira, C.B. Jacobina, A.M.N. Lima, Improved dead-time compensation for sinusoidal pwm inverters operating at high switching frequencies. *IEEE Trans. Ind. Electron.* **54**(4), 2295–2304 (2007)
50. Z. Dongsheng, D.G. Rouaud, Dead-time effect and compensations of three-level neutral point clamp inverters for high-performance drive applications. *IEEE Trans. Power Electron.* **14**(4), 782–788 (1999)
51. IRG4BC20UDPBF Insulated Gate Bipolar Transistor with Ultrafast Soft Recovery Diode (2010) International Rectifier, Jan 2010, available: www.irf.com
52. S.R. Minshull, C.M. Bingham, D.A. Stone, M.P. Foster, Compensation of nonlinearities in diode-clamped multilevel converters. *IEEE Trans. Ind. Electron.* **57**(8), 2651–2658 (2010)
53. J. Holtz, W. Lotzkat, A.M. Khambadkone, On continuous control of pwm inverters in the overmodulation range including the six-step mode. *IEEE Trans. Power Electron.* **8**(4), 546–553 (1993)

54. D.-C. Lee, G.-M. Lee, A novel overmodulation technique for space–vector pwm inverters. *IEEE Trans. Power Electron.* **13**(6), 1144–1151 (1998)
55. A.K. Gupta, A.M. Khambadkone, A general space vector pwm algorithm for multilevel inverters, including operation in overmodulation range. *IEEE Trans. Power Electron.* **22**(2), 517–526 (2007)

Chapter 11

Some Aspects of Nonlinear and Discontinuous Control with Induction Motor Applications

Dariusz L. Sobczuk

Abstract In this Chapter the theory of nonlinear control systems is shortly described. The nonlinear feedback linearization control (FLC) and discontinuous sliding mode control (SMC) are presented. Moreover, several applications of nonlinear control methods for induction motor drive are shown. The FLC guarantees the exactly decoupling of the motor speed and rotor flux control. Thus this control method gives a possibility to get very good behavior in both dynamic and steady states. The SMC approach assures direct control of inverter legs and allows using a simple table instead of performing complicated PWM calculation. Moreover the SMC is robust to drive uncertainties. The good behaviour of rotor flux and mechanical speed Sliding Mode Observers (SMO) is the important feature of the system. Therefore, presented approaches are very useful in a variety of applications and, in particular, in the drive systems and power electronics.

1 Introduction

The induction motor (IM) thanks to simple construction, reliability and low cost has found wide applications in industry, electric vehicles and traction drives. Contrary to the brush DC motor, it can also be used in aggressive or volatile environments. However, there are control problems when using an IM in speed adjustable industrial drives. This is due primarily three reasons:

- (a) the induction motor is high order internally coupled nonlinear dynamic system,
- (b) some state variables: rotor currents and fluxes are directly not measurable,
- (c) rotor resistance (due to heating) and magnetising inductance (due to saturation) varies considerably with a significant impact on the system dynamics.

D. L. Sobczuk (✉)
Warsaw University of Technology, Warsaw, Poland
e-mail: sobczuk@isep.pw.edu.pl

Therefore, in high dynamic performance IM drives, the complex control algorithms should be used. Nevertheless, the advancements in semiconductor power electronic devices and microprocessors technologies enabled to use IM in variable speed applications. Implementation of new control techniques in drive systems has made IM a reasonable alternative to DC motors.

The first high performance IM control method known as *Field Oriented Control* (FOC) or *Vector Control* (VC) has been proposed by Hasse [1] and Blaschke [2]. In this method the IM equations are represented in a coordinate system that rotates with the rotor flux vector and are called *field coordinates*. In field coordinates—for the constant rotor flux magnitude—there is a *linear relationship* between control variables and speed. However, another type of coordinates can also be selected to achieve decoupling and linearization of the induction motor equations. An alternative to the FOC is the *feedback linearization control* (FLC) [3, 4]. The application of this approach can take many forms, depending on the choice of variables used for the linearization. Krzeminski [5] has proposed a nonlinear controller based on *multiscalar motor model*. In this approach, similarly as in field oriented controller, it is assumed that the rotor flux amplitude is regulated at a constant value. Thus, the motor speed is not strictly decoupled from the rotor flux, like in FOC. In [6, 7] was developed a nonlinear control system based on *input–output linearization*. In this system, the IM speed and rotor flux are decoupled exactly. The system, however, uses the transformation in field coordinates. Later, Marino et al. [8, 9] have proposed a nonlinear transformation of the IM state variables, so that in the new coordinates, the speed and rotor flux amplitude are decoupled by feedback. Note that using the *feedback linearization* approach strictly linear and strictly decoupled system are obtained. Next, for the decoupled linear system several control algorithms could be applied. One of the important requirements in the control system is robustness against changing of plant parameters. In this case a discontinuous type of control called *Sliding Mode Control* (SMC) could be used [10–12].

This chapter is divided into four sections. In [Sect. 2](#) the theoretical principles of FLC are introduced. In [Sect. 3](#) the SMC will be presented. In [Sect. 4](#) the application of Sliding Mode and feedback linearization to IM control will be shown. In this section three algorithms will be presented. At first the FLC algorithm with the linear control of state variables will be shown [13, 14]. Next the SMC will be used to control IM linearized in feedback [15]. The application of SMC to such a system allows creating the direct control algorithms of the inverter [16]. Finally, the Sliding Mode Observer (SMO) of rotor flux and speed used in the linearized IM control system will be described [17].

2 Feedback Linearization

2.1 Introduction

In this section the basis of feedback linearization will be introduced and the mathematical description and principles [3, 4] will be shortly presented. At first a description of SISO (single input–single output) systems will be introduced, since it is more understandable. Next, the description of SISO systems will be generalized to MIMO (multi input–multi output) systems. At the beginning some useful definitions will be introduced.

The Lie derivative is defined as below:

Definition 1 Let h is function $\mathbb{R}^n \rightarrow \mathbb{R}$ of class C^∞ . The Lie derivative of the function h along the vector field $f: \mathbb{R}^n \rightarrow \mathbb{R}^n$ is defined by following expression

$$L_f h = (\nabla h)^T f \quad (2.1)$$

where ∇h is the gradient of function h . The Eq. (2.1). can also be written as

$$L_f h = \sum_{i=1}^n \frac{\partial h}{\partial x_i} \cdot f_i \quad (2.2)$$

Note that f_i is function $\mathbb{R}^n \rightarrow \mathbb{R}$, and it is i th coordinate of vector f . Afterwards the lie derivative $L_f h$ is also function $\mathbb{R}^n \rightarrow \mathbb{R}$. So we introduce the following definitions:

$$\begin{aligned} L_f^0 h &= h \\ L_f^1 h &= L_f h \\ L_f^2 h &= L_f(L_f h) \\ &\dots \\ L_f^k h &= L_f(L_f^{k-1} h) \end{aligned} \quad (2.3)$$

2.2 Feedback Linearization of SISO Systems

The nonlinear SISO system is given using following equations:

$$\begin{aligned} \dot{\mathbf{x}} &= \mathbf{f}(\mathbf{x}) + \mathbf{g}(\mathbf{x})u \\ y &= h(\mathbf{x}) \end{aligned} \quad (2.4)$$

where $\mathbf{f}, \mathbf{g} \in \mathbb{R}^n, \mathbf{x} \in \mathbb{R}^n, u, y, h \in \mathbb{R}$.

Definition 2 The SISO system described by (2.4) have relative degree r at a point \mathbf{x}^0 if

$$L_g L_f^k h(\mathbf{x}) = 0 \quad (2.5)$$

for all \mathbf{x} in the neighborhood of \mathbf{x}^0 and all $0 \leq k < r - 1$ and

$$L_g L_f^{r-1} h(\mathbf{x}) \neq 0 \quad (2.6)$$

Assuming, that the system (2.4) has relative degree r . After simple calculations using Definition 2 the following equations are obtained:

$$\begin{aligned} y^{(k)}(t) &= L_f^k h(\mathbf{x}(t)) \quad \text{dla } k = 0, 1, \dots, r - 1 \\ y^{(r)}(t) &= L_f^r h(\mathbf{x}(t)) + L_g L_f^{r-1} h(\mathbf{x}(t)) u(t) \end{aligned} \quad (2.7)$$

Coordinate transformations are introduced to the system with relative degree r by below equations:

$$\begin{aligned} z_1 &= \phi_1(\mathbf{x}) = h(\mathbf{x}) \\ z_2 &= \phi_2(\mathbf{x}) = L_f h(\mathbf{x}) \\ &\dots \\ z_r &= \phi_r(\mathbf{x}) = L_f^{r-1} h(\mathbf{x}) \end{aligned} \quad (2.8)$$

the other $n - r$ functions $\phi_{r+1}(x), \phi_{r+2}(x), \dots, \phi_n(x)$ have been chosen in such a way, that the formula:

$$\Phi(\mathbf{x}) = [\phi_1(\mathbf{x}), \phi_2(\mathbf{x}), \dots, \phi_n(\mathbf{x})]^T \quad (2.9)$$

have nonsingular Jacobian matrix defined by equations:

$$j_{kl} = \frac{\partial \phi_k}{\partial x_l} \quad (2.10)$$

Nonsingularity condition is obtained using following inequality:

$$\det(\mathbf{J}) \neq 0 \quad (2.11)$$

Afterwards, it is necessary to fulfill the additional condition:

$$L_g \phi_j(\mathbf{x}) = 0 \quad \text{dla } r + 1 \leq j \leq n \quad (2.12)$$

From (2.7) and (2.8) derivative of z_k is obtained:

$$\begin{aligned} \dot{z}_k &= (\nabla \phi_k)^T \cdot \dot{\mathbf{x}} = (\nabla L_f^{k-1} h(\mathbf{x}))^T \cdot \dot{\mathbf{x}} \\ &= (\nabla L_f^{k-1} h(\mathbf{x}))^T (\mathbf{f}(\mathbf{x}) + \mathbf{g}(\mathbf{x}) u) \\ &= L_f^k h(\mathbf{x}) = \phi_{k+1}(\mathbf{x}) = z_{k+1} \quad \text{dla } k = 1, 2, \dots, r - 1 \end{aligned} \quad (2.13)$$

The derivative of z_r is equal:

$$\begin{aligned}\dot{z}_r &= (\nabla\phi_r)^T \dot{\mathbf{x}} = (\nabla L_f^{r-1}h(x))^T \cdot \dot{x} \\ &= (\nabla L_f^{r-1}h(x))^T (f(x) + g(x)u) = L_f^r h(x) \\ &\quad + L_g L_f^{r-1}h(x)u = L_f^r h(\Phi^{-1}(z)) + L L_f^{r-1}h(\Phi^{-1}(z))u\end{aligned}\quad (2.14)$$

If below definitions are used:

$$\begin{aligned}a(z) &= L_g L_f^{r-1}h(\Phi^{-1}(z)) \\ b(z) &= L_f^r h(\Phi^{-1}(z))\end{aligned}\quad (2.15)$$

then

$$\dot{z}_r = b(z) + a(z)u \quad (2.16)$$

The derivative of z_k for $k > r$ could be rewritten using condition (2.12):

$$\begin{aligned}\dot{z}_k &= (\nabla\phi_k)^T \cdot \dot{\mathbf{x}} = (\nabla\phi_k)^T (f(\mathbf{x}) + g(\mathbf{x})u) \\ &= L_f\phi_k(\mathbf{x}) + L_g\phi_k(\mathbf{x})u = L_f\phi_k(\mathbf{x}) \\ &= L_f\phi_k(\Phi^{-1}(z)) \quad \text{dla } k = r+1, r+2, \dots, n\end{aligned}\quad (2.17)$$

Assuming that:

$$q_k(z) = L_f\phi_{k+r}(\Phi^{-1}(z)) \quad (2.18)$$

Equation (2.17) is presented in the following form:

$$\dot{z}_{k+r} = q_k(z) \quad \text{dla } k = 1, 2, \dots, n-r \quad (2.19)$$

Thus, the system description in the new coordinates is presented below:

$$\begin{aligned}\dot{z}_1 &= z_2 \\ \dot{z}_2 &= z_3 \\ &\dots \\ \dot{z}_{r-1} &= z_r \\ \dot{z}_r &= b(z) + a(z)u \\ \dot{z}_{r+1} &= q_1(z) \\ &\dots \\ \dot{z}_n &= q_{n-r}(z)\end{aligned}\quad (2.20)$$

and the output is:

$$y = z_1 \quad (2.21)$$

Let us assume, that $r = n$. Then the dynamic of the system is described by:

$$\begin{aligned}
 \dot{z}_1 &= z_2 \\
 \dot{z}_2 &= z_3 \\
 &\dots \\
 \dot{z}_{n-1} &= z_n \\
 \dot{z}_n &= b(\mathbf{z}) + a(\mathbf{z})u \\
 y &= z_1
 \end{aligned} \tag{2.22}$$

If the control is chosen:

$$u = \frac{1}{a(\mathbf{z})} (-b(\mathbf{z}) + v) \tag{2.23}$$

then the closed loop system is described by:

$$\begin{aligned}
 \dot{z}_1 &= z_2 \\
 \dot{z}_2 &= z_3 \\
 &\dots \\
 \dot{z}_{n-1} &= z_n \\
 \dot{z}_n &= v \\
 y &= z_1
 \end{aligned} \tag{2.24}$$

Thus, the system is linear and controllable. The control signal could be rewritten using the previous coordinate system by the following equation:

$$u = \frac{1}{L_g L_f^{n-1} h(\mathbf{x})} (-L_f^n h(\mathbf{x}) + v) \tag{2.25}$$

Note that above considerations are presented for the case $r = n$ and then the system is called *exact linearized*.

The feedback linearization algorithm consists of two steps (Fig. 1):

- coordinates transformation according to Eq. (2.8)
- control signal calculation according to Eq. (2.23)

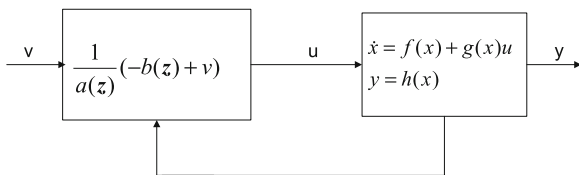
In the case $r < n$ after coordinating transformation (2.8) the system (2.20) is obtained.

If the control signal is chosen:

$$u = \frac{1}{L_g L_f^{r-1} h(\mathbf{x})} (-L_f^r h(\mathbf{x}) + v) \tag{2.26}$$

then partially linearized system will be obtained:

Fig. 1 Scheme of feedback linearization control (FLC)



$$\begin{aligned}
 \dot{z}_1 &= z_2 \\
 \dot{z}_2 &= z_3 \\
 &\dots \\
 \dot{z}_{r-1} &= z_r \\
 \dot{z}_r &= v \\
 \dot{z}_{r+1} &= q_1(z) \\
 &\dots \\
 \dot{z}_n &= q_{n-r}(z)
 \end{aligned}
 \tag{2.27}$$

Note, that this system can be decomposed into two subsystems The first one is linear of dimension r defined by vector ξ

$$\xi = [z_1, z_2, \dots, z_r]^T
 \tag{2.28}$$

Only this subsystem is responsible for the input–output behavior. The second subsystem of dimension $n - r$ is nonlinear. Its behavior does not affect the output and is defined by a vector η :

$$\eta = [z_{r+1}, z_{r+2}, \dots, z_n]^T
 \tag{2.29}$$

and it is responsible for the zero dynamics of the system.

Using the definitions (2.28) and (2.29), system (2.27) could be rewritten in the following form:

$$\begin{aligned}
 \dot{\xi}_1 &= \xi_2 \\
 \dot{\xi}_2 &= \xi_3 \\
 &\dots \\
 \dot{\xi}_{r-1} &= \xi_r \\
 \dot{\xi}_r &= v \\
 \dot{\eta}_1 &= q_1(\xi, \eta) \\
 &\dots \\
 \dot{\eta}_{n-r} &= q_{n-r}(\xi, \eta)
 \end{aligned}
 \tag{2.30}$$

Regarding an additional expression:

$$\mathbf{q} = [q_1, q_2, \dots, q_{n-r}]^T \quad (2.31)$$

The Eq. (2.30) could be presented in shorter form:

$$\begin{aligned} \dot{\xi}_1 &= \xi_2 \\ \dot{\xi}_2 &= \xi_3 \\ &\dots \\ \dot{\xi}_{r-1} &= \xi_r \\ \dot{\xi}_r &= v \\ \dot{\boldsymbol{\eta}} &= \mathbf{q}(\boldsymbol{\xi}, \boldsymbol{\eta}) \end{aligned} \quad (2.32)$$

2.3 Feedback Linearization of MIMO Systems

Let us assume that the MIMO system will be described using the following equations:

$$\begin{aligned} \dot{\mathbf{x}} &= \mathbf{f}(\mathbf{x}) + \mathbf{g}(\mathbf{x})\mathbf{u} \\ \mathbf{y} &= \mathbf{h}(\mathbf{x}) \end{aligned} \quad (2.33)$$

where $\mathbf{f} \in R^n$, $\mathbf{x} \in R^n$, $\mathbf{u}, \mathbf{y}, \mathbf{h} \in R^m$, $\mathbf{g} \in R^{n \times m}$. In this system the number of inputs is equal the number of outputs m .

Definition 3 MIMO system described by Eq. (2.33) has the vector relative degree $\mathbf{r} = [r_1, r_2, \dots, r_m]^T$ at point \mathbf{x}^0 if

$$\mathbf{L}_g \mathbf{L}_f^k h_i(\mathbf{x}) = 0 \quad (2.34)$$

for all \mathbf{x} in neighborhood of \mathbf{x}^0 and all $0 \leq k < r_i - 1$ as well as $1 \leq i \leq m, 1 \leq j \leq m$

and matrix $\mathbf{A}(\mathbf{x})$, which elements a_{ij} are defined by:

$$a_{ij} = \mathbf{L}_{g_j} \mathbf{L}_f^{r_i-1} h_i(\mathbf{x}) \quad (2.35)$$

is nonsingular in $\mathbf{x} = \mathbf{x}^0$.

Note that this definition corresponds to the definition of SISO system (Definition 2).

Let us assume that:

$$\mathbf{r} = \sum_{i=1}^m r_i \quad (2.36)$$

The results from Sect. 2.2.1 are generalized to MIMO system. Thus the coordinate transformation is defined by the mapping Φ :

$$\Phi(\mathbf{x}) = [\phi_1^1(\mathbf{x}), \dots, \phi_{r_1}^1(\mathbf{x}), \dots, \phi_{r_m}^m(\mathbf{x}), \phi_{r+1}, \dots, \phi_n]^T \quad (2.37)$$

where:

$$\phi_j^i(\mathbf{x}) = L_f^{j-1} h_i(\mathbf{x}) \quad (2.38)$$

for all $i = 1, 2, \dots, m$ and $j = 1, 2, \dots, r_i$. Afterwards

$$L_{g_j} \phi_i(\mathbf{x}) = 0 \quad (2.39)$$

for $r+1 \leq i \leq n$ and $1 \leq j \leq m$.

If the following expressions are defined:

$$\begin{aligned} \zeta_j^i &= \phi_j^i(\mathbf{x}) \\ \eta_i &= \phi_{i+r} \end{aligned} \quad (2.40)$$

the vectors are fixed as:

$$\begin{aligned} \boldsymbol{\xi}^i &= [\zeta_1^i, \zeta_2^i, \dots, \zeta_{r_i}^i]^T \\ \boldsymbol{\eta} &= [\eta_1, \eta_2, \dots, \eta_{n-r}]^T \end{aligned} \quad (2.41)$$

and matrix $\boldsymbol{\zeta}$

$$\boldsymbol{\xi} = [\boldsymbol{\xi}^1, \boldsymbol{\xi}^2, \dots, \boldsymbol{\xi}^m]^T \quad (2.42)$$

Then the dynamic of the system could be rewritten by the following equations:

$$\begin{aligned} \dot{\zeta}_{j-1}^i &= \zeta_j^i \\ \dot{\zeta}_{r_i}^i &= b_i(\boldsymbol{\xi}, \boldsymbol{\eta}) + \sum_{k=1}^m a_{ik} u_k \\ y_i &= \zeta_1^i \end{aligned} \quad (2.43)$$

for $1 \leq i \leq m$ and $2 \leq j \leq r_i$.

whereas the equation corresponds to $\boldsymbol{\eta}$ is as follows:

$$\dot{\boldsymbol{\eta}} = \mathbf{q}(\boldsymbol{\xi}, \boldsymbol{\eta}) \quad (2.44)$$

And the transformation parameters are:

$$a_{ij} = L_{g_j} L_f^{r_i-1} h_i(\Phi^{-1}(\boldsymbol{\xi}, \boldsymbol{\eta})) \quad (2.45)$$

$$b_i = L_{g_j} L_f^{r_i} h_i(\Phi^{-1}(\boldsymbol{\xi}, \boldsymbol{\eta})) \quad (2.46)$$

for $i, j = 1, 2, \dots, m$.

In the system (2.33) the control signal is:

$$\mathbf{u} = \boldsymbol{\alpha}(\mathbf{x}) + \boldsymbol{\beta}(\mathbf{x})\mathbf{v} \quad (2.47)$$

where $\boldsymbol{\alpha} \in R^m$, $\boldsymbol{\beta} \in R^{m \times m}$ and \mathbf{v} is the reference input ($\mathbf{v} \in R^m$).

Suppose, that the relative degree of the system (2.33) is equal n and the control signal is:

$$\mathbf{u} = \mathbf{A}^{-1}(\boldsymbol{\xi})(-\mathbf{b}(\boldsymbol{\xi}) + \mathbf{v}) \quad (2.48)$$

then the closed loop system is described by following equations:

$$\begin{aligned} \dot{\zeta}_1^i &= \zeta_2^i \\ \dot{\zeta}_2^i &= \zeta_3^i \\ &\dots \\ \dot{\zeta}_{r_i-1}^i &= \zeta_{r_i}^i \\ \dot{\zeta}_{r_i}^i &= v_i \\ y_i &= \zeta_1^i \end{aligned} \quad (2.49)$$

for $i = 1, 2, \dots, m$. The closed system is linear and controllable.

If the relative degree of the system fulfills the condition $r < n$, then the partially linearized system is obtained, consisting of two subsystems: linear (2.49) and nonlinear (2.45). These equations correspond to the SISO system described by (2.32).

3 Sliding Mode Control

3.1 Introduction

Control Systems are an important part of automation. Sliding Mode Control (SMC) is a type of control using the theory of Variable Structure Systems (VSS). The first works in these fields started in 50th of the twentieth century in the Soviet Union and were developed in 1960s and 1970s (Emelyanow 1967 [10], Itkis 1976 [4], Utkin 1977 [18]).

At the beginning of 1980s started more and more often applying the method of SMC in the real systems. SMC methods found application in:

- systems of automatic control in planes (Singh 1989) [19],
- control of servomechanisms (Hikita 1988) [20],
- design observers (Slotine and de Wit 1991) [21],
- control robots (Slotine and Sastry 1983) [22],
- control electric motors and in power electronics (Sabanowic and Izosimov 1981) [23], and many others.

Today SMC makes a comeback because of discovering second order SMC (2-SMC) by A. Levant [24]. The 2-SMC is sometimes called SMC without chattering, because this disadvantageous phenomenon of classical first order SMC is strongly limited.

3.2 Variable Structure Systems (VSS)

In this section theoretical principles of the VSS will be introduced. The mathematical description of this approach is given in [12]. At the beginning a theoretical description of systems with single input and single output (SISO) will be introduced, since this approach is simpler and more understandable. The importance will be put to the SMC. Further considerations applying SMC to SISO systems will be generalized to systems with multi inputs and multi outputs (MIMO).

It is possible, in the simplest way, to explain the VSS by comparing with the linear controller for SISO systems.

Let us assume, that the object is described by matrix equation:

$$\dot{\mathbf{x}} = \mathbf{A}\mathbf{x} + \mathbf{b}u \quad (3.1)$$

For the linear state regulator the structure of the feedback is defined as follows:

$$u = \mathbf{k}^T \mathbf{x} \quad (3.2)$$

where $\mathbf{A} \in R^{n \times n}$, \mathbf{b} , \mathbf{x} , $\mathbf{k} \in R^n$, $u \in R$.

The VSS can be implemented through state switching between two or more linear controllers (Fig. 2).

Construction of this system includes two problems:

- choice of parameters for every structure,
- defining the switching logic.

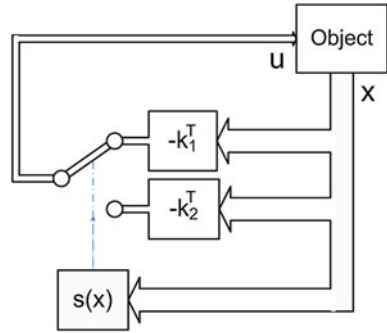
The following advantages are obtained on the costs for the small system complication:

- it is possible to improve control quality combining useful properties for every separated structure,
- the VSS can hold new properties not existing for every structure.

3.3 First Order SMC

This section will be concentrating on the first order SMC, also called simply SMC. SMC occurs if in the neighborhood of the switching surface, trajectories are directed in its direction. The fact that structure is independent of the object

Fig. 2 Strategy of variable structure system



parameters is the most important feature of this approach. It causes the robustness of the system. One should however remember that fulfil two conditions are necessary to obtain SMC:

- trajectories must tend to the switching surface,
- on this surface condition for the occurring sliding mode phenomenon must be fulfilled.

3.3.1 SMC for the Linear SISO Systems

Now the SMC description for the linear SISO system will be presented. The object is written in the canonical form:

$$\begin{aligned} \dot{x}_i &= x_{i+1} \quad \text{for } i = 1, 2, \dots, n - 1 \\ \dot{x}_n &= - \sum_{i=1}^n a_i x_i + u \end{aligned} \tag{3.3}$$

Let us assume that aim of control is zeroing of the output $y = x_l$. Let u will be a function of the vector x with discontinuity surface determined by the equation $s = 0$, where

$$s = \sum_{i=1}^n c_i x_i, c_i = const, c_n = 1 \tag{3.4}$$

If trajectories are directed at the surface $s = 0$, then SMC occurred. The sufficient condition is:

$$\begin{aligned} \lim_{s \rightarrow 0^+} \dot{s} &< 0 \\ \lim_{s \rightarrow 0^-} \dot{s} &> 0 \end{aligned} \tag{3.5}$$

It means that if s is positive, then its derivative should be negative and if s is negative, then its derivative should be positive. So, when the Eq. (3.5) is fulfilled,

trajectories will be attracted to the sliding surface. Thus, the resulting equation of the system working with SMC is as follows:

$$\begin{aligned} \dot{x}_i &= x_{i+1} \quad \text{for } i = 1, 2, \dots, n-2 \\ \dot{x}_{n-1} &= -\sum_{i=1}^n c_i x_i \end{aligned} \quad (3.6)$$

Note, that these equations are not dependent from control parameters but only from parameters c_i .

The main problem is to select control to meet the following properties:

- the sliding mode must exist in all points of the surface $s = 0$,
- control should provide reaching this surface.

In the case of classical SM, the switching function, used in control is function $\text{sign}(\cdot)$.

$$\text{sign}(s) = \begin{cases} +1 & \text{if } s \geq 0 \\ -1 & \text{if } s < 0 \end{cases} \quad (3.7)$$

So the control of the SISO system is equal :

$$u = V_m \text{sign}(s) \quad (3.8)$$

3.3.2 SMC for Nonlinear SISO Systems

A nonlinear SISO system with SMC is described as follows:

$$\begin{aligned} \dot{\mathbf{x}} &= \mathbf{g}(\mathbf{x}, t) + \mathbf{b}(\mathbf{x}, t)u \\ u &= \begin{cases} u^+(\mathbf{x}, t) & \text{dla } s \geq 0 \\ u^-(\mathbf{x}, t) & \text{dla } s < 0 \end{cases} \end{aligned} \quad (3.9)$$

where $\mathbf{x}, \mathbf{f} \in R^n, u \in R$.

Now, the problem is: how to choose functions $u^+(\mathbf{x}, t)$, $u^-(\mathbf{x}, t)$, and switching surface s to obtain the desired system behaviour. In order to describe the dynamics of the SMC system one could use *equivalent control* method. Using this method equation for the ideal sliding mode will be received. Equivalent control fulfil the following equation:

$$\dot{s}(\mathbf{x}) = 0 \quad (3.10)$$

The Eq. (3.14) could be rewritten in the following form:

$$(\nabla s)^T (\mathbf{g}(\mathbf{x}, t) + \mathbf{b}(\mathbf{x}, t)u) = 0 \quad (3.11)$$

The equivalent control is obtained from the Eq. (3.11) and is equal:

$$u_{eq} = -\frac{(\nabla s)^T \mathbf{g}(\mathbf{x}, t)}{(\nabla s)^T \mathbf{b}(\mathbf{x}, t)} \quad (3.12)$$

with assumption

$$(\nabla s)^T \mathbf{b}(\mathbf{x}, t) \neq 0 \quad (3.13)$$

Substituting the Eq. (3.12) to Eq. (3.9) we receive:

$$\dot{\mathbf{x}} = \mathbf{g}(\mathbf{x}, t) - \frac{(\nabla s)^T \mathbf{g}(\mathbf{x}, t)}{(\nabla s)^T \mathbf{b}(\mathbf{x}, t)} \mathbf{b}(\mathbf{x}, t) \quad (3.14)$$

The Eq. (3.14) presents control dynamics of the SMC. Using the equivalent control method we can also receive other SMC conditions different from Eq. (3.5). The following condition must be fulfilled:

$$\min(u^+, u^-) < u_{eq} < \max(u^+, u^-) \quad (3.15)$$

3.3.3 SMC for MIMO Systems

The SMC description of the nonlinear MIMO systems is similar to those presented for the SISO systems. An appropriate equation for this case can be written in the following form:

$$\begin{aligned} \dot{\mathbf{x}} &= \mathbf{g}(\mathbf{x}, t) + \mathbf{B}(\mathbf{x}, t)\mathbf{u} \\ u_i &= \begin{cases} u_i^+(\mathbf{x}, t) & \text{for } s_i \geq 0 \\ u_i^-(\mathbf{x}, t) & \text{for } s_i < 0 \end{cases} \end{aligned} \quad (3.16)$$

for $i = 1, 2, \dots, m$. In addition $\mathbf{x}, \mathbf{f} \in R^n, \mathbf{u} \in R^m$.

Equivalent control is obtained from the equation:

$$\dot{\mathbf{s}}(\mathbf{x}) = 0 \quad (3.17)$$

Let us assume, that $\mathbf{K}(\mathbf{x})$ is a matrix with elements $k_{ij}(\mathbf{x})$ defined as follows:

$$k_{ij} = \frac{\partial s_i}{\partial x_j} \quad (3.18)$$

Note, that the rows of the \mathbf{K} matrix are gradients of the function $s_i(\mathbf{x})$. Thus, the condition Eq. (3.17) can be written in following form

$$\mathbf{K}(\mathbf{x}) (\mathbf{g}(\mathbf{x}, t) + \mathbf{B}(\mathbf{x}, t)\mathbf{u}) = 0 \quad (3.19)$$

From this formula one can get the equivalent control equation:

$$\mathbf{u}_{\text{eq}} = -(\mathbf{K}(\mathbf{x})\mathbf{B}(\mathbf{x}, t))^{-1}\mathbf{K}(\mathbf{x})\mathbf{g}(\mathbf{x}, t) \quad (3.20)$$

with assumption:

$$\det(\mathbf{K}(\mathbf{x})\mathbf{B}(\mathbf{x}, t)) \neq 0 \quad (3.21)$$

Putting the Eq. (3.20) to Eq. (3.16) one receives:

$$\dot{\mathbf{x}} = \mathbf{g}(\mathbf{x}, t) - \mathbf{B}(\mathbf{x}, t)(\mathbf{K}(\mathbf{x}, t)\mathbf{B}(\mathbf{x}, t))^{-1}\mathbf{K}(\mathbf{x}, t)\mathbf{g}(\mathbf{x}, t) \quad (3.22)$$

Note, that the sufficient conditions for sliding mode existence for MIMO systems is:

$$\min(u_i^+, u_i^-) < u_{\text{eq}i} < \max(u_i^+, u_i^-) \quad (3.23)$$

for $i = 1, 2, \dots, m$

3.3.4 Chattering Phenomenon in SMC

So far only an ideal case of Sliding Mode has been considered. However, in the real condition certain vagueness is appearing:

- hysteresis in switching controls (what limits the frequency of switching),
- delay associated with sampling in digital controllers.

This causes that the system dynamics are not working precisely according to dynamics determined by the sliding mode. Therefore in the real conditions high frequency signal is occurring, which is called *chattering*. It is possible to eliminate it using different methods. These methods are called chattering reduction methods. For the purpose of chattering limitation, the continuous switching function approximation is applied. Systems using this approach are called *quasi sliding mode* control systems.

Some other methods of chattering reduction are presented below:

- applying the low-pass filter on the controller output,
- adding switching function to equivalent control u_{eq} function, which causes that the part with saturation can have a smaller amplitude and consequently reduces chattering,
- using sliding control of the higher order,
- applying the integral sliding mode,
- applying the sliding mode with adaptive switching surfaces,
- decoupling plant structures and applying sliding mode control for the new object.

3.4 Second Order SMC

In this section the definition of higher order SMC methods will be introduced [24]. The r order sliding mode control means

$$s = \dot{s} = \ddot{s} = \dots = s^{(r-1)} = 0 \quad (3.24)$$

The higher order system description will be limited to second order system. This is obvious that in first order SMC systems, a value of the function s derivative can obtain high value. This is because, this value is not controlled. Reducing this variable cause also chattering reduction.

In classical SMC, the switching function, used in control is function $\text{sign}(\cdot)$. It means that the control signal is dependent only on switching function s . In the second order SMC this signal is additionally dependent directly or indirectly on the derivative of switching function. If the convergence to the origin of the function $\dot{s}(s)$ in finite time, then occurs second order SMC.

Currently the most popular three following methods exist for achieving the second order SMC:

- twisting algorithm (Levantovsky (Levant) 1985 [25]),
- sub-optimal algorithm (Bartolini et al. 1997 [26]),
- super-twisting algorithm (Levant 1993 [24]).

3.4.1 Twisting Algorithm

The twisting algorithm was introduced by Lewantowski in 1985 [25] (at present Arie Levant). He also introduced the second order SMC term in the paper from 1993 [24].

The control function in twisting algorithm has the following form:

$$u = \begin{cases} -V_m \text{sign}(s) & \text{if } s\dot{s} \leq 0 \\ -V_M \text{sign}(s) & \text{if } s\dot{s} > 0 \end{cases} \quad (3.25)$$

and $V_M > V_m$

Trajectories are twisted around the $s - \dot{s}$ coordinates system. The origin of the coordinate system is reached at the finite time.

3.4.2 Sub-Optimal Algorithm

The sub-optimal algorithm was described by Bartolini et al. in 1998 [26]. Control in this system is described by following equations:

$$u = \begin{cases} -U \operatorname{sign}(s - \beta s_M) & \text{if } (s - \beta s_M)s_M \geq 0 \\ -\alpha^* U \operatorname{sign}(s - \beta s_M) & \text{if } (s - \beta s_M)s_M < 0 \end{cases} \quad (3.26)$$

where $U > 0$, $\alpha^* > 1$, $\beta \in [0; 1)$, and s_M is the last value s measured in the moment when $\dot{s} = 0$.

3.4.3 Super-Twisting the Algorithm

Super-twisting algorithm was published in 1993 by Levant. In this system control signal is described by the following formulas:

$$\begin{aligned} u &= -\lambda |s|^\rho \operatorname{sign}(s) + u_1 \\ \dot{u}_1 &= -W \cdot \operatorname{sign}(s) \end{aligned} \quad (3.27)$$

where $W > 0$, $\lambda > 0$, $\alpha^* > 1$, $\rho \in (0; 0.5]$

Note, that in this algorithm, only information about the s functions is necessary. In the other two methods the information about the derivative of s is required, which is not easy to obtain.

3.5 Comparison of First and Second SMC

Among the advantages of the second order SMC are:

- The second order SMC system is getting smaller chattering towards the first order SMC system,
- in the second order SMC the control signals and state variables are smooth at keeping the robustness of the system,
- in the second order SMC construction of robust differentiating systems based on the super-twisting algorithm is possible.

Among the disadvantages of the second order SMC are:

- in the second order SMC is much difficult to prove and to get the system stability towards the first order SMC,
- in the second order SMC system is more parameters for adjusting, and not so clear construction rules towards the first order SMC system.

This comparison shows that second order SMC systems have better properties towards first order SMC systems, although obtaining this mode is technically more difficult.

3.6 Conclusions

This study presents the mathematical basis of first order SMC and second order SMC. In the systematic way is explained how the VSS and particularly the SMC of the first and second order are constructed. The first order SMC description for linear and nonlinear systems with SISO and MIMO systems are presented. The advantage of this control method i.e. the robustness of parameter changes is clarified. Also, a disadvantageous chattering phenomenon is described, and discussed in which way it is possible to manage with this feature. Then three algorithms for second order SMC controlling are introduced and shortly described. Finally, the short comparison between first order SMC methods and second order SMC is performed.

4 The Application of Feedback Linearization and Sliding Mode to Induction Motor Control

4.1 Introduction

In this section the application of Sliding Mode Control (SMC) and feedback linearization control (FLC) to induction motor (IM) will be presented. Thus three application examples will be shown. At first the FLC algorithm with the linear control of state variables will be investigated. After that the SMC will be used to control linearized induction motor. The SMC application for such a system gives us the possibility creating the direct control algorithms of the inverter. Finally, the Sliding Mode Observer (SMO) of rotor flux and speed used in the linearized induction motor will be described.

4.2 Application of Feedback Linearization to Induction Motor Control

This section presents the application of feedback linearization to induction motor control. The induction motor equations in per unit (pu.) system is described in the following form:

$$\dot{\mathbf{x}} = \mathbf{f}(\mathbf{x}) + u_{s\alpha}\mathbf{g}_\alpha + u_{s\beta}\mathbf{g}_\beta \quad (4.1)$$

where

$$\mathbf{f}(\mathbf{x}) = \begin{bmatrix} -\alpha\psi_{r\alpha} - \omega_m\psi_{r\beta} + \alpha x_M i_{s\alpha} \\ \omega_m\psi_{r\alpha} - \alpha\psi_{r\beta} + \alpha x_M i_{s\beta} \\ \alpha\beta\psi_{r\alpha} + \beta\omega_m\psi_{r\beta} - \gamma i_{s\alpha} \\ -\beta\omega_m\psi_{r\alpha} + \alpha\beta\psi_{r\beta} - \gamma i_{s\beta} \\ \mu(\psi_{r\alpha} i_{s\beta} - \psi_{r\beta} i_{s\alpha}) - \frac{m_e}{\tau_m} \end{bmatrix} \quad (4.2)$$

$$\mathbf{g}_\alpha = [0, 0, 1/\sigma x_s, 0, 0]^T, \quad \mathbf{g}_\beta = [0, 0, 0, 1/\sigma x_s, 0]^T \quad (4.3)$$

$$\mathbf{x} = [\psi_{r\alpha}, \psi_{r\beta}, i_{s\alpha}, i_{s\beta}, \omega_m]^T \quad (4.4)$$

and $\alpha = r_r/x_r$; $\beta = x_M/(\sigma x_s x_r)$; $\gamma = (r_s x_r^2 + r_r x_M^2)/(\sigma x_s x_r^2)$; $\mu = x_M/(\tau_M x_r)\sigma = 1 - x_M^2/(\sigma x_s x_r)$, where motor parameters r_r, r_s are rotor and stator resistance in pu. system, and x_r, x_s, x_M , are rotor, stator and main inductance in pu. system.

Note that $\omega_m, \psi_{r\alpha}, \psi_{r\beta}$, are not dependent on control signals $u_{s\alpha}, u_{s\beta}$. In this case it is easy to choose two variables dependent on \mathbf{x} only. Now the feedback linearization procedure will be applied, which was described in Sect. 2. So we can define [3, 4]:

$$\phi_1(\mathbf{x}) = \psi_{r\alpha}^2 + \psi_{r\beta}^2 = \psi^2 \quad (4.5)$$

$$\phi_2(\mathbf{x}) = \omega_m \quad (4.6)$$

Let $\phi_1(\mathbf{x}), \phi_2(\mathbf{x})$ are the output variables. The aim of control is to obtain:

- constant flux amplitude,
- reference angular speed.

Part of the new state variables we can choose according to (4.5) and (4.6). So, the full definition of new coordinates is given by [8, 9]:

$$\begin{aligned} z_1 &= \phi_1(\mathbf{x}) \\ z_2 &= L_f \phi_1(\mathbf{x}) \\ z_3 &= \phi_2(\mathbf{x}) \\ z_4 &= L_f \phi_2(\mathbf{x}) \\ z_5 &= \arctan\left(\frac{\psi_{r\beta}}{\psi_{r\alpha}}\right) \end{aligned} \quad (4.7)$$

where $L_f h$ is the Lie derivative of h with respect to a vector field f (2.1).

Note, that the fifth variable cannot be linearizable and the linearization can be only partial. Denote:

$$\phi_3(\mathbf{x}) = z_5 \quad (4.8)$$

then the dynamic of the system is given by:

$$\begin{aligned}
\dot{z}_1 &= z_2 \\
\dot{z}_2 &= L_f^2 \phi_1(\mathbf{x}) + L_{g\alpha} L_f \phi_1(\mathbf{x}) u_{s\alpha} + L_{g\beta} L_f \phi_1(\mathbf{x}) u_{s\beta} \\
\dot{z}_3 &= z_4 \\
\dot{z}_4 &= L_f^2 \phi_2(\mathbf{x}) + L_{g\alpha} L_f \phi_2(\mathbf{x}) u_{s\alpha} + L_{g\beta} L_f \phi_2(\mathbf{x}) u_{s\beta} \\
\dot{z}_5 &= L_f^2 \phi_3(\mathbf{x})
\end{aligned} \tag{4.9}$$

In the further part of this section we will consider the system consists of the first four equations, because the fifth variable is only responsible for the zero dynamics of the system. We can define linearizing feedback as [4]:

$$\begin{bmatrix} u_{s\alpha} \\ u_{s\beta} \end{bmatrix} = \mathbf{D}^{-1} \left\{ \begin{bmatrix} -L_f^2 \phi_1 \\ -L_f^2 \phi_2 \end{bmatrix} + \begin{bmatrix} v_1 \\ v_2 \end{bmatrix} \right\} \tag{4.10}$$

\mathbf{D} is given by:

$$\mathbf{D} = \begin{bmatrix} L_{g\alpha} L_f \phi_1 & L_{g\beta} L_f \phi_1 \\ L_{g\alpha} L_f \phi_2 & L_{g\beta} L_f \phi_2 \end{bmatrix} \tag{4.11}$$

After simple calculation, with the assumption that $\det(\mathbf{D}) \neq 0$ what means that $\psi_r \neq 0$, the following equation is fulfilled:

$$\mathbf{D}^{-1} = \frac{\sigma x_s}{2\alpha\mu x_M \psi_r^2} \begin{bmatrix} \mu\psi_{r\alpha} & -2\alpha x_M \psi_{r\beta} \\ \mu\psi_{r\beta} & -2\alpha x_M \psi_{r\alpha} \end{bmatrix} \tag{4.12}$$

and $L_f^2 \phi_1$, $L_f^2 \phi_2$ are equal:

$$\begin{aligned}
L_f^2 \phi_1 &= 2\alpha \left[(2\alpha + \alpha\beta x_M) (\psi_{r\alpha}^2 + \psi_{r\beta}^2) + \alpha x_M^2 (i_{s\alpha}^2 + i_{s\beta}^2) \right. \\
&\quad \left. - (\gamma x_M + 3\alpha x_M) (\psi_{r\alpha} i_{s\alpha} + \psi_{r\beta} i_{s\beta}) + x_M \omega_m (\psi_{r\alpha} i_{s\beta} - \psi_{r\beta} i_{s\alpha}) \right]
\end{aligned} \tag{4.13}$$

$$\begin{aligned}
L_f^2 \phi_2 &= -\mu \left[\omega_m (\psi_{r\alpha} i_{s\alpha} + \psi_{r\beta} i_{s\beta}) + \beta \omega_m (\psi_{r\alpha}^2 + \psi_{r\beta}^2) \right. \\
&\quad \left. + (\gamma + \alpha) (\psi_{r\alpha} i_{s\beta} - \psi_{r\beta} i_{s\alpha}) \right]
\end{aligned} \tag{4.14}$$

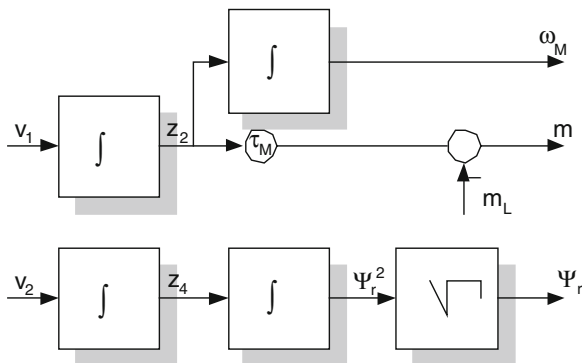
The resulting system is described by the equations:

$$\begin{aligned}
\dot{z}_1 &= z_2 \\
\dot{z}_2 &= v_1 \\
\dot{z}_3 &= z_4 \\
\dot{z}_4 &= v_2
\end{aligned} \tag{4.15}$$

So, the block diagram of the linearized system is shown in the Fig. 3 Control signals can be calculated by the following formulas:

$$v_1 = k_{11}(z_1 - z_{1ref}) - k_{12}z_2 \tag{4.16}$$

Fig. 3 Block diagram of induction motor with control signals v_1, v_2 (feedback linearization)



$$v_2 = k_{21}(z_3 - z_{3ref}) - k_{22}z_4 \tag{4.17}$$

where coefficients $k_{11}, k_{12}, k_{21}, k_{22}$ are chosen to determinate closed loop system dynamic.

Control algorithm consists of two steps (Fig. 4):

- calculations v_1, v_2 according to Eq. (4.16) and (4.17),
- calculations $u_{s\alpha}, u_{s\beta}$ according to Eq. (4.10).

Application of the feedback linearization method gives us a possibility to get very good behaviour in steady and dynamical states. The main features and advantages of the presented control are:

- with control variables v_1, v_2 the FLC guarantee the exactly decoupling of the motor speed and rotor flux control in both dynamic and steady states.
- the FLC is implemented in a state feedback fashion and needs more complex signal processing (full information about motor state variables and load torque is required).

4.3 Feedback Linearization with Sliding Mode

In many publications the SMC is applied to vector controlled IM [5–9]. In this section application of the sliding mode technique to the resulting linear system obtained by feedback linearization is described. The robustness and the discontinuous nature of Variable Structure Control permits to use this control technique to the PWM fed induction motor drives, what is the greatest advantage in this control area.

In SLM [12] the system structure is switched when the system state crosses the predetermined discontinuity line, so that the plant state slides along the reference trajectory. This type of control was described in Sect. 3. The design of SMC requires a suitable control law. The simplest way to solve this problem is to use

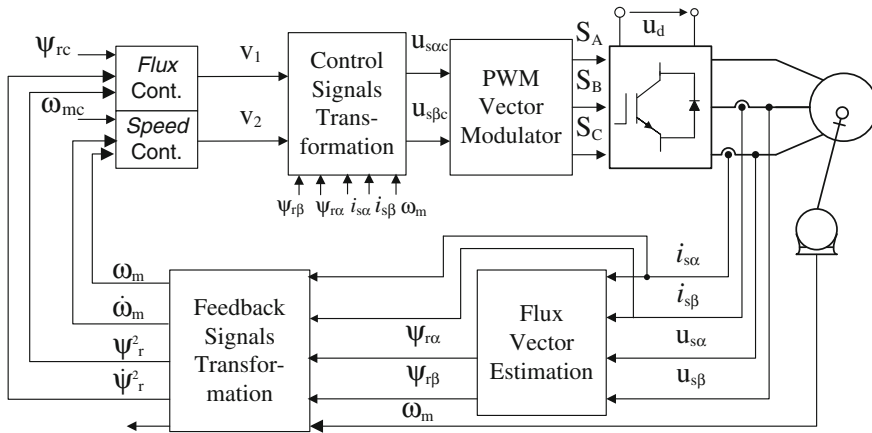


Fig. 4 Block diagram of feedback linearized control of two level three phase voltage source inverter fed induction motor

bang–bang controller. In this case the absolute value of the control command v is constant and the sign is given by the sign of a commutation function s as follows:

$$v = v_{\max} \operatorname{sgn}(s) \tag{4.18}$$

The controller gain v_{\max} can be evaluated based on the existing condition of sliding mode Eq. 3.5:

In the case of linearized motor, there are two error signals:

$$e_1 = z_{1\text{ref}} - z_1 \tag{4.19a}$$

$$e_2 = z_{3\text{ref}} - z_3 \tag{4.19b}$$

two sliding lines defined by:

$$\begin{aligned} s_1 &= e_1 + \tau_1 \dot{e}_1 \\ s_2 &= e_2 + \tau_2 \dot{e}_2 \end{aligned} \tag{4.20}$$

and two control signals:

$$v_1 = v_{1\max} \operatorname{sgn}(s_1) \tag{4.21a}$$

$$v_2 = v_{2\max} \operatorname{sgn}(s_2) \tag{4.21b}$$

Note that for each vector v_1, v_2 the conditions Eq. (3.5) must be fulfilled and this gives us possibilities to choose a vector pattern in PWM inverter.

In many papers [5–9, 27–30], where the nonlinear control of induction motor is described, the inverter model does not take into account. However, in the case of two-level three-phase inverter, it is easy to show that using SLM approach one can find the voltage vector, from the set of eight possible vectors, which assure the

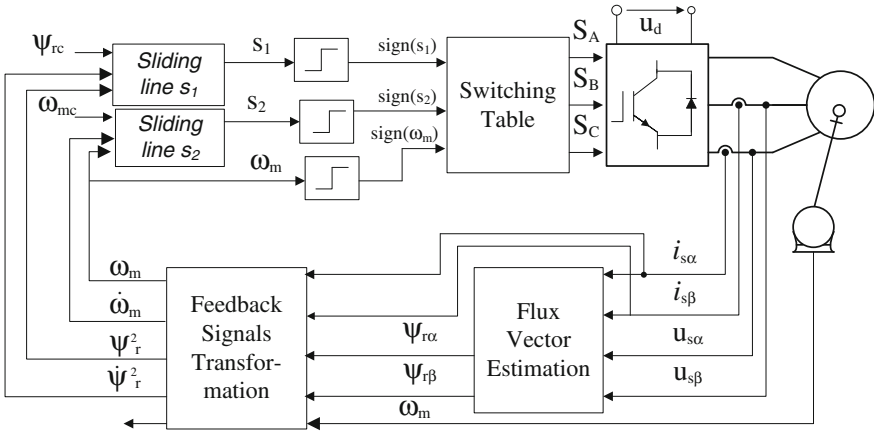


Fig. 5 The sliding mode control with switching table applied to the two-level three-phase inverter fed induction motor

Table 1 Switching table in classical sliding mode

Sector	$s_2 > 0, s_1 > 0$	$s_2 > 0, s_1 < 0$	$s_2 < 0, s_1 > 0$	$s_2 < 0, s_1 < 0$
1	2	3	6	5
2	3	4	1	6
3	4	5	2	1
4	5	6	3	2
5	6	1	4	3
6	1	2	5	4

Table 2 Definition of rotor flux sector

$-\pi/6 < \varphi_{\psi_r} < \pi/6$	1
$\pi/6 < \varphi_{\psi_r} < \pi/2$	2
$\pi/2 < \varphi_{\psi_r} < 5\pi/6$	3
$5\pi/6 < \varphi_{\psi_r} < 7\pi/6$	4
$7\pi/6 < \varphi_{\psi_r} < 3\pi/2$	5
$3\pi/2 < \varphi_{\psi_r} < 11\pi/6$	6

correct system behaviour (i.e. according to sliding mode conditions). It is obvious that this approach is easy to extend for multilevel inverters.

The simplest way of producing the inverter switch states is to check all possibilities and choose this one, which fulfil the sliding mode conditions. The algorithm could be performed in different ways using switching table Fig. 5 (algorithm 1) (Table 1).

where sector is defined by the angle of the rotor flux vector (Table 2):

Table 3 Switching table in modified sliding mode

Sect.	$\omega_m > 0, s_2 > 0,$ $s_1 > 0$	$\omega_m > 0, s_2 > 0,$ $s_1 < 0$	$\omega_m s_2 < 0$	$\omega_m < 0, s_2 < 0,$ $s_1 > 0$	$\omega_m < 0, s_2 < 0,$ $s_1 < 0$
1	2	3	0	6	5
2	3	4	0	1	6
3	4	5	0	2	1
4	5	6	0	3	2
5	6	1	0	4	3
6	1	2	0	5	4

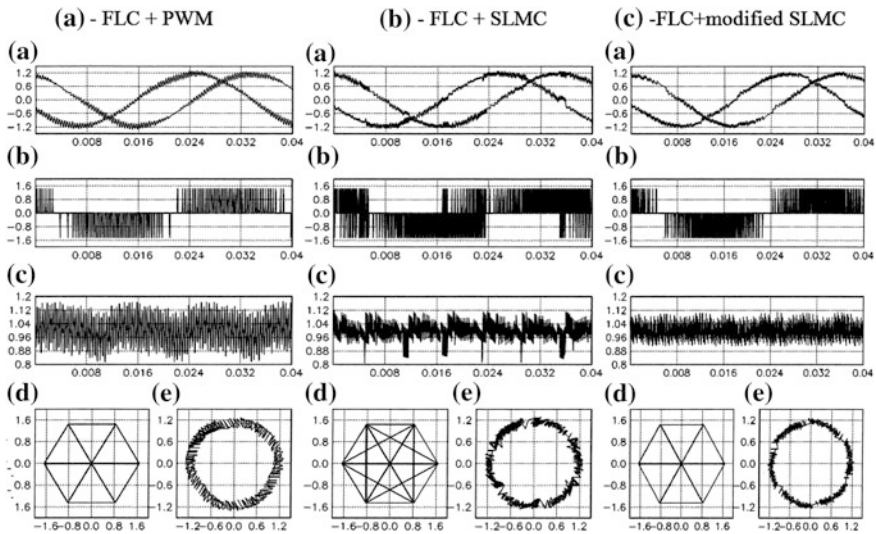


Fig. 6 Steady state operation of the induction motor controlled via feedback linearization with linear feedback and PWM (a) with SLMC (b) with modified SLMC (c): (a) stator currents $i_{s\alpha}, i_{s\beta}$, (b) stator voltage $u_{s\beta}$, (c) electromagnetic torque m , (d) stator voltage vector path $u_{s\beta}(u_{s\alpha})$, (e) stator current vector path $i_{s\beta}(i_{s\alpha})$

The algorithm could be modified in such a way, that in some situations we can choose zero vector instead of active vectors. In this case the sign of mechanical speed is taken to account, and the switching table is (algorithm 2) (Table 3):

This approach is correct in steady state, but not correct in transients, because the SMC condition is not fulfilled in every time instance. In transient state another modification could be used. Inside the ε -neighborhood the algorithm with modification will be used and outside this region the algorithm which strictly fulfilled the sliding mode conditions will be applied. (algorithm 3). The simulations of these algorithms are performed. The oscillograms obtained for FLC with sinusoidal PWM and with linear speed and rotor flux controllers as well as for FLC with sliding mode (algorithm 1) are shown in Fig. 6a, b. These figures show the

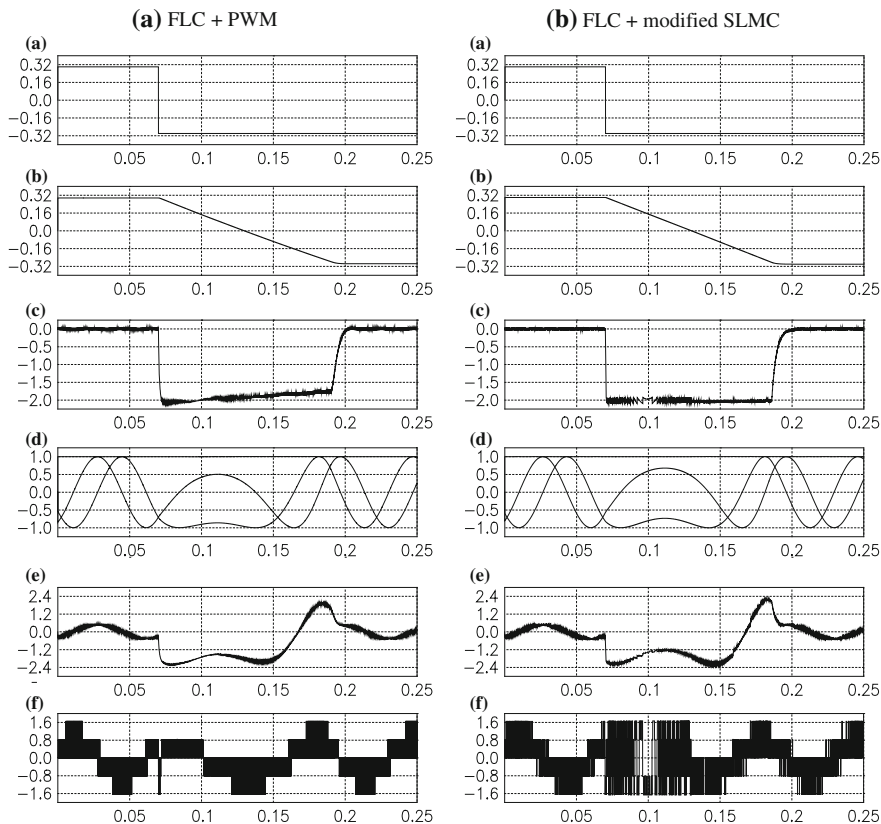


Fig. 7 Simulation results for change of the reference speed with induction motor controlled via feedback linearization with linear feedback and PWM (a) and with the modified SLMC (b): (a) reference speed ω_{mref} , (b) actual speed ω_m , (c) electromagnetic torque m , (d) rotor flux components and absolute value (Ψ_{rz} , $\Psi_{r\beta}$, Ψ_r), (e) stator current component $i_{s\alpha}$, (f) stator voltage component $u_{s\alpha}$

steady state behaviour of the above systems. As can be seen from Fig. 6b that it exists torque stress in some time instances. To guarantee better performance one can apply algorithm 2 presented in the previous section. In Fig. 6c the simulation results obtained for SMC with modification are shown. In Fig. 7 the response to speed reference change is presented. The simulated oscillograms obtained for FLC with sinusoidal PWM and with linear speed and rotor flux controllers as well as for FLC with modified sliding mode (algorithm 3) are shown. These oscillograms show the dynamic behaviour of the above systems, which are similar to each other.

4.4 Sliding Mode Observers

4.4.1 Application of Sliding Mode Observers

The description of sliding mode is presented in [Chap. 3](#). The sliding mode condition should be fulfilled, which imply the convergence to the prescribed surface. The main advantage of SM is the robustness of the system.

Sliding mode could be applied to observers in which the discontinues terms are used. In this section the Sliding Mode Observers (SMO) used for induction motor are applied. Recently many papers devoted to this topic were written [31–37]. In this work two different observers are presented, the parallel and serial SMO.

The parallel Sliding Mode Observer of rotor flux we can calculate using following formulas:

$$\begin{aligned}
 \frac{d\hat{\psi}_{rx}}{dt} &= -\alpha\hat{\psi}_{rx} - \omega_m\hat{\psi}_{r\beta} + \alpha x_M i_{sx} + kV_\alpha \\
 \frac{d\hat{\psi}_{r\beta}}{dt} &= -\alpha\hat{\psi}_{r\beta} + \omega_m\hat{\psi}_{rx} + \alpha x_M i_{s\beta} + kV_\beta \\
 \frac{d\hat{i}_{sx}}{dt} &= \alpha\beta\hat{\psi}_{rx} + \beta\omega_m\hat{\psi}_{r\beta} - \gamma\hat{i}_{sx} + \frac{1}{\sigma x_s} u_\alpha + V_\alpha \\
 \frac{d\hat{i}_{s\beta}}{dt} &= \alpha\beta\hat{\psi}_{r\beta} - \beta\omega_m\hat{\psi}_{rx} - \gamma\hat{i}_{s\beta} + \frac{1}{\sigma x_s} u_\beta + V_\beta
 \end{aligned} \tag{4.22}$$

where $\hat{\psi}_{rx}$, $\hat{\psi}_{r\beta}$, \hat{i}_{sx} , $\hat{i}_{s\beta}$ are estimated values of the rotor flux and stator currents, k is a positive convergence rate coefficient and V_α , V_β are discontinues functions of the current errors:

$$\begin{aligned}
 V_\alpha &= -V_0 \text{sign}(\bar{i}_{sx}) = -V_0 \text{sign}(\hat{i}_{sx} - i_{sx}) \\
 V_\beta &= -V_0 \text{sign}(\bar{i}_{s\beta}) = -V_0 \text{sign}(\hat{i}_{s\beta} - i_{s\beta})
 \end{aligned} \tag{4.23}$$

and $V_0 > 0$.

The scheme of this observer is presented in [Fig. 8](#).

The serial SMO is based on current observer which is calculated by following formula:

$$\begin{bmatrix} \hat{i}_{sx} \\ \hat{i}_{s\beta} \end{bmatrix} = \frac{x_M}{\sigma x_s x_r} \begin{bmatrix} \lambda_{rx} \\ \lambda_{r\beta} \end{bmatrix} - \frac{r_s}{\sigma x_s} \begin{bmatrix} \hat{i}_{sx} \\ \hat{i}_{s\beta} \end{bmatrix} + \frac{1}{\sigma x_s} \begin{bmatrix} u_{sx} \\ u_{s\beta} \end{bmatrix} \tag{4.24}$$

and in this case the flux observer is

$$\begin{bmatrix} \hat{\psi}_{rx} \\ \hat{\psi}_{r\beta} \end{bmatrix} = - \begin{bmatrix} \lambda_{rx} \\ \lambda_{r\beta} \end{bmatrix} \tag{4.25}$$

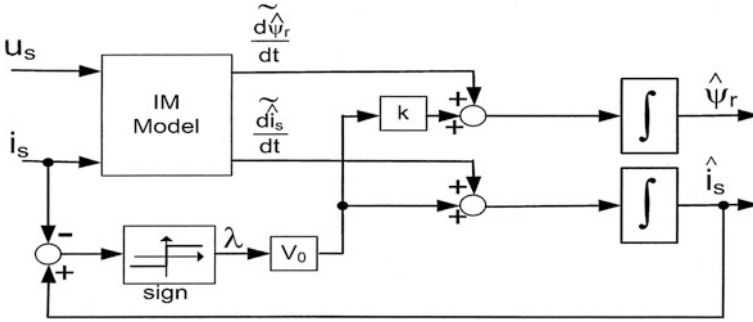


Fig. 8 Parallel sliding mode flux observer

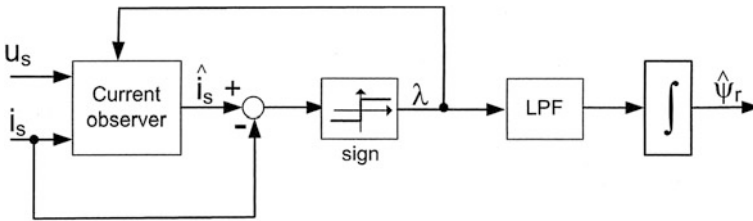


Fig. 9 Serial sliding mode flux observer

$$\begin{aligned} \lambda_{rx} &= -V_0 \text{sign}(\bar{i}_{sx}) = -V_0 \text{sign}(\hat{i}_{sx} - i_{sx}) \\ \lambda_{r\beta} &= -V_0 \text{sign}(\bar{i}_{s\beta}) = -V_0 \text{sign}(\hat{i}_{s\beta} - i_{s\beta}) \end{aligned} \tag{4.26}$$

and $V_0 > 0$.

The scheme of this observer is presented in Fig. 9.

Knowing the estimated current, estimated rotor flux, and λ function values, we can express estimated rotor speed as [33]

$$\hat{\omega}_m = \frac{\hat{\psi}_{r\beta} \cdot \lambda_{rx} - \hat{\psi}_{rx} \cdot \lambda_{r\beta} - \alpha x_M (\hat{i}_{s\beta} \hat{\psi}_{rx} - \hat{i}_{sx} \hat{\psi}_{r\beta})}{\hat{\psi}_{rx}^2 + \hat{\psi}_{r\beta}^2} \tag{4.27}$$

4.4.2 SMO Results

The simulated and experimental oscillograms were obtained for FLC with vector PWM and with Sliding Mode Flux Observers (Fig. 10).

Simulation of two described vector flux estimators is shown in Figs. 11 and 12 (steady state operation). and Figs. 13 and 14 (dynamic behaviour). It is obvious,

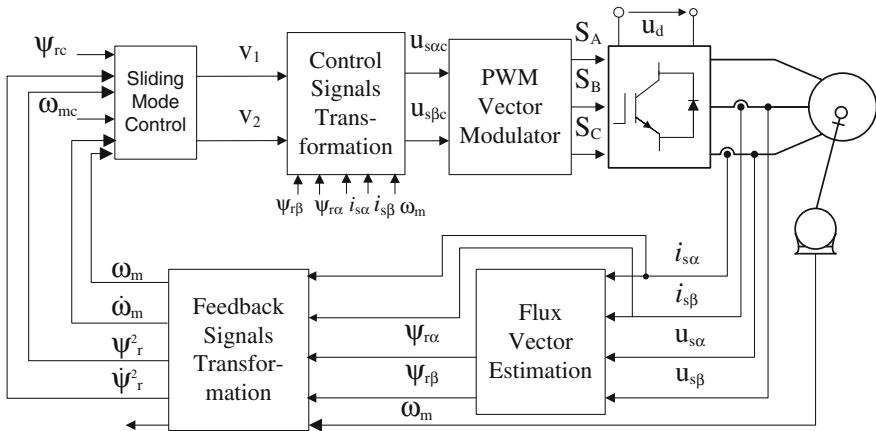


Fig. 10 Control of induction motor via feedback linearization

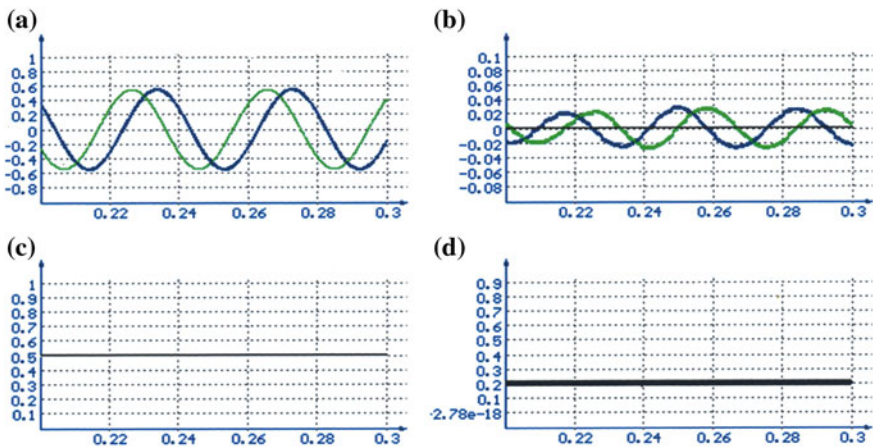


Fig. 11 Simulation results for steady state operation ($\omega_m = 0.5i_{mL} = 0.2$) for parallel SMO **a** current and voltage, **b** speed and speed command, **c** flux estimation errors, **d** electromagnetic torque

that the parallel flux estimator is better compare to serial one, therefore this estimation was selected to experiment.

These oscillograms confirm the good dynamic behaviour of the system, and the correct operation of Sliding Mode Flux Observers. Additionally using a serial SM observer approach there is possible to obtain mechanical speed. It should be noted, that to calculate rotor flux in feedback linearization control the parallel SM observer is used.

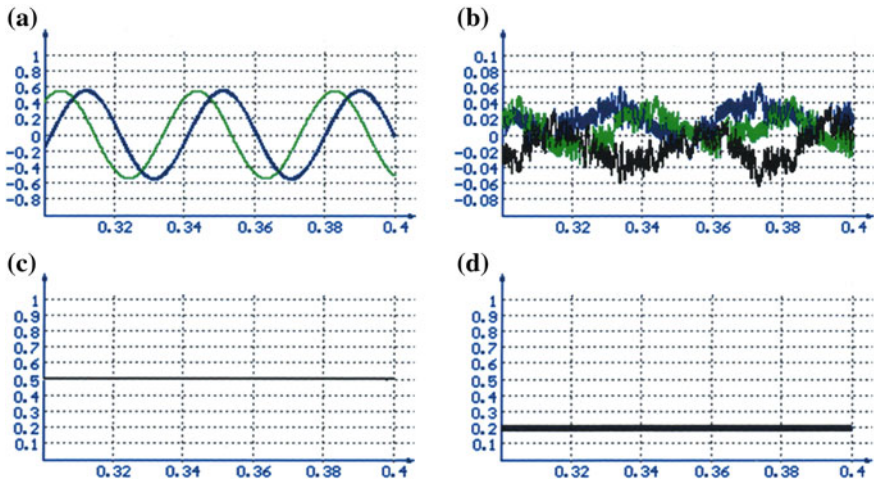


Fig. 12 Simulation results for steady state operation ($\omega_m = 0.5i$ $m_L = 0.2$) for serial SMO **a** current and voltage, **b** speed and speed command, **c** flux estimation errors, **d** electromagnetic torque

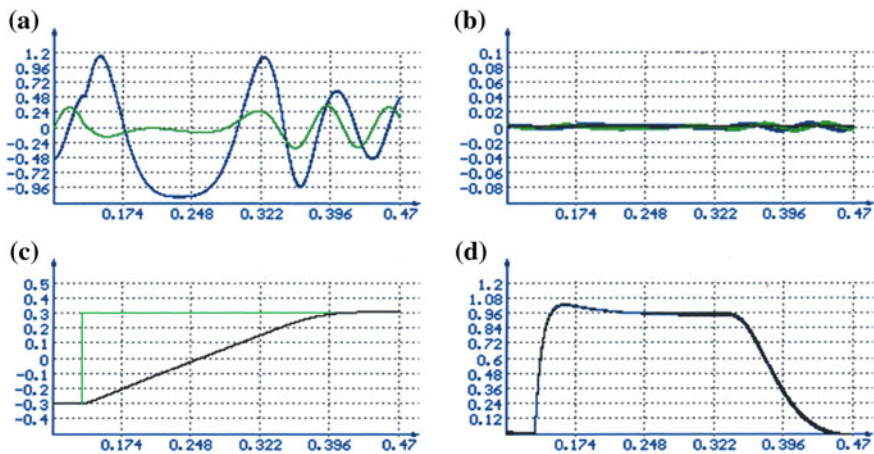


Fig. 13 Dynamic behavior. The speed reversal $\omega_m = -0.3, 0.3$ for parallel SMO. **a** Current and voltage, **b** speed and speed command, **c** flux estimation errors, **d** electromagnetic torque

Figure 15 shows the correct operation of Sliding Mode Speed Observer in simulation, in both dynamic and steady state. We can note, that the response of the system is proper, and the speed sensorless system gives good results.

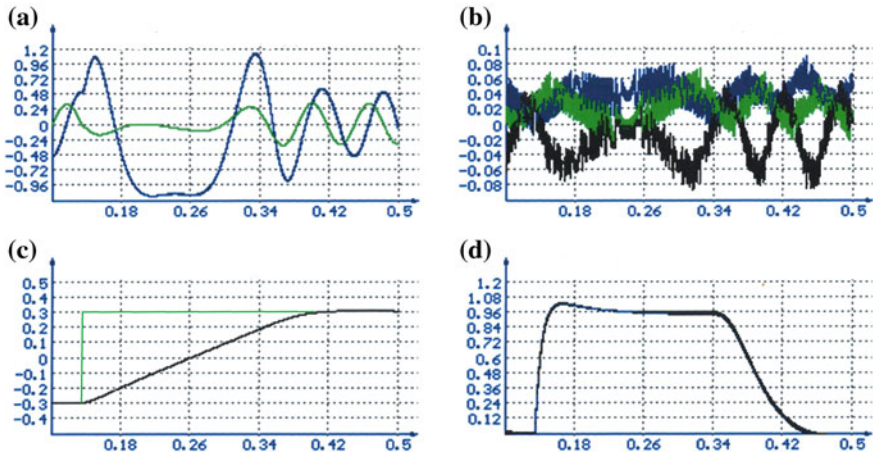


Fig. 14 Dynamic behavior. The speed reversal $\omega_m = -0.3, 0.3$ for serial SMO. **a** Current and voltage, **b** speed and speed command, **c** flux estimation errors, **d** electromagnetic torque

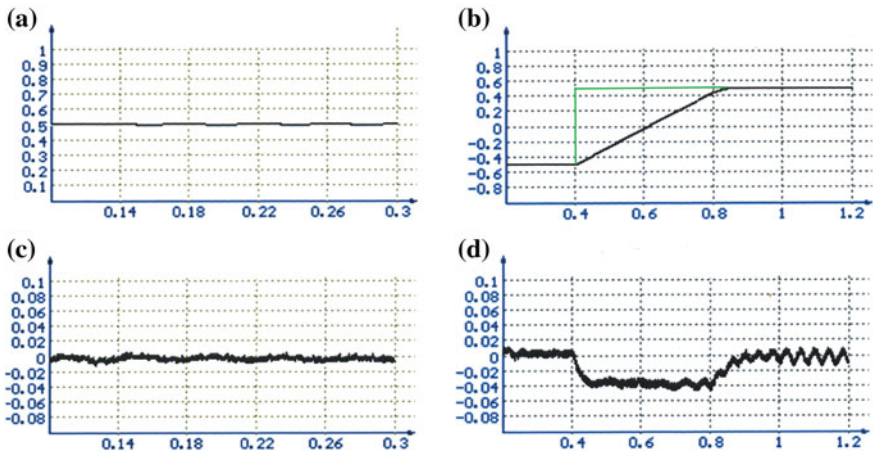


Fig. 15 Simulation results for steady-state (*left side*) and speed reversal (*right side*). **a** Command speed and mechanical speed, **b** speed estimation error

5 Conclusions

In this chapter several applications of feedback linearization (FLC) and sliding mode control (SMC) and observers for inverter fed induction motor is presented. Features and advantages described algorithms can be summarized as follows.

- The FLC guarantees the exactly decoupling of the motor speed and rotor flux control. Thus this control method gives a possibility to get very good behaviour in both dynamic and steady states.
- Since in the FLC chosen variables (ω_m, ψ_r^2) and its derivative ($\dot{\omega}_m, \dot{\psi}_r^2$) are used as new coordinates this approach will be well suited for SMC speed and position controllers. The SMC is robust. Therefore, the combination of these two algorithms allow achieving the advantages of both: decoupled, robust system.
- The SMC approach assures direct control of inverter legs and allows using a simple table instead of performing complicated PWM calculation.
- The good behaviour of rotor flux and speed Sliding Mode Observers (SMO) is the important feature of the system and allows achieving very good results.

Thus the SMC and FLC, both together and separately, offer an interesting perspective in future research. These approaches are also a good alternative to other solutions, such as predictive and adaptive systems, and soft computing. SMOs are frequently used in drive systems. Sliding Mode Controllers work well in switching systems, and in systems which parameters are variable or not accurately set. The FLC approach is applied when we are dealing with non-linear systems, such as for example different types of drive systems. Therefore, we can say that these approaches are very useful in a variety of applications and, in particular, in the drive systems and power electronics.

References

1. K. Hasse, Drehzahlverfahren für schnelle Umkehrantriebe mit stromrichtergespeisten Asynchron—Kurzschlusslaufermotoren. *Regelungstechnik* **20**, 60–66 (1972)
2. F. Blaschke, Das Verfahren der Feldorientierung zur Regelung der Asynchronmaschine. *Siemens Forschungs-und Entwicklungsber* **1**(1), 184–193 (1972)
3. A. Isidori, *Nonlinear Control Systems, Communications and Control Engineering*, 2nd edn. (Springer Verlag, Berlin, 1989)
4. H. Nijmeijer, A. van der Schaft, *Nonlinear Dynamical Control Systems* (Springer Verlag, New York, 1990)
5. Z. Krzemiński, Multi-scalar models of an induction motor for control system synthesis. *Scientia Electrica* **33**(3), 9–22 (1987)
6. M. Bodson, J. Chiasson, R. Novotnak, High performance induction motor control via input-output linearization, in *Proceedings of the IEEE Control Systems*, pp. 25–33 (1994)
7. J. Chiasson, A. Chaudhari, M. Bodson, Nonlinear controllers for the induction motor, in *Proceedings of the IFAC Nonlinear Control System Design Symposium*, Bordeaux, France, pp. 150–155 (1992)
8. R. Marino, S. Peresada, P. Valigi, Adaptive partial feedback linearization of induction motors, in *Proceedings of the 29th Conference on Decision and Control*, Honolulu, Hawaii, pp. 3313–3318 (1990)
9. R. Marino, P. Valigi, Nonlinear control of induction motors: a simulation study, in *Proceedings of the European Control Conference*, Grenoble, France, pp. 1057–1062 (1991)
10. S.V. Emelyanov, *Variable Structure Control Systems* (Nauka, Moskwa, 1967)

11. V.I. Utkin, Variable structure systems with sliding modes: a survey. *IEEE Trans. Autom. Control* **22**(2), 212–222 (1977)
12. V.I. Utkin, *Sliding Modes and their Applications in Variable Structure Systems* (Mir, Moscow, 1981)
13. D.L. Sobczuk, Nonlinear control for induction motor, in *Proceedings of the PEMC '94*, pp. 684–689 (1994)
14. M.P. Kazmierkowski, D.L. Sobczuk, High performance induction motor control via feedback linearization, in *Proceedings of the IEEE-ISIE'95*, pp. 633–638 (1995)
15. M.P. Kazmierkowski, D.L. Sobczuk, Sliding mode feedback linearized control of PWM inverter fed induction motor, in *Proceedings of the IEEE IECON Conference*, pp. 244–249 (1996)
16. M.P. Kazmierkowski, H. Tunia, *Automatic Control of Converter-Fed Drives*, (Elsevier, Amsterdam, 1994)
17. D.L. Sobczuk, M. Malinowski, Feedback linearization control of inverter fed induction motor—with sliding mode speed and flux observers, in *Proceedings of the IECON 06*, Paris, France, pp. 1299–1304 (2006)
18. Y. Itkis, *Control Systems with Variable Structure* (Wiley, New York, 1976)
19. S.N. Singh, Asymptotically decoupled discontinuous control of systems and nonlinear aircraft maneuver. *IEEE Trans. Aeronaut. Electron. Syst.* **25**(3), 380–391 (1989)
20. H. Hikita, Servomechanisms based on sliding mode control. *Int. J. Control* **48**(2), 435–441 (1988)
21. J.J. Slotine, C. Canudas de Wit, Sliding observers for robot manipulators. *Automatica* **27**(5), 859–864 (1991)
22. J.J. Slotine, S.S. Sastry, Tracking control of nonlinear systems using sliding surfaces with application to robot manipulators. *Int. J. Control* **38**(2), 465–492 (1983)
23. A. Sabanovic, D.B. Izosimov, Applications of sliding modes to induction motor control. *IEEE Trans. Ind. Appl.* **17**(1), 41–49 (1981)
24. A. Levant, L.V. Levantovsky, Sliding order and sliding accuracy in sliding mode control. *Int. J. Control* **58**(6), 1247–1263 (1993)
25. L.V. Levantovsky, *Second Order Sliding Algorithms: Their Realization, Dynamics of Heterogenous Systems* (Institute for System Studies, Moscow, 1985), pp. 32–43
26. G. Bartolini, A. Ferrara, E. Usai, Applications of a sub-optimal discontinuous control algorithm for uncertain second order systems, *Int. J. Robust Nonlinear Control* **7**(4), 299–310 (1997)
27. M. Rashed, P.F.A. MacConnell, A.F. Stronach, Nonlinear adaptive state-feedback speed control of a voltage-fed induction motor with varying parameters. *IEEE Trans. Ind. Appl.* **42**(3), 723–732 (2006)
28. T. Orłowska-Kowalska, M. Dybkowski, K. Szabat, Adaptive sliding-mode neuro-fuzzy control of the two-mass induction motor drive without mechanical sensors. *IEEE Trans. Ind. Electron.* **57**(2), 553–564 (2010)
29. M. Rashed, K.B. Goh, M.W. Dunnigan, P.F.A. MacConnell, A.F. Stronach, B.W. Williams, Sensorless second-order sliding-mode speed control of a voltage-fed induction-motor drive using nonlinear state feedback, *IEE Proc. Electr. Power Appl.* **152**(5), 1127–1136 (2005)
30. F. F. M. El-Sousy, Adaptive dynamic sliding-mode control system using recurrent RBFN for high-performance induction motor servo drive. *IEEE Trans. Ind. Inf.* **9**(4), 1922–1936 (2013)
31. C. Lascu, I. Boldea, F. Blaabjerg, A class of speed-sensorless sliding-mode observers for high-performance induction motor drives. *IEEE Trans. Ind. Electron.* **56**(9), 3394–3403 (2009)
32. S. Rao, M. Buss, V. Utkin, Simultaneous state and parameter estimation in induction motors using first- and second-order sliding modes. *IEEE Trans. Ind. Electron.* **56**(9), 3369–3376 (2009)
33. Z. Yongchang, Z. Zhengming, L. Ting, Y. Liqiang, X. Wei, Z. Jianguo, A comparative study of Luenberger observer, sliding mode observer and extended Kalman filter for sensorless

- vector control of induction motor drives, in *Proceedings of the ECCE IEEE*, pp. 2466–2473 (2009)
34. M. Comanescu, An induction-motor speed estimator based on integral sliding-mode current control. *IEEE Trans. Industr. Electron.* **56**(9), 3414–3423 (2009)
 35. H. Rehman, A. Derdiyok, M.K. Guven, L. Xu, A new current model flux observer for wide speed sensorless control of an Induction Machine. *IEEE Trans. Power Electron.* **17**(6), 1041–1048 (2002)
 36. S.M. Gadoue, D. Giaouris, J.W. Finch, MRAS sensorless vector control of an induction motor using new sliding-mode and fuzzy-logic adaptation mechanisms. *IEEE Trans. Energy Convers.* **25**(2), 394–402 (2010)
 37. X. Zhang, Sensorless induction motor drive using indirect vector controller and sliding mode observer for electric vehicle. *IEEE Trans. Veh. Technol.* **62**(7), 3010–3018 (2013)

About the Editors



Teresa Orłowska-Kowalska (M'93–SM'05) is a full professor and director of the Institute of Electrical Machines Drives and Measurements, at Wrocław University of Technology, Poland. She has co-authored close to 400 journal papers conference proceedings, textbooks, and chapters in monographs. Her research interests include the application of modern control methods and artificial intelligence to electrical drives, especially sensorless. Dr. Orłowska-Kowalska is a member of Electrical Engineering Committee of the Polish Academy of Science (since 1996), and member of the Council of 4th Division Provosts of PAS. Since 2004, she has been an Associate Editor for the IEEE Transactions on Industrial Electronics.



Frede Blaabjerg (S'86–M'88–SM'97–F'03) is a full professor of power electronics and drives at Aalborg University, Denmark. His current research interests include power electronics and its applications in wind turbines, PV systems and adjustable speed drives. He has received several research and papers awards, in Denmark and abroad. He was an Editor-in-Chief of the IEEE Transactions on Power Electronics (2006–2012) and a Distinguished Lecturer for the IEEE Power Electronics Society and Industry Applications Society. Recently he received the IEEE William E. Newell Power Electronics Award 2014.



José Rodríguez (M'81–SM'94) is a full professor of the Department of Electronic Engineering and Rector of the Universidad Técnica Federico Santa María, Valparaiso, Chile. He has co-authored more than 350 journals and conference papers. Professor Rodríguez is Associate editor of the *IEEE Transactions on Power Electronics* and *IEEE Transactions on Industrial Electronics* since 2002. He has received several papers awards. Dr. Rodríguez is a member of the Chilean Academy of Engineering and Fellow of the IEEE.